Copyright is owned by the Author of this thesis. Permission is given for a copy to be used by an individual for the purpose of research and private study only. The thesis may not be reproduced elsewhere without the permission of the Author.

Understanding the volcanic response to edifice collapse. A case study of the Poto and Paetahi Formations at Mt. Taranaki.

Shannen Alice Mills

A thesis submitted in partial fulfilment of a
Philosophiae Doctor degree in Earth Science

Supervisors:
Prof. Jonathan Procter
Dr Anke. V. Zernack
Dr Stuart Mead
Prof. Georg Zellmer
A/Prof. Gabor Kereszturi
Prof. Shane Cronin
Dr Ian Schipper

Volcanic Risk Solutions
School of Agriculture and Environment
Massey University, New Zealand

2024

Abstract

Stratovolcanoes are unstable and prone to collapse. Depressurisation from collapse events can possibly impact the subvolcanic plumbing system. This may cause a change in the eruptive size, style and frequency of eruptive activity following a collapse.

Mt. Taranaki in New Zealand provides a unique opportunity to investigate the influence of edifice collapse on eruptive behaviour. The extensive ring plain around Mt. Taranaki is dominated by debris-avalanche deposits (DAD) recording the last > 200 kyr of eruptive history including at least fourteen events. The medial ring plain provides a stratigraphic record of the last 30 ka of eruptive history comprising four DADs including two of the largest to have occurred in Mt. Taranaki's history the 27.3 ka (5.85 km^3) Ngaere and 24.8 ka (> 7.5 km^3) Pungarehu DAD. The (27.3-23.1 ka) Poto and Paetahi Formations deposited across the eastern and southeastern sector of the ring plain are used to investigate the effects of depressurisation on the magmatic system.

A detailed stratigraphic analysis of medial to distal exposures of the Poto and Paetahi Formations was undertaken across the eastern and southeastern sectors of the Taranaki ring plain. Changes in lithosedimentological characteristics were used to identify single and multiphase eruptive events. Isopach and Isopleth mapping of the deposits show a period of increased explosive activity within Mt. Taranaki's history. The deposits were analysed for grain size distributions, componentry, juvenile and density, as well as X-ray tomography to define vesicle and crystal number densities and volumes. Geochemical analysis on whole rock, glass, feldspar, and pyroxene crystals was conducted to create a detailed account of the changes within the Poto and Paetahi Formations and infer the response to edifice collapse. This study found that the relative abundance of lithics informed processes of conduit stability throughout the eruptive period, with increase abundance reflecting conduit excavation. Components were divided into juveniles, lithics and free crystals with subcategories established for each lithology class. Micro-Computed X-ray tomography indicated the high percentage of small bubbles present within the juvenile deposits.

Twenty-eight subplinian eruptions produced at least ~3 km^3 of tephra across the eastern and southeastern Taranaki ring plain within a ~4 kyr period, producing single and multiphase eruptive events with eruption column heights between 10-20 km and individual deposit volumes of 0.01-0.26 km^3. Variations in the relative abundance of lithic clasts and density analysis of juvenile deposits reflect changing conduit conditions throughout the Poto and Paetahi Formations. Connected porosities and the abundance of juvenile clasts increased during stable conduit conditions due to the formation of gas flow pathways. A decrease in connected porosities and increase in the abundance of lithics indicated conduit excavation through unstable/ widening events, disrupting the formation of gas flow networks.

Large populations of small bubbles (2.75 x 10^{-7} mm^{-3}) are indicated through high vesicle number densities (VND) (9.03 x 10^{15} – 1.74 x 10^{16} cm^{-3}), reflecting the domination of late-stage bubble nucleation within the upper conduit by fast ascending magmas occurring throughout the Poto and Paetahi Formations. Vesicle size populations reflect the onset location of bubble nucleation within the system. Changes in vesicle size distributions and oscillatory crystal rims throughout the sequence reflect cycles of magma recharge and storage occurring below Mt. Taranaki. Single stage nucleation events reflect the rapid ascent of magma through the system, while bubble coalescence indicates some magma stalled within the mid-to-upper crustal system. Whole rock compositions from these tephra vary between 3.03 – 5.19 wt.% MgO and reflect an evolution in magmatic composition overtime. Depressurisation from the eastern Ngaere collapse resulted in an increase in MgO wt.% (from 4.06 wt.% to 4.55 wt.%), decrease in VND (from 1.53 x 10^{16} to 9.76 x 10^{15} cm^{-3}), but uniform vesicle volumes (VV) (from 4.9 to 4.8 %). This indicates a change in magmatic overpressure and deactivation of the mid-to-upper crustal system. The younger (23.1 – 24.1 Ka) Paetahi Formation is more evolved than the Poto Formation (27.3-25 Ka), reflecting the re-activation of the mid-to-upper crustal system throughout the regrowth period. Continued evolution in magmatic composition (from 3.62 wt.% to 3.14 wt.% MgO), increase in VND (from 1.15 x10^{16} to 1.29x10^{16} cm^{-3}) and decrease in VV (from 7.1 to 3.3%) following the western Pungarehu collapse (~2,500 years after the Ngaere) reflects no depressurisation on the shallow volcanic system. The observed differences in response to collapse events is due to the relative height of the edifice and location of the conduit/ vent.

The sedimentological, textural, and geochemical analysis of the Poto and Paetahi tephra formations demonstrate the changes to eruptive activity following collapse events. However, these results highlight the relationship between edifice height, lithostatic pressure and the magmatic system. The Ngaere collapse depressurized a fully grown edifice (~ 2500 m), shifting the vent location within the scar and destabilized the remanent cone. The relatively short time between collapse events (~2,500 years) saw the western remanent cone collapse before Mt. Taranaki had fully regrown. This did not cause a significant change on the magmatic system below and allowed for the continued regrowth. This study highlights a need to understand the relationship between hazardous volcanic phenomena to generate more accurate hazard scenarios for stratovolcanoes which are prone to edifice collapse.

Acknowledgements

I would like to thank all of my supervisors for their support and guidance throughout my PhD.

To my main supervisor Professor Jonathan Procter (Massey University), thank you for reaching out and suggesting such an amazing research project and for convincing me to move to Palmerston North. I am grateful for all of your support and guidance throughout the years, for your continued belief in me, and for your help in receiving a Massey Doctoral Scholarship as well as other financial assistance throughout the years.

I would also like to thank my co-supervisors Dr Anke Zernack (Massey University) for taking me in the field and showing me around Taranaki. I appreciated all the in-depth discussions and detailed feedback on written manuscripts. Dr Stuart Mead (Massey University) for his continued support and discussions around all aspects of the PhD and PhD life. I am grateful for Professor Georg Zellmer (Massey University) for his ability to explain all things geochemistry. I would also like to thank Professor Shane Cronin (The University of Auckland), Associate Professor Gabor Kereszturi (Massey university), and Dr Ian Schipper (Victoria University of Wellington) for their helpful and interesting discussions over the past four years.

A massive thank you to the farmers of Taranaki especially Brain Bailey and Phil Meerman who allowed me access onto their land.

My geochemical analysis would not have been possible without the help of David Adams (The University of Auckland); Andres Arcila-River (The University of Auckland), Nessa D'Mello (Massey University) and Daniel Coulthard Jr (Massey University).

I am greatly appreciative of the technicians Andrew Stevenson, Benedicta Arhatari, Darren Thompson, and Anton Maksimenko at the Australian Synchrotron for all of their support in create a project and running our samples. A big thank you to the Australian Synchrotron for the grants to be able to conduct my research using the IMBL and MCT beamlines. I would also like to thank the New Zealand Synchrotron Group for providing travel funding to attend the experiments in person.

I would like to thank Anja Moebis for your support and help in the lab, along with James Ardo and Joesph Fleeming for your assistance with samples.

Thanks to Kate Arentsen, Judith Stepper, and Tara Penketh for all of their help with logistics, support, and organisation. Throughout this project many people have contributed help and knowledge, and their support has been greatly appreciated, I would especially like to thank Matthew Irwin for his continued support with all thing's computers and Mark Bebbington for his statistical modelling and discussions.

Funding for this research was provided by the Transitioning Taranaki to a volcanic future MBIE endeavour project. I am furthermore grateful for receiving the Eileen Fair Doctoral Scholarship as well as a Massey University Doctoral Scholarship and a Massey University Doctoral Conference Grant.

To my examiners Gert Lube, Ben Kennedy and Natalia Pardo thank you for your in-depth comments and discussion around my thesis.

To my fellow PhD comrades in Volcanic Risk Solutions, thank you for your support, friendship, and wisdom. To Sarah, Daniel, Lucas, Maia, Anna, and Brain thank you for your friendship over the years, your continued encouragement got me through the last few months. To Alex Davidson and Brooke Waterson thank you for everything over the years you have both been such a pillar of support since undergrad and I could not have achieved this without you.

To my family, thank you for all of your encouragement and support throughout my life, you have allowed me to achieve my dreams.

And lastly, but certainly not least to my husband Jeremy Cole, thank you for your unconditional love and support. Without you I would not have been able to have achieved this.

Table of Contents

Abstract i

Acknowledgements iii

Table of Figures xi

Table of Tables xiv

Abbreviations xv

1 Introduction 1

1.1 Research Problem and motivation 1

1.2 Literature review 6

1.2.1 Subplinian and plinian eruptions 6

1.2.2 Eruptive deposits and characteristics 9

1.2.3 Buried paleosols. 10

1.2.4 Preservation of deposits 10

1.3 Magma fragmentation and bubble nucleation 10

1.3.1 Bubble nucleation studies on New Zealand volcanoes 13

1.4 Regional geologic setting of New Zealand 15

1.5 Taupo Volcanic Zone (TVZ) 16

1.6 Geology of the Taranaki Peninsula 18

1.7 Taranaki Volcanic Lineament (TVL) 21

1.8 Mt. Taranaki 22

1.8.1 Previous tephrastratigraphy of Mt. Taranaki 26

1.9 Petrology and geochemistry of Mt. Taranaki 33

1.9.1 Mineral assemblages 37

1.9.2 Previous geochemical models for Mt. Taranaki 38

1.10 Taranaki hazards 43

2 Methodology 49

2.1 Fieldwork and physical parameters 49

2.2 Laboratory 53

2.2.1 Grain size analysis 53
2.2.2 Componentry 54
2.2.3 Pumice density 55
2.3 Pyroclastic 3D analysis 56
2.4 Geochemistry 59
2.4.1 Electron microprobe analysis (EMPA) 59
2.4.2 X-ray fluorescence analysis (XRF) 62
2.4.3 Laser ablation inductively coupled plasma mass-spectrometry (ICP-MS) 62
2.5 Limitations of the data 62
2.5.1 Synchrotron Data 62
3 The stratigraphy and physical properties of explosive events from Mt. Taranaki, New Zealand pre- and post-edifice collapse. 64
3.1 Introduction 65
3.2 Geological Setting 66
3.3 Tephrochronology 67
3.4 Methodology 69
3.5 Results. 73
3.5.1 Revised stratigraphy of the Poto and Paetahi Formations 73
3.5.2 Physical properties of the Poto and Paetahi tephras. 89
3.5.3 Componentry 89
3.5.4 Eruptive conditions 93
3.6 Interpretations. 101
3.7 Discussion. 103
3.7.1 Eruption Parameters and uncertainties. 103
3.7.2 The influence of edifice collapse on eruptive behavior 106
3.7.3 Implications for future eruption scenarios and hazard modelling. 108
3.8 Conclusions. 109
4 Assessing the influence of edifice collapse on the shallow volcanic plumbing system of Mt. Taranaki through textural analysis of the subplinian Poto and Paetahi tephra formations. 110
4.1 Introduction 111

4.2 Geological history of Mt. Taranaki 114
4.3 Methodology 116
4.3.1 Sampling 116
4.3.2 Density 117
4.3.3 3D bubble analysis 117
4.3.4 2D Textural analysis 121
4.4 Results 122
4.4.1 Density data 122
4.4.2 Textural features 125
4.4.3 Pyroclast vesicularity and vesicle number density (VND) 128
4.4.4 Stages of nucleation 129
4.5 Interpretation 133
4.5.1 Vesicularity in relation to VND 133
4.5.2 Influence of conduit conditions on the eruptive products 133
4.5.3 Relationship to edifice collapse events 134
4.5.4 Bubble nucleation and growth 135
4.5.5 Vesicle size 136
4.6 Discussion 137
4.6.1 Subvolcanic plumbing system 137
4.6.2 Changes within the Poto and Paetahi Formations 140
4.6.3 Influence of the collapses on the shallow volcanic plumbing system 141
4.7 Conclusion 145
5 Investigating the influence of edifice collapse on the geochemical and mineralogical composition of magma in the subvolcanic plumbing system: A case study of the Poto and Paetahi tephra formations of Taranaki volcano, New Zealand. 146
5.1 Introduction 147
5.2 Geological setting of the Taranaki Peninsula 148
5.3 Mt. Taranaki Volcanic history 149
5.4 Methodology 150
5.4.1 Sampling 150

5.4.2 Electron Microprobe Analysis (EMPA) 150
5.4.3 X-Ray Fluorescence Analysis (XRF) 151
5.4.4 Inductively Coupled Plasma-Mass Spectrometer Analysis (ICP-MS) 151
5.5 Results 152
5.5.1 LOI Weathering of samples 152
5.5.2 Whole-Rock Geochemistry 154
5.5.3 Trace elements 160
5.5.4 Spider diagrams 162
5.5.5 Electron Microprobe glass point analysis 166
5.5.6 Thermobarometry/ Hygrometry 170
5.6 Discussion 173
5.6.1 Impacts of weathering on the samples 173
5.6.2 Compositional variation throughout the Poto and Paetahi Formations 174
5.6.3 Magma ascent and crystal processes 175
5.6.4 Melt characteristics and crystallization conditions 179
5.6.5 Influence of unloading on the volcanic system 180
5.7 Conclusions 184
6 Discussion 186
6.1 Introduction 186
6.2 Magma storage and supply below Mt. Taranaki 188
6.3 The relationship between stratovolcano collapse and eruptions 195
6.4 Eruption frequency and ashfall distribution 204
6.5 Implications for hazard analysis 208
7 Conclusion 210
7.1 Specific findings of this study 210
7.2 Conclusion 212
7.3 Future Work 214
References 216
Appendices 280

Appendix A: Stratigraphy 280
Appendix A1: Stratigraphic sections. 280
Appendix A2: Sample Locations. 286
Appendix A3: Exposure locations across the west/southwestern ring plain. 295
Appendix A4: Stratigraphic Fence Diagrams. 297
Appendix A5: Isopach Calculations. 299
Appendix A6: Isopach maps. Isopach map images for all of the twenty-eight Poto and Paetahi Formations. Road and Topographic data sourced from the LINZ Data Service licensed for reuse under CC by 4.0. 304
Appendix A7: Isopach graphs. 312
Appendix A8: Isopleth Calculations. 315
Appendix A9: Isopleth maps. Isopleth map images for all of the twenty-eight Poto and Paetahi Formations. Road and Topographic data sourced from the LINZ Data Service licensed for reuse under CC by 4.0 318
Appendix B: Grain Size distributions statistics. 326
Appendix B1: Grain size distribution of each sample from the reference locations in half phi. 326
Appendix B2: Grain size distribution statistics. 329
Appendix C: Componentry. 333
Appendix C1: Percentage measurements of the componentry in each unit from the Poto and Paetahi reference locations for -1.5 and 0.5 ϕ size fractions. 333
Appendix D: Density and vesicularity. 336
Appendix D1: Bulk density, and vesicularity measurements using pycnometry for pumices from -2 to -4 ϕ from the Poto and Paetahi Formations at the reference locations. 336
Appendix E: 3D X-ray Tomography. 345
Appendix E1: Vesicle size distribution graphs. 345
Appendix E2: Vesicle size distribution data for the Poto and Paetahi Formations. 348
Appendix E3: Crystal Size distribution graphs. 355
Appendix E4: Crystal size distribution data for the Poto and Paetahi Formations. 358
Appendix E5: Vesicle number densities. 365
Appendix E6: Crystal number densities. 368

Appendix E7: Vesicle Volume. 371
Appendix E8: Crystal volume. 375
Appendix F: Geochemical analysis. 379
Appendix F1: Major elements for whole rock analyses using XRF. 380
Appendix F2: Trace elements for whole rock analyses using ICP-MS 381
Appendix F3: Major element EMPA analyses of glass from epoxy plugs. 382
Appendix F4: Major element EMPA analysis of pyroxene crystals from epoxy plugs. 383
Appendix F5: Major element EMPA analyses of plagioclase crystals from epoxy plugs 385
Appendix G: DRC16 Contributions Form. 387

Table of Figures

Figure 1.1: Schematic of a typical plinian/subplinian eruption column. 8
Figure 1.2: Northern New Zealand's current tectonic setting showing the Taupo volcanic zone and Taranaki Volcano. 17
Figure 1.3: Geological map of the North Island of New Zealand 20
Figure 1.4: Geological map of the Quaternary ring plain succession of Mt. Taranaki 25
Figure 1.5: Schematic of the magma source model below Mt. Taranaki 34
Figure 1.6: Major element whole rock geochemical plots of volcanic products from throughout Mt. Taranaki's evolution. 36
Figure 1.7: Normal mid-ocean ridge basalts (N-MORB) and Chondrite normalized rare earth element patterns for eruptive products from Mt. Taranaki 37
Figure 1.8: Illustration of the early and mature magmatic system beneath Mt, Taranaki, ... 40
Figure 1.9: Schematic of the 3-stage model of high-K arc magma generation at Mt. Taranaki 41
Figure 1.10: Schematic of a low angle subduction system, showing the partial melting of a subduction mélange 42
Figure 1.11: Schematic illustration of magma recharge into the magmatic system below Mt. Taranaki. 43
Figure 1.12: Hazard map for the Taranaki Region 45
Figure 1.13: Eruption modelling diagram showing scenarios for future eruptive events from Mt. Taranaki 47
Figure 1.14: Schematic of eruption scenarios for Mt. Taranaki 48
Figure 2.1: A. Location map of the Poto and Paetahi tephra formations across the Taranaki ring plain. 50
Figure 2.2: A. Sample holder containing pumice clast in the top 7 mm mounted to a magnetic base.. 57
Figure 3.1: Field location map of the Poto and Paetahi Formations across the Taranaki ring plain. 70
Figure 3.2: Images of the different compositional classifications 71
Figure 3.3: Complete depositional sequence for the Poto Formation at the Poto reference location ... 74
Figure 3.4: Field images of the Paetahi tephra formations. 82
Figure 3.5: Stratigraphy of the Poto Formation 87
Figure 3.6: Stratigraphy of the Paetahi Formation 88
Figure 3.7: Compositional variation of the -1.5 and 0.5 ϕ grains from the Poto tephra formation..... 91
Figure 3.8: Compositional variation of the -1.5 and 0.5 ϕ grains from the Paetahi tephra formation. . 92
Figure 3.9: A representative selection of isopach from the Poto and Paetahi Formations 95
Figure 3.10: Representative selection of Isopleth maps of the Poto and Paetahi Formation. 97

Figure 3.11: Representative selection of isopach data plots for the individual eruptive layers of the Poto and Paetahi Formations 98
Figure 3.12: Column height vs. magnitude of the Poto and Paetahi Formation 101
Figure 3.13: Histogram of the duration of eruptions from the Poto and Paetahi Formations. 101
Figure 4.1: Sample holders used for the 3D MCT scanning at the Australian Synchrotron. 118
Figure 4.2: Flow diagram for extracting volume and number density calculations from 3D textural analysis 121
Figure 4.3: Step view of thresholding process showing 121
Figure 4.4: Average Density data for the Poto and Paetahi Formations. 124
Figure 4.5: Representative samples of the different pumice types within the Poto and Paetahi Formations 126
Figure 4.6: Representative 3D reconstructions and 2D slices from MCT scan images 128
Figure 4.7: a.) Vesicle number density vs average bulk density 129
Figure 4.8: Stratigraphic column of the Poto Formation showing vesicle size distribution 132
Figure 4.9: Stratigraphic column of the Paetahi Formation showing vesicle size distribution 133
Figure 4.10: a.) Schematic model of the conduit system below Mt. Taranaki 139
Figure 4.11: Schematic model of Mt. Taranaki edifice morphologies during the Poto and Paetahi Formations. 144
Figure 5.1: Relationship between LOI and whole-rock major element abundance. 153
Figure 5.2: Total Alkali ($Na_2O + K_2O$) vs Silica (TAS) classification of the Poto and Paetahi volcanic rocks 154
Figure 5.3: Whole-rock major element variation diagrams 159
Figure 5.4: Trace element variability (ppm) vs MgO content (wt.%) of the sampled Poto and Paetahi Formations 162
Figure 5.5: Normal mid-ocean ridge basalt (N-MORB) and chondrite normalized rare earth element patterns 163
Figure 5.6: Major element variation diagrams as a function of SiO_2 abundance 167
Figure 5.7: Stratigraphic column of the Poto and Paetahi Formations with the calculated temperature (in °C) and H_2O content (in wt.%) 172
Figure 5.8: Relationship between temperature and H_2O content 172
Figure 5.9: Crystal texture of representative examples from the Poto and Paetahi Formations. 173
Figure 5.10: Representative BSE images of pyroxene crystals from the Poto and Paetahi Formations 177
Figure 5.11: Representative BSE images of plagioclase crystals from the Poto and Paetahi Formations 178
Figure 5.12: Schematic illustration of the relationship between surface load and the mid– to upper crustal system below Mt. Taranaki 184

Figure 6.1: Total Alkali ($Na_2O + K_2O$) vs Silica (SiO_2) (TAS) classification 190
Figure 6.2: MgO vs LOI plot showing no relationship between LOI and the whole rock MgO abundance 190
Figure 6.3: Whole rock major element variation diagrams as a function of MgO abundance..... 191
Figure 6.4: Crystal texture of representative examples from the Poto and Paetahi Formations. 192
Figure 6.5: Whole rock MgO (wt.%) composition for the Poto and Paetahi Formation 195
Figure 6.6: Schematic illustration of the changes occurring at Mt. Taranaki 20 – 30 ka during the Poto and Paetahi eruptive period. 199
Figure 6.7: A. Column height vs composition (MgO wt.%) of the Poto and Paetahi Formation 202
Figure 6.8: Comparison between the distribution of the Poto and Paetahi Formation ash and lapilli fall deposits 206
Figure 6.9: A-B. Fitted α (alpha indicates the shape of the distribution) shape parameters A. all data from the Poto and Paetahi Formations 207

Table of Tables

Table 1.1: Global examples of plinian and subplinian eruptions from historical observations 8
Table 1.2: Tephra stratigraphic and debris-avalanche deposits from Mt. Taranaki with calibrate ages. 29
Table 1.3: Selected Plinian/Subplinian eruptions from Mount Taranaki over the past 5 ka. 32
Table 2.1: Tephra size clasts in relation to grain size parameters phi and mm 54
Table 2.2: EMPA measurement conditions. 61
Table 3.1: Description of the units within the Poto Formation 75
Table 3.2: Description of the units within the Paetahi Formations. 83
Table 3.3: Description table of the components present within the Poto and Paetahi tephra layers. 90
Table 3.4: A representative selection of eruptive volumes calculated using AshCalc 93
Table 3.5: A representative selection of the isopleth parameters for the Poto and Paetahi Formations. 95
Table 3.6: Estimated eruptive parameters for the Poto and Paetahi Formations 98
Table 4.1: Textural features of the Poto and Paetahi Formations 123
Table 5.1: Whole rock major element compositions (wt. %) of Poto and Paetahi pumice clasts determined by XRF analysis. 155
Table 5.2: Whole-rock trace element composition (averages ppm) of Poto and Paetahi pumice clasts determined by ICPMS analysis. 164
Table 5.3: Major element glass composition (averages wt.%) of Poto and Paetahi pumice clasts determined by EMPA. 168
Table 6.1: Global examples of volcanoes that have experienced multiple collapse cycles throughout their life cycles 186

Abbreviations

Locations and stratigraphic units

TVZ – Taupo Volcanic Zone

TgVC – Tongariro Volcanic centre

AV – Alexandra Volcanics

TVL – Taranaki Volcanic lineament

UIG – Upper Inglewood

CEFZ – Cape Egmont Fault Zone

MTZ – Median tectonic zone

Eruptive Parameters

V – Fallout tephra volume ()

H – Eruptive column height (km)

DRE – Eruptive magnitude ()

MER – Mass eruption rate ()

Q – Discharge rate ()

MDR – Mass discharge rate (X)

VEI – Volcanic explosivity index

bt – Thickness half distance

bc – Clast half distance

k – slope

A – Area (km^2)

Grain size parameters

ϕ - Phi

Mdϕ - geometric mean

Sigmaϕ - Graphic standard deviation

SkG – Graphic skewness

Mz – Graphic mean

Sigmai – Graphic standard deviation

Ski – Graphic skewness

Kg – Kurtosis

Density parameters

δbulk – Bulk density (g/cm^3)

vbulk – Bulk volume (mm^3)

3D Bubble parameters

VND – Vesicle number density (cm^{-3})

VSD – Vesicle size distribution

CND – Crystal number density (cm^{-3})

CSD – Crystal size distribution

CV – Crystal volume (%)

VV – Vesicle volume (%)

Deposits

PDC – Pyroclastic density current

DAD – Debris-avalanche deposit

Geochemical

FC – Fractional crystallization

AFC – Assimilation fractional crystallization

LILE – Large ion lithophile elements

TAS – Total alkali silica

LREE – Light rare earth elements

HREE – heavy rare earth elements

Age constraints

Cal. Yr BP – Calibrated years before present

CE – Current Era

BCE – Before current era

Techniques and equipment

MCT – Micro-Computed Tomography

EMPA – Electron Microprobe analysis

ICP-MS – Laser ablation

XRF – X-ray fluorescence analysis

BSE – Back-scatter electron image

1 Introduction

1.1 Research Problem and motivation

Stratovolcanoes can produce a multitude of hazardous phenomena impacting many communities around the world (e.g., Mt. Vesuvius; Carey and Sigurdsson (1987); 1902 Mt. Pelé; Bourdier et al. (1989); 1980 Mt. St. Helens; Tilling et al. (1984); 2008 Chaitén; Carn et al. (2009); 2010 Eyjafjallajökull; Gudmundsson et al. (2010); Langmann et al. (2012)). Past eruptions and their preserved deposits provide information on eruption size, frequency, and style, which are important to characterize the hazards associated with long-lived volcanoes. This information can inform hazard scenarios to mitigate future eruptive impacts (e.g., Houghton et al., 1987; Neall & Alloway, 1996; Connor C, 2001; Sieron et al., 2014; Calder et al., 2015; Torres-Orozco et al., 2018; Alpízar Segura et al., 2019; Gillies et al., 2020).

Activity at a stratovolcano can be divided into periods of quiescence and levels of activity (Zernack et al., 2011; Watt, 2019; Zernack, 2021; Zernack & Procter, 2021). Volcanism associated with subduction zones can experience long periods of quiescence prior to undergoing an abrupt explosive awakening (e.g., 1991 Mt. Pinatubo, Philippines;(Newhall, 1996); 1995-1999 Soufrière Hills, Montserrat; (Druitt & Kokelaar, 2002; Baxter et al., 2005). Once a volcano becomes active, eruptive behaviours can alternate between explosive (e.g., 1980-1986 Mt. St. Helens, USA, 1992 El Chichón, Mexico, 1989-1990 Redoubt, USA, 2007-2008 Chaitén, Chile and 1992 Crater Peak, USA (Woods, 1995; Simkin et al., 2000; Carn et al., 2009; Lara, 2010), and effusive activity (e.g., Mt. Augustine, Alaska; (Begét & Kienle, 1992; Waitt, 2010; Watt, 2019; Siebert & Roverato, 2021; Zernack & Procter, 2021). Alternations between explosive and effusive activity has been observed at Colima, Mexico (O'Callaghan & Francis, 1986; Luhr & Prestegaard, 1988), Merapi, Indonesia (Abdurachman et al., 2000; Schwarzkopf et al., 2005) and Mt. Ruapehu, New Zealand (Hackett & Houghton, 1989; Moebis et al., 2011; Pardo et al., 2012b; Pardo et al., 2012a; Voloschina et al., 2020). Large tephrochronological studies of volcanoes around the globe have typically focused on Holocene records due to the preservation of depositional material (Siebert et al., 1995; Thouret et al., 1995; Scott et al., 1997; Ponomareva et al., 1998; Belousov et al., 1999; Waythomas, 1999; Waythomas & Miller, 1999; Reid et al., 2001; Ponomareva et al., 2006). In this research, we attempt to understand the features of an eruptive period from Mt. Taranaki, New Zealand, investigating a sequence of eruptive products which took place over a 4,000-year period from 22.7 to 19.4 ka (Section 1.7.1) (Alloway et al., 1995).

Within any tectonic setting stratovolcanoes are highly unstable and susceptible to collapse (e.g., Ui, 1983; Siebert, 1984; Ui et al., 1986b; Ui et al., 1986a; Moore et al., 1989; Carracedo, 1994; Vallance et al., 1995; Capra et al., 2002; Masson et al., 2002; Silver et al., 2009; Németh et al., 2011; Delcamp et al., 2012; Watt et al., 2020). The 1980 eruption of Mt. St. Helens provided insights into how important

it is to understand the hazards associated with edifice collapse and the destructive power of debris avalanches (Crandell & Hoblitt, 1986; Voight, 2000). Most stratovolcanoes only experience one major edifice collapse throughout their evolution (Siebert, 1996; Voight & Elsworth, 1997; Voight, 2000; Girina, 2013; Roverato & Dufresne, 2021; Zernack, 2021). However, at a number of stratovolcanoes there is evidence of repeated debris-avalanche deposits from edifice collapses (Zernack & Procter, 2021) e.g., St. Augustine, Alaska (Begét & Kienle, 1992; Waitt, 2010; Siebert & Roverato, 2021), Mt. Rainer, USA (K. M. Scott et al., 1995; W. E. Scott et al., 1995), Lascar, Chile (Clavero et al., 2002), Colima, Mexico (Cortés et al., 2010; Roverato et al., 2011; Cortés et al., 2019), Shiveluch, Russia (Belousov et al., 1999), Mt. Ruapehu, New Zealand (Tost et al., 2014; Tost & Cronin, 2015), including Mt. Taranaki, New Zealand (Zernack et al., 2011). Volcanoes that have experienced multiple edifice collapse events indicate a cyclic pattern of collapse and regrowth occurring on timescales ranging from hundreds to thousands of years (Belousov et al., 1999; Tibaldi, 2004; Zernack et al., 2009; Zernack et al., 2011; Zernack & Procter, 2021). These cyclic patterns indicate there is a natural height at which an edifice becomes unstable, with stratovolcanoes having an average maximum height of 2,000 to 2,500 m prior to collapse (Davidson & De Silva, 2000). Edifice collapse events change the lithostatic pressure of the crust above magma reservoirs which can cause sudden depressurization within the magmatic system as magmatic pressure and stress within the reservoir is decreased driven by a downward propagating decompression wave as a large section of the upper edifice is rapidly removed (Pinel & Jaupart, 2003; Pinel & Jaupart, 2005; Pinel & Albino, 2013; Watt, 2019; Cutler et al., 2022). This change in lithostatic pressure can cause the sudden onset of an eruption if there is eruptible magma present at shallow depths within the system (Watt, 2019). The depressurization can also shift the fragmentation zone deeper within the conduit (Alidibirov & Dingwell, 1996; Alidibirov & Dingwell, 2000; Spieler et al., 2004) and typically results in less evolved magma being erupted e.g., Mt. Pelée, Martinique (Boudon et al., 2013); Stromboli, Italy (Hornig-Kjarsgaard, 1993; Petrone et al., 2009; Vezzoli et al., 2014) and Soufrière Hills, Montserrat (Zellmer et al., 2003; Cassidy et al., 2012; Michael Cassidy et al., 2015) (Watt, 2019). This can result in changes to internal processes which drive eruptions e.g., bubble nucleation and growth (Alidibirov & Dingwell, 2000) influencing the eruptive style, size and frequency of events following large collapses (Tibaldi, 2004; Hora et al., 2009; Manconi et al., 2009; Watt, 2019).

Changes in eruptive style following collapse have been observed globally e.g., Fuego de Colima, Mexico (Robin et al., 1990; Stoopes & Sheridan, 1992; Capra & Macías, 2002); Shiveluch, Russia (Belousov, 1995; Belousov et al., 1999; Gorbach et al., 2013) and Planchón, Chile (Tormey et al., 1995; Tormey, 2010). The volume of material associated with cone collapse events can vary from between 0.1 km^3 to 100 km^3 (e.g., Watt, 2019; Zernack & Procter, 2021). Globally more than 200 volcanoes have a record of a collapse > 1 km^3 (e.g., Watt, 2019), with collapses associated with subduction related volcanism typically between 1 – 5 km^3 (Watt, 2019). Historical edifice collapse events (e.g., 1888 Ritter Island, Papa New Guinea 4.2 km^3; Johnson (1987); and 1980 Mt. St. Helens, USA, 2.5 km^3 ; Siebert

(1984), have been relatively small compared to pre-historic events within the volcanic record (e.g., 4.3 ka Colima, Mexico, 10 km^3;O'Callaghan and Francis (1986); Luhr and Prestegaard (1988); and 60 – 65 ka Chimborazo, Ecuador, 12 km^3 ;(Samaniego et al., 2012; Watt, 2019). Mt. Taranaki in New Zealand has experienced at least fourteen collapse events of varying sizes 0.1 to 7.5 km^3 within its > 200,000-year eruptive period (Zernack et al., 2011). A unique combination of tectonic uplift and coastal erosion has provided access to a detailed stratigraphic record of growth and collapse cycles of a long-lived stratovolcano along the western and south-western coastal ring plain (Ui et al., 1986b; Ui et al., 1986a; Pillans, 1990; Palmer & Neall, 1991; Procter et al., 2009; Zernack et al., 2009; Zernack et al., 2011; Roverato et al., 2015; Cronin et al., 2021; Zernack, 2021).

The 200-ka ring plain around Mt. Taranaki provides a comprehensive record of the cyclic behaviour of growth and collapse at a long-lived stratovolcano. The ring plain contains a record of successive mass flows and pyroclastic deposits compared to the < 14 ka cone (2518 m), where erupted material gets quickly buried by new deposits or eroded through fluvial, aeolian and, redeposition processes (Neall et al., 1986; Alloway et al., 1995; Neall & Alloway, 1996; Procter et al., 2009; Zernack et al., 2011). The (> 150 km^3) ring plain contains approximately ten times the volume of the current edifice (12 km^3) (Neall et al., 1986; Zernack et al., 2012b; Zernack et al., 2012a) recording the multiple growth and collapse cycles which Mt. Taranaki has experienced within its evolution (Neall et al., 1986; Alloway et al., 1995; Procter et al., 2009; Zernack et al., 2011; Damaschke et al., 2017b; Torres-Orozco et al., 2018; Lerner et al., 2019d). The last edifice collapse event to have occurred at Mt. Taranaki was the 2.5 km^3 Opua collapse dated at around 7.5 ka. Ring plain stratigraphy of the > 5 ka sequence has been investigated to quantify the eruptive frequency for Mt. Taranaki (Neall et al., 1986; Alloway et al., 1995; Damaschke et al., 2017b). Analysis of eruptive products at Taranaki has been concentrated on the < 5 ka eruptive record, focusing heavily on the eruptive processes and no other associated volcanic phenomena (see subsequent literature review, Section 1.7.1) (Platz et al., 2007; Turner et al., 2008b; Turner et al., 2009; Torres-Orozco et al., 2018; D'Mello et al., 2021). Investigations of mass flow and debris avalanche occurrence has focused on the geomorphological and geochemical changes associated with growth and collapse cycles through ring plain geological mapping (e.g., Procter et al., 2009; Zernack et al., 2011; Zernack et al., 2012a; Zemeny et al., 2021; Zemeny et al., 2023). However, an in-depth investigation examining primary deposits (e.g., tephra) associated with growth and collapse cycles at a long-lived stratovolcano has not been investigated prior. This study is focused on the Poto and Paetahi Formations, mapped across the eastern and southeastern Taranaki ring plain (Alloway et al., 1995; Damaschke et al., 2017b). Past research on the Poto and Paetahi Formations shows that they occurred during an eruptive period which encompasses two of the largest edifice collapse events in Mt. Taranaki's history producing the 27.3 ka Ngaere debris-avalanche deposit (5.85 km^3) and the 24.8 ka Pungarehu debris-avalanche deposit (7.5 km^3).

This Thesis will provide a contribution toward understanding eruptive processes that may occur in response to edifice collapse events. This work will underpin the defining hazards associated with depressurization on the magmatic system at Mt. Taranaki. An overarching hypothesis for this work is proposed as follows:

Geomorphic changes related to edifice collapse events can impact the style, frequency, and size of subsequent eruptions. Rapid decompression from these collapse events can influence the subvolcanic plumbing system impacting the internal processes driving volcanic eruptions. A detailed analysis of the size, and style of the Poto and Paetahi Formations will be developed to understand the influence that multiple large sector collapses have on the short and long-term eruptive evolution of a long-lived stratovolcano. This will form the basis for including long-term tephrochronological records into future hazard scenarios and assessments.

To test this hypothesis four main objectives are defined below.

Objective 1: *To quantify the variability of eruptive parameters, including eruption volume, column height and mass eruption rates from the Poto and Paetahi tephra formations.*

This objective will investigate the products of the Poto and Paetahi eruptive period to create a detailed eruptive record, including the eruption size, dispersal, and magnitude of the events, along with the number of events which are classified as single or multiphase sequences.

Objective 2: *To quantify the variability of magma vesiculation and fragmentation in these eruptions as a response to edifice collapse.*

This objective will investigate the bubble texture characteristics of pumice clasts produced during the Poto and Paetahi eruptive period to interpret the influence that rapid decompression has on the subvolcanic plumbing system. The timing of the Poto and Paetahi eruptive periods provides a unique opportunity to investigate this influence with the occurrence of two large edifice collapse events occurring within the timeframe of these deposits. This provides the basis for investigating the internal processes pre and post collapse event and to understand how the system responds and evolves across a short and long-term time scale.

Objective 3: *To examine the magmatic history of the magma as a response to depressurization, fractional crystallization and magma recharge leading to an eruption.*

Primary fall deposits will be used to examine how Mt. Taranaki has responded to major edifice collapse events. Major and trace element whole rock and glass point analysis of pumice clasts within each primary fall unit from the Poto and Paetahi Formations allows for the geochemical characterization and evolution of Mt. Taranaki within this studied timeframe. This provides the foundation for understanding the influence of the growth and collapse cycles on the evolution of the volcanic system.

Further insights can be obtained through the P-T-H_2O conditions of the crystals to understand the crystallization and ascent rates of the magma within the system. Thermometry modelling will be undertaken to better understand the complex vertical plumbing system below Mt. Taranaki in combination with objective.2. The results will be compared to datasets from earlier work on Mt. Taranaki to indicate similarities or differences in relation to magma ascent pathways throughout the system.

Objective 4: *To understand the potential hazards posed by the geomorphic change of a stratovolcano on the subvolcanic plumbing system.*

The analysis will focus on understanding how large edifice collapse events may impact the size, frequency, style, and dispersal pattern of eruptions at Mt. Taranaki and how these fit in with the current hazard models and scenarios for the region. Short and long -term records surrounding large edifice collapse events will be investigated to ascertain the direct impact experienced by Mt. Taranaki.

Looking at an eruptive period which encompasses two large edifice collapse events allows for an in-depth look at the direct impact this has on short and long-term eruptive evolutions of the volcano. Comparing this data to previous studies which look at the eruptive frequency and distribution of large explosive events will show similarities and discrepancies in relation to the hazard models and scenarios for the surrounding Taranaki region.

This thesis is composed of **7** chapters and 7 digital appendices. The thesis is divided into three main chapters prepared as separate scientific articles that directly address the four objectives provided here in chapters 3 to 5. This chapter introduces the literature, this is followed by **Chapter 2** where all the methods used to address the proposed objectives are outlined. The core of this thesis comprises the following chapters:

Chapter 3 entitled "The stratigraphy and physical properties of explosive events from Mt. Taranaki, New Zealand pre- and post-edifice collapse." provides the basis for the subsequent chapters investigating the stratigraphic and sedimentological characteristics of the Poto and Paetahi Formations. Create detailed, quantitative dataset of deposit characteristics across the Taranaki ring plain, in terms of sedimentological characteristics to allow for depositional correlations. Reconstruct the eruptive parameters of the Poto and Paetahi Formations using detailed field mapping and descriptions to investigate changes in eruption style and frequency during the Poto and Paetahi eruptive period at Mt. Taranaki.

Chapter 4 entitled "Assessing the influence of edifice collapse on the shallow volcanic plumbing system of Mt. Taranaki through textural analysis of the subplinian Poto and Paetahi tephra formations". Use juvenile pyroclasts to investigate the changes in vesiculation and fragmentation present within the

Poto and Paetahi Formations to understand the changes to the processes occurring within the subvolcanic plumbing system in response to large edifice collapse events.

The geochemical analysis of the Poto and Paetahi Formations is discussed in **Chapter 5** entitled "Investigating the influence of edifice collapse on the geochemical and mineralogical composition of magma in the subvolcanic plumbing system: A case study of the Poto and Paetahi tephra formations of Taranaki volcano, New Zealand." based on analysis of rock, glass, and minerals, focusing on any changes in the system as a response to edifice collapse events.

Chapter 6 is a synthesis chapter that combines the stratigraphy, sedimentological, textural, and geochemical results to discuss how edifice collapse events influence the eruptive styles and hazards at Mt. Taranaki. A summary of the main conclusions of this research is presented in **Chapter 7**.

1.2 Literature review

1.2.1 Subplinian and plinian eruptions

The style, frequency, and size of a volcanic eruption are influenced by the composition and rheology of its magma. Within convergent plate boundaries there is a significant amount of water derived from the subducting slab which can influence the volatile content, viscosity, and location of degassing (Jeanloz, 1999; Perfit & Davidson, 2000; Lautze & Houghton, 2007; Parfitt & Wilson, 2008; Pardo et al., 2014; Cashman & Scheu, 2015; Heinrich et al., 2020a). Plinian and subplinian eruptions are explosive events which are generated by volatile exsolution within the magma driving ascent through the conduit to the surface (Toramaru, 1989; Prousevitch et al., 1993; Sparks et al., 1994; Barclay et al., 1995; Toramaru, 1995; Lyakhovsky et al., 1996; Proussevitch & Sahagian, 1998; Burgisser & Gardner, 2004).

Eruption columns produced during plinian and subplinian events are composed of a mixture of gas and rock (juvenile and lithics), which is ejected out of the vent at 100 to 400 m/s during eruptive periods which can last 2 to 6 hours (Cioni et al., 2015). The generated eruptive jets become buoyant and transform into convective plumes which can reach up into the stratosphere (Figure 1.1) (Carey & Sigurdsson, 1989; Cioni et al., 2015). Plinian events (i.e., 79AD Vesuvius; 1980 Mt. St. Helens; Table 1.1) produce eruptions 20-35 km high, where eruptive volumes range from 0.1 to 10 km^3 and can have a mass discharge rate (MDR) of between 10^6 to 10^8 kg/s and corresponding to VEIs of 4 to 6. Subplinian events (i.e., 1631 Vesuvius and 1970 Hekla; Table 1.1) produce deposits with similar depositional properties as plinian eruptions, but the eruptions are smaller in mass with eruption columns < 20 km in height, and MDRs of 10^6 kg/s (Cioni et al., 2015). These eruptive events can be associated with steady sustained eruption columns but can also experience pulses where new material and gas is rapidly injected into the column causing a collapse. Column collapses are common and can generate pyroclastic density currents (PDCs) (Pardo et al., 2014; Cioni et al., 2015). These large eruptive subplinian and

plinian plumes can disperse pyroclastic material hundreds of kilometres downwind from the vent (i.e., Taupo Pumice > 220 km) (Walker, 1980; Carey & Sigurdsson, 1989). The pumice produced is often highly vesicular due to the degree of gas exsolution and fragmentation occurring within the conduit as the magma reaches the surface generating explosive volcanic eruptions (Walker, 1981b, a). The resulting deposits normally consist of well-sorted pumice lapilli units (64-2 mm). Close to the vent (0 m-5 km) (> 64 mm) blocks and bombs can be present with the furthest historical deposits of volcanic ballistic projectiles found 10.4 km from source (Alatorre-Ibargüengoitia et al., 2012; Fitzgerald et al., 2017; Taddeucci et al., 2017). Further away from the vent the clast size decreases with clast half-distance occurring for subplinian eruptions between 1-3 km and for plinian eruptions between 3-8 km until the dominant grain size is (< 2 mm) ash (Walker, 1981a; Pyle, 1989; Cioni et al., 2015). The half distance for eruptive deposits is the distance where the deposit becomes half as thick as at its maximum point, for subplinian eruptions this range is between 0.5-4 km from source and for plinian eruptions it ranges between 2-10 km from source (Pyle, 1989; Cioni et al., 2015).

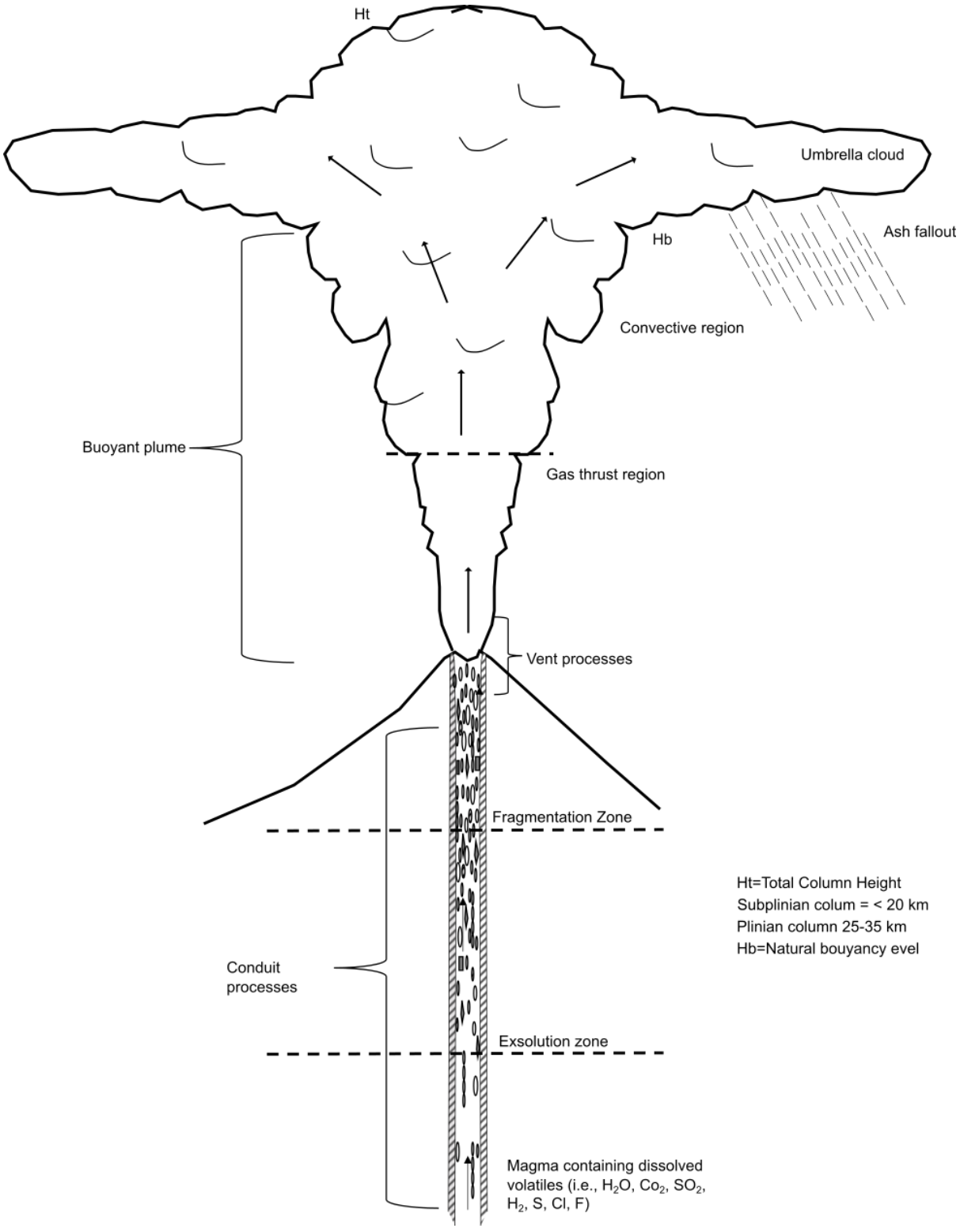


Figure 1.1: Schematic of a typical plinian/subplinian eruption column from magma exsolution through to ash dispersal from the umbrella cloud. Modified from Cioni et al. (2015); Rowell et al. (2022).

Table 1.1: Global examples of plinian and subplinian eruptions from historical observations (Cioni et al., 2015; Bruce Houghton & Rebecca J. Carey, 2015)

Eruption	Plinian/subplinian
18th May 1980 Mt. St. Helens, USA	Plinian
1982 CE El Chichón, Mexico	Plinian
1970 CE Hekla	Subplinian/plinian
1875 CE Askja - D	Plinian
79 CE Vesuvius	Plinian
1631 CE Vesuvius	Subplinian
Pululagua	Plinian

1.2.2 Eruptive deposits and characteristics

Deposits from explosive subplinian to plinian eruptive events consist of up to meters thick ash and lapilli fall units, which can blanket the surrounding landscape with extremely large events covering up to hundreds to thousands of kilometres. (Cioni et al., 2015). Depositional thickness and grain size decreases with distance from source, with the largest clasts falling out due to gravity (Walker, 1981a; Cioni et al., 2015). The proximal region around the source typically is overrepresented in thickness, as a result of the coarsest grains falling out (Cioni et al., 2015). Distal deposits from explosive eruptions are dominated by a ash, which can contain some lithic clasts, however, these become less frequent the further from source (Cioni et al., 2015). Subplinian eruptions have similar depositional characteristics to plinian events, however, this is on a smaller scale (Cioni et al., 2015).

The dispersal of ash and lapilli from explosive volcanic eruptions is controlled by the direction of the wind typically resulting in elliptical patterns of dispersal (Cioni et al., 2015). The influence of wind on the eruptive column means that during a single eruptive event multiple dispersal axes can be present as the wind shifts (Cioni et al., 2015). Subplinian eruptive events are typically recorded with stratification of eruptive beds, as the eruptions are more influenced by external processes i.e., low level winds and vent geometry (Cioni et al., 2015). Pyroclastic density current (PDC) deposits are frequently interbedded within subplinian and plinian eruptive deposits associated with partial or total column collapse (Cioni et al., 2015). Variations in the thickness of deposits across a site location can occur along with changes between sites, this can be associated with external factors such as more heavily vegetated areas resulting in thinner sections or holes in the landscape generating over thickening (Neall, 1972). These can lead to changes across an outcrop, in this the minimum and maximum thickness of a unit is recorded to represent the natural variability of the deposit (Neall, 1972).

1.2.3 Buried paleosols.

Buried paleosols interspersed between volcaniclastic deposits represent soil development through the accumulation of organic material (Neall, 1972). These paleosol layers provide indications of quiescence from the volcano and can be used to reconstruct eruptive time periods for prehistoric events. Around the Taranaki ring plain high vegetation rates throughout the growth phase of Mt. Taranaki have resulted in the formation of layers of allophanic yellow brown soils interspersed between tephra deposits (Neall, 1972). Paleosols are typically easy to identify due to their blocky structure and dark colour, along with the presence of organic matter (i.e., tree roots and charcoal). Paleosols which are less developed between layers are typically identified by the colour and blocky structure of the layer (Neall, 1972).

1.2.4 Preservation of deposits

The preservation of tephra deposits is associated with the age of the deposit and the climatic conditions and vegetative cover of the region (Neall, 1972). Older tephras are harder to correlate between sites due to weathering and burial by subsequent eruptive products. Mass flows and debris avalanches bury and erode older deposits (Neall, 1972). The present-day Taranaki region is dominated by predominantly westerly winds and has annual rainfall between 900 and 1600 mm (Newnham & Alloway, 2004), with rainfall increasing with altitude where above 2000 m annual rainfall is about 8 000 mm (Coulter, 1976). The present-day high rainfall around the Taranaki region leads to high soil production (Dorn et al., 1987; Frostick & Reid, 1989; Ritter et al., 1995; Lavigne & Thouret, 2003; Lavigne, 2004; Zanchetta et al., 2004; Scott et al., 2005; van Westen & Daag, 2005; Zernack, 2008). The Poto and Paetahi Formations occurred during the Last Glacial Maximum (25-14 ka), which is classified as a cold and dry climate, with increased erosion along streams and aeolian redistributions of tephra (Neall, 1975; McGlone et al., 1996). Climate conditions play a critical role on the formation of soils along with rates of erosion and redistribution of volcaniclastics across the ring plain (Dorn et al., 1987; Frostick & Reid, 1989; Ritter et al., 1995; Lavigne & Thouret, 2003; Lavigne, 2004; Zanchetta et al., 2004; Scott et al., 2005; van Westen & Daag, 2005; Zernack, 2008). The climate and vegetation heavily influence the formation of soil within a region, and this increases the stability of the landscape for better preserving deposits (Zanchetta et al., 2004). The climatic conditions during the Poto and Paetahi eruptive period would have led to less vegetative cover than today's climate resulting in an environment which was associated with aeolian remobilization of loose material (Frostick & Reid, 1989; Hubert & Filipov, 1989; Blair & McPherson, 1994; Blair, 2000).

1.3 Magma fragmentation and bubble nucleation

As the solubility decreases the exsolution of volatiles such as H_2O, SO_2, H_2S, CO_2, HF and HCL increases decreasing the decompression rate within a magmatic system (Gonnermann and Manga,

2007). This changes the viscosity of the magma as it reaches the surface and potential energy within the system is converted to kinetic energy generating an explosive eruption (Wilson et al., 1980; Carey & Sparks, 1986; Gonnermann & Manga, 2007).

Magma begins as a gas free liquid until the point of volatile supersaturation is reached (Mangan & Sisson, 2000; Burgisser & Gardner, 2004; Gaonac'h et al., 2005) and volatiles begin to exsolve out of the melt initiating bubble nucleation and driving magma ascent (Sparks, 1978; Toramaru, 1989; Prousevitch et al., 1993; Sparks et al., 1994; Cashman & Blundy, 2000; Burgisser & Gardner, 2004). Bubble nucleation within a magmatic system can occur as heterogeneous or homogeneous processes. Heterogeneous nucleation occurs with crystals acting as nucleation sites where bubbles begin to form at depth along the edge of the crystal walls. This process allows volatile exsolution and bubble nucleation to begin at lower levels of volatile supersaturation (Toramaru, 1989; Hurwitz & Navon, 1994; Navon et al., 1998; Gardner et al., 1999; Mangan & Sisson, 2000; Cashman, 2004; Gardner & Denis, 2004). While homogeneous nucleation occurs when the melt has become supersaturated and volatiles exsolve at shallower depths (Cioni et al., 2000; Cashman, 2004) both of these processes increase the magmatic overpressure generating an explosive eruption.

Numerous stages of bubble nucleation and growth can occur throughout the magmas ascent generating multiple populations of bubbles within the system (Wilson et al., 1980; Klug & Cashman, 1996). At depth bubble growth is controlled by the viscosity of the magma. While continued bubble nucleation drives ascent decreasing the density of the magma and increasing volatile exsolution and nucleation (Proussevitch et al., 1993; Sparks et al., 1994; Barclay et al., 1995; Toramaru, 1995; Lyakhovsky et al., 1996; Proussevitch & Sahagian, 1998; Burgisser & Gardner, 2004). Continued decompression near the surface promotes bubble growth through expansion as the pressure over the bubble's decreases (Cashman & Blundy, 2000). Throughout bubble growth coalescence occurs once the internal pressure within a bubble is reached and the wall between two bubbles ruptures (Toramaru, 1988; Klug & Cashman, 1996). This process can occur because of shearing, fragmentation and inter-bubble wall expansion (Verhoogen, 1951; Alidibirov & Dingwell, 2000). As bubbles continue to grow and connect within the system the permeability of the magma increases. Magmatic permeability is a critical factor in the size and style of eruption which occurs (Klug & Cashman, 1996; Rust & Cashman, 2004). As magma ascends through the conduit shearing can occur and cause vesicles to stretch and interconnect (Klug & Cashman, 1996; Alidibirov & Dingwell, 2000). This generates increased permeability of the magma, reducing the intensity of fragmentation. If bubbles within the magma do not coalesce, they can remain isolated which can cause over pressurization within the system triggering a highly explosive eruption (Martel & Iacono-Marziano, 2015).

Degassing within a magmatic system occurs as the magma ascends, changing decompression rates which influence the process of volatile solubility (Gonnermann & Manga, 2007). Decoupled degassing

is more typically associated with low viscosity basaltic magmas where bubbles rise faster than the surrounding melt causing buoyant rise (Gerlach & Graeber, 1985; Hurwitz et al., 2003; Gonnermann & Manga, 2007). Within these systems gas slugs can form through coalesced bubbles filling the conduit. When these slugs reach the surface, they burst generating a strombolian eruption (Blackburn et al., 1976; Wilson, 1980; Jaupart & Vergniolle, 1988; Parfitt, 2004; Gonnermann & Manga, 2007). While coupled degassing is more likely to be associated with high viscosity silicic system where the bubbles are less mobile within the melt and are correlated with much larger explosive eruptions (Wilson et al., 1980; Sparks et al., 1994; Papale et al., 1998; Sable et al., 2006). Intermediate andesitic magmas have viscosities that produce a wider variety of eruption styles associated with the broader range of andesitic compositions (e.g., Polacci et al., 2006; Clarke et al., 2007; Höskuldsson et al., 2007; Pardo et al., 2012b; Pardo et al., 2012a; Torres-Orozco et al., 2017b; Heinrich et al., 2020b). However, coupled degassing is not solely controlled by the composition of the melt, groundmass crystallization, decompression rate and rate of ascent strongly influence the style of degassing (Sable et al., 2006). Open-system magmatic degassing can occur when gas is lost through magma foam collapse (e.g., lava flows or domes) (Westrich & Eichelberger, 1994), or if gas is trapped within a closed system the magmatic overpressure builds up and generates a large explosive eruption (Bursik, 1993; Hammer et al., 1999; Gonnermann & Manga, 2007).

When the critical pressure difference of the melt is reached magmatic fragmentation occurs as the melt can no longer withstand the overpressure resulting in an explosive eruption (Spieler et al., 2004). This is known as the fragmentation threshold which occurs when bubbles generate and preserve a connected pathway increasing porosity and controlling the magmatic overpressure (Spieler et al., 2004). If the bubble connectivity becomes to high gas can escape resulting in an effusive eruption (Cashman & Blundy, 2000; Cashman, 2004; Rust & Cashman, 2004). For an explosive eruption to occur the connectivity was believed to need to be around 70 vol.% in order for the fragmentation threshold to be reached (Sparks, 1978; Woods, 1995) however, ongoing studies (e.g., Houghton & Wilson, 1989; Klug & Cashman, 1996; Spieler et al., 2004; Scheu et al., 2006) have found that this level could be significantly lower. Experimental studies by Spieler et al. (2004) into the fundamentals of magmatic fragmentation found that crystallinity, bubble size distribution and composition are not critical controlling factors driving magmatic fragmentation. Their study found that the porosity of the magma was the main driver controlling the fragmentation threshold.

Magmatic fragmentation can occur within a low viscosity system when the bubble walls become too thin to withstand expansion within the rapidly ascending foam (Mader, 1998; Cashman, 2004). While changes in decompression within high viscosity melts causes sudden bubble expansion to occur generating a fragmentation wave to propagate down through the system exceeding the brittle tensile strength of the magma and increasing acceleration generating an explosive eruption (Dingwell & Webb, 1989; Dingwell, 1998; Mader, 1998; Alidibirov & Dingwell, 2000; Houghton et al., 2004; Gonnermann

& Manga, 2007). Sudden decompression caused by the collapse of a edifice or dome can cause the magma to fragment below the fragmentation threshold if the brittle tensile point is reached generating a change in magmatic overpressure (Sato et al., 1992; Klug & Cashman, 1994; Kennedy et al., 2005; Alatorre-Ibargüengoitia et al., 2011).

Fragmentation fronts within magmatic systems move in relation to the porosity of the magma and the decompression rate (Mason et al., 2006).The length of an eruption is controlled by the process of volatile exsolution into bubbles during decompression and the equilibrium between exsolved and dissolved gas (Mason et al., 2006; Hajimirza et al., 2022). A short-lived vulcanian style eruption occurs if volatile exsolution is in disequilibrium because the expanding magma cannot reach the critical fragmentation threshold. Whereas a long sustained plinian eruption can occur if volatile exsolution stays in equilibrium throughout the eruption allowing bubbles to continue to expand (Mason et al., 2006; Hajimirza et al., 2022). If the conditions stay near to equilibrium throughout the eruption a subplinian event occurs prior to a decrease in overpressure (Mason et al., 2006).

Textural characteristics of pyroclasts generated during explosive eruptions provide insights on the shape, size and abundance of bubbles (Shea et al., 2010; Shea et al., 2012). This data is used to understand the complex spatial and temporal processes of bubble nucleation and growth (i.e., coalescence, deformation and expansion) of bubbles within the magma as it ascended up through the conduit (Houghton & Wilson, 1989; Polacci et al., 2003; Gonnermann & Manga, 2007; Shea et al., 2010; Mueller et al., 2011; Shea et al., 2012).

Lithic content within pyroclastic deposits increases with conduit widening as magma ascends abrading the conduit walls (Wilson et al., 1980; Macedonio et al., 1994; Valentine & Groves, 1996; Papale et al., 1998; Campbell et al., 2013; Houghton & Carey, 2015). Erosion of the conduit walls occurs when the pressure difference is greatest usually at the fragmentation level (Papale et al., 1998). The presence of increased lithics reflect conduit widening under steady state or decreasing mass eruption rates (Varekamp, 1993; Taddeucci & Wohletz, 2001).

1.3.1 Bubble nucleation studies on New Zealand volcanoes

The variability of the amount of volatiles within magma controls the rate of rise and therefore influences the eruptive style, i.e., shift between explosive and effusive periods during an eruptive episode (Eichelberger et al., 1986; Jaupart & Allègre, 1991; Woods & Koyaguchi, 1994; Jaupart, 1998; Bouvet de Maisonneuve et al., 2009). The generation of bubbles within magma can vary within different volcanic settings and also during eruptive phases as bubbles form through volatile exsolution the amount of connectedness, deformation, and size distribution changes (Belien et al., 2010). Under lower pressures within the conduit the main volatiles (i.e., H_2O; SO_2) are less soluble leading to more bubbles

and thus high porosities within the ejected material (Clarke et al., 2002; Melnik et al., 2002; Kennedy et al., 2005).

Previous studies of bubble nucleation from New Zealand volcanoes and volcanic deposits show that bubbles range (in 2D sections) between 0.0001 to 6 mm^2 with a median area of 0.02 mm^2 from andesites at Mt. Ruapehu (Pardo et al., 2012a; Pardo et al., 2014). The pumice clasts from Mt. Ruapehu indicate that the magma underwent a two-phase nucleation. This suggests that the magma within the system began to ascend and then stalled for a significant length of time before erupting. The second phase of nucleation began in response to crystallisation, triggering an eruption (Mills, 2019). Pumice clasts from two ignimbrites of the 25.6 ka Taupo eruption have large (1-8 mm^2) vesicles, indicating that this magma experienced substantial expansion post-nucleation, leading to bubble coalescence (Houghton et al., 2010). The vesicles within pumices from the ash fall deposits are mostly characterised by small vesicles. The vesicle number densities from erupted pyroclastic material can provide insights into the nucleation and growth phases of bubbles occurring at different stages during an eruptive period. The vesicle size distributions for pumice clasts can be represented by either exponential or power law distribution curves (Klug et al., 2002; Adams et al., 2006b; Carey et al., 2009; Rotella et al., 2014). Pumice clasts that show power law distributions indicate bubble nucleation and growth was generated through solely magmatic processes, while exponential distributions are considered to represent viscosity limited diffusional bubble growth (Toramaru, 1995; Navon et al., 1998; Liu & Zhang, 2000; Klug et al., 2002; Adams et al., 2006b; Toramaru, 2006; Carey et al., 2009; Rotella et al., 2014). Within the ash fall deposits from the 25.6 ka Taupo eruption the bubble nucleation shows an exponential relationship which is characterised by a power law exponent of > 3, suggesting that rapid bubble nucleation was occurring within a high volatile supersaturation (Blower et al., 2003; Houghton et al., 2010). Fitting a single distribution to BSDs for pumice clasts however can be difficult, often with small bubbles plotting along an exponential distribution while the larger bubbles plot along a power law distribution depending on the amount of coalescence which has occurred (Toramaru, 1995; Navon et al., 1998; Liu & Zhang, 2000; Klug et al., 2002; Adams et al., 2006b; Toramaru, 2006; Carey et al., 2009; Rotella et al., 2014). The vesicles characterized indicate that the ash fall was produced during non-steady state bubble growth, which remained fairly consistent throughout the eruption (Blower et al., 2003; Houghton et al., 2010).

The power law exponent of explosive events within rhyolitic volcanic environments range between 3.3 to 4.0 (Klug et al., 2002; Carey et al., 2009; Rotella et al., 2014). For eruptive sequences, the power law varies as the eruption style changes, e.g., Mayor Island's Tuhua eruption showed a power law of 4.52 at the beginning of the sequence and towards the end dropped to 3.42 (Mills, 2019). The initial higher number reflects the onset of an eruption that transitions into a less explosive eruptive phase with a lower power law number as larger bubbles within the magma are erupted out of the conduit (e.g., Okumura et

al., 2008; Okumura et al., 2009; Okumura et al., 2010; Caricchi et al., 2011; Okumura et al., 2013; Rotella et al., 2014; Mills, 2019).

Previous bubble studies from Torres-Orozco et al. (2023) on Mt. Taranaki focussed on the 3300 cal BP Upper Inglewood (Uig) plinian eruptive episode including a range of eruptive styles from plinian eruptions to dome collapse pyroclastic density currents (PDCs) (Torres-Orozco et al., 2023). The vesicle number densities (VNDs) for these events ranged from 1.1 x 10^5 to 2.5 x 10^6 mm^3, with vesicle size distributions (VSDs) indicating that these eruptive events underwent multiple stages of bubble nucleation and growth indicative of different rates of ascent and decompression within the conduit (Torres-Orozco et al., 2023). The different styles of eruptions which occurred throughout the Uig eruptive episode showed different levels of bubble nucleation and growth with bubble shapes ranging from spherical to elongate which indicates that changes in fragmentation and decompression within the conduit can influence the eruption style produced (Torres-Orozco et al., 2023).

1.4 Regional geologic setting of New Zealand

New Zealand is situated along a plate boundary extending over c. 2,800 km from the Tongan Island Arc to New Zealand, where the Pacific Plate is being subducted underneath the Indo-Australian Plate (Figure 1.2) (Karig, 1970; Ewart et al., 1977). Below the Kermadec and Tongan Arc volcanoes the Benioff zone dips at 28-30˚ but steepens to 40-57˚ beneath the Tongan Islands and to 55-71˚ below the Kermadec Islands (Sykes L, 1966; Isacks & Barazangi, 1977). The rate of plate convergence increases from south to north from 51-53 mm yr^{-1} in the Kermadec Arc up to 240 mm yr^{-1} at the northern end of the Tongan Arc (Jarrad R, 1986; DeMets et al., 1990; Bevis et al., 1995; Parson & Wright, 1996). The Tongan-Kermadec plate sector has mostly been intact for the past 45 Ma (Ballance et al., 1982; Davey, 1982; Mortimer et al., 1998).

In the North Island of New Zealand subduction along the Hikurangi Trench represents the southernmost expression of the Tongan-Kermadec Trench (Karig, 1970; DeMets et al., 1994; Henrys et al., 2003; Nicol et al., 2007; Wallace et al., 2012; Damaschke, 2017). Within the Hikurangi Trench the plate motion convergence rate decreases from c. 70 mm yr-1 to c. 40 mm yr-1 from north to south (Walcott, 1978; DeMets et al., 1990; Parson & Wright, 1996; Beavan et al., 2002).280 km west of the Hikurangi Trench the Benioff Zone dips at 50-70 °NE beneath New Zealand (Adams & Ware, 1977; Ewart et al., 1977) to a depth of 100 km below the Taupo Volcanic Zone (TVZ) continuing to a depth of 300 km beneath the Taranaki region (Boddington et al., 2004; Reyners et al., 2006; Reyners et al., 2011). The oceanic crust of the Pacific Plate has a variable thickness (Hikurangi Plateau) causing a clockwise rotation of the North Island at 0.5-3.8˚ Myr^{-1} relative to the Indo-Australian Plate (Wallace et al., 2004; Rowan et al., 2005; Nicol et al., 2007). The South Island of New Zealand is dominated by continental-continental collision that has created a system of strike slip faults, including the Alpine Fault (Van Dissen & Yeats, 1991; Holt & Haines, 1995; Norris & Cooper, 2007; Sutherland et al., 2012).

1.5 Taupo Volcanic Zone (TVZ)

The Tongan-Kermadec Trench is represented on the North Island of New Zealand by the 300 km-long, 200 km-wide Taupo Volcanic Zone (TVZ) where an average extension of 8-10 mm/yr generates tensional stress within the 12-15 km-thick crust (DeMets et al., 1994; Villamor & Berryman, 2001; Henrys et al., 2003). The volcanic and tectonic features within the TVZ are aligned in an south-south-west to north-north-east direction extending from Mt. Ruapehu in the South to Whakaari (White Island) in the North. Active spreading, subvolcanic rifting and widening occurs constantly in this region (Figure 1.2) (Wilson et al., 1995) and the constant crustal deformation generates a thinner crust underneath the TVZ with the offset of the MOHO by 7-10 km) (Turner & Hurst, 2001).

The TVZ is one of the most productive magmatic systems in the world (Stern, 1987; Wilson et al., 1995) with andesitic volcanic activity beginning c. 2 Ma in the central TVZ (Wilson, 1993; B. Houghton et al., 1995; Wilson et al., 1995; Wilson, 2001). A total of over 20,000 km^3 of rhyolitic volcanic material has been erupted over a 1.6 Myr period, mainly from ignimbrites in caldera-forming events (B. F. Houghton et al., 1995; Allan et al., 2008). The northern and southern extremities of the TVZ are dominated by active andesitic stratovolcanoes (Cole et al., 1986; Houghton & Nairn, 1991; Donoghue & Neall, 1996; Price et al., 2005). At the southern end of the TVZ is the Tongariro Volcanic Centre (TgVC) consisting of four major andesitic massifs, Kakaamea, Pihanga, Mt. Tongariro and Mt. Ruapehu, and several satellite cones (Cole, 1978). Volcanism from Mts. Tongariro and Ruapehu is believed to have started c. 340 ka (Gamble et al., 2003) with dates from the oldest exposed lava flows on Mt. Tongariro being K-Ar dated at 230 to 273 ka (Patterson & Graham, 1988; Hobden et al., 1996). Mt. Ruapehu's oldest exposed lavas (Te Herenga Formation) in the Whakapapa gorge date to at least 300 ka (Tanaka et al., 1997). Andesitic clasts found within the O'Leary Conglomerate near Wanganui indicate an age of < 310 ka (Fleming & Survey, 1953; Pillans, 1990; Bussell & Pillans, 1992).

The TVZ is defined by three periods of volcanic activity (Wilson et al., 1995). Activity between 2 Ma to 340 ka is classed as the old TVZ, 340 to 65 ka represents the young TVZ and activity since 65 ka is the modern TVZ (Wilson et al., 1995).

Within the TVZ, andesite volcanism started at approximately 2 Ma, and rhyolitic activity began at 1.6 Ma (Wilson et al., 1995). The TVZ is considered to belong to a migrating arc, which has been active for over 20 Ma (Stern, 1985, 1987; J. W. Cole et al., 1995). The active front of the volcanic arc is believed to have been migrating south-eastward at a rate of c. 20 mm/yr. (Smith & Fritz, 1989; J. W. Cole et al., 1995). The western most expression of subduction related volcanism within New Zealand is the Taranaki Volcanic Lineament situated within the Taranaki Basin, located 140 km west of the TVZ (Adams & Ware, 1977; Reyners, 1983; Price et al., 1999).

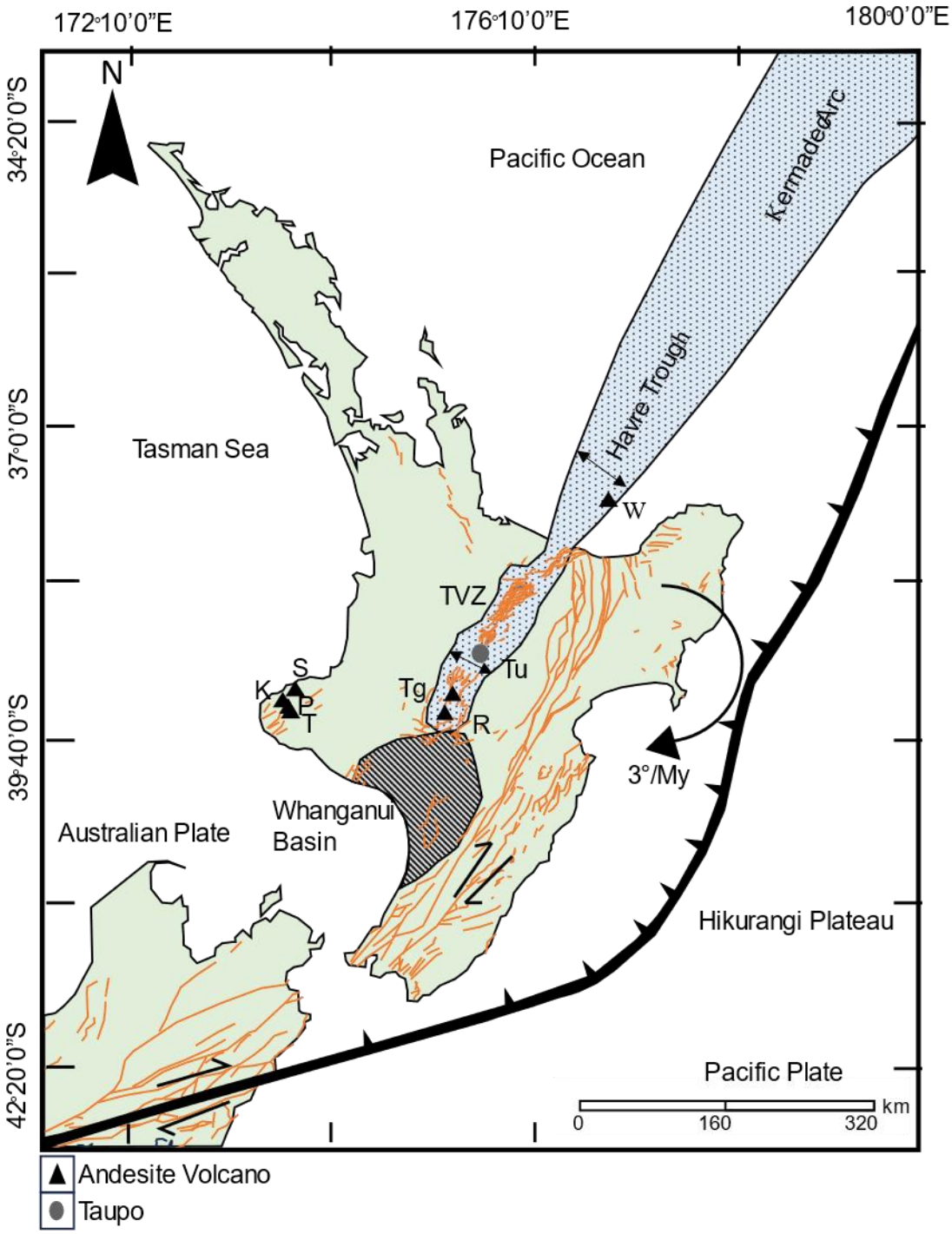


Figure 1.2: Northern New Zealand's current tectonic setting showing the Taupo volcanic zone and Taranaki Volcano. The rotation of the eastern North Island is shown covering 3 Ma to present (Wallace et al., 2004). Volcanoes shown include Tu – Taupo, Tg – Tongariro, R – Ruapehu, T – Taranaki, P – Pouakai, K – Kaitake and S – Paritutu and

sugar loaf islands. To the South of Mt. Ruapehu is the Whanganui Basin. Major faulting is indicated in orange. Modified from Wilson and Rowland (2016); Heinrich (2020).

1.6 Geology of the Taranaki Peninsula

The Taranaki Basin is a large sedimentary basin located along the western side of New Zealand (Thrasher, 1992). The formation of the Taranaki Basin is associated with extension of the breakup of Gondwanaland and the seafloor spreading within the Tasman Sea (Figure 1.3) (Clayton, 2017).

The basin is bounded to the East by the Taranaki Fault, a reverse late-Paleogene (66-23 Ma) to Neogene (23-2.58 Ma) fault that vertically offsets the basement by > 5 km (Figure 1.3) (Thrasher, 1992; Clayton, 2017). To the West of the Taranaki Basin, gradual shallowing of the basement leads into an oceanic bathymetric high, the Challenger Plateau (Thrasher, 1992). Sediments are rich in oil and gas reserves and on average are 6 km thick, however, can be up to 9 km thick (King & Thrasher, 1996). The sequences within the sedimentary basin provide a record of regional transgression comprising silt, mudstone, sand, and intercalated shell beds that indicate higher eustatic sea-level cycles (Kamp et al., 2004).

The Taranaki Basin began as a Late Cretaceous (100–66 Ma) transcurrent rift along the Gondwanaland margin (Thrasher, 1992). During the Late Oligocene (28.5-23.8 Ma), post-rift tectonic activity occurred, increasing the subsidence of the eastern sector of the basin (King et al., 1992; Thrasher, 1992). The eastern margin of the basin was generated as the fault overthrust basin sediments throughout the Miocene (23–5.33 Ma) (Thrasher, 1992).

Subsidence in the North and South Taranaki grabens generated through back-arc rifting resulted in a complicated pattern of erosion, uplift and progradation within the Taranaki Basin (Thrasher, 1992).

The formation of the Taranaki Basin began during the late Cretaceous (100 – 66 Ma) with rifting and transgression generating the Pakawau Group, made up of terrestrial marine sedimentary rocks (Thrasher, 1992). The basin contains normal faults, which trend north to northeast dipping both east and west (Clayton, 2017), with displacement varying from hundreds of meters to kilometres (Clayton, 2017). Across the eastern and central section of the basin normal faults were reactivated generating inversion structures. A transgressive sequence of depositional material was generated during the Paleocene (66–56 Ma) and Eocene (56–33.9 Ma) as a response to post-rift subsidence (Thrasher, 1992). Producing the terrestrial Kapuni Group and the marine Moa Group (Thrasher, 1992). By the end of the Eocene (56–33.9 Ma) the majority of the Taranaki basin was covered by the fine-grained Moa Group sediments. Continued movement within the Taranaki basin during the Oligocene (33.9–23 Ma) generated the Ngatoro Group Carbonates through inundation and deposition related to tectonic subsidence (Thrasher, 1992). This subsidence resulted in the majority of the basin being submerged throughout this time period. The deposits from the Ngatoro Group are thicker along the eastern section

of the basin due to the deposition of coarse shelf carbonates (Thrasher, 1992). The late Miocene (10.4-5 Ma) through to present within the Taranaki basin was characterised by the Wai-iti groups marine terrigenous deposits. Underlying this is the Rotokare Group which represents the past 5 million years forming a thick fine-grained rock sequence across the Taranaki Basin (Thrasher, 1992). The Rotokare group has a higher sedimentation rate than the Wai-iti group and can be over 2 km thick (Thrasher, 1992). There is a widespread unconformity which separates the Wai-iti and Rotokare Groups. Throughout the late Miocene until present the Taranaki basin has gone through little deformation (Clayton, 2017). Volcanism began in the northern part of the basin approximately 16 Ma and is comprised of buried subvolcanic stratovolcanoes situated offshore from the Taranaki Peninsula (Knox, 1982; Neall et al., 1986; Hayward et al., 1987; Thrasher & Cahill, 1990; Bergman S, 1992; King et al., 1992; Herzer, 1995; Giba et al., 2010). The Taranaki Volcanic Lineament displays the youngest on land expression of this volcanic activity with continued activity today with Mt. Taranaki (Neall et al., 1986; Giba et al., 2010).

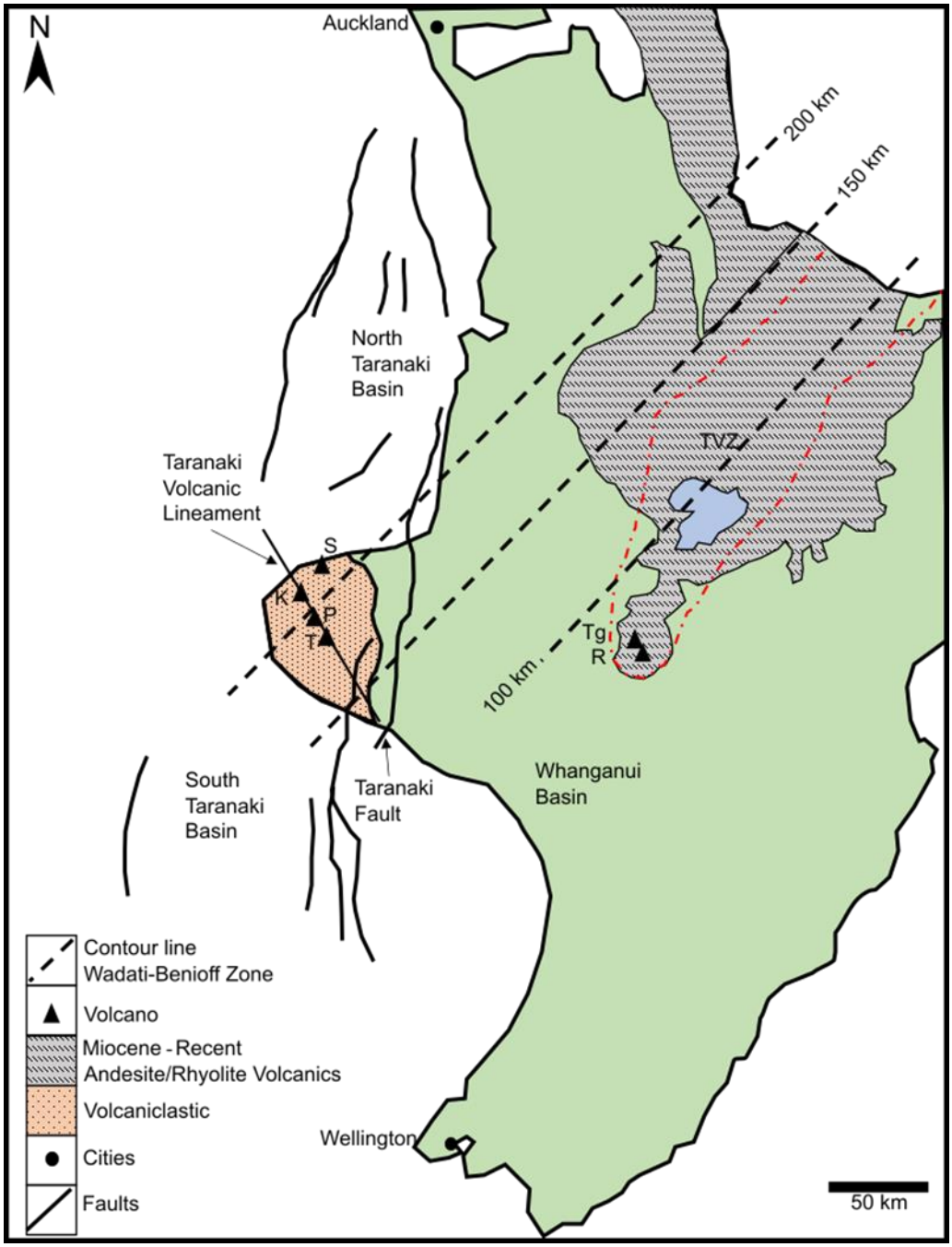


Figure 1.3: Geological map of the North Island of New Zealand showing the Taranaki Basin and the Taranaki Volcanic Lineament made up of Mt. Taranaki (T), Pouakai Volcano (P) and Kaitake Volcano (K), the Sugar Loaf Islands and Paritutu (S) may also be part of the lineament. The Taupo Volcanic Zone (TVZ) Mt. Ruapehu (R) and Mt. Tongariro (Tg) are located to the east at the southern end of the TVZ. Contour lines show the depths of the Wadati-Benioff Zone (Adams & Ware, 1977), modified from Price et al. (1999).

The southern section of the Taranaki Basin provides a gradual transition into the ridges and basins of the north-western South Island. The northern part of the basin is geologically continuous to the

Northland Basin (King & Thrasher, 1996; Coleman, 2018). To the northwest, the basin descends into the Deepwater Taranaki Basin before it grades into the Caledonia Basin (Coleman, 2018).

The Cape Egmont Fault Zone (CEFZ) is a 53 km long 1-5 m high east-facing scarp expressed along the seafloor. The Cape Egmont Fault has been moving over the last 225 kyr with an average slip rate of 0.8 mm/yr (Nodder, 1993). The CEFZ marks the western edge of deformation on the convergent plate boundary, dividing the Taranaki Basin into two structural regions: a tectonically active mobile belt in the East and a passive stable platform on the western side (King, 1991; King & Thrasher, 1996). The two sections of the Taranaki Basin are connected to each other by the Median Tectonic Zone (MTZ) (Kroeger et al., 2013; Coleman, 2018). A large percentage of the MTZ is made up of plutonic rocks (Calc-alkaline gradioritic and diariticic) belonging to the Median Batholith the potential source of some phenocrysts observed in the volcanic lithologies of Taranaki (Kroeger et al., 2013; Coleman, 2018). The Taranaki Peninsula represents the largest onshore section of the Taranaki Basin (King & Thrasher, 1996; Zernack, 2008).

The present-day stress field differs from the orientation of the CEFZ and is indicated by the volcanic vent alignments (Neall, 1971; Sherburn & White, 2006), which typically form perpendicular to the direction of extension (Nakamura, 1977). The migration of the Taranaki Volcanic Lineament from north-north-west to south-south-east, as well as the north to south alignment of the Mt. Taranaki summit, Panitahi (Fanthams Peak) and lava domes indicate the location of the current stress field (Neall, 1971; Sherburn & White, 2006).

1.7 Taranaki Volcanic Lineament (TVL)

The Taranaki Volcanic Lineament (TVL) is situated within the Taranaki Basin about 400 km to the west of the Hikurangi Trench and consists of four high to medium k andesite volcanic edifices (Figure 1.3) (Adams & Ware, 1977; Neall et al., 1986; Stewart et al., 1996; Price et al., 1999; Zernack et al., 2012a; Price et al., 2021). These four volcanic centres are aligned in an north-north-west to south-south-east trend younging to the south-south-east and are parallel to the Benioff zone representing the western most expression of the Hikurangi subduction system (Hatherton, 1969; Adams & Ware, 1977; Neall et al., 1986; Locke et al., 1994; Alloway et al., 1995; Higgins, 1996; Stewart et al., 1996; Boddington et al., 2004; Reyners et al., 2006; Reyners et al., 2011; Gaylord et al., 2014). To the North of the Taranaki Basin, the Alexandra Volcanics (AV) in the western Waikato region have been interpreted as a older analogue for the TVL (Briggs, 1986; Briggs & McDonough, 1990; Price et al., 2021). The AV is perpendicular to the axis of the TVZ dated at 1.6 to 2.7 Ma (Briggs, 1986; Briggs & McDonough, 1990; Price et al., 2021). The youngest rocks in the AV overlap with the oldest rocks from the TVL (Briggs, 1986; Briggs & McDonough, 1990; Price et al., 2021). The oldest volcano in the TVL is Paritutu (Sugar loaf) volcano which is dated at 1.75 Ma and represented by the heavily eroded offshore islands and onshore Paritutu rock (Grant-Taylor, 1964; Neall, 1979). The next youngest is Kaitake Volcano dated

at 0.57 Ma, next to this is Pouakai Volcano with an age of 0.25 Ma, the end of activity at Pouakai is associated with an edifice collapse event producing the Maitahi Formation (Gaylord et al., 1993; Neall, 2003; Zernack et al., 2011; Price et al., 2021). The youngest volcano within the TVL Mt. Taranaki with a date of > 200 ka and its parasitic cone Panitahi (Fanthams Peak) is the only active centre within the TVL. The three youngest volcanoes show different stages of erosion that reflect the different lengths of time since they became extinct (Kaitake and Pouakai Volcanoes) or dormant, in the case of Mt. Taranaki (Neall, 1979).

These volcanic centres within the TVL have predominantly produced basaltic andesites and andesites commonly containing amphiboles and on rare occasions erupting basalts and dacites (Price et al., 2021). There are multiple hypothesis around the generation of magma across the lineament.

1.) Edge effects along the present-day subducting system, where asthenospheric mantle flowing around the subducting slab inducing adiabatic melting (Jacoby, 1973).

2.) Propagating tears and/or fractures along the subducting slab resulting in fluid loss (Price et al., 1992; Price et al., 1999), with seismic data indicating segmentations of the subducting slab beneath the North Island along a series of fractures orthogonal to the Hikurangi Trench (Reyners, 1983; Price et al., 1992; Price et al., 1999; Price et al., 2021).

3.) An alternative hypothesis involves the dehydration of foundering mantle lithosphere with lateral mantle inflow from the northwest (Reyners et al., 2006; Stern et al., 2006; Price et al., 2016). Between Mts. Ruapehu and Taranaki, a transition in crustal thickness occurs with an increase from ~25 km in the north and west to ~35 km to the south and east (Salmon et al., 2011). This transition does not have a topographic expression (Salmon et al., 2011) but is interpreted to reflect the delamination and decent of the lithospheric mantle and lower crust from beneath the western North Island, generating a compensating flow of low-density mantle from the northwest (Stern et al., 2006; Salmon et al., 2011; Stern et al., 2013; Dimech et al., 2017).

1.8 Mt. Taranaki

Mt. Taranaki (2518 m) is the youngest volcano within the Taranaki Volcanic lineament, activity was previously assumed to have started approximately 130 ka based on the estimated age of the Motunui DAD (Neall et al., 1986; Alloway et al., 2005). However, the identification of an even older Mt. Taranaki sourced DAD, the Mangati Formation, suggests an inception of volcanism for this centre prior to 200 ka (Zernack et al., 2011) (Figure 1.4).

The older volcanic record for Mt. Taranaki is preserved in the surrounding ring plain, which comprises > 150 km^3 of volcaniclastics, pyroclastic flows, tephra fall, debris avalanche, lahars, and fluvial deposits (Neall et al., 1986; Palmer & Neall, 1991; Alloway et al., 2005; Zernack et al., 2011; Zernack, 2021),

providing insights into the growth and collapse cycles which have occurred throughout the volcano's evolution (Zernack et al., 2011; Zernack, 2021). Compared to the surrounding ring plain the < 10 ka present day edifice above 1400 m elevation has a volume of ~12 km^3 and is dominated by andesitic lava flows (Downey et al., 1994; Procter et al., 2009; Zernack et al., 2012b). The ring plain is volumetrically dominated by debris-avalanche deposits (DADs), with fourteen major collapses having occurred within Mt. Taranaki's history, the most recent occurring 7.5 ka creating the Opua Formation (Zernack et al., 2011). Within the last 30 ka there have been four edifice collapse events including two of the largest events: the Pungarehu Formation (7.5 km^3) at c. 24.8 ka and the Ngaere Formation (5.85 km^3) at c. 27.3 ka (Neall, 1979; Ui et al., 1986b; Zernack et al., 2011). The oldest stratigraphic sequence for Mt. Taranaki is best preserved within coastal sequences where paleosols, lahars and tephra falls are intercalated with debris-avalanche deposits, recording the last 200 ka of activity from Mt. Taranaki (Neall, 1972; Zernack et al., 2011; Zemeny et al., 2021).

The younger ring plain record < 30 ka provides the most complete eruptive history for Mt. Taranaki with tephra layers found predominantly in the northeastern to southeastern sector of the ring plain downwind from Mt Taranaki's summit vent (Alloway et al., 1995; Turner et al., 2009; Damaschke et al., 2017b). More than sixteen tephra formations comprising at least 228 individual eruptions as identified by Alloway et al. (1995); Damaschke et al. (2017b); Torres-Orozco et al. (2017a); Torres-Orozco et al. (2017b) have been recorded within the stratigraphic record.

The present-day edifice (c. 10, 000 years old; Neall et al. (1986)), is comprised of lava flows, scoria, pyroclastic flows, and tephra fall deposits (Alloway et al., 1995). However, the preserved record is incomplete due to weathering, erosion, rapid burial of material by subsequent eruptions and the complete removal of large stratigraphic sequences through secondary remobilization events triggering volcanic mass flows (Alloway et al., 1995). On the present-day edifice there are two vents, the summit vent which contains a lava dome produced during the final eruptive period 1790 CE (Platz et al., 2012; Damaschke et al., 2017b; Lerner et al., 2019a), and Panitahi (Fanthams Peak) (1966 m) a parasitic cone ~ 1.5 km due south of the main summit vent, creating a north to south axis between the two summits (Neall et al., 1986; Turner et al., 2008b; Cronin et al., 2021). Panitahi (Fanthams Peak) is believed to be approximately 7 ka, with eruptions known to have occurred from the vent between 3 and 1.2 ka (Neall, 1972; Turner et al., 2008b; Torres-Orozco et al., 2017a; Torres-Orozco et al., 2017b). The majority of Holocene activity has occurred from the summit vent or Panitahi (Fanthams Peak) with the exception of four isolated lava domes (Neall et al., 1986; Stewart et al., 1996; Torres-Orozco et al., 2017a; Torres-Orozco et al., 2017b; Lerner et al., 2019d; Cronin et al., 2021). These lava domes formed on the lower flanks of Taranaki, controlled by radial faults extending from the summit (Neall et al., 1986; Stewart et al., 1996; Torres-Orozco et al., 2017a; Torres-Orozco et al., 2017b; Lerner et al., 2019d; Cronin et al., 2021). On the upper flanks of Mt. Taranaki there has been two main periods of lava flow production from the summit vent and Panitahi (Fanthams Peak) indicated by palaeomagnetism between

7 ka and 2.8 ka and 700 and 400 years ago, with the younger flows being associated with the main summit vent (Lerner et al., 2019d). The last 1000 years of activity from Mt. Taranaki created a pyroclastic fan on the north-western flank which was built up during the Maero eruptive period. This eruptive period occurred following a 480-year quiescence following eruptions from Mt. Taranaki's Panitahi (Fanthams Peak) (Torres-Orozco et al., 2017a; Lerner et al., 2019a) and consisted of large explosive eruptions, explosive collapses of hot lava domes, block and ash flows and minor ash eruptions (Lerner et al., 2019a). There are over fifty streams on the present-day cone which deeply incise into the flanks radially draining away and eroding material (Grant-Taylor, 1964; Davies & Lambert, 2015).

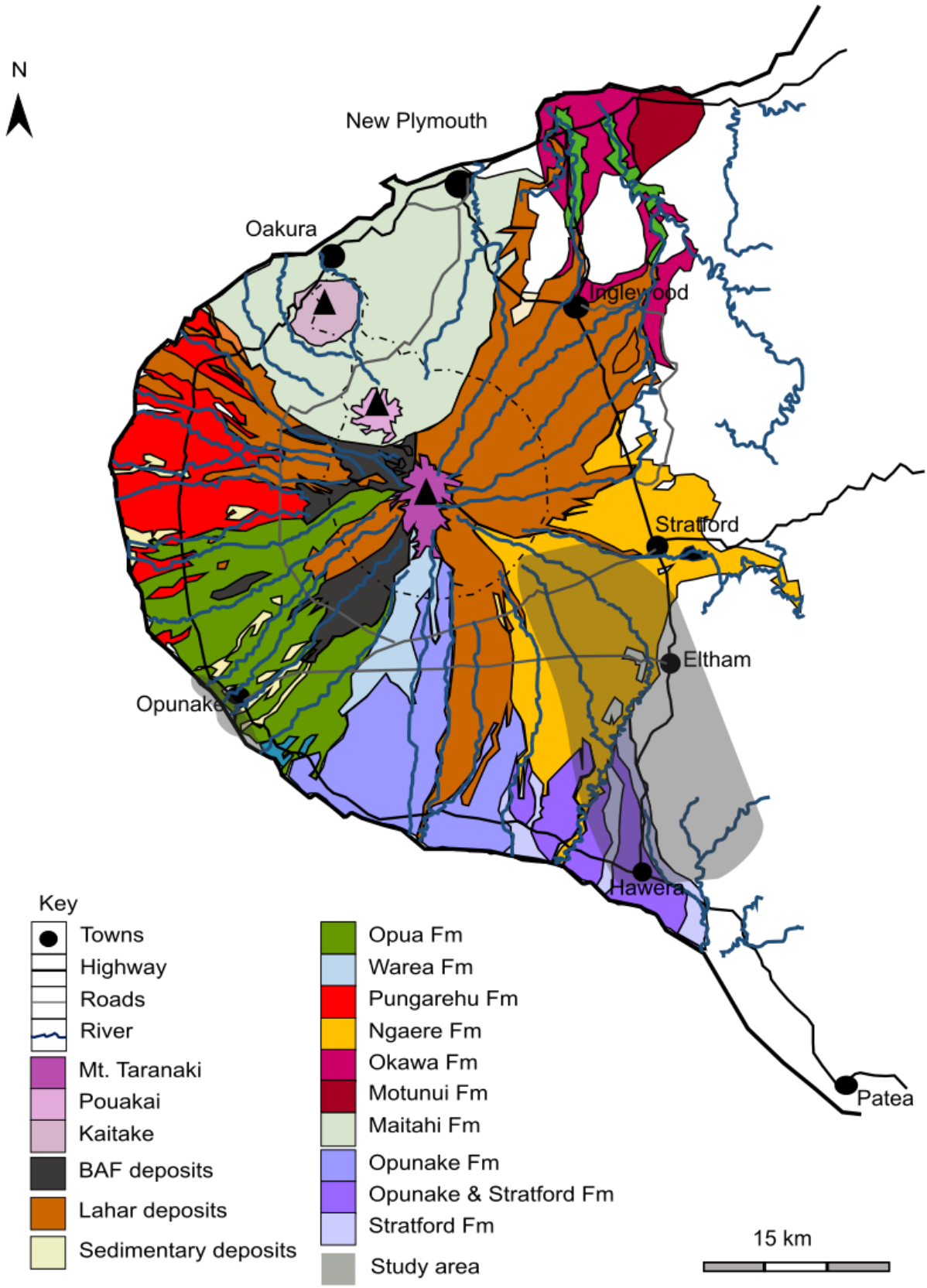


Figure 1.4: Geological map of the Quaternary ring plain succession of Mt. Taranaki (after Neall and Alloway, 2004), showing the location of the Taranaki Volcanic Lineament massifs, Kaitake, Pouakai and Taranaki. Identified

distributions of debris-avalanche, block and ash flow, lahars and sedimentary deposits across the Taranaki ring plain including the location of the study areas in the eastern, southeastern, and southwestern sectors of the ring plain modified from Zernack et al. (2011).

1.8.1 Previous tephrastratigraphy of Mt. Taranaki

The first age constraint on historic eruptions from Mt. Taranaki was from A.W. Burrell (1883) (Oliver, 1931; Druce, 1966), who found pumice fragments in the forks of a Matai (Podocarpus Spicatus) tree, indicating that the last eruption had occurred within the past few hundred years (Druce, 1966). Skeet (1901) referenced ash and lapilli layers interbedded with paleosol layers across the Taranaki ring plain (Druce, 1966). Charcoal within buried Māori ovens discovered near Stratford Mountain house underneath 15 inches of pumice and ash were dated and provided ages of 400 ± 60 yr BP and 360 ± 60 yr BP (Oliver, 1931; Fergusson, 1957). Tree ring dating by Burrell of Matai trees in the region provides a similar age estimate of 1430 CE, for this deposit now formally known as the Burrell Lapilli (Oliver, 1931). Further dendrochronological analysis of Kaikawaka (Libocedrus bidwillii) trees provided the most commonly used age of the Burrell eruption as 1655 CE (Druce, 1966). The work done by Oliver (1931) around Taranaki may be the first example of tephrochronology in New Zealand (Lowe, 1990). Early surveys of soil and peat around the Taranaki region by (Taylor, 1954) refers to the ash layers found around the mountain including the occurrence of the Newall ash which was first recognized by Grange and Taylor (1933); Gibbs, pers. Comm Druce (1966). Vegetation survey work from 1959-1964 around the "Egmont National Park" identified separate beds describing three individual layers within the previously identified Burrell ash and four layers within the previously identified Newall ash (Druce, 1966). Field mapping of intercalated tephra and paleosol layers around the mountain found that the thickness and depths of ash and lapilli beds had a natural variation due to the influence from trees and shrubs, along with redistribution from rain and wind (Druce, 1966).

The first tephrochronology studies around Mt. Taranaki focused on the younger < 500-year eruptive record, from the Newall formation to the Tahurangi Formation (Oliver, 1931; Taylor, 1954; Druce, 1966). In the 1930's Grange and Taylor identified two tephra falls within the Taranaki ring plain mapping the Stratford ash in the east which overlaid the Egmont ash dispersed from north to south-east (Grange & Taylor, 1933; Alloway et al., 1995). Studies by Wellman (1962) along the northern coastline identified multiple andesitic tephra layers which correlated to the Burrell Lapilli (Oliver, 1931); Newall Ash and Stratford Ash (Taylor, 1954). Beneath these three more tephra groups were identified as the Stent ash and two into the Onaero group (Wellman, 1962). The youngest < 500 years of explosive activity was further mapped out by Druce (1966), who identified nine layers including the Newall ash, Newall lapilli, Waiweranui lapilli, Waiweranui ash, Burrell ash, Burrell Lapilli, Puniho lapilli 1, Puniho

lapilli 2 and Tahurangi ash. The age of the Tahurangi eruption was calculated at 1755 CE through analysis of the peat accumulation between the present-day soil and the Burrell Lapilli by Druce (1966).

Panitahi (Fanthams Peak) was thought to be the youngest eruptive vent from Mt. Taranaki however, isopach mapping by Tonkin (1970) indicated that this is not the case, and the most recent eruptions occurred from the present-day summit crater. Studies by Tonkin (1970), focused on the Dawson Falls and Mountain House sector of the ring plain looking at how the three tephra formations identified by Druce (1966) 1). Tahurangi Formation (1755 CE), 2). Burrell Formation (1655 CE), and 3). Newall Formation (Prior to 1604 CE) influenced the production of soil across Taranaki. The soils indicate an interbedded system with preserved tephra layers providing a record of the eruptive history of Mt. Taranaki (Tonkin, 1970). The dispersal pattern and depositional characteristics of the Burrell lapilli was further analysed through (Topping, 1972). Cronin et al. (2003) classified activity at Mt. Taranaki from 1040 CE to present as the Maero Eruptive Period.

A more detailed investigation into the tephrastratigraphy of Mt. Taranaki was conducted by Neall (1972) across western Taranaki region. A region encompassing Okato to Inglewood and north to New Plymouth was examined and described to correlate depositional units across the ring plain and to determine a frequency of eruptions which had occurred at Mt. Taranaki. From this work a frequency of one small eruption on average at least every 500 years was determined for the older tephrostratigraphic sequence and one every 150 years for the younger sequence related to the preservation of the younger eruptive units within the stratigraphy (Neall, 1972). Tephra records from this study across the north-western flanks of Mt. Taranaki were deposited over the last 100 ka, including the newly identified Inglewood (P2 Druce, 1966), Korito (P1 Druce, 1966), Carrington, Koru, Pukeiti and Weld tephra formations which were identified within the stratigraphy. The previously identified Egmont showers (Grange & Taylor, 1933) were split and renamed as two separate units 1). Oakura Tephra (~6970±76 yr BP) and 2). Okato tephra and Ahuahu lapilli (c. 14,000 yr BP). This layer is underlain by the Saunders ash (16,100 ± 220 yr BP) which is confined to a small sector around Saunders Road in northwestern Taranaki and considered to be a pyroclastic flow unit (Neall, 1972). The Carrington tephra formation is situated below the Saunders ash and is made up of nine localized tephra units which are confined to a small region and therefore not assigned specific formations (Neall, 1972). The Koru tephra below is made up of two units and is found in deposits covering Okato to Inglewood, the lower Koru lapilli is a key marker horizon within the north-western stratigraphy (Neall, 1972).

Whitehead (1976) informally named the Manganui (3200 yr BP) and Kaupokanui (1200 yr BP) tephras (P4 Druce, 1966; Tonkin, 1970) generating isopach maps for correlated layers. The Manganui tephra isopachs indicate that the source vent for these eruptions was Panitahi (Fanthams Peak) rather than the main summit cone (Whitehead, 1976). Work on the paleosols and tephrastratigraphy of central Taranaki by Franks (1984) identified a number of prominent tephra layers within the eastern ring plain of

Taranaki below the Manganui tephra which includes the informally named Maketawa (McGlone et al., 1988); Mahoe (oldest), 1 (Konini; Alloway et al., 1995) (1), E2 (Kaponga; Alloway et al., 1995), E3 (Waipuku; Alloway et al., 1995), E4 (Tariki; Alloway et al., 1995), and E5 (Mangatoki; Alloway et al., 1995) tephras which were correlated to the previously defined Oakura and Okato Tephra Formations of (Neall, 1972). Franks (1984) also mapped the locations of the 25.6 ka Aokautere (Kawakawa-Oruanui) ash across the Taranaki ring-plain an important rhyolitic marker layer present within the stratigraphy. These initial studies across the ring plain form the basis for Alloway et al. (1995) which provides a comprehensive record of the past 28 ka across the northeastern and central ring plain of Taranaki.

Alloway et al. (1995) provides the most complete record of tephrastratigraphy over the past 28 ka recorded in the northeastern and central Taranaki ring plain. Sixteen Taranaki Formations across at least 76 tephra events were recorded with volumes which exceed 10^7 m^3 producing an eruptive record of one event every c. 330 years, this is viewed as a minimum recurrence rate due to the absence of smaller eruptions preserved within the stratigraphic sequence (Lowe, 1986; Alloway et al., 1995). This is comparative to Turner et al., (2008b); Turner et al., (2009) who examined the last c. 9.5 ka of eruptive history from Mt. Taranaki looking at 123 events providing a probability of 0.37-0.48 for a new eruption to occur in the next 50 years, and the last < 5 ka by (Torres-Orozco et al., 2018) showed a recurrence rate of 300 years for large subplinian to plinian eruptions.

The identified formations by Alloway et al. (1995) within the ring-plain (Table 1.2) are broken down into three broad sequences according to major variations within the morphology and minerology of inter-bedded andic soils. The upper tephra sequence includes the Manganui (c. 3.1 ka) to Mahoe tephras (c. 11.0 – 11.4 ka); the upper section of the lower tephra sequence includes the Kaihouri (c. 12.9 – 18.8 ka) to Poto tephras (c. 20.9 – 22.7 ka) and the lower section of the lower sequence including the Tuikonga (c. 23.4 – 24.0 ka) to Waitepuku tephras (c. 27.5 - 28 ka) (Alloway et al., 1995). These tephra formations predominantly cover the north-north-east to the south-south-east sectors of the ring plain. Alloway et al. (1995) also described two silicic tephra beds within the stratigraphy which are used as marker bed layers and improve the correlations between sites across the ring plain. The younger Stent tephra (Wellman, 1962; Alloway & Neall, 1994) provides a late Holocene correlation intercalated with paleosols and tephras from the andesitic Mt. Taranaki and the older Aokautere Ash (Kawakawa-Oruanui tephra) (Froggatt & Lowe, 1990) is interbedded within Pleistocene aged deposits sitting within the Poto Formation sequence across the central Taranaki ring plain (Alloway et al., 1995). The Aokautere Ash (Kawakawa-Oruanui tephra) first identified in Taranaki by J.F. Aitken in 1971 is a comparatively thick (up to 10 cm) thick yellowy fine ash layer which is easily identifiable in field deposits (Geddes et al., 1981; Franks, 1984; Alloway et al., 1995).

The Poto and Paetahi tephra formations identified by (Alloway et al., 1995) within the upper lower tephra sequence, preserved in the eastern stratigraphy are made up of 21 individual depositional ash and

lapilli fall units which are interbedded with paleosol layers. The Poto Formation was originally identified by (Alloway et al., 1995) in central Taranaki as a closely interbedded sequence of 15 ash and lapilli fall units which sits above the 23.4 – 24.0 ka Tuikonga Formation. The formation named after Poto Road, which joins Opunake Road between Cardiff and Mahoe dated at c. 20.9 to 22.7 ka intercalates the Aokautere ash (Kawakawa-Oruanui) between layers Poto.e and f and the Ngaere debris-avalanche deposit between Poto.b and c (Alloway et al., 1995). The Paetahi formation (c. 19.4 to 20.2 ka) is situated above the Poto Formation and is separated by a prevalent paleosol layer which defined the end of the Poto Formation and the start of the Paetahi Formation (Alloway et al., 1995). Six ash and lapilli fall units make up the Paetahi tephra formation sequence named after Paetahi Stream near Stratford (Alloway et al., 1995). Paetahi.a is the coarsest unit within the formation and the most widely distributed unit across the central to southeast Taranaki ring plain (Alloway et al., 1995). The Paetahi Formation underlies the 12.9 – 18.8 ka Kaihouri tephra formation separated by a 15 cm paleosol (Alloway et al., 1995).

Table 1.2: Tephra stratigraphic and debris-avalanche deposits from Mt. Taranaki with calibrate ages. Age references as followed: (a) (Platz, 2007); (b) (Druce, 1966); (c) (Grant-Taylor & Rafter, 1971); (d) (Grant-Taylor & Rafter, 1963); (e) (Cronin et al., 2003); (f) (Turner et al., 2008b); (g) (Topping, 1974); (h) (Neall & Jansen, 1984); (i) (Alloway et al., 1995); (j) (Torres-Orozco et al., 2017a); (k) (Vandergoes et al., 2013); (l) (Zernack et al., 2011); (Damaschke et al., 2017b).

Age Cal. Age (ka)	DAD	Tephra	No. of eruptive units in the formation	Age Ref
1860 CE		Pyramid	1	a
1755 CE		Tahurangi	2	b
1465-1583 CE		Burrell	2	d
346 +/_ 73		Puniho	2	e, f
1390-1520 CE		Waiweranui	2	e, f
431 +/_62 CE		Newall	2	c
1438 CE		Waingongoro	1	g
1173 CE		Hooker	1	e, f
1.3		Kaupokonui	1	h
3.1		Manganui	7	i
3.6		Inglewood	10	i
3.5-3.8		Kapuni	6	j
4.1		Korito	9	i

4.4		Mangatoki	2	i
4.6-4.7		Kokowai	8	j
4.6 – 4.7		Tariki	6	i
5.2		Waipuku	1	i
7.5	Opua			l
8 – 10		Kaponga	10	i
10.1		Konini	2	i
11 – 11.4		Mahoe	4	i
12.9 – 18.8		Kaihouri	8	i
c. 14	Motumate			l
24.1 – 23.1		Paetahi	6	i, l
24.8	Pungarehu			l
25.4		Kawakawa Oruanui		k
27.3 – 25		Poto	15	i, l
27.3	Ngaere			l
28.7 – 28.1		Tuikonga	4	i, l
30.4 29.7		Koru	2	i, l
31.4		Pukeiti	1	i, l
33.4 – 33.3		Waitepuke	3	i, l
34	Te Namu			l
c. 40 – 45	Rama			l
c. 45.1		Rotoehu		l
c. 50 – 55	Otakeho			l
c. 60	Tokaora			l
c. 70	Waihi			l
c. 75	Waingongoro			l
c. 85 – 90	Oeo			l
100 – 80		Epiha		l
c. 105	Okawa			l
c. 115 – 105		Ninia		l
> 130	Motunui			l
c. 200	Mangati			l

Previous work on peat cores across the Taranaki region has been completed by McGlone and Neall (1994) and Damaschke et al. (2017b), identifying andesitic and silicic tephras within the cores. Early vegetation studies by (McGlone & Neall, 1994) within the Eltham Swamp c. 25 km southeast of Mt. Taranaki identified five tephra layers within the core which correlated to the Burrell Lapilli, Kaupokanui Tephra, Manganui Tephra, Inglewood Tephra and Korito Tephra. A more detailed investigation by Damaschke et al. (2017b) studied 11 sediment cores from swamps across the Taranaki ring plain which provided a new composite tephrostratigraphic record building on previous work by Druce (1966); Neall (1972) and Alloway et al. (1995), encompassing at least 228 tephra eruptions over the last 30 ka.

Correlations between cores was conducted allowing for the overall 30 ka eruption record to be divided into six tephra sequences (A-F) (Damaschke et al., 2017b). The six tephra sequences are subdivided by geochemically and stratigraphically distinct features which are characterized by their dominant titanomagnetite group (Damaschke et al., 2017b). The tephra sequences are traceable across all of the different cores and is divided up with tephra sequence F (30-23.5 cal ka BP), E (17.5-14 cal ka BP), D (14-19.5 cal ka BP), C (9.5-4 cal ka BP), B (4-3 cal ka BP) and A (3-0.5 cal ka BP) (Damaschke et al., 2017b). Tephra sequence F which contains the rhyolitic Aokautere Ash (Kawakawa-Oruanui tephra) and some of the Poto Formation layers are only represented within the Eltham Swamp core (Damaschke et al., 2017b). Tephra deposits from Mt. Taranaki have also been found in lake deposits across different regions of the North Island of New Zealand i.e., c. 200 km to the north-north-east in the Waikato Lakes, Hamilton (Lowe, 1988); c. 250 km East in the Hawkes Bay (Eden et al., 1993); > 270 km north to northwest in Lake Pupuke, Onepoto and Orakei Basins, Hopua Crater and Pukaki Lagon, in Auckland (Sandiford et al., 2001; Shane & Hoverd, 2002; Shane, 2005; Molloy et al., 2009). Lake deposits from within the region and further away are important for understanding the small and large-scale eruptions which occurred from Mt. Taranaki providing a sequence of continuous sedimentation which is useful for determining the eruption frequency occurred at Mt. Taranaki throughout its evolution (Damaschke et al., 2017b).

Recent studies on the last ~ 5 ka from Mt. Taranaki by Torres-Orozco et al. (2017a, 2017b) identified at least 53 eruptive episodes having occurred from either the summit crater or Panitahi (Fanthams Peak). Within this time period Mt. Taranaki has experienced at least 16 large explosive subplinian to plinian eruptions including within the c. 4.7 – 4.6 ka Kokowai; 3.3 ka upper Inglewood; 2.6 ka Manganui D; 1.2 ka Kaupokanui Formations and the 1655 CE Burrell Lapilli (Table 1.3) (Torres-Orozco et al., 2017a; Torres-Orozco et al., 2017b). The Kokowai 4 and Upper Inglewood 7 units represent the largest volume and highest energy eruptions studied at Mt. Taranaki from the main summit vent with Kokowai 7 and the Burrell Lapilli deposits producing smaller subplinian eruptions. Erupted fallout volumes ranged from 0.1 to 1.1 km^3 and had column heights of 12 to 29 km, the Kokowai 4 eruption had a magnitude of 5.1 with eruption columns comparable to Tarawera 1886 CE and Hatepe 186 CE (Bonadonna & Costa, 2013b; Torres-Orozco et al., 2017a; Torres-Orozco et al., 2017b). These large explosive eruptions

all occurred from Mt. Taranaki's summit vent and had multiple phases of different eruption styles associated with them including block and ash flow, lava dome effusion and pyroclastic density currents (Torres-Orozco et al., 2017a; Torres-Orozco et al., 2017b). Large explosive eruptions from Mt. Taranaki's parasitic cone Panitahi (Fanthams Peak) have also occurred throughout the volcano's evolution including the Manganui and Kaupokanui eruptive periods (Torres-Orozco et al., 2017a; Torres-Orozco et al., 2017b). The 1.3 ka Kaupokanui fall deposit was produced by a subplinian eruption with an eruption column 12 to 16 km high while the Manganui-D eruption produced a plinian eruption column 24 to 27 km high (Torres-Orozco et al., 2017a; Torres-Orozco et al., 2017b). The eruptive episodes of the Upper Inglewood and Manganui D were almost identical in magnitude, intensity, column height, and duration even though they erupted from two different vents (Torres-Orozco et al., 2017a; Torres-Orozco et al., 2017b).

Table 1.3: Selected Plinian/Subplinian eruptions from Mount Taranaki over the past 5 ka. Data sourced from (Torres-Orozco et al., 2017a; Torres-Orozco et al., 2017b, 2018).

Eruptive Episode	Age (Cal Yr B.P)	Column Height (km)	Min Vol (km^3)	MDR (kg/s)	Magnitude$^+$	Eruption Type
Burrell	300	14 – 17	0.10	1.3×10^7	4.1	Subplinian
Kaupokanui	1200	14 – 16	0.13	1.2×10^7	4.3	Subplinian
Manganui-D	2600	25 – 27	0.50	1.1×10^8	4.9	Plinian
Upper Inglewood	3300	22 – 24	0.30	7.6×10^7	4.7	Plinian
Kokowai 7	4700-4600	21 – 22	0.10	5.8×10^7	4.2	Subplinian
Kokowai 4	4700-4600	27 - 29	1.10	1.8×10^8	5.1	Plinian
$^+$ obtained from (Torres-Orozco et al., 2018), original data following (Pyle, 2000).						

In-depth studies into the eruptive dynamics and parameters of eruptions from Mt. Taranaki have primarily focused on the last 5 ka due to the poor preservation of proximal deposits for the older eruptive sequence. The > 5 ka sequence has typically been focused on the correlation of tephra units across the ring plain to better understand the eruptive frequency for Mt. Taranaki, rather than on the eruptive parameters and size of the older eruptive units. This has led to an over representation of large explosive eruptions within the younger Taranaki eruptive record.

1.9 Petrology and geochemistry of Mt. Taranaki

Magmas associated with Subduction zones originate within the mantle wedge above a subducting plate where fluids derived from the subducting slab metasomatize the mantle wedge, promoting partial melting by lowering the peridotite solidus (Gill, 1981; Annen et al., 2006; Blundy & Cashman, 2008; Price et al., 2016; Cashman et al., 2017). Slab dehydration increases the H_2O content within the magma (Nicholls & Ringwood, 1973; Ringwood, 1974; Hawkesworth et al., 1979; Tatsumi & Eggins, 1995; Schmidt & Poli, 1998; Ulmer, 2001; Grove et al., 2002; Zheng et al., 2016). Magmas derived from the mantle primarily interact in deep crustal "hot zones" with sub-arc lithosphere (Hildreth & Moorbath, 1988; Price et al., 2005; Annen et al., 2006; Reubi & Blundy, 2009). Primary magma compositions rarely erupted from continental arc volcanoes, a key challenge is determining the processes which occur in these "hot zones" through differentiation (Turner et al., 2003). No two volcanic systems are the same, this complicates the understanding around the relative importance of fractional crystallization, crystal melting and assimilation on the differentiation of the magma (Melekhova et al., 2017). These melts have complex storage and plumbing systems, characterised by a combination of processes which can influence fractional crystallization (FC; Bowen, 1928; Gill, 1981; Grove et al., 2003); magma mixing (Eichelberger, 1978; Clynne, 1999; Tepley et al., 2000), and assimilation fractional crystallization (AFC; Grove & Kinzler, 1986; Graham & Hackett, 1987). These multi-level plumbing and storage systems produce a mixture of melt and crystals derived from mixing a range of crustal and mantle sources (Figure 1.5) (Davidson et al., 2005).

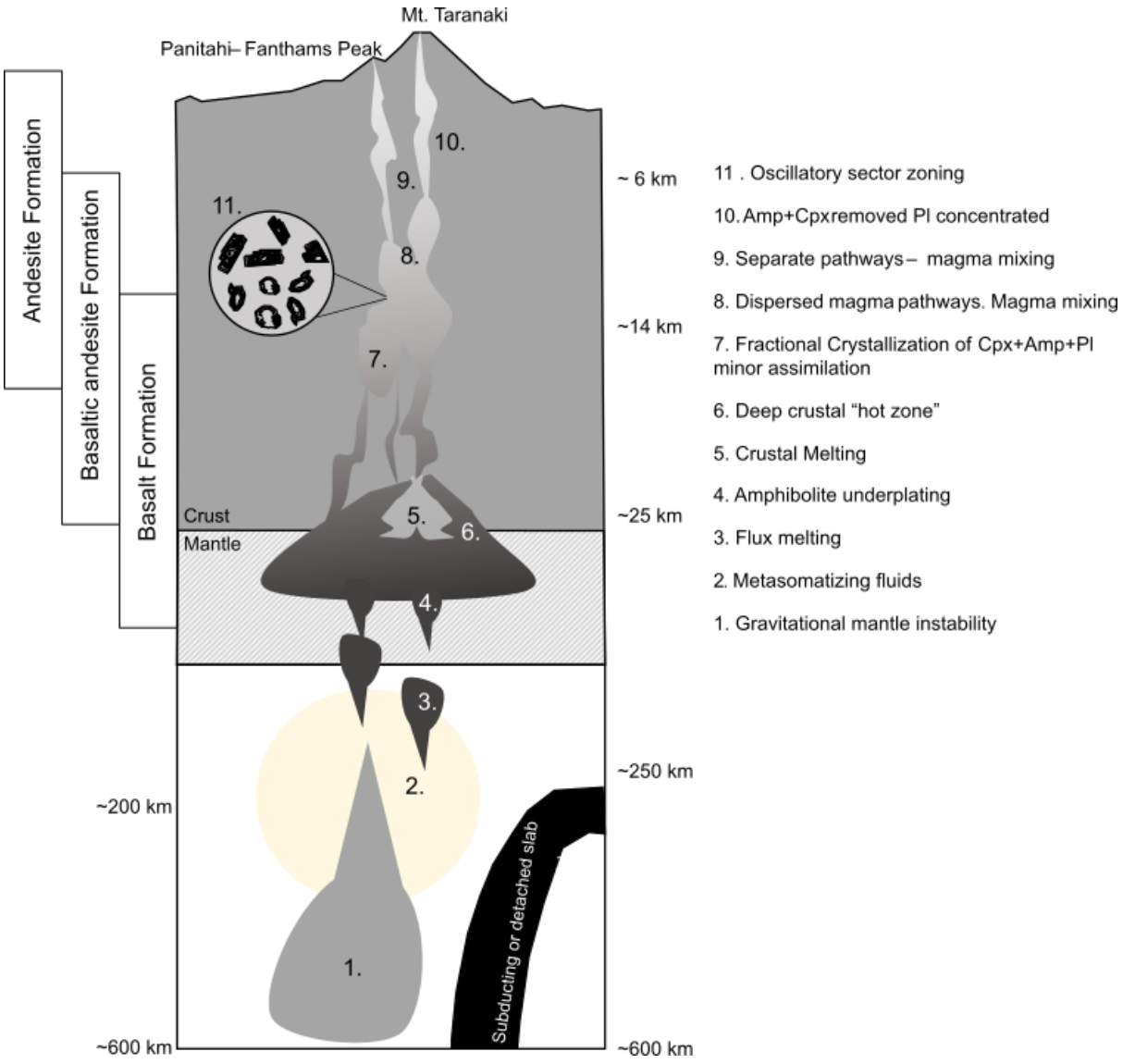


Figure 1.5: Schematic of the magma source model below Mt. Taranaki with metasomatizing fluids releasing basaltic magma into the system. Magma assimilation occurs in the deep crustal "hot zone" at the base of the crust where basalt magma becomes more evolved. More evolved magma ascends through the system with continued assimilation and fractional crystallization occurring. Separate pathways near the surface, with continued magma mixing and assimilation occurring feeding the satellite and summit vents Modified from Cronin et al., (2021); Price et al., (2021).

The eruptive products from Mt. Taranaki can be classified from high-alumina-basalts to andesites, however, the system is dominated by high-K basaltic andesites (Neall et al., 1986; Price et al., 1992; Stewart et al., 1996; Price et al., 1999; Price et al., 2005; Turner et al., 2008b; Zernack et al., 2012a). The Holocene record for Mt. Taranaki has seen eruptions from both the summit vent and from the parasitic cone Panitahi (Fanthams Peak) (< 7 ka) (Neall et al., 1986). The main summit vent is characterized by high-K basaltic andesites and andesites, while Panitahi (Fanthams Peak) has erupted

more basaltic less evolved compositions (Turner et al., 2008b). The magmatic system feeding Panitahi (Fanthams Peak) is thought to be separated from that of the summit vent as past eruptions have occurred from the two vents at the same time with evidence of dark grey tephra's intercalated with light grey tephras within the stratigraphy between 3 and 1.5 kyr CE (Torres-Orozco et al., 2017a; Torres-Orozco et al., 2017b).

The majority of eruptive products from Mt. Taranaki's summit vent have bulk compositions that are high-K, low-Si, however the compositions range from medium-K and high-K basalts and basaltic andesite to high-K, high-Si andesites (Price et al., 1999). The young Taranaki eruptive products are generally significantly more K rich than eruptives from the TgVC (Price et al., 1992; Price et al., 1999). Throughout its evolution Mt. Taranaki has shown a trend towards more potassic and siliceous compositions, however there is natural variability seen within eruptive periods which can cover the spectrum of eruptive products for Mt. Taranaki (Figure 1.6) (Stewart et al., 1996; Zernack et al., 2012a). Edifice collapse events have been frequent at Mt. Taranaki with a recurrence every 8-9 ka influencing the geochemical evolution (Zernack et al., 2012a; Zemeny et al., 2021; Zemeny et al., 2023). Throughout a regrowth cycle following an edifice collapse event, the magma becomes more evolved as the edifice regrows (Zernack et al., 2012a; Zemeny et al., 2021; Zemeny et al., 2023). The long-term evolutionary trend of Mt. Taranaki from debris avalanches shows a gradual enrichment of K_2O and LILE overtime (Zernack et al., 2012a). On a shorter timescale, studies by Zemeny (2021) show no enrichment of K_2O and LILE within growth period 1 (GP1) to growth period 3 (GP3). Instead during individual growth cycles there is a petrogenic trend from a more mafic to a more evolved composition (Figure 1.6) (Zemeny, 2021). Throughout a growth cycle as the lithostatic pressure increases the mid-upper crustal system becomes re-established this increases the compositional range of eruptive products from Mt. Taranaki (Zemeny, 2021). Eruptive products from Mt. Taranaki according to the total alkali silica (TAS) classification scheme of (Le Maitre, 1989) shows 14 % of rocks classified as basalts, 73 % as basaltic andesites and 13 % as andesites (Price et al., 2016).

Compared to andesites from within the TVZ, 130 km to the east, the Taranaki eruptives are alkali rich while eruptives from Mt. Ruapehu are a lot less potassic (Neall et al., 1986; Price et al., 1992; Price et al., 1999; Turner et al., 2008b; Zernack et al., 2012a; Lerner et al., 2019a). The typical whole rock compositions for Mt. Taranaki varies between 53–60 wt.% SiO_2, with the largest proportion of primitive magmas present within the oldest debris-avalanche deposits (Neall et al., 1986; Price et al., 1992; Stewart et al., 1996; Price et al., 1999; Platz et al., 2007; Zernack et al., 2012a; Price et al., 2016). The Holocene 3.1 ka Manganui tephra from Panitahi (Fanthams Peak) produced a more mafic composition (48-53 wt.% SiO_2) than what was typically produced during the Holocene from Mt. Taranaki (Price et al., 1999; Turner et al., 2011; Torres-Orozco et al., 2017a; Torres-Orozco et al., 2017b; Lerner et al., 2019d). This highlights that more primitive compositions are produced from Panitahi (Fanthams Peak)

and informs a model that Fantham's Peak is feed by a different magmatic source than that of the summit vent (Damaschke, 2017).

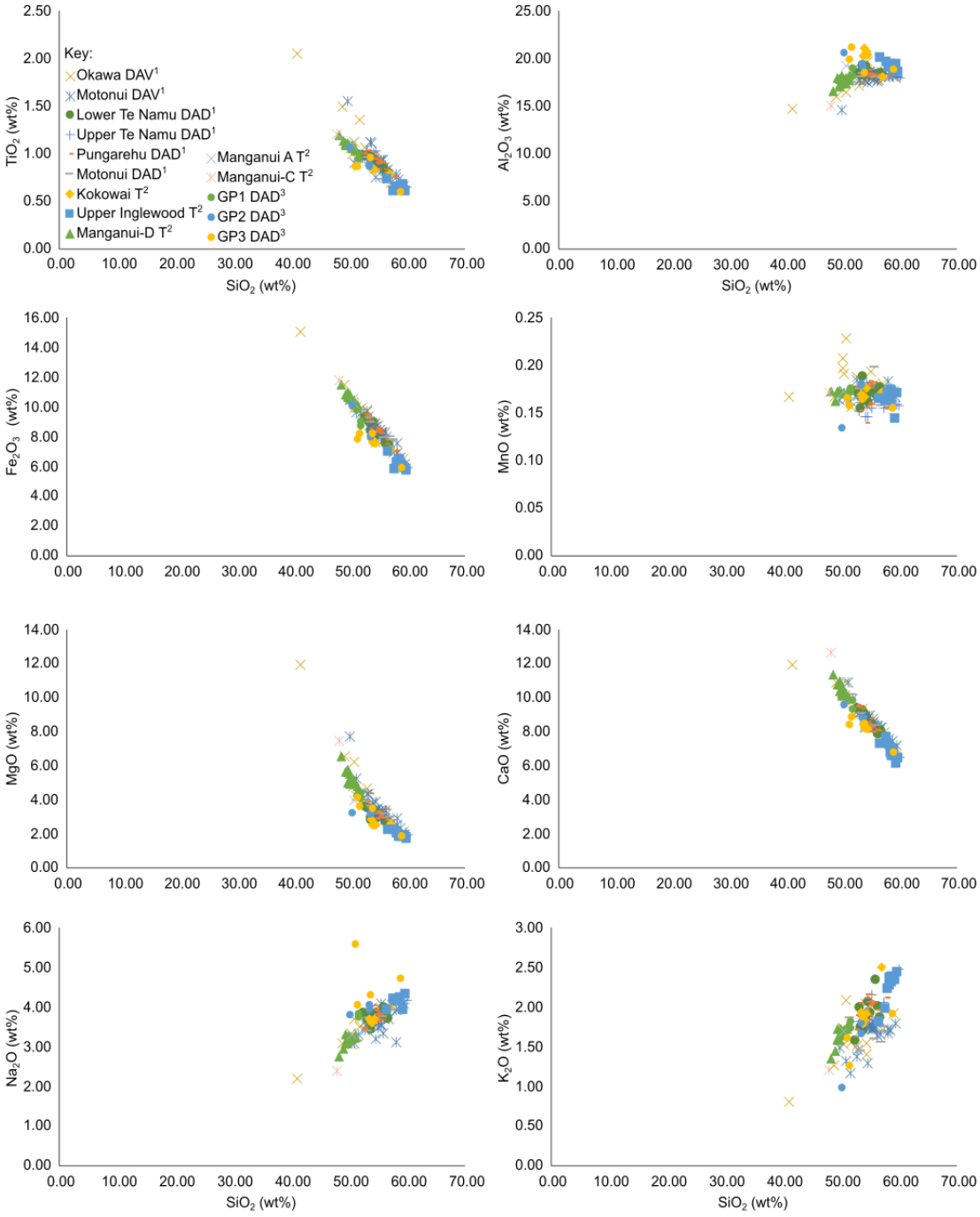


Figure 1.6: Major element whole rock geochemical plots of volcanic products from throughout Mt. Taranaki's evolution. Data obtained from ([1]Zernack et al., 2012a; [2]Torres-Orozco et al., 2017b; [3]Zemeny et al., 2023).

Trace element signatures from Mt. Taranaki are typical of subduction related volcanism and continental crust assimilation (Price et al., 1992; Price et al., 1999; Zernack et al., 2012a). The eruptive products show relative enrichment of Rb, K, and light rare earth elements (LREE) in relation to Zr and Y, along

with enrichment of heavy rare earth elements (HREE), and Pb in relation to Ce (Figure 1.7) (Price et al., 1992; Price et al., 1999; Zernack et al., 2012a). The eruptive products show a strong depletion in Nb relative to K and Th (Price et al., 1992; Price et al., 1999; Zernack et al., 2012a). The more evolved magmas (basaltic andesites and andesites) show a stronger arc signature than the less evolved basaltic eruptives (Zernack et al., 2012a). Andesitic volcanoes within the TVZ also show an arc signature within mantle normalized trace element plots, with enrichments in Pb and Ce and depletions in Nb relative to La. Mt. Taranaki shows a higher abundance of LREEs, Rb, Ba, Th and Cs compared to the TVZ volcanoes (Price et al., 1992). This higher abundance in LREEs at Mt. Taranaki may be related to partial melting which is occurring within the system at depth (Price et al., 1992).

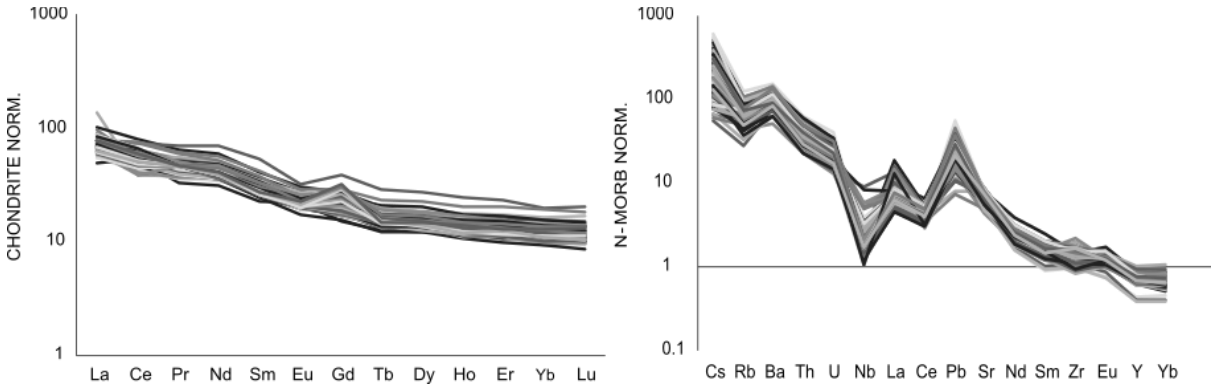


Figure 1.7: Normal mid-ocean ridge basalts (N-MORB) and Chondrite normalized rare earth element patterns for eruptive products from Mt. Taranaki throughout its evolution. Data obtained from (Zernack et al., 2012a; D'Mello et al., 2023; Zemeny et al., 2023).

1.9.1 Mineral assemblages

Stratigraphic sequences from Mt. Taranaki that include tephra fall, debris-avalanche deposits, block and ash flows and lavas can show the temporal geochemical evolution of the volcano (Platz et al., 2007; Turner et al., 2008b; Zernack et al., 2012a; Damaschke et al., 2017b). Lava flows on the cone show an array of lithologies which range from porphyritic lavas with basaltic andesite to andesite compositions (Neall et al., 1986; Price et al., 1992; Stewart et al., 1996; Price et al., 1999; Platz et al., 2007; Zernack et al., 2012a). These lithologies are present as lithic fragments within different eruptive units throughout the eruptive record. Mt. Taranaki lavas are typically holocrystalline to hypo crystalline comprising of 25-55 % crystals with phenocryst assemblages being dominated by plagioclase, clinopyroxene, titanomagnetite and hornblende with accessory apatite and zircon. Orthopyroxene is rare, and olivine is only present in more primitive lavas (Neall et al., 1986; Stewart et al., 1996; Platz et al., 2007; Zernack et al., 2012a). Glomerocrysts are common and are typically comprised of clinopyroxene ± titanomagnetite ± plagioclase ± olivine with rare amphiboles (Stewart et al., 1996; Zernack et al., 2012a). Lava flows from Panitahi (Fanthams Peak) are predominantly porphyritic basaltic andesites

(40-50 % crystals) with small (0.5-2 mm) phenocrysts (Price et al., 1992). Clinopyroxenes and magnetite's dominate the mineral assemblages from Panitahi (Fanthams Peak) with some units dominated by plagioclase (Price et al., 1992). A proportion of Panitahi (Fanthams Peak) lava flows contain 10-20 % modal olivine crystals which is unusual for Taranaki lavas (Price et al., 1992).

Within the Taranaki eruptive deposits, plagioclase is the most abundant crystal (12-40 %) (Neall et al., 1986; Price et al., 1992; Higgins, 1996), clinopyroxenes are the second most common (2-26 %) (Neall et al., 1986) and often associated with titanomagnetite crystals (1-6 %) (Gow, 1968; Neall et al., 1986). Amphibole (0-20 %) and olivine crystals are less common within the Taranaki eruptives, with amphiboles often having resorption rims and olivine's occurring as phenocrysts, xenocrysts or glomerocrysts (Gow, 1968; Price et al., 1992; Higgins, 1996; Stewart et al., 1996; Cronin et al., 2021). Plagioclase and pyroxene phenocrysts within eruptive products from Mt. Taranaki often show resorption and overgrowth oscillatory zoning (Price et al., 1992; Shane et al., 2023). These characteristic features within the phenocrysts show evidence for new magmas entering and mixing within the system (e.g., Davidson et al., 2007; Ginibre et al., 2007; Ubide & Kamber, 2018; Costa et al., 2020). Oscillatory zones within the phenocrysts show that the magma in the system could have been sitting for decades to centuries, going through multiple episodes of replenishment (Costa & Chakraborty, 2004; Metcalfe et al., 2021; Mangler et al., 2022). Oscillatory zones within the plagioclase, amphibole and pyroxene phenocrysts indicate disequilibrium crystallisation occurring within the magmatic system (Price et al., 1992). The disequilibrium in crystal rims and melt show that there is a complex process with multiple periods of magma mixing, assimilation fractional crystallization and fractional crystallization (Bowen, 1928; Eichelberger, 1978; Gill, 1981; Grove & Kinzler, 1986; Graham & Hackett, 1987; Clynne, 1999; Tepley et al., 2000; Grove et al., 2003; Davidson et al., 2005; Lormand et al., 2021; Shane et al., 2023).

1.9.2 Previous geochemical models for Mt. Taranaki

Previous studies on geochemical models of Mt. Taranaki have focused on eruptive products from young tephra falls, block and ash flows/dome formation and lava flows while the older record remains preserved in the debris-avalanche deposits within the ring plain (Neall et al., 1986; Price et al., 1992; Price et al., 1999; Platz et al., 2007; Turner et al., 2008b; Zernack et al., 2012a; Price et al., 2016; Damaschke, 2017; Torres-Orozco et al., 2017b) indicating that Mt. Taranaki has evolved to a high-K magmatic system throughout its lifetime.

The high-K arc volcanic signature of Mt. Taranaki was originally used to estimate the depth of a subducting slab within a subduction related volcanic system (Dickinson & Hatherton, 1967). Geochemical studies of eruptives from Mt. Taranaki have shown that the high-K signature is time dependent rather than slab generated with the volcano evolving over time (Price et al., 1992; Stewart et al., 1996; Price et al., 1999; Price et al., 2005). A model of a deep crustal "hot zone" has been

hypothesized for the younger < 8 ka Taranaki andesites by Stewart et al. (1996); and Price et al. (1999) where aspects of the deep crustal "hot zone" model by Annen et al. (2006) fit in with the data from Mt. Taranaki. Work on older lithological units > 200 ka, by Zernack et al. (2012a) examining clasts within debris-avalanche deposits shows that the geochemistry of the lithologies align to the deep crustal "hot zone" model (Annen et al., 2006; Zernack et al., 2012a). This study highlighted that the evolution of Mt. Taranaki towards a high-K system over time is likely related to more crystal input over time (Price et al., 1992; Stewart et al., 1996; Price et al., 1999; Price et al., 2005; Zernack et al., 2012a). The magmatic system began with a hot zone beneath Mt. Taranaki with basaltic melts derived from the mantle intruding into the lower crust (Zernack et al., 2012a). Changes in the composition of the magma over time was related to increased lower crustal material (Graham & Hackett, 1987; Stewart et al., 1996; Zernack et al., 2012a) and changes in the degree of partial melting within the system, with additional fluid influx from the mantle (Price et al., 1999). This change in composition overtime for Mt. Taranaki reflects a multistage model which was initially proposed by Stewart et al. (1996) and further confirmed by Price et al. (1999); Price et al. (2005); and Zernack et al. (2012a) (Figure 1.8).

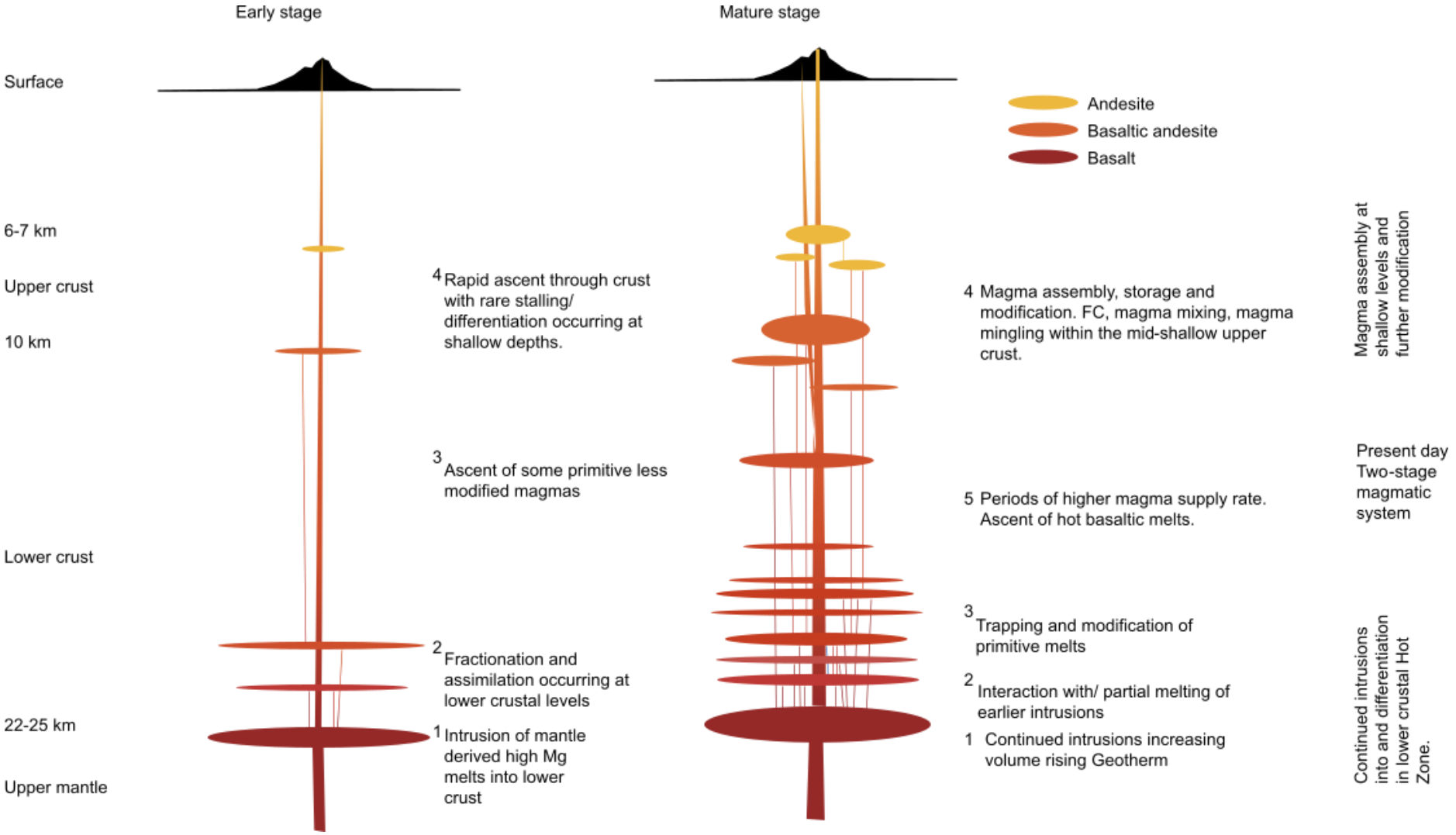


Figure 1.8: Illustration of the early and mature magmatic system beneath Mt, Taranaki, based on the magma crustal "hot zone" model of (Annen et al., 2006), showing the gradual development of a magma crustal "hot zone" beneath Mt. Taranaki. Modified from Annen et al., (2006); Turner et al., (2008b); Zernack et al., (2012a).

Stewart et al. (1996) hypothesized a three-stage magmatic model for Mt. Taranaki's high-K evolution (Figure 1.9).

Stage 1) High-Al basaltic magmas pond against the base of the lower crust, resulting in the start of crystallization and the formation of amphiboles.

Stage 2) Basaltic and basaltic andesite magmas begin to evolve which melts amphiboles in the wall rock increasing the Potassium content of the magmas.

Stage 3) At shallower depths within the magma chamber plagioclase fractionation occurred, along with melt segregation. This evolved the melt along a calc-alkaline trend towards dacitic compositions (Stewart et al., 1996). Drier melts within the system evolved to andesites as amphibole fractionation did not occur (Stewart et al., 1996).

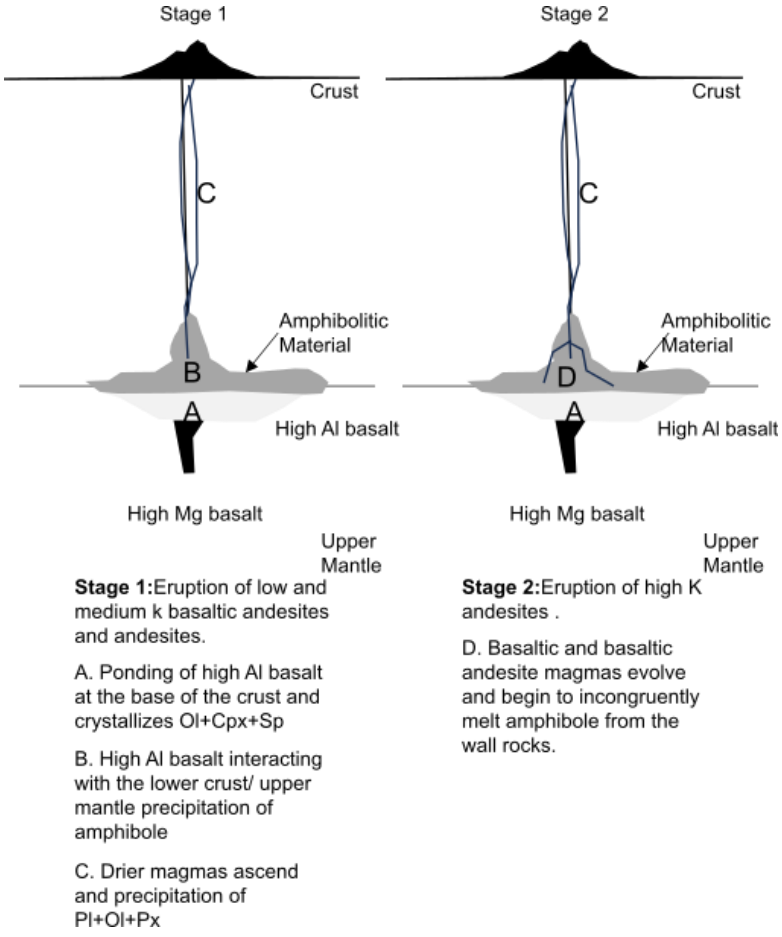


Figure 1.9: Schematic of the 3-stage model of high-K arc magma generation at Mt. Taranaki modified from Stewart et al., (1996).

Price et al. (2016), examined xenoliths from Taranaki identified that overtime, magmas within the multi-stage system (Figure 1.8) (Zernack et al., 2012a) became more fractionated and dispersed throughout the upper regions of the system. (Price et al., 2016). At the beginning of Taranaki's evolution primitive

magmas would have been able to move up to the surface more freely before the deep crustal “hot zone” formed and trapped primitive magmas on their ascent up through the plumbing system (Price et al., 2016).

Studies by D'Mello et al. (2023) on the youngest lava flows from Taranaki suggested that a deep crustal “hot zone” may not be required to explain the subcrustal evolution of andesitic to dacitic magmas within the plumbing system below Mt. Taranaki (D'Mello et al., 2023). This model suggests that aphyric (55-68 wt.% SiO_2) hot melts ascend through colder lower silica rocks entraining crystals as they pass through (D'Mello et al., 2023). The H_2O content within plagioclase rims from the young lava flows indicate that H_2O undersaturation occurred and the magmas did not reach H_2O saturation at depth, suggesting that differentiation within the deep crustal “hot zone” may not be occurring below Mt. Taranaki (D'Mello et al., 2023). The presence of data indicating both primitive magmas with signatures from the mantle and evidence of crustal assimilation can be related to the subduction mélange model (Figure 1.10) (D'Mello et al., 2023). Subduction mélanges are mixtures of altered oceanic crust, hydrous ultramafic matrix and forearc crust which forms between the subduction slab and the mantle within a subduction system (Marschall & Schumacher, 2012; Hao et al., 2016; Parolari et al., 2021; D'Mello et al., 2023). Melting begins in the forearc before continuing in the mantle where partial melting of the different components results in a diverse range of compositions (Gerya & Yuen, 2003; Behn et al., 2011; D'Mello et al., 2023).

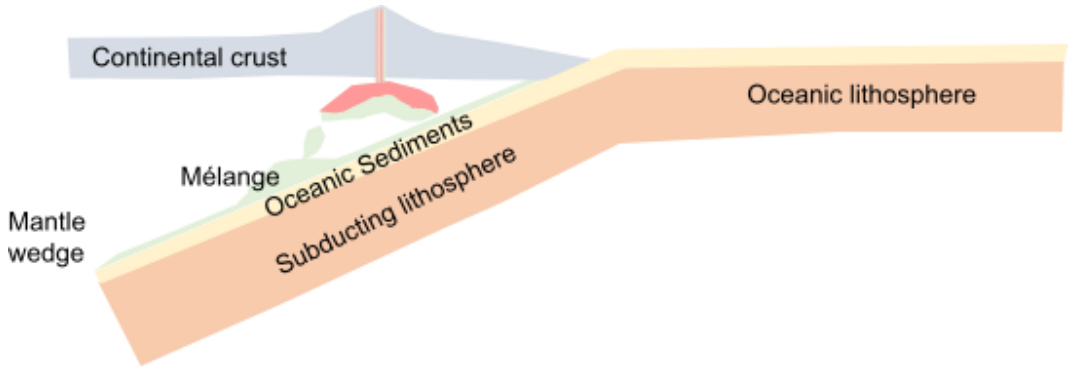


Figure 1.10: Schematic of a low angle subduction system, showing the partial melting of a subduction mélange containing a mixture of altered oceanic crust, hydrous ultramafic matrix, and forearc crust in the mantle wedge forming a primary melt. Modified from Hao et al. (2016).

Turner et al. (2008b) suggested a magma recharge model for Mt. Taranaki looking at the geochemistry and phenocryst textural characteristics which are present within andesites (Price et al., 2005; Turner et al., 2008b), it was suggested that these features could be a result of small magma bodies present within the system experiencing coalescence (Coleman et al., 2004; Humphreys et al., 2006). This model is similar to Price et al. (2005) who suggested that andesite magmas are formed in the lower crust and then ascend as lithic and crystal rich melts, if there is a recharge into the system with similar

compositions this can be hard to differentiate (D'Lemos, 1996; Turner et al., 2008b). This model suggests that magma at depth can rise mixing with another magma body in the upper magmatic system (7-10 km depth) recharging the system (Turner et al., 2008b). This mixing resulted in patchy textured plagioclase phenocryst cores and rounded clinopyroxene and amphibole phenocrysts (Figure 1.11). The occurrence of crystallization in the upper magmatic system generated phenocryst rims with different compositions (Turner et al., 2008b). The presence of titanomagnetite micro phenocrysts lacking diffusion within the co-existing minerals suggests that these recharging events occurred within days to weeks of an eruption indicating that the recharge event was likely an eruptive trigger (Turner et al., 2008b).

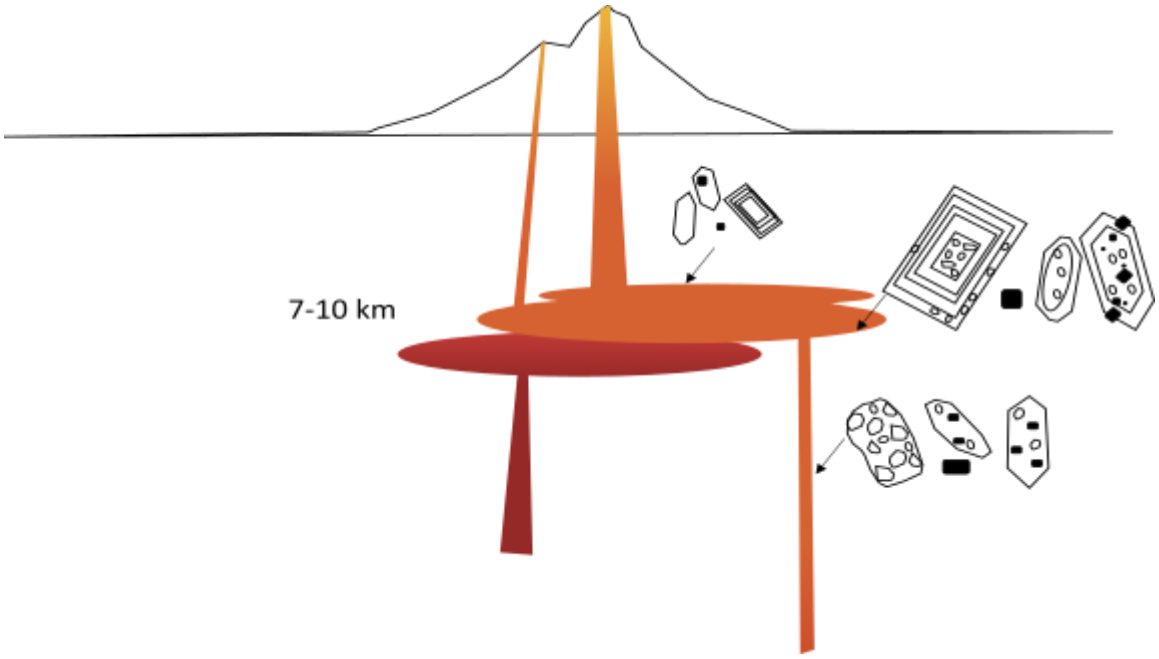


Figure 1.11: Schematic illustration of magma recharge into the magmatic system below Mt. Taranaki. Recharge events incorporate phenocrysts of amphiboles, clinopyroxenes, titanomagnetites and plagioclases which are reabsorbed. This generates oscillatory zones within the crystal rims representing multiple periods of magma recharge into the system. Modified from Turner et al. (2008b).

1.10 Taranaki hazards

Mt. Taranaki has experienced an array of different volcanic processes across its > 200 ka history (Neall, 1979; Neall et al., 1986; Alloway et al., 1995; Procter et al., 2009; Zernack et al., 2011; Damaschke et al., 2017a; Torres-Orozco et al., 2017a; Torres-Orozco et al., 2017b, 2018; Cronin et al., 2021; Weir et al., 2022). Volcanic eruptions are typically multi hazard events with different hazards affecting different sectors at varying times throughout an eruptive period (Neall, 1979; Neall et al., 1986; Alloway et al., 1995; Procter et al., 2009; Zernack et al., 2011; Damaschke et al., 2017a; Torres-Orozco et al., 2017a; Torres-Orozco et al., 2017b, 2018; Cronin et al., 2021).

Primary hazards from Mt. Taranaki include lava flows, pyroclastic density currents (PDCs) from column or dome collapse, tephra fall and debris avalanches from edifice collapse events (Figure 1.12) (Zernack et al., 2011; Damaschke et al., 2017b; Torres-Orozco et al., 2017a; Torres-Orozco et al., 2017b; Lerner et al., 2019d; Lerner et al., 2019b; Zernack, 2021) with secondary hazards occurring through remobilization of volcaniclastics through lahars (Procter et al., 2009). Lava flows and dome growth on Mt. Taranaki are mainly confined to the upper flanks of the edifice (Turner et al., 2009; Cronin et al., 2021; D'Mello, 2021; D'Mello et al., 2023). PDCs can pose a significant hazard being able to travel tens of kms away from the source, moving up to 200 km/h (Lerner et al., 2019d; Lerner et al., 2019a; Lerner et al., 2019c; Cronin et al., 2021). Their potential travel distance (> 25 km Lerner et al. (2019c)) means that they could affect populated areas around Mt. Taranaki.

Debris avalanches are one of the largest and most dangerous hazards to have occurred historically as large quantities of the edifice collapses and rapidly move across the landscape inundating everything (Zernack et al., 2011; Zernack, 2021). The destructive nature of debris avalanches was highlighted during the 1980 Mt. St. Helens eruption. For Mt. Taranaki, the recurrence rate of an edifice collapse event is one every 8-9 kyr with the last collapse producing the Opua debris-avalanche deposit 7.5 ka (Zernack, 2008; Zernack et al., 2009; Zernack et al., 2011; Zernack et al., 2012b; Zernack & Procter, 2021). Although DADs from Mt. Taranaki have a low probability of occurring (0.02 % Cronin et al. (2021)), there is likely to be another one within its future and this would be catastrophic for the sector of the ring plain in which it occurs, covering everything in Tens of meters worth of debris (Zernack et al., 2011; Zernack, 2021; Weir et al., 2022).

The most common hazard from Mt. Taranaki is tephra fall with eruption frequency records indicating that there is a recurrence time of between 300 and 500 years for large explosive subplinian to plinian events (Alloway et al., 1995; Turner et al., 2008b; Damaschke et al., 2017b; Cronin et al., 2021) and ~50-80 years for smaller vulcanian-style or strombolian events (Alloway et al., 1995; Platz et al., 2007; Turner et al., 2011; Torres-Orozco et al., 2017a; Torres-Orozco et al., 2017b). The last large explosive eruption from Mt. Taranaki was the Burrell eruption in 1655 CE (Platz, 2007; Platz et al., 2007), with the final eruptive activity occurring in 1790 CE, which involved effusive and explosive activity before the emplacement of a lava dome currently present at the summit vent (Neall, 1972; Platz et al., 2012). Tephrostratigraphic analysis of tephra layers around Taranaki by Damaschke et al. (2017b) estimate that in the next 50 years there is a 33-42 % chance of an eruption occurring at Mt. Taranaki.

Tephra fall from Mt. Taranaki has the potential to travel 100s of km from source with large historical eruptions being recorded in lake cores as far north as Auckland 270 km away (Shane, 2005; Molloy et al., 2009). The distribution of tephra fall as a hazard can be problematic and it is controlled by the wind and therefore can change and cover different sectors of the ring plain all within the same eruption (Cioni et al., 2015). Isopach maps are used to identify historical distributions of tephra fall to gain an

understanding of the parameters of an eruption (i.e., grain size, thickness, column height, eruption volume and wind direction) (Rosi, 1998; Bonadonna, 2006) which is used to inform future hazard scenarios through numerical modelling (Wadge & Isaacs, 1988; Barberi et al., 1990; Heffter & Stunder, 1993; Wadge et al., 1994; Hill et al., 1998; Iverson et al., 1998; Searcy et al., 1998; Canuti et al., 2002; Bonadonna, 2006).

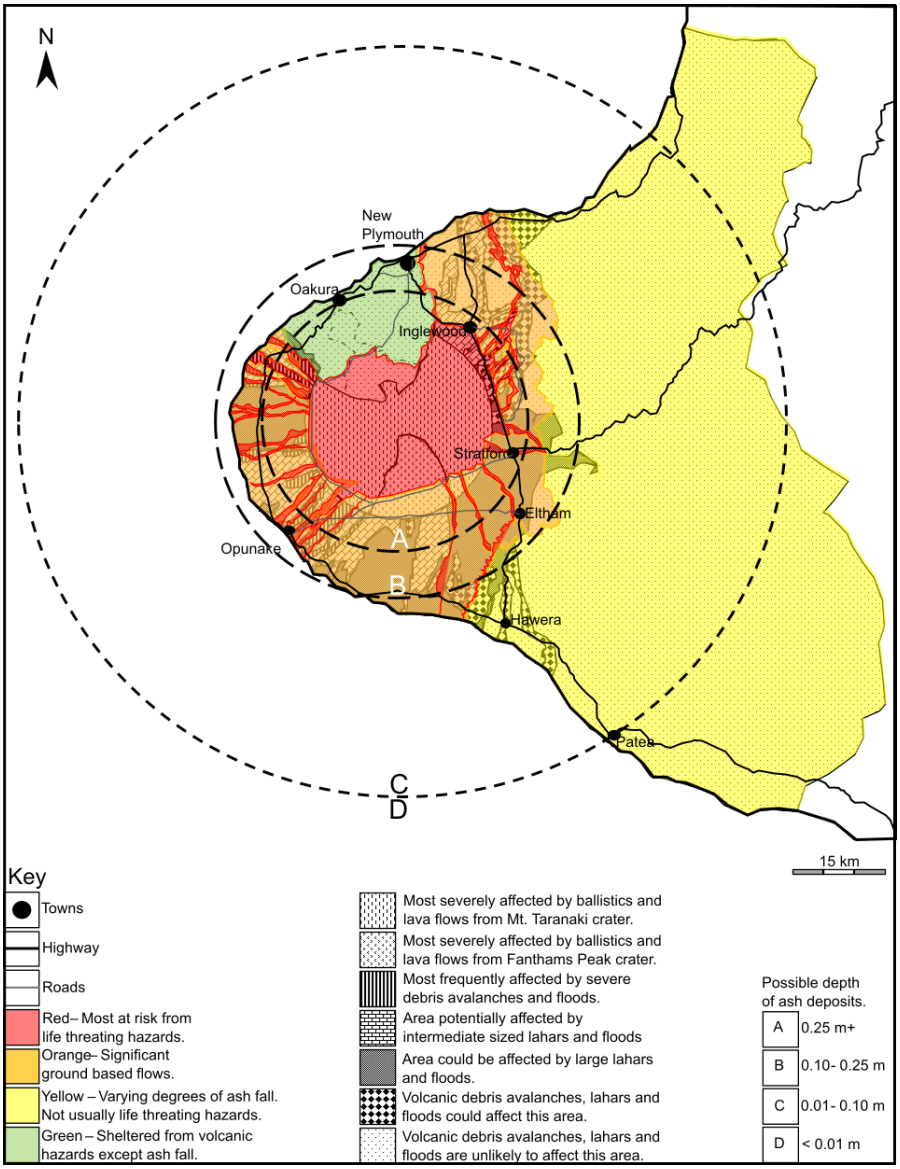


Figure 1.12: Hazard map for the Taranaki Region showing the risk zones and hazard type across the Taranaki ring plain. Modified from CDEM, (2004); TRC, (2004); Becker et al., (2010).

Numerical modelling for Mt. Taranaki simulates potential hazard scenarios which could occur based on past eruptive behaviour to inform the likelihood of impact and hazard impact regions for the different eruptive products seen from Mt. Taranaki (Druce, 1966; Neall, 1979; Platz et al., 2007; Procter et al., 2009; Procter et al., 2010; Platz et al., 2012; McDonald et al., 2017; Weir et al., 2022).

The last eruptive period from Mt. Taranaki, the Tahurangi eruptive period, provides an example of the most common eruption type with an annual probability of ~ 0.010-0.012 producing small tephra fall < 0.06 km^3, along with pyroclastic density currents (Druce, 1966; Neall, 1979; Platz et al., 2007; Procter et al., 2009; Procter et al., 2010; Platz et al., 2012; McDonald et al., 2017). These events are typical of a VEI 2-3 event which is accompanied by extrusion of a summit lava dome (McDonald et al., 2017). Modelling shows an eruption like this would produce thin ash fall layers millimetres to sub-millimetres thick, which would be mainly contained within the Egmont National Park with some easterly distribution possible under a strong prevailing wind (Turner et al., 2009; Damaschke et al., 2017b; McDonald et al., 2017). The Inglewood scenario (Figure 1.13) represents a much larger Mt. Taranaki event with an annual probability of 0.003 (McDonald et al., 2017). This event involves a subplinian to plinian eruption column accompanied by PDCs during unstable episodes, which could reach 19 km from source (McDonald et al., 2017; Torres-Orozco et al., 2017b). The main eruption column produced during this event would range between 14-22 km high ejecting volumes of 0.5 to 1.1 km^3 (Platz et al., 2007; McDonald et al., 2017; Torres-Orozco et al., 2017b). Tephra fall produced during an event this size would deposit 1 mm-thick tephra east of Stratford, covering a large agricultural zone and neighbouring towns (McDonald et al., 2017). The Opua scenario (Figure 1.13) shows an example of an edifice collapse creating a debris avalanche across the southwestern ring plain of Mt. Taranaki with an annual probability of 0.02 % (Cronin et al., 2021). A collapse event like this could generate a debris avalanche of 1 to > 7.5 km^3 to move down the flanks. Proximal areas could be buried in 10–30 m of debris-avalanche deposit destroying everything around it (McDonald et al., 2017), with runout distances up to 45 km from source.

Hazard scenarios from Weir et al. (2022) show that an eruption from Mt. Taranaki is unlikely to be just a single event, instead when the volcano re awakens it is more likely that it will be a multi-hazard event occurring over days to years (Figure 1.14) (e.g., Torres-Orozco et al., 2017a; Torres-Orozco et al., 2017b; 2018). This can also include a wide spectrum of volcanic hazardous phenomena (Bebbington et al., 2018). A series of eruption scenarios were created for Mt. Taranaki which range from small magnitude (S1, S2 and S3), medium magnitude (M1, M2, and M3) and large magnitude (L1, L2, and L3), these scenarios increase in magnitude (Pyle, 2015), as they progress (i.e., M2 is larger than M1 (Figure 1.14) (Weir et al., 2022). These scenarios took into consideration four factors 1). The location of the eruption 2). The eruption style, 3). The duration of the eruptive phase and 4). The hazard and frequency of the phase (Weir et al., 2022).

Eruption forecast probabilities for Mt. Taranaki for the next 50 years calculated the likelihood of a VEI > 3 was 37-52 % (Turner et al., 2009), using a 10,150-year record. (Damaschke et al., 2017a), used an eruption record over the past 14,500 years CE to generate a 33-42 % probability of eruption in the next 50 years. A study by (Bebbington et al., 2018) reported a likelihood of 50% of an eruption occurring in the next 50 years, with a 76% chance that this will be over a VEI 3 (Carman, 2023).

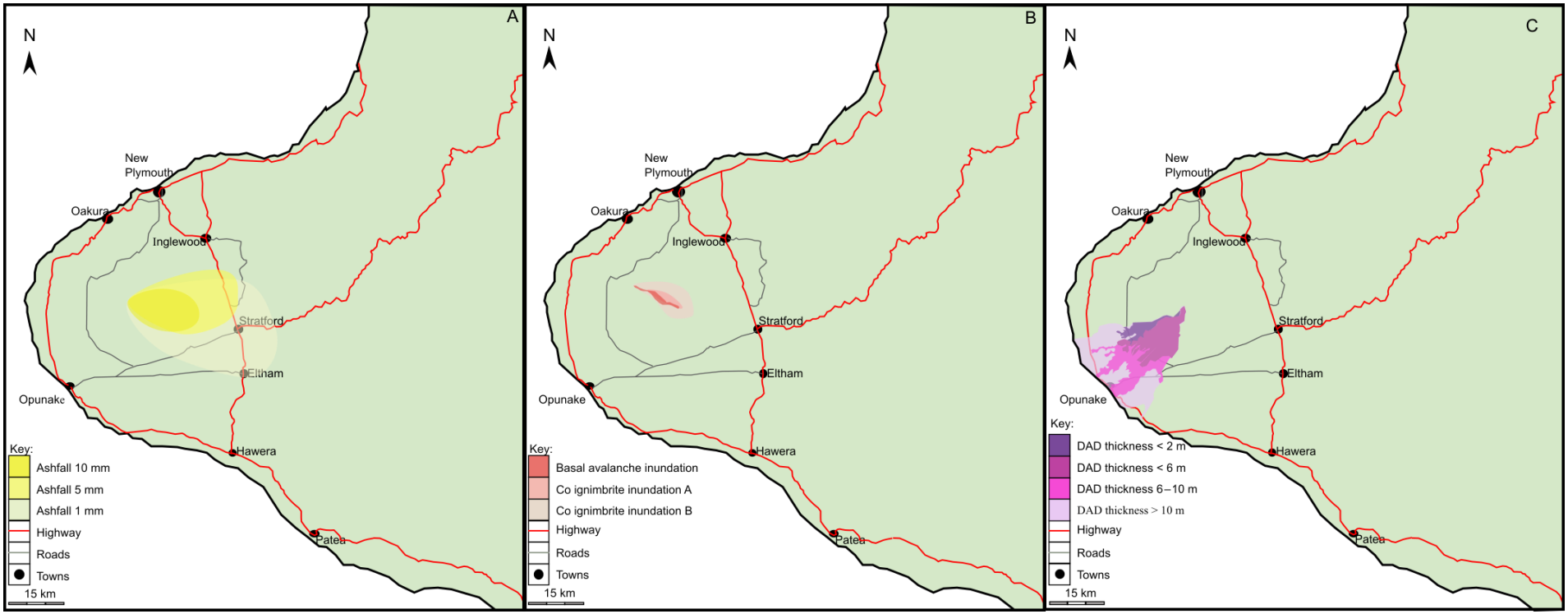


Figure 1.13: Eruption modelling diagram showing scenarios for future eruptive events from Mt. Taranaki. A). The Inglewood sub-plinian to Plinian eruption scenario showing zones of tephra dispersal. B). The Tahurangi eruptive scenario showing the extent of the basal avalanche and ash fall dispersal. C). The Opua debris avalanche scenario showing the extent of debris avalanche dispersal modified from McDonald et al. (2017).

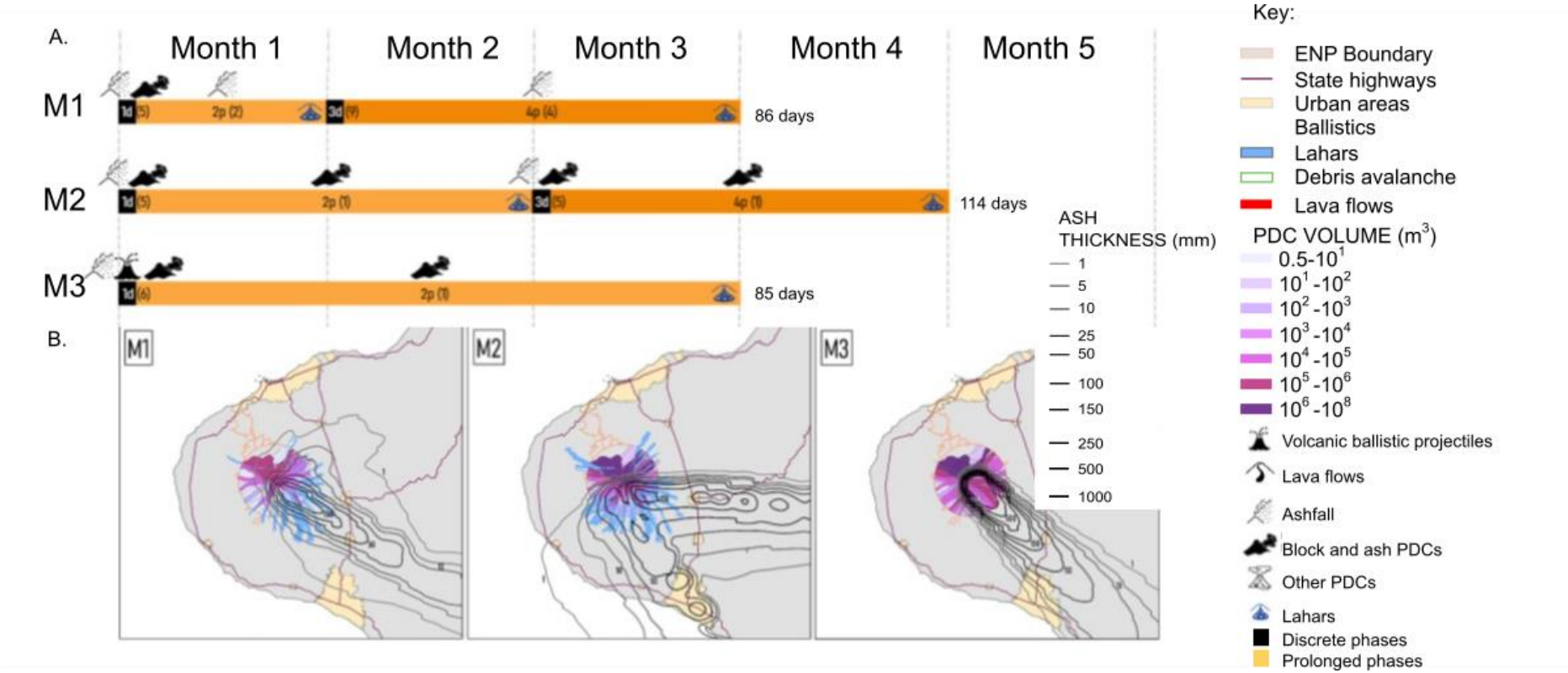


Figure 1.14: Schematic of eruption scenarios for Mt. Taranaki modified from Weir et al. (2022). A. shows eruption scenarios for M1-M3 magnitude events throughout a 6-month duration indicating prolonged (p) phases lasting weeks to months and discrete (d) phases lasting 1 day, with the total length of the scenario displayed at the end (Weir et al., 2022). B. Indicates the aggregated outputs for the medium sized sub-suites from Weir et al. (2022), showing the depositional material produced during an eruptive period highlighted in A

.

2 Methodology

2.1 Fieldwork and physical parameters

The pyroclastic deposits of the Poto and Paetahi tephra formations from Mt. Taranaki are mapped across the Taranaki ring plain and dated from 27.3 to 23.1 ka (Alloway et al., 1995). The reference localities (Ronald Road: 39°21'41.64"S; 174°13'20.02"E; Opunake Road: 39°21'21.45"S; 174°14'38.09"E; Cardiff Road: 39°20'34.71"S; 174°13'41.90"E) for the formations are found on the south-eastern ring plain, where 18 Poto layers were identified and 10 Paetahi tephras were identified (Figure 2.1). Parts of the formations were discovered at 16 sites across the eastern, southeastern, and southwestern sectors of the ring plain where detailed descriptions of the layers were recorded (Appendix A). Observations noted grain size, sorting, colour, layering, sedimentary structures including paleosols and thickness. Textural parameters including clast framework (clast supported vs. consolidated), clast weathering, and lithic content were also originally described in the field. At field locations tephra samples were collected for further analysis, such as grain size analysis, componentry, textural analysis, and geochemistry.

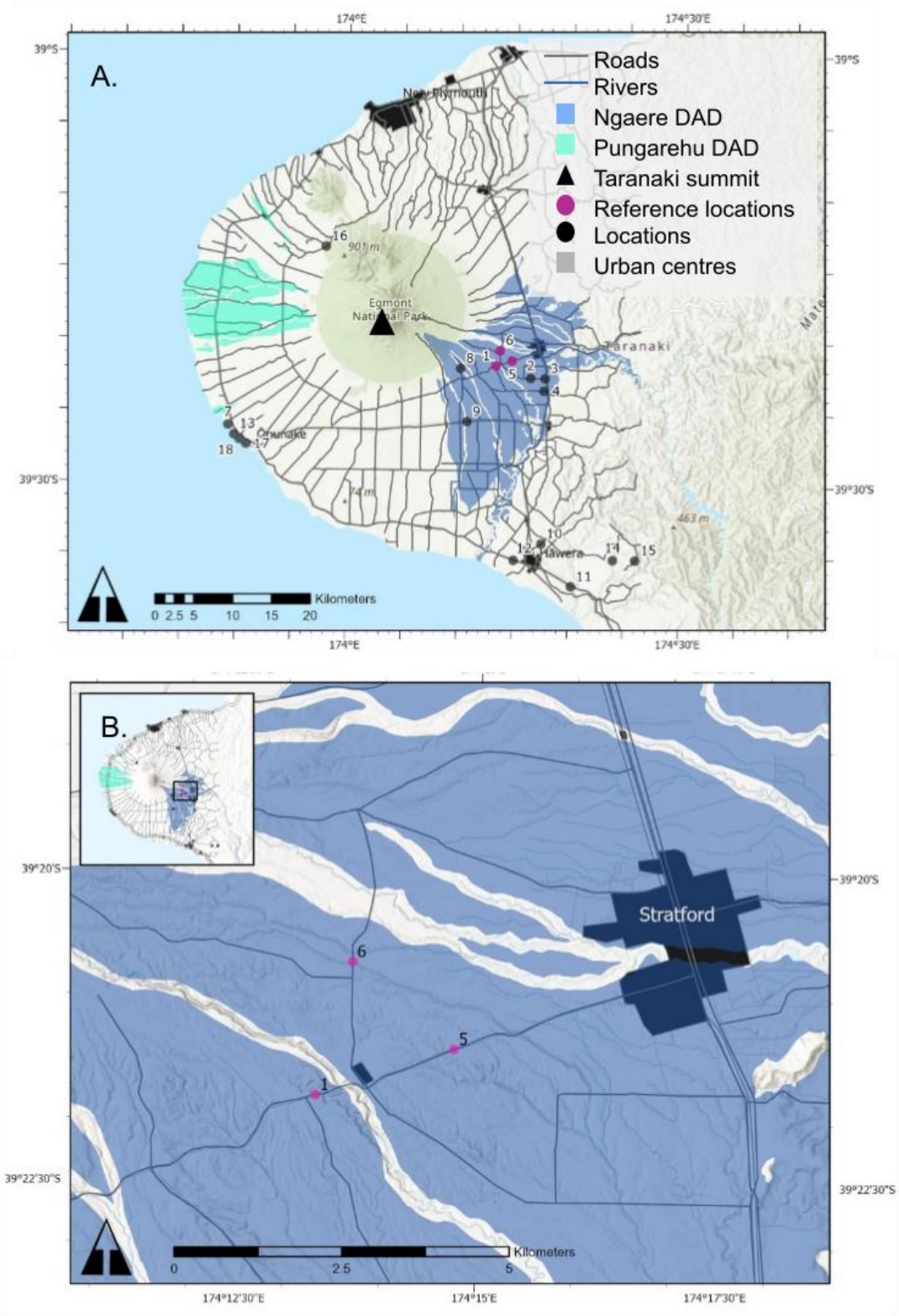


Figure 2.1: A. Location map of the Poto and Paetahi tephra formations across the Taranaki ring plain. B. Inset map of the Poto and Paetahi reference locations. Road and Topographic data sourced from the LINZ Data Service licensed for reuse under CC by 4.0.

Detailed descriptions of the layers identified contributed to tephrostratigraphic correlations across the ring plain. Paleosols within the sequence indicate pauses between eruptive events (Fisher & Schmincke, 1984; Miall, 1996). Preservation of tephras is varied across the landscape in relation to the age of the deposits with the Poto and Paetahi eruptive period occurring during the Last Glacial Maximum (25-14 ka). This time period was associated with a cold dry climate, with an increase in erosion along streams and redistribution of tephra through aeolian processes (Neall, 1975; McGlone et al., 1996). Due to the age of the tephra only medial and distal outcrops where accessible as proximal deposits have been buried by subsequent eruptive events or eroded away. The 25.6 ka Rhyolitic Kawakawa-Oruanui tephra (Vandergoes et al., 2013) and the 27.3 ka Ngaere debris-avalanche deposit are intercalated with tephra deposits within the Poto Formation providing key marker units. Key locations of the Kawakawa-Oruanui tephra identified by Franks (1984) were used to determine stratigraphic positions of the Poto and Paetahi Formation units. Initial identification of the deposits from the Poto and Paetahi Formations was made by Alloway et al. (1995), this study is extending and contributing to the understanding of the eruptive activity during this time period from Mt. Taranaki (for more details see Chapters 3-6).

Detailed stratigraphic profiles of the depositional layers for the Poto and Paetahi Formations provide the basis for correlations and interpretations of the deposits (see more details in Chapter 3). At each location the depositional thickness (cm) and largest pumice lapilli clasts of each layer was recorded and used to construct isopach and isopleth maps for the Poto and Paetahi Formations (Appendix A). The contours were digitally drawn using ArcMap 10.8 and ArcGIS Pro, to assist in the calculation of areas, distances, and circularity (expressed as shape factor: = ((4 πArea)/Perimeter^2)). The long axis was measured from the last known vent to the end of the contour and the short axis was measured across the smallest section of the contour.

The **Fallout tephra volume (V)** was estimated using the program AshCalc (Daggitt et al., 2014) using inputs of (T) and ($A^{1/2}$) using the Weibull method (Bonadonna & Costa, 2012; Bonadonna & Costa, 2013a) where they describe the thinning of data on semilog plots of T vs. $A^{1/2}$. Where T is the thickness (m), and $A^{1/2}$ is the square root of the Area (km). This method uses the assumption that T scales with $A^{1/2}$ according to the relationship below where they relate x to the thickness using:

$$(T(x) = \theta(\frac{x}{\lambda})^{k-2} e(\frac{x}{\lambda})^k$$

(1)

This model has incorporated ʎ as a parameter to allow for the variation in thinning rate that is seen in tephra deposits with multiple segments (Pyle, 1989; Fierstein & Nathenson, 1992; Bonadonna & Costa, 2012; Bonadonna & Costa, 2013a; Daggitt et al., 2014), reporting the ʎ, Θ and k values. Θ represents the thickness scale. Tephra volumes were calculated using a minimum of 1 isopach. How the isopachs were calculated influences the volumes produced and therefore the eruption dynamic values. Plots of

the thickness (T_k) logarithm vs. the square root of the area ($A^{1/2}$) for the different isopachs from each layer were produced. AshCalc (Daggitt et al., 2014) also produces the slope (k) of the volumes, while T_0 expresses the extrapolated thickness at the vent (Pyle, 1989).

The Eruptive Column Height (H) (km) was determined using the method by Mastin et al. (2009) which uses the relationship between eruption rate and plume height. Studies by Mastin et al. (2009) showed a positive correlation between plume height (km) and eruptive volume (DRE V) (km^3). Eruptive column height was calculated using the following equation:

$$\mathrm{H} = 25.9 + 6.4log^{10}(dreV) \quad (2)$$

Comparative column heights were calculated using the model from Carey and Sparks (1986), applying the same isopach data that was used for the calculations of column height from Mastin et al. (2009). The column heights calculated from the two methods produced considerable differences in column heights (e.g., 18.67 vs. 30.1 km). For this study the heights produced for the Poto and Paetahi Formations by Mastin et al. (2009) were determined to be more reliable in relation to eruptions from a global context (e.g., Thorarinsson & Sigvaldason, 1972; Sarna-Wojcicki et al., 1981; Carey & Sigurdsson, 1985; Fierstein & Nathenson, 1992; Gudmundsson et al., 1992; Rosi et al., 1993; P. D. Cole et al., 1995; Höskuldsson et al., 2007; Carey et al., 2009).

Column heights determined using the model from Carey and Sparks (1986) used the downwind and crosswind axis from the isopleths of the different eruptive events to calculate the eruption heights. The crosswind and downwind ranges of 8 mm clast isopleths were used with an approximated density of 2.5 g/cm^3 to estimate the mean column height and wind speed.

Once H for each eruption was estimated, the **Volume Discharge Rate (Q) DRE (m^3/s)** was calculated using the following equation from Sparks et al. (1997) and Mastin et al. (2009):

$$Q = ((\frac{H}{1.67})^{3.86}) \quad (3)$$

The **Total Erupted Mass (mT)** was calculated following Wilson (1976) using the equation:

$$mT = volume * 1000\ kg/m^3 \quad (4)$$

The **Eruptive Magnitudes (DRE)** was calculated using the equations by Pyle (2000) using a rock density of 2500 kg/ m^3:

$$DRE = \frac{mass}{rock\ density} * 10^{-9}$$

(5)

The **Mass Eruption Rate (MER) (kg/s)** indicates the mass of material which erupted out of the vent per second and was calculated using Sparks et al. (1997) and Mastin et al. (2009):

$$MER = DRE * density$$

(6)

The **Magnitude (M) and Duration (hours)** of each eruption was calculated following Pyle (2000), and Wilson (1976):

$$Magnitude = Log10(Erupted\ mass)^{-7}$$

(7)

$$Duration = (\left(\frac{mT}{MER}\right) * 3600)$$

(8)

2.2 Laboratory

2.2.1 Grain size analysis

Field grain-sizes of the deposits were described using the simple and practical Udden (1914) scale which was modified by (Wentworth, 1922). More precise analysis of the samples was completed in the laboratory. Pyroclastic fall deposit samples ranging from 0.1 to 1 kg were dried at ~45 °C in an oven for 7 days, then weighed and manually hand sieved to avoid pumice breakage at 0.5 ϕ intervals between -4 and 4 ϕ. This study uses the logarithmic phi scale for grain size classification defined by Krumbein (1934; 1938) as:

$$\Phi = -\log 2d$$

(9)

Φ is defined as the phi size of the particle and d is the diameter of the mesh used in the sieve in mm (Tanner, 1969; Boggs, 2012). The tephra size classification in relation to phi and mm is shown in Table 2.1 (White & Houghton, 2006), grain size terminology within this thesis is based on the classification by White and Houghton (2006), while Folk and Ward (1957) are used for descriptive terms (i.e., median mode and sorting) of the deposits.

Table 2.1: Tephra size clasts in relation to grain size parameters phi and mm from White and Houghton (2006).

Grain size (φ)	Grain size (mm)	Tephra size clasts
>4	<0.0625	Extremely fine ash
3 - 4	0.0625-0.125	Very fine ash
2 - 3	0.125-0.25	Fine ash
1 - 2	0.25-0.5	Medium ash
0 - 1	0.5-1	Coarse ash
-1 - 0	1-2	Very coarse ash
-2 - -1	2-4	Fine lapilli
-4 - -2	4-16	Medium lapilli
-6 - -4	16-64	Coarse lapilli
<-6	>64	Block/bomb

Grain size distribution and sorting were analysed through Gradistat (Blott & Pye, 2001), producing statistical parameters following Inman (1952), producing the geometric (graphic) mean (Mdϕ), the graphic standard deviation (Sigmaϕ) the graphic skewness (SkG), and after Folk and Ward (1957), quantifying the graphic mean (Mz), inclusive graphic standard deviation (Sigmai), inclusive graphic skewness (Ski), and kurtosis (Kg). These sorting classifications followed the criteria from Cas and Wright (1987). Detailed results are found in Appendix B.

2.2.2 Componentry

Component analysis was conducted on the -1.5 and 0.5 ϕ size fraction of sieved samples from the reference section locations (Figure 2.1). These grains were cleaned four times with distilled water inside the ultrasonic bath for three minutes each round until the water ran clean. The deposits were characterized by lithologies looking at juvenile pumice, lithic clasts and crystals which provides information on the fragmentation mechanisms, conduit conditions and eruption styles (e.g., Macedonio et al., 1994; Paredes-Mariño et al., 2019). The terminologies for the different lithologies are defined as follows:

- *Juvenile:* Primary material erupted from magma during the Poto and Paetahi eruptive period i.e., ash, lapilli, blocks.
- *Lithic:* Secondary material of foreign origin excavated from the subvolcanic basement and conduit walls or at the surface during the Poto and Paetahi eruptive period i.e., basement and conduit wall rock (Sparks, 1976; Fisher & Schmincke, 1984; Carey & Houghton, 2010; Campbell et al., 2013; Paredes-Mariño et al., 2019).

- *Crystal:* Crystals erupted out of the vent free from juvenile or lithic material, predominantly Feldspars, Pyroxenes, Amphiboles and Cumulates (e.g., Sparks, 1976; White & Houghton, 2006; Paredes-Mariño et al., 2019).

Between 300 and 500 grains per sample for the -1.5 and 0.5 ϕ size fraction was conducted from the reference sections of the Poto and Paetahi Formations. These size fractions were selected as they are present within all depositional layers and allowed for identification of foreign lithics present within the deposits. The size fractions were split multiple times using a splitter until there was approximately 300 grains remaining. To remove biases all of the grains in the split sample were counted and this was done before any other analysis which removed grains from those size fractions. The grains were counted under a binocular microscope where classification of grains was consistent throughout the layers separating the lithologies into two juvenile classes: 1) Grey pumice; 2) Brown pumice; four main lithic classes: 3) Altered pumice; 4) Grey lithics; 5) Altered lithics; 6) White clay; and four main crystal classes: 7) Feldspars; 8) Pyroxene; 9) Amphiboles; 10) Cumulates. (Chapter 3; Table 3.3; Figure 3.2)

To allow for comparison between eruptive layers individual component classes were normalized to the number of clasts counted within each size fraction. Detailed results are found in Appendix C.

2.2.3 Pumice density

Juvenile pumice clasts between -4 to -2 ϕ were selected for density measurements. This grainsize was selected as it reduces the effects of post-fragmentation expansion and bubble coalescence, which can be used to quantitatively infer magmatic processes within the conduit (Houghton & Wilson, 1989; Thomas & Sparks, 1992; Klug & Cashman, 1994; Klug & Cashman, 1996; Mangan & Cashman, 1996). Grains which are greater than 16 mm are not used as they do not cool fast enough in the eruption column to preserve the initial bubble structure, these cooling processes can take 10-15 seconds (Thomas & Sparks, 1992; Klug & Cashman, 1994). A total of 5-40 (depending on available material) juvenile clasts were selected from each of the lapilli bearing layers. Pumice clasts were cleaned using distilled water in the ultrasonic bath 3 times for at least 3 minutes each time, dried in a 65° C oven overnight before being analysed. Once dry, pumice clasts were weighed to 4 decimal places before being analysed.

Bulk density (δbulk) (g/cm^3):

The envelope volume of small irregular shaped pumices was calculated using a Micrometrics Geopyc 1360 Envelope Density analyser (geopyc) through the use of the Archimedes principal. Displacement measurements are conducted using DryFlo a quasi-fluid composed of small rigid spheres. The displacement data is collected between a blank run with DryFlo and a sample run containing the exact same amount of DryFlo and the irregular shaped clast. A total of five blank and five sample runs were completed per grain with a compact pressure of 100 Newtons. Samples which had a standard deviation

> 5 % were excluded as an unreliable data point. The envelope density of each sample was used as a proxy for bulk density (δbulk). Detailed results are found in Appendix D.

Vesicularity was calculated using the equation by Houghton and Wilson (1989):

$$\text{Vesicularity} = (100 * \frac{(\text{DRE } - \text{bulk density})}{DRE})$$

(10)

2.3 Pyroclastic 3D analysis

X-ray computed tomography has become increasingly common (e.g., Song et al., 2001; Polacci et al., 2006b; Zandomeneghi et al., 2010; Voltolini et al., 2011; Baker et al., 2012; Pardo et al., 2014; Berg et al., 2016; Heinrich et al., 2020b; Torres-Orozco et al., 2023) in the use to reconstruct 3D images of juvenile pyroclasts to analyse and quantify vesicle networks and crystal contents produced during volcanic eruptions. These measures are used to understand the processes around nucleation and bubble growth looking at the size and distribution of bubbles within juvenile material (Song et al., 2001; Polacci et al., 2006b; Zandomeneghi et al., 2010; Voltolini et al., 2011; Baker et al., 2012; Pardo et al., 2014; Berg et al., 2016; Heinrich et al., 2020b; Torres-Orozco et al., 2023).

The reconstruction of 3D micro-textures within juvenile clasts required the use of Synchrotron radiation Micro-Computed Tomography (MCT) as benchtop MCTs did not have high enough energies to penetrate the high atomic number mafic compositions of the pumice clasts. The Micro-Computed Tomography Beamline facility at the Australian Synchrotron was used as it provides high energy scanning capabilities coupled with high resolution scans.

The Australian Synchrotron is a third-generation electron light source which accelerates an electron beam through a vacuum chamber within a 216m circumference storage ring. Accelerated electrons are held within the storage ring at high levels (200 mA) for over 20 hours. Synchrotron light produced by the storage ring is captured by fourteen beamlines situated around the outside of the storage ring, designed for selected wavelength acquisition.

The MCT beamline was built as a compliment to the pre-existing Imaging and Medical beamline (IMBL), with the capability of scanning images at a higher resolution. The second hutch was chosen for use in this study at a distance of 24 m from the bending-magnet source point. The MCT operates with x-ray energies ranging from 8 – 40 Kev using monochromatic, pink, and white x-rays. With differing magnification on the whitebeam detector, the effective pixel size varies with 1 x magnification producing an effective pixel size of 6.5 um using a field of view of 16.6 x 4 mm^2.

Samples used for this study were cylinders drilled out of pumice clasts with densities calculated beforehand using the Geopyc (see 2.2.3 Pumice density) (e.g., Heinrich et al., 2020b). The samples

were selected due to representative densities identified through histograms providing the average bulk density for each deposit. The cylinders have a diameter of 8 x 7 mm which was chosen to achieve the highest possible resolution to capture the smallest bubbles within the clasts which represent the final stage of magmatic fragmentation (Sparks & Brazier, 1982; Genareau et al., 2013). These pumice clasts have a high proportion of small bubbles and little to no large bubbles allowing for the small cylinder size to be obtained for high resolution analysis.

The cylinders were drilled with a handheld power drill and a diamond core drill bit with an internal diameter of 10 mm. The pumice cores were mounted inside a 50 mm high solid aluminium tube which contained an 8 x 7 mm core to house the sample. The aluminium rim around the sample was < 1mm to allow for the x-rays to pass through without disruption. A plastic cap was placed over each sample to secure the sample in place. The uniformity in tube size and height reduced the sample change time and meant each sample was well aligned within the beam field of view with no rotation axis correction required. Sample holders were mounted on a magnetic platform with industrial double-sided tape to lock the tube in place and stop movement of the sample during rotation (Figure 2.2).

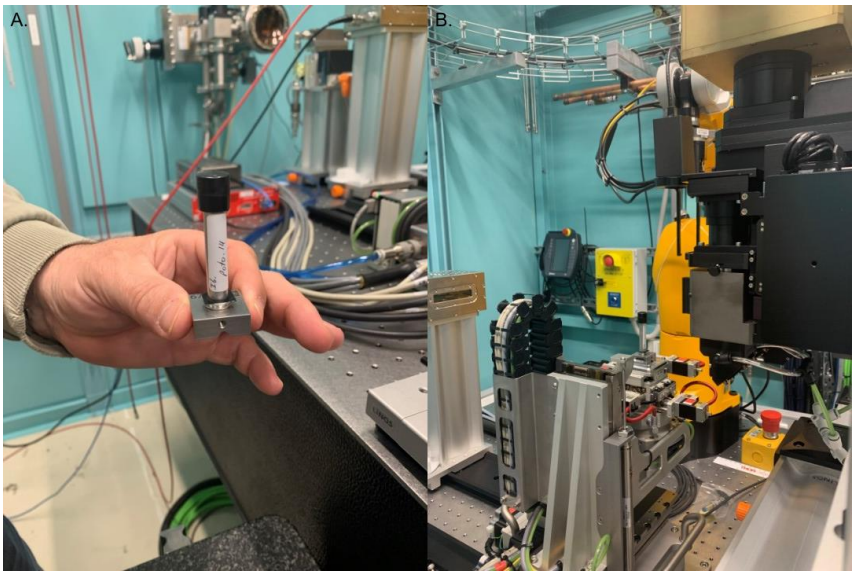


Figure 2.2: A. Sample holder containing pumice clast in the top 7 mm mounted to a magnetic base. B. Sample mounted onto the sample stage in front of the whitebeam detector on the MCT beamline at the Australian Synchrotron.

Once samples were mounted on the sample stage in front of the beam the axis of rotation was defined by moving the stage vertically and horizontally to ensure that the sample always remained in the field of view. Following each sample change a check on the stage axis was undertaken to ensure the sample remained in the field of view. The whitebeam detector was used with the beam energy kept at 35 keV and rotation steps of 0.15° to complete 180°.

During each scan a set of dark and flat fields are undertaken where an image is acquired with and without the X-ray beam turned on to allow for the removal of background noise and correct for image

oversaturation (Van Nieuwenhove et al., 2015). The background analysis is conducted by moving the sample stage out of the beam. This can then be subtracted from the sample scans, resulting in a less noisy image. A flat field is run to calibrate the exposure time to avoid oversaturation of the images. For this study we set the exposure time at 0.019 s to acquire the best resolution and the least noise in the image. Step and shoot image acquisition was used to capture the sequence with a complete scan of 1201 images in 1 hour.

Image reconstruction was conducted using MCT processing software through the Australian Synchrotron. This processing corrects for oversaturation, background noise, ring artifacts and beam-hardening. In rare occasions the centre of rotation for the sample needs to be corrected this can be done through the MCT processing software. To start 100 images are reconstructed to check the parameters before the stack of 1201 images are reconstructed. Image reconstruction for 1201 images into hdf5. files take approximately 5 minutes. Image TIFF sequences along with brightness and contrast can be adjusted through Image-J allowing for samples to be saved as 32-bit Tiff sequence files used for 3D image rendering.

Image rendering of the 3D stacks was completed using the rendering software Dragonfly 2022.2. Intensity threshold segmentation, and image filtering were used on each of the image sequences (see further details in Chapter 4; Section 4.3.3). Intensity threshold segmentation segments the vesicles from the matrix and crystals, this process was manually checked on multiple sections of the sequence to evaluate the conditions that were used (Chapter 4; Figures 4.2 and 4.3). If required, the intensity threshold was tested on different sections to allow for the incorporation of all pixels corresponding to a particular group. Extracting connected facies was used to generate statistical properties of the four identified groups 1) vesicles 2) matrix 3) mafic crystals 4) total volume.

The final files contained information on the size and number of vesicles, mafic crystals, matrix, and total volume and allowed for individual calculations on the **Vesicle Volume (VV) (%)** and **Crystal Volume (CV) (%)**:

$$VV = \frac{\text{Total vesicle volume}}{\text{Total volume}} * 100 \quad (11)$$

$$CV = \frac{\text{Total crystal volume}}{\text{Total volume}} * 100 \quad (12)$$

Along with the **Vesicle Number Densities (VND) (cm^{-3})** and **Crystal Number Densities (CND) (cm^{-3})** which were calculated using:

$$VND = \frac{\text{No. of bubbles}}{\text{Total crystal} + \text{Melt volume}}$$

(13)

$$CND = \frac{\text{No. of crystals}}{\text{Total vesicle volume} + \text{Melt volume}}$$

(14)

The resolution of the scans was 6.5 um allowing for the capture of vesicles down to 2.7 x 10^{-7} mm^3. All pixel sizes analysed were included in the calculations of VND, these were manually checked during 3D rendering to determine the accuracy of the detection. The high-resolution scans allowed for confidence in the presence of these small vesicles and the decision to not remove them from the above calculations. The presence of large vesicles in the samples are scarce, therefore we focus on the populations of small vesicles within the samples which provide the most information about the vesiculation stage and fragmentation (Klug et al., 2002; Castro et al., 2003; Shea et al., 2010; Shea et al., 2012; Rotella et al., 2014). Detailed results are found in Appendix E.

2.4 Geochemistry

2.4.1 Electron microprobe analysis (EMPA)

Juvenile pumice clasts from -1 to -2 ϕ were cleaned in distilled water 3 times for 3 minutes using an ultrasonic bath and then were dried in an oven overnight at 65 °C. These clasts were then impregnated under vacuum with a low viscosity EpoThin 2-part epoxy resin with a ratio of 4:1, 4 parts Epoxy Resin to 1 Part Epoxy Hardner. Multiple vacuum rounds are necessary to remove bubbles from within the epoxy plugs. The epoxy mounds may require multiple rounds of impregnation to allow for all vesicles to be filled with epoxy. The mounts were polished with 220, 400, 600 and 1000 grit and 6, 3, and 1 um diamond paste. Each mount was cleaned for 2 minutes between each grit size in the ultrasonic bath with distilled water to remove polish residue. Throughout the grinding process samples may need to be re-impregnated if bubbles have not been filled all the way through and are exposed. Following re-impregnation, the polishing process needs to re start.

These 1-inch epoxy mounts were carbon coated before major and minor phases were analysed using a JEOL 8530F plus field emission gun electron microscope at The University of Auckland. Analysis was conducted using a focused beam (1-15 um), at 15 kV accelerating voltage and 20 nA beam current. The instrument was calibrated for optimal analysis of elements, using a variety of mineral, oxide, and glass standards (Table 2.2) (Jarosewich et al., 1980). Elemental measurements were conducted using program settings which are optimized for different mineral phases. Analysed glass points less than 98 % and

more than 102 % were excluded. The remaining data was normalized to 100 %. Standards used for different analysis were VG-A99 for glass, labradorite for feldspars and clinopyroxene for pyroxenes.

Detailed information about the standards, spot size, beam current, accelerating voltage and counting times for each phase are in Table 2.2.

Table 2.2: EMPA measurement conditions.

Phase	Standard	Element, standard and crystal	Beam size (um)	Beam Current (nA)	Accelerating voltage (kV)	Counting time on peak (s) (element)	Counting time background (s) (element)
Glass	VG-A99, VG-2, VG-568 Rhyolite	**Si** (Orthoclase – OR – 1 TAP), **Ti** (Ti LiFL), **Al** (Anorthite TAP), **Fe** (Fayalite LiFL), **Mn** (Manganosite LiFL), **Mg** (Periclase TAPL), **Ca** (Anorthite PETL), **Sr** (Strontonite TAPL), **Ba** (Barite PETL), **Na** (Jadeite TAPL), **K** (Orthoclase – OR – 1 PETL), **P** (USNM HoPO4 PETL), **S** (Barite PETL), **Cl** (Sodalite PETL), **F** (CaF2 TAPL).	1	20	15	10 (Na), 30 (all)	5 (Na), 15 (all)
Pyroxene	Clinopyroxene	**Si** (Orthoclase – OR – 1 TAP), **Ti** (Ti PETL), **Al** (Augite TAP), **V** (V2O5 LiFL), **Cr** (Cr LiFL), **Fe** (Fayalite LiFL), **Ni** (Ni Olivine LiFL), **Mn** (Rhodochrosite LiFL), **Mg** (Fo88 Olivine TAPL), **Ca** (Anorthite PETL), **Na** (Jadeite TAPL), **K** (Orthoclase – OR – 1 PETL).	1-2	20	15	10 (Na), 30 (all)	5 (Na), 15 (all)
Plagioclase	Labradorite	**Si** (Orthoclase – OR – 1 TAP), **Ti** (Ilmenite PETL), **Al** (Anorthite (TAP), **Fe** (Fayalite LiFL), **Mn** (Rhodochrosite LiFL), **Mg** (Spring Water Olivine TAPL), **Ca** (Anorthite PETL), **Sr** (SrF2 for TAPL), **Ba** (Barite PETL), **Na** (Albite TAPL), **K** (KCl PETL).	15	20	15	10 (Na), 30 (all)	5 (Na), 15 (all)

2.4.2 X-ray fluorescence analysis (XRF)

Unaltered pumice clasts from each of the Poto and Paetahi Formations were cleaned in an ultrasonic bath with distilled water and dried in the oven at 110°C for at least two hours. The samples were then powdered in a tungsten grinding machine to avoid Fe contamination and kept in the oven at 110°C for at least two hours. Loss on ignition (LOI) was determined by weighting c. 2 g of powder before and after heating in an oven at c. 900°C for three hours. After heating, c. 0.8 g of the powdered sample was mixed with c. 8.0 g (± 0.0010 g) of lithium tetraborate: lithium metaborate (12: 22) flux mixture, followed by fusion to produce a glass disc using a XRFuse2 electric fusion apparatus at Massey University.

Glass discs were analysed for major element concentrations using a 1 kW Bruker Tiger S8 Series II WD-XRF spectrometer at Massey University in Palmerston North, New Zealand. Interference-corrected spectra intensities were converted to oxide concentrations using calibration curves consisting of natural standards. Long-term reproducibility of the instrument was assessed using the basaltic Oreas 24c and granodioritic Oreas 24b standard reference materials. 1σ reproducibility is typically ± 0.5-1% relative for major oxides and better than ± 3% relative for minor oxides, except for P_2O_5 (± 5-10%).

2.4.3 Laser ablation inductively coupled plasma mass-spectrometry (ICP-MS)

Rock powders previously fused with x-ray flux for XRF major element analysis was used for trace element analysis for whole rock samples. Analysis of 35 trace and minor elements was conducted. Analysis was run as 50 um spots on the surface of the disks. Minor and trace element analysis was obtained using an Agilent 7500 Quadrupole ICP-MS equipped with a Resonetics RESOlution M-50-LR Excimer (193 nm) laser ablation system and a Laurin Technic sample cell housed at the University of Otago Centre for Trace Element Analysis. Standard National Institute of Standards and Technology Standard Reference (NIST SRM 610 and 612) were used as reference standards for calibration, error analysis and drift correction. The laser settings for analysis were set at 10 Hz pulse frequency, 29 kV voltage and 140 mJ energy. The on-sample flux was c. 2.5 J/cm^2. ^{43}Ca was used as the normalizing isotope, with data reduction conducted using the LAtools package (Branson et al., 2019) on Jupyter Notebook.

2.5 Limitations of the data

2.5.1 Synchrotron Data

Due to the increased resolution obtained through synchrotron radiation there is an increased number of small bubbles analysed within the pumice clasts. However, with this there is also the

detection of small apertures which would not have been previously detected through 2D analysis interconnecting a large network. Each sample had evidence of one large bubble corresponding to either large permeable connected bubble pathways or edges of the pumice core where vesicle walls had been removed during sample preparation. These large, connected pathways were not separated into individual vesicles due to their natural connected behaviour (e.g., Colombier et al., 2018; Torres-Orozco et al., 2023) and were not included in measurements as they created an outlier for vesicle size distributions.

With the removal of this large bubble, bubble size distributions and calculations on vesicle number densities and vesicle volumes are looking at the large population of small bubbles that exclude this large bubble. This is then only looking at 5-20 % of the vesicularity of the clast.

3 The stratigraphy and physical properties of explosive events from Mt. Taranaki, New Zealand pre- and post-edifice collapse.

Abstract

Edifice collapse events produce one of the most hazardous phenomena known at stratovolcanoes; debris avalanches that move rapidly down the flanks of the volcano burying the surrounding ring plain in meters to tens of meters of volcaniclastic material. The sudden removal of large portions of the edifice can furthermore cause depressurisation in the subvolcanic magmatic system, influencing the nature of subsequent eruptions. At Mt. Taranaki, New Zealand, these events have occurred frequently and at different time scales throughout the volcanic history forming a broad pattern of cyclic collapse and regrowth. About 20 – 30,000 years ago, Mt. Taranaki experienced two such cycles in short succession, where emplacement of the collapse-generated Ngaere debris-avalanche deposit at 27.3 ka (5.85 km^3) and the 24.8 ka Pungarehu debris-avalanche deposit (7.5 km^3) were preceded and followed by a sequence of twenty-eight closely spaced tephra deposits generating the Poto (lower) and Paetahi (upper) Formations during subsequent edifice regrowth. This research focuses on reconstructing the tephrostratigraphic framework of the Poto and Paetahi Formations, which record an increase in explosive activity that generated twenty-eight subplinian eruptions. We used stratigraphic mapping and sedimentological characterisation of the tephra layers, coupled with componentry and grain-size analysis to better understand potential variations in eruptive activity during these complex growth cycles. The thickness and distribution of the deposits revealed a minimum total eruptive volume of 1.6 km^3 for the Poto Formation and 1.4 km^3 for the Paetahi Formation, with some of the tephra beds identified up to 45 km from the present-day edifice. While eruptions directly following edifice failure were larger compared to those prior to collapse, this 4 kyr eruptive period had consistent large subplinian eruptions. In contrast large explosive events within the younger Holocene sequence are less frequent with more multiphase periods of effusive and explosive activity recorded. The number of large subplinian to plinian events from Mt. Taranaki during the Holocene was significantly lower than during the generation of the Poto and Paetahi Formations. Our new data furthermore highlights the need to include longer-term eruptive records in volcanic hazard modelling since the most recent volcanic history might not cover the full nature of volcanic processes occurring at long-lived stratovolcanoes.

3.1 Introduction

Stratovolcanoes around the world experience edifice or flank collapse events at least once during their lifetimes, which pose a major hazard to the surrounding landscape (McGuire, 1996; Siebert, 1996; Voight & Elsworth, 1997; Voight, 2000; Girina, 2013; Roverato & Dufresne, 2021). Major edifice failures also dramatically modify the morphology of the edifice, with changes to increased eruption rate (frequency and/or magnitude), magmatic composition or eruptive style observed at some volcanoes globally (Siebert et al., 2004; Tibaldi, 2004; Hora et al., 2009; Manconi et al., 2009; Zernack & Procter, 2021), while some volcanoes see no change in eruptive behaviour (e.g., Ponomareva et al., 2006; Zernack et al., 2012b; Zernack & Procter, 2021). The proximity of the failure to the source of magma can influence the response of the magmatic system influencing the eruption style, such as Pacaya Volcano, Guatemala changing from Strombolian prior to collapse to Phreatic and Phreatomagmatic erupting styles after collapse (Vallance et al., 1995; Rose et al., 2013; Gonzalez-Santana & Wauthier, 2021). Depending on how close the failure is to the magma source volcanoes can experience explosive activity (i.e., tephra fall, pyroclastic density currents and lateral blasts), through to effusive activity (i.e., lava flows and lava domes) (O'Callaghan & Francis, 1986; Luhr & Prestegaard, 1988; Vallance et al., 1995; Siebert, 1996; Vallance et al., 2001; Pallister et al., 2017).

Generating accurate eruption scenarios for hazard mitigation from potential future eruptions requires an extensive understanding of the eruptive history of a volcano. However, most eruption histories for volcanoes around the world are limited to the Holocene period due to better access and preservation of the younger records. As a result, the effects of large (prehistoric) edifice collapse events on subsequent eruptive activity are still poorly understood (Watt, 2019).

At Mt. Taranaki, the long-term (200 kyr) volcanic history and predominant landscape-shaping processes are well understood and have been reconstructed based on volcaniclastic records preserved in the surrounding ring plain (Neall, 1979; Alloway et al., 1995; Procter et al., 2009; Zernack et al., 2009; Zemeny et al., 2021; Zernack, 2021). These studies have shown that one of the major hazards at Mt. Taranaki is edifice failure with fourteen major collapses identified in its eruptive history (Zernack et al., 2011; Zernack et al., 2012b). Yet only data on eruptive behaviour, and changes in the patterns of eruptive styles of the last 5,000 years (Platz et al., 2007; Turner et al., 2008b; Torres-Orozco et al., 2018; Lerner et al., 2019d) were used to generate a modular framework for likely future hazard scenarios from this long-lived stratovolcano (Weir et al., 2022). This period is too short to encompass the much longer timeframes of cyclic behaviour of Mt. Taranaki. It also fails to take into account the volcano's history of frequent edifice failure and the impacts such large-scale events have on the subvolcanic plumbing system and eruptive behaviour, with the last event, the 7.5 ka Opua collapse, pre-dating this framework by more than 2,000 years.

While most studies on eruptive histories and processes are limited to the Holocene record (< 12 ka), we focused on the 20-30 ka period which broadly coincides with the Last Glacial Maximum (LGM) (25-14 ka) (McGlone et al., 1996). In the Taranaki region the LGM was associated with a cold dry climate with increased erosion along streams and high rates of aeolian redistribution of tephra (Neall, 1975; McGlone et al., 1996). Preservation of tephra deposits within the stratigraphic record is highly dependent on local climate and vegetative cover (Neall, 1972). Older eruptive deposits are typically underrepresented within the volcanic record due to erosion and subsequent burial by younger eruptive products. During the LGM in Taranaki there was less vegetation due to the cooler climate increasing the amount of erosion occurring on the Poto and Paetahi tephras (Frostick & Reid, 1989; Hubert & Filipov, 1989; Blair, 2000). Present day climatic conditions in the Taranaki region leads to high soil production and large percentage of vegetative cover further adding to the erosion and weathering of older tephra deposits (Dorn et al., 1987; Frostick & Reid, 1989; Ritter et al., 1995; Lavigne & Thouret, 2003; Lavigne, 2004; Zanchetta et al., 2004; Scott et al., 2005; van Westen & Daag, 2005; Zernack, 2008). This time period in Mt. Taranaki's history is characterized by two closely spaced large edifice collapse events producing the 27.3 ka (5.85 km^3) Ngaere and 24.8 ka (> 7.5 km^3) Pungarehu debris-avalanche deposits (DAD). Eruptive activity preceding and following the collapse events involved a series of tephra deposits providing a unique opportunity to investigate the influence that a large edifice has on the eruptive size, style, and frequency at a long-lived stratovolcano. Globally this data is sparse within volcanic records due to poor preservation of eruptive material around DAD's. This research examines the response of a long-lived stratovolcano to large edifice collapse.

3.2 Geological Setting

Mt. Taranaki (formally known as Egmont Volcano) is the second highest stratovolcano in New Zealand (2,518 m a.s.l.) and almost symmetrical except for the parasitic cone Panitahi (Fanthams Peak) at 1,952 m (Neall et al., 1986; Cronin et al., 2021). Mt. Taranaki has experienced at least fourteen collapse events throughout its > 200 kyr history (Zernack et al., 2012b; Cronin et al., 2021; Zernack & Procter, 2021), due to this the present-day edifice is comprised of only a small percentage of the total volume of erupted material (c. 12 km^3) (Procter, 2009) representing eruptive material from the last 10,000 years (Druce, 1966; Neall, 1979; Neall et al., 1986; Platz et al., 2007; Turner et al., 2008b; Zernack et al., 2009; Turner et al., 2011; Platz et al., 2012; Torres-Orozco et al., 2017a; Cronin et al., 2021). These Holocene volcanic deposits depict activity from explosive plinian eruptions to effusive periods involving minor lava flows and dome building events (Alloway et al., 1995; Stewart et al., 1996; Price et al., 1999; Turner et al., 2008b; Damaschke, 2017; Damaschke et al., 2017b; Torres-Orozco et al., 2017a; Torres-Orozco et al., 2017b; Turner et al., 2018). The edifice stratigraphic record is patchy due to unconsolidated pyroclastic material being prone to erosion and mass-wasting events and new eruptions burying the older sequences (Alloway et al., 1995; Cronin et al., 2021).

Mt. Taranaki is surrounded by a voluminous (> 150 km^3) ring plain comprised of volcaniclastic sequences that provide a record of the older volcanic history (Chapter 1; Figure 1.4) (Neall et al., 1986; Palmer & Neall, 1991; Alloway et al., 2005; Zernack et al., 2011; Damaschke et al., 2017b; Cronin et al., 2021; Zemeny et al., 2021). Along the northern coastline, the older (> 100 ka) ring-plain succession is dominated by DADs and intercalated tephra beds (Alloway et al., 1995), including the Mangati Formation, the oldest recognised DAD from Mt. Taranaki, which indicates that volcanism started prior to 200 ka (Zernack et al., 2011). A unique combination of uplift and coastal erosion has provided access to the volcaniclastic succession of the western to southern ring plain allowing a detailed reconstruction of Mt. Taranaki's long-term growth and collapse history predominantly comprising < 100 ka DA, lahar and fluvial deposits, exposed along the coastal cliffs (Ui et al., 1986b; Pillans, 1990; Palmer & Neall, 1991; Procter et al., 2009; Zernack et al., 2009; Zernack et al., 2011; Roverato et al., 2015; Cronin et al., 2021; Zernack, 2021). While primary deposits are rare in these coastal cross-sections due to distance from source (20 -35 km) and off-wind direction, tephra sequences from the last 30 kyr are accessible downwind from Mt. Taranaki's summit vent in the southeastern to northeastern ring-plain sector, where the full spectrum of primary and reworked volcanic material is recorded due to the predominant westerly winds (Alloway et al., 1995; Zernack et al., 2011; Cronin et al., 2021).

However, the most complete eruptive record is preserved in the youngest, < 30 ka ring-plain succession with at least 272 individual eruptions having been identified and grouped into formations (Alloway et al., 1995; Turner et al., 2009; Damaschke et al., 2017b; Torres-Orozco et al., 2017a; Torres-Orozco et al., 2017b; Cronin et al., 2021). During this period, four edifice failures occurred, including two of the largest recorded events producing the Pungarehu DAD (7.5 km^3) at c. 24.8 ka to the west and the Ngaere DAD (5.85 km^3) at c. 27.3 ka to the southeast, intercalated tephra sequences representing subsequent growth phases are well exposed within this timeframe (Neall, 1979; Ui et al., 1986b; Alloway et al., 2005; Zernack et al., 2011; Cronin et al., 2021).

3.3 Tephrochronology

The most complete tephra record from Mt. Taranaki is preserved in the north-north-east to south-south-east sector of the ring-plain, due to prevailing westerly winds (Neall, 1972; Alloway, 1989; Alloway et al., 1995; Turner et al., 2009; Damaschke et al., 2017b; Cronin et al., 2021). The older tephras are exposed in peats within coastal cliff sections in the north, south and western parts of the peninsula providing a tephrostratigraphic framework for the past > 130-25 kyr (Alloway, 1989; Newnham & Alloway, 2004; Alloway et al., 2005; Zernack et al., 2011). Distal lakes and peat on the eastern ring plain have preserved the most complete tephra record for the past 30 kyr, where 272 individual tephra beds were identified (Damaschke et al., 2017b; Torres-Orozco et al., 2017a; Torres-Orozco et al., 2017b). The last large explosive eruption at Mt. Taranaki was the Burrell eruption in 1655 CE (Druce, 1966), which produced widespread tephra fall across the central North Island (Platz et al., 2007). Mt.

Taranaki's last known activity occurred between 1700-1800 CE and included many small explosive to effusive eruptions before the extrusion of the current summit dome (Platz et al., 2012; Lerner et al., 2019d; Lerner et al., 2019a; Lerner et al., 2019b).

An extensive period of eruptive activity between 20-30 ka produced the Poto and Paetahi Formations. The Poto Formation was identified as having fifteen depositional layers, including fourteen tephra layers, and one pyroclastic surge deposit (Alloway et al., 1995). Dating of the Formation has revealed an age range of 27.3-25 ka sitting between the 28.7-28.1 ka Tuikanga tephras and the 24.1-23.1 ka Paetahi tephras, the latter comprising six depositional layers (Alloway et al., 1995). At the base of the Poto Formation it is separated from the four Tuikonga tephras by a < 15 cm paleosol. The Paetahi Formation sits between the Poto Formation and the 15,326 ± 354 ka Kaihouri tephras (Alloway et al., 1995), it is separated from the eight Kaihouri tephras by a 14 cm Paleosol. The Kaihouri tephra layers are each separated by thin lenses of aeolian andesitic soils correlated to the Katikara Formation (Neall, 1975; Alloway, 1989; Alloway et al., 1995). Paetahi.a is an important marker layer within the Poto and Paetahi eruptive period as it is widely dispersed across the eastern sector of the Taranaki ring plain situated above a very well developed paleosol (Alloway et al., 1995). This unique stratigraphic position within the ring plain allows for relative correlations of other tephra layers from within the Poto and Paetahi Formations as some individual tephra layer correlations are difficult on their own due to similarities between layers and weathering of deposits. The presence of the rhyolitic Kawakawa-Oruanui Tephra (KOT previously referred to as Aokautere Ash) derived from the 25.4 ka Oruanui Eruption of Taupo Volcano (Pillans et al., 1993; Wilson, 2001; Lowe et al., 2008; Vandergoes et al., 2013) a yellowish-white, glass rich coarse ash layer easily identifiable in the stratigraphy around Mt. Taranaki (Geddes et al., 1981; Franks, 1984; Alloway et al., 1995; Alloway et al., 2005) and in eastern and southeastern sectors of the ring plain is situated in-between Poto.e and Poto.f layers that closely overlie the Ngaere DAD (Alloway et al., 1995).

Another key time marker intercalated with Poto tephras and directly overlying Poto.b is the Ngaere DAD (Alloway et al., 1995; Neall & Alloway, 2004; Alloway et al., 2005). The Ngaere DAD (27.3 ka) is one of the largest debris avalanches to have occurred from Mt. Taranaki with a volume of > 5.85 km^3 covering 320-500 km^2 of the southeastern ring plain and southeastern lower flanks (Alloway, 1989; Neall & Alloway, 2004; Alloway et al., 2005). Across the western sector of the Taranaki ring plain the occurrence of the KOT is sparse, typically confined to coastal cliff sections or aeolian dunes which boarder the 24.8 ka Pungarehu DAD across the northeastern sector of the ring plain. The absence of accessible deposits of the KOT across western Taranaki is associated with burial by the 24.8 ka Pungarehu DAD, the largest recorded DAD from Mt. Taranaki with a volume > 7.5 km^3 covering an area of 200-250 km^2 with a thickness that exceeds 70 m in proximal regions of the ring plain (Neall, 1979). The emplacement of the Pungarehu DAD co-insides with the timing of the Poto and Paetahi tephras (Zernack et al., 2009), with the presence of the KOT underneath the Pungarehu within

southwestern coastal cliffs distinguishing pumice deposits which post-date the emplacement of the eastern Ngaere DAD.

3.4 Methodology

The Poto and Paetahi tephra beds were originally identified on the southeastern ring plain interbedded with andic paleosols (Alloway et al., 1995), with subsequent additional localities extended across a wide east to southeastern arc between 11 and 45 km from the present-day summit vent (Figure 3.1). Preservation of tephras across the landscape were varied, especially towards the northeastern sector of the ring plain where subsequent burial underneath younger deposits associated with the dominant wind direction and industrialisation have removed or buried deposits. Previously identified deposits to the northeast (Alloway et al., 1995) were not identifiable in the field. Preservation of these deposits does not appear to exist. Because of this these deposits have not been used in volume calculations or isopach maps in this study. Extended locations identified in this study were used to correlate individual depositional layers across the Taranaki region. Individual depositional layers were identified through differences in lithosedimentological characteristics from the surrounding layers. Boundaries were marked by a sharp contact or a blurred contact with changes in lithosedimentological characteristics (i.e., lithology, contained within a clay-rich paleosol or clast supported, grain size, presence, or lack of a paleosol).

Eruptive events were divided into single-phase (individual events) or multiphase (multiple events) due to their depositional characteristics (e.g., Voloschina et al., 2020) which were classified as below.

- Single phase (SB) layers appear in pockets within the stratigraphy creating a wavy appearance with boundaries characterised by paleosols, or distinct/blurred contacts between depositional units. Internal variations are not quantifiable within the individual layers. Some layers have distinguishable features in relation to others which assist with correlations of single-phase events between locations.
- Multi-phase (MB) layers were originally recognised as single bed layers by (Alloway et al., 1995) which had internal depositional characteristics (i.e., Paetahi.a referred to shower bedding). These layers have been reclassified as multi-phase layers within this study as they showed internal variations in deposits which are marked by lithosedimentological features such as lithology, grainsize, deposit texture or colour (e.g., Voloschina et al., 2020). Depositional distributions of these multi-phase layers are found across the eastern and southeastern sectors of the Taranaki ring plain within the stratigraphic set (lower to upper) or as individual subunits.

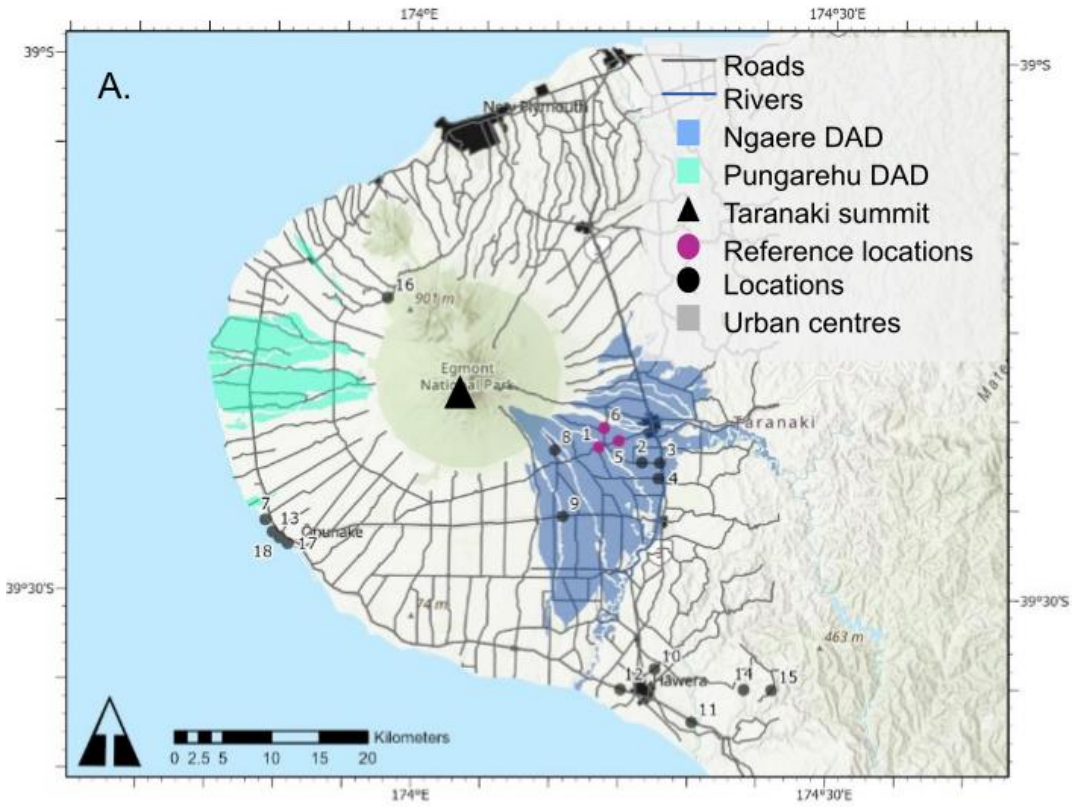


Figure 3.1: Field location map of the Poto and Paetahi Formations across the Taranaki ring plain.Road and Topographic data sourced from the LINZ Data Service licensed for reuse under CC by 4.0.

Lithosedimentological features of each layer was recorded including consolidation, grain size characteristics following (Wentworth, 1922; White & Houghton, 2006), grading, sorting, componentry, thickness and contact types (Torres-Orozco et al., 2017b).

Further grain size analysis and point counts were performed on selected samples. Manual dry sieving at 0.5 ϕ intervals between -4 and 4 ϕ was conducted and individual grain sizes were weighed and normalised to 100. Statistical parameters (Folk & Ward, 1957) for grain size were obtained through GradiSTAT (Blott & Pye, 2001) using a size scale modified after (Udden, 1914; Wentworth, 1922).

The -1.5 and 0.5ϕ size fractions were chosen for componentry analysis, allowing comparison between the dominant lapilli-bearing deposits and the finer grained ash beds. On average, at least 300-500 grains were used for point count analyses, although for some layers this is less in the -1.5 ϕ clast size due to a lack of coarser particles within the deposit. The percentages of the individual componentry classes were calculated relative to the total number of grains counted, distinguishing between juveniles (primary erupted material), lithics (secondary material that has been brought up during the eruptions i.e., lithic clasts comprised within pyroclastic deposits can be from older eruptive products or material excavated from the conduit wall and basement rock (Sparks, 1976; Fisher & Schmincke, 1984)) and thus provide information on the lithologies making up the conduit and subvolcanic basement along with the conduit

geometry (Carey & Houghton, 2010; Campbell et al., 2013; Paredes-Mariño et al., 2019) and free crystal components, (i.e., matrix-free crystals generated through the fragmentation of crystal rich pumices during the eruptive phase (Sparks, 1976; White & Houghton, 2006; Paredes-Mariño et al., 2019). With these lithologies, we further distinguished subgroups with two main juvenile classes: 1. Grey pumice, 2. Brown pumice ; four main lithic classes; 3. Altered pumice; 4. Grey lithics, 5. Altered lithics, 6. White clay and four main crystal classes: 7. Feldspars, 8. Pyroxenes, 9. Amphiboles and 10. Glomerocrysts (Figure 3.2).

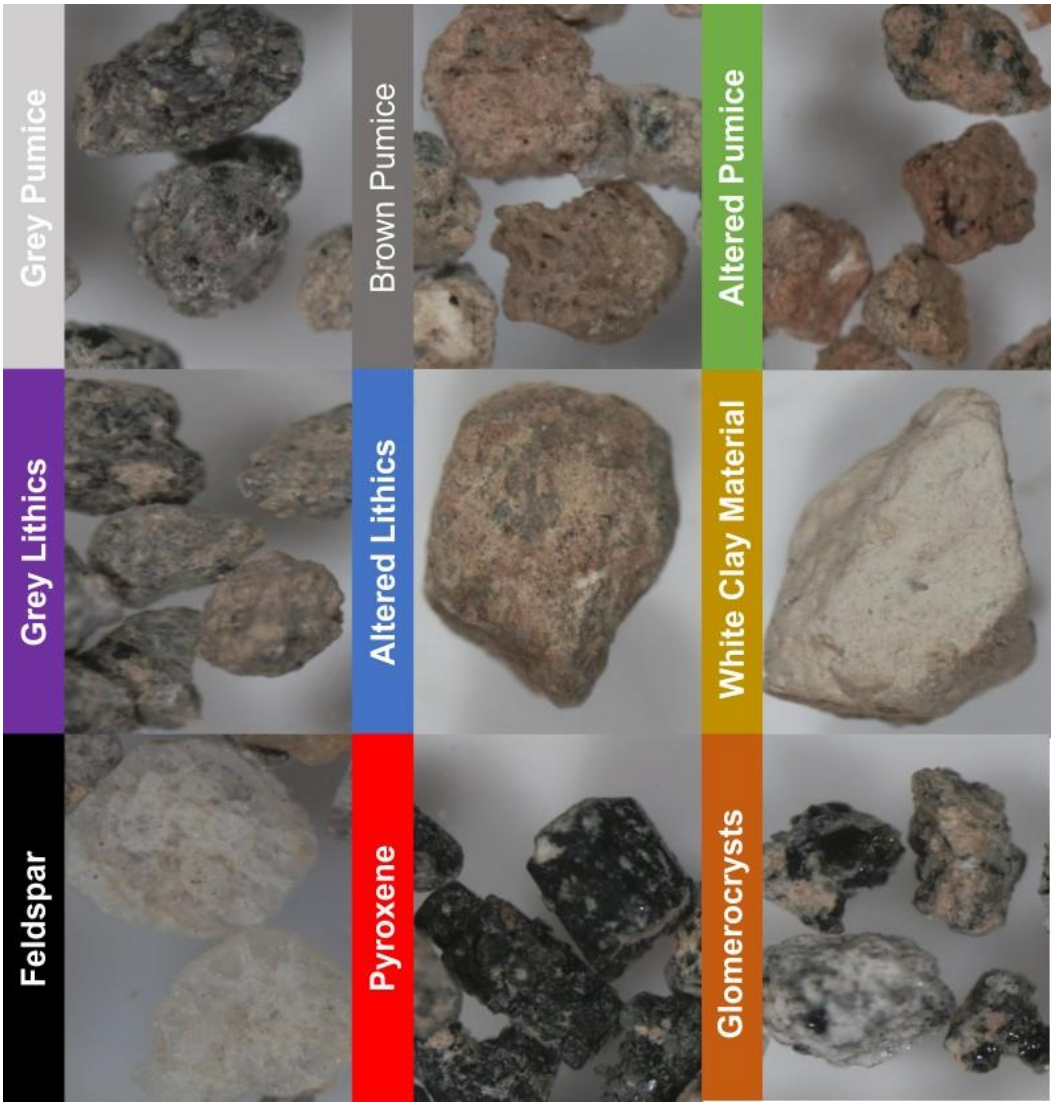


Figure 3.2: Images of the different compositional classifications used in characterizing deposits from the Poto and Paetahi Formation. Grains are from the -1.5 phi and 0.5phi grain size. Descriptions of the different components in located in Table 3.3.

The age and location of the Poto and Paetahi Formations means that a lot of the tephras are consolidated within a yellowish-brown clay-rich paleosol which consists of strongly weathered soft orange lapilli (Tables 3.1 and 3.2) (e.g., Neall, 1977). This impacts analysis through analytical methods as these

tephras are visible in the outcrop but are not able to be sampled whole. To reduce the effects of analytical bias on componentry and grain size, analysis was conducted on samples from the reference locations: 1. Ronald Road: (15km from present day edifice), 5. Opunake Road (17 km from present day edifice) and 6. Paetahi Stream (15 km from present day edifice), so that deposits would have been subjected to similar weathering processes. This weathering process may have had an impact on the percentage of pumice clasts within a layer. However, lithic dominated layers contain a significantly higher proportion of lithic clasts than pumice clasts. The amount of pumice weathering at the reference locations should be fairly similar allowing for the comparison of components between depositional layers.

Deposit thicknesses in centimetres was used to construct isopachs for each identified tephra layer. At more distal locations it becomes difficult to take reliable thickness measurements for some of the Poto and Paetahi tephras. The dispersal limits for these layers were set to where scattered clasts are no longer visibly present. Isopleth maps were generated using the largest grainsize within the deposit at each of the studied locations, determined through dry sieving. With increasing distance from the edifice, the grainsize decreases. The weathering of some of the layers may have affected the grainsize in some locations, in this case some of the layers were not classified as reliable enough for use in isopleths. Preservation and accessibility of deposits from the Poto and Paetahi tephras across the ring plain means that calculated eruptive parameters would be minimum values. Volume estimates for individual layers were calculated using the Weibull model (Bonadonna & Costa, 2012; Bonadonna & Costa, 2013a) produced in AshCalc (Daggitt et al., 2014) using the equation

$$((T(x) = \theta(\frac{x}{\lambda})^{k-2} e(\frac{x}{\lambda})^{k})$$

(15)

where the thickness, *T*, is related to the square root of the isopach area, *x*. Input parameters for the model used isopach thickness (m) and √Area (km) ($A^{1/2}$). This model has incorporated ʎ as a parameter to allow for the variation in thinning rate that is seen in tephra deposits with multiple segments (Daggitt et al., 2014), which works well with the more medial and distal deposits with a decrease in the thickness as we move away from the source (Bonadonna & Costa, 2012; Bonadonna & Costa, 2013a). Eruption column heights (H) were calculated using the (Mastin et al., 2009) equation

$$(H = 25.9 + 6.64\log^{10}(\text{dreV})).$$

(16)

The total erupted mass (mT) was calculated after the equation

$$\text{mT} = (\text{volume} * 1000\ \text{kg/m}^3)$$

(17)

from Wilson (1976). Mass eruption and discharge rates (MER and Q) were calculated using methods from (Sparks, 1976; Mastin et al., 2009).

$$\text{MER} = (\text{mass}/ (\text{rock density}) * 10^{-9}) \quad (18)$$

$$Q = ((\frac{H}{1.67})^{3.86}) \quad (19)$$

Eruptive magnitudes were calculated using equations

$$\log^{10}(\text{DRE[kg]})^{-7} \quad (20)$$

from Pyle, (2000). To estimate the minimum duration (hours) of the eruption the equation

$$((\text{mT/MER}) * 3600) \quad (21)$$

from Wilson (1976) was used.

3.5 Results.

3.5.1 Revised stratigraphy of the Poto and Paetahi Formations

The Poto Formation was named after Poto Road along Opunake Road in southeast Taranaki and occurs across the eastern, southeastern, and southwestern ring plain (Alloway et al., 1995). Across the ring plain, the majority of locations are situated between 11-25 km from source, with the most distal site being 45 km from the summit vent. Within the stratigraphy there are single and multiphase events with some layers separated by paleosols. At its reference section (location 1 Figure 3.1) east of Ronald Road along Opunake Road nineteen depositional layers are preserved (Table 3.1; Figure 3.3). At the base of the sequence two ash and lapilli fall layers occur (Poto.a and Poto.b) prior to the Ngaere DAD. Four ash and lapilli layers (Poto-c. l to e) and one pyroclastic density current (PDC) deposit (situated above Poto.e) occur above the Ngaere DAD and are overlain by the 25.4 ka rhyolitic Kawakawa tephra (c.f., Vandergoes et al., 2013). Situated above the Kawakawa tephra are twelve ash and lapilli layers (Poto.f to o).

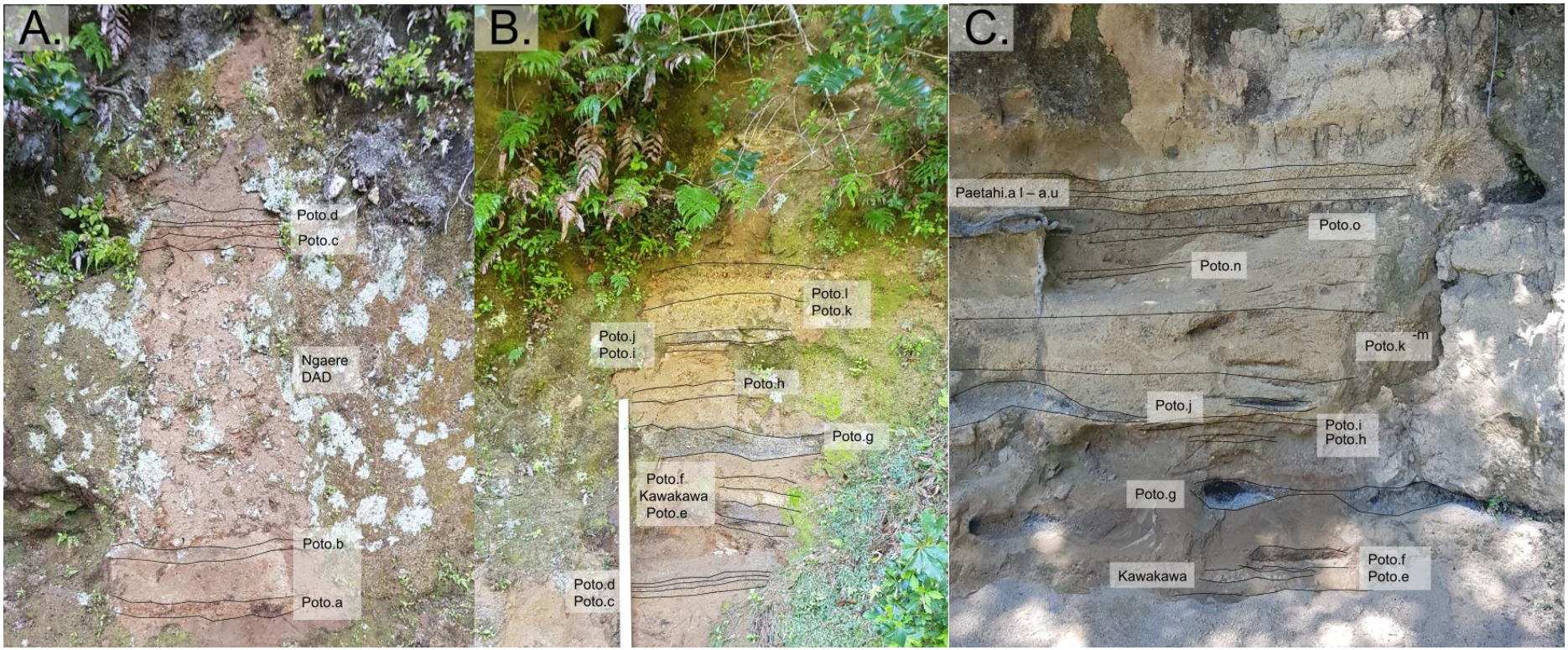


Figure 3.3: Complete depositional sequence for the Poto Formation at the Poto reference location (1. Opunake Ronald Road) including the Ngaere DAD and the Kawakawa tephra. a). Poto.a-Poto.d including the Ngaere DAD, b). Ngaere DAD-Poto.l, c). Poto.e - Poto.o including the Kawakawa Tephra.

Table 3.1: Description of the units within the Poto Formation. Grain size parameters determined through dry sieving and GradiSTAT analysis (Blott & Pye, 2001) (Descriptions are of deposits from the Poto reference location).

Name	**Maximum Thickness (cm)**	**Modality**	**Sorting**	**Grain Size (mean)**	**Componentry**	**Contact**	**Description**
Poto.a	9	Bimodal	Poorly	Very Fine Lapilli	Brown Pumice	Sharp contact at the base with 18cm soil. Gradual contact above with 9cm soil.	An unconsolidated clast supported deposit within a yellow-brown clay-rich paleosol which is distinctive at the base of the Poto Formation. At the base, the grains appear more reddish brown in the field.
Poto.b	5	Unimodal	Moderately	Very Fine Coarse Ash	Grey Lithics	Sharp contact below with 9cm soil. Sharp contact above the Ngaere DAD.	Unconsolidated dark grey deposit. Some small clasts present in the layer, mostly ash particles.
Poto.c lower	4	Polymodal	Very Poorly	Very Coarse Ash	Brown Pumice	Irregular contact at base with 4cm soil. Gradual contact above with Poto.c upper.	Loosely consolidated layer which fines upwards, contained within a yellow-brown clay-rich paleosol.

Poto.c upper	3	Unimodal	Poorly	Coarse Ash	Grey Pumice in coarser fraction. Grey lithics in finer fraction.	Gradual contact below with Poto.c lower. Sharp contact above with 3cm soil.	Layer appears in pockets across the outcrop. Dominated by unconsolidated material. Layer appears to erode more easily than Poto.c lower.
Poto.d	3	Bimodal	Poorly	Coarse Ash	Grey Pumice in coarser fraction. Brown Pumice in finer fraction.	Wavy contact below with 3cm soil. Wavy contact above with 3cm soil.	Unconsolidated material within a yellow-brown clay-rich material. The layer appears in pockets across the outcrop.
Poto.e	4	Trimodal	Very Poorly	Fine Ash	Grey Lithics	Gradual contact below with 3cm soil. Gradual contact above with PDC deposit.	Unconsolidated fall layer underneath a PDC deposit.
PDC deposit	4					Gradual contact above with Rhyolitic Kawakawa tephra.	Dark brown/grey clay-rich material containing light grey flecks of pumice. Small pumice 1-2 mm. A layer which is only present at the Ronald Road

							field site. Only appears in small pockets. The Kawakawa tephra is present directly above.
Poto.f	6	Polymodal	Very Poorly	Very Coarse Ash	Brown Pumice	Below sharp contact with Rhyolitic Kawakawa tephra. Gradual contact above with 7cm soil.	Orange-brown consolidated clay-rich paleosol supported layer. A range of pumice and lithic clasts present. No apparent grading.
Poto.g	3-8	Unimodal	Moderately	Very Coarse Ash	Grey Lithics	Sharp contact below with soil 7cm. Gradual contact above with 1-2cm soil.	Unconsolidated layer which thickens and thins across the outcrop. Layer has eroded out in areas.
Poto.h	4	Polymodal	Very Poorly	Coarse Ash	Grey Lithics	Wavy contact at base with 1-2cm soil. Wavy contact above with 3cm soil.	Orangey grey consolidated clay-rich material layer. Layer appears to be dominated by grey clasts. Clasts range between 1 mm to 1 cm.

Poto.i	4-7	Polymodal	Very Poorly	Very fine Lapilli	Brown Pumice	Wavy contact below with 3cm soil. Sharp contact above with Poto.j.	Yellowish brown clay-rich paleosol layer containing weathered pumice. There are some bands containing more grey clasts.
Poto.j	3	Trimodal	Poorly	Very Coarse Ash	Grey Lithics	Sharp contact at base with Poto.i. Sharp contact above with Poto.k lower.	Easily eroded unconsolidated layer which contains a band through the middle which has lighter grey material present. The layer has been eroded out in patches.
Poto.k lower	8	Polymodal	Very Poorly	Very Coarse Ash	White clay material in coarser fraction. Brown Pumice in finer fraction.	Sharp contact below with Poto.j. Sharp contact above with Poto.k upper.	Layer is within a yellow, brown clay-rich material Appears to contain more grey clasts in the field.
Poto.k upper	4	Polymodal	Poorly	Very Fine Lapilli	Brown Pumice	Sharp contact below with Poto.k lower. Gradual contact	Heavily weathered layer, within a yellowish-brown clay-rich material. This layer contains more

						above with l. lower.	brown lapilli than Poto.k lower visible in the field.
Poto.l lower	5	Trimodal	Very Poorly	Very Coarse Ash	Grey Lithics in coarser fraction. Brown Pumice in finer fraction.	Gradual contact below with Poto.k upper. Gradual contact with Poto.l upper.	Yellow-brown consolidated clay-rich paleosol layer containing a higher percentage of clasts 0.5-1cm diameter.
Poto.l upper	7	Trimodal	Poorly	Very Fine Lapilli	Brown Pumice in coarser fraction. Grey Lithics in finer fraction.	Gradual contact below with Poto.l lower. Gradual contact above with Poto.m.	Yellow-brown consolidated clay-rich material layer, although more clast supported than Poto.l lower. There is reverse grading within the layer.
Poto.m	11	Polymodal	Very Poorly	Very Coarse Ash	Brown Pumice in coarser fraction. Grey lithics in finer fraction.	Gradual contact below with Poto.m. Gradual contact above with 5cm soil.	Heavily weathered consolidated clay-rich layer. Pumice is soft and easily erodible. There is a mix of grey and brown clasts present.
Poto.n	8	Polymodal	Very Poorly	Very Coarse Ash	Brown Pumice	Gradual contact below with 5cm soil. Gradual contact	Yellow-brown consolidated clay-rich paleosol layer. Towards the top of this layer

						above with 6cm soil.	there is a band of orange clasts present.
Poto.o	5	Polymodal	Very Poorly	Coarse Ash	Grey Lithics in coarser fraction. Feldspars and Pyroxenes in finer fraction.	Gradual contact below with 6cm soil. Sharp contact above with well-defined dark brown 6cm soil.	Yellow-brown consolidated clay-rich material., containing pumice and lithic clats. The top section of this layer has a darker orange band present.

The majority of individual layers of the Poto Formation were originally described as ash and lapilli fall layers with one layer (Poto.i) tentatively described as a thin PDC bed based on sorting and the occurrence of cross laminations (Alloway et al., 1995). Within this study the tephrastratigraphy of the Poto Formation has been expanded identifying layers as single phase and multiphase layers dependent on depositional characteristics. This has added three new subunits to the original Poto stratigraphy (Poto.c upper, k upper and l upper). The majority of individual Poto Formation layers are ash and lapilli fall layers with one PDC deposit located directly above Poto.e. This PDC layer is only found at the Poto reference section. Poto.i was previously recorded as a PDC deposit (Alloway et al., 1995). This study has reclassified Poto.i as a fall due to the layer containing moderately sorted pumice and lithic clasts. Poto.i appears within pockets across the outcrop with no bedding features. The Poto.b fall deposit directly underlies the Ngaere DAD which has been postulated as an indicator that the Ngaere collapse event was magmatically triggered (Alloway et al., 2005; Zernack, 2008) due to the stratigraphic relationship between the deposits and the subsequent tephra fall layers following the collapse generating the Poto tephra formation (Druitt, 1992; Sisson, 1995; Belousov et al., 2007).

The identified ash and lapilli fall layers have varying grain sizes ranging from fine ash to coarse lapilli, with the majority being dominated by very coarse ash (Tables 3.1 and 3.2). Most of the Poto layers are supported by a yellow-brown consolidated clay-rich paleosol containing orange pumice. The included pumice clasts are soft, indicating that these layers are more strongly weathered. Less consolidated grey layers are also found throughout the sequence and have been more easily eroded out of the stratigraphic profile. Capping the Poto Formation is a 6 cm thick, well defined paleosol with a darker brown colour than the paleosols within the Poto Formation, marking the boundary to the overlying Paetahi Formation.

The Paetahi Formation was named after Paetahi Stream along Cardiff Road in southeast Taranaki (Alloway et al., 1995). This formation is located across the eastern, southeastern, and southwestern Taranaki ring plain (Figure 3.1) and is made up of ten ash and lapilli fall layers comprising grainsizes that range from medium ash to very fine lapilli with the majority of layers having very coarse ash texture. Within this study the tephrastratigraphy of the Paetahi Formation has been expanded identifying layers as single phase and multiphase layers dependent on depositional characteristics. This has added four new subunits to the original Paetahi stratigraphy (Paetahi.a middle, upper, e middle and upper). The majority of the locations are situated between 11-25 km from source, with some layers up to 45 km away from the present-day summit vent. The reference section for the lower six layers is located along Opunake Road west of Stratford (location 5 Figure 3.1) while the reference section for the upper four layers is located along Cardiff Road (location 6 Figure 3.1) on the southern side of Paetahi Stream (Table 3.2; Figure 3.4). At the Opunake Road reference section, 8 of the 10 depositional layers are present and the lower contact is sharp and marked by the well-defined paleosol at the top of the Poto Formation. One multiphase event is recorded at this site in the stratigraphy (Paetahi.a lower – upper) and four single-phase events and one subunit of a multiphase sequence (Paetahi.b – f including Paetahi.e middle). At the Paetahi Stream reference section eight depositional layers are recorded including two multiphase events Paetahi.a lower – middle (upper is missing at this location) and Paetahi.e lower – upper (Paetahi.e middle is found at the Opunake Road reference section) and three single-phase events (Paetahi.c, d, and f). The identified multiphase eruptions within the Paetahi Formation produced similar depositional characteristics both starting with an unconsolidated orange coarse ash to lapilli dominated layer followed by a change to a finer grainsize and a shift to a grey slightly more consolidated coarse ash layer. The upper beds record a shift back to orange dominated layers, with Paetahi.a upper being unconsolidated while Paetahi.e upper is strongly consolidated. Paetahi.e middle is the most widely distributed layer of the Paetahi.e multiphase event.

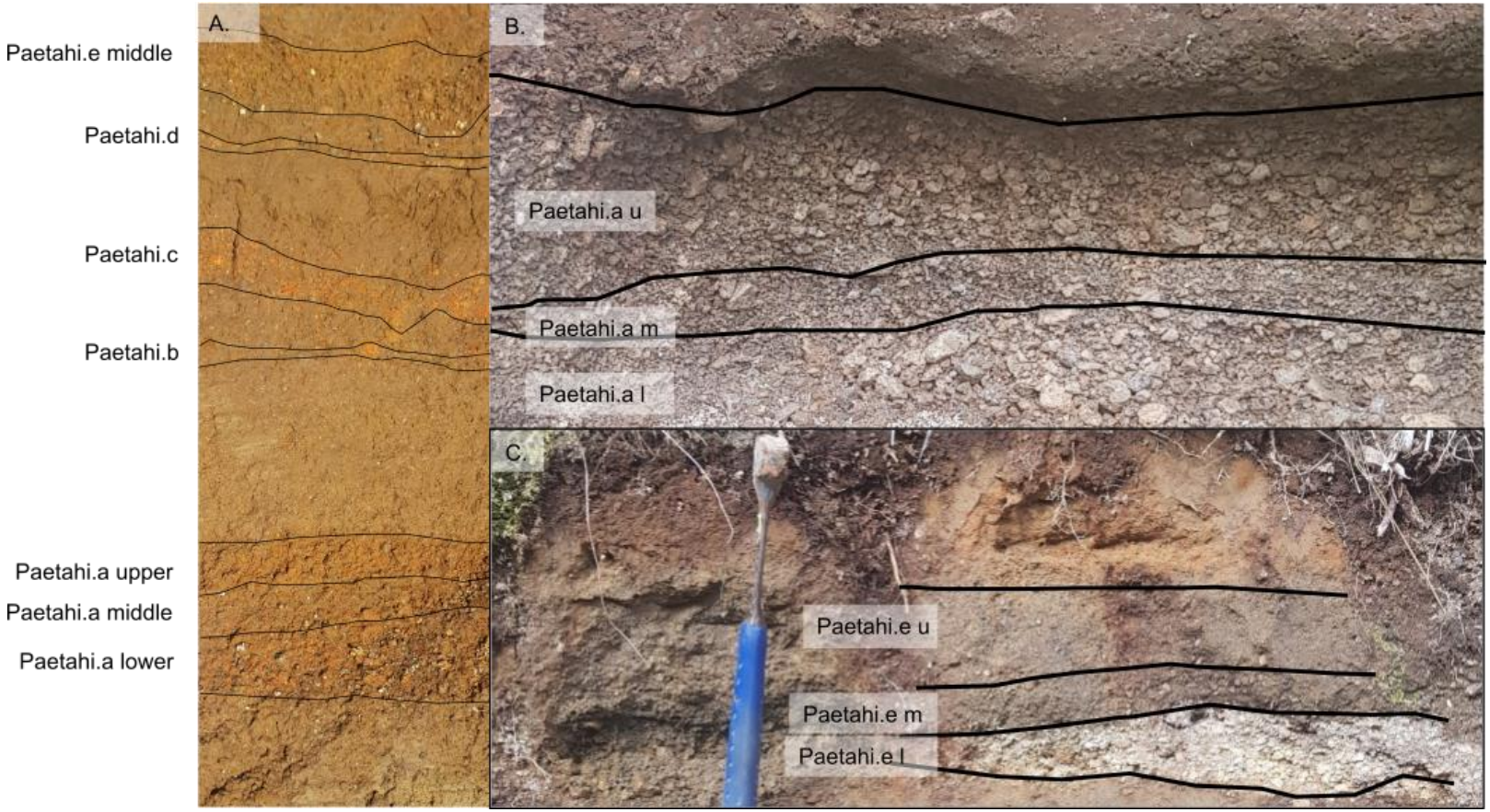


Figure 3.4: Field images of the Paetahi tephra formations. A. Depositional sequence of the Paetahi Formation at the Opunake Road (5.) reference location. B. Close up image of the Paetahi.a multiphase sequence showing the internal variation present within the layer allowing for the reclassification into Paetahi.a lower, middle, and upper at the Poto reference location (1. Opunake/ Ronald Road). C. Close up of the Paetahi.e multiphase sequence showing the internal variation present within the layer allowing for the division into Paetahi.e lower, middle, and upper at the Paetahi Stream (6.) reference location.

Table 3.2: Description of the units within the Paetahi Formations Grain size parameters determined through dry sieving and GradiSTAT analysis (Blott & Pye, 2001) (Descriptions are of deposits from the two Paetahi reference locations).

Name	**Maximum Thickness (cm)**	**Modality**	**Sorting**	**Grain Size (mean)**	**Componentry**	**Contact**	**Description**
Paetahi.a lower	8	Polymodal	Poorly	Very Coarse Ash	Grey pumice in coarser fraction. Brown Pumice in finer fraction.	Sharp contact below with the 6cm soil. Gradual contact above with Paetahi.a middle.	Unconsolidated layer, which is the most identifiable across the ring plain.
Paetahi.a middle	2	Unimodal	Poorly	Very Coarse Ash	Grey Pumice in coarser fraction. Brown Pumice in finer fraction.	Gradual contact below with Paetahi.a lower. Gradual contact with Paetahi.a upper.	Loosely consolidated layer. This layer is a thin band that appears greyer than Paetahi.a lower and Paetahi.a upper.
Paetahi.a upper	4	Bimodal	Poorly	Very Fine Lapilli	Brown Pumice	Gradual contact below with Paetahi.a middle. Sharp contact above with	Unconsolidated layer containing predominantly orange/ brown pumice clasts. Very similar to the Paetahi.a lower.

						13cm soil.	
Paetahi.b	2	Trimodal	Very Poorly	Coarse Ash	Grey Lithics	Gradual contact below with 13cm soil. Gradual contact above with 10cm soil.	Heavily weathered within a yellow-brown consolidated clay-rich material. This layer appears in pockets across the outcrop. Pumice is very soft and weathered at the surface.
Paetahi.c	13	Polymodal	Very Poorly	Medium Ash	Grey Lithics in coarser fraction. Pyroxenes in finer fraction.	Gradual contact below with 10cm soil. Sharp contact above with 8cm soil.	Heavily weathered within a yellow-brown consolidated clay-rich material. The layer thickens and thins across the outcrop. Pumice is very soft and weathered at the surface.
Paetahi.d	2	Polymodal	Very Poorly	Coarse Ash	Grey Pumice in coarser fraction. Brown Pumice in finer fraction.	Sharp contact below with 8cm soil. Gradual contact above with 6cm soil.	Heavily weathered orange, brown consolidated clay-rich material. Appears in pockets across the deposits.

							Pumice clasts are very soft.
Paetahi.e lower	7	Trimodal	Poorly	Fine Lapilli	Brown Pumice	Sharp contact below with 6cm soil. Gradual contact above with Paetahi.e middle.	Unconsolidated layer. Dominated by very coarse orange lapilli with some grey clasts present.
Paetahi.e middle	6	Bimodal	Poorly	Very Coarse Ash	Grey Lithics	Gradual contact below with Paetahi.e lower. Gradual contact above with Paetahi.e upper.	Loosely consolidated layer within an orange, brown clay-rich material, dominated by grey pumice/ lithic clasts.
Paetahi.e upper	9	Trimodal	Very Poorly	Coarse Ash	Grey Lithics in coarser fraction. Grey pumice in finer fraction.	Gradual contact below with Paetahi.e middle. Sharp contact above with Paetahi.f.	Orange, brown consolidated clay-rich material layer dominated by grey pumice/ lithics. This layer is very well consolidated and is very hard.
Paetahi.f	5	Polymodal	Very Poorly	Medium Ash	Grey lithics in coarser fraction.	Sharp contact below	Heavily weathered within an

					Brown Pumice in finer fraction.	with Paetahi.f. Gradual contact above with > 10cm soil.	orange, brown consolidated clay-rich material . The pumice in this layer is very soft and breaks apart easily. This layer is present within pockets.

The multiphase events of the Paetahi Formation are coarser grained and less consolidated than any of the other depositional layers in either formation across the ring plain they protrude out of the outcrop and appear to weather less easily compared to the surrounding layers. However, the Poto Formation comprises more of the grey unconsolidated layers. Both types of deposits allow for easier recognition and correlation across the ring plain (Appendix A). The majority of eruptive events within the Poto Formation (66 %) are single-phase (SB) events, compared to the Paetahi Formation where most (60%) of the eruptive events are multiphase (MB) (Figures 3.5 and 3.6). The single-phase events in the Paetahi Formation sequence are within a yellow-brown consolidated clay-rich paleosol containing a larger amount of soft pumice than the multiphase events. The upper boundary of the formation is characterised by a gradual contact to the overlying Kaihouri Tephra that is marked by a > 10 cm thick paleosol. The multiphase eruptions recorded within the Poto Formation are made up of two events compared to those within the Paetahi Formation, which comprise three events that also show internal variation in lithosedimentological characteristics (i.e., grain size, componentry, consolidation). Between the two formations the yellow brown consolidated clay-rich layers show very similar characteristics in the field meaning these more identifiable layers along with stratigraphic markers are vital for correlation.

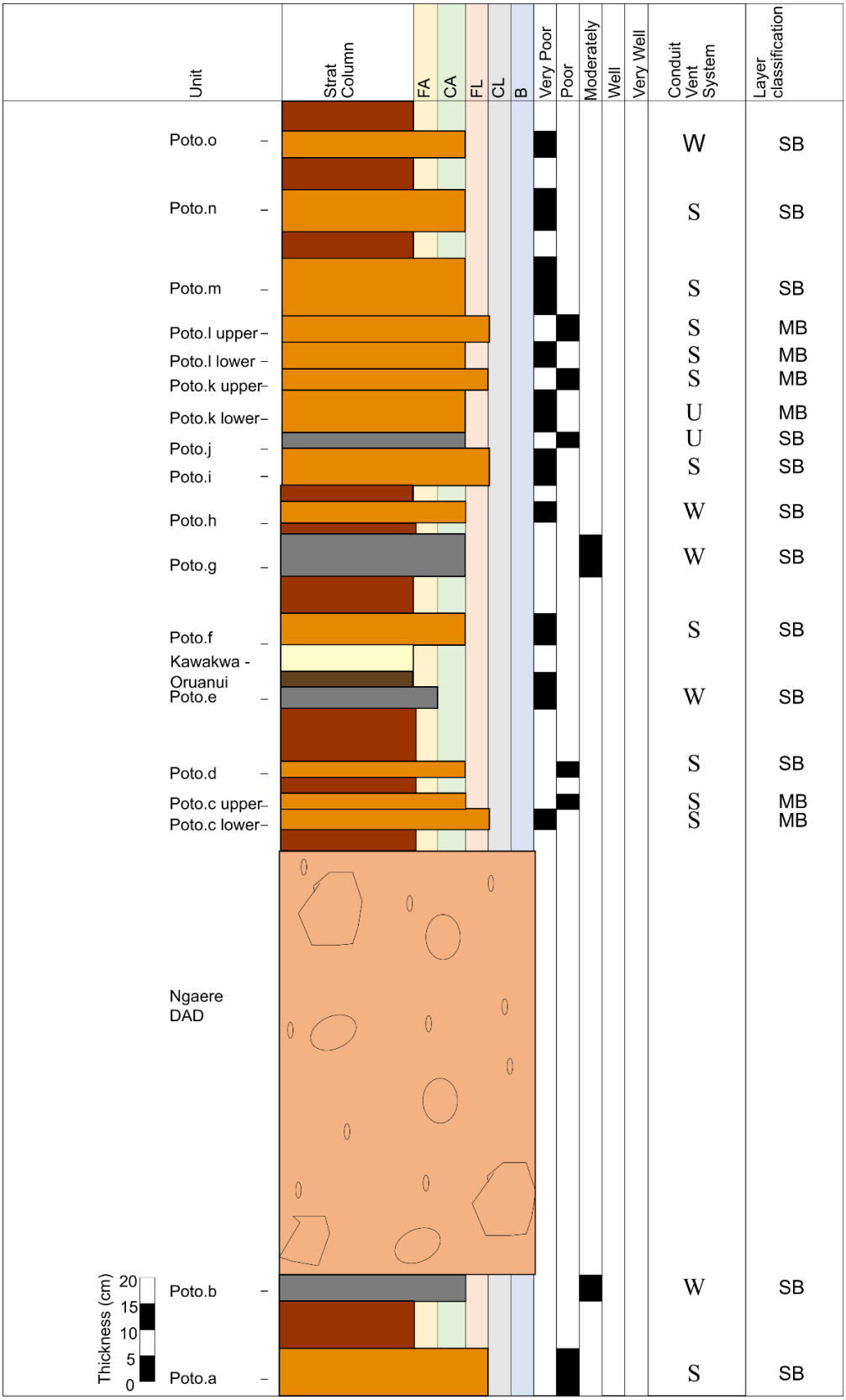


Figure 3.5: Stratigraphy of the Poto Formation showing the coarseness of the deposits, the sorting, vent system S). Stable conduit vent system, W). Conduit vent system widening and U). Unstable column/ conduit wall collapse. The layer

classification MB). Multiphase eruptive layer, SB). Single phase eruptive layer. Grain size, FA – Fine ash; CA – Coarse ash; FL – Fine lapilli; CL – Coarse lapilli; B – Blocks.

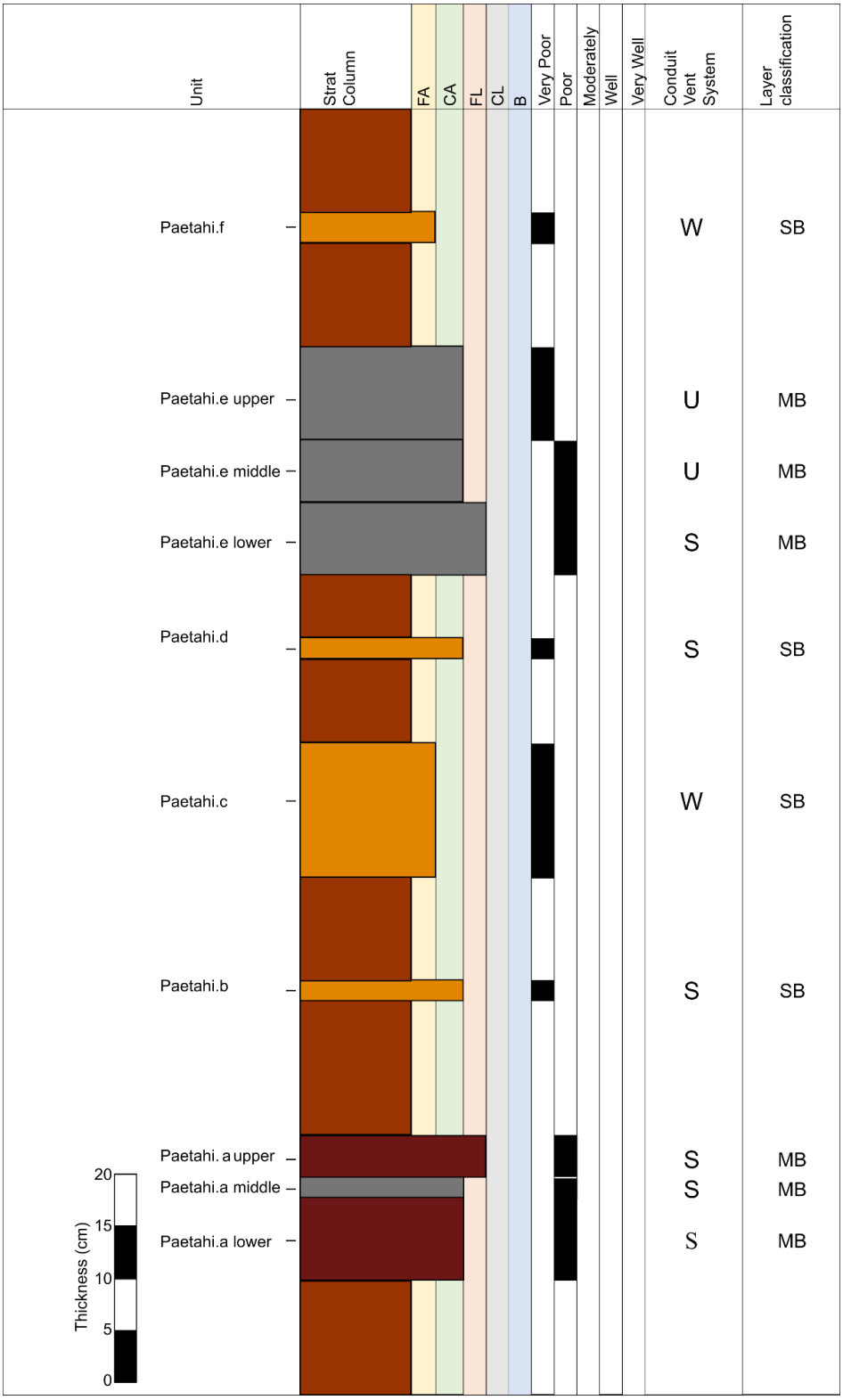


Figure 3.6: Stratigraphy of the Paetahi Formation showing the coarseness of the deposits, the sorting, vent system S). Stable conduit vent system, W). Conduit vent system widening and U). Unstable column/ conduit wall collapse. The layer

classification MB). Multiphase eruptive layer, SB). Single phase eruptive layer. Grain size, FA – Fine ash; CA – Coarse ash; FL – Fine lapilli; CL – Coarse lapilli; B – Blocks.

In addition to the main depositional fan to the east, tephras have been located along the southwestern coastline (Figure 3.1) that were emplaced within the timeframe of the Poto and Paetahi Formations as indicated by the presence of the rhyolitic Kawakawa Tephra. However, due to limited exposure and/or preservation across the southwestern ring plain sector we were not able to correlate these layers with individual events within this eruptive sequence. The Carrington Tephras identified in the western stratigraphy also occurred at a similar point in time (Neall, 1972; Franks, 1991; Alloway et al., 1995; Damaschke et al., 2017b). However, further work is required to link the eastern and western stratigraphic sequences for this time period since tephra records are missing in the south due to preservation of the deposits by erosion and burial by subsequent younger events.

3.5.2 Physical properties of the Poto and Paetahi tephras.

The depositional layers within the Poto and Paetahi Formations are very poorly to moderately sorted, with the majority of the layers being very poorly sorted. They display a diverse range of mean grain sizes from fine ash to very fine lapilli with coarse ash being the dominant grain size (Tables 3.1 and 3.2; Appendix B) throughout the depositional layers ranging from 4-55 wt.%.

3.5.3 Componentry

Analysis of components (Table 3.3) was undertaken on samples from the reference sections (locations 1,5 and 6 Figure 3.1) to cover the complete stratigraphic record of the Poto and Paetahi Formations. Within the Poto Formation, the majority of tephra beds in the -1.5 and 0.5 phi size fractions are dominated by brown pumice (ranging from 0-75 %) with some being dominated by lithic clasts (0-87 %), e.g., Poto.g and Poto.j (Figure 3.7). Of the ten Paetahi tephras the lower and upper layers contain mostly grey lithics (5-74 %) while the more heavily weathered middle layers are rich in brown pumice (5-50 %) (Figure 3.8). Juvenile dominated layers within the two formations (Poto.a, cl, cu, d, f, I, ku, ll, lu, m, n and Paetahi.al, am, au, b, d and el) are dominated by either grey (7-55 %) or brown (0-75 %) pumice. Grey lithic clasts show the largest variation in abundance throughout the tephra sequence varying from ~0 to 87% with lithic-rich layers occurring at various stratigraphic levels (Poto.b, e, g, h, j, kl, o and Paetahi.c, em, eu and f) (Figures 3.7 and 3.8). Lithic clasts within the Poto and Paetahi tephras are dense grey fragments of pre-Poto andesitic lavas (Figure 3.2; Table 3.3). Altered lithics are typically red/orange and sub-angular to sub-rounded dense clasts. Two of the depositional layers contain sedimentary white chalky claystone that breaks easily (7% in Poto.i and 29% in Poto.kl) (Figure 3.7) and was excavated from the basement during the eruptions. However, in contrast to Poto.kl, Poto.i is not a lithic-dominated layer.

Crystal abundance is predominantly represented in the 0.5ϕ size fraction (ranging from 4-63 %) and were rarely found in the -1.5ϕ size fraction (0-10 %). Six stratigraphic layers in the Poto Formation display a larger crystal percentage in the small size fraction, i.e., at the start of the Poto Formation (31%), following the Ngaere DAD (40%), through the middle of the sequence (30-32 %) and at the end of the Poto Formation (63%). There is also a marked increase in crystal proportions towards the middle and upper Paetahi Formation (37-50 %). The end of each of the formations is marked by a higher proportion of free crystals in the small size fraction.

Table 3.3: Description table of the components present within the Poto and Paetahi tephra layers.

Lithology	Subgroup	Description
Juveniles	Brown Pumice	Brown to orange pumice clasts which cover the range of densities in the Poto and Paetahi Formations. Differences in vesicularity were not observable in hand specimen through componentry.
	Grey Pumice	Light to dark grey pumice clasts which cover the range of densities in the Poto and Paetahi Formations. Differences in vesicularity were not observable in hand specimen through componentry.
Lithics	Altered Pumice	Brown and grey pumice clasts of previously erupted material which have an orange, white coating over all or part of the clast
	Grey Lithics	Dark grey andesitic lava fragments
	Altered Lithics	Dark grey andesitic lava fragments which have an orange, white coating over all or part of the clast
	White Clay Material	White claystone
Free Crystals	Feldspars	Glassy, white translucent blocky brittle crystal
	Pyroxenes	Dark monoclinic crystals
	Glomerocrysts	Accumulation of crystals

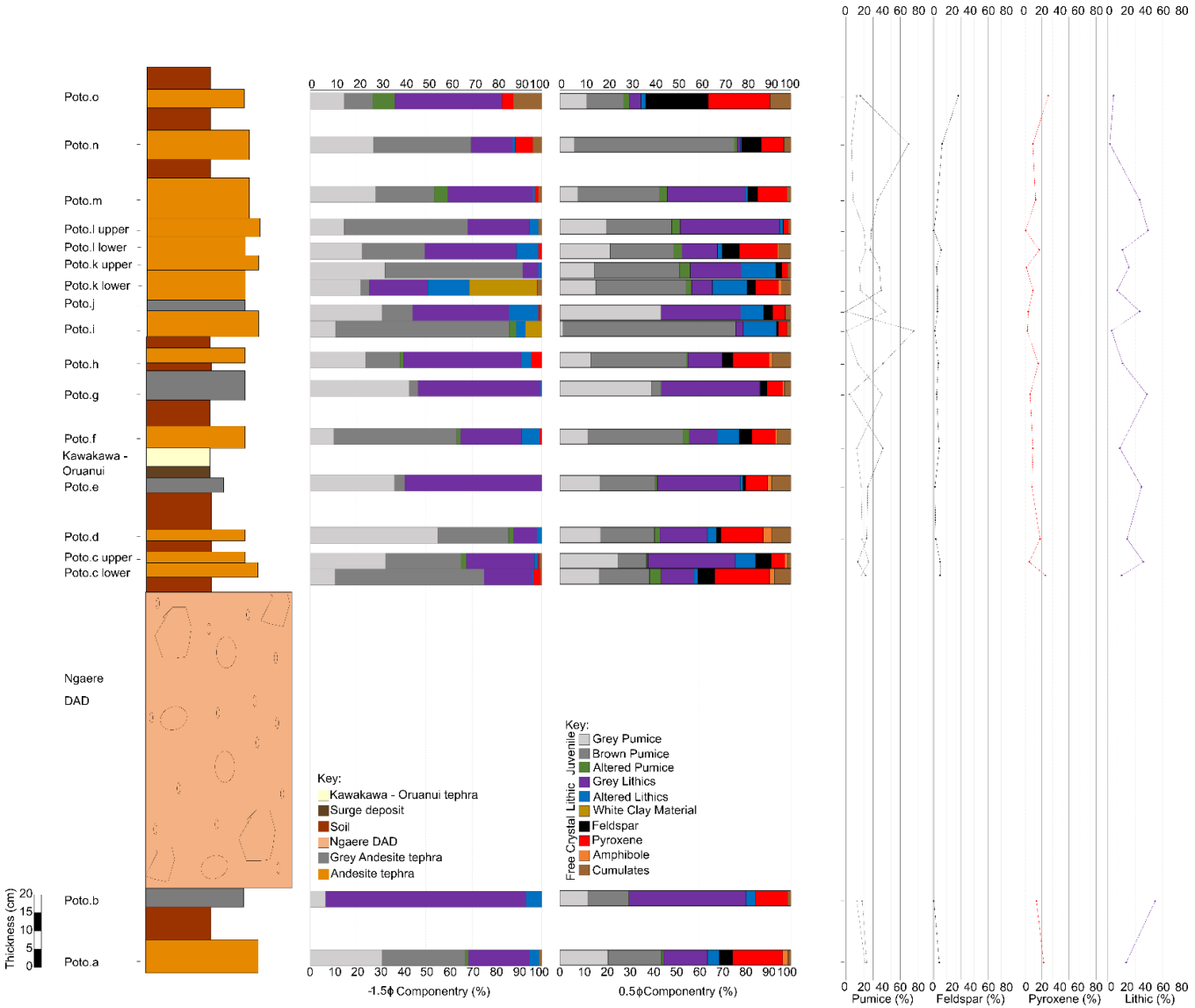


Figure 3.7: Compositional variation of the -1.5 and 0.5 ϕ grains from the Poto tephra formation. Detailed results are found in Appendix C.

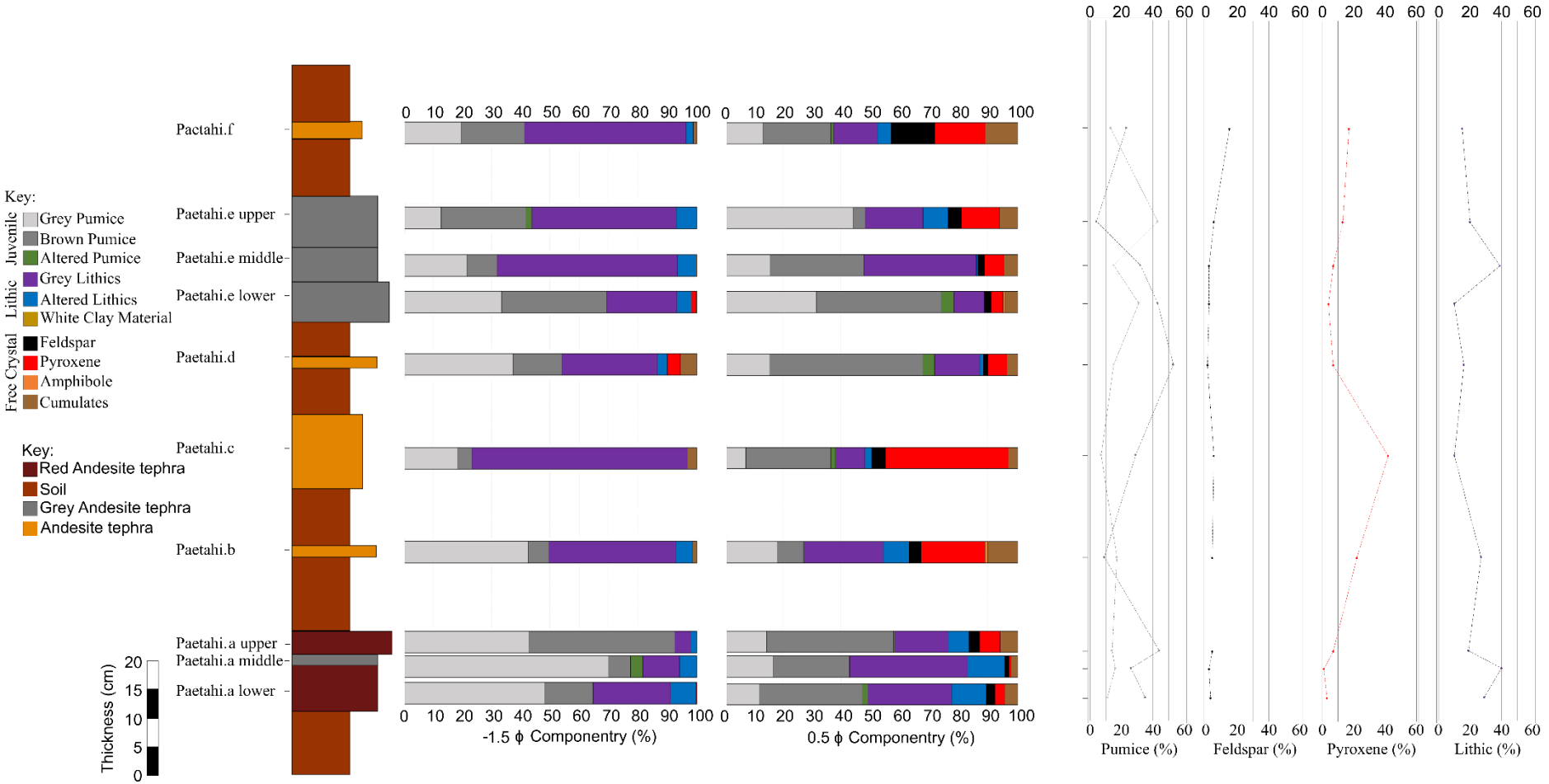


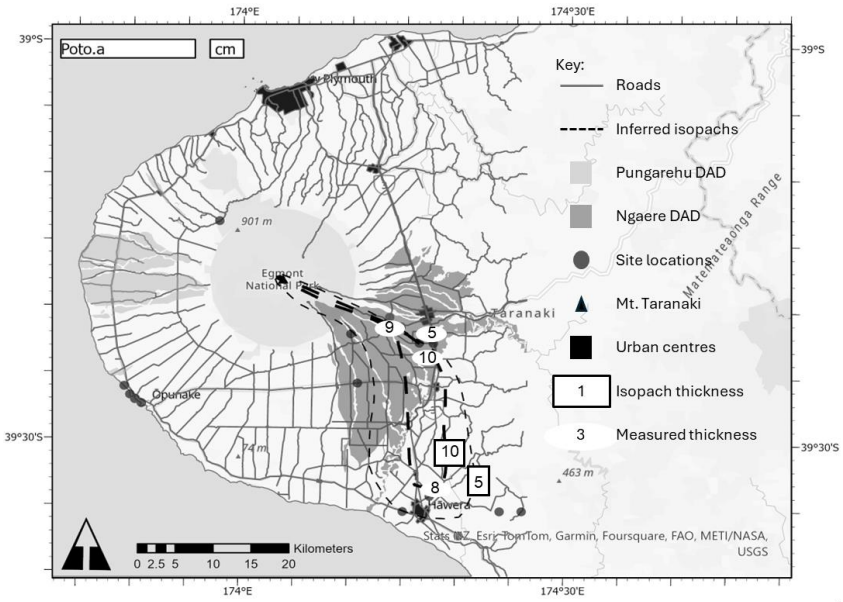
Figure 3.8: Compositional variation of the -1.5 and 0.5 ϕ grains from the Paetahi tephra formation. Detailed results are found in Appendix C.

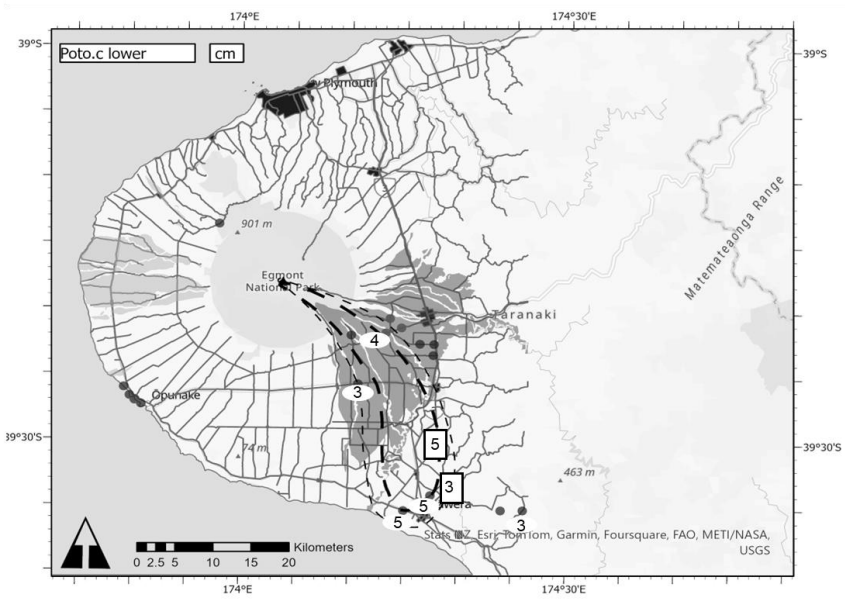
3.5.4 Eruptive conditions

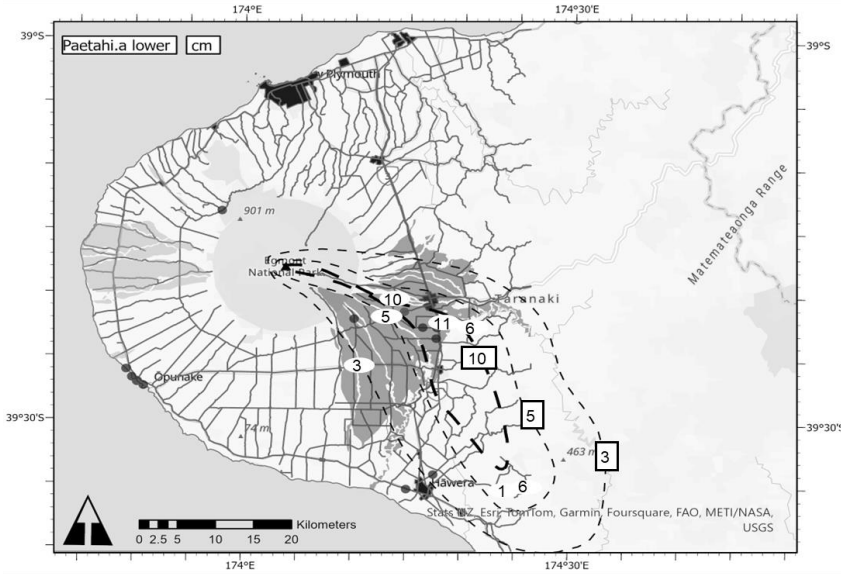
Isopach and isopleth maps for the Poto and Paetahi tephras have elliptical shapes and aspect ratios that range from 0.1 to 0.7 (Tables 3.4 and 3.5; Figures 3.9-3.11; Appendix A). The most widespread fallout deposits are Poto.h, Paetahi.a lower, Paetahi.e lower and Paetahi.e upper, which have the largest isopach areas ($A^{1/2}$ = 23.65, 32.29, 26.88 and 30.31 km^2). The coarsest layers with the largest pumice isopleths are Poto.a, Poto.f, Poto.g, Paetahi.b, Paetahi.d ($A^{1/2}$ =7.75, 9.58, 7.94, 12.2, 8.54 km^2). Poto.b shows the smallest dispersal (isopach $A^{1/2}$ = 4.94 km^2), and layers Poto.l upper, Poto.m, Poto.n, Paetahi.a middle and Paetahi.f have the smallest pumice isopleths ($A^{1/2}$=5.92, 5.92, 6.0, 5.1, 6.0 km^2). Paetahi.a lower shows the largest dispersal ($A^{1/2}$ = 32.29 km^2) with an isopleth area of $A^{1/2}$ = 6.7 km^2. The thickness of proximal deposits was not available because the older sequences are buried beneath younger material closer to the volcano. This has led to a potential underestimation of eruptive volumes with the parameters calculated here representing minimum volumes. Most tephra layers show a similar dispersal direction with main dispersal axes to the east and southeast. However, several layers produced during the studied timeframe were dispersed to the southwest. The deposits to the southwest need further investigation to allow correlation to the eastern stratigraphy.

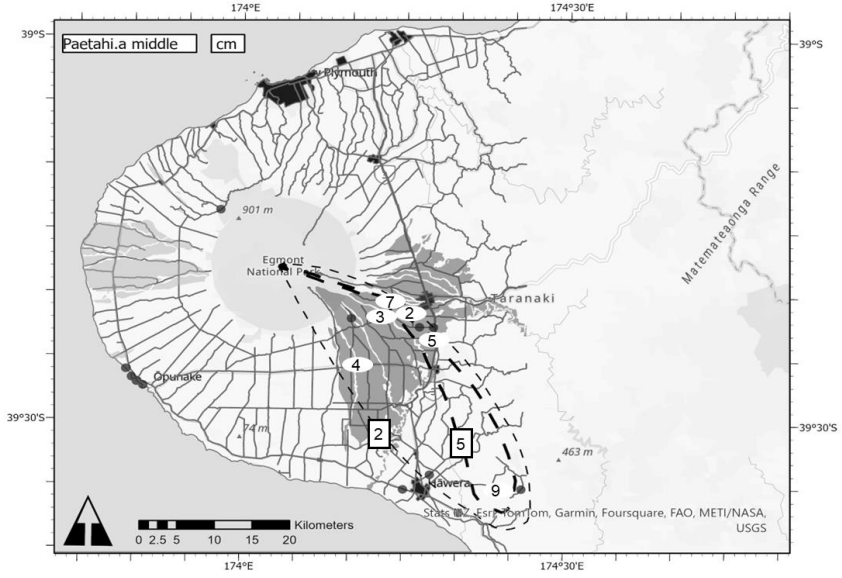
Table 3.4: A representative selection of eruptive volumes calculated using AshCalc (Daggitt et al., 2014), using isopachs from the Poto and Paetahi Formations. Appendix A contains the remainder of the isopach parameters for the Poto and Paetahi Formations.

T (m)	A (km^2)	A1/2	Perimeter (km)	Shape factor	Long axis	Short axis	Aspect ratio	k	theta	lambda	AshCalc Volume (km^3)
Poto.a								0.9774	0.01208	90.85	0.204
0.1	104.95	10.24	85	0.18	40.62	5.03	0.12				
0.05	340.01	18.44	97	0.45	43.93	13.78	0.31				
Poto.c lower								0.3398	0.004603	76.62	0.1717
0.05	185.03	13.6	83	0.34	39.68	7.54	0.19				
0.03	320.66	17.91	92	0.48	42.26	11.96	0.28				
Paetahi.a lower								0.932	0.01	99.36	0.26
0.1	157.23	12.54	93	0.23	43.43	7.58	0.17				
0.05	419.26	20.48	114.00	0.41	52.02	11.31	0.22				
0.03	1042.52	32.29	138.00	0.69	58.19	23.53	0.40				
Paetahi.a middle								1.13	0.02	41.16	0.06
0.05	131.87	11.48	103.0	0.16	50.10	5.75	0.11				
0.02	550.64	23.47	107	0.60	48.97	14.50	0.30				


Poto.a
cm
Key:
Roads
Inferred isopachs
Pungarehu DAD
Ngaere DAD
Site locations
Mt. Taranaki
Urban centres
1 Isopach thickness
3 Measured thickness
174°E
174°30'E
39°S
39°30'S
Plymouth
Egmont National Park
Taranaki
Matemateaonga Range
Opunake
Hawera
901 m
74 m
463 m
9
5
10
10
8
5
Kilometers
0 2.5 5 10 15 20
Esri, TomTom, Garmin, Foursquare, FAO, METI/NASA, USGS


Poto.c lower
cm
174°E
174°30'E
39°S
39°30'S
Plymouth
Egmont National Park
Taranaki
Matemateaonga Range
Opunake
Hawera
901 m
74 m
463 m
4
3
5
3
5
5
3
Kilometers
0 2.5 5 10 15 20
Esri, TomTom, Garmin, Foursquare, FAO, METI/NASA, USGS


Paetahi.a lower
cm
174°E
174°30'E
39°S
39°30'S
Plymouth
Egmont National Park
Taranaki
Matemateaonga Range
Opunake
Hawera
901 m
74 m
463 m
10
5
11
6
10
3
5
3
1
6
Kilometers
0 2.5 5 10 15 20
Esri, TomTom, Garmin, Foursquare, FAO, METI/NASA, USGS

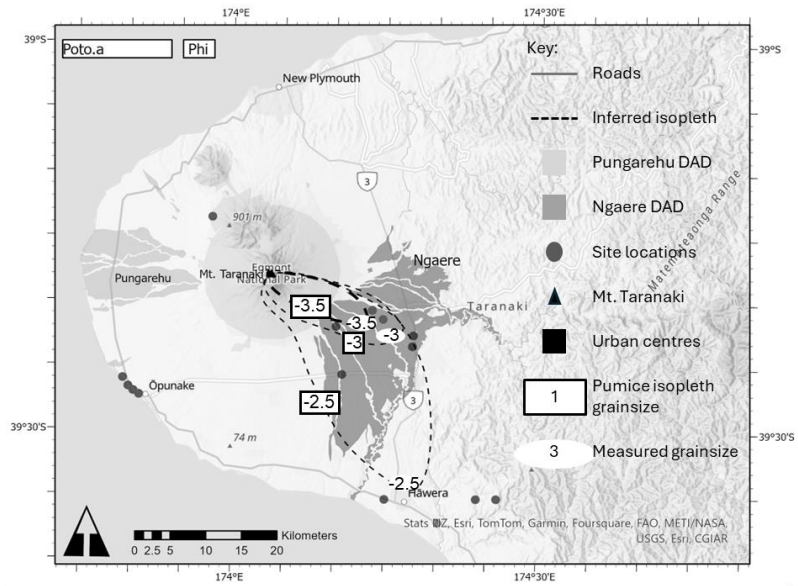

Paetahi.a middle
cm
174°E
174°30'E
39°S
39°30'S
Plymouth
Egmont National Park
Taranaki
Matemateaonga Range
Opunake
Hawera
901 m
74 m
463 m
7
3
2
5
4
2
5
9
Kilometers
0 2.5 5 10 15 20
Esri, TomTom, Garmin, Foursquare, FAO, METI/NASA, USGS

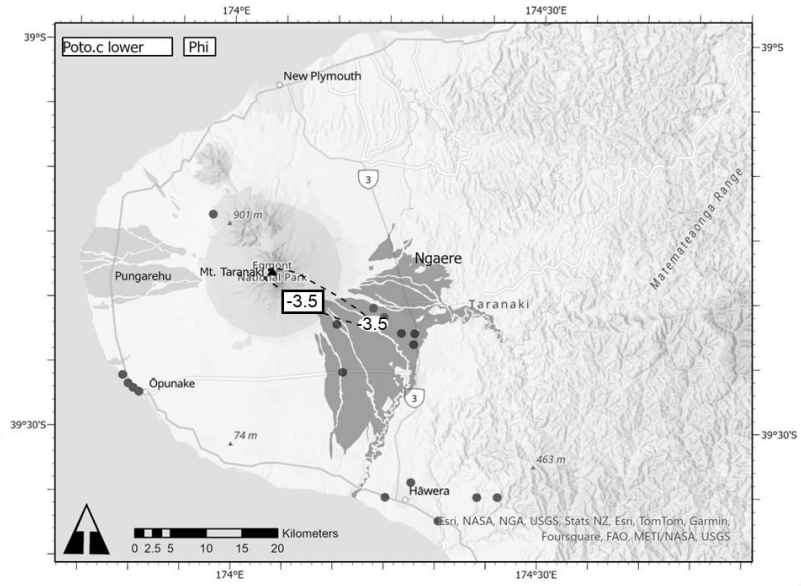
.

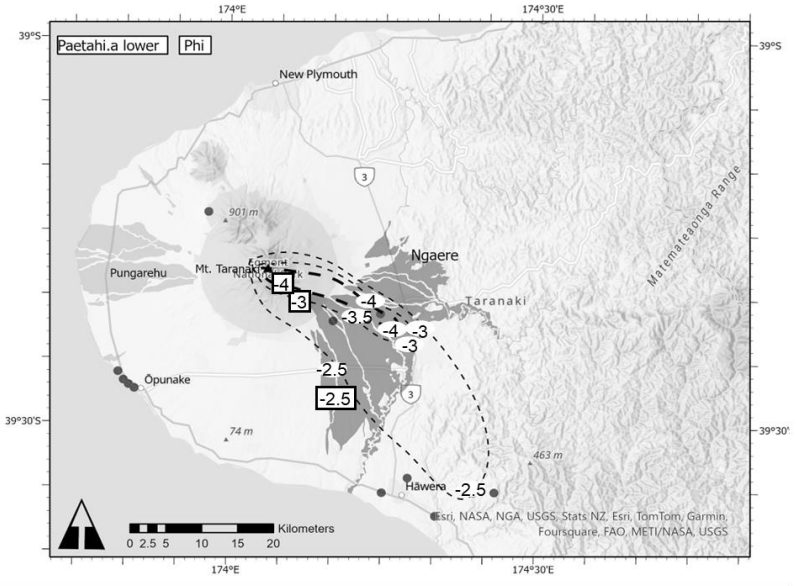
Figure 3.9: A representative selection of isopach from the Poto and Paetahi Formations showing the distribution of tephra layers across the Taranaki ring plain. The black dots show the site locations containing the whole or partial sections of the Poto and Paetahi Formations. Appendix A contains the remainder of the isopach maps for the Poto and Paetahi Formations. Road and Topographic data sourced from the LINZ Data Service licensed for reuse under CC by 4.0

Table 3.5: A representative selection of the isopleth parameters for the Poto and Paetahi Formations. Appendix A contains the remainder of the isopleth parameters for the Poto and Paetahi Formations.

Phi (Θ)	A (km^2)	A1/2	Perimeter (km)	Shape factor
Poto.a				
-2.5	415	20.37	86	0.71
-3	112	10.58	47	0.64
-3.5	60	7.75	35	0.62
Poto.c lower				
-0.5	43	6.56	29	0.64
-3.5	45	6.71	35	0.46
Paetahi.a lower				
-2.5	601	24.52	124	0.49
-3	206	14.35	77	0.44
-4	132	11.49	69	0.35
Paetahi.a middle				
-3.5	85	9.22	52	0.4
-4	26	5.1	34	0.28


Poto.a
Phi
Key:
Roads
Inferred isopleth
Pungarehu DAD
Ngaere DAD
Site locations
Mt. Taranaki
Urban centres
1 Pumice isopleth grainsize
3 Measured grainsize
New Plymouth
Ngaere
Pungarehu
Mt. Taranaki
Egmont National Park
Taranaki
Matemateaonga Range
Ōpunake
Hāwera
901 m
74 m
-3.5
-3
-2.5
Kilometers
0 2.5 5 10 15 20
Stats NZ, Esri, TomTom, Garmin, Foursquare, FAO, METI/NASA, USGS, Esri, CGIAR
174°E
174°30'E
39°S
39°30'S


Poto.c lower
Phi
New Plymouth
Ngaere
Pungarehu
Mt. Taranaki
Egmont National Park
Taranaki
Matemateaonga Range
Ōpunake
Hāwera
901 m
74 m
463 m
-3.5
Kilometers
0 2.5 5 10 15 20
Esri, NASA, NGA, USGS, Stats NZ, Esri, TomTom, Garmin, Foursquare, FAO, METI/NASA, USGS
174°E
174°30'E
39°S
39°30'S


Paetahi.a lower
Phi
New Plymouth
Ngaere
Pungarehu
Mt. Taranaki
Egmont National Park
Taranaki
Matemateaonga Range
Ōpunake
Hāwera
901 m
74 m
463 m
-4
-3
-3.5
-2.5
Kilometers
0 2.5 5 10 15 20
Esri, NASA, NGA, USGS, Stats NZ, Esri, TomTom, Garmin, Foursquare, FAO, METI/NASA, USGS
174°E
174°30'E
39°S
39°30'S

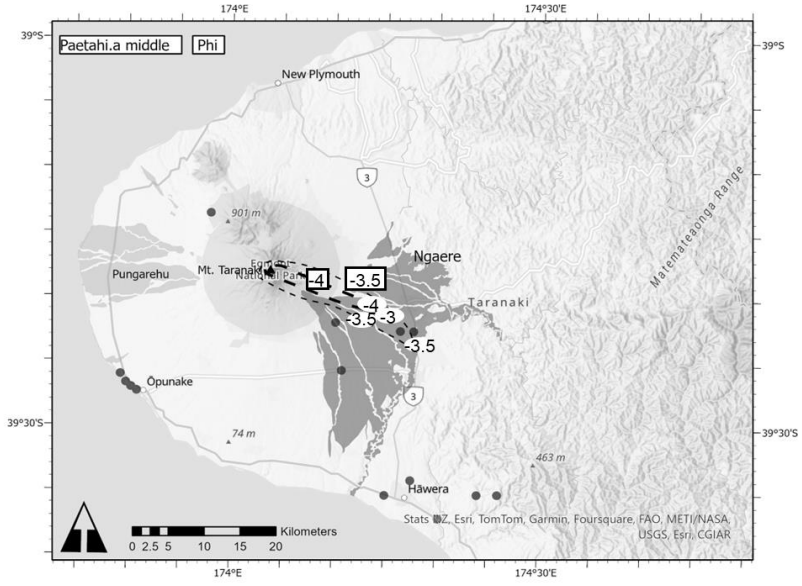

Paetahi.a middle
Phi
New Plymouth
Ngaere
Pungarehu
Mt. Taranaki
Egmont National Park
Taranaki
Matemateaonga Range
Ōpunake
Hāwera
901 m
74 m
463 m
-4
-3.5
-3
Kilometers
0 2.5 5 10 15 20
Stats NZ, Esri, TomTom, Garmin, Foursquare, FAO, METI/NASA, USGS, Esri, CGIAR
174°E
174°30'E
39°S
39°30'S

Figure 3.10: Representative selection of Isopleth maps of the Poto and Paetahi Formation. Appendix A contains the remainder of the isopleth maps for the Poto and Paetahi Formations. Road and Topographic data sourced from the LINZ Data Service licensed for reuse under CC by 4.0

Some layers show a dog-leg depositional pattern that trend towards the east before bending south-eastwards (e.g., Poto.j and Paetahi.e middle). The dog-leg feature can impact the volume calculations due to the bend in the isopachs affecting the measurements of the long access of dispersal. This feature could be due to preservation and access to the deposits in the stratigraphy, especially for deposits to the south as these deposits have been eroded by subsequent activity or buried under tens of meters of younger material. Deposits of the Poto and Paetahi Formations in the northeast have also potentially been buried due to the dominant wind dispersal of the younger eruptive products and through industrialisation in this region. However, it could also be an influence of different wind directions at different heights, i.e., the column reaches a certain height with distance from the vent where a changing wind direction disperses the tephra to the southeast after initial deposition to the east (Sarna-Wojcicki et al., 1981). Eruption column tephra models by Weir et al. (2022) for large explosive eruptions from Mt. Taranaki show tephra dispersal across the eastern and southeastern ring plain once the eruption column becomes high enough.

Tephra volumes for the Poto and Paetahi depositional layers vary between 0.01-0.26 km^3 (Table 3.4; Appendix A) with a total volume of 1.6 km^3 for the Poto Formation and 1.4 km^3 for the Paetahi Formation. Paetahi.a lower and Paetahi.e middle have the largest eruptive volumes (0.26 km^3) within the formations.

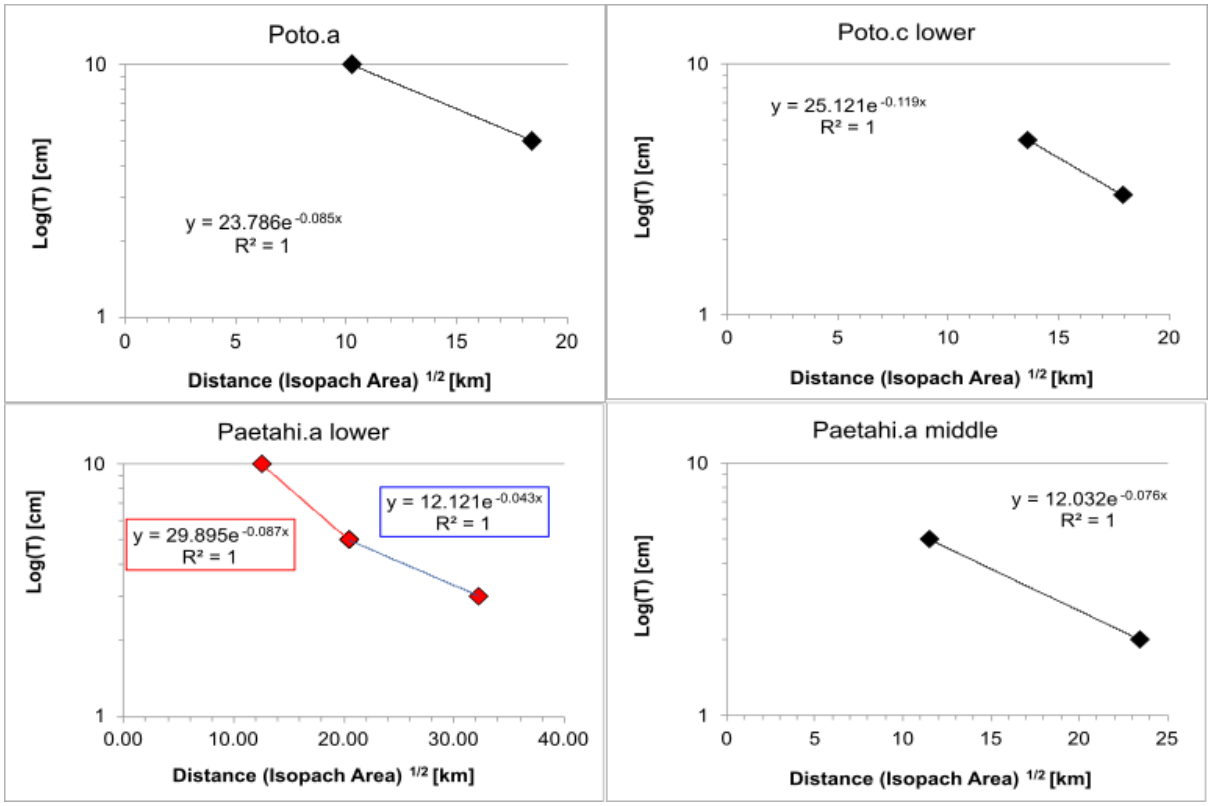


Figure 3.11: Representative selection of isopach data plots for the individual eruptive layers of the Poto and Paetahi Formations showing one to two segments with different slopes. Colours in Paetahi.a lower separate the different segments. Appendix A contains isopach data plots for the remainder of the Poto and Paetahi Formations.

Table 3.6: Estimated eruptive parameters for the Poto and Paetahi Formations based on the volumes calculated in Table 3.4. Appendix A through AshCalc (Daggitt et al., 2014), calculated using (Pyle, 2000; Mastin et al., 2009).

Formation	**Layer**	**Column height (H) (Mastin et al., 2009)**	**Volume Discharge m^3/s (Q) (Mastin et al., 2009)**	**Log10 Mass eruption rate (MER) (kg/s)**	**Eruptive magnitude (Pyle, 2000)**	**Duration (hours)**
Poto	a	18.7	11149.5	7.45	4.31	2.03
	b	13.3	3044.6	6.88	3.51	1.17
	c.l	18.2	10046.8	7.4	4.23	1.9
	c.u	14.6	4260.9	7.03	3.69	1.28
	d	14.0	3710.5	6.97	3.61	1.23
	e	14.6	4333.9	7.03	3.70	1.28
	f	16.8	7425.8	7.27	4.03	1.6
	g	16.7	7253.9	7.26	4.01	1.58
	h	15.8	5875.9	7.17	3.88	1.43

	i	14.6	4270.9	7.03	3.69	1.28
	j	11.9	1984.2	6.70	3.30	1.11
	k.l	16.1	6260.1	7.19	3.92	1.47
	k.u	12.8	2614.5	6.82	3.43	1.14
	l.l	10.2	1097.5	6.44	3.04	1.11
	l.u	14.9	4669.6	7.07	3.74	1.31
	m	13.1	2867.3	6.86	3.48	1.16
	n	11.7	1827.6	6.66	3.26	1.10
	o	17.5	8723.3	7.34	4.14	1.74
Paetahi	a.l	19.4	12850.0	7.51	4.41	2.25
	a.m	15.1	4967.2	7.09	3.78	1.34
	a.u	16.9	7572.1	7.28	4.04	1.61
	b	15.1	4967.2	7.09	3.78	1.34
	c	15.1	4967.2	7.09	3.78	1.34
	d	10.0	992.1	6.39	3	1.12
	e.l	19.2	12369.7	7.49	4.39	2.19
	e.m	19.4	12850.0	7.51	4.41	2.25
	e.l	19.1	12179.5	7.48	4.37	2.16
	f	12.0	2007.6	6.70	3.30	1.11

Calculated column heights for the individual eruptive events range from 10-20 km. These column heights indicate subplinian eruptive columns across the formations (Table 3.6; Figure 3.12). Mass discharge rates (Q) for the eruptive events are in the order of 10^3 to 10^5 m^3/s, with the corresponding mass eruption rates (MER) ranging from 10^6 to 10^8 kg/s (Table 3.6). These numbers are minimum values due to the lack of proximal data. Across the two formations, Paetahi.d has the smallest plume height (9.98 km) and MER (10^6 kg/s), Poto.l lower has the smallest plume height (10.24 km) and MER (10^6 kg/s) for the Poto Formation. Paetahi.a lower and Paetahi.e middle have the largest plume height (19.37 and 19.18 km) and MER (10^7 kg/s) of the two formations, with Poto.a having the largest plume height (18.67 km) and MER (10^7 kg/s) for the Poto Formation. This eruptive period from Mt. Taranaki saw eruptive magnitudes between 3 and 4.5 (Table 3.6; Figure 3.12). The plume height and magnitudes of these eruptions indicate subplinian events that had VEIs ranging from 3 (moderately large) to 4 (large) (Newhall & Self, 1982; Cioni et al., 2015). The calculated minimum duration of the individual subplinian eruptive events of the Poto and Paetahi Formations ranged between 1 to 2.5 hours (Table 3.6; Figure 3.13).

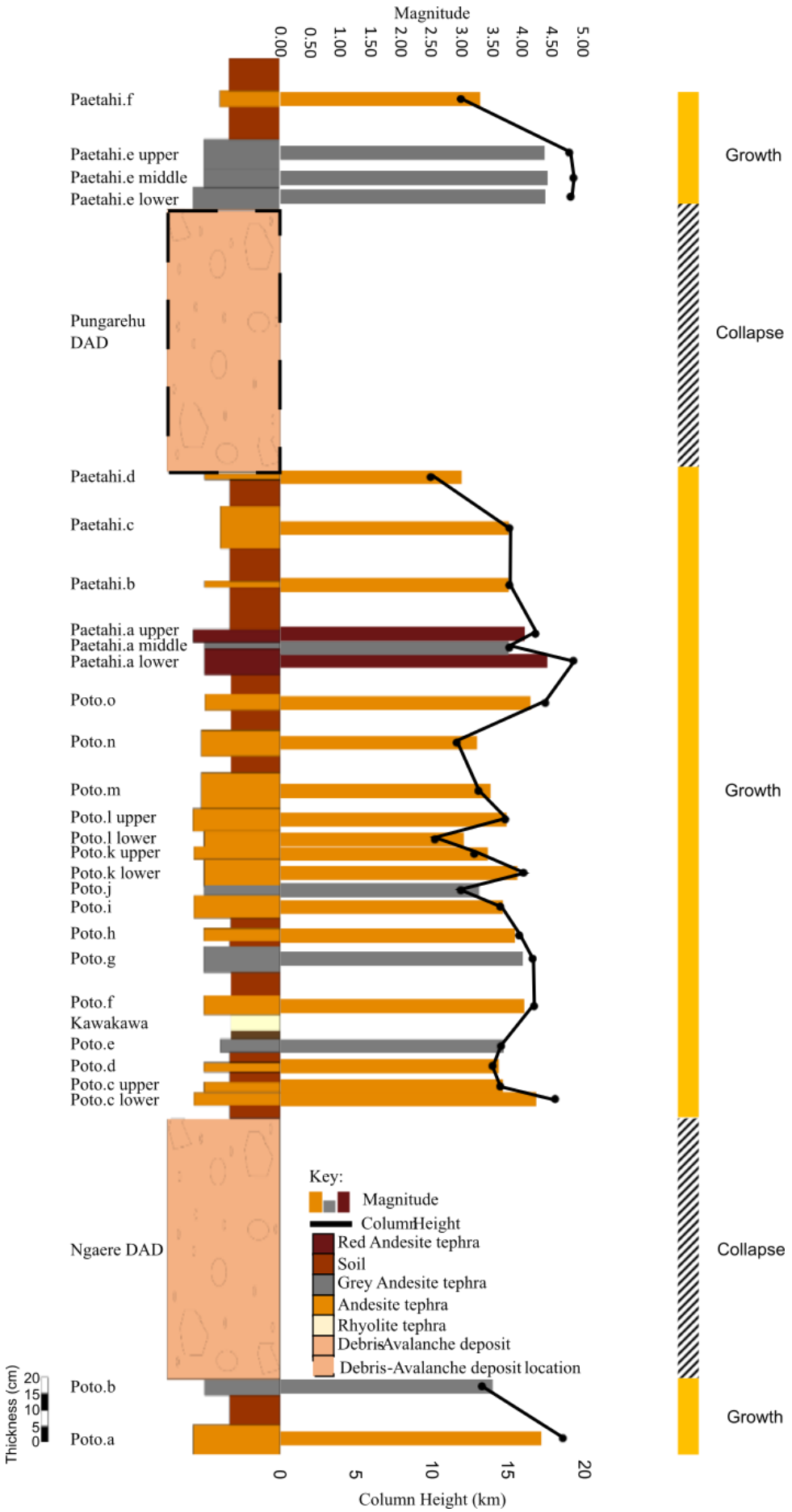

Magnitude
0.00
0.50
1.00
1.50
2.00
2.50
3.00
3.50
4.00
4.50
5.00
Paetahi.f
Paetahi.e upper
Paetahi.e middle
Paetahi.e lower
Pungarehu DAD
Paetahi.d
Paetahi.c
Paetahi.b
Paetahi.a upper
Paetahi.a middle
Paetahi.a lower
Poto.o
Poto.n
Poto.m
Poto.l upper
Poto.l lower
Poto.k upper
Poto.k lower
Poto.j
Poto.i
Poto.h
Poto.g
Poto.f
Kawakawa
Poto.e
Poto.d
Poto.c upper
Poto.c lower
Ngaere DAD
Poto.b
Poto.a
Growth
Collapse
Growth
Collapse
Growth
Key:
Magnitude
Column Height
Red Andesite tephra
Soil
Grey Andesite tephra
Andesite tephra
Rhyolite tephra
Debris Avalanche deposit
Debris-Avalanche deposit location
Thickness (cm)
20
15
10
5
0
0
5
10
15
20
Column Height (km)

Figure 3.12: Column height vs. magnitude of the Poto and Paetahi Formation across the stratigraphic column. Showing changes in the eruption size across the formation of the Poto and Paetahi eruption sequence. The dashed lines around the Pungarehu DAD show the hypothesized location of the western Pungarehu DAD within the eastern stratigraphic sequence.

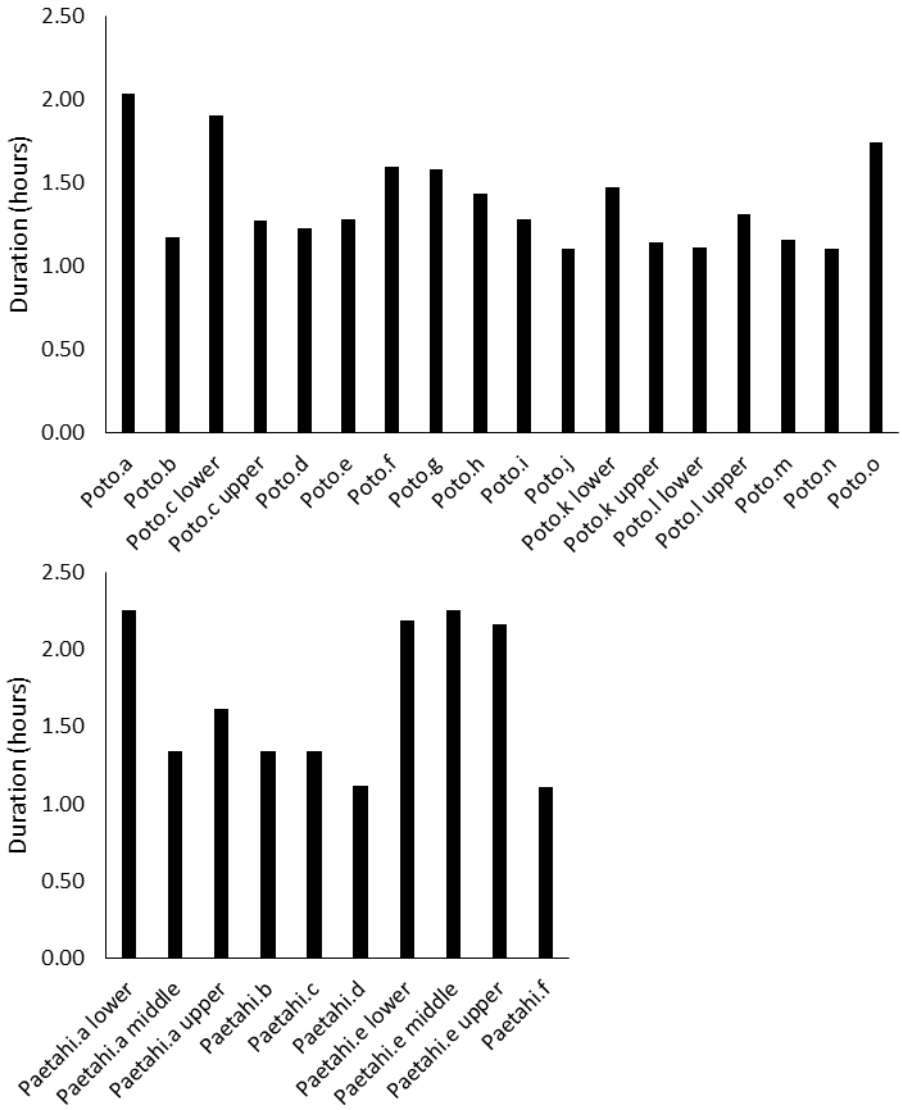


Figure 3.13: Histogram of the duration of eruptions from the Poto and Paetahi Formations.

3.6 Interpretations.

This in-depth view of the tephrastratigraphy and lithosedimentological features of the Poto and Paetahi Formations builds on the < 30 ka record of primary deposits from Mt. Taranaki. Similar eruptive styles were observed during the eruptive period encompassing the Ngaere and Pungarehu collapses. This differs from the younger eruptive periods from Mt. Taranaki, which consist of less frequent large explosive eruptions within the multiphase effusive and explosive events. The large eruptions which did

occur were predominantly distributed to the northeast differing from the east and southeastern distribution seen by the Poto and Paetahi subplinian events (e.g., Platz et al., 2007; Platz et al., 2012; Torres-Orozco et al., 2017a; Torres-Orozco et al., 2017b, 2018; Lerner et al., 2019d; Lerner et al., 2019a; Cronin et al., 2021).

The timing of the Poto and Paetahi Formations between 20-30 ka provides a unique opportunity to investigate the impacts of edifice collapse on the eruptive processes at a stratovolcano, influencing the size of the eruptive events which occurred. This period of time saw an increase in the frequency of large explosive eruptions compared to what has previously been recorded within the younger eruptive record and the direction of deposits. This 4 kyr eruptive period is characterised by two major collapse events that removed large portions of the edifice: 5.85 km^3 as a result of the 27.3 ka Ngaere and 7.5 km^3 during the 24.8 ka Pungarehu collapse (Neall, 1979; Zernack et al., 2011). The latter failure was equivalent to 60% of the present-day volume of the Mt. Taranaki edifice above 1400 m elevation (Zernack et al., 2011; Cronin et al., 2021). Removing such large volumes of material from the upper edifice can significantly influence the post-collapse eruption style depending on the location of the magma source in relation to the upper edifice. Age dating of the Pungarehu DAD puts the collapse within the time period of the Poto and Paetahi Formations (Alloway et al., 2005) and the presence of < 5 ash fall layers underneath the Pungarehu DAD within coastal cliff sections within the southwestern sector of the ring plain allowed for the hypothesis of where the Pungarehu DAD fits into the eastern stratigraphy (Figure 3.12).

The percentage of components (juvenile, lithic and free crystals) present within the different depositional fall layers of the Poto and Paetahi Formations provides insights into changes in conduit geometry, which can impact eruption styles (Macedonio et al., 1994; Paredes-Mariño et al., 2019). The dominance of lithics within a fall layer indicates conduit widening where lithic clasts are ripped off the conduit wall by the rapidly ascending magma (Campbell et al., 2013; Houghton & Carey, 2015). Changes in the percentage of lithic clasts throughout the eruptive sequence can indicate pressure changes within the conduit, coupled with the change of depth where fragmentation is occurring (Varekamp, 1993; Taddeucci & Wohletz, 2001). The geometries of the volcanic plumbing and conduit vent systems control the dynamics of magma ascent and impact the magma supply and discharge rate during an eruption (Scandone & Malone, 1985; Bursik, 1993; de' Michieli Vitturi et al., 2008; Aravena et al., 2018). Layers dominated by juvenile clasts indicate that magma fragmentation was the dominating process along with a stable conduit vent system (Taddeucci & Wohletz, 2001). The Poto and Paetahi Formations comprise seventeen events characterised by a stable conduit, seven conduit widening events represented by lithic dominated layers that occurred following time breaks (a soil layer was present between layers), and four unstable column/conduit wall collapse events marked by lithic dominated layers that follow previous eruptions without a break in time (no soil present) (Figures 3.6 and 3.6). Within the stratigraphy only one PDC deposit was identified. This was found at the Ronald

Road reference section for the Poto Formation as a thin 4 cm very fine dark brown silty layer directly overlying Poto.e. Poto.i was previously described as a surge deposit (Alloway et al., 1995), but further investigation (i.e., lack of depositional features, grain size distribution) indicates this is a heavily weathered fall deposit. No other pyroclastic flow or lahar deposits have been observed within the stratigraphic record of these two formations.

Fluctuations in the size of the eruptions can be seen throughout the formation (Figure 3.12). For the Poto and Paetahi Formations leading into a collapse event we see smaller subplinian eruptions occurring. Prior to the Ngaere collapse the conduit was widening emplacing Poto.b. Trigger mechanisms for edifice collapse events at Mt. Taranaki are not known with the exception of the Ngaere DAD due to the close stratigraphic relationship with Poto.b it has been postulated as a Bezymianny type failure (Alloway et al., 1995; Zernack, 2008) where magma is involved in triggering the collapse, which is common at other volcanoes around the globe (Siebert et al., 1987; Vallance et al., 1995; Girina, 2013; Pallister et al., 2017). Eruptive activity prior to the Pungarehu DAD is characterised by stable conduit conditions, making determination of the cause of collapse difficult to define. The collapse trigger for the Pungarehu DAD is unknown however, it could have been seismically induced (Alloway et al., 2005; Zernack, 2008) due to the edifice's instability caused by the Ngaere collapse. The time between collapse events (c. 2,500 years) might have been too short to fully rebuild Mt. Taranaki's edifice. The failures furthermore occurred in opposite directions, resulting in the eastern portion of the edifice being destroyed during the Ngaere and the western portion of the edifice during the Pungarehu collapse. This would have drastically changed the morphology of the edifice and subsequent conduit system. Prior to the collapse events eruptive parameters indicate smaller eruptions compared to those which occurred following the collapse. Figure 3.12 shows that the edifice regrowth phase between the two collapses was marked by fluctuations in the size of subplinian events.

Following deposition of the uppermost lithic rich tephra, Paetahi.f, Mt. Taranaki entered a period of quiescence until the next eruption recorded in the eastern stratigraphy, the 15,326 ± 354 ka Kaihouri Tephra (Alloway et al., 1992; Alloway et al., 1995).

3.7 Discussion.

3.7.1 Eruption Parameters and uncertainties.

Previous analysis of eruptive activity from Mt. Taranaki has predominantly focussed on Holocene events, primarily due to the limited preservation of and access to older material. Studies of primary deposits have mostly involved deposits that have contributed to the construction of the present-day edifice. However, this represents only < 10 kyr of stratigraphy and a limited range of primary deposits. In contrast, the ring plain preserves deposits extending from present day through to approximately 200 ka (Neall, 1979; Neall et al., 1986; Alloway et al., 1995; Alloway et al., 2005; Procter et al., 2009;

Zernack et al., 2009; Zernack et al., 2011; Damaschke et al., 2017b; Zernack, 2021). Deposits older than 20 ka are very rarely studied because they are typically buried under tens to hundreds of meters of younger volcaniclastic material (Zernack et al., 2011) and can be significantly altered. Older volcaniclastic sequences (< 100 ka) from Mt. Taranaki are exposed along coastal cliffs around the southern and western ring plain due to uplift and coastal erosion (Pillans, 1990; Palmer et al., 1991; Zernack et al., 2011; Zernack, 2021) Some primary fall deposits can be found embedded in soil or peat layers within these coastal cliffs; exhibiting limited distribution due to the lack of preservation in the mass-flow dominated succession.

The Poto and Paetahi Formations, as a sequence of eruptive events, both have distinct spatial patterns of distribution due to erosion and subsequent burial of deposits inland especially by the Pungarehu and Opua DADs (c.f., Neall, 1979; Neall et al., 1986; Zernack et al., 2011). In this study we primarily find the eruptive deposits of the Poto and Paetahi Formations to the east and southeast with isolated locations of Poto and Paetahi correlatives in coastal sites to the southwest. The presence of the (< 5) Poto and Paetahi tephra layers in the southwestern ring plain creates some uncertainty when determining the physical conditions of these eruptives. The deposits are found over a small stretch of coastline within a < 100 m^2 area showing a consistent thickness of 1-2 cm. The limited exposure and lack of distinguishing physical and geochemical features made correlation to the reference section impossible. Including these deposits as part of the isopach analysis would significantly skew the results, reporting unusually large eruptions. It could be feasible to consider them as part of a multiphase sequence of eruptives where the wind direction had changed during that phase of the eruption. However, none of the deposits at the distal locations indicate any multiphase eruptive activity within the stratigraphic age range they are assigned to. Finally, the deposits to the southwest could be considered as stand-alone, single-phase eruptions with a completely different wind direction and should be analysed as separate eruptive events with isopachs constructed to represent their distribution. The complication with this is that these deposits are only found in an isolated small area with no variation in thickness. Preservation of tephra deposits within the southwestern sector is diminished due to the domination of mass flows within the depositional sequence. Tephras that are preserved in the sector are predominantly located along the coastal cliffs within soil or peat sequences which are not preserved across the whole coastal region. Erosion of these soils and peats by mass flows lead to tephra deposits only being recorded within a few small, isolated regions within the volcaniclastic succession. Due to these limitations those points cannot credibly be associated to the eruptive layers analysed.

The variable preservation and exposure of these primary deposits across the ring plain generates uncertainties when trying to reliably recreate the size of prehistoric events. Due to the age of the studied deposits, proximal records are deeply buried by subsequent events. The closest location to access these depositional layers is 11 km from the present-day summit vent. The lack of proximal data means all

eruptive parameters produced are minimum values based on medial and distal locations (Brown et al., 2014; Watt, 2019).

Multiple models are used for calculating the volume of ash produced during an eruptive event, e.g., Exponential (Pyle, 1989), Power law (Bonadonna et al., 1998; Bonadonna & Houghton, 2005) and Weibull (Bonadonna & Costa, 2012). The volume of a deposit can be significantly underestimated when either proximal, medial, or distal regions are missing (Pyle, 1989; Fierstein & Nathenson, 1992; Rose, 1993; Pyle, 1995; Bonadonna & Costa, 2012). For datasets where large sections of the deposit are missing the Weibull model provides the smallest uncertainties compared to other models, which extrapolate areas of missing data (Bonadonna & Costa, 2012; Bonadonna & Costa, 2013a). Reducing uncertainties at this step is important to decrease the amount of uncertainty for other eruptive parameters which are all calculated using eruptive volumes. Although our proximal data is missing the medial and distal data was robust enough to apply the Weibull model through AshCalc (Bonadonna & Costa, 2012; Daggitt et al., 2014).

Column height calculations using the methods of Mastin et al. (2009) and the Carey and Sparks (1986) model for the same isopach data produced considerable differences in column heights (e.g., 18.67 km vs. 30.1 km). These discrepancies indicate the levels of uncertainty that can develop when studying prehistoric eruptive events. This study determined that the values generated using Mastin et al. (2009) provided more reliable heights for the Poto and Paetahi eruptive events in the context of global examples (Thorarinsson & Sigvaldason, 1972; Sarna-Wojcicki et al., 1981; Carey & Sigurdsson, 1985; Fierstein & Nathenson, 1992; Gudmundsson et al., 1992; Rosi et al., 1993; P. D. Cole et al., 1995; Höskuldsson et al., 2007; Carey & Houghton, 2010).

The total Poto tephra volume is at least 1.6 km^3 with individual events ranging from 0.01 to 0.2 km^3 and DREs between 3 to 4.5 (Table 3.6) and eruption column heights between 10 and 19 km. The total Paetahi tephra volume is at least 1.4 km^3 with individual events ranging from 0.01 to 0.26 km^3, magnitudes between 3 to 4.5 (Table 3.6) and eruption column heights of 9.98 to 20 km. Our study highlights that Mt. Taranaki is capable of producing multiple magnitude 3 to 4.5 eruptions at regular intervals within an eruptive period a much higher frequency of large explosive events than previously recorded within the younger volcanic history (c.f., Alloway et al., 1995; Platz, 2007; Platz et al., 2007; Platz et al., 2012; Torres-Orozco et al., 2017a; Torres-Orozco et al., 2017b, 2018). The lack of internal variability and contacts between depositional layers indicate that the majority of events within the formations were recorded as single-phase events consisting of one subplinian eruption, with a time break either long (soil formation between layers), or short with a defined change between layers. Internal variability in lithosedimentological characteristics of the layers representing multiphase events record changes within the deposit during the eruption. Due to the age of the Poto and Paetahi Formations proximal deposits are not accessible or preserved within the stratigraphic record. This lack of

preservation means there may have been smaller eruptive events occurring during this eruptive period which are not referenced in this study. Younger eruptive records for Mt. Taranaki (e.g., Platz et al., 2007; Torres-Orozco et al., 2017a; Torres-Orozco et al., 2017b) indicate that effusive eruptive events coupled with smaller explosive activity was common at Mt. Taranaki, there is the potential that there was directed pyroclastic density currents occurring during this eruptive period. However, these were likely confined to the proximal sector of the ring plain (e.g., Torres-Orozco et al., 2017a; Torres-Orozco et al., 2017b; Torres-Orozco et al., 2018; Lerner et al., 2019d; Lerner et al., 2019a; Lerner et al., 2019c).

Increased lithic content within some layers showed the conduit system was experiencing widening or instability. Lithic percentage increases within multiphase events could be related to conduit wall collapses as the mass eruption rate during these eruptions decreased reducing the height of the eruption column without resulting in a column collapse (Taddeucci & Wohletz, 2001; Carey & Houghton, 2010; Campbell et al., 2013; Paredes-Mariño et al., 2019).

Although conduit wall collapse or widening is evident within several layers, only Poto.e shows evidence of a column collapse with a thin PDC deposit preserved at the reference location (location 1 Figure 3.1). However, the lack of PDCs during large explosive events is seen globally around the world (Wilson et al., 1980; Sparks et al., 1997; Taddeucci & Wohletz, 2001). While bubble and geochemical analysis of pumices are subject to a separate study, our lithosedimentological analysis provides an initial hypothesis around the magmatic plumbing system. Layers dominated by juvenile material are indicative of increased levels of fragmentation occurring (Taddeucci & Wohletz, 2001; Cioni et al., 2015). Stable conduit events are indicated through a higher presence of juvenile clasts as the magma ascends freely through the conduit without excavating the conduit walls (Carey & Houghton, 2010; Paredes-Mariño et al., 2019).

3.7.2 The influence of edifice collapse on eruptive behavior

Eruption triggered edifice collapse events can occur in three different scenarios: 1. The absence of an eruption (e.g., Unzen); 2. A magmatic eruption (e.g., Bezymianny type); or, 3. A Phreatic eruption (e.g., Bandai type) (Moriya, 1980; Siebert et al., 1987; Roverato et al., 2021). For prehistoric collapses the cause can be difficult to determine due to the preservation of the deposits around DADs (Watt, 2019). The presence of pumice within collapse deposits is not indicative of an eruption induced collapse occurring (Watt, 2019). If the collapse is accompanied by eruptive activity (i.e., Poto.b directly below the Ngaere DAD), the collapse was likely associated with magmatic intrusion similar to the 1980 collapse at Mt. St. Helens (Druitt, 1992; Belousov et al., 2007). Even if it was not linked with magmatic intrusion, eruptions can be triggered by a reduction of lithostatic pressure if eruptible magma is present at shallow levels (Watt, 2019).

Edifice collapse events can change the lithostatic pressure above the magmatic system, which may influence the eruptive behaviour at a volcano if there is eruptible magma present (Watt, 2019). Following a collapse event there can be responses from the magmatic system, where there can be changes in eruptive style, increased eruption rate (frequency and/ or magnitude), or a shift in composition to a more mafic setting (c.f., Siebert et al., 2004; Tibaldi, 2004; Hora et al., 2009; Manconi et al., 2009; Watt, 2019), while some volcanoes display no apparent change in eruptive behaviour following collapse (Ponomareva et al., 2006; Zernack et al., 2012b; Zernack & Procter, 2021). Globally changes in eruptive styles following collapse have been observed e.g., Pacaya, Guatemala showing a shift between Strombolian activity, Phreatomagmatic and Phreatic eruptions along with lahars (Vallance et al., 1995; Rose et al., 2013; Gonzalez-Santana & Wauthier, 2021) and Cerro Quemado, Guatemala (1200 BCE) with pyroclastic flows and lahars following the collapse (Vallance et al., 1995). Large explosive events flowing the collapse was subsequently followed by effusive activity at Mt. St. Helens in 1980 (Glicken, 1996), Bezymianny in 1956 (Belousov et al., 2007) and Augustine in 1883 (Siebert et al., 1987; Watt, 2019). The effusive stage at these volcanoes following collapse events began to fill in the collapse scar (Watt, 2019).

At Mt. Taranaki the Poto and Paetahi Formations indicate a period of time where there was a higher frequency of large explosive events compared to the younger eruptive record (c.f., Neall, 1972; Alloway et al., 1995; Platz et al., 2007; Damaschke et al., 2017b; Torres-Orozco et al., 2017a; Torres-Orozco et al., 2017b). Within these two formations there are larger explosive events with column heights of 18.18 and 19.18 km following the Ngaere and Pungarehu Collapses compared to the eruptions prior with heights of 13.34 (Poto.b) and 9.98 km (Paetahi.d). This increase in frequency of large explosive events has also been observed at Shiveluch, Kamchatka (Belousov et al., 1999; Gorbach et al., 2013) and Mt. Pelée, Martinique (32 ka) (Boudon et al., 2013; Germa et al., 2015).

Observed historical collapses have been relatively small (e.g., Ritter Island, Papa New Guinea in 1888 4.2 km^3 (Johnson, 1987); and Mt. St. Helens in 1980 2.5 km^3 (Siebert, 1984), compared to those identified in the volcanic record (e.g., the 4.3 ka 10 km^3 Colima, Mexico (O'Callaghan & Francis, 1986; Luhr & Prestegaard, 1988), and the 60-65 ka 12 km^3 Chimborazo, Ecuador (Samaniego et al., 2012; Watt, 2019). A lack of direct stratigraphic correlations with prehistoric collapse can complicate interpretations around the influence of collapse on the eruptive system. However, the volume of the collapse seems to be less important than the proportion of the collapse volume compared to the edifice volume. The 1980 collapse at Mt. St. Helens and the 1888 Ritter Island collapse only mobilised approximately 10-20 % of the total edifice volume (Grosse et al., 2013; Day et al., 2015; Watt, 2019), compared to the 24.8 ka 7.5 km^3 Pungarehu collapse at Mt. Taranaki which was equivalent to approximately 60 % of the total present-day edifice volume above ~1400 m elevation being mobilised (Zernack et al., 2011; Cronin et al., 2021). The relationship between collapse volume and edifice volume

could be the link to what impacts the magmatic system experiences from the removal of rock mass above it.

3.7.3 Implications for future eruption scenarios and hazard modelling.

Globally, pre-Holocene volcanic deposits are underrepresented within the stratigraphic record due to poor preservation of deposits around the volcano. Hazard modelling and mitigation plans for Mt. Taranaki have typically focussed on the < 5 ka eruptive history investigating the styles and frequency of eruptive events (e.g., McDonald et al., 2017; Torres-Orozco et al., 2018; Weir et al., 2022). This short eruptive record from Mt. Taranaki used for hazard modelling fails to account for changing eruptive hazard associated with morphological changes associated with large edifice collapse events. Our study highlights the importance of including long term volcanic records to generate more accurate hazard models for long-lived stratovolcanoes that experience frequent edifice collapse events with the Poto and Paetahi Formations providing the unique opportunity to investigate the volcanic response to repeated collapse.

Furthermore, during this 4 kyr eruptive period 20 – 30,000 years ago more large explosive events occurred corresponding to major explosive eruption with eruption column c. 10-20 km of (Bebbington & Jenkins, 2019). This contrasts the eruptive hazard forecasting for Mt. Taranaki based on the younger record where a lot fewer major explosive to plinian eruptions occurred, and a wider range of eruptive styles were observed (e.g., effusive to large explosive) (Torres-Orozco et al., 2017a; Torres-Orozco et al., 2017b, 2018; Bebbington & Jenkins, 2019; Weir et al., 2022). Within the last 5 ka, sixteen large explosive subplinian to plinian eruptions have been recorded with the last occurring in 1655 CE (Platz, 2007; Platz et al., 2007; Torres-Orozco et al., 2018). This indicates during the Poto and Paetahi Formations there was a higher frequency of large explosive eruptions occurring in response to the morphological changes on the edifice following a large edifice collapse event.

The deposits from the Poto and Paetahi Formations also show that during this eruptive period, these large events were distributed to the southeastern sector of the ring plain which differs from the predominant north-eastern distribution seen for < 5 ka tephras (Torres-Orozco et al., 2017a; Torres-Orozco et al., 2017b, 2018). This dispersal is supported by modelling which shows that eruptions of a certain size are being distributed across the southeastern sector of the ring plain (Weir et al., 2022). Thus, our results have significant implications for future hazard work in the Taranaki region. They also highlight the limitations of using only the Holocene records for risk assessments, which might not fully capture how eruptive styles and the dispersal of eruptives may be changing over a longer time scale or in response to external factors.

3.8 Conclusions.

Investigating a sequence of eruptions around two major edifice collapses at a stratovolcano exposed the complexity of long-term volcanic processes and their role in eruption behaviour. Our revised stratigraphy for the Poto and Paetahi Formations shows that this period of time in Mt. Taranaki's history was marked by an increase in explosive activity that resulted in the production of twenty-eight subplinian events and one PDC deposit. These tephra formations differ from the previously studied younger eruptive periods at Mt. Taranaki where there is a wider array of eruptive styles and less frequent large explosive events. The 4 kyr Poto and Paetahi eruptive period was characterised by frequent and consistently large explosive events with a total eruptive volume of 3 km^3 and individual eruptive events producing 0.01 to 0.26 km^3 of tephra. Eruption column heights ranged from 10-20 km with eruption magnitudes of 3 – 4.5. Eruptive events following the collapses were larger than the events seen beforehand and variable eruption sizes between the two collapse events as Mt. Taranaki rebuilt its edifice. Throughout this increase in large explosive events, observed changes within the componentry of the depositional layers indicate varying conditions within the conduit system. The sequence comprises seventeen stable conduit events, seven conduit widening events and four unstable column/ conduit wall collapse events.

The dispersal of the studied Poto and Paetahi tephras to the east and southeast differs from younger deposits at Mt. Taranaki, with some additional layers identified along the southwestern coastline that fall within the same time period. However, further work is required to integrate these into the stratigraphy. While the distribution of the Poto and Paetahi tephras diverges from the predominant northeasterly distribution due to the prevailing westerly winds, it supports tephra fall models for the area which show eruptions of a certain size being distributed to the southeast.

The relationship between the volume of the collapse and the total volume of the edifice appears to play a role in the size of the eruptions following a collapse event and the changes or lack of changes seen in the eruptive styles at a volcano. The Pungarehu and Ngaere DADs represent a significant percentage of the cone (up to approximately 60%) being removed, depressurising the system, and resulting in a 4, 000 year-long period of heightened explosive activity at Mt. Taranaki. Understanding how eruptive behaviour may change not only due to magmatic processes but external influences is critical for hazard forecasting and planning. These collapse events and the generation of the Poto and Paetahi tephra formations highlight the need to extend eruptive histories for hazard modelling at volcanoes around the world to longer-term records. The concept of large edifice collapses leading to an increase in large eruptive events without changing eruptive styles might be applicable for repeatedly collapsing stratovolcanoes elsewhere.

4 Assessing the influence of edifice collapse on the shallow volcanic plumbing system of Mt. Taranaki through textural analysis of the subplinian Poto and Paetahi tephra formations.

Abstract

Edifice collapse events can alter the shallow volcanic plumbing system and thus influence short- to long-term eruptive processes occurring at stratovolcanoes. Mt. Taranaki in New Zealand has experienced at least fourteen large-scale collapse events within its > 200 kyr eruptive history. The 20-30 ka Poto and Paetahi tephra formations encompass two of the largest collapse events recognised in Mt. Taranaki's history, providing a unique opportunity to explore the impact that major edifice failure has on the shallow volcanic plumbing system. Pumice clasts from representative layers within the explosive eruptive sequence were analysed in 3D using the Micro-Computed Tomography (MCT) beamline at the Australian Synchrotron. Vesicle number densities (VND) and vesicle size distributions (VSD) for nineteen eruptive events were compared to investigate potential changes before and after collapse events. The obtained VNDs indicate that the pyroclasts of the Poto and Paetahi Formations are dominated by small bubbles with the 27.3 ka 5.85 km^3 Ngaere collapse having a significantly larger impact on the shallow volcanic plumbing system than the 24.8 ka 7.5 km^3 Pungarehu collapse. A decrease in VND and increase in the percentage of large bubbles within Poto. c lower indicates a change in over pressurization within the system in response to the Ngaere collapse. Removal of the upper conduit system during the Ngaere collapse changed the lithostatic pressure, causing rapid decompression on the magmatic system below resulting in an explosive eruption. However, an increase in the percentage of small bubbles within Paetahi.e lower following the Pungarehu collapse indicates a rapid decompression event did not occur as the western remnant cone collapsed. The data suggests that the relative proportion of the upper conduit that is removed during edifice failure controls subsequent processes occurring in the shallow volcanic plumbing system.

4.1 Introduction

Volcanic ash is produced through explosive eruptive events and can be harmful to human health and disrupt/damage infrastructure and aviation. Therefore, understanding the processes which generate ash is critically important for hazard analysis and planning (Sparks, 1978; Gardner et al., 1996; Papale, 1999; Sahagian, 1999; Zhang, 1999; Alidibirov & Dingwell, 2000; Koyaguchi & Mitani, 2005; Genareau et al., 2012). Eruptive style and explosivity of a volcano are controlled by both internal magmatic processes and external factors. The main internal drivers of explosivity are magma rheology and composition, which in turn influence viscosity, volatile content, and degassing controlling bubble nucleation (e.g., Lautze & Houghton, 2007; Pardo et al., 2014; Cashman & Scheu, 2015; Heinrich et al., 2020b; Toramaru, 2022). Additional internal influences on eruption style include the timing and nature of where degassing begins (e.g., Wilson et al., 1980; Woods & Koyaguchi, 1994; Mangan & Sisson, 2000; Gaonac'h et al., 2005) the proportion of juvenile particles to accidental lithics (e.g., Shea et al., 2011), and the amount of crystallisation occurring during magma degassing (Gardner et al., 1998; Hammer et al., 1999; Pistone et al., 2012). External factors such as interaction of magma with groundwater (e.g., Wohletz, 1986; Caricchi et al., 2007; Andújar & Scaillet, 2012; Okumura et al., 2013; Pistone et al., 2013; Cassidy et al., 2018), changes to the size and geometry of the conduit wall (Wilson et al., 1980; Macedonio et al., 1994; Caricchi et al., 2007; Andújar & Scaillet, 2012; Okumura et al., 2013; Pistone et al., 2013; Cassidy et al., 2018), or decompression through processes such as edifice collapse (McBirney & Murase, 1970; Wilson et al., 1980; Lipman & Mullineaux, 1981; Alidibirov & Dingwell, 2000) also influence eruptive style.

The viscosity of the magma plays a critical role in the process of bubble nucleation and growth, e.g., low viscosity basalt compositions rarely produce explosive plinian events but are more commonly associated with Hawaiian and Strombolian-type eruptions (e.g., Parfitt & Wilson, 1995; Pioli et al., 2008; Pérez et al., 2009). However, intermediate andesite systems have a broader range of compositions and viscosities, resulting in a wider array of eruptive styles (e.g., Polacci et al., 2006a; Clarke et al., 2007; Höskuldsson et al., 2007; Pardo et al., 2012b; Pardo et al., 2012a; Torres-Orozco et al., 2017a; Torres-Orozco et al., 2017b; Heinrich et al., 2020a; Heinrich et al., 2020b). Explosive eruptions are

dependent on the ability of gas flow pathways to form within the liquid magma while volatile exsolution is driving magma ascent to the surface (Klug & Cashman, 1996; Mangan & Sisson, 2000; Burgisser & Gardner, 2004; Gaonac'h et al., 2005; Wright et al., 2009; Rust & Cashman, 2011) once volatile saturation or supersaturation is reached and gas phases start to influence magma viscosity (Mangan & Sisson, 2000; Burgisser & Gardner, 2004; Gaonac'h et al., 2005) bubble nucleation begins, as bubbles begin to grow the density of the magma decreases (Toramaru, 1989; Sparks et al., 1994; Barclay et al., 1995; Toramaru, 1995; Lyakhovsky et al., 1996; Proussevitch & Sahagian, 1998; Burgisser & Gardner, 2004). This drives magma ascent to the surface, forming more bubbles and causing increased exsolution of volatiles from the melt. Small bubbles merge as bubble nucleation and growth continues, resulting in coalescence and the increased separation of gas from the melt (Gonnermann & Manga, 2007). Bubbles continue to form (Klug & Cashman, 1996; Wright et al., 2009; Rust & Cashman, 2011) until the percentage of the vesicles exceeds the tensile strength of the magma and fragmentation ensues, resulting in an explosive eruption (McBirney & Murase, 1970; Sparks, 1978; Prousevitch et al., 1993; Alidibirov, 1994; Proussevitch & Sahagian, 1996; Proussevitch & Sahagian, 1998; Zhang, 1999; Alidibirov & Dingwell, 2000; Pinkerton et al., 2002; Proussevitch & Sahagian, 2005; Sahagian, 2005; Gonnermann & Manga, 2007; Castro et al., 2012; Genareau et al., 2013).

External events such as edifice collapse can disrupt the process of bubble nucleation and growth due to the rapid decompression (Alidibirov & Dingwell, 2000). The location of the fragmentation zone within the conduit is considered to be associated with the lithostatic pressure above it (Wilson et al., 1980). A collapse of the edifice changes this lithostatic pressure, which can generate magmatic overpressure triggering an explosive eruption through the rapid fragmentation of the melt, caused by the propagation of a fragmentation front (Alidibirov & Dingwell, 2000; Sato et al., 1992; Klug & Cashman, 1994; Kennedy et al., 2005; Alatorre-Ibarguengoitia et al., 2011).

Bubbles within pumice clasts are a frozen record of the processes occurring within the magmatic system; their size, shape and connectedness being the result of magma rheology, permeability, volatile degassing, and fragmentation within the conduit (Houghton & Wilson, 1989; Polacci et al., 2003; Gonnermann & Manga, 2007; Shea et al., 2010; Mueller et al., 2011; Shea et al., 2012). Investigation

of these parameters provides insights into the relative location and timing of bubble nucleation, coalescence, and volatile degassing within the system and how this changes the eruptive behaviour throughout an eruptive sequence (Mangan & Sisson, 2000; Toramaru, 2006; Gurioli et al., 2008; Belien et al., 2010; Shea et al., 2010; Shea et al., 2012).

Changes in lithostatic pressure above a magmatic system following an edifice collapse can influence the eruptive composition, style, size, and frequency of subsequent eruptive activity (Watt, 2019). Observations from global examples e.g., Stromboli, Italy (Hornig-Kjarsgaard, 1993; Tibaldi, 2001; Romagnoli et al., 2009); Fuego de Colima, Mexico (Robin et al., 1990; Stoopes & Sheridan, 1992; Capra & Macías, 2002) reflect the relationship between lithostatic pressure and the magmatic system. Historical collapse events have been relatively small e.g., 1888 Ritter Island Papa New Guinea 4.2 km^3 (Johnson, 1987) in comparison to prehistoric failures e.g., 60 – 65 ka Chimborazo, Ecuador, 12 km^3; (Samaniego et al., 2012; Watt, 2019) however, studies into eruptive events pre- and post-dating these large prehistoric failures is difficult due to the preservation of deposits (Watt, 2019).

Sector collapse triggering sudden decompression on the system can cause magmatic overpressure resulting in the initiation of an explosive eruption (e.g., 1980 Mt. St. Helens (Siebert, 1984)). In order to investigate the role sudden decompression has on the magmatic system the textural characteristics of pumice clasts from explosive eruptions within a stratigraphic sequence that encompasses two large edifice collapse events were investigated to better understand the short- and long-term effects of the associated sudden decompression on the subvolcanic plumbing system. The units were selected to test the hypothesis that sudden decompression causes a critical change in the magmatic overpressure generating a fragmentation front. The sequence before and after two collapse events at Mt. Taranaki were selected to compare the pre and post collapse deposits and determine the influence sudden collapse has on the processes of bubble nucleation. The eruptions within the regrowth phase provide information on the changes in magmatic processes occurring below the surface.

Mt. Taranaki has experienced at least fourteen major edifice collapse events within its > 200 kyr eruptive history (Zernack et al., 2011; Zernack et al., 2012b; Zernack & Procter, 2021) with two of the largest edifice failures the 27.3 ka 5.85 km^3 Ngaere and 24.8 ka 7.5 km^3 Pungarehu collapses occurring within

close succession (~2.5 kyr) (Neall, 1979; Neall & Alloway, 2004; Alloway et al., 2005). These two events are encompassed by the Poto and Paetahi tephra formations (Alloway et al., 1995) a sequence of twenty-eight subplinian events which occurred over ~4,000 years (Chapter 3). The pumices from these pre- and post- failure explosive eruptions provide a unique opportunity to examine how eruptive behaviour at a long-lived stratovolcano is impacted by edifice collapse.

4.2 Geological history of Mt. Taranaki

Mt. Taranaki is situated on the west coast of the North Island of New Zealand, 140 km west of the Taupō Volcanic Zone (TVZ) and 180 km west of the Hikurangi Trench (Stewart et al., 1996). It is situated 180 km above a westward dipping Wadati-Benioff Zone (Chapter 1; Figure 1.3) (Adams & Ware, 1977; Stewart et al., 1996). Mt. Taranaki is the youngest volcano (> 200 kyr) of the Taranaki Volcanic Lineament, which is a north-north-west to south-south-east trending succession of three volcanoes that is younging to the south-south-east (Neall et al., 1986). At (2518 m), Mt. Taranaki is an almost completely symmetrical stratovolcano, except for the parasitic cone Fantham's Peak on the upper southern flank. The present-day edifice is composed of pyroclastic material and lava flows less than 10,000 years old (Neall, 1979; Turner et al., 2011) with a volume of ~12 km^3 (Neall et al., 1986; Procter et al., 2009; Zernack et al., 2012a).

The older volcanic history is recorded in an extensive ring plain surroundings Mt. Taranaki, which comprises predominantly volcanic debris-avalanche and lahar deposits with minor fluvial and aeolian sediments (Chapter 1; Figure 1.4) (Neall, 1979; Alloway et al., 1995; Procter et al., 2009; Zernack et al., 2009; Cronin et al., 2021; Zernack, 2021). Collapse-generated debris avalanche deposits have contributed the largest volume of material to the ring plain with at least 14 edifice failures with volumes > 1 km^3 being recognised (Neall, 1979; Alloway et al., 2005; Zernack et al., 2011; Zernack et al., 2012b). The medial ring plain around Mt. Taranaki provides a record of eruptive activity over the past 30-50 kyr comprising four debris-avalanche deposits including two of the largest (Zernack et al., 2011). The majority of fall deposits are preserved across the north-north-east to south-south-east sector of the ring plain due to the prevailing westerly winds (Neall, 1972; Neall, 1979; Alloway, 1989; Alloway et al.,

1995; Turner et al., 2009). Recent studies (Damaschke et al., 2017b) using lake cores have identified at least 272 tephra producing eruptions from Mt. Taranaki over the past 30 kyr.

The 20-30 ka Poto and Paetahi tephra formations consist of twenty-eight subplinian events of varying size with eruption volumes of 0.01 to 0.26 km^3 covering the eastern and southeastern sectors of the ring plain (Chapter 3). These formations are unique as they encompass two of the largest known collapse events at Mt. Taranaki, recording the regrowth of the edifice between major failures. Paleosols between individual tephra layers mark breaks in eruptive activity during regrowth, while lithosedimentological variations within the tephra deposits preserve evidence for the onset of new eruptive phases (Chapter 3**).**

The present-day edifice > 1200 m provides the most detailed stratigraphic record of activity for Mt. Taranaki over the last ~8 ka (Druce, 1966; Neall, 1979; Platz et al., 2007; Turner et al., 2008a; Turner et al., 2011; Platz et al., 2012; Torres-Orozco et al., 2017a; Torres-Orozco et al., 2017b). The edifice consists of overlapping, interbedded or spatially diverse units of domes, lava flows, ballistics, block and ash flows, pyroclastic density currents, surges and associated lahars indicating the array of eruptive activity occurring at Mt. Taranaki (Torres-Orozco et al., 2018; Cronin et al., 2021). Within the last 5 ka at least 53 eruptive episodes have occurred from Mt. Taranaki, including sixteen subplinian and plinian eruptions produced from the Summit Crater and Panitahi (Fanthams Peak) (Turner et al., 2009; Torres-Orozco et al., 2017a; Torres-Orozco et al., 2017b). These proximal fall deposits preserve a detailed record of individual eruptive phases.

Previous bubble studies investigated magmatic vesiculation and crystallisation of the 3300 cal BP Upper Inglewood (Uig) plinian eruptive episode (Torres-Orozco et al., 2023). This eruptive episode included an array of eruptive styles ranging from dome collapse pyroclastic density currents (PDCs) to climactic plinian eruptive events that produced pumice with vesicle number densities (VNDs) ranging from 1.1 x 10^5 to 2.5 x 10^6 mm^{-3} and mafic crystal number densities (CNDs) ranging from 8.0 x 10^4 to 5.1 x 10^6 mm^{-3} (Torres-Orozco et al., 2023). Vesiculation studies of the Uig indicate multiple processes occurring in the subvolcanic plumbing system during this eruptive period, with different rates of magma decompression and ascent through the conduit resulting in the observed spectrum of eruptive styles

(Torres-Orozco et al., 2023). The most explosive eruptive phases, Uig4-Uig5, and the climactic plinian phase Uig7, showed the highest VNDs and CNDs of the entire Uig eruptive episode. The climactic plinian phase (Uig7) had VNDs of > 1.5 x 10^6 mm^{-3} and produced subspherical to highly spherical uniform sized bubbles (Torres-Orozco et al., 2023), compared to other eruptive styles within the Uig eruptive period where bubble shapes ranged from subspherical to elongated. This variation in bubble shapes indicates pulses of bubble nucleation and growth within the system (Torres-Orozco et al., 2023). This study hypothesized the Uig eruptive period was associated with a new cycle of mafic magma recharge below Mt. Taranaki, and that any slight changes in magmatic decompression and fragmentation within the conduit can influence the eruption scenario at Mt. Taranaki (Torres-Orozco et al., 2023).

In-depth investigations into eruptive dynamics at Mt. Taranaki have predominantly focussed on the < 5 ka eruptive record due to the poor preservation of proximal sequences from older eruptive phases (e.g., Platz, 2007; Platz et al., 2007; Turner et al., 2009; Turner et al., 2011; Torres-Orozco et al., 2017a; Torres-Orozco et al., 2017b; Lerner et al., 2019d; Lerner et al., 2019a; Lerner et al., 2019c; Lerner et al., 2019b; D'Mello et al., 2021; D'Mello et al., 2023). The eruptive record > 5 ka has typically been investigated to correlate tephras to better understand the frequency of eruptive activity (e.g., Neall, 1972; Neall, 1979; Neall et al., 1986; Alloway et al., 1995; Procter et al., 2009; Zernack et al., 2011; Damaschke et al., 2017b). However, investigating the changes in > 5 ka eruptive dynamics at a frequently collapsing long lived stratovolcano in response to edifice failure are critical for understanding the changes in eruptive behaviour which occur.

4.3 Methodology

4.3.1 Sampling

Twenty-one of the twenty-eight subplinian Poto and Paetahi tephras were sampled for density analysis, selecting 5 – 40 pumice clasts between -4 to -2 phi for each unit. Using pumice clasts from this size fraction reduces the effects of bubble coalescence and post-fragmentation expansion and allows quantitative inference of magmatic processes within the conduit (Houghton & Wilson, 1989; Thomas

& Sparks, 1992; Klug & Cashman, 1994; Klug & Cashman, 1996; Mangan & Cashman, 1996). Seven units were not used for density analysis, due to small grains not providing accurate and reliable data (Appendix D). Sixteen of the twenty-one units used for density and three of the remaining seven units were selected for 3D analysis. These nineteen units dispersed throughout the Poto and Paetahi Formations represent different stages within the collapse and regrowth cycle, along with different conduit conditions identified in (Chapter 3).

4.3.2 Density

Densities were measured on 5 - 40 (depending on available material) pumice clasts from twenty-one Poto and Paetahi units. Envelope density was conducted using the Micrometrics Geopyc 1365 dry flow pycnometer with 5 re-run measurements to provide standard deviations of max 5 %. The envelope density of the samples is a proxy for the bulk density of the pumice clasts.

Pumice vesicularities were calculated using the equation by Houghton and Wilson (1989)

$$(100*(\text{DRE g/cm}^3\text{-bulk density g/cm}^3)/ \text{DRE g/cm}^3) \quad (22)$$

and a DRE of 2.4 g/cm^3 as an average for andesitic rocks (Houghton & Wilson, 1989).

4.3.3 3D bubble analysis

Nineteen clasts from nineteen different eruptive units dispersed throughout the Poto and Paetahi Formations were chosen for 3D textural quantitative analysis. Density data obtained through pycnometry was used for sixteen units to select a representative clast (average bulk density) for analysis at the Australian Synchrotron. Density calculations for units Poto.d, m and Paetahi.a middle were not possible due to the small size of the clasts. These units were chosen for 3D analysis as they represented significant events within the sequence. For these three units the largest non-weathered clast was used whole as a representative sample while 8 mm by 7 mm diameter cores were extracted from the other sixteen clasts. All nineteen samples were placed inside aluminium tubes with a plastic cap for analysis at the Australian Synchrotron (Figure 4.1). The selected units represent important stages within the

collapse and regrowth cycle and different conduit conditions as identified in (Chapter 3) as well as covering the range of eruption sizes observed within the Poto and Paetahi Formations rather than targeting specific eruption types or single events (e.g., Pardo et al., 2014; Heinrich et al., 2020b; Torres-Orozco et al., 2023).

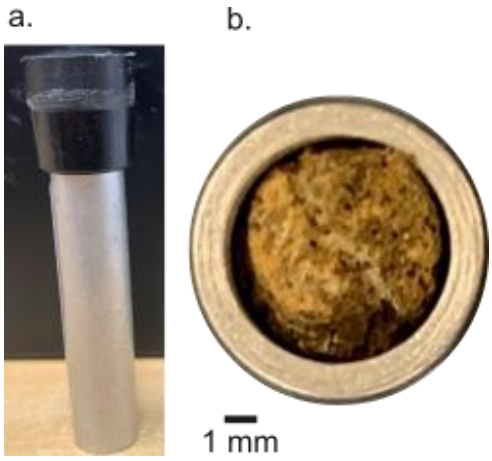


Figure 4.1: Sample holders used for the 3D MCT scanning at the Australian Synchrotron.a) 5 cm long aluminum cylinder with plastic cap. b) Sample within the upper cut out 7 mm x 8 mm core within the cylinder.

The pumice cores were placed inside aluminium tubes and analysed using the Micro-Computed Tomography (MCT) Beamline at the Australian Synchrotron. A total of 1201 images were recorded for each sample with a voxel size of 6.5 microns using a whitebeam with a sample to detector distance of 0.16 m, 1 x magnification at 35 keV energy, and 180° rotation in 0.150-degree angle increments. Filters 0.2 mm diamond, 5.0 mm Aluminium and 0.5 mm Copper were used. The 2D slices were reconstructed into 3D volumes and corrected using MCT Processing. The MCT beamline at the Australian Synchrotron allows for higher resolution imaging on the pumices than what has been achieved in the past (c.f., Pardo et al., 2014; Rotella et al., 2014; Torres-Orozco et al., 2023). This higher resolution allowed for improved detection of smaller bubbles preserved within pumice clasts, enabling a more in-depth investigation of the eruptive processes forming the juvenile products.

Pre-processing was completed in Dragonfly version 2022.2 (Figure 4.2), which involved the cropping of the cylinders to create a subset which was completely contained within the sample and removal of any void space created between the grain and sample holder. This subset was then

used for further analysis. The total volume of the subset was determined and used for calculating vesicle and crystal number densities, and vesicle- and crystal-size distributions. This sample subset was segmented using intensity thresholds into vesicles (< 0.8 intensity), matrix (> 0.8 intensity) and mafic crystals (< 1.48 intensity) (Figure 4.3). Each 3D model was then processed in Dragonfly to identify the segmented elements and quantify the sample properties (count, voxel count and volume). Processing of the subset for analysis (see Figure 4.2) included filling internal enclosed portions of the area of interest and reduction of pixel noise using erosion morphological operations (kernel size of 3 voxels) to remove any isolated pixels from the scans. This processed data set was separated into four components (vesicle, matrix, crystals, and total volume) by analysing connectivity of voxel faces to generate statistical properties for the different units.

The individual volumes were used to calculate

$$\text{vesicle volume percentages} = \left(\frac{\text{Vesicle volume}}{\text{Total volume}} * 100\right), \tag{23}$$

$$\text{vesicle number densities} = \left(\frac{\text{No. of vesicles}}{\text{Total crystal + melt}}\right), \tag{24}$$

$$\text{crystal volume percentages} = \left(\frac{\text{Crystal volume}}{\text{Total volume}} * 100\right) \tag{25}$$

$$\text{and crystal number densities} = \left(\frac{\text{No. of crystals}}{\text{Total vesicles + melt}}\right) \tag{26}$$

for each of the erupted grains. The resolution of the scans were 6.5 microns allowing for the capture of vesicles down to 2.7×10^{-7} mm^3. Our samples have a small percentage of larger vesicles. However, the smallest vesicles provide the most information about the last vesiculation stage during fragmentation (Klug et al., 2002; Castro et al., 2003; Rotella et al., 2014). Within the 3D vesicle analysis each pumice clast had evidence of one large bubble corresponding to either large permeable connected bubble pathways or edges of the pumice core where vesicle walls had been removed during sample preparation. These large, connected pathways were not separated into individual vesicles due to their natural connected behaviour (e.g., Colombier et al.,

2018; Torres-Orozco et al., 2023) and were not included in measurements as they created an outlier for vesicle size distributions.

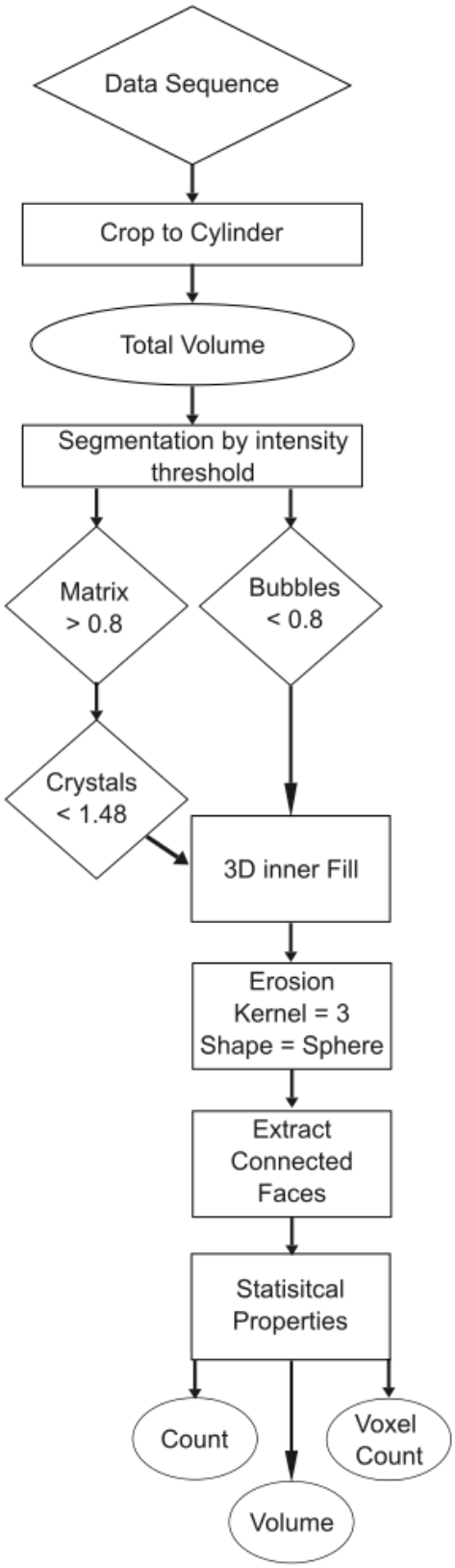


Figure 4.2: Flow diagram for extracting volume and number density calculations from 3D textural analysis to produce vesicle number densities (VND), mafic crystal number densities (CND), Total volume and Matrix Volume.

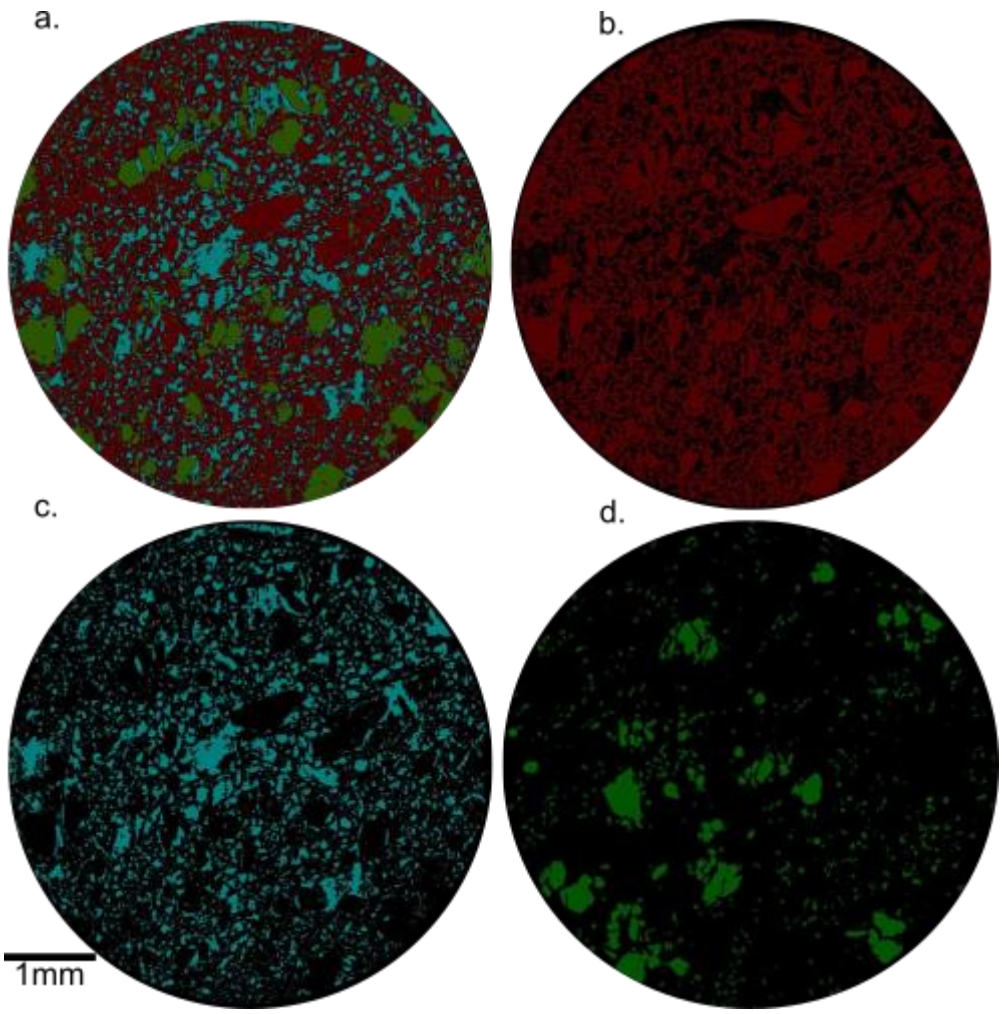


Figure 4.3: Step view of thresholding process showing a) Juvenile grain with the different sections thresholds for bubbles, matrix and crystals overlaid, b) Matrix threshold (red), c) Thresholding of the vesicles (voids) (blue), and d) Thresholding of the mafic crystals (pyroxenes and titano-magnetite) (green).

4.3.4 2D Textural analysis

Two-dimensional image slices from the 3D scans were used to explore the different textural characteristics within the pumice clasts, i.e., isolated pores, coalescence, and shearing (Verhoogen, 1951; Lyakhovsky et al., 1996; Gardner et al., 1998; Gardner et al., 1999; Alidibirov & Dingwell, 2000; Klug et al., 2002; Castro et al., 2012). The 2D slices were enhanced to increase contrast and highlight the three main features (Figure 4.3), bubbles (blue), matrix (inclusive of Feldspar crystals) (red) and Mafic crystals (Pyroxenes and Titanomagnetites) (green).

4.4 Results

4.4.1 Density data

Pumices from the Poto and Paetahi Formations were analysed and plotted (Table 4.1; Figure 4.4) to investigate the relationship between stratigraphic position, conduit conditions and collapse/growth cycles identified in (Chapter 3), to understand what influence these processes have on the density of erupted material.

The bulk densities for the Poto Formation range from 0.7 to 2.4 g/cm^3 with an average of 1.3 g/cm^3 and from 0.7 to 2.6 g/cm^3 for the Paetahi Formation with an average of 1.2 g/cm^3(Figure 4.4). Conduit conditions throughout the eruption sequence vary between phases of stable, unstable, and widening conduit systems.

Stable conduit pumice bulk densities range between 0.7 and 2.6 g/cm^3.Unstable conduit eruption bulk densities have a range of 1 to 2.4 g/cm^3, and conduit widening events have a bulk density range of 1 to 2.4 g/cm^3.

The Poto and Paetahi Formations were emplaced during stages of collapse and regrowth, where bulk densities were 1 to 1.7 g/cm^3 pre-Ngaere collapse. Following the Ngaere collapse during edifice regrowth of Mt. Taranaki the bulk density ranged from 0.7 to 2.6 g/cm^3.Following the Pungarehu collapse the bulk density ranged between 1 to 1.5 g/cm^3.

Table 4.1: Textural features of the Poto and Paetahi Formationsshowing the average bulk densities, and vesicularities calculated using pycnometry. Vesicle number densities (VND), mafic Crystal number densities (CND), Vesicle volume (VV), and Crystal volumes (CV) were calculated from 3D MCT scans. Conduit conditions from (Chapter 3). Detailed results are found in Appendix D and E.

Name	Conduit conditions	Bubble number density (BND) (cm^{-3})	Bubble Volume (%)	Crystal number density (CND) (cm^{-3})	Crystal volume (%)	Vesicularity (%)	Bulk density g/cm^3
Paetahi.f	Widening	$9.03x10^{15}$	4.2	$3.72x10^{15}$	21.9	52.59	1.3
Paetahi.e upper	Unstable	-	-	-	-		
Paetahi.e middle	Unstable	$1.38x10^{16}$	6.8	$7.95x10^{14}$	6.2	54.81	1.2
Paetahi.e lower	Stable	$1.29x10^{16}$	3.3	$8.3x10^{14}$	9.1	52.22	1.3
Pungarehu DAD	DAD	DAD	DAD	DAD	DAD	DAD	DAD
Paetahi.d	Stable	$1.15x10^{16}$	7.1	$1.5x10^{15}$	11.5	56.67	1.2
Paetahi.c	Widening	-	-	-	-		
Paetahi.b	Stable	-	-	-	-	58.15	1.1
Paetahi.a upper	Stable	$1.52x10^{16}$	8.2	$1.18x10^{15}$	8.7	58.52	1.1
Paetahi.a middle	Stable	$1.59x10^{16}$	4.9	$1.15x10^{15}$	8		
Paetahi.a lower	Stable	$1.56x10^{16}$	3.5	$1.20x10^{15}$	7.7	63.33	1.0
Poto.o	Widening	$1.54x10^{16}$	5.5	$1.71x10^{15}$	11.9	51.48	1.3
Poto.n	Stable	-	-	-	-	56.67	1.2
Poto.m	Stable	$1.74x10^{16}$	6.5	$9.94x10^{14}$	1.4		
Poto.l upper	Stable	$1.09x10^{16}$	6.4	$1.93x10^{15}$	13.2	48.15	1.4
Poto.l lower	Stable	$1.36x10^{16}$	5	$1.78x10^{15}$	15.1	46.3	1.5
Poto.k upper	Stable	-	-	-	-	62.59	1.0
Poto.k lower	Unstable	$1.64x10^{16}$	5.3	$2.24x10^{15}$	13.3	45.56	1.5
Poto.j	Unstable	$1.17x10^{16}$	5.5	$1.62x10^{15}$	14.8	43.7	1.5
Poto.i	Stable	-	-	-	-	70.74	0.8
Poto.h	Widening	$1.49x10^{16}$	6.5	$9.45x10^{14}$	9.6	39.63	1.6
Poto.g	Widening	$1.65x10^{16}$	9	$1.41x10^{15}$	13.7	41.11	1.6
Poto.f	Stable	-	-	-	-		
Poto.e	Widening	$1.5x10^{16}$	3.9	$2.99x10^{15}$	24.5	49.63	1.4
Poto.d	Stable	$1.1x10^{16}$	3.4	$9.96x10^{14}$	20.2		
Poto.c upper	Stable	-	-	-	-	61.85	1.0
Poto.c lower	Stable	$9.76x10^{15}$	4.8	$9.15x10^{14}$	10.2	59.63	1.1
Ngaere DAD	DAD	DAD	DAD	DAD	DAD	DAD	DAD
Poto.b	Widening	-	-	-	-	-	-
Poto.a	Stable	$1.53x10^{16}$	4.9	$3.11x10^{15}$	6.6	54.44	1.2

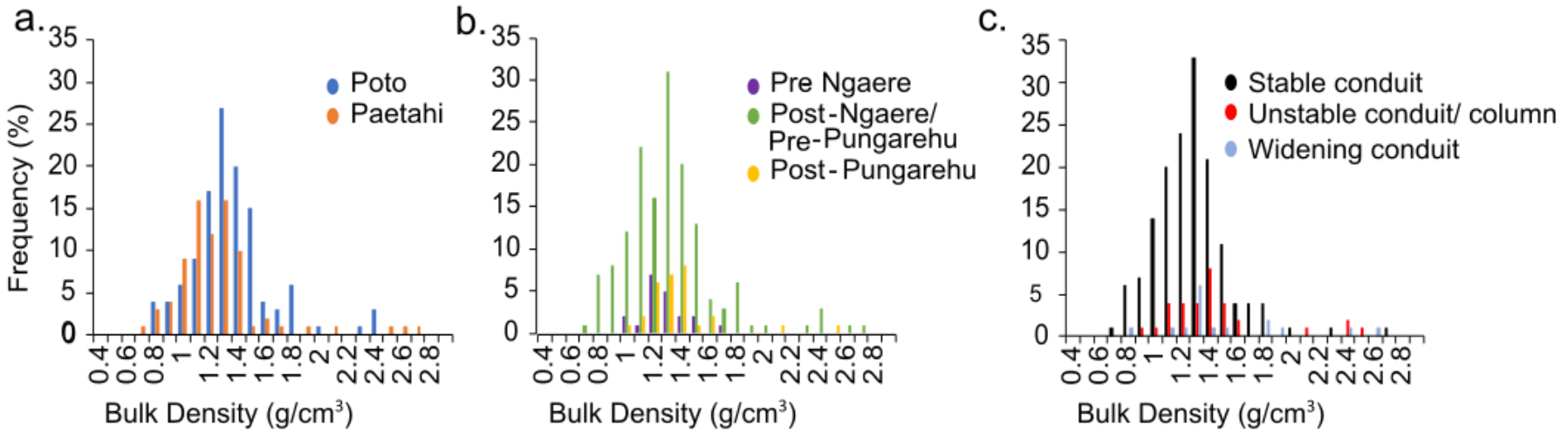


Figure 4.4: Average Density data for the Poto and Paetahi Formations. a) The Poto and Paetahi Formations relative to each other. b) In relation to the collapse and regrowth cycles. c) In relation to the conduit conditions identified in Chapter 3. Detailed results are found in Appendix D.

4.4.2 Textural features

Poto and Paetahi pumice clasts show a high percentage of small vesicles (2.75 x 10^{-7} mm^3) for all eruptive units. The 2D textural analysis indicates three main textural classes, micro-vesicular, transitional, and foamy (Figures 4.5 and 4.6).

1. Micro-vesicular clasts (Poto.a; Figures 4.5a and 4.6a) are dominated by small vesicles with thick vesicle walls (c.f., Pardo et al., 2014; Heinrich et al., 2020b). A small percentage of larger vesicles (< 0.02 mm^3) is present within the clast, and macro-vesicles occur along the edge of some pyroxene crystals. Vesicle walls are thicker than within foamy textured clasts (Figure 4.6).
2. Transitional clasts show a combination of both micro-vesicular and foamy characteristics, typically displaying foamy lenses throughout the clast. Paetahi.a lower has the largest foamy textured lens surrounded by micro-vesicular textures (Figures 4.5d and 4.6d). Other clasts (Poto.l upper Figures 4.5c and 4.6c) comprise patches of foamy lenses that are surrounded by micro-vesicular lenses.
3. Foamy clasts have thinner vesicle walls than observed in micro-vesicular clasts. No evidence of shearing is present within the clasts; however, larger vesicles (< 0.07 mm^3) are more elongated and subspherical. Poto. c lower and Paetahi.e middle are examples of foamy clasts (Figures 4.5b, 4.5e and 4.6b).

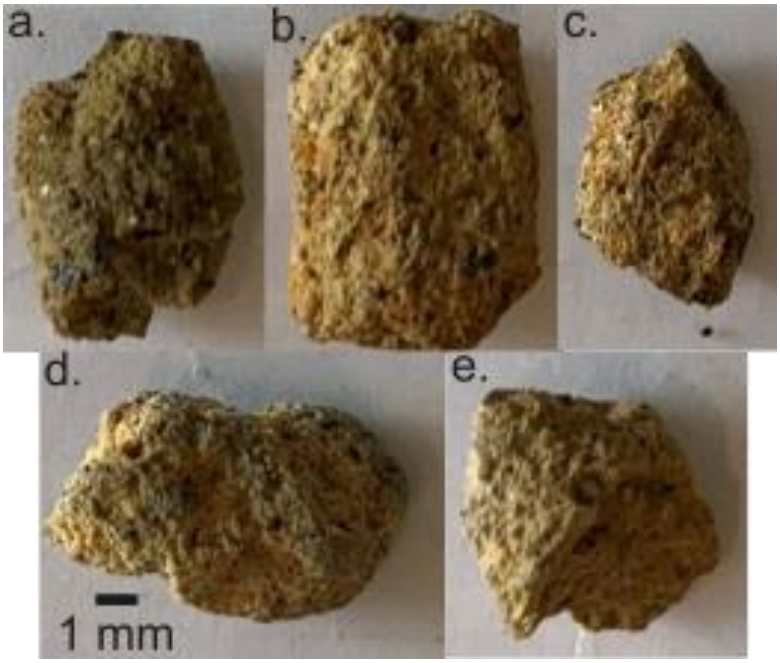


Figure 4.5: Representative samples of the different pumice types within the Poto and Paetahi Formations that were used for 3D analysis at the Australian Synchrotron. a) Poto.a. b) Poto.c lower. c) Poto.l upper. d) Paetahi.a lower. e) Paetahi.e middle.

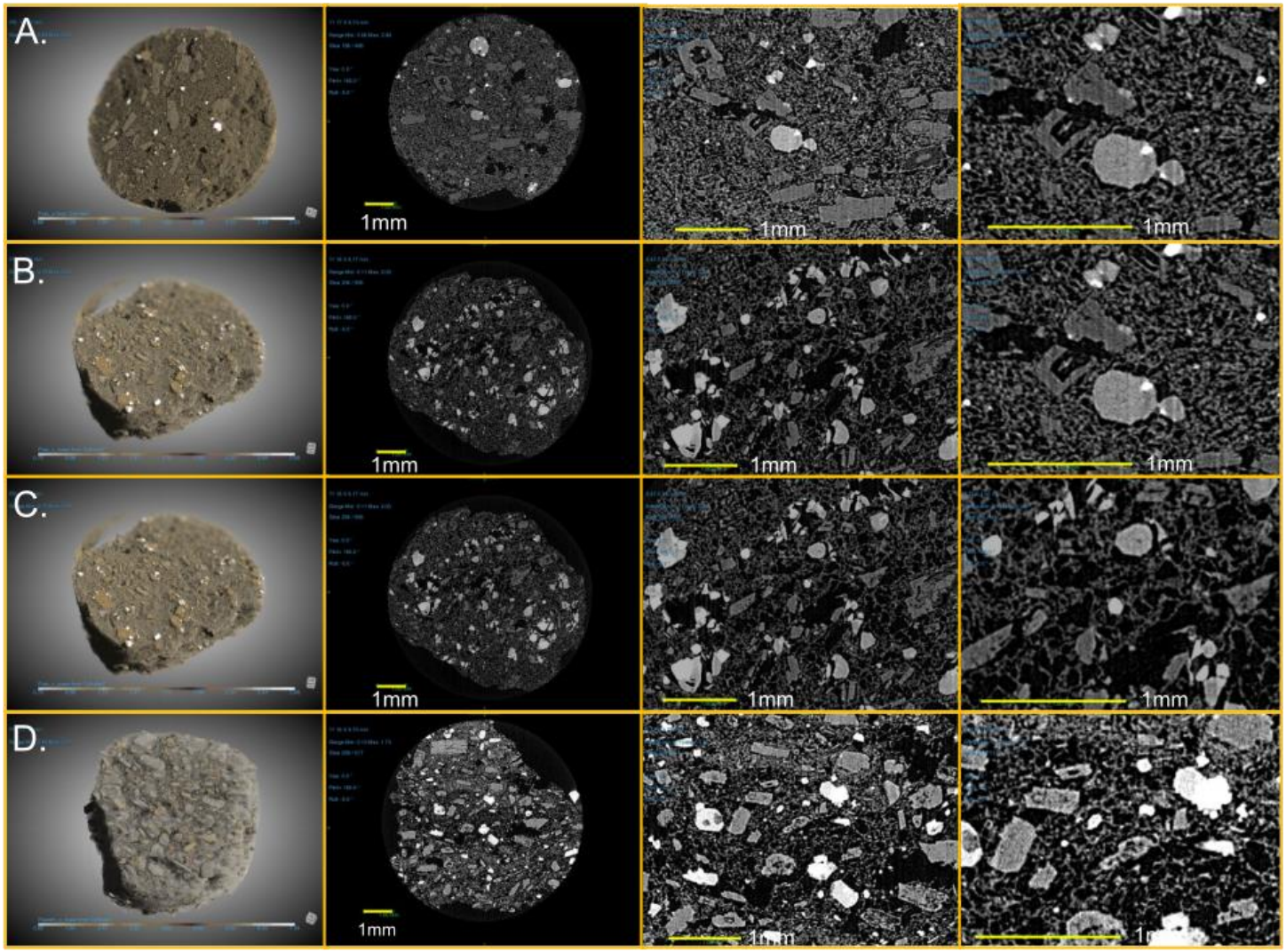

A.
1mm
1mm
1mm
B.
1mm
1mm
1mm
C.
1mm
1mm
1mm
D.
1mm

Figure 4.6: Representative 3D reconstructions and 2D slices from MCT scan images of the Poto and Paetahi Formations showing textural characteristics of the different grains at different levels of zoom. a) Poto.a micro-vesicular dominated clast b) Poto.c lower foamy vesicle clast. c) Poto.l upper transitional clast showing a combination of micro-vesicular and foamy vesicles. d) Paetahi.a lower transitional clast displaying a combination of both textures with a large zone of foamy vesicles through the center.

4.4.3 Pyroclast vesicularity and vesicle number density (VND)

Vesicularities of Poto and Paetahi pumices range between 39 to 70 % with an average of 47.92 % (Table 4.1) and can thus be classified as poorly to highly vesicular (Houghton & Wilson, 1989). The majority of pumice clasts are considered moderately vesiculated based on the Houghton and Wilson (1989) classification. These clasts have a higher proportion of small bubbles (2.75 x 10^{-7} mm^3) with vesicle number densities (VND) between 9.03 x 10^{15} cm^{-3} and 1.74 x 10^{16} cm^{-3}. This is significantly higher than most other published data of similar compositions (Shea et al., 2012; Pardo et al., 2014; Heinrich et al., 2020b), which can be attributed to the improved resolution of our scans that allow for a more accurate quantification of small vesicles within the pumice clasts. Figure 4.7b shows no apparent correlation between vesicularity and VND within the samples. The dominance of small bubbles within the pumices indicate little to no bubble growth and coalescence has occurred within the system during ascent. The high proportion of small bubbles seen in the VNDs together with low VVs with only 3.3 to 9.0 % of the clast volume made of bubbles (Table 4.1) imply that the vesicles present within the pumices are very small as to not become the dominant volume, comparative to pumices seen in rhyolitic systems (e.g., Raoul Island; Rotella et al. (2014), where large vesicles dominate.

The Poto and Paetahi Formations also have high mafic crystal number densities (CND) ranging from 7.95 x 10^{14} to 3.72 x 10^{15} cm^{-3} with crystal volumes (CV) ranging between 1.4 to 24.5 %. The crystal analysis is limited to mafic crystals such as pyroxene and titanomagnetite crystals due to the similarities in compositional range feldspar crystals are unable to be segmented from the matrix through thresholding.

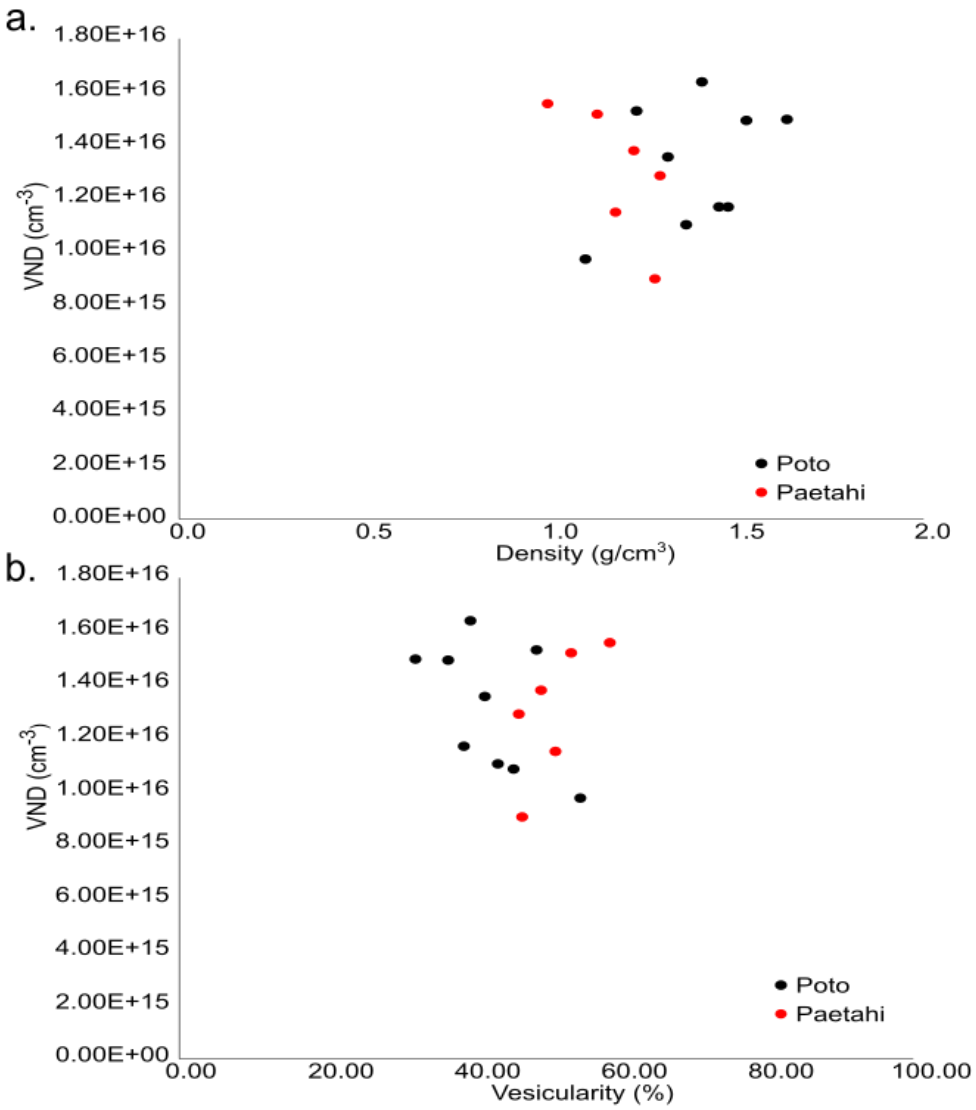


Figure 4.7: a.) Vesicle number density vs average bulk density b.) Vesicle number density vs vesicularity of the different eruptive units from the Poto and Paetahi Formations.

4.4.4 Stages of nucleation

Changes observed in the vesicle size distributions (Figures 4.8 and 4.9) can be used to infer the nucleation history of erupted pumice clasts (e.g., Klug & Cashman, 1994; Shea et al., 2010), including distinct phases of nucleation and growth within the magmatic system and fragmentation processes (Klug et al., 2002; Polacci et al., 2003; Lautze & Houghton, 2007; Shea et al., 2010). Centred unimodal distributions reflect single stage nucleation, whereas positively skewed bimodal distributions and/or

wider dispersed ranges reflect the occurrence of coalescence (Adams et al., 2006b; Gurioli et al., 2008; Shea et al., 2010). Centred bimodal distributions can reflect multiple stages of nucleation occurring within the system (Shea et al., 2010) while positively skewed unimodal distributions indicate a state of continuous/accelerating bubble nucleation and growth (Shea et al., 2010). The Poto and Paetahi Formations display a wide array of distributions representing single stage nucleation, multiple stages of nucleation and growth, continuous/accelerating nucleation and growth, and coalescence (Figures 4.8 and 4.9). Some bubble distributions suggest transitions between two different processes and are indicated by an Asterix (*). Single stage nucleation is found in Poto.a, c.l*, e, h*, k.l, m, Paetahi. a.l, a.m*, e.m*, while multiple stage nucleation and growth is identified within Poto.j and Paetahi. e.l, f. Coalescence is seen within Poto.d, h*, l.l, l.u*, o, Paetahi. a.m*, a.u, d, e.m* and there is evidence for continuous / accelerating nucleation and growth within Poto.m, l.u* and, c. l*.

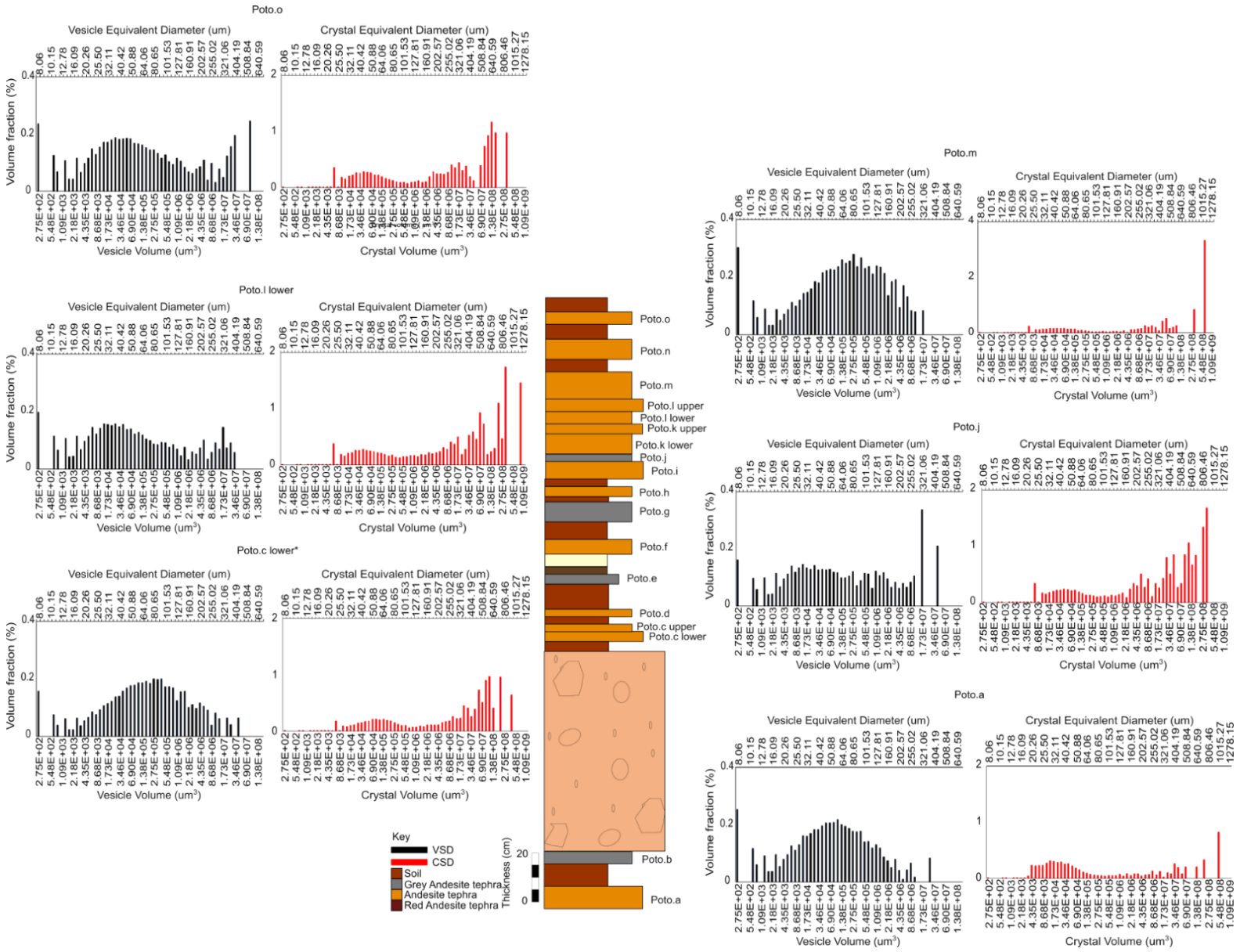

Poto.o
Vesicle Equivalent Diameter (um)
Crystal Equivalent Diameter (um)
Volume fraction (%)
Vesicle Volume (um3)
Crystal Volume (um3)
Poto.l lower
Poto.c lower*
Poto.m
Poto.j
Poto.a
Poto.n
Poto.l upper
Poto.k upper
Poto.k lower
Poto.i
Poto.h
Poto.g
Poto.f
Poto.e
Poto.d
Poto.c upper
Poto.c lower
Poto.b
Key
VSD
CSD
Soil
Grey Andesite tephra
Andesite tephra
Red Andesite tephra
Thickness (cm)

*Figure 4.8: Stratigraphic column of the Poto Formation showing vesicle size distribution (VSD) and crystal size distribution (CSD) plots of representative units, calculated from the 3D MCT analysis of the different pumice clasts. Units with a * display multiple modes of nucleation. (Detailed results are found in Appendix E.).*

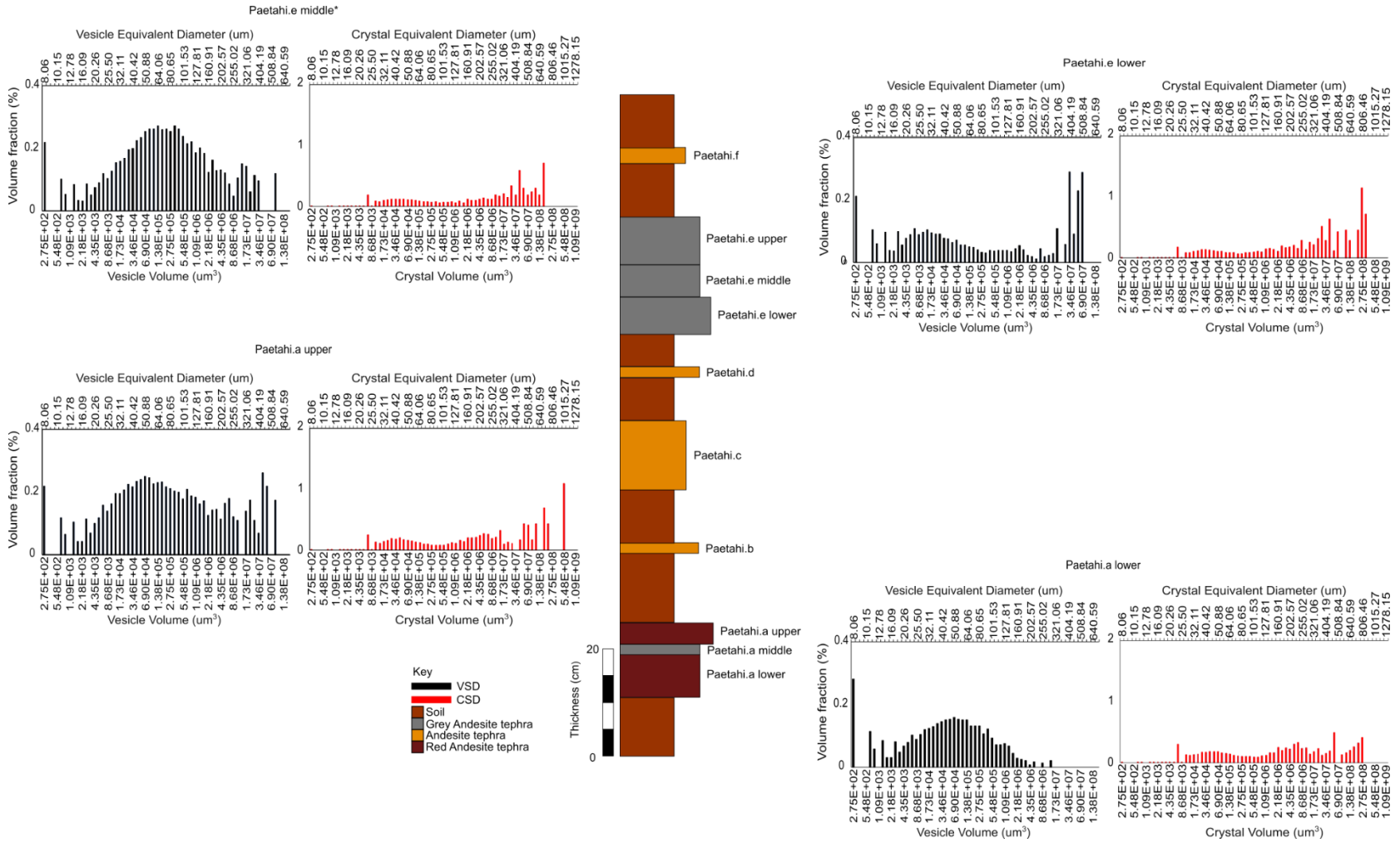


*Figure 4.9: Stratigraphic column of the Paetahi Formation showing vesicle size distribution (VSD) and crystal size distribution (CSD) plots of representative units, calculated from the 3D MCT analysis of the different pumice clasts. with a * show multiple modes of nucleation. (Detailed results are found in Appendix E).*

4.5 Interpretation

4.5.1 Vesicularity in relation to VND

The range of VNDs (9.03 x 10^{15} – 1.74 x 10^{16} cm^{-3}) within the Poto and Paetahi Formations do not directly correlate with higher or lower vesicularity rates (39 – 70 %). This differs from what has been described in other studies (e.g., Rotella et al., 2014), where pumice clasts are dominated by large bubbles significantly influencing the vesicularity of the clasts. This study shows that the vesicularity of the Poto and Paetahi Formations range between 39-70 % indicating poorly to highly vesicular clasts (Houghton & Wilson, 1989), with most pumices classed as moderately vesiculated. VNDs throughout the sequence do not vary significantly with the units ranging from 10^{15} to 10^{16} cm^{-3}. The dominance of small vesicles identified here due to the increased resolution of the MCT scans influence the relationship between VND and vesicularity. Pumice vesicularity correlates to the volume of bubbles present within the clast. The high VNDs but low VVs (3.3 to 9.0 %) relate to the large population of small bubbles present within the clast. The lack of large bubbles within the Poto and Paetahi pyroclasts reduces the vesicularity of the clasts.

4.5.2 Influence of conduit conditions on the eruptive products

VNDs for these events vary from 9.76 x 10^{15} to 1.74 x 10^{16} cm^{-3} with an average of 1.3 x 10^{16} cm^{-3} and vesicle volumes (VV) ranging from 3.3 to 8.2 %. The VNDs for stable conduit eruptions are predominantly in the 10^{16} cm^{-3} range apart from a VND in the 10^{15} cm^{-3} range for Poto.c lower*. CND for stable conduit events of the Poto and Paetahi Formations range from 8.31 x 10^{14} to 3.11 x 10^{15} cm^{-3} with CVs between 1.4 to 20.2 %.

VNDs for conduit widening events are relatively high with the exception of Paetahi.f (9.03 x 10^{15} cm^{-3}) which also has the highest CND (3.72 x 10^{15} cm^{-3}) corresponding to the final eruption before Mt. Taranaki entered a period of quiescence. Overall, the VNDs of the eruptive products produced during

conduit widening events ranged from 9.03 x 10^{15} to 1.65 x 10^{16} cm^{-3} with an average of 1.42 x 10^{16} cm^{-3} and VVs ranging from 3.9 to 9.0 %. The CNDs for conduit widening events sit within middle number of standard deviations of the mean of the measured grains which range from 9.45 x 10^{14} to 3.72 x 10^{15} cm^{-3} with CVs also ranging from 9.6 to 24.5 %.

For unstable conduit events a wide range of VNDs is observed with values of 1.17 x 10^{16} to 1.64 x 10^{16} cm^{-3} with an average of 1.40 x 10^{16} cm^{-3}, while VVs range from 5.3 to 6.8 %. The CNDs also cover the spectrum of values for all conditions with values of 7.95 x 10^{14} to 2.24 x 10^{15} cm^{-3}. The crystal volumes for Poto.j and Poto.k lower are similar 14.8 and 13.3 %, while Paetahi.e middle* has a much lower CV of 6.2 %. The Paetahi.e middle* eruption occurred towards the end of a period of activity in Mt. Taranaki's evolution prior to a significant period of quiescence.

4.5.3 Relationship to edifice collapse events

The relationship between pumice density and porosity appears to be more strongly influenced by the variability of the conduit system (e.g., stable conduit events; Poto.a, c lower*, d, l lower, l upper*, m, Paetahi.a lower, a middle*, a upper, d and e lower; unstable conduit events; Poto. j, k lower and Paetahi.e middle* and widening conduit events; Poto.e, g, h*, o and Paetahi.f) rather than the collapse and subsequent depressurization, with three of the four post-Pungarehu eruptions being associated with unstable and widening conduits. The regrowth phase between the two collapses is dominated by stable conduit systems reflected in higher connected porosities compared to post-Pungarehu eruptives.

The density data of pumice clasts from the Poto and Paetahi Formations indicates that the variability of the conduit played a critical role in the eruptive processes at Mt. Taranaki. Compared to the collapse events where we see a minor influence on the density of the deposits from the formations there are some changes however, in the 3D bubble analysis of clasts from eruptions directly following a edifice collapse event. Paetahi.e lower shows a large decrease in the VV (3.3 %) following the Pungarehu collapse compared to Paetahi.d (7.1 %), however there is a minor decrease in VV between Poto.a and Poto.c lower* (4.9 % to 4.8 %) following the Ngaere collapse. Although Poto.c lower* shows a significant decrease in VND following the Ngaere collapse (Poto.a 1.53 x 10^{16} cm^{-3}, Poto.c lower* 9.76 x 10^{15} cm^{-}

^{3}), this decrease in VND and minimal decrease in VV indicates an increase in larger bubbles within the pumice clast following the collapse. This is not reflected in Paetahi.e lower following the Pungarehu collapse where there is an increase in VND (Paetahi.d 1.15 x 10^{16} cm^{-3}, Paetahi.e lower 1.29 x 10^{16} cm^{-3}). The decrease in VV and increase in VND following the Pungarehu collapse indicates an increase in the percentage of small bubbles present within the pumices.

4.5.4 Bubble nucleation and growth

Vesicle size distributions (VSD) of the pumices within the Poto and Paetahi Formations record the nucleation and growth phases of bubbles influenced by magma storage within the system and the decompression pathway (Shea et al., 2010). VSDs for the Poto and Paetahi eruptives indicate that the magmatic system underwent a number of processes; single stage nucleation, continuous/accelerating nucleation and growth, multiple stages of nucleation and growth and coalescence (Shea et al., 2010), at different stages throughout the sequence. These different bubble nucleation and growth processes relate to bubble nucleation originating at different depths and magma ascending at different rates through the system as well as stalling at different depths between eruptions. Stalling generates a population of large bubbles (< 0.135 mm^3), indicated by the presence of multiple stages of nucleation and/or coalescence of bubbles within the pumice clasts. Units which indicate single-stage nucleation events represent magma that ascended quickly to the surface with nucleation occurring at a shallow depth (Sparks & Brazier, 1982; Genareau et al., 2013). Some units show one distinct pattern of bubble nucleation and growth, while others display indicators of multiple processes. Within the Poto and Paetahi Formations three textural classes of different nucleation and growth phases are observed in 2D textural data (Figure 4.6). Micro-vesicular clasts are dominated by small bubbles, with little apparent coalescence, while foamy clasts are dominated by a population of large bubbles and thinner bubble walls and more coalescence. Some of the pumices are transitional and display zones of micro vesicular and foamy sections. However, there is no shearing evident within the 2D textures.

Throughout the sequence four units (Poto.a. Poto. e, Poto. k lower and Paetahi. a lower) display only single stage nucleation processes. Poto.a and Paetahi.a lower represent the onset of new stratigraphic

formations from Mt. Taranaki. These single stage nucleation phases are dominated by the smallest population of bubbles and indicate magma moving up throughout the system without stalling. Prior to each of these replenishment events (Shea et al., 2010; Heinrich et al., 2020b) an increase in the population of large bubbles is seen within the pumices (Poto.d, l upper* and Poto.o). An increase in the percentage of large bubbles within Poto.o and Paetahi.f indicates the eruption of stalled magma being cleared out of the system prior to an extended period of quiescence. Thick defined paleosols following these two eruptive events indicate eruptible magma had been removed from the system. A new recharge event triggered the start of a new eruptive formation.

4.5.5 Vesicle size

Vesicles sizes across the Poto and Paetahi Formations range from 2.75 x 10^{-7} to 0.153 mm^3 indicating rapid bubble growth within the upper sections of the conduit system and little to no coalescence recorded suggesting that the magma was not stalled for long periods of time. Average vesicle size distributions of 2.34 x 10^{-6} to 6.59 x 10^{-6} mm^3 are significantly smaller than for compositionally similar volcanoes where mean bubble sizes range for example from 0.04 to 0.8 mm for the Bullot Formation at Mt. Ruapehu (Pardo et al., 2014) and 0.025 to 0.035 mm for the CE79 Vesuvius eruption (Shea et al., 2012). This supports the observations that the Poto and Paetahi pumices are dominated by small bubbles, which contrasts with previous studies (Shea et al., 2010; Lin et al., 2015), where scan resolution would be insufficient to identify bubble sizes down to 2.75 x 10-7 mm^3. These studies removed anything with a pixel size < 5 voxels due to scan errors and relative accuracy of the image (Shea et al., 2010; Lin et al., 2015). The improved scan resolution in this study significantly alters the VND, VV, CND, and CV calculations for the pumices. The percentage of small bubbles present within the pumices of the Poto and Paetahi Formations also leads to a smaller mean bubble size compared to previous work. A resolution similar to previous studies would remove over 75 % of bubbles recorded in this study (all of those less than 5 voxels), and result in inaccuracies.

4.6 Discussion

4.6.1 Subvolcanic plumbing system

Vesicle size distributions of Poto and Paetahi pumices indicate different zones of bubble nucleation and growth at different depths below the volcano. Magma systems below volcanoes can typically be divided into three zones (i.e., Zone 1,2 and 3), which represent different regions of bubble nucleation and growth (Wilson et al., 1980; Sparks & Brazier, 1982; Genareau et al., 2013).

The largest bubbles within the pumice clasts (Figure 4.10a) represent the first stages of bubble nucleation and growth. These occur within zone 1 (Figure 4.10b) where the pressure is typically high enough for volatiles to be completely dissolved within the melt (Wilson et al., 1980) until a change in pressure or supersaturation of the volatiles is reached leading to the onset of bubble nucleation (Sparks & Brazier, 1982; Mangan & Sisson, 2000; Gaonac'h et al., 2005; Genareau et al., 2013). Bubble nucleation within this zone can form over weeks, months, years, or centuries while the magma is stalled within the magmatic system (Sparks & Brazier, 1982). The presence of coalesced bubbles within the pumices indicates that bubble nucleation for this eruption started in zone 1. For the Poto and Paetahi Formations the presence of large, coalesced bubbles which would have been generated within zone 1 is limited to the units Poto.d, h*, l.l, l.u*, o, Paetahi. a.m*, a.u, d, e.m*.

As bubble nucleation increases the magma begins to ascend towards the surface, where the pressure within the system begins to decrease. This allows more volatiles to exsolve out of the magma increasing the proportion of bubbles within the system (Wilson et al., 1980; Sparks & Brazier, 1982; Takeuchi et al., 2005). This change in pressure occurs between zones 1 and 2 and is referred to as the exsolution surface (Wilson et al., 1980). Bubbles growing within zone 2 create connected networks forming permeable gas flow pathways (Takeuchi et al., 2005), with bubbles in this zone forming within minutes to hours (Sparks & Brazier, 1982). As the magma continues to ascend to the surface more bubbles form as nucleation and growth continues. Any bubbles produced within zone 1 continue to grow and coalescence of bubbles begins. Near the top of zone 2 the pressure decreases further fragmenting the

magma into pyroclasts and releases gas as it enters zone 3. The boundary between zone 2 and 3 is regarded as the fragmentation surface (Wilson et al., 1980).

The final zone (zone 3) is the fragmentation zone, which controls if the eruption is effusive or explosive. The final stage of bubble nucleation occurs in this zone and is responsible for the smallest population of bubbles recorded in the pumice clasts (Figures 4.10a and b) (Sparks & Brazier, 1982; Genareau et al., 2013). Vesicle size distribution data for the Poto and Paetahi Formations indicate that zones 2 and 3 were the dominant source for bubble nucleation and growth at Mt. Taranaki (Figures 4.8 and 4.9). All of the studied pumice clasts show a dominance of small to medium sized bubble populations. These populations are indicative of single phase to continuous nucleation occurring within a magmatic system where little to no stalling had occurred. Geochemistry data from younger eruptive events at Mt. Taranaki (Turner et al., 2008b) showed that in some events an influx of mafic melt into the system a few days before the event triggered an eruption (Turner et al., 2008b; Shane et al., 2023). Similar trends have been observed at Mt. Hood and the Soufrière Hills where geochemical analysis has indicated an influx of mafic magma into the system days prior to an eruption (Kent et al., 2010; Didonna et al., 2022). The high proportion of small bubbles within the Poto and Paetahi Formations could indicate that Mt. Taranaki had an influx of mafic magma into the system which triggered an eruption, with bubble nucleation occurring within zones 2 and 3. Within the pumices there are very high CND recorded, predominantly related to high microlite contents within the erupted material.

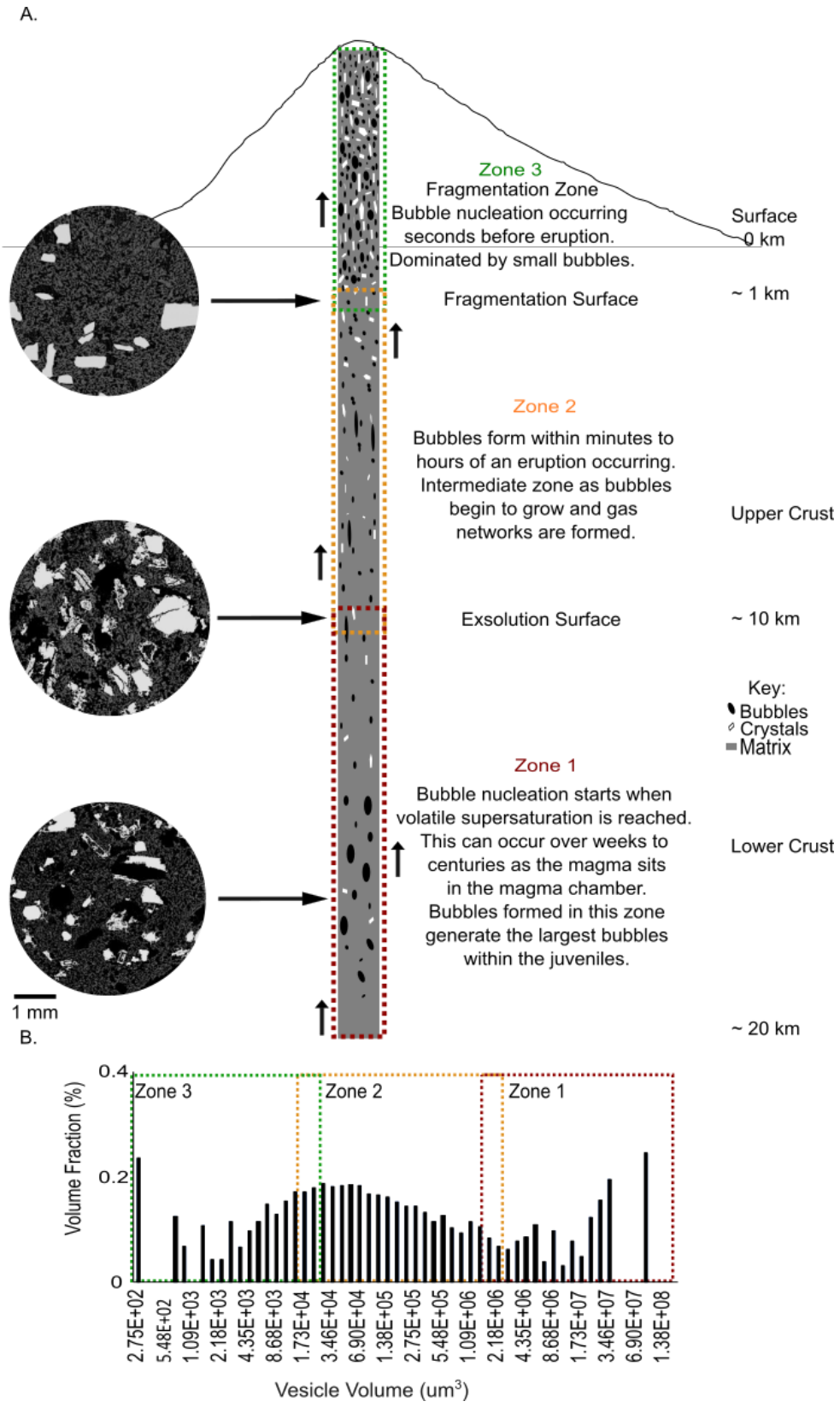


Figure 4.10: a.) Schematic model of the conduit system below Mt. Taranaki showing the different zones where the stages of nucleation occur. b.) Plot showing the distribution of bubble populations in relation to the zones identifies in the conduit diagram VSD of unit Poto.o.

4.6.2 Changes within the Poto and Paetahi Formations

Changes recorded in the vesicle size distributions throughout the sequence reflect periods of recharge and stalling within the magmatic system. Units with a higher level of coalescence indicate that bubble nucleation began in zone 1 while the magma was stalled at depth, before nucleation and growth continued in zone 2 (Wilson et al., 1980; Sparks & Brazier, 1982; Mangan & Sisson, 2000; Gaonac'h et al., 2005; Genareau et al., 2013). At different stages throughout the sequence pumice is dominated by single stage nucleation (e.g., Poto.a, c lower*, e, h*, k lower, m, Paetahi.a lower, a middle* and e middle*) (Figures 4.8 and 4.9; Appendix E) (Shea et al., 2010), indicating an influx of new magma which moved up through the system with no nucleation occurring until it reached zone 2 from where it ascended quickly before volatile supersaturation is reached and volatile exsolution begins, not allowing for coalescence to dominate. These influxes of new magma appear to recharge the system, with not all of the material being erupted in the one event. Magma is then stored (stalled) in a reservoir, leading to differing amounts of bubble nucleation and growth present within subsequent eruptive events. The VSDs indicate that the system goes through recharge phases dominated by single stage nucleation, followed by events showing continuous/multiple nucleation events (e.g., Poto.c lower*, j, l upper*, m, Paetahi.e lower and f) and coalescence (e.g., Poto.d, h*, l lower, l upper*, o, Paetahi.a middle*, a upper, e lower and e middle*) (Figures 4.8 and 4.9; Appendix E) (Shea et al., 2010), providing evidence that the magma stalled within the system. Events following coalescence-dominated units are again dominated by single stage nucleation suggesting there was another recharge of magma into the system.

The final stages of both the Poto and Paetahi Formations (Poto.o and Paetahi.f) were dominated by coalescence, suggesting that bubble nucleation started lower in the system. The explosive events which generated these eruptions systematically cleared the magma reservoir below Mt. Taranaki leading to a period of quiescence in the eruptive record. The start of the Paetahi Formation (Paetahi.a lower) was dominated by single stage nucleation indicating a new influx of magma into the system (Shea et al., 2010). Throughout the multistage Paetahi.a eruption different stages of nucleation and some coalescence are recorded, indicating the potential eruption of some residual magma that had stalled within the system at the end of the Poto Formation. The changes in BSD within the Paetahi.a multi-

phase eruption coincide with changes in eruption column height and eruptive magnitude (Chapter 3). The dominance of coalescence together with low VNDs and high CNDs in Paetahi.f at the end of the Paetahi Formation indicate that the remaining eruptible magma was cleared from the system and not recharged. This signalled the end of this eruptive period at Mt. Taranaki where a period of quiescence was entered until the Kaihouri tephra eruption 600 years later (12.9 – 18.8 ka) (Alloway et al., 1995).

4.6.3 Influence of the collapses on the shallow volcanic plumbing system

The influence of edifice collapse on the shallow volcanic plumbing system and associated depressurisation was investigated through analysing pre- and post-collapse eruptive products of the Poto and Paetahi Formations to determine the impact that sudden depressurisation has on the magmatic system. The VNDs and VVs of post- and pre-collapse pumices were compared to identify changes within the nucleation zones of the volcanic conduit.

The collapse event which produced the 27.3 ka Ngaere debris-avalanche deposit near the start of the Poto Formation removed approximately 5.85 km^3 of material from the upper edifice including a section of the upper conduit, thus depressurising the system in a propagating wave (Figure 4.11). Within post-Ngaere pumice clasts of Poto.c lower* the VND decreases while the VV remains similar evidenced by lower proportions of small bubbles compared to pre-collapse (Poto.a) (Table 4.1). This indicates that the depressurisation triggered by the collapse caused over pressurization within the system generating a fragmentation front to move down throughout the system. The fragmentation front produced by the Ngaere collapse event led to rapid decompression between zones 2 and 3 (Figure 4.10a) resulting in an explosive eruption. Vesicle size distributions for Poto.c lower* indicate the presence of a foamy magma within the system prior to collapse. This allowed eruptible magma to be present when the decompression event occurred resulting in an eruption (Watt, 2019). Rapid decompression of the shallow magmatic system following an edifice collapse was seen during the 1964 Shiveluch collapse resulting in an explosive plinian eruption (Belousov, 1995).

Mt. Taranaki experienced another major edifice failure only ~2,500 years after the Ngaere event producing the 7.5 km^3 Pungarehu debris-avalanche deposit that buried a large sector of the western ring

plain. Throughout the regrowth period between the two collapse events twenty-two subplinian eruptions occurred covering the eastern and southeastern sectors of the ring pain in ash and lapilli. While the Ngaere collapse had removed a significant portion of the upper edifice leaving a large scar on the eastern side, the Pungarehu event involved a large sector of the edifice from the opposite (western) side of the volcano while Mt. Taranaki was still in the process of rebuilding itself. 3D bubble analysis of pumices from Paetahi.e lower following the Pungarehu indicates that even though this collapse was significantly larger than the Ngaere event, it did not have the same lithostatic depressurisation effect on the subvolcanic plumbing system (as seen in Poto.c lower*). In the post-Pungarehu (Paetahi.e lower) tephra a decrease in VV together with an increase in VND compared to Paetahi.d indicate a higher proportion of smaller bubbles than coalesced ones. The VSD of Paetahi.d shows a higher percentage of bubble coalescence occurring within the system due to the magma stalling for some time before ascending to the surface.

The lack of evidence of depressurisation on the subvolcanic plumbing system following the Pungarehu collapse could be due to several different contributing factors. Bubble nucleation and growth analysis of pumices from Paetahi.e lower indicate that continuous/accelerated nucleation occurred within the system during magma ascent (Shea et al., 2010; Shea et al., 2012). The observed small percentage of coalescence suggests that the magma had not stalled in the system for a long period of time, indicating that at the time of the Pungarehu collapse there may not have been enough eruptible magma within the system to result in an eruption. This would eliminate any impact or decompression a collapse-generated propagation fragmentation front could have had on the nucleation and fragmentation zones within the system (Watt, 2019).

However, another hypothesis is that due to the close succession of the two edifice failures, the lithostatic pressure change resulting from the Pungarehu collapse was not large enough to depressurise the system (Pinel & Jaupart, 2005; Watt, 2019; Zemeny et al., 2023). Davidson and De Silva (2000) suggest that stratovolcanoes can grow to a natural maximum height of 2000 – 2500 m before they become unstable. Debris-avalanche deposit volumes as a measure of collapse sizes indicate that Mt. Taranaki would have been of a similar height to the present-day edifice (2518 m) prior to the 27.3 ka Ngaere collapse. The

5.85 km^3 collapse dramatically altered the morphology of Mt. Taranaki removing a large volume of the upper edifice and conduit system potentially shifting the vent location to the southeast within the collapse scar (Figure 4.11). Although Mt. Taranaki went through a regrowth period between the Ngaere and Pungarehu collapse events, it is unlikely that the edifice completely rebuilt itself to previous heights of 2000-2500 m during this short period of time, i.e. over ~2,500 years. Instead, it is more feasible to assume that the Pungarehu event predominantly involved failure of the remaining (western) sector of the pre-Ngaere edifice. Thus, since the main controlling factor for lithostatic pressure is height, the Pungarehu collapse did not impact the subvolcanic plumbing system despite its large volume of at least 7.5 km^3. This is because the upper edifice had already been removed during the 5.85 km^3 Ngaere collapse (and had not regrown to pre-Ngaere heights (Figure 4.11). Therefore, while the post-Ngaere Poto.c lower* tephra exhibits features that indicate depressurisation from collapse-induced lithostatic changes impacting the shallow volcanic plumbing system, these are absent in the post-Pungarehu Paetahi.e lower tephra.

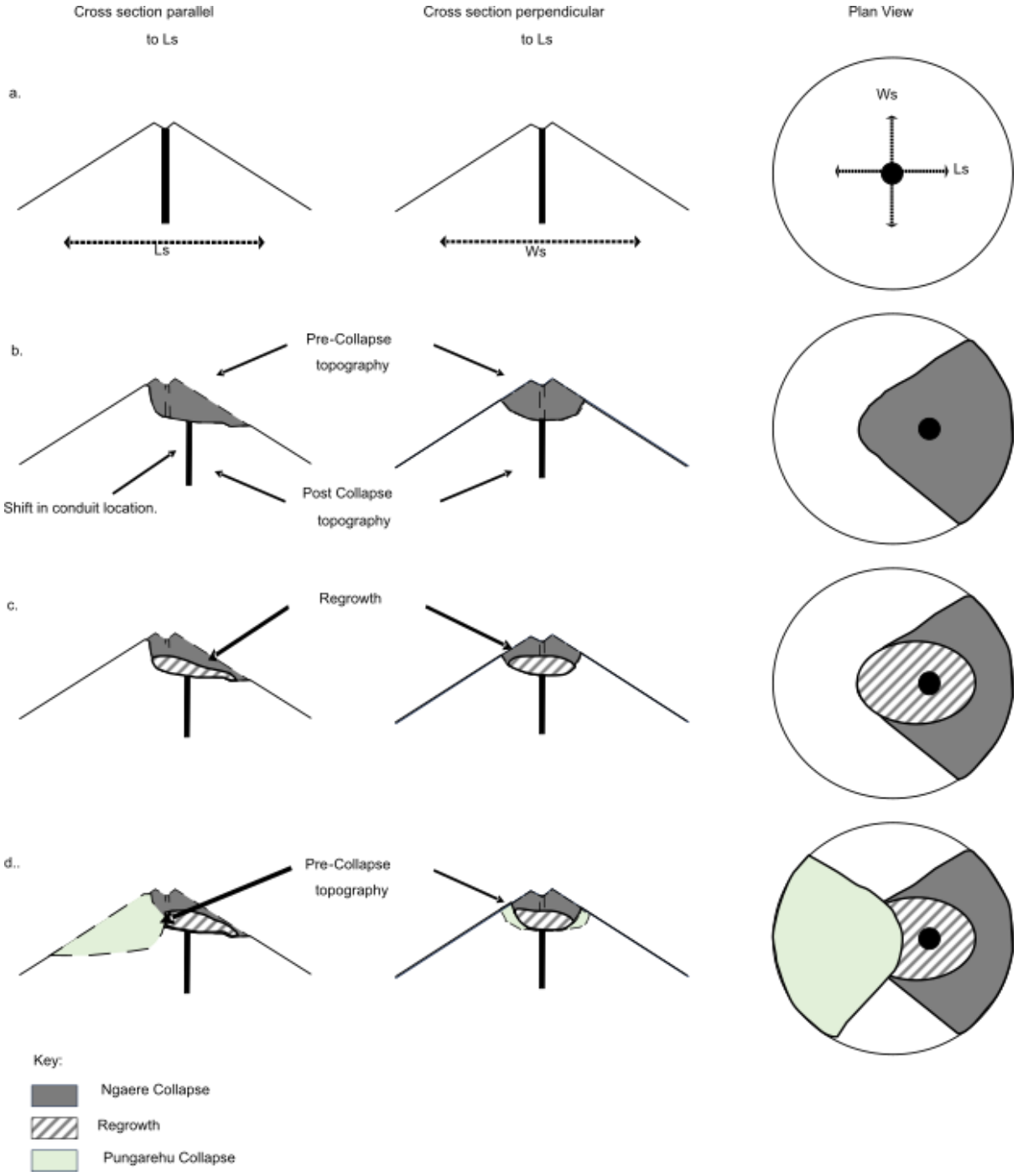


Figure 4.11: Schematic model of Mt. Taranaki edifice morphologies during the Poto and Paetahi Formations. a) Mt. Taranaki at the start of the Poto Formation prior to the 27.3 ka Ngaere collapse to the East. b) post-Ngaere Mt. Taranaki edifice showing shift in conduit location within the Ngaere scar. c) Edifice regrowth reflected in the twenty-two eruptive events of the Poto and Paetahi Formations prior to the Pungarehu collapse. d). Mt. Taranaki

edifice following the 24.8 ka Pungarehu edifice collapse to the West. Cross section and plan view configuration from (Bernard et al., 2021).

4.7 Conclusion

The 3D textural data of pumice clasts produced during the eruptions of the Poto and Paetahi Formations help to better understand the influence that edifice collapses have on the magmatic system below. Over a ~4 ka period twenty-eight subplinian eruptions occurred at Mt. Taranaki which encompassed two large edifice collapse events. The Ngaere edifice collapse at 27.3 ka mobilised 5.85 km^3 of material from the upper edifice, removing the upper conduit generating magmatic overpressure producing a fragmentation front which moved down through the magma. The resulting impact on the fragmentation zone within the shallow volcanic system is recorded within the VNDs of Poto.c lower*. The change seen in the magmatic system is not repeated following the 24.8 ka 7.5 km^3 Pungarehu collapse. This is due to the close succession in which these two collapse events, occurred which did not allow the edifice to completely rebuild itself and experience the same impact on the conduit and fragmentation front as seen post-Ngaere. The response of the shallow volcanic plumbing system to collapse is relative to the impact on the upper conduit system and change in magmatic overpressure producing a fragmentation front. The pumice clast data from the Poto and Paetahi Formations show that zones 2 and 3 are the main drivers of bubble nucleation and growth, with only a small percentage of bubble nucleation occurring within zone 1. During this eruptive period at Mt. Taranaki the magmatic system went through cycles of recharge and storage as indicated by the stages of nucleation and growth recorded in the vesicle size distributions. The final stages of each formation contained more bubble coalescence signalling that the magma had stalled for some time before erupting, which emptied the system causing Mt. Taranaki to enter a period of quiescence. Thick well defined paleosol deposits following the Poto.o and Paetahi.f eruptions indicate a long period of quiescence marking the boundary between eruptive periods. The start of both formations is characterised by a single stage nucleation event where small to medium sized bubble populations dominated indicating a recharge of magma into the system which ascended to the surface quickly.

5 Investigating the influence of edifice collapse on the geochemical and mineralogical composition of magma in the subvolcanic plumbing system: A case study of the Poto and Paetahi tephra formations of Taranaki volcano, New Zealand.

Abstract

Globally, many long-lived stratovolcanoes experience cycles of collapse and regrowth. The influence that these cycles may have on the volcanic system and the subsequent eruptive products are recorded in the deposits of the surrounding ring plains. Mt. Taranaki in New Zealand has experienced at least fourteen major edifice failures during its c. 200 kyr eruptive history and provides a unique opportunity to investigate the impact that collapse/decompression events have on the magmatic system. The Poto and Paetahi tephra formations (23.1-27.3 ka) encompass the 27.3 ka (5.85 km^3) Ngaere and the 24.8 ka (7.5 km^3) Pungarehu debris-avalanche deposits. Geochemical data shows a more primitive composition of pumices produced during the Poto Formation which become more evolved throughout the regrowth phase of Mt. Taranaki into the Paetahi Formation. Textures within pyroxene and plagioclase crystals indicate that there were multiple stages of magma influx into the system, leading to resorption and regrowth zones within crystal rims. Rim to melt equilibrium tests for pyroxene crystals show that only nine of the tephras comprise pyroxene crystals in equilibrium with the surrounding melt. The crystals in equilibrium show temperature ranges between 1024 to 1137 °C and water contents of 1.7 to 6.9 %, indicating that these are hot magmas moving from depth. Crystal textures reveal that magma ascended quickly, within a couple of days, before triggering the eruptions. The geochemical data from the Poto and Paetahi Formations show that there were multiple stages of magma recharge into the system prior to the final magma influx triggering the eruption. The crystal textures indicate the speed at which the magma within the system ascends following the final influx providing vital information for future eruption scenarios at Mt. Taranaki.

5.1 Introduction

Mt. Taranaki (Taranaki Mounga) is a high-K andesitic volcano on the western side of the North Island of New Zealand, which is associated with the subduction of the Pacific Plate underneath the Australian Plate along the Hikurangi Margin. The volcano has been active for at least 200,000 years (Zernack et al., 2011) and produced an array of basaltic, basaltic-andesite and andesite compositions over its eruptive history (Price et al., 1992; Stewart et al., 1996; Platz et al., 2007; Turner et al., 2008b; Zernack et al., 2012a; D'Mello et al., 2021; D'Mello et al., 2023). Magmatic systems in subduction zones are primarily believed to be related to the partial melting of the mantle wedge increasing the influx of volatiles into the system (Nicholls & Ringwood, 1973; Hawkesworth et al., 1979; Arculus & Powell, 1986; Tatsumi et al., 1986; McCulloch & Gamble, 1991; Zellmer et al., 2015; Zemeny et al., 2023). However, there is evidence that a small amount of this mantle derived material reaches the surface without being significantly modified. Magmas derived from the mantle are typically thought to interact with deep crustal hot zones (Hildreth & Moorbath, 1988; Price et al., 2005; Annen et al., 2006; Reubi & Blundy, 2009; Price et al., 2016) as the magmas migrate up to the surface. Variable degrees of crystal fractionization may take place at depth (Dungan et al., 2001; Price et al., 2005; Eichelberger et al., 2006; Price et al., 2012; Price et al., 2016).

Crystal rim chemistry within juvenile material provides information on the storage processes of magma within the reservoir (Agostini et al., 2013; Allan et al., 2013). The textures of the crystal cores and melts record the history of growth reflecting the storage of magma within the system and can indicate the injection of compositionally distinct magma (Sparks et al., 1977; Ubide & Kamber, 2018). Models for understanding the magmatic plumbing system have been used to explain the complexities within the crystal cargo of the magma (e.g., Lormand et al., 2021). The presence of different crystal textures indicates changes occurring during crystal growth within these systems. Resorption and overgrowth zones in the plagioclase crystals show the occurrence of magma mixing with multiple stages of magma influx into the system over time (e.g., Lormand et al., 2021; Shane et al., 2023).

A better understanding of the effects of edifice failure on the magmatic system can be obtained from investigating chemical variations over short and long timescales (i.e., individual events, different formations) recorded within the erupted material (Newhall, 1979; Gill, 1981). Unloading of the system through edifice collapse events decreases the pressure on the upper magmatic system (Pinel & Jaupart, 2005; Gudmundsson, 2012; Pinel & Albino, 2013). This depressurization can trigger an eruption if eruptible magma is present within the system (Watt, 2019). As the edifice regrows the load on the upper crust increases again, impacting the stress field and magmatic processes within the shallow crustal magmatic zone as the ascending melts become more directed beneath the edifice (e.g., Pinel & Jaupart, 2000; Muller et al., 2001; Pinel & Jaupart, 2003; Pinel & Jaupart, 2005; Karlstrom et al., 2010; Pinel et al., 2010; Gudmundsson, 2012). Previous studies on the evolution of magmatic systems throughout a

collapse and regrowth cycle (Belousov et al., 1999; Capra & Macías, 2002; Galipp et al., 2006; Carracedo et al., 2007; Longpré et al., 2009; Manconi et al., 2009; Petrone et al., 2009; Boulesteix et al., 2012; Hildner et al., 2012; Samaniego et al., 2012; Gorbach et al., 2013; Vezzoli et al., 2014; M. Cassidy et al., 2015; Day et al., 2015; Tost & Cronin, 2016; Karstens et al., 2019; Watt, 2019; Watt et al., 2020; Zemeny et al., 2023) show that there are variations in the response to edifice collapse events between volcanic centres and within the same system. Understanding the changes that can occur is import as they can influence subsequent eruption styles and magma ascent rates (Williams & McBirney, 1979; Cas & Wright, 1987; Neri et al., 1998; Papale et al., 1998).

Sector collapse at stratovolcanoes can impact the magmatic system resulting in more mafic compositions following collapse. Throughout the regrowth period following collapse the system becomes more evolved. The re-establishment of the magmatic system can take thousands of years. Does a short timeframe between collapse events play a role in the response that a collapse has on a system or will a collapse trigger a shift in composition. To test this hypothesis pumice clasts from the Poto and Paetahi Formations were used to investigate potential geochemical changes before and after edifice collapse events. The aim was to assess how the depressurization of the edifice failures that generated the Ngaere and Pungarehu debris-avalanche deposits (DADs) modified the composition of the Poto and Paetahi Formations of Mt. Taranaki (Chapter 3), and to explore the crystal textures within individual eruptive units to understand the processes that were occurring in the subvolcanic plumbing system.

5.2 Geological setting of the Taranaki Peninsula

The Taranaki Peninsula is part of the Taranaki Basin that formed as a result of extension during the breakup of Gondwanaland during the lower Eocene – upper Oligocene (30- 25 Ma) and is expressed as a ~350 km-long and 120 km-wide basin that is mostly situated offshore underlying the continental shelf to the west of the North Island (Chapter 1; Figure 1.3) (Knox, 1982; King et al., 1992; Thrasher, 1992; King & Thrasher, 1996; Clayton, 2017). During this time, back-arc extension coincided with subduction initiation 400 km to the east at the Hikurangi Trench (Stern & Holt, 1994). To the east the basin is bounded by the reverse Late Paleogene to Neogene Taranaki Fault, which vertically offsets the basement by > 5 km (Thrasher, 1992; Clayton, 2017).

The western edge of deformation along the convergent plate boundary is confined by the Cape Egmont Fault Zone (CEFZ), a 53 km-long 1- to 5 m-high east-facing scarp, which is expressed along the seafloor dividing the Taranaki Basin into two structural regions (King, 1991; King & Thrasher, 1996); a tectonically active mobile belt in the east and a passive stable platform in the west (King, 1991; King & Thrasher, 1996) connected by the Median Tectonic Zone (MTZ) (Kroeger et al., 2013; Coleman, 2018).

The basement geology below Mt. Taranaki comprises early Palaeozoic terranes in the western province, and late Palaeozoic-Mesozoic terranes in the eastern province, separated by the MTZ that is made up of a suite of Carboniferous - Cretaceous arc related igneous rocks (Sutherland, 1999). The upper 6-7 km of crust underneath Mt. Taranaki consists of Cretaceous to Tertiary sedimentary rocks (King & Thrasher, 1996). Below 6-7 km the geology is related to the Median Batholith consisting of plutonic and metamorphic rocks (Wodzicki, 1974; Knox, 1982; Gamble et al., 1994; King & Thrasher, 1996; Mortimer et al., 1997; Sutherland, 1999).

The Taranaki Peninsula is located 150 km west of the Taupō Volcanic Zone, a 300 km-long, 200 km-wide on-land expression of the Tonga-Kermadec Trench (Adams & Ware, 1977; Stewart et al., 1996). Mt. Taranaki lies 400 km west of the Hikurangi Trench where the Pacific Plate is being subducted under the Indo-Australian Plate (Karig, 1970; DeMets et al., 1994; Henrys et al., 2003; Wallace et al., 2004; Reyners et al., 2006; Stern et al., 2006; Nicol et al., 2007; Wallace et al., 2012; Damaschke, 2017; Cronin et al., 2021).

Mt. Taranaki is the youngest volcano in the NNW-SSE trending Taranaki Volcanic Lineament (Adams & Ware, 1977; Neall et al., 1986; Alloway et al., 1995; Higgins, 1996; Stewart et al., 1996; Gaylord et al., 2014), which lies180-250 km above the Wadati-Benioff Zone and sits on 25-35 km thick continental crust (Adams & Ware, 1977; Stern & Davey, 1987; Boddington et al., 2004; Reyners et al., 2006). It is made up of Mt. Taranaki > 200 ka, Pouakai 0.25 Ma, and Kaitake 0.57 Ma on land and the Sugar Loaf Islands 1.75 Ma offshore (Neall, 1979; Neall et al., 1986). Pouakai and Kaitake show different stages of erosion, reflecting the length of time since they became extinct (Neall, 1979). The migration of the Taranaki volcanic lineament from north-north-west to south-south-east, as well as the north to south alignment of Mt. Taranaki's summit vent, satellite cone Panitahi (Fanthams Peak) and lava domes on the lower flanks indicate the location of the current extensional stress field (Neall, 1971; Sherburn & White, 2006).

5.3 Mt. Taranaki Volcanic history

Mt. Taranaki (2518 m) is the second highest stratovolcano in the North Island of New Zealand with the edifice above 1400 m having a volume of ~12 km^3 (Neall et al., 1986; Procter et al., 2009; Zernack et al., 2011; 2012a). The > 150 km^3 ring plain surrounding Mt. Taranaki comprises pyroclastic material, debris-avalanche, lahar, and fluvial deposits (Chapter 1; Figure 1.4) (Neall et al., 1986; Palmer & Neall, 1991; Alloway et al., 2005; Procter et al., 2009; Zernack et al., 2009; Zernack et al., 2011; Zernack, 2021). A more complete eruptive record is preserved in the younger < 30 ka ring plain with at least 272 individual eruptions identified and grouped into formations (Alloway et al., 1995; Turner et al., 2009; Damaschke et al., 2017b; Torres-Orozco et al., 2017a; Torres-Orozco et al., 2017b; Cronin et al., 2021 Chapter 3). Mt. Taranaki is currently in a period of quiescence with the last know eruptive event, the Pyramid episode (c. 1790 CE), emplacing the present-day summit dome (Platz, 2007; Lerner et al.,

2019a). Throughout Mt. Taranaki's eruptive history, it has experienced at least fourteen major and several smaller edifice collapse events (Zernack et al., 2011; Zernack et al., 2012b), which have been followed by periods of regrowth. Between 20-30 ka two of these collapse and regrowth cycles emplaced the Ngaere and Pungarehu DADs and the Poto and Paetahi tephras. These tephra formations record twenty-eight subplinian eruptive events, which produced ~3 km^3 of pyroclastic material (Chapter 3).

The Poto and Paetahi tephras are found across the east to southeastern ring plain (Chapter 3; Figure 3.1) and individual units' range in volume from 0.01 to 0.26 km^3. These events record the influence of edifice collapse on the volcanic system of Mt. Taranaki and subsequent changes in eruptive activity (Chapters 3 and 4). Throughout the eruptive sequence, variations in the proportion of lithics within the tephras indicate changes in conduit conditions (Chapter 3). The Poto and Paetahi eruptive periods were characterized by an increased occurrence of large explosive eruptions at Mt. Taranaki compared to the younger volcanic history (Neall et al., 1986; Alloway et al., 1995; Damaschke et al., 2017b; Torres-Orozco et al., 2017a; Torres-Orozco et al., 2018; Cronin et al., 2021).

5.4 Methodology

5.4.1 Sampling

Pumice clasts from the Poto and Paetahi Formations were selected with the utmost care to avoid as much weathering as possible to allow for an accurate and reliable analysis of the geochemistry for each depositional unit. Sampling was conducted at the Poto and Paetahi reference sections (Chapter 3; Section 3.4) to allow for comparison of material that had been exposed to the same external weathering processes. The selected pumices were prepared for the different geochemical analyses in accordance with the methodologies below.

5.4.2 Electron Microprobe Analysis (EMPA)

Glass, feldspar, and pyroxene major-element compositional data was obtained using the JEOL 8530F Plus field-emission gun electron microprobe at The University of Auckland. Analysis was conducted with a focused (1-15 μm) beam, at 15 kV accelerating voltage and 20 nA beam current. Data was collected using 1 inch round carbon coated epoxy plugs with 1 plug per unit each containing 6-8 grains. The instrument was calibrated for optimized analysis of minerals of interest using a variety of mineral, oxide, and glass standards (Jarosewich et al., 1980). Counting times were 10/5 s peak/background for Na and 30/15 s peak/background for all other elements. Analysis of the pyroxene and plagioclase crystals was focused on crystal rims. Standards used for different analysis were VG-A99, VG-2, VG-568 Rhyolite for glass, labradorite for feldspars and clinopyroxene for pyroxenes.

Using standard calibration of synthetic standard minerals of known compositions, the measured X-ray intensities were ZAF-corrected using various diffracting crystals.

For glass point analysis the following were used: Orthoclase – OR – 1 for Si with TAP crystal, Ti for Ti with LiFL crystal, Anorthite for Al (TAP), Fayalite for Fe (LiFL), Manganosite for Mn (LiFL), Periclase for Mg with TAPL crystal, Anorthite for Ca with PETL, Strontonite for Sr (TAPL), Barite for Ba (PETL), Jadeite for Na (TAPL), Orthoclase-OR-1 for K (PETL), USNM HoPO4 for P (PETL), Barite for S (PETL), Sodalite for Cl (PETL) and CaF2 for F (TAPL).

For Plagioclase analysis the following were used: Orthoclase – OR – 1 for Si (TAP), Ilmenite for Ti (PETL), Anorthite for Al (TAP), Fayalite for Fe (LiFL), Rhodochrosite for Mn (LiFL), Spring Water olivine for Mg (TAPL), Anorthite for Ca (PETL), SrF2 for Sr (TAPL), Barite for Ba (PETL), Albite for Na (TAPL) and KCl for K (PETL).

For Pyroxene analysis the following were used: Orthoclase – OR – 1 for Si (TAP), Ti for Ti (PETL, Augite for Al (TAP), V2O5 for V (LiFL), Cr for Cr (LiFL), Fayalite for Fe (LiFL), Ni olivine for Ni (LiFL), Rhodochrosite for Mn (LiFL), Fo88 olivine for Mg (TAPL), Anorthite for Ca (PETL), Jadeite for Na (TAPL) and Orthoclase – OR – 1 for K (PETL).

5.4.3 X-Ray Fluorescence Analysis (XRF)

Unaltered pumice clasts from each of the Poto and Paetahi units were cleaned in an ultrasonic bath with distilled water and dried in the oven at 110°C for at least two hours. The samples were then powdered in a tungsten carbide ring grinding machine and kept in the oven at 110°C for at least two hours. For major oxide analysis, loss on ignition (LOI) was determined by weighting c. 2 g of powder before and after heating in an oven at c. 900°C for three hours. After heating, c. 0.8 g of the powdered sample was mixed with c. 8.0 g of lithium tetraborate: lithium metaborate (12:22) flux mixture, followed by fusion to produce a glass disc using a XRFuse2 electric fusion apparatus.

Major element concentrations were measured with a 1 kW Bruker Tiger S8 Series II WD-XRF spectrometer at Massey University in Palmerston North, New Zealand. Interference-corrected spectra intensities were converted to oxide concentrations using calibration curves consisting of natural standards. Long-term reproducibility of the instrument was assessed using the basaltic Oreas 24c and granodioritic Oreas 24b standard reference materials. 1σ reproducibility is typically ± 0.5-1% relative for major oxides and better than ± 3% relative for minor oxides, except for P_2O_5 (± 5-10%).

5.4.4 Inductively Coupled Plasma-Mass Spectrometer Analysis (ICP-MS)

Whole-rock minor and trace element compositions was conducted on the same samples analysed for whole-rock geochemistry using the XRF. Minor and trace elements were analysed using an Agilent

7500 Quadrupole ICP-MS equipped with a Resonetics RESOlution M-50-LR Excimer (193 nm) laser ablation system and a Laurin Technic sample cell housed at the University of Otago Centre for Trace Element Analysis. The laser spot diameter was set to 50 μm for all samples, the laser settings were 10 Hz (pulse frequency), 29 kV (voltage) and 140 mJ (energy). The on-sample flux was c. 2.5 J/cm^2. Standards NIST glass SRMs 610 and 612 were used for calibration, drift correction and error analysis. 43Ca was used as the normalizing isotope, with data reduction conducted using the LAtools package (Branson et al., 2019) on Jupyter Notebook. Multiple measurements were undertaken on each sample using fused glass beads. Reproducibility is $2\sigma < 5\%$ for Nd, Y, Ti, K, Sr, Zr, Ba, Ce and La, < 10% for Rb, Th, Nb and Hf, < 15% for Eu, Yb, Gd and V, <20 % for Pb, Sm and Lu and 32% for Cs.

5.5 Results

5.5.1 LOI Weathering of samples

The Poto and Paetahi Formations were deposited across the eastern, southeastern, and southwestern sectors of the Taranaki ring plain and sit within a high weathering environment interbedded with allophanic soil. The whole-rock chemistry of pumices within the deposits indicates that varying degrees of weathering have occurred, reflected in the high LOI numbers ranging from 3.27 to 9.94 wt.%. This weathering has influenced some of the more mobile elements within the pumices. Figure 5.1 illustrates the relationship between LOI and whole-rock major elements. SiO_2, Na_2O, and K_2O show a strong correlation with LOI, where the higher the LOI the lower the concentration of these oxides. Al_2O_3, Fe_2O_3, P_2O_5 and TiO_2 show a slight correlation with LOI, and CaO, MnO and MgO show no correlation with LOI. Because MgO contents are not correlated with LOI, this oxide is here used as a differentiation index for all whole-rock major oxide and trace element discrimination diagrams.

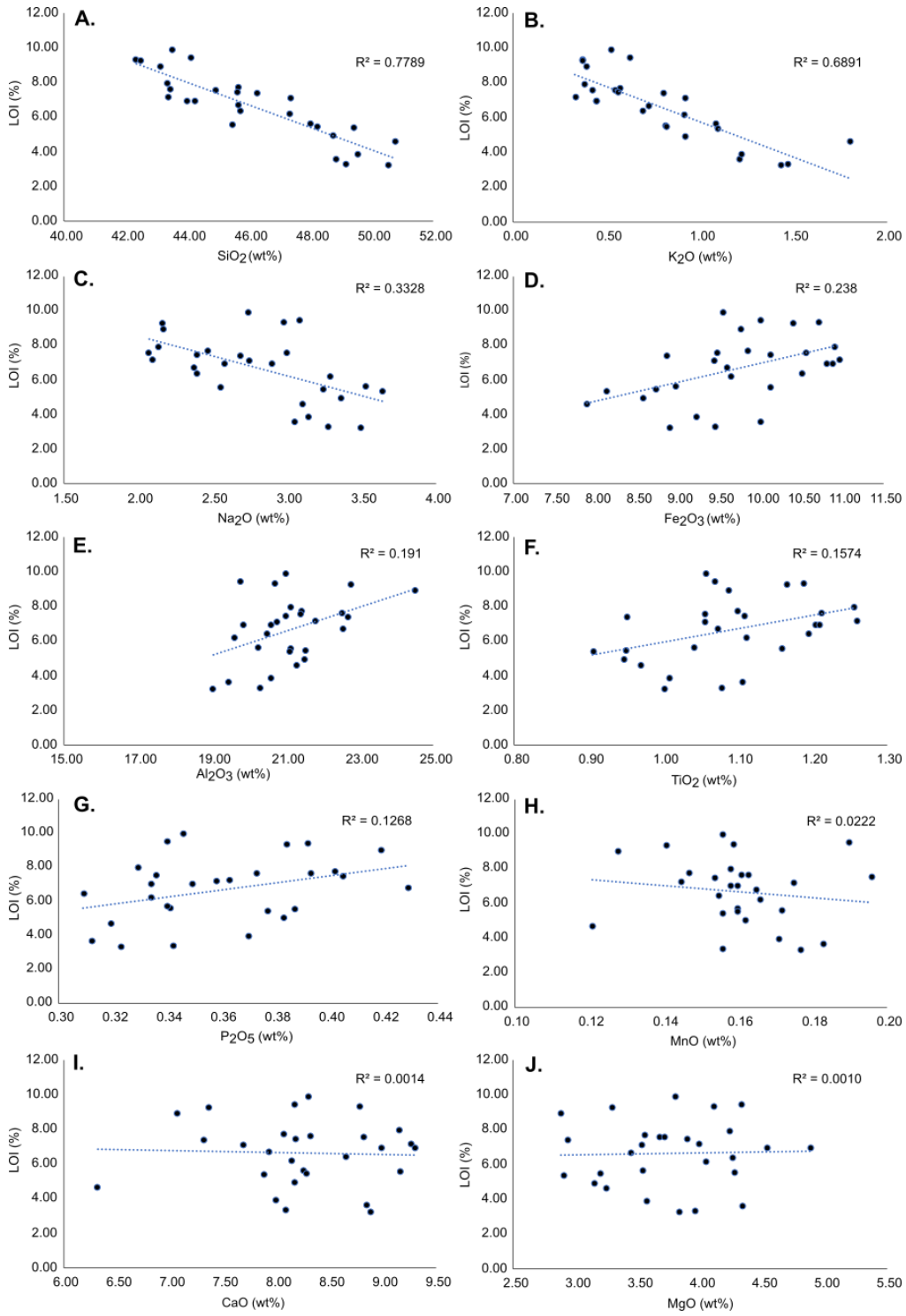


Figure 5.1: Relationship between LOI and whole-rock major element abundance. A - C, show elements that strongly correlate with LOI. D - G show a moderate relationship with LOI. H - J show no relationship with LOI.

5.5.2 Whole-Rock Geochemistry

The Poto and Paetahi tephras have SiO_2 concentrations between 46 wt.% to 53 wt.% and total alkali compositions ($Na_2O + K_2O$) range from 2.6 to 5.1 wt.%. (Table 5.1; Figure 5.2). Within the total alkali vs silica (TAS) classification of Le Maitre (2002) the pumices plot as basalts with one sample plotting as basaltic-andesite and two on the boundary between basalt and basaltic-andesite (Figure 5.2). The TAS diagram for the Poto and Paetahi Formations is affected by the high LOI of the whole-rock samples. Silica and alkali (Na_2O+K_2O) show a strong relationship with LOI; therefore, the plotted data indicate that the terms basaltic to basaltic andesites are unreliable and will not be used again within this thesis.

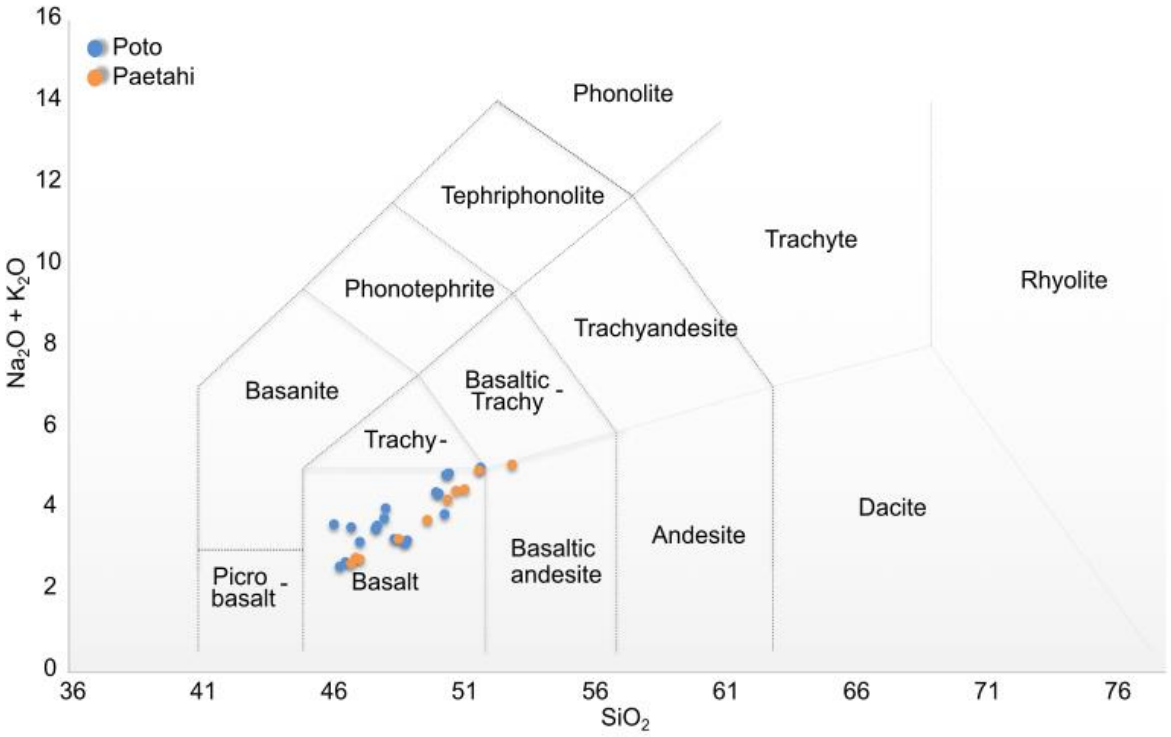


Figure 5.2: Total Alkali ($Na_2O + K_2O$) vs Silica (TAS) classification of the Poto and Paetahi volcanic rocks from whole-rock XRF analysis (after Le Maitre, 2002).

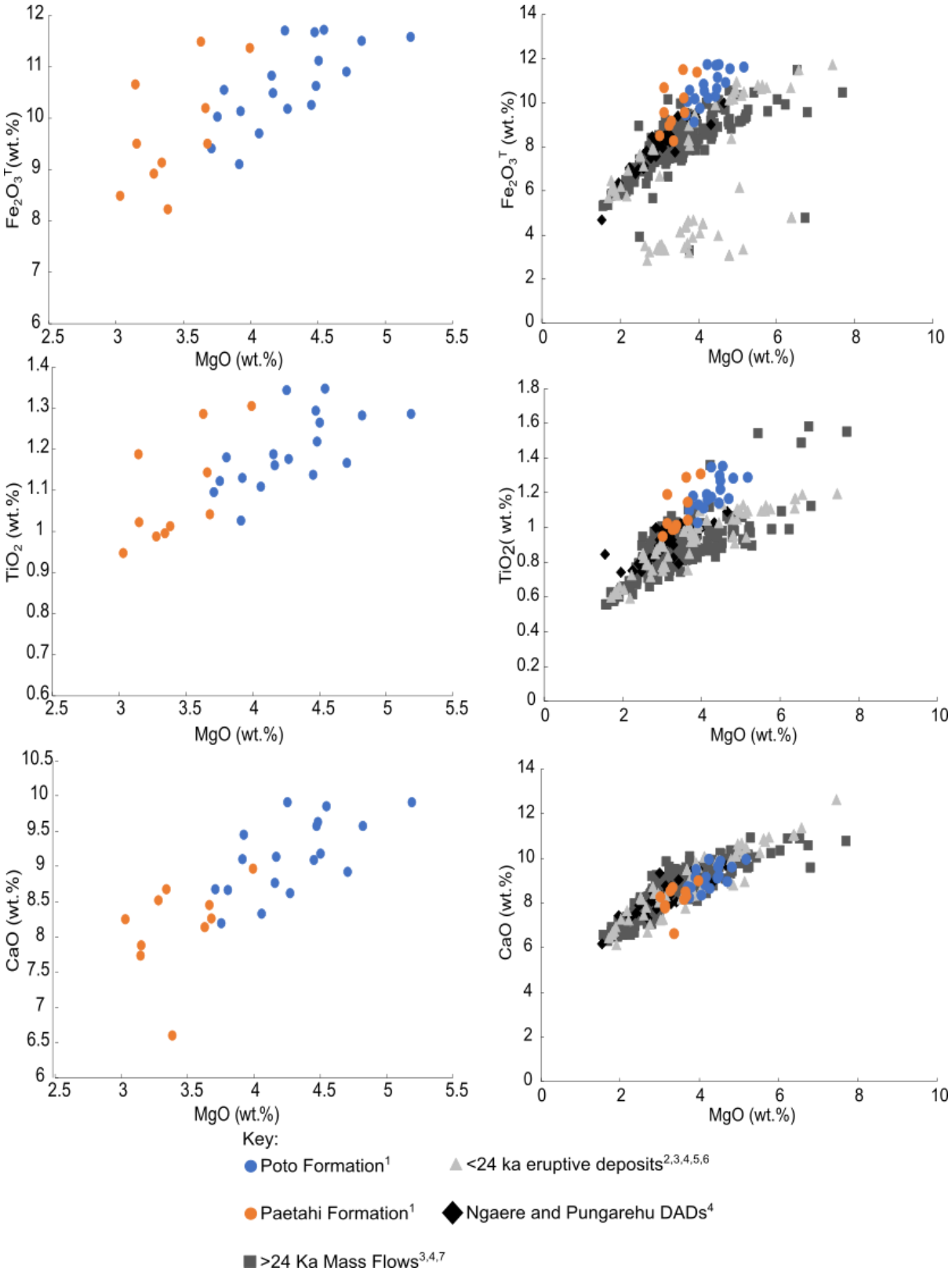
Table 5.1: Whole rock major element compositions (wt. %) of Poto and Paetahi pumice clasts determined by XRF analysis.

Name	SiO_2 (%)	Al_2O_3 (%)	TiO_2 (%)	MnO (%)	Fe_2O_3 (%)	MgO (%)	CaO (%)	Na_2O (%)	K_2O (%)	P_2O_5 (%)	Alkali Na_2O + K_2O	LOI	Total with LOI
Paetahi.f	46.3	22.69	0.95	0.15	8.85	2.93	7.32	2.69	0.80	0.41	3.49	7.43	100.53
Paetahi.e upper	49.58	20.61	1.01	0.17	9.22	3.56	8.00	3.15	1.22	0.37	4.37	3.91	100.80
Paetahi.e middle	50.78	21.31	0.97	0.12	7.89	3.24	6.32	3.11	1.80	0.32	4.91	4.65	100.50
Paetahi.e bottom	43.16	24.52	1.09	0.13	9.76	2.88	7.07	2.17	0.39	0.42	2.56	8.95	100.54
Paetahi.d	42.53	22.78	1.17	0.14	10.40	3.29	7.37	2.17	0.37	0.38	2.54	9.31	99.91
Paetahi.c	43.47	22.53	1.21	0.16	10.55	3.71	8.32	2.08	0.42	0.39	2.50	7.62	100.46
Paetahi.b	45.68	22.57	1.07	0.17	9.59	3.44	7.94	2.38	0.72	0.43	3.10	6.72	100.69
Paetahi.a upper	48.25	21.56	0.95	0.16	8.73	3.19	8.29	3.25	0.82	0.39	4.07	5.50	101.09
Paetahi.a middle	48.77	21.54	0.95	0.16	8.57	3.15	8.17	3.36	0.92	0.38	4.28	4.96	100.94
Paetahi.a bottom	49.44	21.14	0.91	0.16	8.12	2.90	7.89	3.64	1.09	0.38	4.73	5.40	101.05
Poto.o	45.66	21.03	1.11	0.20	10.12	3.89	8.18	2.39	0.56	0.34	2.95	7.49	100.96
Poto.n	47.38	20.77	1.06	0.18	9.43	3.53	7.70	2.75	0.92	0.36	3.67	7.15	101.21
Poto.m	47.37	19.62	1.11	0.17	9.64	4.05	8.15	3.29	0.91	0.33	4.20	6.20	100.83
Poto.l upper	44.02	19.87	1.21	0.16	10.88	4.88	9.31	2.90	0.44	0.35	3.34	6.97	101.00

Poto.l lower	44.29	20.62	1.20	0.16	10.80	4.54	8.99	2.58	0.44	0.33	3.02	6.98	100.93
Poto.k upper	44.15	19.80	1.07	0.19	10.00	4.32	8.18	3.09	0.62	0.34	3.71	9.47	101.24
Poto.k lower	43.53	21.03	1.06	0.16	9.55	3.80	8.31	2.74	0.52	0.35	3.26	9.94	100.98
Poto.j	50.56	19.05	1.00	0.18	8.89	3.83	8.89	3.50	1.43	0.32	4.93	3.27	100.92
Poto.i	44.94	21.41	1.06	0.16	9.48	3.67	8.83	3.00	0.54	0.37	3.54	7.59	101.05
Poto.h	42.36	20.72	1.19	0.16	10.71	4.11	8.89	2.98	0.37	0.39	3.35	9.35	101.11
Poto.g	48.85	19.46	1.11	0.18	10.00	4.34	8.85	3.05	1.21	0.31	4.26	3.63	100.98
Poto.f	48.04	20.26	1.04	0.16	8.97	3.53	8.26	3.53	1.08	0.34	4.61	5.67	100.89
Poto.e	45.74	20.51	1.19	0.16	10.50	4.26	8.66	2.39	0.69	0.31	3.08	6.42	100.84
Poto.d	43.40	21.82	1.26	0.15	10.96	3.99	9.27	2.10	0.33	0.36	2.43	7.19	100.84
Poto.c upper	45.49	21.15	1.16	0.17	10.12	4.28	9.16	2.56	0.81	0.34	3.37	5.58	100.83
Poto.c lower	43.37	21.15	1.26	0.16	10.90	4.23	9.16	2.14	0.38	0.33	2.52	7.96	101.04
Poto.b	49.17	20.32	1.08	0.16	9.45	3.96	8.09	3.28	1.47	0.34	4.75	3.34	100.67
Poto.a	45.69	21.46	1.10	0.15	9.87	3.55	8.08	2.47	0.57	0.40	3.04	7.73	101.03

The variability in whole-rock element abundance within the Poto and Paetahi Formations is best illustrated using MgO variation diagrams (Figure 5.3) with MgO contents ranging between 3 to 5.2 wt.% (Table 5.1; Figure 5.3). The compositions of FeO (8.2 to 11.7 wt.%), CaO (6.6 to 9.9 wt.%) and Al_2O_3 (19.5 to 26.8 wt.%) display a wider distribution, while MnO (0.1 to 0.2 wt.%), TiO_2 (0.9 to 1.3 wt.%) and P_2O_5 (0.3 to 0.5 wt.%) show a narrower spread. Fe_2O_3 and CaO show a strong positive correlation with MgO while MnO and TiO_2 only slightly increase with increasing MgO. In contrast, P_2O_5 and Al_2O_3 contents decrease with decreasing MgO. Major elements generally show a more scattered distribution at lower MgO abundances that becomes narrower towards higher MgO contents. The whole-rock geochemistry of the Paetahi Formation reveals overall lower MgO concentrations indicating a more evolved magmatic composition than the Poto Formation.

The Poto and Paetahi Formations plot within the range of compositions of volcanic deposits from Mt. Taranaki reported by previous studies. However, compared to DAD clasts, lavas, pumice clasts from lahars and < 30 ka tephra (Price et al., 1992; Price et al., 1999; Zernack et al., 2012a; Torres-Orozco et al., 2017a; D'Mello et al., 2023; Zemeny et al., 2023), the studied pumices have higher TiO_2, Al_2O_3, Fe_2O_3 and P_2O_5 concentrations (Table 5.1; Figure 5.3).This relates to the high LOIs of the rocks where these elements show a positive correlation with LOI. On the other hand, CaO and MnO contents fall within the trend observed for all Mt. Taranaki rocks with a positive correlation of CaO and no correlation of MnO with MgO.


Fe2O3T (wt.%)
MgO (wt.%)
TiO2 (wt.%)
TiO2(wt.%)
CaO (wt.%)
Key:
Poto Formation[1]
Paetahi Formation[1]
>24 Ka Mass Flows[3,4,7]
<24 ka eruptive deposits[2,3,4,5,6]
Ngaere and Pungarehu DADs[4]

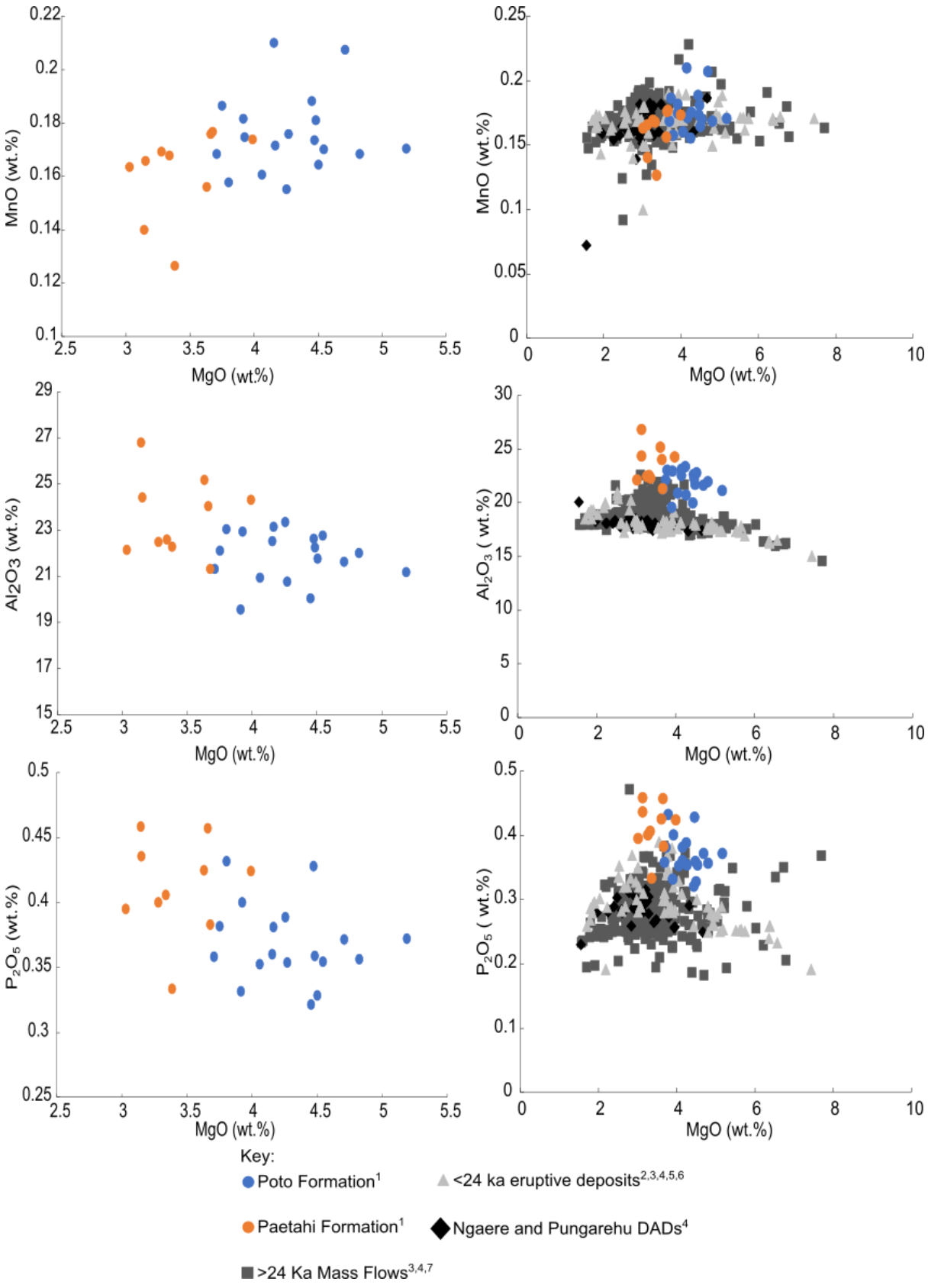


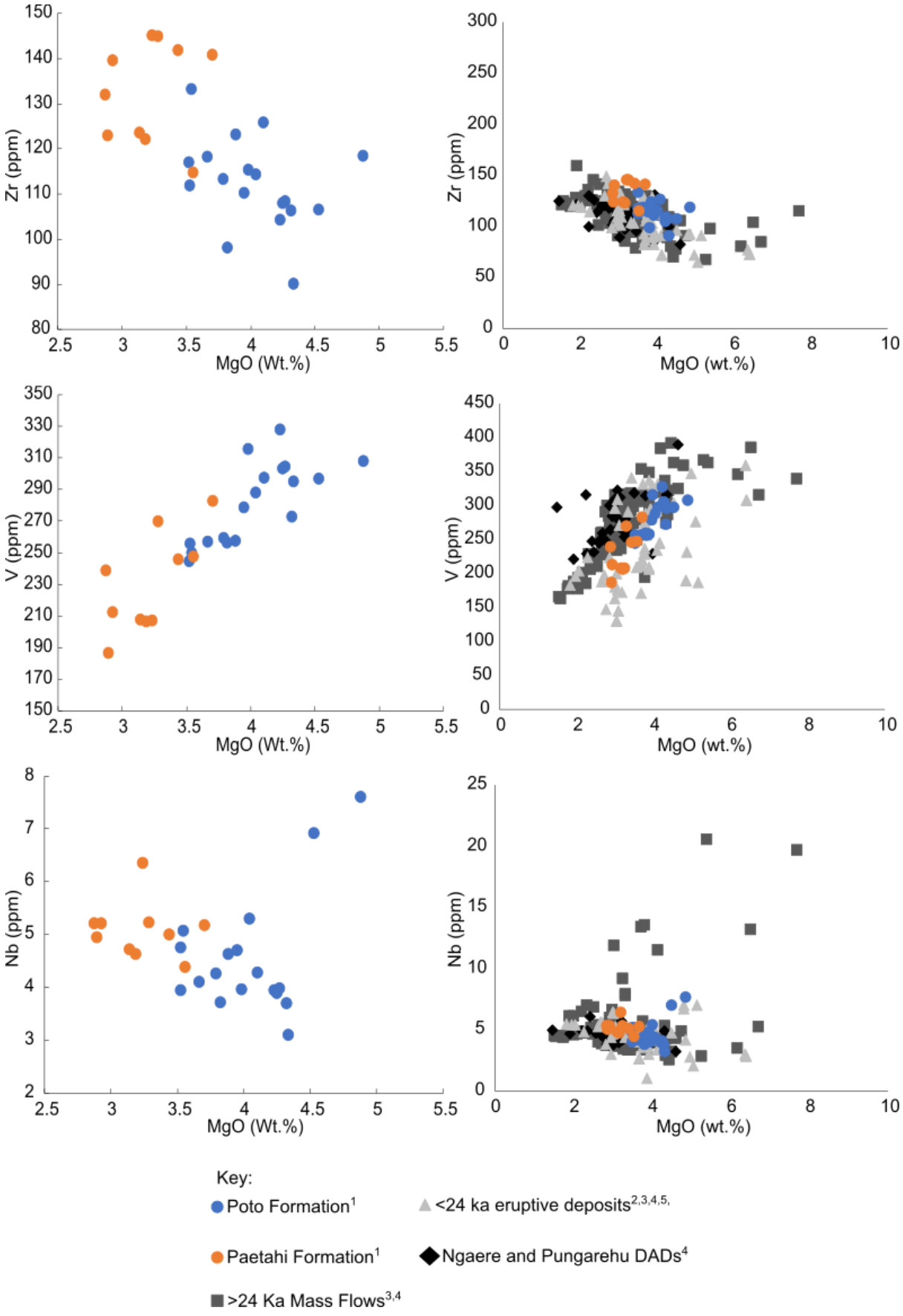
Figure 5.3: Whole-rock major element variation diagrams as a function of MgO abundance for the analysed pumices from the Poto and Paetahi Formations compared to published data from younger and older Taranaki eruptives. Elements P_2O_5, Al_2O_3, Fe_2O_3 and TiO_2 show the relationship that the Poto and Paetahi Formations have with the

high LOI percentages compositions are plotting above previous literature but following the same trends as previous studies ([1.]This study, [2.]Price et al., 1992; [3.]Price et al., 1999; [4.]Zernack et al., 2012a; [5.]Torres-Orozco et al., 2017a; [6.]D'Mello et al., 2023; [7.]Zemeny et al., 2023).

5.5.3 Trace elements

Like the major element XRF results, some minor and trace elements show a correlation with the observed high LOI percentages. The mobile large ion lithophile elements Rb, Ba, and Cs are strongly correlated with LOI and have been excluded from interpretations of the compositional variations of the Poto and Paetahi Formations. Light Rare Earth Elements La and Ce show a moderate correlation but have been included in the trace element diagrams. The elements Zr, V, Sr, and Ni yield a slight correlation with LOI.

On trace element discrimination diagrams using MgO as the differentiation index (Table 5.2; Figure 5.4) Sc and V show a strong positive correlation with MgO compared to a weak and slightly scattered positive trend for Ni. Zr and Sr, and to a lesser extent Nb, decrease with increasing MgO. Previous studies on clast assemblages from DA and lahar deposits along with lava flows show the magmatic evolution of Mt. Taranaki over the past 200 kyr with magmas becoming gradually more evolved over time (Price et al., 1992; Price et al., 1999; Zernack et al., 2012a; D'Mello et al., 2023). The Poto and Paetahi compositions overlap with previous Mt. Taranaki samples suits and overall follow the same trends. However, in comparison the Poto Formation is less evolved than the majority of trace element concentrations derived from debris-avalanche and lahar clasts and lava flows with magmas becoming more evolved throughout the Poto and Paetahi Formation as best displayed in V vs MgO and Sc vs MgO plots (Figure 5.4).


Zr (ppm)
MgO (Wt.%)
MgO (wt.%)
V (ppm)
Nb (ppm)
Key:
Poto Formation[1]
Paetahi Formation[1]
>24 Ka Mass Flows[3,4]
<24 ka eruptive deposits[2,3,4,5,]
Ngaere and Pungarehu DADs[4]

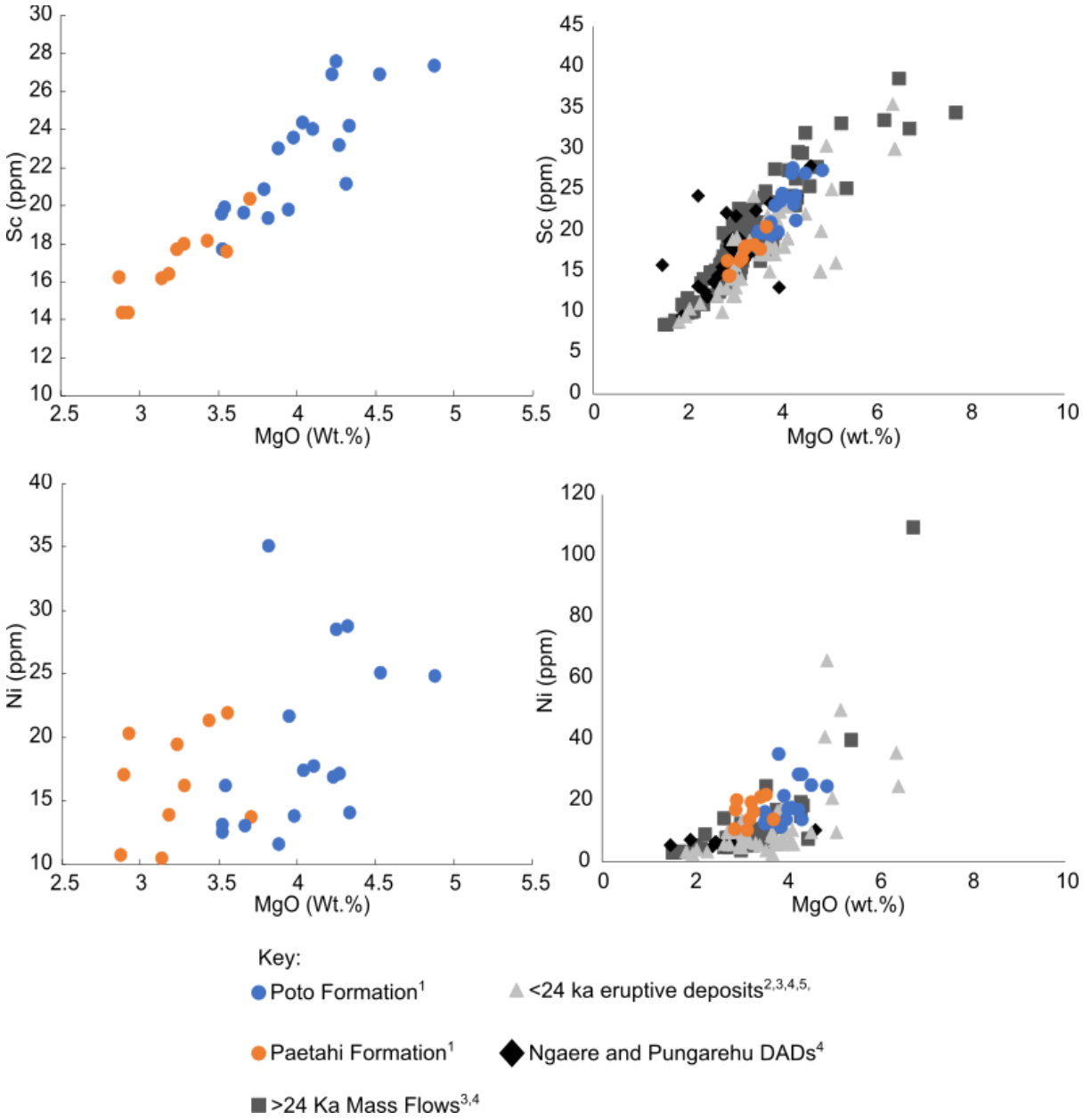


Figure 5.4: Trace element variability (ppm) vs MgO content (wt.%) of the sampled Poto and Paetahi Formations compared to published data for younger and older Mt. Taranaki eruptives. Elements V, Sr and Ni are weakly correlated with the observed high LOI percentages of the Poto and Paetahi Formations ([1.]This study., [2.]Price et al., 1992; [3.]Price et al., 1999; [4.]Zernack et al., 2012a; [5.]D'Mello et al., 2023).

5.5.4 Spider diagrams

Normalized extended trace element diagrams for the Poto and Paetahi Formations and other Mt. Taranaki sample suites studied by Price et al. (1992); Price et al. (1999); Zernack et al. (2012a); D'Mello et al. (2023); Zemeny et al. (2023) (Table 5.2; Figure 5.5) show a strong enrichment in Th, Pb and La

and to lesser extents in Eu and U relative to the normal mid-ocean ridge basalts (N-MORB). Nb and Ce are strongly depleted relative to N-MORB.

Within the N-MORB and chondrite normalized diagrams (Figure 5.5). The patterns of LILE and heavy rare earth elements (HREE) within the N-MORB and chondrite normalized diagrams of the 20-30 ka Poto and Paetahi Formations are very similar to those observed in younger (< 12 ka) Taranaki lavas (Price et al., 1992; Price et al., 1999; D'Mello et al., 2023) and older (< 200 ka) mass flow deposits (Zernack et al., 2012a; Zemeny et al., 2023).

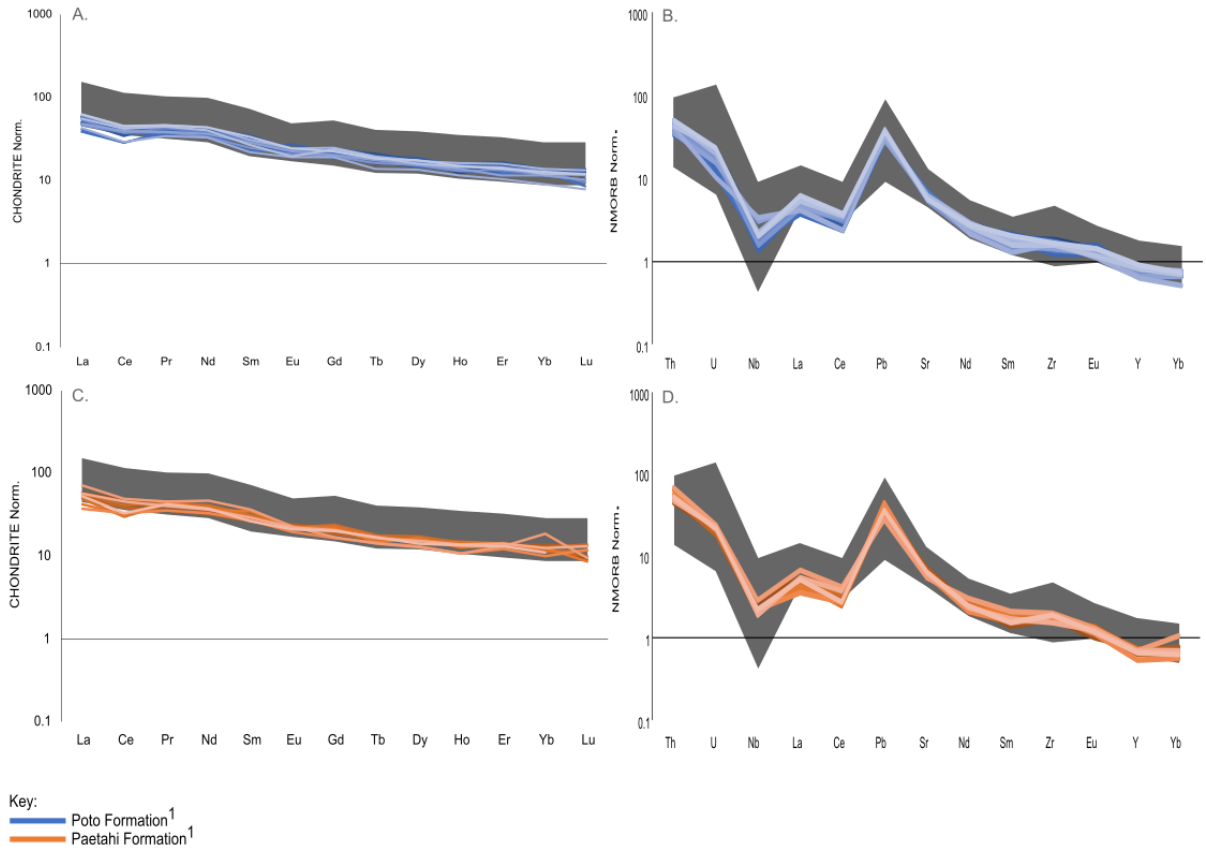


Figure 5.5: Normal mid-ocean ridge basalt (N-MORB) and chondrite normalized rare earth element patterns for: a-b). The Poto Formation, c-d). The Paetahi Formation compared to older and younger Mt. Taranaki eruptives (in grey field) (Price et al., 1992; Price et al., 1999; Zernack et al., 2012a; D'Mello et al., 2023; Zemeny et al., 2023). Normalizing values are from Sun and McDonough (1989). Only elements which do not show strong correlations with LOI (due to weathering) have been plotted.

Table 5.2: Whole-rock trace element composition (averages ppm) of Poto and Paetahi pumice clasts determined by ICPMS analysis.

Name	Cs	Rb	Ba	Th	U	Nb	K	La	Ce	Pb	Sr	Nd	Sm	Zr	Hf	Eu	Ti	Gd	Y	Yb	Lu
Paetahi.f	0.95	16.90	406.11	6.34	1.02	5.20	6339	12.52	20.42	10.93	559.52	17.60	4.08	139.42	4.21	1.23	5450	4.16	18.46	1.89	
Paetahi.e upper	1.44	25.04	598.77	5.68	1.06	4.38	9974	13.48	27.76	10.28	582.87	17.02	4.48	114.48	3.72	1.29	5828	4.25	19.27	2.13	0.33
Paetahi.e middle	1.43	36.98	663.71	7.66	1.19	6.33	14366	16.05	30.78	8.90	490.05	18.18	4.39	144.86	4.62	1.36	5559	4.19	18.79	2.25	0.29
Paetahi.e lower	0.29	5.96	312.54	6.53	1.00	5.20	3139	8.89	20.08	13.31	527.60	15.31	4.19	131.78	3.81	1.14	6271	3.38	15.10	1.72	0.31
Paetahi.d	0.38	5.65	328.14	7.21	1.13	5.21	3005	10.93	18.9	13.41	526.01	18.36	4.6	144.62	4.15	1.33	6769	4.5	18.81	2.02	0.27
Paetahi.c	0.42	7.16	307.47	7.78	0.95	5.15	3333	11.68	18.20	10.94	533.38	18.60	4.69	140.56	4.31	1.43	6882	4.65	20.19	1.95	0.30
Paetahi.b	0.79	14.42	357.22	6.66	0.98	4.99	5739	13.19	25.33	11.52	507.22	19.17	4.84	141.63	4.42	1.28	6142	4.97	20.46	2.16	0.35
Paetahi.a upper	0.83	14.62	4440.9	5.61	0.79	4.61	6572	11.85	24.02	10.41	606.37	16.97	4.28	121.84	3.74	1.13	5428	4.01	18.41	1.97	0.31
Paetahi.a middle	0.90	16.82	517.78	6.03	0.86	4.71	7377	12.62	25.55	11.31	631.69	16.85	4.40	123.35	3.81	1.44	5414	4.56	19.41	2.38	0.33
Paetahi.a lower	1.29	22.02	529.25	5.96	0.85	4.93	8548	13.81	29.47	7.85	609.32	18.04	4.45	122.72	3.21	1.27	5112	4.48	20.11	2.14	0.23
Poto.o	0.88	11.14	382.31	5.96	1.07	4.62	4334	15.01	27.64	10.77	497.44	20.27	5.14	122.89	3.63	1.41	6455	4.66	24.53	2.20	0.31
Poto.n	1.16	18.53	465.24	5.26	1.10	4.74	7476	13.09	25.83	11.68	495.05	18.79	4.09	116.76	3.48	1.14	6067	4.93	22.14	2.05	0.30
Poto.m	1.18	19.52	604.59	5.55	0.96	5.29	7703	14.67	26.75	10.68	556.13	20.55	4.72	114.2	3.05	1.42	6668	5.17	22.65	2.38	0.34

Poto.l upper	0.65	7.65	390.12	4.78	0.49	7.59	3542	10.20	17.94	9.44	559.93	15.36	3.40	118.14	3.67	1.10	7007	3.93	17.00	1.55	0.20
Poto.l lower	0.39	6.26	358.96	4.29	0.73	6.90	3511	11.45	24.46	8.38	535.15	17.06	4.42	106.25	3.17	1.30	6808	4.19	18.58	1.95	0.26
Poto.k upper	1.05	13.18	337.79	4.72	0.83	3.68	4978	11.01	23.43	9.83	478.41	15.65	3.82	106.20	2.91	1.21	6108	4.03	18.59	1.97	0.26
Poto.k lower	0.80	10.61	344.20	5.29	0.83	4.25	4304	12.7	23.00	10.66	523.62	17.9	4.51	113.14	3.49	1.33	6289	4.61	20.13	2.25	0.24
Poto.j	1.84	30.40	637.30	4.36	0.78	3.70	12361	13.64	27.45	9.43	620.38	18.31	4.57	97.94	3.34	1.31	5884	4.25	22.37	2.20	0.30
Poto.i	0.64	8.67	341.63	5.59	0.54	4.09	4277	9.74	17.66	8.58	625.91	16.80	3.50	118.05	3.6	1.35	6065	3.83	18.79	2.22	0.22
Poto.h	0.33	5.31	335.13	5.53	0.66	4.27	2945	9.23	17.49	10.03	558.55	18.03	5.27	125.69	4.05	1.32	7245	4.65	20.36	1.97	0.31
Poto.g	1.27	21.79	554.37	3.99	0.83	3.08	9616	11.19	23.07	9.09	539.28	16.14	4.43	89.89	3.03	1.25	6392	4.44	19.66	1.95	0.26
Poto.f	1.37	20.99	597.25	5.40	0.86	3.94	9193	13.32	25.19	9.61	611.93	17.13	3.45	111.72	2.90	1.58	6101	4.47	19.92	2.22	0.35
Poto.e	0.78	12.01	453.60	5.41	0.93	3.88	5721	11.64	25.95	11.23	514.71	17.75	4.67	107.76	3.41	1.31	7027	4.73	19.69	2.32	0.33
Poto.d	0.30	4.28	331.38	5.55	0.73	3.94	2687	11.86	20.88	10.91	553.13	19.31	5.42	115.25	3.67	1.37	7274	5.16	21.32	2.25	0.31
Poto.c upper	0.72	13.65	509.92	5.12	0.74	3.97	6536	11.42	23.30	9.06	554.75	18.23	4.55	108.23	3.38	1.43	6640	4.57	20.50	2.15	0.32
Poto.c lower	0.08	2.85	446.18	5.06	0.78	3.94	2917	11.61	22.73	10.47	516.09	19.49	4.49	104.10	3.28	1.29	7176	4.87	21.90	2.37	0.31
Poto.b	1.46	26.40	710.70	5.17	1.02	4.68	11900	13.76	26.45	9.45	567.18	18.02	4.63	110.05	3.56	1.39	6281	4.47	19.11	1.97	0.27
Poto.a	0.70	9.56	387.37	6.01	1.10	5.06	4572	14.00	22.09	10.92	532.87	20.53	4.98	133.04	4.35	1.43	6347	4.97	22.46	2.08	0.33

5.5.5 Electron Microprobe glass point analysis

Silica contents of glass within the Poto and Paetahi pumices range from 53 to 64 wt.% (Table 5.3; Figure 5.6). The compositions of Al_2O_3 and CaO show a narrow-confined relationship with SiO_2 compared to FeO, TiO_2, MgO and MnO which show a wide scatter. The elements SiO_2, K_2O, and BaO have a distribution pattern in between these.

The Poto glass analyses display a wider compositional variation than the Paetahi. With increasing SiO_2 the Poto Formation shows a stronger decrease in CaO and overall higher K_2O contents than the Paetahi Formation (Table. 5.3; Figure 5.6), while Na_2O abundances overlap.

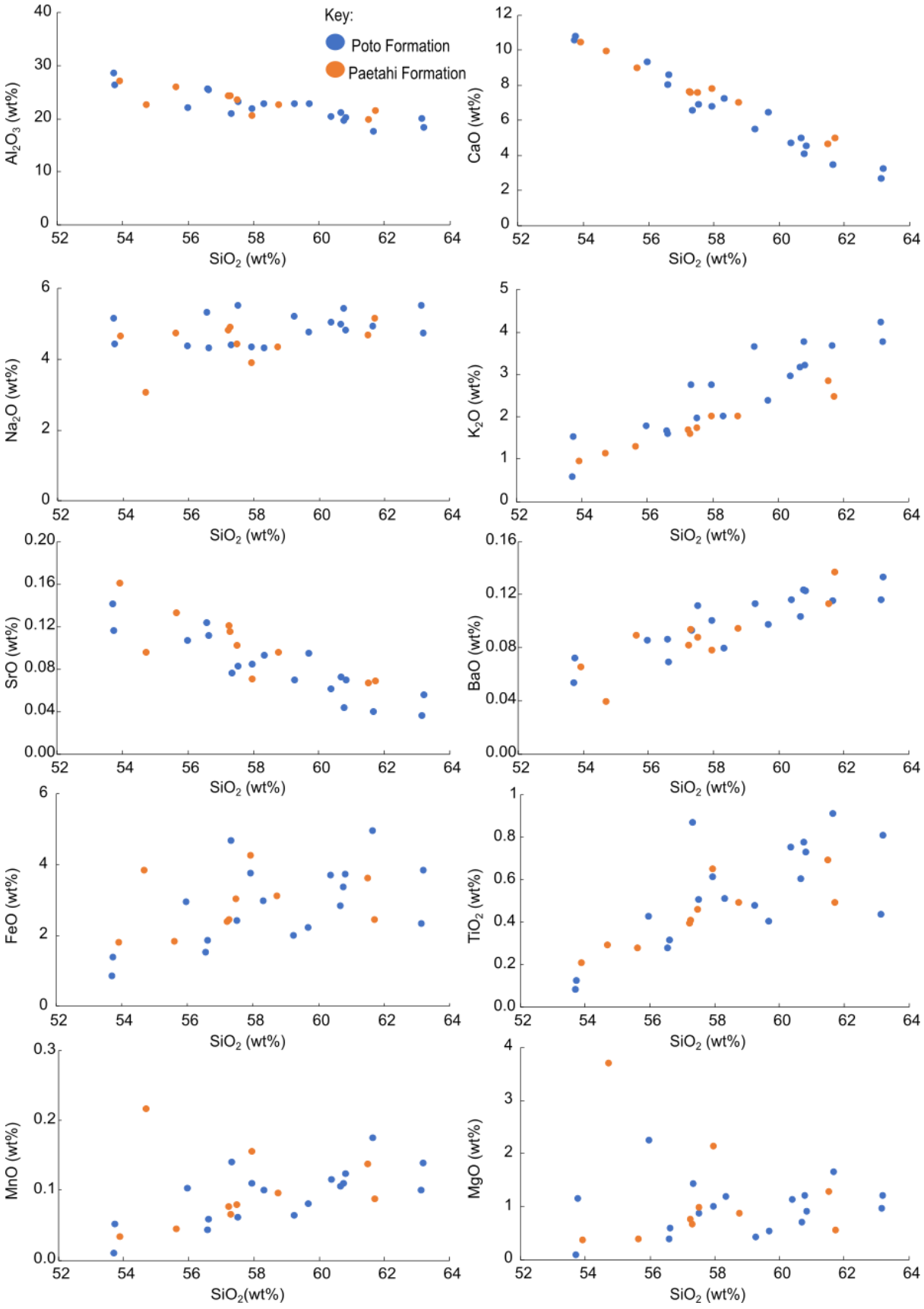


Figure 5.6: Major element variation diagrams as a function of SiO_2 abundance (wt.%) from glass point analysis of Poto and Paetahi pumice clasts.

Table 5.3: Major element glass composition (averages wt.%) of Poto and Paetahi pumice clasts determined by EMPA.

Name	SiO_2	TiO_2	Al_2O_3	FeO	MnO	MgO	CaO	SrO	BaO	Na_2O	K_2O	P_2O_5	SO_3	Cl	F	Total
Paetahi.f	54.09	0.25	24.29	3.35	0.18	3.13	10.55	0.11	0.04	3.21	0.97	0.07	0.00	0.06	0.00	100.29
Paetahi.e upper	56.06	0.28	26.34	1.86	0.04	0.39	9.06	0.13	0.09	4.81	1.31	0.38	0.01	0.06	0.03	100.81
Paetahi.e middle	57.50	0.39	24.65	2.42	0.08	0.76	7.70	0.12	0.08	4.87	1.69	0.20	0.00	0.07	0.02	100.54
Paetahi.e lower	57.37	0.41	24.57	2.47	0.07	0.66	7.64	0.12	0.09	4.92	1.61	0.18	0.01	0.07	0.03	100.19
Paetahi.d	59.68	0.78	21.33	4.82	0.11	0.66	5.13	0.08	0.13	5.14	2.31	0.17	0.01	0.10	0.02	100.42
Paetahi.c	58.04	0.46	23.93	3.09	0.08	0.99	7.67	0.10	0.09	4.50	1.75	0.21	0.01	0.09	0.02	101.02
Paetahi.b	61.25	0.69	19.89	3.61	0.14	1.26	4.68	0.07	0.11	4.69	2.84	0.27	0.02	0.15	0.03	99.64
Paetahi.a upper	57.50	0.66	21.76	3.84	0.12	1.78	7.77	0.09	0.09	4.15	1.87	0.21	0.01	0.09	0.02	99.94
Paetahi.a middle	57.99	0.65	20.70	4.28	0.16	2.14	7.86	0.07	0.08	3.93	2.02	0.21	0.01	0.10	0.01	100.19
Paetahi.a lower	53.39	0.21	27.01	1.80	0.03	0.36	10.35	0.16	0.07	4.62	0.94	0.09	0.01	0.03	0.01	99.06
Poto.o	54.39	0.08	29.04	0.89	0.01	0.09	10.73	0.14	0.05	5.24	0.60	0.01	0.00	0.01	0.00	101.28
Poto.n	58.11	0.51	22.86	2.96	0.10	1.16	7.25	0.09	0.08	4.33	2.01	0.18	0.01	0.10	0.04	99.74
Poto.m	59.35	0.66	21.49	3.36	0.10	1.02	5.43	0.07	0.11	5.13	2.58	0.24	0.01	0.16	0.04	99.69
Poto.l upper	57.23	0.87	21.07	4.69	0.14	1.43	6.56	0.08	0.09	4.43	2.76	0.35	0.01	0.19	0.05	99.88
Poto.l lower	60.94	0.90	17.57	4.92	0.17	1.62	3.43	0.04	0.11	4.89	3.64	0.38	0.02	0.23	0.04	98.85

Poto.k upper	62.97	0.81	18.35	3.84	0.14	1.20	3.22	0.06	0.13	4.73	3.76	0.29	0.01	0.17	0.04	99.67
Poto.k lower	56.85	0.32	25.82	1.88	0.06	0.59	8.69	0.11	0.07	4.38	1.59	0.11	0.01	0.10	0.00	100.55
Poto.j	59.96	0.40	23.10	2.25	0.08	0.54	6.53	0.10	0.10	4.82	2.40	0.16	0.01	0.12	0.03	100.56
Poto.i	64.13	0.44	20.38	2.39	0.10	0.96	2.72	0.04	0.12	5.63	4.32	0.18	0.01	0.12	0.02	101.53
Poto.h	60.65	0.58	21.68	2.76	0.11	0.69	5.33	0.08	0.10	5.01	3.06	0.25	0.01	0.17	0.03	100.46
Poto.g	60.94	0.73	20.39	3.75	0.12	0.90	4.59	0.07	0.12	4.86	3.23	0.34	0.01	0.19	0.06	100.23
Poto.f	55.66	0.26	26.01	1.47	0.04	0.35	8.41	0.13	0.08	5.28	1.51	0.11	0.01	0.08	0.47	99.64
Poto.e	60.91	0.78	19.80	3.40	0.11	1.21	4.12	0.04	0.12	5.47	3.79	0.35	0.01	0.15	0.05	100.26
Poto.d	56.25	0.43	22.44	2.96	0.10	2.25	9.44	0.11	0.09	4.43	1.80	0.16	0.01	0.10	0.03	100.57
Poto.c upper	59.81	0.48	23.07	2.03	0.06	0.43	5.56	0.07	0.12	5.29	3.70	0.20	0.01	0.11	0.06	100.95
Poto.c lower	54.48	0.13	26.89	1.42	0.05	1.16	10.94	0.12	0.07	4.51	1.57	0.03	0.00	0.01	0.00	101.38
Poto.b	57.63	0.51	23.45	2.44	0.06	0.86	6.94	0.08	0.11	5.55	1.98	0.51	0.01	0.07	0.04	100.23
Poto.a	58.09	0.61	22.19	3.76	0.11	0.99	6.84	0.09	0.10	4.38	2.76	0.28	0.00	0.13	0.05	100.34

5.5.6 Thermobarometry/ Hygrometry

Thermobarometry and hygrometry were conducted on pyroxene and plagioclase crystals from each of the Poto and Paetahi units to determine the temperature and water contents of the melt, respectively. For each unit three to ten crystals were analysed along the rim and compared to the average glass point analysis of the groundmass. Using the ($Fe\text{-}Mg^{cpx\text{-}liq}$) equilibrium test (Putirka et al., 1996; Putirka, 2008) across the twenty-eight Poto and Paetahi eruptive events, only fourteen pyroxene crystals from nine units were found to be in equilibrium within the surrounding melt. The units comprising crystals in equilibrium are scattered throughout the sequence (Figure 5.7) with temperatures varying from 1024-1137 °C and H_2O contents ranging between 1.7-6.9 wt.% (Figures 5.7 and 5.8). There does not appear to be a relationship between the temperature of the melt and its calculated H_2O content nor a trend with stratigraphic position of the respective units throughout the Poto and Paetahi Formations. Overall, the Poto Formation contains the units with the highest temperature and the lowest H_2O content while Paetahi.e. middle produced both the lowest temperature and highest water content.

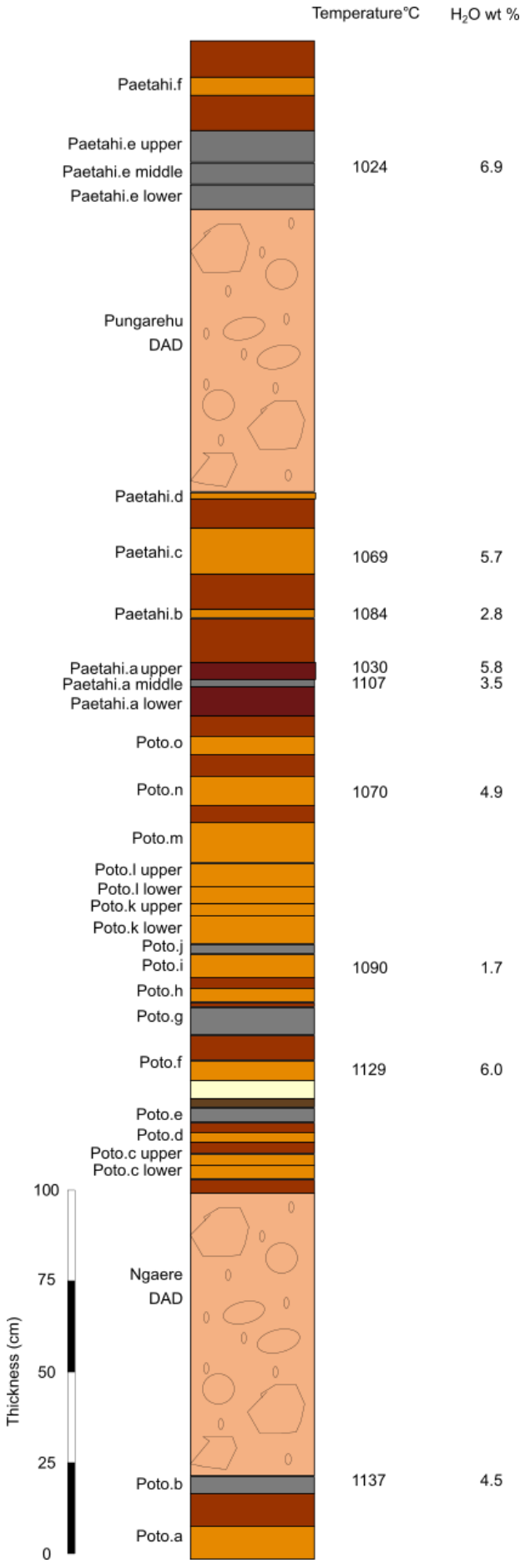

Temperature°C
H2O wt %
Paetahi.f
Paetahi.e upper
Paetahi.e middle
Paetahi.e lower
1024
6.9
Pungarehu
DAD
Paetahi.d
Paetahi.c
1069
5.7
Paetahi.b
1084
2.8
Paetahi.a upper
Paetahi.a middle
Paetahi.a lower
1030
1107
5.8
3.5
Poto.o
Poto.n
1070
4.9
Poto.m
Poto.l upper
Poto.l lower
Poto.k upper
Poto.k lower
Poto.j
Poto.i
Poto.h
Poto.g
1090
1.7
Poto.f
1129
6.0
Poto.e
Poto.d
Poto.c upper
Poto.c lower
Ngaere
DAD
Poto.b
Poto.a
1137
4.5
Thickness (cm)
100
75
50
25
0

Figure 5.7: Stratigraphic column of the Poto and Paetahi Formations with the calculated temperature (in °C) and H_2O content (in wt.%) shown for units that contained crystals in equilibrium.

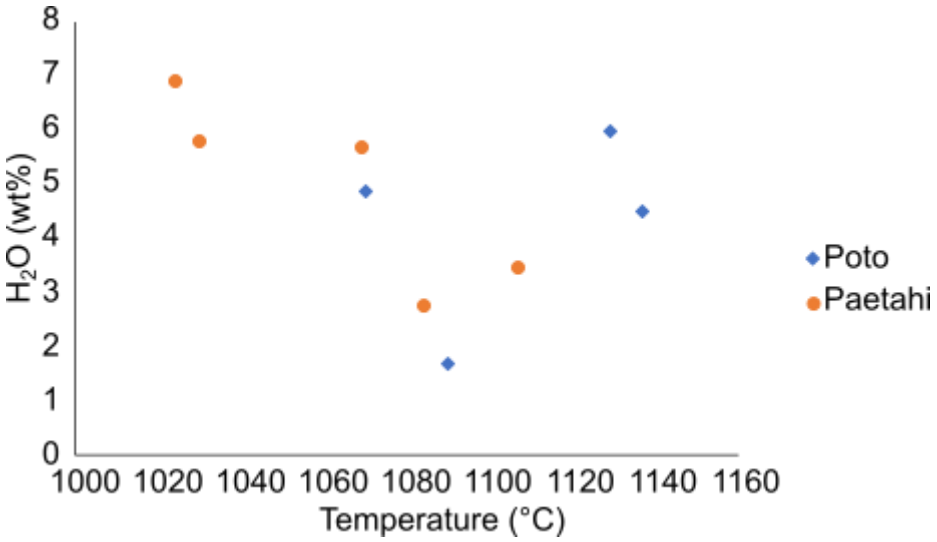


Figure 5.8: Relationship between temperature and H_2O content for the Poto and Paetahi Formations from pyroxene to melt thermobarometry.

Pyroxene and plagioclase crystal rims record multiple episodes of growth and break down stages which have occurred throughout the crystals' life cycles (Figure 5.9). The rims of the crystals show periods of resorption and overgrowth at various stages. Oscillatory zoning rims are visible in both pyroxene and plagioclase crystals.

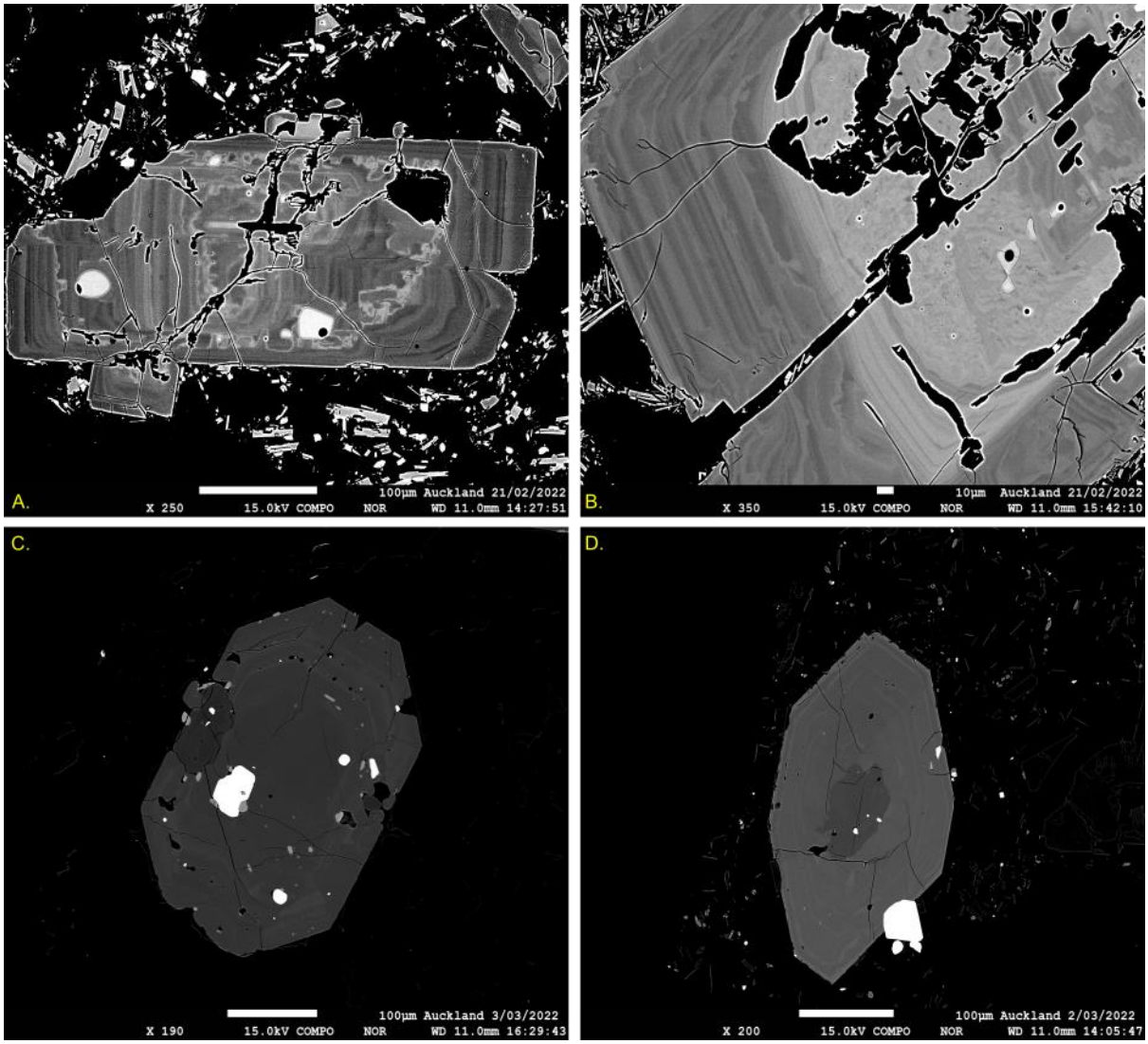


Figure 5.9: Crystal texture of representative examples from the Poto and Paetahi Formations. A-B plagioclase crystals, C-D pyroxene crystals.

5.6 Discussion

5.6.1 Impacts of weathering on the samples

Weathering and alteration are processes that affect all volcanic and nonvolcanic rocks and deposits on the Earth's surface, especially when exposed to sea/river water, hydrothermal systems, and biological organisms (Kerr & Poldervaart, 1955; Wilson, 2004; Cockell, 2011). Older rocks typically exhibit a higher degree of weathering/alteration due to the longer exposure times to the elements. Within volcanic rocks weathering processes can alter their internal textures, and geochemical and mineralogical characteristics (Duzgoren-Aydin et al., 2002). The primary order of weathering for alkali-rich minerals begins with predominantly feldspars, followed by pyroxenes and amphiboles, which results in the loss of sodium and potassium within the volcanic rocks (Regassa et al., 2014).

Loss on ignition (LOI) is used as a tool for assessing the extent of weathering/alteration and the associated impact on the whole-rock geochemistry of volcanic rocks. Sueoka et al. (1985) use LOI parameters as an indicator for understanding the degree of weathering within rocks, distinguishing: a) unweathered (LOI < 2.5 wt.%), b) intermediate (2.5 wt.% < LOI < 8 wt.%), c) weathered (8 wt.% < LOI < 16 wt.%), and d) highly weathered (LOI > 16 wt.%) (Regassa et al., 2014). In addition to an increased LOI, weathering is also indicated by some major elements, i.e. a decrease in sodium and potassium contents as well as silica with leaching occurring during weathering.

When sampling for geochemical analysis the utmost care is taken to choose the freshest clasts to attain the most accurate representation of the original composition of the erupted material while reducing the influence of post-depositional processes. The Poto and Paetahi tephra formations have LOIs ranging from 3.27 to 9.94 wt.%, and the majority (twenty-three units) of fall units show intermediate levels of weathering/alteration (Table 5.1). The observed intermediate LOIs are not unexpected for pumice clasts from primary fall deposits that were emplaced more than 20,000 years ago, especially in an area of high rainfall and soil production. Because of the relationship between LOI, K_2O, Na_2O and SiO_2 (Figure 5.1), these major elements have been disregarded for the interpretation of the Poto and Paetahi whole-rock geochemistry to limit mistaking any affects from post-depositional processes as primary features. Elements that have minor correlations with LOI were included in the differentiation plots although the influence of weathering on the compositions can be seen when comparing the data to the Mt. Taranaki sample suites of Price et al. (1992); Price et al. (1999); Zernack et al. (2012a); Torres-Orozco et al. (2017a); D'Mello et al. (2023); Zemeny et al. (2023). The abundances of TiO_2, Al_2O_3, Fe_2O_3 and P_2O_5 show this relationship and plot at higher values than previously published compositions while following the same trend and positive correlation with MgO. The Poto and Paetahi pumices also show a slight correlation between LOI and the trace element concentrations for Zr, V, Sr and Ni compared to previous work (e.g., Price et al., 1992; Price et al., 1999; Zernack et al., 2012a; D'Mello et al., 2023).

5.6.2 Compositional variation throughout the Poto and Paetahi Formations

The temporal variation in the composition of eruptives at Mt. Taranaki have been well studied using clast assemblages found in secondary volcanic mass-flow deposits, i.e., debris-avalanche and lahar deposits (e.g., Zernack et al., 2012a; Zemeny et al., 2021; Zemeny et al., 2023). This has contributed to understanding the long-term magmatic evolution of the volcano and magmatic processes in the subvolcanic plumbing system (Price et al., 1992; Stewart et al., 1996; Price et al., 1999; Price et al., 2005; Zernack et al., 2012a). Fractional crystallization and partial melting of the lower crust are attributed to Mt. Taranaki's magmatic evolution overtime (Zernack et al., 2012a). Previous studies have also investigated the long-term trends that collapse (unloading), and growth (loading) cycles had on the magmatic evolution of Mt. Taranaki. This long-term record shows significant compositional changes during growth and collapse cycles (e.g., Zernack et al., 2012a; Zemeny et al., 2023). The regrowth phase

of Mt. Taranaki between the Ngaere and Pungarehu edifice collapses was relatively short, occurring over only ~2,500 years. During this time, sixteen Poto and six Paetahi subplinian tephra units were produced with likely many more smaller events and proximal activity not being recorded in the medial to distal ring plain succession that this study focused on. Thus, the primary fall deposits of the Poto and Paetahi Formations provide a unique opportunity to investigate both short- and long-term influences of growth and collapse on the eruptive behaviour of a long-lived stratovolcano within a constrained stratigraphic sequence.

Geochemical variability needs to be accounted for when comparing whole-rock and groundmass datasets since there is a direct correlation between crystal/groundmass proportions and SiO_2 content of the bulk rock. Glass SiO_2 concentrations vary from 53 to 64 wt.% compared to whole-rock SiO_2 contents that vary from 46 to 53 wt.%, although the SiO_2 abundance of the latter is significantly influenced by weathering reflected in the high LOI percentages from the whole rock analysis.

Both bulk rock major and element glass compositions of the studied pumices show that the Paetahi tephras are more evolved than the Poto Formation (Figures 5.3 and 5.4). The whole rock major and trace element analysis of the Poto and Paetahi Formations are comparable with previous studies by Price et al. (1992); Price et al. (1999); Zernack et al. (2012a); Torres-Orozco et al. (2017a); D'Mello et al. (2023); Zemeny et al. (2023), which show a trend of more evolved magma throughout the regrowth of Mt. Taranaki following edifice collapse events. However, the Poto Formation plot within some of the least evolved compositions observed in previous studies on Mt. Taranaki eruptives (Price et al., 1992; Price et al., 1999; Zernack et al., 2012a; Torres-Orozco et al., 2017a; D'Mello et al., 2023; Zemeny et al., 2023). Zemeny et al. (2023) observed a shift to more mafic compositions following edifice collapse events within three older collapse phases at Mt. Taranaki. Throughout the subsequent regrowth phase the magmatic system became more evolved exhibiting a wider distribution of magmatic compositions. This finding is comparable with the Poto and Paetahi Formations with the magmatic composition distribution becoming more evolved throughout the regrowth phase. Similar shifts in the magmatic composition and evolution following edifice collapse have been observed elsewhere e.g., Soufriere Hills, Mt. Pelée, Stromboli, and Parinacota (Hornig-Kjarsgaard, 1993; Zellmer et al., 2003; Hora et al., 2009; Petrone et al., 2009; Cassidy et al., 2012; Vezzoli et al., 2014; Michael Cassidy et al., 2015) where there is a shift towards more mafic compositions directly following the collapse and a gradual magmatic evolution following regrowth.

5.6.3 Magma ascent and crystal processes

Crystal textures within erupted magmas provide an insight into the magmatic processes and history as they grew (Agostini et al., 2013; Allan et al., 2013; Lormand et al., 2021). Changes within the crystals record pressure/temperature differences in the system (Nelson & Montana, 1992; Berlo et al., 2007;

Coote & Shane, 2016); influx of fresh compositionally distinct magma bodies (Sparks et al., 1977; Ubide & Kamber, 2018); degassing rates (Cashman & Blundy, 2000; Giacomoni et al., 2014; Renjith, 2014), and cooling rates of the melt (Mollo et al., 2011b; Mollo et al., 2011a; Pankhurst et al., 2018). These different conditions control the speed at which magma ascends to the surface, impacting the nature of subsequent eruptions and the amount of warning time pre-eruption.

Within the Poto and Paetahi Formations crystal textures show resorption and regrowth rims. Resorption crystal textures indicate magmatic processes such as fluctuations in temperature and pressure (Nelson & Montana, 1992; Cashman & Blundy, 2000), recycling of old crystals (Armienti et al., 2007), and recharge/magma mixing (Agostini et al., 2013; Tost et al., 2016; Shane et al., 2017; Bennett et al., 2019).

Resorption and regrowth zones within plagioclase crystals from younger Mt. Taranaki eruptions (e.g., Shane et al., 2023) suggest multiple stages of melt injection into the system. Resorption and regrowth of crystal rims was observed in all Poto and Paetahi rocks (Figures 5.10 and 5.11), indicating that they underwent a multi-stage process within the magma system prior to the onset of the eruption. However, the lack of crystals in equilibrium with the surrounding melt in the erupted material indicates that the final injection of magma occurred only a few days prior to eruption (e.g., Shane et al., 2023). Crystals from younger Mt. Taranaki eruptives (< 10 Ka) infer multiple episodes of magma influx and storage within the system (Shane et al., 2023). Some of the crystal rim textures indicate continuous rim growths consistent with fractional crystallization of the cooling magma while others recorded the input of a mafic melt just days before the eruption (Shane et al., 2023). Similar textures, indicating fast ascent times following the injection of new magmas into the system, have been observed in plagioclase crystals at Mt. Hood and Soufrière Hills, Montserrat, where magma influx into the system triggered eruptions (Kent et al., 2010; Didonna et al., 2022).

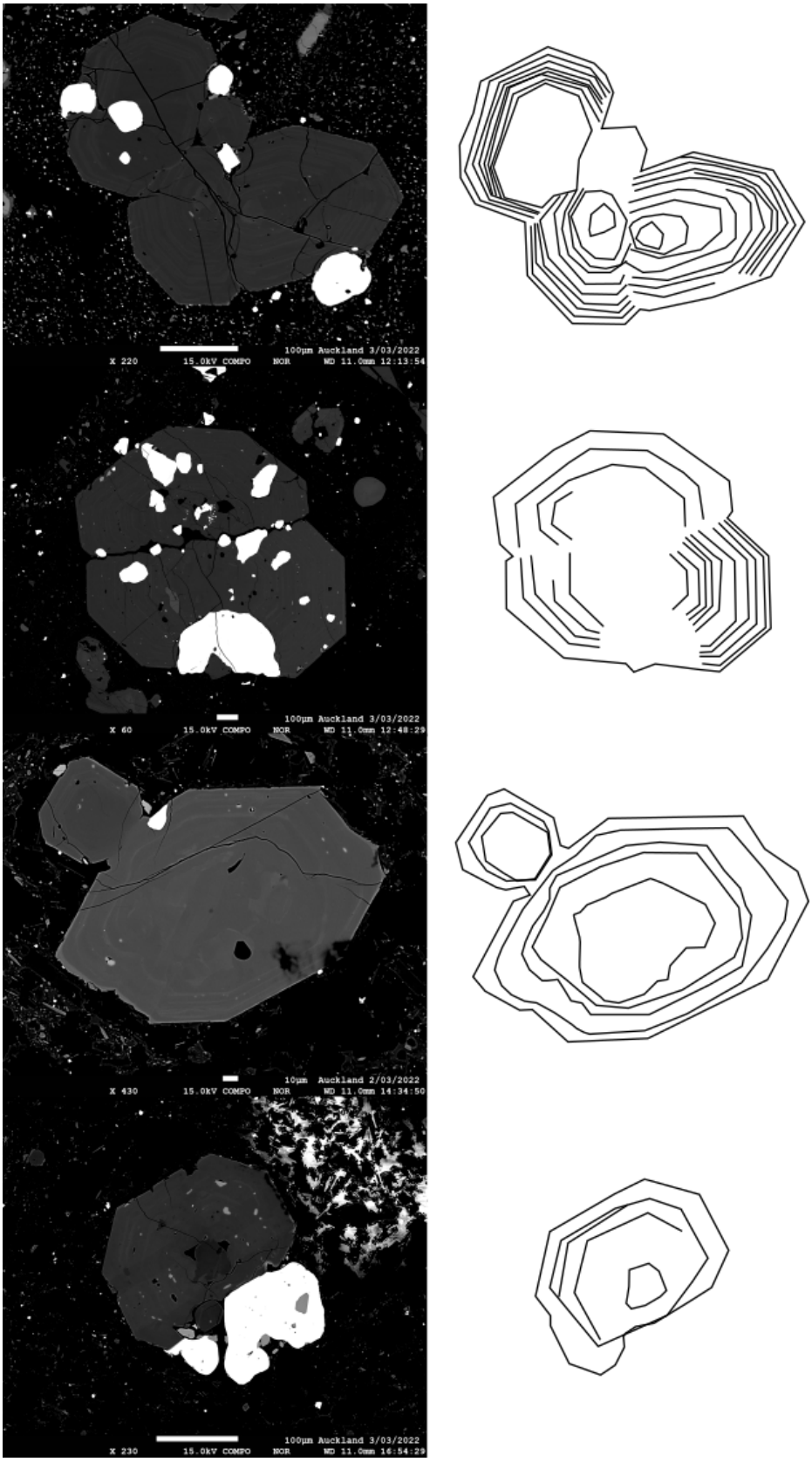


Figure 5.10: Representative BSE images of pyroxene crystals from the Poto and Paetahi Formations showing the resorption and regrowth zones of crystal rims, along with sketches of compositional zones highlighting the growth history of the crystals within the magmatic system.

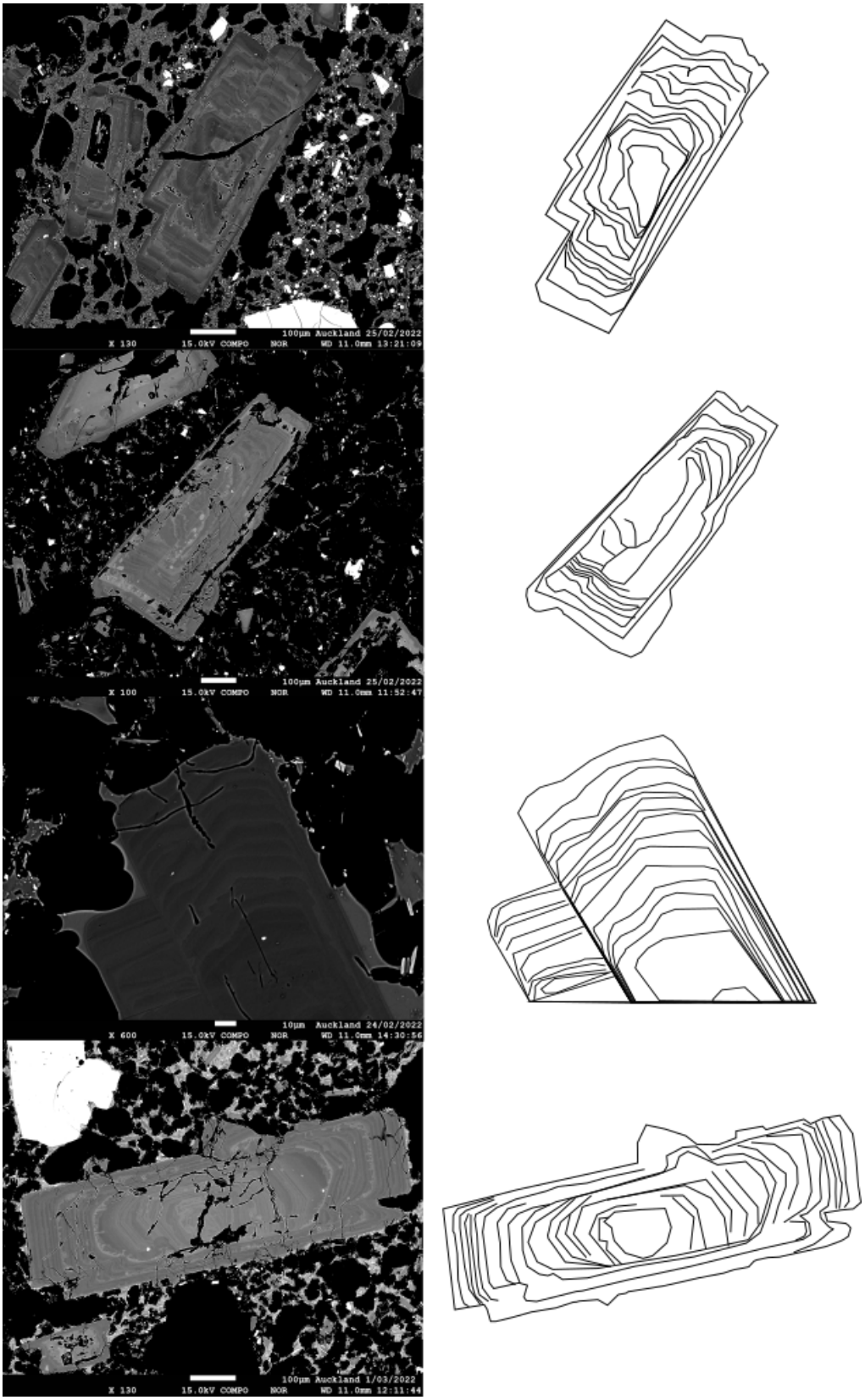


Figure 5.11: Representative BSE images of plagioclase crystals from the Poto and Paetahi Formations showing the resorption and regrowth zones of the crystal rims along with sketches of the rim regrowth to display the growth history of the crystals within the magmatic system.

5.6.4 Melt characteristics and crystallization conditions

Crystallisation conditions within a magmatic system can be calculated using mineral-melt thermobarometers (e.g., Putirka, 2008). Combining compositions of glass with clinopyroxene rims that formed in equilibrium to the surrounding melt provides an indicator for the temperature at which the final stages of crystallization occurred. Clinopyroxene rim-melt equilibrium was calculated using the Putirka (2008) model checking the KD $(Fe\text{-}Mg)^{cpx\text{-}liq}$ exchange which should be 0.27 ± 0.03 to indicate equilibrium. The Poto and Paetahi Formations are dominated by disequilibrium textures, and only nine eruptive events out of twenty-eight show any crystals in equilibrium with the melt. Three to ten clinopyroxene crystals were analysed for each of the eruptive units, and only fourteen crystals within nine units were in equilibrium. This indicates that most crystals were recycled from crystal mush zones and picked up by the ascending melt (c.f., D'Mello et al., 2023).

Putirka's (2008) clinopyroxene rim-melt thermobarometer was used to estimate the melt temperatures, and with the Waters and Lange's (2015) hygrometer to estimate the H_2O content of the melt. Anorthite (An) contents from plagioclase crystals were calculated and used in the Waters and Lange (2015) model along with the temperatures derived from pyroxene crystals from the Putirka (2008) model. Temperatures obtained from clinopyroxene crystals were high, ranging from 1024 to 1137 °C. The Waters and Lange (2015) model produced low to high H_2O contents for Mt. Taranaki pumices, ranging from 1.5 to 6.9 wt.%. Because of the high proportion of clinopyroxene crystals that are in disequilibrium with the melt, the pressure values that were produced were not believed to be reliable.

The temperatures and H_2O contents for the Poto and Paetahi pumices are significantly higher than those of younger lavas (D'Mello et al., 2023), for which clinopyroxene rim-melt temperatures ranged between 970-1000 °C (± 40 °C) and H_2O concentrations varied from 1 – 3 % (± 0.78 wt.%.).

The textural features recorded in Poto and Paetahi plagioclase crystals indicate that they went through multiple stages of resorption and regrowth. This can be associated with magma recharge into the system causing overgrowth of crystal rims present within the crystal mush zone or recycling of old crystals that are within the system (Lormand et al., 2021). The presence of resorption textures within the crystals further supports our thermobarometry results indicating disequilibrium between the crystals and the host melt, which can be attributed to pressure and temperature fluctuations within the system (e.g., Nelson & Montana, 1992; Cashman & Blundy, 2000; Lormand et al., 2021). This is related to the fast ascent of hot deep magmas through the system following a final injection, indicating that magma could be entering the system only days prior to an eruptive episode (c.f., Shane et al., 2023).

5.6.5 Influence of unloading on the volcanic system

A volcanic edifice causes a deviation in the lithostatic stress field of the Earth's crust that impacts the magmatic plumbing system (Pinel & Jaupart, 2005; Watt, 2019). The depth of the stress field is related to the radius of the edifice, with increasing height and mass the lithostatic pressure increases to a maximum three times deeper than the radius of the edifice (Pinel & Jaupart, 2003; Watt, 2019). An edifice collapse event can remove a large height/mass (e.g., Mt. St. Helens, USA, 2.5 km^3 (Siebert, 1984) ; Mt. St. Augustine, Alaska, 0.1-0.5 km^3 (Begét & Kienle, 1992; Siebert et al., 1995) ; Shiveluch Volcano, Russia, 1-2.5 km^3 (Belousov et al., 1999); Mt. Taranaki, New Zealand, 1-7.5 km^3 (Neall, 1979; Alloway et al., 2005; Zernack et al., 2011; Zernack et al., 2012a; Procter et al., 2021; Zernack & Procter, 2021); Volcán de Colima, Mexico, 0.4-35 km^3 (O'Callaghan & Francis, 1986; Luhr & Prestegaard, 1988; Stoopes & Sheridan, 1992; Capra & Macías, 2002; Cortés et al., 2019); and 60-65 ka Chimborazo Ecuador 12 km^3 (Samaniego et al., 2012; Watt, 2019). This changes the lithostatic stress field through rapid decompression which can influence the size, style, frequency, and composition of subsequent eruptive events (Presley et al., 1997; Pinel & Jaupart, 2005; Hora et al., 2009; Manconi et al., 2009; Boudon et al., 2013; M. Cassidy et al., 2015; Zemeny et al., 2023). At some volcanoes, changes in eruptive size and style following edifice collapse have been recorded e.g., Fuego de Colima, Mexico (Robin et al., 1990; Stoopes & Sheridan, 1992; Capra & Macías, 2002) and Stromboli, Italy (Bertagnini & Landi, 1996; Tibaldi, 2001; Petrone et al., 2009; Vezzoli et al., 2014), while compositional changes have been observed e.g., at Mt Pelée, Martinique(Germa et al., 2011; Boudon et al., 2013); at Planchon, Chile (Schindlbeck et al., 2014); Soufrière Hills, Montserrat (Zellmer et al., 2003; Cassidy et al., 2012; Michael Cassidy et al., 2015); Stromboli, Italy (Hornig-Kjarsgaard, 1993; Petrone et al., 2009; Vezzoli et al., 2014); Tungurahua, Ecuador (Hall et al., 1999); and Ritter Island, Papa New Guinea (Johnson, 1987; Day et al., 2015; Karstens et al., 2019; Watt, 2019). Prior to collapse surface load pressure on the magmatic system can inhibit denser mafic magmas from ascending to the surface causing stalling within the upper crust with depressurization from a collapse event promoting a shift towards more mafic compositions as magma can ascend to the surface more freely (Pinel & Jaupart, 2004; Watt, 2019).

At Mt. Taranaki, a previous study by Zemeny et al. (2023) focused on pumice assemblages from lahar deposits at Mt, Taranaki to better understand the geochemical variation of three growth and collapse cycles between 65 – 34 ka. Their data show that throughout the second and third growth periods pumice compositions become broader and more evolved from the early to later stages of edifice regrowth. This was interpreted to reflect reloading through gradual edifice growth reactivating the mid to upper crustal storage system (Zemeny et al., 2023). The here studied primary tephra deposits also show a trend towards a more evolved magma source from the Poto to the Paetahi Formation following the Ngaere collapse reflecting the same processes of magma compositions becoming more evolved due to reloading. Similarly, the widening range of geochemical compositions during edifice regrowth,

indicates the gradual reactivation of the mid to upper crustal system (Figure 5.12). However, the Pungarehu collapse did not generate the same response of the subvolcanic plumbing system as seen for the Ngaere event (Chapter 4), with all Paetahi tephras showing more evolved compositions than the Poto Formation.

The size of the Ngaere and Pungarehu collapse events indicate that the proto-Taranaki edifice would have been of a comparable size to the present-day cone (~2500 m high with a volume of ~20 km^3) (Zemeny et al., 2023) (Figure 5.12). The 27.3 ka 5.85 km^3 Ngaere collapse removed a large section of the fully grown edifice's eastern flank, reducing the height of the volcano and destabilizing the remnant cone (Figure 5.12). Post-collapse eruptive activity indicates the influence of the lithostatic pressure change on the upper magmatic system resulting in eruption of a more primitive composition and a the generation of a fragmentation front down through the magma (Chapter 4). The change in surface load following the Ngaere collapse and potential shift in conduit location to the southeast within the collapse scar deactivated the mid- to upper crustal reservoir (e.g., Watt, 2019; Zemeny et al., 2023) and promoted the ascent of mafic magma to the surface (Figure 5.12). A post-collapse shift in conduit location is common and has been observed at Planchon (Tormey, 2010), Ollagüe and Stromboli (Tibaldi et al., 2008), where the collapse event focused the conduit towards the scar (Tibaldi et al., 2008; Watt, 2019). Subsequent edifice rebuilding increases the surface load on the magmatic system which may lead to the reestablishment of the upper crustal storage system resulting in the eruption of more evolved compositions. This process has been observed at Mt Pelée, Martinique following the 32 ka collapse with evolved compositions reoccurring within ~10 kyr (Boudon et al., 2013) and at Stromboli, Italy where multiple collapse cycles induced a shift to more mafic compositions which gradually evolved throughout the subsequent regrowth phases (Hornig-Kjarsgaard, 1993; Petrone et al., 2009; Vezzoli et al., 2014). Older collapse cycles at Mt. Taranaki have also exhibited the reactivation of the mid- to upper crustal system following collapse (Zemeny et al., 2023), where over a 10 kyr period the reloading has reactivated the reservoir. This cyclic pattern of compositional change following collapse is not seen everywhere with responses varying for each volcano. However, recent studies indicate a commonality in the relationship between surface load and the mid-to upper crustal system in response to edifice growth (Zemeny et al., 2023). This time period allows for the height and surface load to be restored. Different responses can be seen following the Ngaere and Pungarehu collapse events that reflect the relationship between surface load, the natural maximum height of a volcano and the influence on the magmatic system (c.f., Watt, 2019). The Pungarehu debris avalanche was generated by the collapse of a unstable remnant cone to the west ~2,500 years after the Ngaere collapse before the scar had time to refill (Figure 5.12). The uninterrupted gradual magmatic evolution following the Pungarehu collapse indicates that Mt. Taranaki had not regrown enough to generate a surface load large enough to cause depressurization. This contrasts with the hypothesis that there is a connection between higher volume loss and more significant whole-rock geochemistry (Zemeny et al., 2023). This study highlights that the

interaction of these processes is heavily dependent on the original height of the volcano. For this eruptive period in Mt. Taranaki's history the proximity between collapse events (~2,500 years) limited the impact the second (Pungarehu) collapse had on the subvolcanic plumbing system (Figure 5.12). Therefore, the mid- to upper crustal system was not de-activated and the gradual evolution of magmatic compositions continued.

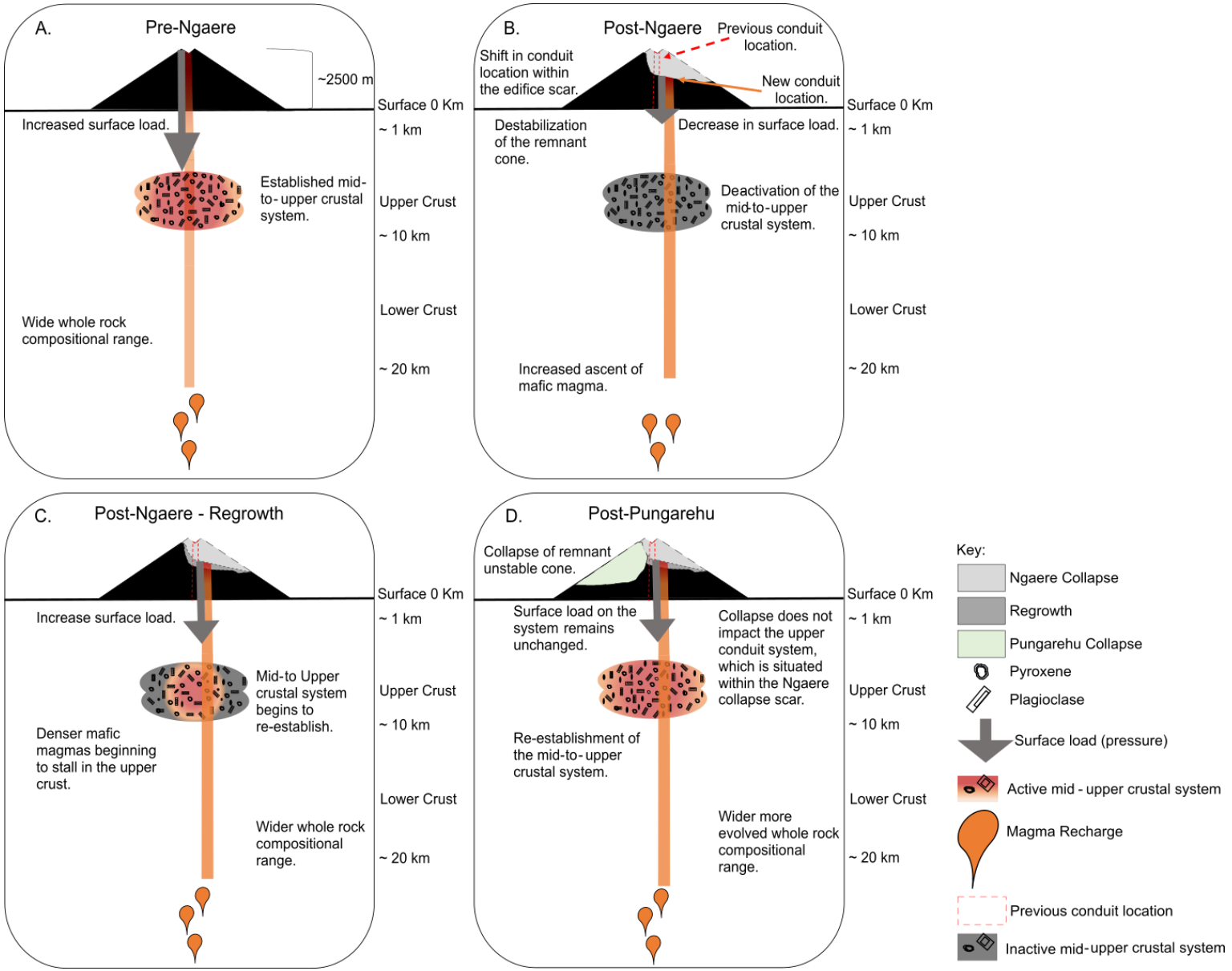

A.
Pre-Ngaere
~2500 m
Increased surface load.
Established mid-to-upper crustal system.
Wide whole rock compositional range.
Surface 0 Km
~ 1 km
Upper Crust
~ 10 km
Lower Crust
~ 20 km
B.
Post-Ngaere
Previous conduit location.
Shift in conduit location within the edifice scar.
New conduit location.
Destabilization of the remnant cone.
Decrease in surface load.
Deactivation of the mid-to-upper crustal system.
Increased ascent of mafic magma.
Surface 0 Km
~ 1 km
Upper Crust
~ 10 km
Lower Crust
~ 20 km
C.
Post-Ngaere - Regrowth
Increase surface load.
Mid-to Upper crustal system begins to re-establish.
Denser mafic magmas beginning to stall in the upper crust.
Wider whole rock compositional range.
Surface 0 Km
~ 1 km
Upper Crust
~ 10 km
Lower Crust
~ 20 km
D.
Post-Pungarehu
Collapse of remnant unstable cone.
Surface load on the system remains unchanged.
Collapse does not impact the upper conduit system, which is situated within the Ngaere collapse scar.
Re-establishment of the mid-to-upper crustal system.
Wider more evolved whole rock compositional range.
Surface 0 Km
~ 1 km
Upper Crust
~ 10 km
Lower Crust
~ 20 km
Key:
Ngaere Collapse
Regrowth
Pungarehu Collapse
Pyroxene
Plagioclase
Surface load (pressure)
Active mid - upper crustal system
Magma Recharge
Previous conduit location
Inactive mid-upper crustal system

Figure 5.12: Schematic illustration of the relationship between surface load and the mid– to upper crustal system below Mt. Taranaki. A. Fully grown edifice pre-Ngaere collapse with an increased surface load on the magmatic system resulting in a well-established mid– to upper crustal plumbing system. B. Post-Ngaere destabilized edifice and deactivated mid– to upper crustal zone prompting the ascent of more mafic magma and a shift of the conduit southeast into the collapse scar. C. Regrowth period begins to increase the surface load on the magmatic system re-activating the mid– to upper crustal system. D. Collapse of the remnant unstable cone to the west, which does not impact the surface load above the magmatic system allowing for magmatic evolution to continue as the mid– to upper crustal system is re-established.

5.7 Conclusions

This study provides insights into the short- and long-term volcanic response to edifice collapse. The presented whole-rock, glass, and mineral compositions for the Poto and Paetahi Formations along with pyroxene and plagioclase crystal textures highlight the complexity of the geochemical changes observed following collapse-induced decompression of the mid– to upper crustal magmatic system. The key findings of geochemical and mineralogical characteristics of pumices produced before and after the two-edifice collapse events that generated the Ngaere and Pungarehu debris-avalanche deposits respectively are as follows:

a) Whole-rock geochemistry data indicate intermediate to strong weathering of pumice samples of the Poto and Paetahi Formations with LOIs ranging from 3.27 to 9.94 wt.%. These high LOI values show correlations with some major elements (K_2O, Na_2O and SiO_2), which were removed from variation plots to avoid interpreting post-depositional processes.
b) Variations in whole-rock major and trace elements reveal that the Paetahi Formation had more evolved magma compositions than the Poto Formations reflecting a reactivation of the mid to upper magmatic system as the volcano was rebuilding itself.
c) Pyroxene and plagioclase crystal textures indicate that multiple stages of magma injection into the system occurred during the Poto and Paetahi eruptive periods, generating resorption and regrowth zones within the crystal rims.
d) Fe-Mg exchange equilibria of pyroxene crystals and their host rock is only present for a small number of crystals in nine eruptive units of the Poto and Paetahi Formations. The lack of crystals in equilibrium with the surrounding melt is related to a final influx of magma into the system triggering the eruptions. The calculated high temperatures (1024 – 1137 °C) and varying water contents (1.7 – 6.9 %) of the crystals are associated with a deep hot magma moving quickly up through the system following this final injection. This indicates that magma could be entering the system and ascending rapidly within only days prior to an eruptive event occurring (e.g., Shane et al., 2023).

e) The edifice collapse that generated the Ngaere DAD had a greater impact on the upper crustal magmatic system than the collapse that generated the Pungarehu DAD causing significant depressurization as reflected in the eruption of less evolved more mafic magmas being erupted post-Ngaere and the relocation of the eruptive conduit. Such a shift in composition is not seen post- Pungarehu with the Paetahi Formation being more evolved than the Poto. This is related to the close succession of the two collapse events that did not provide enough time for the cone to rebuilt. The Pungarehu collapse involved the remnant unstable sector of the edifice on the opposite side to the Ngaere, which did not directly influence the conduit location (Figure 5.12) or the height of the edifice, therefore, not resulting in a depressurization event.

6 Discussion

6.1 Introduction

The majority of stratovolcanoes experience one large edifice collapse event within their lifetime, however, there are global examples of volcanoes that have experienced multiple collapse events e.g., Mt. St. Augustine (Begét & Kienle, 1992; Waitt, 2010; Siebert & Roverato, 2021), Mt. Rainier (Crandell, 1971; K. M. Scott et al., 1995; W. E. Scott et al., 1995; Vallance & Scott, 1997), Colima (Cortés et al., 2010; Roverato et al., 2011; Cortés et al., 2019), Shiveluch (Ponomareva et al., 1998; Belousov et al., 1999), Mt. St. Helens (Hausback & Swanson, 1990; Glicken, 1996; Clynne et al., 2008), Reunion Island (Lénat et al., 1989; Labazuy, 1996), Canary Islands (Holcomb & Searle, 1991; Carracedo, 1994; Masson et al., 2002; Walter & Schmincke, 2002; Hunt et al., 2013; Hunt et al., 2014), Hawaii (Fornari & Campbell, 1987; Moore et al., 1989), Mt. Ruapehu (Tost et al., 2014), and Mt. Taranaki (Procter et al., 2009; Zernack et al., 2011) (Table 6.1).

Table 6.1: Global examples of volcanoes that have experienced multiple collapse cycles throughout their life cycles (data from Zernack & Procter, 2021).

Name	Number of DADs	References
Mt. St. Augustine	12	(Begét & Kienle, 1992; Siebert et al., 1995; Waitt, 2010).
Mt. Rainier	6	(Crandell, 1971; K. M. Scott et al., 1995; W. E. Scott et al., 1995; Vallance & Scott, 1997).
Volcan de Colima	8	(Cortés et al., 2010; Cortés et al., 2019 and references therein).
Shiveluch	8	(Ponomareva et al., 1998; Belousov et al., 1999).
Mt. St. Helens	4	(Hausback & Swanson, 1990; Glicken, 1996; Clynne et al., 2008).
Reunion Island	> 50	(Lénat et al., 1989; Labazuy, 1996; Oehler et al., 2008).
Canary Islands	11	(Carracedo, 1994; Masson et al., 2002; Hunt et al., 2013; Hunt et al., 2014).

Hawaii (Big Island)	9	(Moore et al., 1989; James et al., 1994).
Mt. Ruapehu	10	(Keigler et al., 2011; Tost et al., 2014; Tost & Cronin, 2016).
Mt. Taranaki	16	(Zernack et al., 2009; Zernack et al., 2011; Zernack et al., 2012b; Cronin et al., 2021 and references therein).

Debris-avalanche deposits from collapse events are well recorded within volcanic records around these volcanoes (e.g., Voight, 1981; Crandell et al., 1984; Siebert, 1984; Ui et al., 1986a; Vallance et al., 1995; Glicken, 1996; de Vries et al., 2000; Capra et al., 2002; Waythomas & Wallace, 2002; Concha-Dimas et al., 2005). However, the changes in eruptive behaviour following edifice collapse events are still poorly understood with the majority of volcanic eruptive histories following collapse events being confined to the Holocene period due to older eruptive events being buried under 10s to 100s of meters of volcaniclastics (Siebert et al., 1995; Thouret et al., 1995; Scott et al., 1997; Ponomareva et al., 1998; Belousov et al., 1999; Waythomas, 1999; Waythomas & Miller, 1999; Reid et al., 2001; Ponomareva et al., 2006; Watt, 2019; Zernack, 2021). At long lived volcanoes, pre-Holocene eruptive events record key changes in eruptive conditions following large edifice collapse events (Watt, 2019). Changes to the morphology of a volcanic edifice following a large collapse event can influence the size, style, and frequency of an eruption which can impact the subsequent hazards which occur e.g. post collapse activity at Shiveluch was dominated by repetitive small collapses and an increase in lava domes in response to a higher magmatic viscosity creating a steeper less stable edifice (McBirney & Murase, 1970; Wilson et al., 1980; Lipman & Mullineaux, 1981; Belousov et al., 1999; Alidibirov & Dingwell, 2000; Gorbach et al., 2013; Watt, 2019). Studying the eruptions which bound edifice collapse events provides insights into the short and long-term response of eruptive cycles. Previous studies have examined secondary volcaniclastic deposits between debris-avalanche deposits to understand geochemical processes associated with cone regrowth (e.g., Zemeny et al., 2021; Zemeny et al., 2023). However, tephra directly predating or postdating collapse events can be used to examine the influence an edifice collapse has on the subvolcanic plumbing system, magmatic evolution, and conduit processes. Primary fall deposits are therefore preferred to understand the relationship between collapse events and eruption cycles (Watt,2019).

The Taranaki region within New Zealand has a unique combination of erosion and uplift which has resulted in the preservation of > 200 kyr of volcanic activity from Mt. Taranaki across a > 150 km^3 ring plain (Neall, 1972; Neall, 1979; Neall et al., 1986; Pillans, 1994; Alloway et al., 1995; Zernack et al., 2011). Within this time Mt. Taranaki has experienced at least fourteen major and several minor edifice

collapse events that are preserved across the different sectors of the ring plain. Mt. Taranaki also has a long preserved stratigraphic record of eruptions that provides a better understanding of the evolution of a long-lived stratovolcano (Neall, 1972; Neall, 1979; Neall et al., 1986; Alloway et al., 1995; Procter et al., 2009; Zernack et al., 2009; Zernack et al., 2011; Damaschke et al., 2017b; Torres-Orozco et al., 2017b; D'Mello, 2021). The medial ring plain around Mt. Taranaki provides a record for the past 30-50 kyr of eruptive activity comprising four large debris avalanches including two of the largest to have occurred in Mt. Taranaki's history. The 27.3 ka 5.85 km^3 Ngaere and the 24.8 ka 7.5 km^3 Pungarehu debris-avalanche deposits (Zernack et al., 2011), are encompassed by the Poto and Paetahi tephra Formations with the Ngaere DAD intercalated with twenty-eight primary ash and lapilli fall units across the eastern and southeastern sector of the ring plain (Alloway et al., 1995). This prehistoric record of primary deposits is examined to understand the magmatic response to a large edifice collapse on a short and long-term scale directly following an event and throughout a regrowth phase.

The Poto and Paetahi Formations contains twenty-eight subplinian eruptions across twenty-one eruptive events consisting of single phase and multi-phase eruptive episodes (Chapter 3). These subplinian events had eruption columns which ranged from 10-20 km high with eruptive volumes varying between 0.01 to 0.26 km^3 covering the eastern and southeastern sector of the ring plain in ash and lapilli deposits. Two eruptions occurred prior to the Ngaere edifice collapse event with Poto.b directly underlying the Ngaere debris-avalanche deposit suggesting a Bezymianny (Moriya, 1980; Siebert et al., 1987; Roverato et al., 2021) style trigger event generated this collapse. Changing vent conditions throughout this eruptive period was highlighted through compositional characteristics of the deposits (Chapter 3) and indicates that Mt. Taranaki was experiencing periods of stable, unstable, and widening conduit conditions throughout the generation of the Poto and Paetahi tephra formations. Twenty-two eruptions occurred over ~2.5 kyr between the Ngaere and Pungarehu collapse events while Mt. Taranaki was undergoing a regrowth period.

6.2 Magma storage and supply below Mt. Taranaki

Throughout the Poto and Paetahi Formations ~3 km^3 of magma erupted over ~ 4 kyr with individual events producing between 0.01 to 0.26 km^3 (Chapter 3). The eruptive volumes for the Poto and Paetahi Formations indicate there was a large complex plumbing system present below Mt. Taranaki during this eruptive period capable of producing large subplinian explosive eruptions (Heinrich, 2020). To understand this complex plumbing system, the geochemical and thermobarometry data for all of the eruptive units (Chapter 5) is integrated with the pumice textural data (Chapter 4), vent conditions and eruptive dynamics of the (23.1-27.3 ka) Poto and Paetahi Formations (Chapter 3).

The age of the Poto and Paetahi Formation deposits mean that some weathering of pumice clasts within the individual units has occurred. This has resulted in high LOI percentages that have influenced some

of the whole rock elements (e.g., SiO_2 shows a strong correlation with LOI; Chapter 5 Section 5.5.2). The TAS diagram classifications (Le Maitre, 2002 Figure 6.1) for the Poto and Paetahi Formations are therefore unable to be used. However, MgO does not show a correlation with LOI and provides a good differentiation index for looking at the magmatic evolution throughout the sequence (Figure 6.2). The whole rock geochemical compositions (Figure 6.3) for the Poto and Paetahi Formations indicate that throughout this eruptive period the magmatic system became more evolved overtime with MgO ranging from 3.03 to 5.19 wt.% (Figure 6.3). The Paetahi Formation (MgO 3.03-4.0 wt.%) is more evolved than the Poto Formation (3.71-5.19 wt.%), suggesting Mt. Taranaki become more evolved throughout the regrowth period following the Ngaere edifice collapse event (Chapter 5; Section 5.5.3) (Figure 6.3). Similarities in the geochemical evolution of Mt. Taranaki during the regrowth stage of older edifice collapse cycles was observed by Zemeny et al. (2023). Glass point analysis for the formations indicate SiO_2 compositions range between 53 to 64 wt.% with the Poto Formation having a wider compositional variation than the Paetahi Formation. Comparisons in composition between the whole rock and glass point analysis is related to the crystal proportion present within the sample.

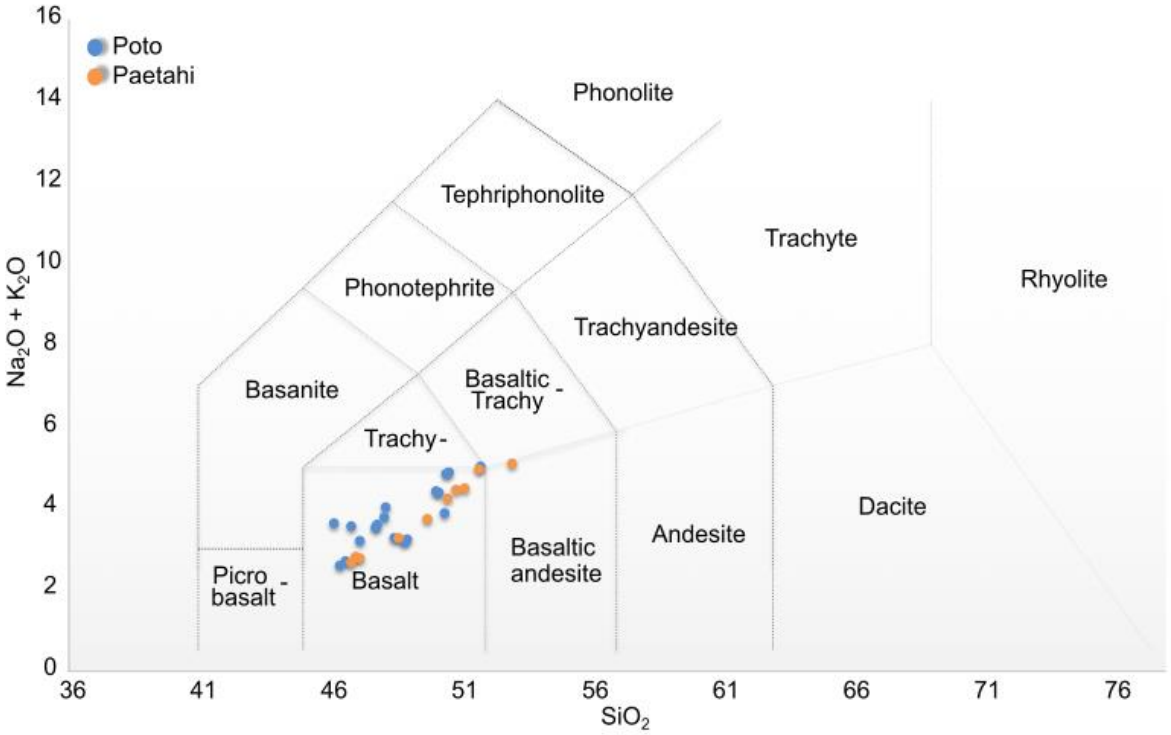


Figure 6.1: Total Alkali ($Na_2O + K_2O$) vs Silica (SiO_2) (TAS) classification (Le Maitre, 2002) showing the compositions of the Poto and Paetahi Formations from whole rock XRF analysis.

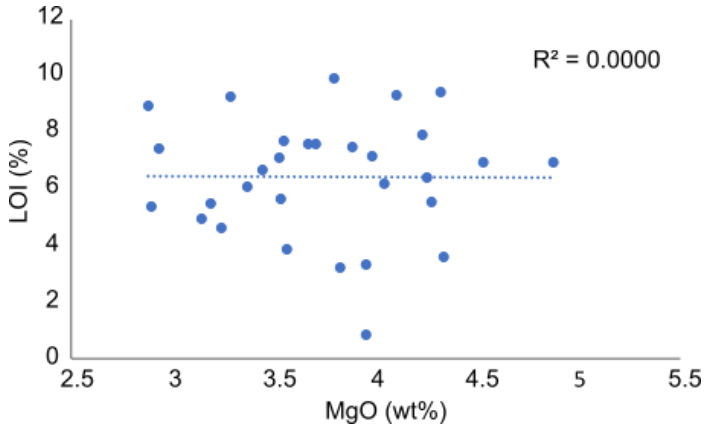


Figure 6.2: MgO vs LOI plot showing no relationship between LOI and the whole rock MgO abundance for the Poto and Paetahi Formations.

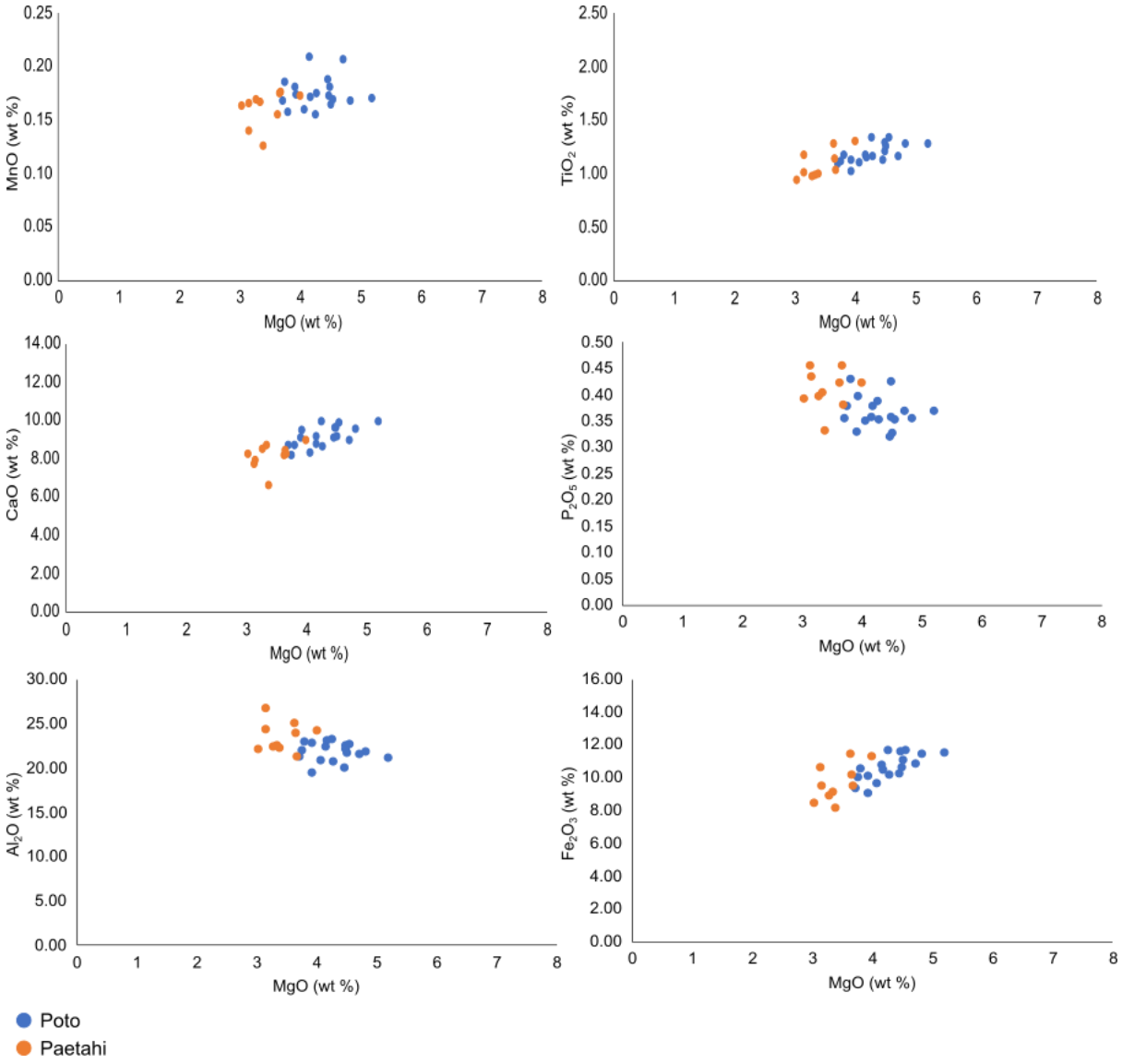


Figure 6.3: Whole rock major element variation diagrams as a function of MgO abundance showing the magmatic evolution throughout the Poto and Paetahi eruptive period.

Thermobarometry from pyroxene crystal rims and pumice bubble textural analysis of the Poto and Paetahi Formations indicate that primitive magma was entering the plumbing system and interacting with a crystal mush zone indicated by the continued overgrowth and resorption features within pyroxene and plagioclase crystals (Figure 6.4). Studies examining thermobarometry and hygrometry for the Poto and Paetahi Formations showed that the majority of crystals within the deposits were out of equilibrium with the surrounding melt. Out of the twenty-eight eruptive units only nine had crystals in equilibrium with temperatures ranging from 1024-1137°C and H_2O ranging between 1.7-6.9 wt.%. These temperatures are comparable with younger Mt. Taranaki lava flows and large explosive eruptions from Mt.'s Ruapehu and Tongariro. Eruptive units with similar temperature ranges 970 – 1120 °C have pressure estimates between 32 – 400 MPa (Pardo et al., 2012a; Heinrich et al., 2020b; D'Mello et al., 2023). These wide pressure ranges indicate a rapidly changing environment of P-T-X conditions within

the magmatic system related to magma recharge and eruption (Higgins, 1996; Price et al., 2016; D'Mello, 2021). Each unit within the Poto and Paetahi Formations had three to ten crystals analysed with only fourteen grains across the whole sequence in equilibrium (Chapter 5; Section 5.5.6). This supports the presence of a complex crystal mush zone below Mt. Taranaki.

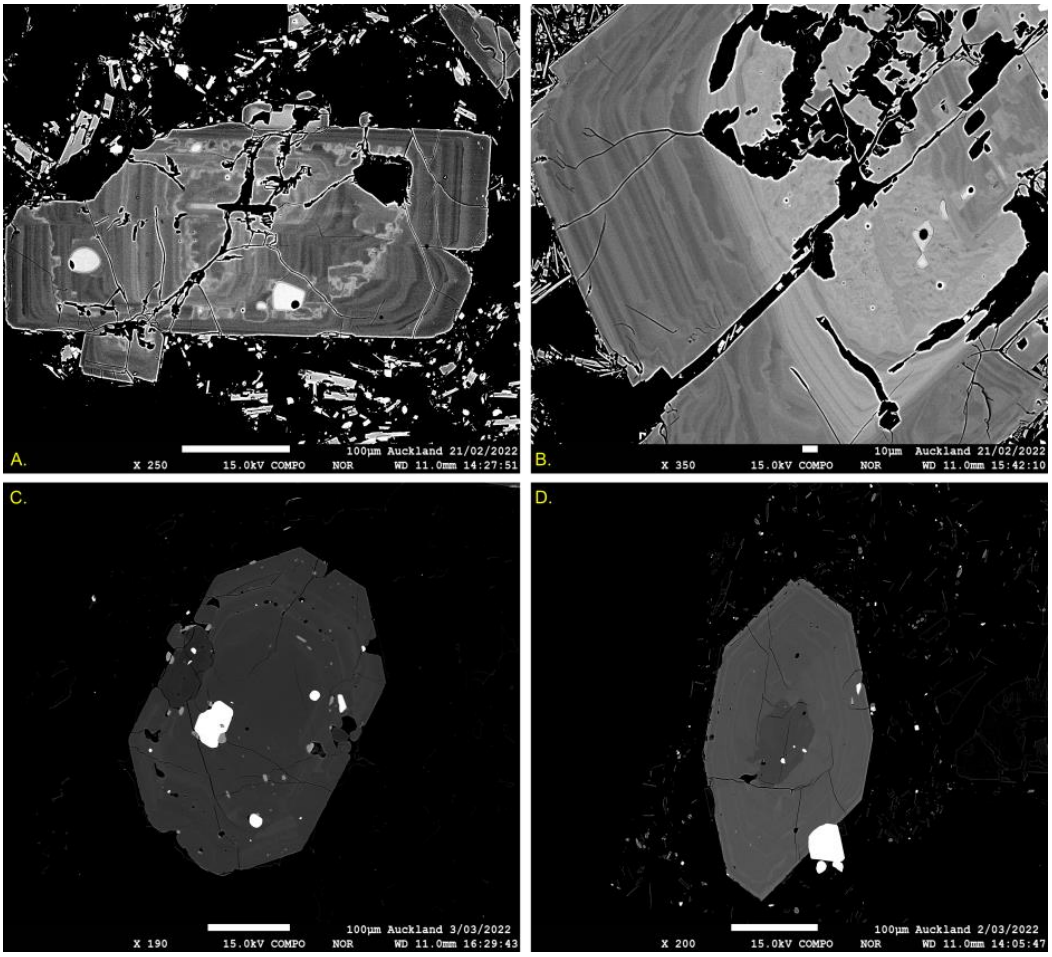


Figure 6.4: Crystal texture of representative examples from the Poto and Paetahi Formations. A-B plagioclase crystals, C-D pyroxene crystals.

This study did not investigate isotopic characteristics for these deposits, however isotopic analysis on some of the Poto eruptives were analysed by Davidson (2023). Results from Davidson (2023) found that the isotopic signature of the Poto units (Poto.a, d, g, and l.u) were consistent with previously analysed Taranaki samples (e.g., Price et al., 1999). $^{87}Sr/^{86}Sr$ ratios for the Poto units range from 0.704723 to 0.704613 and $\delta^{18}O$ (%) range from 5.43-4.78 % (Davidson, 2023). These values are concurrent with values from Oceanic Island arcs not reaching the high $\delta^{18}O$ values that are found at continental arcs, where there is an interaction between continental crust and magma occurring at depth (Cronin et al., 2021; Davidson, 2023). Phenocrysts and groundmass from Mt. Taranaki indicate that magma equilibrated with the lack of isotopically contrasting material (Davidson et al., 2007; Deegan et al., 2021). The absence of co-variation in the erupted material at Mt. Taranaki rules out significant upper

crustal assimilation during magmatic evolution (Davidson, 2023). Mt. Taranaki magmas more typically correspond with eruptives from the Kermadec Arc where magmatic signatures indicate the addition of fluids and sediment melt derived from the subduction of Pacific Oceanic Crust (Turner et al., 2009; Myeong et al., 2023). This is in contrast to eruptives from Mt. Ruapehu and Whakaari (White Island), which clearly show a signal of crustal involvement (Turner et al., 2009; Davidson, 2023; Myeong et al., 2023). Fractional crystallization studies by Davidson (2023) on the Poto eruptives shows that they share a parental magma and have varying degrees of fractional crystallization reflected in the whole rock compositions. Compositional variations between Poto.a and Poto.d can be modelled and reflect 26.55 % fractional crystallization occurring between eruptive units (Davidson, 2023). Previous studies have discussed a deep crustal "hot zone" or crystal mush present below Mt. Taranaki (Stewart et al., 1996; Price et al., 1999), which is responsible for the high-K arc evolution. The erupted products represent a mixture of melt and crystal components, reflecting the occurrence of different zones within the magmatic system (Davidson et al., 2005) while similar compositional influxes can be hard to differentiate in samples at the surface (D'Lemos, 1996; Coleman et al., 2004; Price et al., 2005; Humphreys et al., 2006; Turner et al., 2008b).

Previous crystal mush models suggest that crystals within a crystal mush zone could exist at different depths within the crust and these could correlate with the different depths at which fragmentation occurs (Métrich & Deloule, 2014; Stock et al., 2018; Tucker et al., 2019). Processes occurring within the crystal mush zone beneath a volcano can influence the composition of the erupted magma and unerupted sections resulting in changes in the evolution of the magmatic system (Cashman & Blundy, 2013), this can then change in relation to interactions with subsequent batches overtime (Browne et al., 2005; Botcharnikov et al., 2008; Streck et al., 2008; Kent et al., 2010; Ruprecht et al., 2012; Parat et al., 2014; Higgins et al., 2015; Melekhova et al., 2015; Wanke et al., 2019; Di Stefano et al., 2020; Namur et al., 2020).

The vesicle size distributions (VSDs) for the erupted pumice clasts indicate that for the Poto and Paetahi Formations there was not a lot of stalled magma present within the system evidenced by the lack of large, coalesced bubbles and the dominance of small bubbles within the system (Chapter 4). Bubble and crystal textures within the Poto and Paetahi Formations indicate that the system went through cycles of magma recharge triggering eruptive events (Figure 6.4) (Chapters 4 and 5). Cyclic trends of bubble nucleation and growth are observed within the BSD of the Poto and Paetahi Formations (Chapter 4; Section 4.5.4) and supported by the resorption and regrowth features present within pyroxene and plagioclase rims (Chapter 5; Section 5.6.3). Recharge events are reflected in BSD by single stage nucleation events (Poto.a, c.l, e, h, k.l, m, Paetahi.a.l, a.m, and e.m), where magma has ascended quickly through the system evidenced by the high proportion of small bubbles present within the erupted pumices. This indicates that bubble nucleation began later in the system within hours of an eruption occurring (e.g., Wilson et al., 1980; Sparks & Brazier, 1982), and the upper conduit was the main

location for nucleation processes throughout this eruptive period (Chapter 4; Section 4.6.1). Following these recharge single stage nucleation events, a series of subsequent eruptions present varying degrees of bubble nucleation and growth at different depths. The final eruption in each recharge cycle (Figure 6.4) is represented by a higher proportion of coalesced bubbles (Poto.d, h*, l.l, l.u, o, Paetahi.a.m, a.u, e.l, and e.m) before a new recharge event occurs, represented by single stage nucleation and the dominance of small bubbles (< 2.7 $x10^{-7}$ cm^{-3}) within the system (Figure 6.4) (Chapter 4; Figures 4.8 and 4.9).

Eruptive compositions from the Poto and Paetahi Formations vary between primitive to more evolved which is related to the process of magma mixing occurring between fast ascending primitive melts interacting with crystal mush zones. The ascending magma is picking up more evolved magma on the way to the surface indicated by the oscillatory zones in the crystals which reflect multiple periods of growth (Figure 6.4) (Platz et al., 2007; Turner et al., 2008b; Zernack et al., 2012a; D'Mello et al., 2021; D'Mello et al., 2023; Davidson, 2023; Shane et al., 2023). Oscillatory zones within plagioclase and pyroxene crystals in erupted pumices indicated patches of stalled “dry” crystal mush zones within the magmatic system which explains the geochemical evolution overtime while small bubble populations within the Poto and Paetahi pumices are attributed to the high mafic crystal number densities (CND) within the samples and the crystal mush zone with crystals acting as nucleation points for further bubble nucleation processes (Cashman, 2004: Hildreth, 2004; Annen et al., 2015; Bachmann & Huber, 2016; Cashman et al., 2017; Edmonds et al., 2019; Lissenberg et al., 2019; Maclennan, 2019; Caracciolo et al., 2020; van Gerve et al., 2020; Zemeny, 2021). The overall magmatic evolution throughout the Poto and Paetahi Formations did not influence the size of the eruptions occurring within this eruptive period. Throughout the Poto and Paetahi Formations there are fluctuations in the magmatic composition of the eruptive deposits reflective of the recharge events into the system (Figure 6.5). Eruptive rates for these subplinian eruptive products also fluctuate throughout the sequence (Figure 6.5). However, there does not appear to be a relationship between the fluctuations in composition and eruption rate with one of the least evolved (Poto.c lower 4.55 wt.% MgO) and most evolved (Paetahi.a lower 3.03 wt.% MgO) having some of the largest eruptive events (18.2 and 19.4 km) (Figure 6.5).

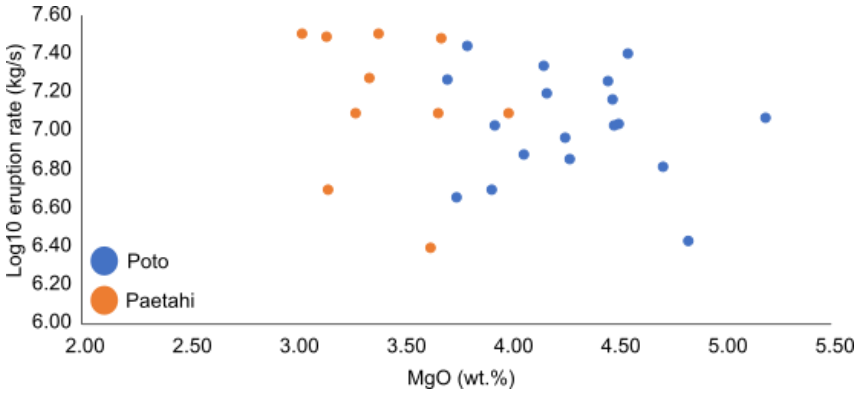


Figure 6.5: Whole rock MgO (wt.%) composition for the Poto and Paetahi Formation in relation to the Log10 eruption rate of the erupted subplinian events.

6.3 *The relationship between stratovolcano collapse and eruptions*

Internal (magmatic, structural), and external (morphological) processes are key factors involved in stratovolcano edifice stability (Elsworth & Voight, 1995, 1996; McGuire, 1996; Roverato et al., 2021; Zernack & Procter, 2021). Volcanoes that experience multiple collapse events also have successive and related periods of regrowth, with the collapse deposits being recorded in the volcanic ring plain intercalated within primary and secondary volcaniclastics from the regrowth period (Zernack et al., 2011; Zernack & Procter, 2021). Repeated collapse events erode or bury the older sequences, removing the record of deposition in proximal to medial locations, limiting preservation beyond the last regrowth event unless the foci of activity changes (Watt, 2019).

The recurrence rate of collapse and regrowth cycles varies from 0.1-1 kyr (Begét & Kienle, 1992; Belousov et al., 1999; Tibaldi, 2001), 1-10 kyr (K. M. Scott et al., 1995; Zernack et al., 2011; Zernack et al., 2012b; Tost et al., 2014) to 10-100 kyr (Moore et al., 1989; James et al., 1994; Carracedo et al., 1999; Oehler et al., 2008) yet is highly dependent on the volcanic setting. The recurrence rate of collapse is directly related to the magmatic production rate of the volcano (Zernack & Procter, 2021) yet cycles of collapse and regrowth indicate that stratovolcanoes have a natural maximum height of 2000 – 2500 m where they become unstable and more susceptible to collapse (Davidson & De Silva, 2000). Edifice collapse events significantly impact the morphology of the upper edifice and can influence the eruptive behaviour including style, size, and frequency at a stratovolcano (McBirney & Murase, 1970; Wilson et al., 1980; Lipman & Mullineaux, 1981; Alidibirov & Dingwell, 2000). Collapse events can change the lithostatic pressure that in turn impacts its magmatic plumbing system through the propagation of a pressure wave down through the conduit. This can trigger an eruption if there is eruptible magma present within the system (Watt, 2019). A change in eruptive behaviour following an edifice collapse event has been observed at volcanoes within the Holocene record e.g. Fuego de Colima, Mexico (Robin et al., 1990; Stoopes & Sheridan, 1992; Capra & Macías, 2002), Tungurahua, Ecuador (Hall et al., 1999),

Stromboli, Italy (Hornig-Kjarsgaard, 1993; Tibaldi, 2001, 2004; Romagnoli et al., 2009), Ritter Island, Papa New Guinea (Johnson, 1987; Day et al., 2015; Karstens et al., 2019; Watt, 2019). However, these observations highlight the short-term response to an edifice collapse event, as opposed to the long-term (> 1000 yrs.) changes which can occur (Robin et al., 1990; Stoopes & Sheridan, 1992; Belousov et al., 1999; Germa et al., 2011; Watt et al., 2012; Boudon et al., 2013; Watt, 2019). Holocene edifice collapse events e.g., 1980 Mt. St Helenes 2.5 km^3 (Siebert, 1984) and 1888 Ritter Island Papa New Guinea 4.2 km^3 (Johnson, 1987), have been relatively small in comparison to pre-Holocene collapses e.g., 4.3 ka Colima, Mexico, 10 km^3; (O'Callaghan & Francis, 1986; Luhr & Prestegaard, 1988) and 60 – 65 ka Chimborazo, Ecuador, 12 km^3; (Samaniego et al., 2012; Watt, 2019). There is limited preservation of older stratigraphic sequences around these large pre-Holocene debris-avalanche deposits, reducing the chance to investigate the impact that there is on the long-term behaviour of the volcano.

The size and stability of large explosive eruptions is controlled by both internal and external processes such as the volatile content, chemistry, and supply rate of the magma along with vent, and conduit geometry (Wilson, 1976; Carey & Sigurdsson, 1989; Woods, 1995; Cioni et al., 2003; Houghton et al., 2004; Adams et al., 2006a). Changes in the gas content, vent radius and gas velocity within a system can influence the size of an explosive eruption and can control the supply of magma and discharge rate within the system (Sparks & Wilson, 1976; Wilson et al., 1980; Bursik, 1993; Cioni et al., 2003; Arce et al., 2005; Cioni et al., 2015).

The ash and lapilli fall units of the Poto and Paetahi Formations produce a unique opportunity to investigate primary fall deposits from within a collapse and regrowth cycle at a long-lived stratovolcano through changes in the eruptive behaviour (Chapter 3), pumice textural data (Chapter 4) and geochemistry (Chapter 5) to understand the short and long-term influence edifice collapse events have on the magmatic system. The Poto and Paetahi Formations are represented by twenty-eight subplinian eruptions covering the eastern and southeastern sectors of the Taranaki ring plain. Specific locations across the eastern and southeastern ring plain allow access to preserved fall deposits (Poto.a and b) which are situated below the Ngaere debris-avalanche deposit which is intercalated within the Poto Formation across the eastern sector of the ring plain. Ash fall units at cliff outcrops across the southwestern sector of the ring plain allowed for the hypothesis of the stratigraphic location of the Pungarehu collapse within the Poto and Paetahi eruptive period.

The Ngaere edifice collapse and following Poto eruptive events indicates the start of a new cycle of cone growth at Mt. Taranaki (e.g., Zernack et al., 2011). The collapse generating the Ngaere DAD removed 5.85 km^3 of material from the eastern flank of the volcano and would have dramatically altered the morphology of the proto-Taranaki edifice compared to the present-day Taranaki cone (2518 m) which has a volume of ~ 12 km^3 above 1400 m (Neall et al., 1986; Zernack et al., 2011). This resulted

in removal of approximately 1000 m in height from the upper edifice and conduit, impacting the lithostatic pressure on the magmatic system causing magmatic over pressurization generating a fragmentation front deeper into the system (Figure 6.6). This resulted in a lower proportion of small bubbles and a less evolved magma being erupted causing an observable change in bubble nucleation and growth recorded within erupted pumice clasts (Chapter 4; Section 4.6.3).

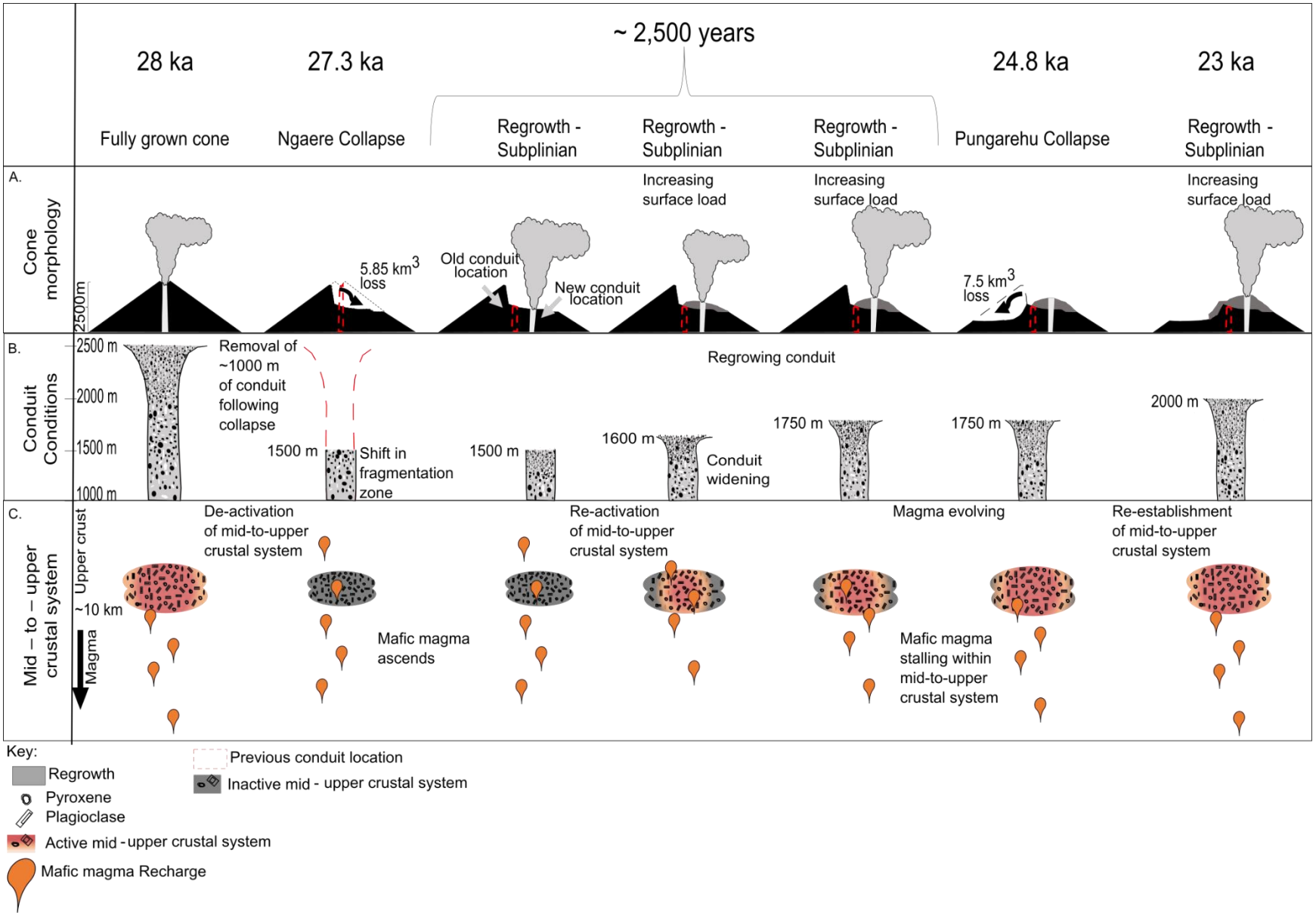

~ 2,500 years
28 ka
27.3 ka
24.8 ka
23 ka
Fully grown cone
Ngaere Collapse
Regrowth - Subplinian
Regrowth - Subplinian
Regrowth - Subplinian
Pungarehu Collapse
Regrowth - Subplinian
A.
Cone morphology
2500m
5.85 km3 loss
Old conduit location
New conduit location
Increasing surface load
Increasing surface load
7.5 km3 loss
Increasing surface load
B.
Conduit Conditions
2500 m
2000 m
1500 m
1000 m
Removal of ~1000 m of conduit following collapse
1500 m
Shift in fragmentation zone
1500 m
Regrowing conduit
1600 m
Conduit widening
1750 m
1750 m
2000 m
C.
Mid – to – upper crustal system
Upper crust
~10 km
Magma
De-activation of mid-to-upper crustal system
Mafic magma ascends
Re-activation of mid-to-upper crustal system
Magma evolving
Mafic magma stalling within mid-to-upper crustal system
Re-establishment of mid-to-upper crustal system
Key:
Regrowth
Pyroxene
Plagioclase
Active mid - upper crustal system
Mafic magma Recharge
Previous conduit location
Inactive mid - upper crustal system

Figure 6.6: Schematic illustration of the changes occurring at Mt. Taranaki 20 – 30 ka during the Poto and Paetahi eruptive period. A.) Changes in cone morphology throughout the collapse and regrowth cycles following the Ngaere and Pungarehu collapse showing the shift in vent location southeast into the Ngaere collapse scar. B.) Changes in the conduit conditions throughout the eruptive sequence. Following the Ngaere collapse ~1000 m of the upper conduit was removed. Throughout the regrowth stage the conduit was redeveloping periods of conduit widening was expanding the conduit as it increased in size during the volcano's regrowth. C.) Indicates the relationship between the mid – to – upper crustal system and surface load underneath Mt. Taranaki. The Ngaere collapse event changed the surface load causing depressurization on the upper magmatic system, allowing mafic melt to ascend to the surface. As the surface load increased the mid – to – upper crustal system begins to re-establish, inhabiting the ascent of mafic melt and leading to wider compositional range and more evolved magmatic compositions. Continued mafic magma recharge into the system throughout this eruptive period, triggered eruptions where some events resulted in these recharge events moving quickly through the system identified through the vesicle size distribution as single stage events where there is the domination of a single population of bubbles. Periods of stalled magma allowed for bubble coalescence to occur erupting following new smaller recharge events with the history of recharge and stalling recorded in the vesicle size distributions of pumice clasts and the oscillatory zoning of crystals.

Following the Ngaere collapse event there is a larger subplinian eruption (18.2 km plume height) (Chapter 3) than what is seen prior (13.3 km), while Poto.c lower shows a decrease in the vesicle number density (VND) (9.76 x 10^{15} cm^{-3}) and increase in the percentage of large bubbles (Vesicle Volume VV = 4.8%). This indicates a change in magmatic overpressure and the generation of a fragmentation front protruding deeper into the system compared to Poto.a (VND = 1.53 x 10^{16} cm^{-3} & VV = 4.9 %) (Chapter 4; Table 4.1). There is also an increase in the whole rock MgO wt.% (4.55 wt.%), indicative of a less evolved magma being erupted following the Ngaere collapse event (Figure 6.7A) and suggesting that the system is tapping magmas that are not being impeded or spending long durations within a crystal mush. Following this collapse event Mt. Taranaki entered a period of regrowth that was characterized by fluctuations in eruption height (10-19.4 km), composition (3.0-5.2 wt.%), and bubble nucleation processes, typical of a volcano going through a regrowth period as it rebuilds an edifice (Figure 6.7A). Following the Pungarehu collapse there is an increase in the eruption column height (19.2 km) compared to the event prior (10 km). However, there does not appear to be the same lithostatic pressure change as observed in the Ngaere collapse. Paetahi.e lower shows a decrease in VV (3.3 %) while there is an increase in VND (1.29 x 10^{16} cm^{-3}) compared to Paetahi.d (VND = 1.15 x 10^{16} cm^{-3} VV = 7.1), indicating a higher percentage of small bubbles in Paetahi.e lower along with a more evolved magmatic composition (MgO = 3.14 wt.%) (Chapters 4 and 5). Throughout this collapse and regrowth cycle fluctuations are observed in the eruptive parameters and in the stability of the conduit conditions.

Changes observed in the componentry of the ash and lapilli fall units indicate changing conduit conditions throughout the Poto and Paetahi eruptive period (Figure 6.7A). Pumice dominated units indicate stable conduit conditions where magma was able to move through the system freely, while lithic dominated units indicate unstable and widening conduit conditions where sections of the conduit wall were being plucked away disrupting the magmas flow path to the surface (Figure 6.7B).
These changes in the conduit conditions, however, are not reflected in the 2D and 3D bubble textural analysis. The lack of shearing within the 2D data and no observable pattern in the VND and VV within changing conduit units reflect the main location of bubble nucleation and growth occurring during the Poto and Paetahi eruptive period was within the fragmentation zone.

The average debris avalanche recurrence rate at Mt. Taranaki over the last 105 ka is 8-9 kyr (Zernack & Procter, 2021), with a magma supply rate of 0.45 km^3/kyr (Zernack et al., 2012b; Zernack & Procter, 2021). Mt. Taranaki's magma supply rate is much slower (Adams et al., 2006a; Germa et al., 2011) compared to volcanoes which have experienced numerous collapses during the Holocene e.g., Shiveluch (Belousov et al., 1999) and Mt. St. Augustine (Begét & Kienle, 1992; Zernack & Procter, 2021). Mt. St. Augustine has had twelve small < 1 km^3 collapses over c. 2.3 ka equating to 5-10 % of the total edifice volume being removed (Begét & Kienle, 1992; Siebert et al., 1995). This corresponds to a debris avalanche recurrence rate of 150-200 years and reflects the high rate of magma recharge (1-3 x 10^6 m^3/yr = 1-3 km^3/kyr) (Begét & Kienle, 1992; Zernack & Procter, 2021). Shiveluch in Russia has experienced eight larger collapses over the past < 5.7 ka with a debris avalanche recurrence rate of 800 years with collapse volumes ranging between 1-2.5 km^3 (Belousov et al., 1999). Shiveluch has a magma recharge rate of (36 x 10^6 tons/yr or 15 km^3/yr (Fedotov, 1991; Ponomareva et al., 2007; Zernack & Procter, 2021). These volcanoes have high collapse recurrence rates which corresponds to a high rate of magma recharge. In comparison to the large size of the Ngaere (5.85 km^3) and Pungarehu (> 7.5 km^3) collapses from Mt. Taranaki, Mt. St. Augustine and Shiveluch's collapses are relatively small allowing for a shorter regrowth time required before the next collapse occurs. The relationship between the size of the collapse and the regrowth period plays a critical role in controlling the lithostatic decompression on the magmatic system (e.g., Pinel & Jaupart, 2003; Pinel et al., 2010; Watt, 2019). The loci of lithostatic pressure on a volcano is centred around the top of the edifice and around the conduit (Pinel & Jaupart, 2003; Watt, 2019), when a large collapse occurs it removes a significant proportion of height and volume from the edifice removing the upper section of the conduit moving the upper magmatic system down deeper (Figure 6.6) (Chapter 4; Figure 4.11; Chapter 5; Figure 5.12) or changing the location of the vent (e.g., Mt. Ruapehu following the Mangaio collapse (Donoghue et al., 1988; Hodgson et al., 2007). Following a collapse event subsequent eruptions infill the edifice scar rebuilding the height of the volcano (e.g., dome growth following the 1980 Mt. St. Helens eruption (Swanson & Holcomb, 1990).

The lithostatic pressure on a magmatic system is directly related to the height of an edifice, therefore volcanoes which have a higher magma supply rate get to the natural maximum height (2000 – 2500 m) (Davidson & De Silva, 2000) faster and are more prone to collapse events. Studies by Zemeny et al. (2023) focused in on three collapse and regrowth cycles to investigate how edifice collapse events influenced the magmatic system through identifying geochemical changes from samples of pumices within mass flows during the regrowth phases. Within the Poto and Paetahi eruptive period similarities are observed in the regrowth period following the Ngaere collapse to that of older regrowth periods examined by Zemeny et al. (2023) where the magmatic system trends from a more primitive to more evolved composition overtime. Evidence of the restoration of the mid-to-upper crustal magma storage system following collapse which generated the Ngaere DAD is seen in the evolution from a more primitive Poto Formation (3.71-5.19 wt.%) to a more evolved Paetahi Formation (3.03-4.0 wt.%). However, unlike Zemeny et al. (2023) this trend is not repeated following the Pungarehu collapse event, instead the composition of the Paetahi Formation eruptives are more evolved than the Poto Formation indicating that the Pungarehu collapse did not start a new regrowth cycle. Rather, the restoration of the mid-to-upper crustal magma storage continued following the Ngaere collapse event (Chapter 5; Figure 5.12). Patterns of geochemical evolution within individual regrowth cycles was not identified by Zernack et al. (2011; 2012), who looked at sedimentological/ geomorphic collapse and regrowth cycles to identify fourteen collapse events within Mt. Taranaki's eruptive history. However, not all of these geomorphic collapse and regrowth cycles correspond to geochemical ones (e.g., Pungarehu collapse). The study by Zernack et al. (2011; 2012) did not identify individual collapse cycle changes between geochemical evolution and conduit conditions as the study was an overview of geomorphic collapse/ regrowth at a large scale and was not at a high enough resolution between events to identify any relationships.

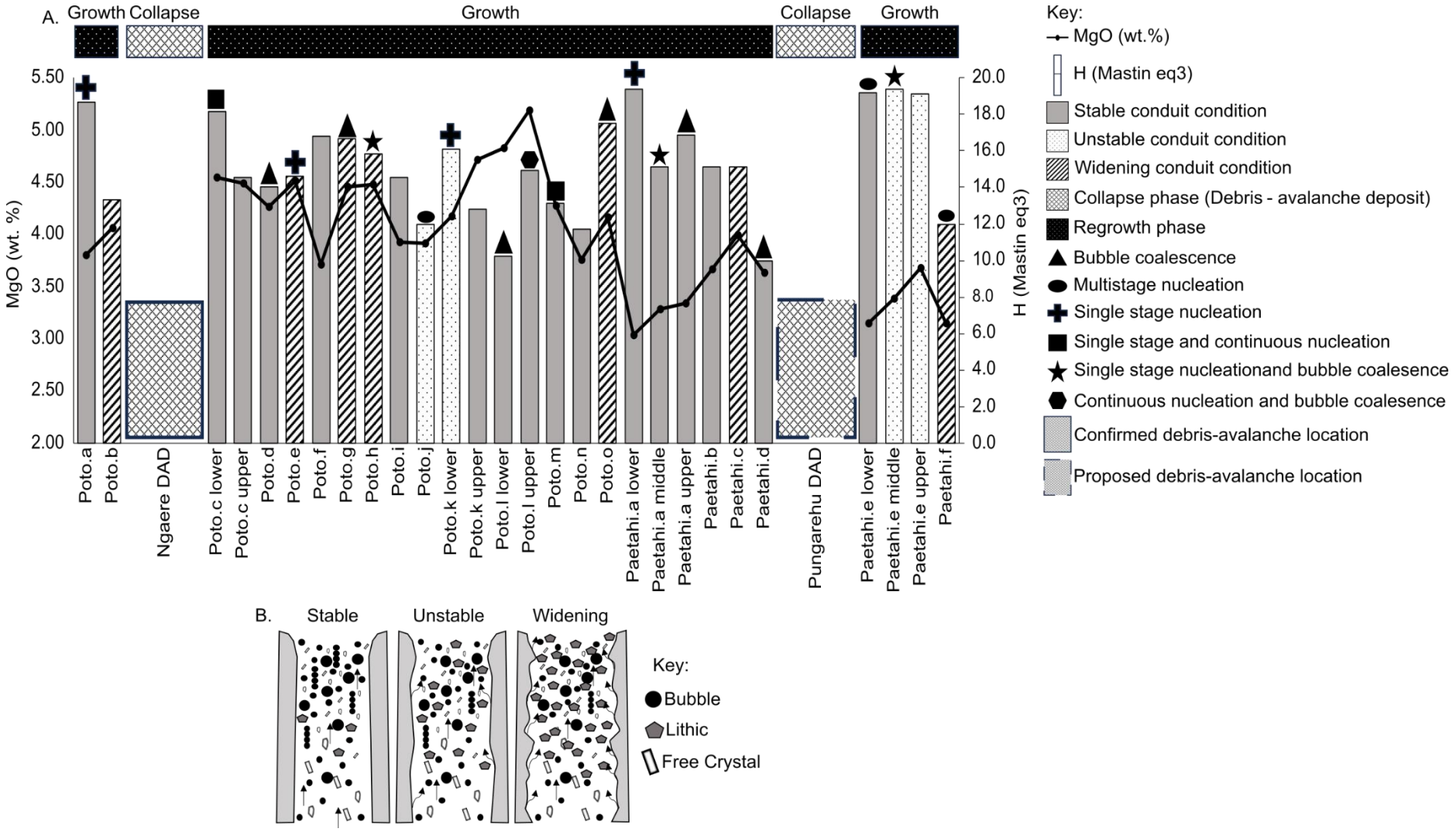


Figure 6.7: A. Column height vs composition (MgO wt.%) of the Poto and Paetahi Formation in relation to the changing conduit conditions occurring up through the eruptive sequence and changing nucleation events. B. Schematic of the changing conduit conditions indicated in the column patterns in A.

The subplinian deposits of the Poto and Paetahi Formations from Mt. Taranaki show that not all collapse events have the same impact on the magmatic plumbing system. The eruption following the Ngaere collapse event indicates rapid decompression caused by magmatic over pressurization of a porous magma generating a fragmentation front which moves through the magma moving erupting a less evolved magma with lower VND's (Chapters 4 and 5). The geologically short period between the Ngaere and Pungarehu collapse events resulted in ~13.35 km^3 of material being removed from the cone of Mt. Taranaki within a ~2.5 kyr period. The size of these two collapse events suggests that the proto-Taranaki edifice would have been a similar size to the present-day cone (~2500 m). The Pungarehu collapse would have equated to approximately 60 % of the cone above 1400 m collapsing away. However, the change in lithostatic pressure on the magmatic plumbing system is reliant on the height above the surface (e.g., Davidson & De Silva, 2000; Pinel & Jaupart, 2003). The removal of 5.85 km^3 of material during the Ngaere edifice collapse event removed a large section of the upper conduit system (Chapter 4; Figure 4.11) and volume from the upper edifice changing the lithostatic pressure which is reflected in the whole rock geochemistry and bubble textural analysis of Poto.c lower with an increase in MgO and decrease in VND (Chapters 4 and 5). Geochemical analysis of the Poto and Paetahi Formations show a shift to more primitive compositions following the Ngaere collapse event (Poto.b 4.06 wt.% MgO and Poto.c lower 4.54 wt.% MgO). Following the collapse event fluctuations in the compositions of erupted magma is observed concurrently with the re-establishment of the upper magmatic system. Whole rock geochemistry's for the Poto and Paetahi Formations vary between 3 to 5.2 wt.%. A decrease in the VND for Poto.c lower following the Ngaere collapse corresponds with the removal of 1000 m from the upper edifice of Mt. Taranaki and subsequent removal of 1000 m from the upper conduit. Fluctuation in eruption size, composition, and conduit processes (Figure 6.7A) throughout the Poto and Paetahi eruptive period are observed with similarities in composition seen between Poto.i and j (3.92-3.91 wt.% MgO), Poto.k lower and o (4.17-4.16 wt.% MgO) and Paetahi.e lower and f (3.14-3.15). The textural analysis of the Poto and Paetahi Formation during the regrowth phase following the Ngaere collapse except for Poto.c lower show a high VND with 10^{16} cmm^{-3} (VNDs) except for Paetahi.f which has a high CND reflecting the final stage of the Poto and Paetahi eruptive period before Mt. Taranaki entered a period of quiescence. The high CND impacts bubble nucleation resulting in a lower VND (Chapter 4; Table 4.1).

This data shows that the impact a subsequent collapse has on the magmatic system is reliant on the regrowth that occurs following the collapse. The lack of regrowth following the 5.85 km^3 Ngaere collapse and the possible shift of the vent to the southeast prior to the > 7.5 km^3 Pungarehu collapse ~2.5 kyr later highlights why the impact on the magmatic system is not as great as the Ngaere collapse (Chapter 4; Figure 4.11). More mafic compositions (from 4.06 wt.% to 4.55 wt.%), following the Ngaere collapse reflect the deactivation of the mid-to-upper crustal system following edifice depressurization. Changes in the magmatic system observed through geochemical analysis (Chapter 5)

indicates a wider more evolved compositional distribution throughout the regrowth period. The Paetahi Formation is more evolved (3.03-4.0 wt.%. MgO) than the Poto Formation (3.71-5.19 wt.% MgO), coinciding with cone regrowth reloading the system, reestablishing the mid-to-upper crustal system.

6.4 Eruption frequency and ashfall distribution

In-depth studies on the eruptive parameters and dynamics of eruptions from Mt. Taranaki have predominantly been focussed on the last 5 ka, primarily due to the poor preservation of proximal deposits from the older sequence (e.g., Platz, 2007; Platz et al., 2007; Turner et al., 2009; Turner et al., 2011; Torres-Orozco et al., 2017a; Torres-Orozco et al., 2017b, 2018; Lerner et al., 2019d; Lerner et al., 2019a; Lerner et al., 2019c; Lerner et al., 2019b; D'Mello et al., 2021; D'Mello et al., 2023) and exposure/ease of access to the younger sequences. The majority of future hazard scenarios for the Taranaki region (e.g., McDonald et al., 2017; Torres-Orozco et al., 2018; Weir et al., 2022) have focused on styles of eruptions which occurred throughout this < 5 ka period. The eruptive record > 5 ka has typically been examined in cores where tephrochronological studies, correlate tephra deposits to better understand frequency of events rather than eruptive parameters (e.g., Neall, 1972; Neall, 1979; Neall et al., 1986; Alloway et al., 1995; Procter et al., 2009; Zernack et al., 2011; Damaschke et al., 2017b). Within the last 5 ka at least sixteen large explosive subplinian to plinian eruptions have been recorded producing eruption columns 14-29 km high, erupting 0.1 to 1.1 km^3 of magma (Torres-Orozco et al., 2017b, 2018). The last subplinian eruptive event occurred in 1655 CE (Platz, 2007; Platz et al., 2007). This study reveals that Mt. Taranaki is capable of producing eruptive periods consisting of sustained large explosive subplinian events with magnitudes ranging from 3 to 4.5 VEI and eruption columns ranging from 10-20 km high. The Poto and Paetahi eruptive period saw twenty-eight subplinian eruptions produced over ~4 kyr covering the eastern and southeastern sectors of the ring plain.

The age of the Poto and Paetahi Formations along with the close time proximity and size of the Ngaere and Pungarehu collapse events has influenced the poor preservation of theses deposits across the Taranaki ring plain. The predominant westerly wind in the Taranaki region has resulted in repeated accumulation of tephra across the eastern ring plain towards Stratford and Inglewood. Overtime changes in wind direction have also distributed historic eruptions west and south towards Okato, Pungarehu and Opunake (Neall, 1972; Neall, 1979; Neall et al., 1986) along with large historic explosive events being recorded within lake cores as far north as Auckland (Sandiford et al., 2001; Shane & Hoverd, 2002; Shane, 2005; Molloy et al., 2009). The Poto and Paetahi eruptive period, however, indicates that these large explosive eruptions consistently deposited ash and lapilli across the eastern and southeastern ring plain towards Stratford and Hawera. Proximal deposits of the formations were not accessible due to subsequent burial of the deposits by the younger eruptive sequences. Erosion of the deposits also influences the dispersal pattern making the isopachs more defined to the eastern and southeastern sector.

Eruptive volumes calculated for the Poto and Paetahi Formations represent minimum values based on medial and distal locations.

All twenty-eight eruptive units of the Poto and Paetahi Formation were produced during the Last Glacial Maximum which was associated with a cold and dry climate around the Taranaki ring plain, where there was more erosion occurring along streams and redistribution of tephra deposits (Neall, 1975; McGlone et al., 1996). These conditions influenced the preservation of the primary fall deposits and highlight why pre-Holocene eruptive events have been typically excluded from volcanic records globally (Watt, 2019). However, the changes seen to the eruptive behaviour at Mt. Taranaki in relation to large edifice collapse events highlights why longer eruptive histories need to be considered within hazard forecasting and eruptive scenarios at volcanoes.

The distribution of the Poto and Paetahi Formations primarily across the eastern and southeastern sectors of the ring plain (Chapter 3) could be due to the preservation conditions in this sector of the ring plain. However, it is most likely related to the size of the eruptive events and the distribution of the Ngaere DAD. Hazard scenarios and computational ashfall simulations generated by Weir et al. (2022) shows that eruptions above a certain size can have a distribution across the eastern and southeastern sector of the ring plain due to the eruption column entering the stratosphere, where different wind patterns take effect (Figure 6.8C and D). This can explain the change in the depositional direction compared to the younger eruptive record (e.g., Torres-Orozco et al., 2018). These modelled eruptive distributions correspond to the (Weir et al., 2022) M1-3 and L2 eruptive events (Figure 6.8C and D). The explosive phases for these scenarios relate to minor to explosive eruptive events ranging from 3-6+ VEI from (Bebbington & Jenkins, 2019), recognised as discrete events with a duration < 1 day for each explosive episode (Weir et al., 2022). The Poto and Paetahi subplinian eruptive events correspond to major explosive eruptions with eruption columns c. 10-20 km of (Bebbington & Jenkins, 2019), related to large subplinian events. Eruptive durations for the Poto and Paetahi subplinian events were calculated at between 1 to 2.5 hours (Chapter 3; Table 3.6). The period and climate in which these events occurred corresponds to the Last Glacial Maximum with stronger westerly winds during summer and weaker for the winter months, in the Taranaki region there was a stronger south-westerly wind during this time (Alloway et al., 1992; Drost et al., 2007; Williams et al., 2015). Changes to the morphology of Mt. Taranaki following the Ngaere collapse may have contributed to the direction of the eruptive column's dispersal axis during the Poto and Paetahi eruptive period (Chapter 4; Figure 4.11).

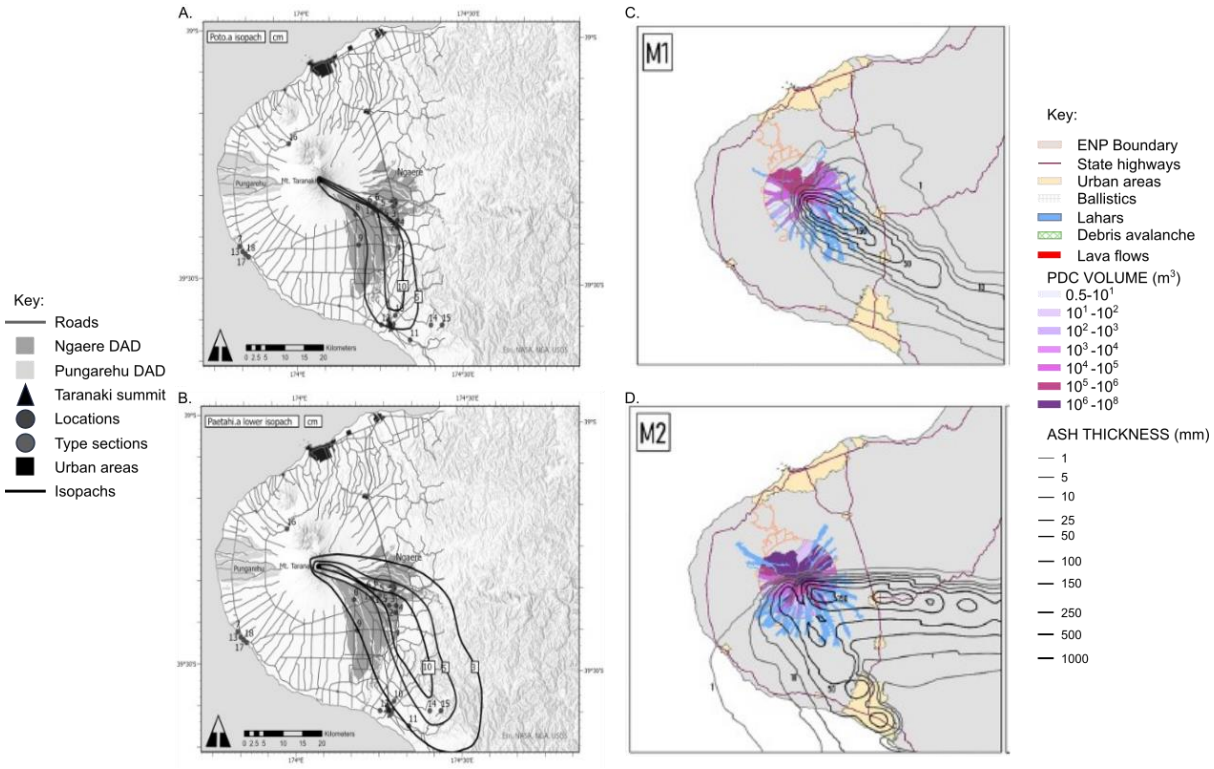


Figure 6.8: Comparison between the distribution of the Poto and Paetahi Formation ash and lapilli fall deposits from this study and modelled ash dispersal of large magnitude eruptive phases modified from Weir et al. (2022). A. Poto.a eruptive unit. B. Paetahi.a lower. C. Magnitude M1 (Weir et al., 2022). D. Magnitude M2 (Weir et al., 2022).

Geomorphological changes to Mt. Taranaki's edifice as a result of the 27.3 ka Ngaere collapse also impacted the eruptive frequency of large explosive eruptions in comparison to the younger Holocene record. Throughout the Poto and Paetahi eruptive period there was twenty-eight subplinian eruptions consisting of sixteen single phase and five multi-phase eruptive events over a period of ~4,000 kyr (Chapter 3; Section 3.6). These eruptions covered the eastern to southeastern sectors of the Taranaki ring plain which ranged in heights from 10 to 20 km with MDRs (Q) of 10^3 to 10^5 $m^{3/s}$ and magnitudes of 3 to 4.5 VEI. From previous studies by (Turner et al., 2008a; Damaschke et al., 2017b; Torres-Orozco et al., 2017b, 2018) the recurrence rate of large explosive subplinian to plinian events from Mt. Taranaki is 300 to 500 years (Cronin et al., 2021). Comparatively the recurrence rate for the Poto and Paetahi eruptive period indicates a much more frequent rate of large explosive subplinian eruptions than what was seen during the Holocene record, with a subplinian event approximately every 190 years.

The Weibull distribution model indicates the regularity of the eruptions within an eruptive period identifying the regularity or clustering of eruptive events which have occurred in the past (e.g., Bebbington & Lai, 1996). If a = 1 it reduces to an exponential distribution, if $\alpha < 1$ this is indicative of clustering as the model is over-dispersed, whereas if a > 1 this indicates a more periodic distribution and that there is a more regular occurrence of eruptive events (e.g., Bebbington & Lai, 1996). The shape parameter for the whole Poto and Paetahi eruptive period is ($\alpha = 1.94 \pm 0.28$) compared with data

following the Ngaere collapse of (α= 2.01 ± 0.34) (Figure 6.9). These results are significant, and both more than 1 that implies a degree of regularity was occurring within this eruptive period. The value of α increases following the Ngaere, indicating that the collapse and subsequent eruptions became more regular post collapse. However, the record prior to the collapse is thin with only two eruptive units occurring prior to the Ngaere DAD making the post collapse record a more comprehensive dataset than the full dataset. Compared to the previous shape parameters for Mt. Taranaki this eruptive period implies a more regular occurrence. Turner et al. (2008a) examined 103 eruptions from a peat core at Lake Umutekai covering an 11 ka period and estimated a shape parameter of (α = 1.17). A combined record from Lakes Rotokare and Umutekai by Green et al. (2013) estimated (α = 1.08) and a combined record of 4 cores by Damaschke et al. (2017a) identified over 200 eruptions over a 14.5 ka period estimating (α = 0.99). These younger eruptive records for Mt. Taranaki show numbers much closer to 1 and indicate clustering periods occurring rather than regular intervals of eruptions. Compared to the post Ngaere collapse these previous studies appear to have far less regular patterns of eruptions.

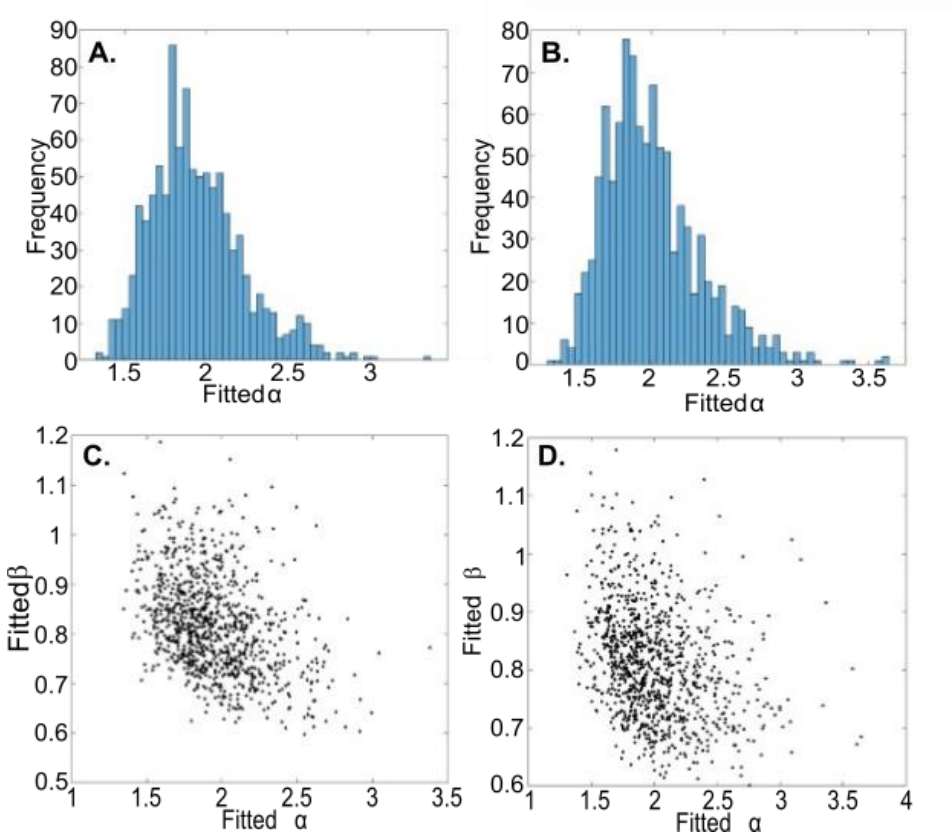


Figure 6.9: A-B. Fitted α (alpha indicates the shape of the distribution) shape parameters A. all data from the Poto and Paetahi Formations and B. Poto and Paetahi eruptions post-Ngaere DAD. C-D. Fitted parameters between the

filled α and β (Beta indicates the scale of the distribution where the bulk of the data is situated). C. all data from the Poto and Paetahi Formations and D. Poto and Paetahi eruptions post-Ngaere DAD.

The Ngaere collapse removed the top section of the conduit system, leaving a large collapse scar on the eastern flanks of Mt. Taranaki which generated an open conduit allowing magma to ascend quickly up through the system. Magma recharge events into the system triggering eruptions where not stalled by overlying rock increasing pressures and this increased the regularity of large explosive events during this time period. The (negative) correlation between the parameters is reduced by removing the pre-Ngaere data, which in relation with the almost unintelligible β of 0.819 ± 0.095 (all data) and 0.813 ± 0.095 (Figure 6.8C and D) indicates that the pre-Ngaere eruptive events may have been less regular than post-Ngaere. The lack of events following the Pungarehu collapse did not allow for a comparison of eruptions from Pre-Pungarehu and Post-Pungarehu to see how this collapse influenced the intervals of events, these eruptive units were included in the post-Ngaere calculations.

The younger 5 ka eruptive record for Mt. Taranaki by Torres-Orozco et al. (2017b) identified sixteen subplinian and plinian eruptive events within the stratigraphy providing a recurrence of one event every 300 years, compared with Neall (1972) who had a recurrence rate of one small event every 500 years for a 16 ka record and Damaschke et al. (2017a) who identified eruptive frequencies over the last 18 ka varying between ~5 – 10 events/kyr and ~25 – 30 events/kyr (Cronin et al., 2021). This change in the recurrence rate could be related to the preservation of tephra within the stratigraphy with the younger volcanic record having better preserved deposits and being overrepresented in the historical record than older eruptive units (e.g., Neall, 1972; Alloway et al., 1995; Turner et al., 2008a; Damaschke et al., 2017b; Cronin et al., 2021). This is the same for the Poto and Paetahi eruptive period occurring 23.1 to 27.3 ka (Alloway et al., 1995) it is likely that there were smaller eruptions which occurred within this period that are not preserved within the stratigraphy or have been subsequently eroded by younger volcanic and geomorphic processes. This would influence the recurrence rate for this eruptive period.

6.5 Implications for hazard analysis

Large edifice collapse events at Mt. Taranaki have an influence on the eruptive frequency and regularity of large explosive subplinian to plinian events. In addition, the distribution of ashfall from the Poto and Paetahi Formations across the eastern and southeastern sectors of the ring plain is different to the predominant distribution to the east and northeast seen in the younger Holocene record. These results should be considered in hazard analyses as well as scenarios and hazard maps where the recurrence of an eruptive period like the Poto and Paetahi Formations would significantly impact the southeastern sector of the ring plain covering it in thick deposits of ash and lapilli on a regular interval.

The limiting factor in creating hazard models and scenarios around collapse events is uncertainty through sparse data and lack of modern-day observations. The changes in the eruptive behaviour at Mt.

Taranaki following collapse events has not been recorded in the eruptive hazard scenarios due to this uncertainty. From this study we can imply that the impact from a large edifice collapse on the eruptive processes at a stratovolcano are complex and can vary. This is highlighted in the deposits which encompass the Ngaere and Pungarehu edifice collapse events where we see a clear influence on the system following the first collapse but not following the second. The data from this study indicates that the Ngaere collapse event had the largest impact on the eruptive dynamics at Mt. Taranaki influencing the magmatic plumbing system, causing the sudden decompression of porous magma causing magmatic over pressurization and generating a fragmentation front through the system. In this studied sequence magma recharge into the system appears to be the greatest influence on the trigger of eruptions. With a large section of the edifice removed the magma is able to freely ascend to the surface without stalling as indicated by the bubble textures and the geochemical analysis of the deposits. This shows that eruptions following a collapse event are more capable of making their way to the surface and explosively erupting out. This resulted in a regular interval of large explosive subplinian events at Mt. Taranaki with an event every ~190 years.

The increase in regularity of large explosive eruptive events following an edifice collapse at Mt. Taranaki is important for future hazard forecasts and scenarios. At some point in the future Mt. Taranaki will experience an edifice collapse event which will change the eruptive behaviour, and this should be accounted for in hazard scenarios and mitigation plans. This is particularly pertinent in the present day considering the current edifice is at an inferred maximum height for stratovolcanoes and possibly more susceptible to collapse.

7 Conclusion

7.1 Specific findings of this study

This research investigated the physical properties of the Poto and Paetahi tephra formations from Mt. Taranaki to understand the eruptive response to large edifice collapse events. The eruption dynamics and pre-eruptive magmatic storage system was examined through detailed stratigraphy, mapping, componentry, density, textural studies using x-ray microtomography and geochemical analysis. Changes in eruptive conditions, bubble nucleation, conduit conditions and magmatic evolution of the system, were determined from these datasets. This study identified a complex relationship between internal and external processes at stratovolcanoes, and that edifice collapse events can influence subsequent eruptive behaviour with one of the greatest factors simply being the change in the height of the volcano and the time between collapse events. A summary of the specific findings from this study are as follows.

1. Detailed stratigraphic mapping across the Taranaki ring plain was introduced in Chapter 3 and built upon the initial work by (Alloway et al., 1995), who had identified fifteen Poto and six Paetahi units. This study has added an additional seven individual tephra units to these formations resulting in a total of twenty-eight tephra units (18 Poto and 10 Paetahi). The thickness and distribution of these units indicate that this period was dominated by large explosive subplinian single phase and multiphase eruptions. The Poto Formation is primarily composed of single-phase events, with multiphase events being preserved in two eruptive episodes. Compared to the Poto Formation, multiphase events within the Paetahi Formation dominate the depositional sequence. These multiphase events consist of three eruptive episodes which are generally less consolidated and with coarser grained deposits in comparison with other depositional units within the formation. The age of these deposits (23.1-27.3 ka) during the Last Glacial Maxima means that the proximal data has been eroded and is missing, therefore all the eruptive parameters calculated are minimum values. Isopach and isopleths fit to the present-day summit vent location and individual volumes, column heights, magnitudes, and mass eruption rates were calculated. Throughout this eruptive period a minimum of ~ 3 km^3 of material was erupted with individual tephra volumes ranging between 0.01 to 0.26 km^3 and column heights varying between 10-20 km. Mass eruption rates vary between 10^6 to 10^8 kg/s resulting in magnitudes of 3 to 4.5.
2. Investigations into the compositional variation of depositional units from the Poto and Paetahi Formations was conducted in Chapter 3 and indicates that changes in conduit geometry were occurring throughout this eruptive period. Lithic dominated units indicates that the conduit was widening through ascending magma excavating sections of the conduit wall. Juvenile

dominated units reflect stable conduit conditions where magma fragmentation was dominant allowing gas flow pathways to easily form throughout the system.

3. Vesicle size distributions of pumice clasts within the Poto and Paetahi Formations examined in Chapter 4 indicate the small bubbles dominate measurements and percentages. This is reflected in the high vesicle number densities (VND) ($10^{15} – 10^{16}$ cm^{-1}) recorded throughout this eruptive period indicating that the fragmentation zone and the upper conduit was the dominant location for bubble nucleation and growth. Large, coalesced bubbles indicate an earlier onset of bubble nucleation lower within the system. Bubble coalescence only occurs within some units (e.g., Poto.d, h*, l.l, l.u, o and Paetahi. a.m, a.u, e.l, and e.m). Throughout the Poto and Paetahi eruptive period variations between bubble nucleation and growth correlate with phases of magma injection and storage indicated by single stage nucleation and coalescence.
4. The influence of edifice collapse on the magmatic system is seen within the deposits predating and postdating the Ngaere Formation collapse event within Chapter 4. Sector collapse removed ~1000 m of height and 5.85 km^3 of material from the eastern side of Mt. Taranaki. Height causing the sudden decompression of a porous magma resulting in magma over pressurization and the generation of a fragmentation front down through the magma. This resulted in a lower VND and higher percentage of large, coalesced bubbles present within the pumice clasts. In relation to the current massif, the large Ngaere Formation collapse event would have produced a significant scarp towards the eastern/southeastern sectors of Mt. Taranaki and likely shifted the conduit (vent) to this location. This vent shift coupled with climatic changes during the last glacial maximum meant subsequent eruptive activity became directed towards the eastern and southeastern ring plain. Fluctuations in column height, magnitude, composition, and VNDs following the collapse is typical of a rebuilding phase (Watt, 2019). The Pungarehu collapse removed the western side of Mt. Taranaki ~ 2.5 kyr after the Ngaere removing another > 7.5 km^3 of material. Changes to the magmatic system and subsequent eruptive products are not observed following the Pungarehu Formation collapse event as compared to those post the Ngaere Formation collapse event. Instead, the results show that there is an increase in VND following the Pungarehu Formation debris avalanche as the height of the volcano had already been removed and Mt. Taranaki had not yet rebuilt the ~1000 m of additional elevation and ~5.85 km^3 it had prior to the Ngaere Formation collapse event. This indicates that the upper conduit system was not directly affected by the Pungarehu Formation collapse event.
5. The geochemical analysis in Chapter 5 obtained from pumice clasts within the Poto and Paetahi Formations eruptive show an evolution of the magmatic system throughout this period (4,000 yrs), as the mid- to upper magmatic system reestablished as the edifice rebuilt. Analysis of the whole rock compositions showed intermediate to heavy weathering of samples with LOIs ranging from 3.27 to 9.94 %. This level of weathering is expected for primary fall deposits emplaced over 20,000 years ago. The MgO compositions (Chapter 5; Figure 5.3) show the

magmatic evolution of Mt. Taranaki throughout time, with the younger Paetahi Formation being more evolved than the older Poto Formation tephra's. This shows that the Pungarehu Formation collapse event during the Paetahi Formation did not start a new geochemical regrowth period as seen following the Ngaere Formation collapse. Instead, the Pungarehu Formation collapse occurred within the Ngaere regrowth period.

6. Entrainment of crystals from within crystal mush zones by ascending melts is common across all crystal populations throughout this eruptive period as evidenced by resorption and regrowth rims (Chapter 5; Figures 5.9 - 5.11). Disequilibrium between crystal rims and melt is observed in all but nine eruptive units dispersed throughout the sequence (Chapter 5; Figure 5.7). Thermobarometry and hygrometry analysis result in temperatures between 1024 – 1137 °C and H_2O concentrations between 1.7 to 6.9 wt.% associated with hot deep magmas ascending to the surface. The complex crystal structures reflect multiple periods of magma recharge into the system interacting with crystal mush zones.
7. The detailed stratigraphic analysis of the Poto and Paetahi Formations indicates more regular intervals of large explosive eruptions occurring during this eruptive period (Chapter 6) compared with younger (< 14.5 ka) Taranaki eruptive events (Turner et al., 2008a; Green et al., 2013; Damaschke, 2017). Currently the recurrence rate for large subplinian to plinian eruptions from Mt. Taranaki is one every 300 years for the < 5 ka eruptive record (Torres-Orozco et al., 2017b). Results from this study indicate that the recurrence rate of subplinian events was more common during the Poto and Paetahi Formations eruptive period with one event every ~ 190 years with individual eruptions lasting for longer than 1 to 2.5 hours. This eruptive period was likely coupled with smaller eruptive events where deposits have been eroded or buried by subsequent younger eruptive products.

7.2 Conclusion

Field analysis along with laboratory analytical techniques were combined to investigate the impact of edifice collapse events on the upper magmatic system and how this influences eruptive behaviour at a stratovolcano. Edifice failure events at Mt. Taranaki have been recorded at least fourteen times while studies into the cycles and changes around these collapses have previously focused on geomorphic features (Zernack et al., 2011) and secondary deposits (Zemeny, 2021). The 27.3 – 23.1 ka Poto and Paetahi Formations provided a unique opportunity to investigate the impact edifice collapse events have on the volcanic system through analysing primary fall deposits pre and post event.

The 27.3 ka Ngaere edifice collapse event removed 5.85 km^3 of material from the southeastern flanks of a fully grown (~2500 m) edifice, destabilizing the remnant cone. Eruptive products following the collapse events indicate a shift towards a more mafic magmatic composition through an increase in MgO wt.% (4.55 wt.%). Coupled with a decrease in vesicle number density (VND) (from 1.53 x 10^{16}

to 9.76 x 10^{15} cm^{-3}), the results indicate the collapse removed a large height/mass (~1000 m height and 5.85 km^3 mass) from the upper edifice and conduit. The increased percentage of large bubbles and decrease in VND within Poto.c lower following the collapse reflects the sudden decompression event producing a fragmentation front down through the system. This reduction in mass changed the lithostatic pressure on the magmatic system causing the deactivation of the mid – to – upper crustal system and allowed denser mafic magma to ascend to the surface.

Continued regrowth following the Ngaere collapse produced twenty-six eruptive events (the Poto and Paetahi Formations) distributed across the eastern and southeastern sectors of the ring plain. This spatial distribution indicates a change in the conduit location, with a migration towards the southeast into the Ngaere collapse scar. The regrowth of Mt. Taranaki during the Poto and Paetahi eruptive period saw an increase in the amount of large subplinian eruptions throughout this ~4, 000-year period in comparison to the < 5 ka eruptive history (Torres-Orozco et al., 2017b). Eruptive frequencies for the Poto and Paetahi eruptive period indicates a large subplinian episode every ~190 years with events becoming more regular following the Ngaere collapse event. The Paetahi Formation (3.03 – 4.0 wt.% MgO) is more evolved than the Poto Formation (3.71 – 5.19 wt.% MgO), the latter of which has a wider geochemical compositional range. This suggests re-activation of the mid – to – upper crustal system as the lithostatic pressure increased following continued regrowth. Reactivation of the crustal system resulted in more magma mixing as the increased surface load inhibited the ascent of denser mafic magma to the surface. The high percentage of small bubbles, VNDs, and oscillatory crystal textures within juvenile eruptives along with the disequilibrium between crystals and melt suggests that mafic recharge into the system was triggering eruptive events, with magma ascending quickly to the surface with little stalling occurring. This is also supported by the low percentage of large bubbles present within the pumice clasts, showing that the magma had not been stalled for long within the upper crustal zone and that the main location of bubble nucleation was within the upper conduit, occurring seconds before the explosive event.

Cycles of bubble nucleation events indicate that not all the magma in a recharge event was erupted at once, the presence of single stage nucleation reflects magma rising quickly, however subsequent eruptive events followed with various stages of nucleation. This may be explained by stalled magma in the crustal system from previous recharge events being carried to the surface by the next recharge event that triggers an eruption. Continued cycles indicate multiple periods of magma influx also reflected in the absorption and regrowth zones of plagioclase and pyroxene rims. Changes in the compositional variation of deposits throughout the Poto and Paetahi Formations show changing percentages of juvenile and lithic dominated eruptions indicating that throughout the eruptive period systematic conduit widening was occurring periodically throughout the system as the conduit rebuilt.

The western side of the unstable remnant cone collapsed ~2,500 years later, producing the large 7.5 km^3 Pungarehu debris-avalanche deposit. Eruptive products following this collapse indicate a continued evolution in magmatic composition (3.14 wt.% MgO), an increase in VND (from 1.15 $x10^{16}$ to $1.29x10^{16}$ cm^{-3}) and an increase in the percentage of small bubbles within the pumice clasts. This shows that the upper conduit and lithostatic pressure on the magmatic system were not impacted by this collapse event. This may be attributed to the short time period between the Ngaere and Pungarehu collapse events that did not allow Mt. Taranaki to re-establish its height and lithostatic pressure. This resulted in no depressurization event occurring following the Pungarehu collapse, allowing the continued re-establishment of the mid – to – upper crustal system and growth within the Ngaere regrowth cycle.

Decreased lithostatic pressure caused by removal of the edifice allowed for enhanced magma ascent. This increased the regularity of explosive subplinian events between 27.3-23.1 ka. The variation in eruptive products following the Ngaere collapse reflects a relationship between edifice height, lithostatic pressure and the magmatic system. However, a similar change did not occur following the Pungarehu event. This study highlights that the edifice height governs the magmatic response rather than volume of a collapse. Using Mt. Taranaki as a case study; this research shows how the collapse of a ~2500 m edifice can de-activate the mid-to-upper magmatic system and allow denser mafic magma to ascend. This increased the frequency of large explosive eruptions as magma ascended freely without the inhibition of surface load. Understanding changes in eruptive processes following morphological changes (e.g., collapse events) will improve future hazard scenarios globally for volcanoes prone to collapse.

7.3 Future Work

This study produces new insights into the relationship between eruptive behaviour and magmatic evolution following a collapse event and the subsequent regrowth cycle. Future research could help significantly improve our knowledge of the long-term evolution of stratovolcanoes and a more accurate understanding of future hazards from Mt. Taranaki and other stratovolcanoes globally that are susceptible to collapse.

1. Changes to the conduit conditions throughout this eruptive period have been studied in detail with respect to componentry, and bubble nucleation and growth from erupted pumice clasts. Melt inclusion analysis to investigate the volatile content of the magmatic system would add to the understanding of changes occurring in the upper magmatic system from eruptive material before and after collapse events to enhance the accuracy of conduit models.
2. Complex crystal zoning has been identified in both plagioclase and pyroxene crystals throughout the Poto and Paetahi Formations indicating the presence of a crystal mush zone and repeated magma recharge events triggering eruptions. More in depth analysis of crystal rims

and melt coupled with elemental mapping of crystal grains and diffusion modelling would allow for calculations of more precise timescales of magmatic processes occurring below Mt. Taranaki.

3. The Poto and Paetahi Formations have been previously dated by (Alloway et al., 1995) through their relative stratigraphic location to the Ngaere DAD, Kawakawa-Oruanui tephra and paleosols situated between depositional tephra units. If zircons can be identified within the tephra, then this provides for the chance to constrain the age of individual tephra units and eruptive events. This would improve the calculation of recurrence rates for these large subplinian eruptions.
4. This study correlated distal tephra's across the eastern and southeastern ring plain. Additional field work across the western and southwestern ring plain coupled with sediment cores from both the eastern and western sectors could improve and better confirm the stratigraphic correlations made in this study.
5. The increased eruptive frequency for large explosive eruptions and changes in the regularity of events surrounding large edifice collapses have been calculated in this study. This study also highlights that long-term volcanic histories should be considered when quantifying hazard and risk around long-lived volcanoes. This dataset could be developed as a standard model of future hazard scenarios for stratovolcanoes.
6. The distribution of the Poto and Paetahi tephra formations differs to that of the younger Taranaki eruptive periods where the prevailing westerly wind has distributed Holocene tephras across the eastern and northeastern sectors of the ring plain. Modelling by (Weir et al., 2022) shows that large explosive eruptions from Mt. Taranaki can distribute tephra across the southeastern sector under modern day wind patterns. Exploring the eruptive parameters calculated during this study and applying these parameters as inputs into computational simulations will enhance modelled forecasts applied as future hazard scenarios at Mt. Taranaki. These scenarios could also be applied as an analogue for hazard analysis at similar volcanoes around the globe.

References

Abdurachman, E. K., Bourdier, J. L., & Voight, B. (2000). Nuées ardentes of 22 November 1994 at Merapi volcano, Java, Indonesia. *Journal of Volcanology and Geothermal Research, 100*(1), 345-361. https://doi.org/https://doi.org/10.1016/S0377-0273(00)00144-X

Adams, N. K., Houghton, B. F., & Hildreth, W. (2006a). Abrupt transitions during sustained explosive eruptions: examples from the 1912 eruption of Novarupta, Alaska. *Bulletin of Volcanology, 69*(2), 189-206. https://doi.org/10.1007/s00445-006-0067-4

Adams, N. K., Houghton, B. F., Fagents, S. A., & Hildreth, W. (2006b). The transition from explosive to effusive eruptive regime: The example of the 1912 Novarupta eruption, Alaska. *GSA Bulletin, 118*(5-6), 620-634. https://doi.org/10.1130/b25768.1

Adams, R. D., & Ware, D. E. (1977). Subcrustal earthquakes beneath New Zealand; Locations determined with a laterally inhomogeneous velocity model. *New Zealand Journal of Geology and Geophysics, 20*(1), 59-83. https://doi.org/10.1080/00288306.1977.10431592

Agostini, C., Fortunati, A., Arzilli, F., Landi, P., & Carroll, M. R. (2013). Kinetics of crystal evolution as a probe to magmatism at Stromboli (Aeolian Archipelago, Italy). *Geochimica et cosmochimica acta, 110*, 135-151. https://doi.org/https://doi.org/10.1016/j.gca.2013.02.027

Alatorre-Ibargüengoitia, M. A., Scheu, B., & Dingwell, D. B. (2011). Influence of the fragmentation process on the dynamics of Vulcanian eruptions: An experimental approach. *Earth and planetary science letters, 302*(1), 51-59. https://doi.org/https://doi.org/10.1016/j.epsl.2010.11.045

Alatorre-Ibargüengoitia, M. A., Delgado-Granados, H., & Dingwell, D. B. (2012). Hazard map for volcanic ballistic impacts at Popocatépetl volcano (Mexico). *Bulletin of Volcanology, 74*(9), 2155-2169. https://doi.org/10.1007/s00445-012-0657-2

Alidibirov, M., & Dingwell, D. B. (1996). An experimental facility for the investigation of magma fragmentation by rapid decompression. *Bulletin of Volcanology, 58*, 411-416. https://doi.org/10.1007/s004450050149

Alidibirov, M., & Dingwell, D. B. (2000). Three fragmentation mechanisms for highly viscous magma under rapid decompression. *Journal of Volcanology and Geothermal Research, 100*(1), 413-421. https://doi.org/https://doi.org/10.1016/S0377-0273(00)00149-9

Alidibirov, M. A. (1994). A model for viscous magma fragmentation during volcanic blasts. *Bulletin of Volcanology, 56*(6), 459-465. https://doi.org/10.1007/BF00302827

Allan, A. S. R., Baker, J. A., Carter, L., & Wysoczanksi, R. J. (2008). Reconstructing the Quaternary evolution of the world's most active silicic volcanic system: insights from an ~1.65Ma deep ocean tephra record sourced from Taupo Volcanic Zone, New Zealand. *Quaternary Science Reviews, 27*(25), 2341-2360. https://doi.org/https://doi.org/10.1016/j.quascirev.2008.09.003

Allan, A. S. R., Morgan, D. J., Wilson, C. J. N., & Millet, M.-A. (2013). From mush to eruption in centuries: assembly of the super-sized Oruanui magma body. *Contributions to Mineralogy and Petrology, 166*(1), 143-164. https://doi.org/10.1007/s00410-013-0869-2

Alloway, B., & Neall, V. (1994). Late Quaternary Volcaniclastic Stratigraphy of Central & North-east Taranaki. Briggs R and Moon V (eds) 1994 Annual Conference. Field Trip Guides, Geological Society of New Zealand Miscellaneous Publication B,

Alloway, B., Neall, V. E., & Vucetich, C. G. (1995). Late Quaternary (post 28,000 year B.P.) tephrostratigraphy of northeast and central Taranaki, New Zealand. *Journal of the Royal Society of New Zealand, 25*(4), 385-458. https://doi.org/10.1080/03014223.1995.9517496

Alloway, B., McComb, P., Neall, V., Vucetich, C., Gibb, J., Sherburn, S., & Stirling, M. (2005). Stratigraphy, age, and correlation of voluminous debris-avalanche events from an ancestral Egmont Volcano: Implications for coastal plain construction and regional hazard assessment. *Journal of the Royal Society of New Zealand, 35*(1-2), 229-267. https://doi.org/10.1080/03014223.2005.9517782

Alloway, B. V. (1989). *The late quaternary cover bed stratigraphy and tephrochronology of north-eastern and central Taranaki, New Zealand: a thesis presented in partial fulfullment of the requirements for the degree of Doctor of philosophy in soil science at Massey University, Palmerston North, New Zealand* Massey University].

Alloway, B. V., McGlone, M. S., Neall, V. E., & Vucetich, C. G. (1992). The role of Egmont-sourced tephra in evaluating the paleoclimatic correspondence between the bio- and soil-stratigraphic records of central Taranaki, New Zealand. *Quaternary international, 13-14*, 187-194. https://doi.org/https://doi.org/10.1016/1040-6182(92)90027-Y

Alpízar Segura, Y., Fernández Arce, M., Ramírez Umaña, C., & Arroyo Alpízar, D. (2019). Hazard Map of Rincón de la Vieja Volcano, Costa Rica: Qualitative Integration of Computer Simulations and Geological Data. *Anuario do Instituto de Geociencias, 42*(3).

Andújar, J., & Scaillet, B. (2012). Experimental Constraints on Parameters Controlling the Difference in the Eruptive Dynamics of Phonolitic Magmas: the Case of Tenerife (Canary Islands). *Journal of Petrology, 53*(9), 1777-1806. https://doi.org/10.1093/petrology/egs033

Annen, C., Blundy, J. D., & Sparks, R. S. J. (2006). The Genesis of Intermediate and Silicic Magmas in Deep Crustal Hot Zones. *Journal of Petrology, 47*(3), 505-539. https://doi.org/10.1093/petrology/egi084

Annen, C., Blundy, J. D., Leuthold, J., & Sparks, R. S. J. (2015). Construction and evolution of igneous bodies: Towards an integrated perspective of crustal magmatism. *Lithos, 230*, 206-221. https://doi.org/https://doi.org/10.1016/j.lithos.2015.05.008

Aravena, Á., Cioni, R., de'Michieli Vitturi, M., & Neri, A. (2018). Conduit stability effects on intensity and steadiness of explosive eruptions. *Scientific reports, 8*(1), 4125. https://doi.org/10.1038/s41598-018-22539-8

Arce, J., Cervantes, K., Macías, J., & Mora, J. (2005). The 12.1 ka Middle Toluca Pumice: A dacitic Plinian–subplinian eruption of Nevado de Toluca in central Mexico. *Journal of Volcanology and Geothermal Research, 147*(1-2), 125-143.

Arculus, R. J., & Powell, R. (1986). Source component mixing in the regions of arc magma generation. *Journal of Geophysical Research, 91*, 5913-5926. https://doi.org/10.1029/JB091iB06p05913

Armienti, P., Francalanci, L., & Landi, P. (2007). Textural effects of steady state behaviour of the Stromboli feeding system. *Journal of Volcanology and Geothermal Research, 160*(1), 86-98. https://doi.org/https://doi.org/10.1016/j.jvolgeores.2006.05.004

Bachmann, O., & Huber, C. (2016). Silicic magma reservoirs in the Earth's crust. *American Mineralogist, 101*(11), 2377-2404. https://doi.org/doi:10.2138/am-2016-5675

Baker, D. R., Mancini, L., Polacci, M., Higgins, M. D., Gualda, G., Hill, R., & Rivers, M. (2012). An introduction to the application of X-ray microtomography to the three-dimensional study of igneous rocks. *Lithos, 148*, 262-276.

Ballance, P. F., Pettinga, J. R., & Webb, C. (1982). A model of the Cenozoic evolution of northern New Zealand and adjacent areas of the southwest Pacific. *Tectonophysics, 87*(1), 37-48. https://doi.org/https://doi.org/10.1016/0040-1951(82)90220-7

Barberi, F., Macedonio, G., Pareschi, M. T., & Santacroce, R. (1990). Mapping the tephra fallout risk: an example from Vesuvius, Italy. *Nature, 344*(6262), 142-144. https://doi.org/10.1038/344142a0

Barclay, J., Riley, D. S., & Sparks, R. S. J. (1995). Analytical models for bubble growth during decompression of high viscosity magmas. *Bulletin of Volcanology, 57*(6), 422-431. https://doi.org/10.1007/BF00300986

Baxter, P. J., Boyle, R., Cole, P., Neri, A., Spence, R., & Zuccaro, G. (2005). The impacts of pyroclastic surges on buildings at the eruption of the Soufrière Hills volcano, Montserrat. *Bulletin of Volcanology, 67*(4), 292-313. https://doi.org/10.1007/s00445-004-0365-7

Beavan, J., Tregoning, P., Bevis, M., Kato, T., & Meertens, C. (2002). Motion and rigidity of the Pacific Plate and implications for plate boundary deformation. *Journal of Geophysical Research (Solid Earth), 107*, 2261. https://doi.org/10.1029/2001jb000282

Bebbington, M. S., & Lai, C. D. (1996). On nonhomogeneous models for volcanic eruptions. *Mathematical Geology, 28*(5), 585-600. https://doi.org/10.1007/BF02066102

Bebbington, M. S., & Jenkins, S. F. (2019). Intra-eruption forecasting. *Bulletin of Volcanology, 81*(6), 34. https://doi.org/10.1007/s00445-019-1294-9

Bebbington, M. S., Stirling, M. W., Cronin, S., Wang, T., & Jolly, G. (2018). National-level long-term eruption forecasts by expert elicitation. *Bulletin of Volcanology, 80*(6), 56. https://doi.org/10.1007/s00445-018-1230-4

Becker, J., Saunders, W., Robertson, C., Leonard, G., & Johnston, D. (2010). A synthesis of challenges and opportunities for reducing volcanic risk through land use planning in New Zealand. *The Australasian Journal of Disaster and Trauma Studies. ISSN*, 1174-4707.

Begét, J. E., & Kienle, J. (1992). Cyclic formation of debris avalanches at Mount St Augustine volcano. *Nature, 356*(6371), 701-704. https://doi.org/10.1038/356701a0

Behn, M. D., Kelemen, P. B., Hirth, G., Hacker, B. R., & Massonne, H.-J. (2011). Diapirs as the source of the sediment signature in arc lavas. *Nature Geoscience, 4*(9), 641-646. https://doi.org/10.1038/ngeo1214

Belien, I. B., Cashman, K. V., & Rempel, A. W. (2010). Gas accumulation in particle-rich suspensions and implications for bubble populations in crystal-rich magma. *Earth and planetary science letters, 297*(1), 133-140. https://doi.org/https://doi.org/10.1016/j.epsl.2010.06.014

Belousov, A., Belousova, M., & Voight, B. (1999). Multiple edifice failures, debris avalanches and associated eruptions in the Holocene history of Shiveluch volcano, Kamchatka, Russia. *Bulletin of Volcanology, 61*(5), 324-342. https://doi.org/10.1007/s004450050300

Belousov, A., Voight, B., & Belousova, M. (2007). Directed blasts and blast-generated pyroclastic density currents: a comparison of the Bezymianny 1956, Mount St Helens 1980, and Soufrière Hills, Montserrat 1997 eruptions and deposits. *Bulletin of Volcanology, 69*(7), 701-740. https://doi.org/10.1007/s00445-006-0109-y

Belousov, A. B. (1995). The Shiveluch volcanic eruption of 12 November 1964—explosive eruption provoked by failure of the edifice. *Journal of Volcanology and Geothermal Research, 66*(1), 357-365. https://doi.org/https://doi.org/10.1016/0377-0273(94)00072-O

Bennett, E. N., Lissenberg, C. J., & Cashman, K. V. (2019). The significance of plagioclase textures in mid-ocean ridge basalt (Gakkel Ridge, Arctic Ocean). *Contributions to Mineralogy and Petrology, 174*(6), 49. https://doi.org/10.1007/s00410-019-1587-1

Berg, S. E., Troll, V. R., Deegan, F. M., Burchardt, S., Krumbholz, M., Mancini, L., Polacci, M., Carracedo, J. C., Soler, V., Arzilli, F., & Brun, F. (2016). Heterogeneous vesiculation of 2011 El Hierro xeno-pumice revealed by X-ray computed microtomography. *Bulletin of Volcanology, 78*(12), 85. https://doi.org/10.1007/s00445-016-1080-x

Bergman S, C. (1992). The Kola Miocene submarine andesite stratovolcano hydrocarbon reservoir, northern Taranaki Basin, New Zealand. *Proc. 1991 New Zealand Oil Expl. Conf.*, 178-206. https://cir.nii.ac.jp/crid/1571980074486637312

Berlo, K., Blundy, J., Turner, S., & Hawkesworth, C. (2007). Textural and chemical variation in plagioclase phenocrysts from the 1980 eruptions of Mount St. Helens, USA. *Contributions to Mineralogy and Petrology, 154*(3), 291-308. https://doi.org/10.1007/s00410-007-0194-8

Bernard, B., Takarada, S., Andrade, S. D., & Dufresne, A. (2021). Terminology and Strategy to Describe Large Volcanic Landslides and Debris Avalanches. In *Volcanic Debris Avalanches* (pp. 51-73). Springer.

Bertagnini, A., & Landi, P. (1996). The Secche di Lazzaro pyroclastics of Stromboli volcano: a phreatomagmatic eruption related to the Sciara del Fuoco sector collapse. *Bulletin of Volcanology, 58*(2), 239-245. https://doi.org/10.1007/BF03395970

Bevis, M., Taylor, F. W., Schutz, B. E., Recy, J., Isacks, B. L., Helu, S., Singh, R., Kendrick, E., Stowell, J., Taylor, B., & Calmantli, S. (1995). Geodetic observations of very rapid convergence and back-arc extension at the Tonga arc. *Nature, 374*(6519), 249-251. https://doi.org/10.1038/374249a0

Blackburn, E. A., Wilson, L., & Sparks, R. S. J. (1976). Mechanisms and dynamics of strombolian activity. *Journal of the Geological Society, 132*, 429-440. https://doi.org/10.1144/gsjgs.132.4.0429

Blair, T. C. (2000). Sedimentology and progressive tectonic unconformities of the sheetflood-dominated Hell's Gate alluvial fan, Death Valley, California. *Sedimentary Geology, 132*(3), 233-262. https://doi.org/https://doi.org/10.1016/S0037-0738(00)00010-5

Blair, T. C., & McPherson, J. G. (1994). Alluvial fans and their natural distinction from rivers based on morphology, hydraulic processes, sedimentary processes, and facies assemblages. *Journal of*

sedimentary research, 64(3a), 450-489. https://doi.org/10.1306/d4267dde-2b26-11d7-8648000102c1865d

Blott, S. J., & Pye, K. (2001). GRADISTAT: a grain size distribution and statistics package for the analysis of unconsolidated sediments. *Earth surface processes and Landforms, 26*(11), 1237-1248.

Blower, J. D., Keating, J. P., Mader, H. M., & Phillips, J. C. (2003). The evolution of bubble size distributions in volcanic eruptions. *Journal of Volcanology and Geothermal Research, 120*(1), 1-23. https://doi.org/https://doi.org/10.1016/S0377-0273(02)00404-3

Blundy, J., & Cashman, K. (2008). Petrologic Reconstruction of Magmatic System Variables and Processes. *Reviews in Mineralogy and Geochemistry, 69*(1), 179-239. https://doi.org/10.2138/rmg.2008.69.6

Boddington, T., Parkin, C. J., & Gubbins, D. (2004). Isolated deep earthquakes beneath the North Island of New Zealand. *Geophysical Journal International, 158*(3), 972-982. https://doi.org/10.1111/j.1365-246X.2004.02340.x

Boggs, S. (2012). Principles of sedimentology and stratigraphy.

Bonadonna, C. (2006). Probabilistic modelling of tephra dispersion. In H. M. Mader, S. G. Coles, C. B. Connor, & L. J. Connor (Eds.), *Statistics in Volcanology* (Vol. 1, pp. 0). Geological Society of London. https://doi.org/10.1144/iavcei001.19

Bonadonna, C., & Houghton, B. F. (2005). Total grain-size distribution and volume of tephra-fall deposits. *Bulletin of Volcanology, 67*(5), 441-456. https://doi.org/10.1007/s00445-004-0386-2

Bonadonna, C., & Costa, A. (2012). Estimating the volume of tephra deposits: A new simple strategy. Geology, 40(5), 415-418. https://doi.org/10.1130/g32769.1

Bonadonna, C., & Costa, A. (2013a). Plume height, volume, and classification of explosive volcanic eruptions based on the Weibull function. *Bulletin of Volcanology, 75*(8), 742. https://doi.org/10.1007/s00445-013-0742-1

Bonadonna, C., & Costa, A. (2013b). Plume height, volume, and classification of explosive volcanic eruptions based on the Weibull function. *Bulletin of Volcanology, 75*(8), 1-19.

Bonadonna, C., Ernst, G. G. J., & Sparks, R. S. J. (1998). Thickness variations and volume estimates of tephra fall deposits: the importance of particle Reynolds number. *Journal of Volcanology and Geothermal Research, 81*(3), 173-187. https://doi.org/https://doi.org/10.1016/S0377-0273(98)00007-9

Botcharnikov, R. E., Almeev, R. R., Koepke, J., & Holtz, F. (2008). Phase Relations and Liquid Lines of Descent in Hydrous Ferrobasalt—Implications for the Skaergaard Intrusion and Columbia River Flood Basalts. *Journal of Petrology, 49*(9), 1687-1727. https://doi.org/10.1093/petrology/egn043

Boudon, G., Villemant, B., Friant, A. L., Paterne, M., & Cortijo, E. (2013). Role of large flank-collapse events on magma evolution of volcanoes. Insights from the Lesser Antilles Arc. *Journal of Volcanology and Geothermal Research, 263*, 224-237. https://doi.org/https://doi.org/10.1016/j.jvolgeores.2013.03.009

Boulesteix, T., Hildenbrand, A., Gillot, P.-Y., & Soler, V. (2012). Eruptive response of oceanic islands to giant landslides: New insights from the geomorphologic evolution of the Teide–Pico Viejo volcanic complex (Tenerife, Canary). *Geomorphology, 138*(1), 61-73. https://doi.org/https://doi.org/10.1016/j.geomorph.2011.08.025

Bourdier, J. L., Boudon, G., & Gourgaud, A. (1989). Stratigraphy of the 1902 and 1929 nuée-ardente deposits, Mt. Pelée, Martinique. *Journal of Volcanology and Geothermal Research, 38*(1), 77-96. https://doi.org/https://doi.org/10.1016/0377-0273(89)90031-0

Bouvet de Maisonneuve, C., Bachmann, O., & Burgisser, A. (2009). Characterization of juvenile pyroclasts from the Kos Plateau Tuff (Aegean Arc): insights into the eruptive dynamics of a large rhyolitic eruption. *Bulletin of Volcanology, 71*(6), 643-658. https://doi.org/10.1007/s00445-008-0250-x

Bowen, N. L. (1928). *The evolution of the igneous rocks*. Princeton University Press.

Branson, O., Fehrenbacher, J. S., Vetter, L., Sadekov, A. Y., Eggins, S. M., & Spero, H. J. (2019). LAtools: A data analysis package for the reproducible reduction of LA-ICPMS data. *Chemical Geology, 504*, 83-95. https://doi.org/https://doi.org/10.1016/j.chemgeo.2018.10.029

Briggs, R. M. (1986). Volcanic rocks of the Waikato region, western North Island, and some possible petrologic and tectonic constraints on their origin [Article]. *Late Cenozoic Volcanism in New Zealand, Vol. 23*, 76-91. https://www.scopus.com/inward/record.uri?eid=2-s2.0-0022887293&partnerID=40&md5=9e75a65d5ac2fe0ecb551bc7a2182a09

Briggs, R. M., & McDonough, W. F. (1990). Contemporaneous Convergent Margin and Intraplate Magmatism, North Island, New Zealand. *Journal of Petrology, 31*(4), 813-851. https://doi.org/10.1093/petrology/31.4.813

Brown, S. K., Crosweller, H. S., Sparks, R. S. J., Cottrell, E., Deligne, N. I., Guerrero, N. O., Hobbs, L., Kiyosugi, K., Loughlin, S. C., Siebert, L., & Takarada, S. (2014). Characterisation of the Quaternary eruption record: analysis of the Large Magnitude Explosive Volcanic Eruptions (LaMEVE) database. *Journal of Applied Volcanology, 3*(1), 5. https://doi.org/10.1186/2191-5040-3-5

Browne, B. L., Eichelberger, J. C., Patino, L. C., Vogel, T. A., Dehn, J., Uto, K., & Hoshizumi, H. (2005). Generation of Porphyritic and Equigranular Mafic Enclaves During Magma Recharge Events at Unzen Volcano, Japan. *Journal of Petrology, 47*(2), 301-328. https://doi.org/10.1093/petrology/egi076

Burgisser, A., & Gardner, J. E. (2004). Experimental constraints on degassing and permeability in volcanic conduit flow. *Bulletin of Volcanology, 67*(1), 42-56. https://doi.org/10.1007/s00445-004-0359-5

Bursik, M. (1993). Subplinian eruption mechanisms inferred from volatile and clast dispersal data. *Journal of Volcanology and Geothermal Research, 57*(1), 57-70. https://doi.org/https://doi.org/10.1016/0377-0273(93)90031-L

Bussell, M. R., & Pillans, B. (1992). Vegetational and climatic history during oxygen isotope stage 9, Wanganui district, New Zealand, and correlation of the Fordell Ash. *Journal of the Royal Society of New Zealand, 22*(1), 41-60. https://doi.org/10.1080/03036758.1992.10420816

Calder, E., Wagner, K., & Ogburn, S. (2015). Volcanic hazard maps. *Global volcanic hazards and risk*, 335-342.

Campbell, M. E., Russell, J. K., & Porritt, L. A. (2013). Thermomechanical milling of accessory lithics in volcanic conduits. *Earth and planetary science letters, 377-378*, 276-286. https://doi.org/https://doi.org/10.1016/j.epsl.2013.07.008

Canuti, P., Casagli, N., Catani, F., & Falorni, G. (2002). Modeling of the Guagua Pichincha volcano (Ecuador) lahars. *Physics and Chemistry of the Earth, Parts A/B/C, 27*(36), 1587-1599. https://doi.org/https://doi.org/10.1016/S1474-7065(02)00180-8

Capra, L., & Macías, J. L. (2002). The cohesive Naranjo debris-flow deposit (10 km3):: A dam breakout flow derived from the Pleistocene debris-avalanche deposit of Nevado de Colima Volcano (México). *Journal of Volcanology and Geothermal Research, 117*(1), 213-235. https://doi.org/https://doi.org/10.1016/S0377-0273(02)00245-7

Capra, L., Macías, J. L., Scott, K. M., Abrams, M., & Garduño-Monroy, V. H. (2002). Debris avalanches and debris flows transformed from collapses in the Trans-Mexican Volcanic Belt, Mexico – behavior, and implications for hazard assessment. *Journal of Volcanology and Geothermal Research, 113*(1), 81-110. https://doi.org/https://doi.org/10.1016/S0377-0273(01)00252-9

Caracciolo, A., Bali, E., Guðfinnsson, G. H., Kahl, M., Halldórsson, S. A., Hartley, M. E., & Gunnarsson, H. (2020). Temporal evolution of magma and crystal mush storage conditions in the Bárðarbunga-Veiðivötn volcanic system, Iceland. *Lithos, 352-353*, 105234. https://doi.org/https://doi.org/10.1016/j.lithos.2019.105234

Carey, R. J., & Houghton, B. F. (2010). "Inheritance": An influence on the particle size of pyroclastic deposits. *Geology, 38*(4), 347-350. https://doi.org/10.1130/g30573.1

Carey, R. J., Houghton, B. F., & Thordarson, T. (2009). Abrupt shifts between wet and dry phases of the 1875 eruption of Askja Volcano: Microscopic evidence for macroscopic dynamics. *Journal of Volcanology and Geothermal Research, 184*(3), 256-270. https://doi.org/https://doi.org/10.1016/j.jvolgeores.2009.04.003

Carey, S., & Sigurdsson, H. (1985). The May 18, 1980 eruption of Mount St. Helens: 2. Modeling of dynamics of the Plinian Phase. *Journal of Geophysical Research, 90*, 2948-2958. https://doi.org/10.1029/JB090iB04p02948

Carey, S., & Sparks, R. S. J. (1986). Quantitative models of the fallout and dispersal of tephra from volcanic eruption columns. *Bulletin of Volcanology, 48*(2), 109-125. https://doi.org/10.1007/BF01046546

Carey, S., & Sigurdsson, H. (1987). Temporal variations in column height and magma discharge rate during the 79 A.D. eruption of Vesuvius. *GSA Bulletin, 99*(2), 303-314. https://doi.org/10.1130/0016-7606(1987)99<303:Tvicha>2.0.Co;2

Carey, S., & Sigurdsson, H. (1989). The intensity of plinian eruptions. *Bulletin of Volcanology, 51*(1), 28-40. https://doi.org/10.1007/BF01086759

Caricchi, L., Burlini, L., Ulmer, P., Gerya, T., Vassalli, M., & Papale, P. (2007). Non-Newtonian rheology of crystal-bearing magmas and implications for magma ascent dynamics. *Earth and planetary science letters, 264*(3), 402-419. https://doi.org/https://doi.org/10.1016/j.epsl.2007.09.032

Caricchi, L., Pommier, A., Pistone, M., Castro, J., Burgisser, A., & Perugini, D. (2011). Strain-induced magma degassing: insights from simple-shear experiments on bubble bearing melts. *Bulletin of Volcanology, 73*, 1245-1257.

Carman, J. (2023). *Forecasting Future Eruptions using Hierarchical Renewal, and Trend Renewal Processes* University of Otago].

Carn, S. A., Zogorski, J. S., Lara, L., Ewert, J. W., Watt, S., Prata, A. J., Thomas, R. J., & Villarosa, G. (2009). The unexpected awakening of Chaitén Volcano, Chile. *Eos, Transactions, American Geophysical Union, 90*(24), 205-206. https://doi.org/10.1029/2009EO240001

Carracedo, J. C. (1994). The Canary Islands: An example of structural control on the growth of large oceanic-island volcanoes. *Journal of Volcanology and Geothermal Research, 60*(3), 225-241. https://doi.org/https://doi.org/10.1016/0377-0273(94)90053-1

Carracedo, J. C., Day, S. J., Guillou, H., & Pérez Torrado, F. J. (1999). Giant Quaternary landslides in the evolution of La Palma and El Hierro, Canary Islands. *Journal of Volcanology and Geothermal Research, 94*(1), 169-190. https://doi.org/https://doi.org/10.1016/S0377-0273(99)00102-X

Carracedo, J. C., Rodríguez Badiola, E., Guillou, H., Paterne, M., Scaillet, S., Pérez Torrado, F. J., Paris, R., Fra-Paleo, U., & Hansen, A. (2007). Eruptive and structural history of Teide Volcano and rift zones of Tenerife, Canary Islands [Article]. *Bulletin of the geological society of America, 119*(9-10), 1027-1051. https://doi.org/10.1130/B26087.1

Cas, R. A. F., & Wright, J. V. (1987). Volcanic Successions Modern and Ancient. *Volcanic Successions: Modern and Ancient.* https://doi.org/10.1007/978-94-009-3167-1

Cashman, K., & Blundy, J. (2000). Degassing and Crystallization of Ascending Andesite and Dacite. *Philosophical Transactions: Mathematical, Physical and Engineering Sciences, 358*(1770), 1487-1513. http://www.jstor.org/stable/2666925

Cashman, K., & Blundy, J. (2013). Petrological cannibalism: the chemical and textural consequences of incremental magma body growth. *Contributions to Mineralogy and Petrology, 166*(3), 703-729. https://doi.org/10.1007/s00410-013-0895-0

Cashman, K. V., & Scheu, B. (2015). Magmatic fragmentation. In H. Sigurdsson (Ed.), *The Encyclopedia of Volcanoes (Second Edition)* (pp. 459-471). Academic Press. https://doi.org/https://doi.org/10.1016/B978-0-12-385938-9.00025-0

Cashman, K. V., Sparks, R. S. J., & Blundy, J. D. (2017). Vertically extensive and unstable magmatic systems: A unified view of igneous processes. *Science, 355*(6331), eaag3055. https://doi.org/doi:10.1126/science.aag3055

Cashman, K. V. (2004). Volatile controls on magma ascent and eruption. *Geophysical Monograph Series, 150*, 109-124. https://doi.org/10.1029/150gm10

Cassidy, M., Manga, M., Cashman, K., & Bachmann, O. (2018). Controls on explosive-effusive volcanic eruption styles. *Nature Communications, 9*(1), 2839. https://doi.org/10.1038/s41467-018-05293-3

Cassidy, M., Edmonds, M., Watt, S. F. L., Palmer, M. R., & Gernon, T. M. (2015). Origin of Basalts by Hybridization in Andesite-dominated Arcs. *Journal of Petrology, 56*(2), 325-346. https://doi.org/10.1093/petrology/egv002

Cassidy, M., Taylor, R. N., Palmer, M. R., Cooper, R. J., Stenlake, C., & Trofimovs, J. (2012). Tracking the magmatic evolution of island arc volcanism: Insights from a high-precision Pb isotope record of Montserrat, Lesser Antilles. *Geochemistry, Geophysics, Geosystems, 13*, Q05003. https://doi.org/10.1029/2012gc004064

Cassidy, M., Watt, S. F. L., Talling, P. J., Palmer, M. R., Edmonds, M., Jutzeler, M., Wall-Palmer, D., Manga, M., Coussens, M., Gernon, T., Taylor, R. N., Michalik, A., Inglis, E., Breitkreuz, C., Le Friant,

A., Ishizuka, O., Boudon, G., McCanta, M. C., Adachi, T., Hornbach, M. J., Colas, S. L., Endo, D., Fujinawa, A., Kataoka, K. S., Maeno, F., Tamura, Y., & Wang, F. (2015). Rapid onset of mafic magmatism facilitated by volcanic edifice collapse [Article]. *Geophysical research letters, 42*(12), 4778-4785. https://doi.org/10.1002/2015GL064519

Castro, J. M., Cashman, K. V., & Manga, M. (2003). A technique for measuring 3D crystal-size distributions of prismatic microlites in obsidian. *American Mineralogist, 88*(8-9), 1230-1240. https://doi.org/10.2138/am-2003-8-906

Castro, J. M., Burgisser, A., Schipper, C. I., & Mancini, S. (2012). Mechanisms of bubble coalescence in silicic magmas. *Bulletin of Volcanology, 74*(10), 2339-2352. https://doi.org/10.1007/s00445-012-0666-1

CDEM, T. G. (2004). Taranaki civil Defence emergency management group volcanic strategy 2004. Taranaki Regional Council, Stratford.

Cioni, R., Sulpizio, R., & Garruccio, N. (2003). Variability of the eruption dynamics during a Subplinian event: the Greenish Pumice eruption of Somma–Vesuvius (Italy). *Journal of Volcanology and Geothermal Research, 124*(1), 89-114. https://doi.org/https://doi.org/10.1016/S0377-0273(03)00070-2

Cioni, R., Pistolesi, M., & Rosi, M. (2015). Plinian and subplinian eruptions. In H. Sigurdsson (Ed.), *The Encyclopedia of Volcanoes (Second Edition)* (pp. 519-535). Academic Press. https://doi.org/https://doi.org/10.1016/B978-0-12-385938-9.00029-8

Clarke, A. B., Voight, B., Neri, A., & Macedonio, G. (2002). Transient dynamics of vulcanian explosions and column collapse. *Nature, 415*(6874), 897-901. https://doi.org/10.1038/415897a

Clarke, A. B., Stephens, S., Teasdale, R., Sparks, R. S. J., & Diller, K. (2007). Petrologic constraints on the decompression history of magma prior to Vulcanian explosions at the Soufrière Hills volcano, Montserrat. *Journal of Volcanology and Geothermal Research, 161*(4), 261-274. https://doi.org/https://doi.org/10.1016/j.jvolgeores.2006.11.007

Clavero, J., Sparks, R., Huppert, H., & Dade, W. (2002). Geological constraints on the emplacement mechanism of the Parinacota debris avalanche, northern Chile. *Bulletin of Volcanology, 64*(1), 40-54. https://doi.org/10.1007/s00445-001-0183-0

Clayton, S. (2017). 3-D Geometry and kinematic evolution of the kupe inversion structure, southern taranaki basin, new zealand.

Clynne, M. A. (1999). A Complex Magma Mixing Origin for Rocks Erupted in 1915, Lassen Peak, California. *Journal of Petrology, 40*(1), 105-132. https://doi.org/10.1093/petroj/40.1.105

Clynne, M. A., Calvert, A. T., Wolfe, E. W., Evarts, R. C., Fleck, R. J., & Lanphere, M. A. (2008). *The Pleistocene eruptive history of Mount St. Helens, Washington, from 300,000 to 12,800 years before present* [Report](1750-28). (Professional Paper, Issue. U. S. G. Survey. https://pubs.usgs.gov/publication/pp175028

Cockell, C. S. (2011). Biological Volcanic Rock Weathering. In J. Reitner & V. Thiel (Eds.), *Encyclopedia of Geobiology* (pp. 143-147). Springer Netherlands. https://doi.org/10.1007/978-1-4020-9212-1_219

Cole, J., Graham, I., Hackett, W., & Houghton, B. (1986). Volcanology and petrology of the Quaternary composite volcanoes of Tongariro volcanic centre, Taupo volcanic zone. In *Late Cenozoic Volcanism in New Zealand* (Vol. 23, pp. 224-250). Royal Society of NZ Bulletin 23.

Cole, J. W. (1978). Andesites of the Tongariro volcanic centre, North Island, New Zealand. *Journal of Volcanology and Geothermal Research, 3*(1), 121-153. https://doi.org/https://doi.org/10.1016/0377-0273(78)90007-0

Cole, J. W., Darby, D. J., & Stern, T. A. (1995). Taupo Volcanic Zone and Central Volcanic Region Backarc Structures of North Island, New Zealand. In B. Taylor (Ed.), *Backarc Basins: Tectonics and Magmatism* (pp. 1-28). Springer US. https://doi.org/10.1007/978-1-4615-1843-3_1

Cole, P. D., Queiroz, G., Wallenstein, N., Gaspar, J. L., Duncan, A. M., & Guest, J. E. (1995). An historic subplinian/phreatomagmatic eruption: the 1630 AD eruption of Furnas volcano, Sa˜o Miguel, Azores. *Journal of Volcanology and Geothermal Research, 69*(1), 117-135. https://doi.org/https://doi.org/10.1016/0377-0273(95)00033-X

Coleman, D. S., Gray, W., & Glazner, A. F. (2004). Rethinking the emplacement and evolution of zoned plutons: Geochronologic evidence for incremental assembly of the Tuolumne Intrusive Suite, California. *Geology, 32*(5), 433-436. https://doi.org/10.1130/g20220.1

Coleman, R. D. (2018). *The Tectonic Evolution of Taranaki Basin, Offshore New Zealand* (Publication Number 10975053) [M.S., Colorado School of Mines]. ProQuest Dissertations & Theses A&I. United States -- Colorado.

Colombier, M., Gurioli, L., Druitt, T., Shea, T., Boivin, P., Miallier, D., & Cluzel, N. (2017). Textural evolution of magma during the 9.4-ka trachytic explosive eruption at Kilian Volcano, Chaîne des Puys, France. *Bulletin of Volcanology, 79*(2), 17.

Colombier, M., Scheu, B., Wadsworth, F. B., Cronin, S., Vasseur, J., Dobson, K. J., Hess, K.-U., Tost, M., Yilmaz, T. I., Cimarelli, C., Brenna, M., Ruthensteiner, B., & Dingwell, D. B. (2018). Vesiculation and Quenching During Surtseyan Eruptions at Hunga Tonga-Hunga Ha'apai Volcano, Tonga. *Journal of Geophysical Research (Solid Earth), 123*, 3762-3779. https://doi.org/10.1029/2017jb015357

Concha-Dimas, A., Cerca, M., Rodríguez, S. R., & Watters, R. J. (2005). Geomorphological evidence of the influence of pre-volcanic basement structure on emplacement and deformation of volcanic edifices at the Cofre de Perote–Pico de Orizaba chain and implications for avalanche generation. *Geomorphology, 72*(1), 19-39. https://doi.org/https://doi.org/10.1016/j.geomorph.2005.05.004

Connor C, B. (2001). Estimation of volcanic hazards from tephra fallout. *Natural Hazards Review, 2*, 33-42. https://cir.nii.ac.jp/crid/1571980074189142784

Coote, A. C., & Shane, P. (2016). Crystal origins and magmatic system beneath Ngauruhoe volcano (New Zealand) revealed by plagioclase textures and compositions. *Lithos, 260*, 107-119. https://doi.org/https://doi.org/10.1016/j.lithos.2016.05.017

Cortés, A., Macías, J. L., Capra, L., & Garduño-Monroy, V. H. (2010). Sector collapse of the SW flank of Volcán de Colima, México: The 3600yr BP La Lumbre–Los Ganchos debris avalanche and associated debris flows. *Journal of Volcanology and Geothermal Research, 197*(1), 52-66. https://doi.org/https://doi.org/10.1016/j.jvolgeores.2009.11.013

Cortés, A., Komorowski, J. C., Macías, J. L., Capra, L., & Layer, P. W. (2019). Late Pleistocene-Holocene Debris Avalanche Deposits from Volcán de Colima, Mexico. In N. Varley, C. B. Connor, & J.-C. Komorowski (Eds.), *Volcán de Colima: Portrait of a Persistently Hazardous Volcano* (pp. 55-79). Springer Berlin Heidelberg. https://doi.org/10.1007/978-3-642-25911-1_4

Costa, F., & Chakraborty, S. (2004). Decadal time gaps between mafic intrusion and silicic eruption obtained from chemical zoning patterns in olivine. *Earth and planetary science letters, 227*(3), 517-530. https://doi.org/https://doi.org/10.1016/j.epsl.2004.08.011

Costa, F., Shea, T., & Ubide, T. (2020). Diffusion chronometry and the timescales of magmatic processes. *Nature Reviews Earth & Environment, 1*(4), 201-214. https://doi.org/10.1038/s43017-020-0038-x

Coulter, J. D. (1976). Weather in Egmont National Park. *In: Fullarton, J. H. (ed.)*

Egmont National Park Handbook., 3rd ed, 51-55.

Crandell, D. R. (1971). Postglacial lahars from Mount Rainier volcano, Washington. *Professional Paper*.

Crandell, D. R., & Hoblitt, R. P. (1986). Lateral blasts at Mount St. Helens and hazard zonation. *Bulletin of Volcanology, 48*(1), 27-37. https://doi.org/10.1007/BF01073511

Crandell, D. R., Miller, C. D., Glicken, H. X., Christiansen, R. L., & Newhall, C. G. (1984). Catastrophic debris avalanche from ancestral Mount Shasta volcano, California. *Geology, 12*(3), 143-146. https://doi.org/10.1130/0091-7613(1984)12<143:Cdafam>2.0.Co;2

Cronin, S., Stewart, R., Neall, V., Platz, T., & Gaylord, D. (2003). The AD1040 to present Maero eruptive period of Egmont volcano, Taranaki, New Zealand. *Geol Soc NZ Misc Publ A, 116*, 43.

Cronin, S. J., Zernack, A. V., Ukstins, I. A., Turner, M. B., Torres-Orozco, R., Stewart, R. B., Smith, I. E. M., Procter, J. N., Price, R., Platz, T., Petterson, M., Neall, V. E., McDonald, G. S., Lerner, G. A., Damaschcke, M., & Bebbington, M. S. (2021). The geological history and hazards of a long-lived stratovolcano, Mt. Taranaki, New Zealand. *New Zealand Journal of Geology and Geophysics, 64*(2-3), 456-478. https://doi.org/10.1080/00288306.2021.1895231

Cutler, K. S., Watt, S. F. L., Cassidy, M., Madden-Nadeau, A. L., Engwell, S. L., Abdurrachman, M., Nurshal, M. E. M., Tappin, D. R., Carey, S. N., Novellino, A., Hayer, C., Hunt, J. E., Day, S. J., Grilli, S. T., Kurniawan, I. A., & Kartadinata, N. (2022). Downward-propagating eruption following vent unloading implies no direct magmatic trigger for the 2018 lateral collapse of Anak Krakatau. *Earth and planetary science letters, 578*, 117332. https://doi.org/https://doi.org/10.1016/j.epsl.2021.117332

D'Lemos, R. S. (1996). Mixing between granitic and dioritic crystal mushes, Guernsey, Channel Islands, UK. *Lithos, 38*(3), 233-257. https://doi.org/https://doi.org/10.1016/0024-4937(96)00007-2

D'Mello, N. (2021). *Unravelling magma generation, storage, and ascent processes from the crystal cargo and their host lavas: a case study of Taranaki Volcano, New Zealand: a dissertation presented in partial fulfilment of the requirements for the degree of Doctor of Philosophy in Earth Sciences at Massey University (Manawatū campus), Palmerston North, New Zealand* Massey University].

D'Mello, N. G., Zellmer, G. F., Kereszturi, G., Ubide, T., Procter, J. N., & Stewart, R. B. (2023). Crystal entrainment from cool, low-silica rocks into hot, high-silica melts: diverse primary melt compositions at Taranaki volcano, New Zealand. *Journal of the Geological Society, 180*(3). https://doi.org/10.1144/jgs2022-036

D'Mello, N. G., Zellmer, G. F., Negrini, M., Kereszturi, G., Procter, J., Stewart, R., Prior, D., Usuki, M., & Iizuka, Y. (2021). Deciphering magma storage and ascent processes of Taranaki, New Zealand, from the complexity of amphibole breakdown textures. *Lithos, 398-399*, 106264. https://doi.org/https://doi.org/10.1016/j.lithos.2021.106264

Daggitt, M. L., Mather, T. A., Pyle, D. M., & Page, S. (2014). AshCalc–a new tool for the comparison of the exponential, power-law and Weibull models of tephra deposition. *Journal of Applied Volcanology, 3*(1), 7. https://doi.org/10.1186/2191-5040-3-7

Damaschke, M. (2017). *High-precision tephrostratigraphy: tracking the time-varying eruption pulse of Mt. Taranaki, North Island, New Zealand: a thesis presented in partial fulfilment of the requirements for the degree of Doctor of Philosophy in Earth Science, Massey University, Palmerston North, New Zealand* Massey University].

Damaschke, M., Cronin, S. J., & Bebbington, M. S. (2017a). A volcanic event forecasting model for multiple tephra records, demonstrated on Mt. Taranaki, New Zealand. *Bulletin of Volcanology, 80*(1), 9. https://doi.org/10.1007/s00445-017-1184-y

Damaschke, M., Cronin, S. J., Holt, K. A., Bebbington, M. S., & Hogg, A. G. (2017b). A 30,000 yr high-precision eruption history for the andesitic Mt. Taranaki, North Island, New Zealand. *Quaternary Research, 87*, 1-23. https://doi.org/10.1017/qua.2016.11

Davey, F. J. (1982). The structure of the South Fiji basin. *Tectonophysics, 87*(1), 185-241. https://doi.org/https://doi.org/10.1016/0040-1951(82)90227-X

Davidson, A. (2023). Insights into the genesis of young (<24 ka) magmas from Mt. Taranaki, New Zealand: a thesis submitted for the degree of Doctor of Philosophy in Earth and Planetary Sciences, Macquarie University, Australia.

Davidson, J., & De Silva, S. (2000). Composite volcanoes. In Sigurdsson H, Houghton B, McNutt S, Rymer H, & S. J (Eds.), *The Encyclopedia of Volcanoes* (pp. 663-681). Elsevier.

Davidson, J., Turner, S., Handley, H., Macpherson, C., & Dosseto, A. (2007). Amphibole "sponge" in arc crust? *Geology, 35*(9), 787-790. https://doi.org/10.1130/g23637a.1

Davidson, J. P., Hora, J. M., Garrison, J. M., & Dungan, M. A. (2005). Crustal forensics in arc magmas. *Journal of Volcanology and Geothermal Research, 140*(1), 157-170. https://doi.org/https://doi.org/10.1016/j.jvolgeores.2004.07.019

Davies, R., & Lambert, R. (2015). Under the Mountain-how a volcanic peak has influenced the culture, ecology and landscape history of Taranaki, New Zealand.

Day, S., Llanes, P., Silver, E., Hoffmann, G., Ward, S., & Driscoll, N. (2015). Submarine landslide deposits of the historical lateral collapse of Ritter Island, Papua New Guinea. *Marine and Petroleum Geology, 67*, 419-438. https://doi.org/https://doi.org/10.1016/j.marpetgeo.2015.05.017

de' Michieli Vitturi, M., Clarke, A. B., Neri, A., & Voight, B. (2008). Effects of conduit geometry on magma ascent dynamics in dome-forming eruptions. *Earth and planetary science letters, 272*(3), 567-578. https://doi.org/https://doi.org/10.1016/j.epsl.2008.05.025

de Vries, B. v. W., Kerle, N., & Petley, D. (2000). Sector collapse forming at Casita volcano, Nicaragua. *Geology, 28*(2), 167-170. https://doi.org/10.1130/0091-7613(2000)28<167:Scfacv>2.0.Co;2

Deegan, F. M., Whitehouse, M. J., Troll, V. R., Geiger, H., Jeon, H., le Roux, P., Harris, C., van Helden, M., & González-Maurel, O. (2021). Sunda arc mantle source δ18O value revealed by intracrystal isotope analysis. *Nature Communications, 12*(1), 3930. https://doi.org/10.1038/s41467-021-24143-3

Delcamp, A., Troll, V. R., van Wyk de Vries, B., Carracedo, J. C., Petronis, M. S., Pérez-Torrado, F. J., & Deegan, F. M. (2012). Dykes and structures of the NE rift of Tenerife, Canary Islands: a record of stabilisation and destabilisation of ocean island rift zones. *Bulletin of Volcanology, 74*(5), 963-980. https://doi.org/10.1007/s00445-012-0577-1

DeMets, C., Gordon, R. G., Argus, D. F., & Stein, S. (1990). Current plate motions. *Geophysical Journal International, 101*(2), 425-478. https://doi.org/10.1111/j.1365-246X.1990.tb06579.x

DeMets, C., Gordon, R. G., Argus, D. F., & Stein, S. (1994). Effect of recent revisions to the geomagnetic reversal time scale on estimates of current plate motions. *Geophysical research letters, 21*(20), 2191-2194.

Di Stefano, F., Mollo, S., Ubide, T., Petrone, C. M., Caulfield, J., Scarlato, P., Nazzari, M., Andronico, D., & Del Bello, E. (2020). Mush cannibalism and disruption recorded by clinopyroxene phenocrysts at Stromboli volcano: New insights from recent 2003–2017 activity. *Lithos, 360-361*, 105440. https://doi.org/https://doi.org/10.1016/j.lithos.2020.105440

Dickinson, W. R., & Hatherton, T. (1967). Andesitic Volcanism and Seismicity around the Pacific. *Science, 157*(3790), 801-803. https://doi.org/doi:10.1126/science.157.3790.801

Didonna, R., Costa, F., Handley, H., Turner, S., & Barclay, J. (2022). Dynamics and timescales of mafic–silicic magma interactions at Soufrière Hills Volcano, Montserrat. *Contributions to Mineralogy and Petrology, 177*(2), 28. https://doi.org/10.1007/s00410-022-01891-z

Dimech, J.-L., Stern, T., & Lamb, S. (2017). Mantle earthquakes, crustal structure, and gravitational instability beneath western North Island, New Zealand. *Geology, 45*(2), 155-158. https://doi.org/10.1130/g38476.1

Dingwell, D. B. (1998). The glass transition in hydrous granitic melts. *Physics of the Earth and Planetary Interiors, 107*(1), 1-8. https://doi.org/https://doi.org/10.1016/S0031-9201(97)00119-2

Dingwell, D. B., & Webb, S. L. (1989). Structural relaxation in silicate melts and non-Newtonian melt rheology in geologic processes. *Physics and Chemistry of Minerals, 16*(5), 508-516. https://doi.org/10.1007/BF00197020

Donoghue, S., Neall, V., & Palmer, A. (1988). Holocene geology of the upper Whangaehu River, Mt. Ruapehu. *NZ Geol Soc Misc Publ, 41*, 61.

Donoghue, S. L., & Neall, V. E. (1996). Tephrostratigraphic studies at Tongariro Volcanic Centre, New Zealand: An overview. *Quaternary international, 34-36*, 13-20. https://doi.org/https://doi.org/10.1016/1040-6182(95)00065-8

Dorn, R. I., DeNiro, M. J., & Ajie, H. O. (1987). Isotopic evidence for climatic influence on alluvial-fan development in Death Valley, California. *Geology, 15*(2), 108-110. https://doi.org/10.1130/0091-7613(1987)15<108:Iefcio>2.0.Co;2

Downey, W. S., Kellett, R. J., Smith, I. E. M., Price, R. C., & Stewart, R. B. (1994). New palaeomagnetic evidence for the recent eruptive activity of Mt. Taranaki, New Zealand. *Journal of Volcanology and Geothermal Research, 60*, 15-27. https://doi.org/10.1016/0377-0273(94)90095-7

Drost, F., Renwick, J., Bhaskaran, B., Oliver, H., & McGregor, J. (2007). A simulation of New Zealand's climate during the Last Glacial Maximum. *Quaternary Science Reviews, 26*(19), 2505-2525. https://doi.org/https://doi.org/10.1016/j.quascirev.2007.06.005

Druce, A. (1966). Tree-ring dating of recent volcanic ash and Lapilli, Mt Egmont. *New Zealand journal of botany, 4*(1), 3-41. https://doi.org/10.1080/0028825X.1966.10443951

Druitt, T. H. (1992). Emplacement of the 18 May 1980 lateral blast deposit ENE of Mount St. Helens, Washington. *Bulletin of Volcanology, 54*(7), 554-572. https://doi.org/10.1007/BF00569940

Druitt, T. H., & Kokelaar, B. P. (2002). *The Eruption of Soufrière Hills Volcano, Montserrat from 1995 to 1999*. Geological Society of London. https://doi.org/10.1144/gsl.Mem.2002.021

Dungan, M. A., Wulff, A., & Thompson, R. (2001). Eruptive stratigraphy of the Tatara-San Pedro complex, 36°S, sourthern volcanic zone, Chilean Andes: Reconstruction method and implications for magma evolution at long-lived arc volcanic centers [Article]. *Journal of Petrology, 42*(3), 555-626. https://www.scopus.com/inward/record.uri?eid=2-s2.0-0035074655&partnerID=40&md5=133b683c718f3860b5936d63cdc229d5

Duzgoren-Aydin, N. S., Aydin, A., & Malpas, J. (2002). Re-assessment of chemical weathering indices: case study on pyroclastic rocks of Hong Kong. *Engineering Geology, 63*(1), 99-119. https://doi.org/https://doi.org/10.1016/S0013-7952(01)00073-4

Eden, D., Froggatt, P., Trustrum, N., & Page, M. (1993). A multiple-source Holocene tephra sequence from Lake Tutira, Hawke's Bay, New Zealand. *New Zealand Journal of Geology and Geophysics, 36*(2), 233-242.

Edmonds, M., Cashman, K. V., Holness, M., & Jackson, M. (2019). Architecture and dynamics of magma reservoirs. *Philosophical Transactions of the Royal Society of London Series A, 377*, 20180298. https://doi.org/10.1098/rsta.2018.0298

Eichelberger, J. C. (1978). Andesitic volcanism and crustal evolution. *Nature, 275*(5675), 21-27. https://doi.org/10.1038/275021a0

Eichelberger, J. C., Izbekov, P. E., & Browne, B. L. (2006). Bulk chemical trends at arc volcanoes are not liquid lines of descent. *Lithos, 87*(1), 135-154. https://doi.org/https://doi.org/10.1016/j.lithos.2005.05.006

Eichelberger, J. C., Carrigan, C. R., Westrich, H. R., & Price, R. H. (1986). Non-explosive silicic volcanism. *Nature, 323*(6089), 598-602. https://doi.org/10.1038/323598a0

Elsworth, D., & Voight, B. (1995). Dike intrusion as a trigger for large earthquakes and the failure of volcano flanks. *Journal of Geophysical Research, 100*, 6005-6024. https://doi.org/10.1029/94jb02884

Elsworth, D., & Voight, B. (1996). Evaluation of volcano flank instability triggered by dyke intrusion. *Geological Society, London, Special Publications, 110*(1), 45-53. https://doi.org/doi:10.1144/GSL.SP.1996.110.01.03

Ewart, A., Brothers, R. N., & Mateen, A. (1977). An outline of the geology and geochemistry, and the possible petrogenetic evolution of the volcanic rocks of the Tonga-Kermadec-New Zealand island arc. *Journal of Volcanology and Geothermal Research, 2*(3), 205-250. https://doi.org/https://doi.org/10.1016/0377-0273(77)90001-4

Fedotov, S. A. (1991). *Active volcanoes of Kamchatka*. Nauka.

Fergusson, G. J., Rafter, T. A. (1957). N.Z. 14C age measurements - 3. *N.Z. Journal of Science and Technology, 38*(7), 732-749.

Fierstein, J., & Nathenson, M. (1992). Another look at the calculation of fallout tephra volumes. *Bulletin of Volcanology, 54*(2), 156-167. https://doi.org/10.1007/BF00278005

Fisher, R. V., & Schmincke, H.-U. (1984). Pyroclastic Rocks and Tectonic Environment. In R. V. Fisher & H.-U. Schmincke (Eds.), *Pyroclastic Rocks* (pp. 383-409). Springer Berlin Heidelberg. https://doi.org/10.1007/978-3-642-74864-6_14

Fitzgerald, R. H., Kennedy, B. M., Wilson, T. M., Leonard, G. S., K, T., & H, K. (2017). The Communication and Risk Management of Volcanic Ballistic Hazards. *Advances in Volcanology*, 121-147. https://doi.org/10.1007/11157_2016_35

Fleming, C. A., & Survey, N. Z. G. (1953). *The geology of Wanganui subdivision*. Department of Scientific and Industrial Research.

Folk, R. L., & Ward, W. C. (1957). Brazos River bar [Texas]; a study in the significance of grain size parameters. *Journal of sedimentary research, 27*(1), 3-26. https://doi.org/10.1306/74d70646-2b21-11d7-8648000102c1865d

Fornari, D. J., & Campbell, J. F. (1987). Submarine topography around the Hawaiian Islands. *US Geol. Surv. Prof. Pap, 1350*, 109-124.

Franks, A. M. (1984). *Soils of Eltham county and the tephrochronology of central Taranaki: a thesis presented in partial fulfilment of the requirements for the degree of Doctor of Philosophy in Soil Science* Massey University].

Franks, A. M. (1991). *No. 14-Soils of part Eltham County, North Island, New Zealand*. DSIR Land Resources.

Froggatt, P. C., & Lowe, D. J. (1990). A review of late Quaternary silicic and some other tephra formations from New Zealand: their stratigraphy, nomenclature, distribution, volume, and age. *New Zealand Journal of Geology and Geophysics, 33*(1), 89-109.

Frostick, L. E., & Reid, I. A. N. (1989). Climatic versus tectonic controls of fan sequences: lessons from the Dead Sea, Israel. *Journal of the Geological Society, 146*(3), 527-538. https://doi.org/10.1144/gsjgs.146.3.0527

Galipp, K., Klügel, A., & Hansteen, T. H. (2006). Changing depths of magma fractionation and stagnation during the evolution of an oceanic island volcano: La Palma (Canary Islands). *Journal of Volcanology and Geothermal Research, 155*(3), 285-306. https://doi.org/https://doi.org/10.1016/j.jvolgeores.2006.04.002

Gamble, J., McKee, J., Grapes, R., & Bennett, D. (1994). The crust beneath Taranaki volcanoimaged by xenoliths from andesites in the Stratford lahars. *Geological Society of New Zealand Miscellaneous Publication, 80*, 70.

Gamble, J. A., Price, R. C., Smith, I. E. M., McIntosh, W. C., & Dunbar, N. W. (2003). 40Ar/39Ar geochronology of magmatic activity, magma flux and hazards at Ruapehu volcano, Taupo Volcanic Zone, New Zealand. *Journal of Volcanology and Geothermal Research, 120*(3), 271-287. https://doi.org/https://doi.org/10.1016/S0377-0273(02)00407-9

Gaonac'h, H., Lovejoy, S., & Schertzer, D. (2005). Scaling vesicle distributions and volcanic eruptions. *Bulletin of Volcanology, 67*(4), 350-357. https://doi.org/10.1007/s00445-004-0376-4

Gardner, C. A., Cashman, K. V., & Neal, C. A. (1998). Tephra-fall deposits from the 1992 eruption of Crater Peak, Alaska: implications of clast textures for eruptive processes. *Bulletin of Volcanology, 59*(8), 537-555. https://doi.org/10.1007/s004450050208

Gardner, J. E., & Denis, M.-H. (2004). Heterogeneous bubble nucleation on Fe-Ti oxide crystals in high-silica rhyolitic melts1 1Associate editor: J. K. Russell. *Geochimica et cosmochimica acta, 68*(17), 3587-3597. https://doi.org/https://doi.org/10.1016/j.gca.2004.02.021

Gardner, J. E., Hilton, M., & Carroll, M. R. (1999). Experimental constraints on degassing of magma: isothermal bubble growth during continuous decompression from high pressure. *Earth and planetary science letters, 168*(1), 201-218. https://doi.org/https://doi.org/10.1016/S0012-821X(99)00051-5

Gardner, J. E., Thomas, R. M. E., Jaupart, C., & Tait, S. (1996). Fragmentation of magma during Plinian volcanic eruptions. *Bulletin of Volcanology, 58*(2), 144-162. https://doi.org/10.1007/s004450050132

Gaylord, D., Neall, V., & Palmer, A. (1993). The Maitahi Formation; a Mid-Pleistocene volcanic debris avalanche assemblage, Taranaki, New Zealand [abs.]. *Volcanic Activity and the Environment: Ancient Vol canism and Modern Analogues, International Association of Volcanology and Chemistry of the Earth's Interior (IAVCEI), Canberra, Australia 1993 General Assembly Abstracts*, 38.

Gaylord, D. R., Neall, V. E., & Palmer, A. S. (2014). The Middle Pleistocene Maitahi Formation, Taranaki, New Zealand: a new formal lithostratigraphic unit. *New Zealand Journal of Geology and Geophysics, 57*(4), 369-377. https://doi.org/10.1080/00288306.2014.914041

Geddes, A., Neall, V., & Stewart, R. (1981). Recent discovery of the westernmost occurrences of Aokautere Ash and implications for the late Quaternary in Taranaki. *R. Howorth et al*, 29-32.

Genareau, K., Proussevitch, A. A., Durant, A. J., Mulukutla, G., & Sahagian, D. L. (2012). Sizing up the bubbles that produce very fine ash during explosive volcanic eruptions. *Geophysical research letters, 39*, L15306. https://doi.org/10.1029/2012gl05247 1

Genareau, K., Mulukutla, G. K., Proussevitch, A. A., Durant, A. J., Rose, W. I., & Sahagian, D. L. (2013). The size range of bubbles that produce ash during explosive volcanic eruptions. *Journal of Applied Volcanology, 2*(1), 4. https://doi.org/10.1186/2191-5040-2-4

Gerlach, T. M., & Graeber, E. J. (1985). Volatile budget of Kilauea volcano. *Nature, 313*(6000), 273-277. https://doi.org/10.1038/313273a0

Germa, A., Lahitte, P., & Quidelleur, X. (2015). Construction and destruction of Mont Pelée volcano: Volumes and rates constrained from a geomorphological model of evolution. *Journal of Geophysical Research (Earth Surface), 120*, 1206-1226. https://doi.org/10.1002/2014jf003355

Germa, A., Quidelleur, X., Lahitte, P., Labanieh, S., & Chauvel, C. (2011). The K–Ar Cassignol–Gillot technique applied to western Martinique lavas: A record of Lesser Antilles arc activity from 2Ma to Mount Pelée volcanism. *Quaternary Geochronology, 6*(3), 341-355. https://doi.org/https://doi.org/10.1016/j.quageo.2011.02.001

Gerya, T. V., & Yuen, D. A. (2003). Rayleigh–Taylor instabilities from hydration and melting propel 'cold plumes' at subduction zones. *Earth and planetary science letters, 212*(1), 47-62. https://doi.org/https://doi.org/10.1016/S0012-821X(03)00265-6

Giacomoni, P. P., Ferlito, C., Coltorti, M., Bonadiman, C., & Lanzafame, G. (2014). Plagioclase as archive of magma ascent dynamics on "open conduit" volcanoes: The 2001–2006 eruptive period at Mt. Etna. *Earth-Science Reviews, 138*, 371-393. https://doi.org/https://doi.org/10.1016/j.earscirev.2014.06.009

Giba, M., Nicol, A., & Walsh, J. J. (2010). Evolution of faulting and volcanism in a back-arc basin and its implications for subduction processes. *Tectonics, 29*, TC4020. https://doi.org/10.1029/2009tc002634

Gill, J., B. (1981). Orogenic Andesites and Plate Tectonics. *Minerals and Rocks*, 390. https://doi.org/10.1007/978-3-642-68012-0

Gillies, J. K., Kennedy, B. M., Gravley, D. M., Leonard, G. S., & Cowlyn, J. (2020). Identifying pyroclastic density currents from partial outcrop exposure on Mt Ruapehu, New Zealand. *Frontiers in Earth Science, 8*, 402. https://doi.org/10.3389/feart.2020.542932

Ginibre, C., Wörner, G., & Kronz, A. (2007). Crystal Zoning as an Archive for Magma Evolution. *Elements, 3*(4), 261-266. https://doi.org/10.2113/gselements.3.4.261

Girina, O. A. (2013). Chronology of Bezymianny volcano activity, 1956–2010. *Journal of Volcanology and Geothermal Research, 263*, 22-41.

Glicken, H. (1996). *Rockslide-debris avalanche of may 18, 1980, Mount St. Helens volcano, Washington*. US Geological Survey, Cascades Volcano Observatory.

Gonnermann, H. M., & Manga, M. (2007). The Fluid Mechanics Inside a Volcano. *Annual Review of Fluid Mechanics, 39*(1), 321-356. https://doi.org/10.1146/annurev.fluid.39.050905.110207

Gonzalez-Santana, J., & Wauthier, C. (2021). Unraveling long-term volcano flank instability at Pacaya Volcano, Guatemala, using satellite geodesy. *Journal of Volcanology and Geothermal Research, 410*, 107147. https://doi.org/10.1016/j.jvolgeores.2020.107147

Gorbach, N., Portnyagin, M., & Tembrel, I. (2013). Volcanic structure and composition of Old Shiveluch volcano, Kamchatka. *Journal of Volcanology and Geothermal Research, 263*, 193-208. https://doi.org/https://doi.org/10.1016/j.jvolgeores.2012.12.012

Gow, A. J. (1968). Petrographic and petrochemical studies of MT Egmont andesites. *New Zealand Journal of Geology and Geophysics, 11*(1), 166-190. https://doi.org/10.1080/00288306.1968.10423683

Graham, I. J., & Hackett, W. R. (1987). Petrology of Calc-alkaline Lavas from Ruapehu Volcano and Related Vents, Taupo Volcanic Zone, New Zealand. *Journal of Petrology, 28*(3), 531-567. https://doi.org/10.1093/petrology/28.3.531

Grange, L. I., & Taylor, N. H. (1933). Report on soil surveys for 1932-33. NZ Department of Scientific and Industrial Research, Annual Report 1932–33.

Grant-Taylor, T. L. (1964). Volcanic history of Western Taranaki. *New Zealand Journal of Geology and Geophysics, 7*(1), 78-86. https://doi.org/10.1080/00288306.1964.10420158

Grant-Taylor, T. L., & Rafter, T. A. (1963). New Zealand natural radiocarbon measurements IV. *American Journal of Science*.

Grant-Taylor, T. L., & Rafter, T. A. (1971). New Zealand radiocarbon age measurements — 6. *New Zealand Journal of Geology and Geophysics, 14*, 364-402. https://doi.org/10.1080/00288306.1971.10421932

Green, R. M., Bebbington, M. S., Cronin, S. J., & Jones, G. (2013). Geochemical precursors for eruption repose length. *Geophysical Journal International, 193*(2), 855-873. https://doi.org/10.1093/gji/ggt044

Grosse, P., Euillades, P. A., Euillades, L. D., & van Wyk de Vries, B. (2013). A global database of composite volcano morphometry. *Bulletin of Volcanology, 76*(1), 784. https://doi.org/10.1007/s00445-013-0784-4

Grove, T., Parman, S., Bowring, S., Price, R., & Baker, M. (2002). The role of an H2O-rich fluid component in the generation of primitive basaltic andesites and andesites from the Mt. Shasta region, N California. *Contributions to Mineralogy and Petrology, 142*(4), 375-396. https://doi.org/10.1007/s004100100299

Grove, T., L., & Kinzler, R., J. (1986). Petrogenesis of Andesites. *Annual Review of Earth and Planetary Sciences, 14*(1), 417-454. https://doi.org/10.1146/annurev.ea.14.050186.002221

Grove, T. L., Elkins-Tanton, L. T., Parman, S. W., Chatterjee, N., Müntener, O., & Gaetani, G. A. (2003). Fractional crystallization and mantle-melting controls on calc-alkaline differentiation trends. *Contributions to Mineralogy and Petrology, 145*(5), 515-533. https://doi.org/10.1007/s00410-003-0448-z

Gudmundsson, A. (2012). Magma chambers: Formation, local stresses, excess pressures, and compartments. *Journal of Volcanology and Geothermal Research, 237-238*, 19-41. https://doi.org/https://doi.org/10.1016/j.jvolgeores.2012.05.015

Gudmundsson, A., Oskarsson, N., Gronvold, K., Saemundsson, K., Sigurdsson, O., Stefansson, R., Gislason, S. R., Einarsson, P., Brandsdottir, B., Larsen, G., Johannesson, H., & Thordarson, T. (1992). The 1991 eruption of Hekla, Iceland. *Bulletin of Volcanology, 54*(3), 238-246. https://doi.org/10.1007/BF00278391

Gudmundsson, M. T., Pedersen, R., Vogfjörd, K., Thorbjarnardóttir, B., Jakobsdóttir, S., & Roberts, M. J. (2010). Eruptions of Eyjafjallajökull Volcano, Iceland. *EOS Transactions, 91*, 190-191. https://doi.org/10.1029/2010eo210002

Gurioli, L., Harris, A. J. L., Houghton, B. F., Polacci, M., & Ripepe, M. (2008). Textural and geophysical characterization of explosive basaltic activity at Villarrica volcano. *Journal of Geophysical Research (Solid Earth), 113*, B08206. https://doi.org/10.1029/2007jb005328

Hackett, W. R., & Houghton, B. F. (1989). A facies model for a quaternary andesitic composite volcano: Ruapehu, New Zealand. *Bulletin of Volcanology, 51*(1), 51-68. https://doi.org/10.1007/BF01086761

Hajimirza, S., Gardner, J. E., & Gonnermann, H. M. (2022). Experimental demonstration of continuous bubble nucleation in rhyolite. *Journal of Volcanology and Geothermal Research, 421*, 107417. https://doi.org/https://doi.org/10.1016/j.jvolgeores.2021.107417

Hall, M. L., Robin, C., Beate, B., Mothes, P., & Monzier, M. (1999). Tungurahua Volcano, Ecuador: structure, eruptive history and hazards. *Journal of Volcanology and Geothermal Research, 91*(1), 1-21. https://doi.org/https://doi.org/10.1016/S0377-0273(99)00047-5

Hammer, J. E., Cashman, K. V., Hoblitt, R. P., & Newman, S. (1999). Degassing and microlite crystallization during pre-climactic events of the 1991 eruption of Mt. Pinatubo, Philippines. *Bulletin of Volcanology, 60*(5), 355-380. https://doi.org/10.1007/s004450050238

Hao, L.-L., Wang, Q., Wyman, D. A., Ou, Q., Dan, W., Jiang, Z.-Q., Yang, J.-H., Li, J., & Long, X.-P. (2016). Andesitic crustal growth via mélange partial melting: Evidence from Early Cretaceous arc dioritic/andesitic rocks in southern Qiangtang, central Tibet. *Geochemistry, Geophysics, Geosystems, 17*, 1641-1659. https://doi.org/10.1002/2016gc006248

Hatherton, T. (1969). The Geophysical significance of calc-alkaline andesites in New Zealand. *New Zealand Journal of Geology and Geophysics, 12*(2-3), 436-459. https://doi.org/10.1080/00288306.1969.10420292

Hausback, B. P., & Swanson, D. A. (1990). Record of Prehistoric Debris Avalanches on the North Flank of Mount St. Helens Volcano, Washington. *Geoscience Canada, 17*(3). https://journals.lib.unb.ca/index.php/GC/article/view/3666

Hawkesworth, C. J., Norry, M. J., Roddick, J. C., Baker, P. E., Francis, P. W., & Thorpe, R. S. (1979). 143Nd/144Nd,87Sr/86Sr, and incompatible element variations in calc-alkaline andesites and plateau lavas from South America. *Earth and planetary science letters, 42*(1), 45-57. https://doi.org/https://doi.org/10.1016/0012-821X(79)90189-4

Hayward, W., King, R., & Fordyce, R. (1987). Paleogeography and tectonic history of Taranaki Basin. *Geological Society of New Zealand Miscellaneous Publication, 37*.

Heffter, J. L., & Stunder, B. J. B. (1993). Volcanic Ash Forecast Transport And Dispersion (VAFTAD) Model. *Weather and forecasting, 8*, 533-541. https://doi.org/10.1175/1520-0434(1993)008<0533:Vaftad>2.0.Co;2

Heinrich, M. (2020). *Drivers, Dynamics and Hazards of the largest pyroclastic eruptions of Tongariro Volcano, Central North Island, New Zealand* ResearchSpace@ Auckland].

Heinrich, M., Cronin, S. J., & Pardo, N. (2020a). Understanding multi-vent Plinian eruptions at Mt. Tongariro Volcanic Complex, New Zealand. *Bulletin of Volcanology, 82*(3), 30. https://doi.org/10.1007/s00445-020-1369-7

Heinrich, M., Cronin, S. J., Torres-Orozco, R., Colombier, M., Scheu, B., & Pardo, N. (2020b). Micro-porous pyroclasts reflecting multi-vent basaltic-andesite Plinian eruptions at Mt. Tongariro, New Zealand. *Journal of Volcanology and Geothermal Research*, 106936.

Henrys, S., Reyners, M., & Bibby, H. (2003). Exploring the plate boundary structure of the North Island, New Zealand. *EOS Transactions, 84*, 289-295. https://doi.org/10.1029/2003eo310002

Herzer, R. H. (1995). Seismic stratigraphy of a buried volcanic arc, Northland, New Zealand and implications for Neogene subduction. *Marine and Petroleum Geology, 12*(5), 511-531. https://doi.org/https://doi.org/10.1016/0264-8172(95)91506-K

Higgins, M. D. (1996). Crystal size distributions and other quantitative textural measurements in lavas and tuff from Egmont volcano (Mt. Taranaki), New Zealand. *Bulletin of Volcanology, 58*(2), 194-204. https://doi.org/10.1007/s004450050135

Higgins, M. D., Voos, S., & Vander Auwera, J. (2015). Magmatic processes under Quizapu volcano, Chile, identified from geochemical and textural studies. *Contributions to Mineralogy and Petrology, 170*(5), 51. https://doi.org/10.1007/s00410-015-1209-5

Hildner, E., Klügel, A., & Hansteen, T. H. (2012). Barometry of lavas from the 1951 eruption of Fogo, Cape Verde Islands: Implications for historic and prehistoric magma plumbing systems. *Journal of Volcanology and Geothermal Research, 217-218*, 73-90. https://doi.org/https://doi.org/10.1016/j.jvolgeores.2011.12.014

Hildreth, W. (2004). Volcanological perspectives on Long Valley, Mammoth Mountain, and Mono Craters: several contiguous but discrete systems. *Journal of Volcanology and Geothermal Research, 136*(3), 169-198. https://doi.org/https://doi.org/10.1016/j.jvolgeores.2004.05.019

Hildreth, W., & Moorbath, S. (1988). Crustal contributions to arc magmatism in the Andes of Central Chile [Article]. *Contributions to Mineralogy and Petrology, 98*(4), 455-489. https://doi.org/10.1007/BF00372365

Hill, B. E., Connor, C. B., Jarzemba, M. S., La Femina, P. C., Navarro, M., & Strauch, W. (1998). 1995 eruptions of Cerro Negro volcano, Nicaragua, and risk assessment for future eruptions. *GSA Bulletin, 110*(10), 1231-1241. https://doi.org/10.1130/0016-7606(1998)110<1231:Eocnvn>2.3.Co;2

Hobden, B. J., Houghton, B. F., Lanphere, M. A., & Nairn, I. A. (1996). Growth of the Tongariro volcanic complex: New evidence from K-Ar age determinations. *New Zealand Journal of Geology and Geophysics, 39*(1), 151-154. https://doi.org/10.1080/00288306.1996.9514701

Hodgson, K. A., Lecointre, J. A., & Neall, V. E. (2007). Onetapu Formation: The last 2000 yr of laharic activity at Ruapehu volcano, New Zealand. *New Zealand Journal of Geology and Geophysics, 50*(2), 81-99. https://doi.org/10.1080/00288300709509823

Holcomb, R. T., & Searle, R. C. (1991). Large landslides from oceanic volcanoes. *Marine Geotechnology, 10*(1-2), 19-32. https://doi.org/10.1080/10641199109379880

Holt, W. E., & Haines, A. J. (1995). The kinematics of northern South Island, New Zealand, determined from geologic strain rates. *Journal of Geophysical Research, 100*, 17,991-918,010. https://doi.org/10.1029/95jb01059

Hora, J. M., Singer, B. S., Wörner, G., Beard, B. L., Jicha, B. R., & Johnson, C. M. (2009). Shallow and deep crustal control on differentiation of calc-alkaline and tholeiitic magma. *Earth and planetary science letters, 285*(1), 75-86. https://doi.org/https://doi.org/10.1016/j.epsl.2009.05.042

Hornig-Kjarsgaard, I. (1993). Geology, stratigraphy and volcanological evolution of the island of Stromboli, Aeolian arc, Italy. *Acta Vulcanologica, 3*, 21-68. https://cir.nii.ac.jp/crid/1570572699956686080

Höskuldsson, Á., Óskarsson, N., Pedersen, R., Grönvold, K., Vogfjörð, K., & Ólafsdóttir, R. (2007). The millennium eruption of Hekla in February 2000. *Bulletin of Volcanology, 70*(2), 169-182. https://doi.org/10.1007/s00445-007-0128-3

Houghton, B., & Carey, R. J. (2015). In H. Sigurdsson (Ed.), *The Encyclopedia of Volcanoes (Second Edition)* (pp. 599-616). Academic Press. https://doi.org/https://doi.org/10.1016/B978-0-12-385938-9.00034-1

Houghton, B., Wilson, C., McWilliams, M., Lanphere, M., Weaver, S., Briggs, R., & Pringle, M. (1995). Chronology and dynamics of a large silicic magmatic system: Central Taupo Volcanic Zone, New Zealand. *Geology, 23*(1), 13-16.

Houghton, B. F., & Wilson, C. J. N. (1989). A vesicularity index for pyroclastic deposits. *Bulletin of Volcanology, 51*(6), 451-462. https://doi.org/10.1007/BF01078811

Houghton, B. F., & Nairn, I. A. (1991). The 1976–1982 Strombolian and phreatomagmatic eruptions of White Island, New Zealand: eruptive and depositional mechanisms at a 'wet' volcano. *Bulletin of Volcanology, 54*(1), 25-49. https://doi.org/10.1007/BF00278204

Houghton, B. F., Latter, J. H., & Hackett, W. R. (1987). Volcanic hazard assessment for Ruapehu composite volcano, taupo volcanic zone, New Zealand. *Bulletin of Volcanology, 49*(6), 737-751. https://doi.org/10.1007/BF01079825

Houghton, B. F., Wilson, C. J. N., Del Carlo, P., Coltelli, M., Sable, J. E., & Carey, R. (2004). The influence of conduit processes on changes in style of basaltic Plinian eruptions: Tarawera 1886 and Etna 122 BC. *Journal of Volcanology and Geothermal Research, 137*(1), 1-14. https://doi.org/https://doi.org/10.1016/j.jvolgeores.2004.05.009

Houghton, B. F., Carey, R. J., Cashman, K. V., Wilson, C. J. N., Hobden, B. J., & Hammer, J. E. (2010). Diverse patterns of ascent, degassing, and eruption of rhyolite magma during the 1.8ka Taupo eruption, New Zealand: Evidence from clast vesicularity. *Journal of Volcanology and Geothermal Research, 195*(1), 31-47. https://doi.org/https://doi.org/10.1016/j.jvolgeores.2010.06.002

Houghton, B. F., Wilson, C. J. N., McWilliams, M. O., Lanphere, M. A., Weaver, S. D., Briggs, R. M., & Pringle, M. S. (1995). Chronology and dynamics of a large silicic magmatic system: Central Taupo Volcanic Zone, New Zealand. *Geology, 23*(1), 13-16. https://doi.org/10.1130/0091-7613(1995)023<0013:Cadoal>2.3.Co;2

Hubert, J. F., & Filipov, A. J. (1989). Debris-flow deposits in alluvial fans on the west flank of the White Mountains, Owens Valley, California, U.S.A. *Sedimentary Geology, 61*(3), 177-205. https://doi.org/https://doi.org/10.1016/0037-0738(89)90057-2

Humphreys, M. C. S., Blundy, J. D., & Sparks, R. S. J. (2006). Magma Evolution and Open-System Processes at Shiveluch Volcano: Insights from Phenocryst Zoning. *Journal of Petrology, 47*(12), 2303-2334. https://doi.org/10.1093/petrology/egl045

Hunt, J. E., Wynn, R. B., Talling, P. J., & Masson, D. G. (2013). Turbidite record of frequency and source of large volume (>100 km³) Canary Island landslides in the last 1.5 Ma: Implications for landslide triggers and geohazards. *Geochemistry, Geophysics, Geosystems, 14*, 2100-2123. https://doi.org/10.1002/ggge.20139

Hunt, J. E., Talling, P. J., Clare, M. A., Jarvis, I., & Wynn, R. B. (2014). Long-term (17 Ma) turbidite record of the timing and frequency of large flank collapses of the Canary Islands. *Geochemistry, Geophysics, Geosystems, 15*, 3322-3345. https://doi.org/10.1002/2014gc005232

Hurwitz, S., & Navon, O. (1994). Bubble nucleation in rhyolitic melts: Experiments at high pressure, temperature, and water content. *Earth and planetary science letters, 122*(3-4), 267-280.

Hurwitz, S., Goff, F., Janik, C. J., Evans, W. C., Counce, D. A., Sorey, M. L., & Ingebritsen, S. E. (2003). Mixing of magmatic volatiles with groundwater and interaction with basalt on the summit of Kilauea Volcano, Hawaii. *Journal of Geophysical Research (Solid Earth), 108*, 2028. https://doi.org/10.1029/2001jb001594

Inman, D. L. (1952). Measures for describing the size distribution of sediments. *Journal of sedimentary research, 22*(3), 125-145. https://doi.org/10.1306/d42694db-2b26-11d7-8648000102c1865d

Isacks, B. L., & Barazangi, M. (1977). Geometry of Benioff zones: Lateral segmentation and downwards bending of the subducted lithosphere. *Island Arcs, Deep Sea Trenches and Back-Arc Basins, 1*, 99-114.

Iverson, R. M., Schilling, S. P., & Vallance, J. W. (1998). Objective delineation of lahar-inundation hazard zones. *Geological Society of America Bulletin, 110*, 972-984. https://doi.org/10.1130/0016-7606(1998)110<0972:Odolih>2.3.Co;2

Jacoby, W. R. (1973). Model Experiment of Plate Movements. *Nature Physical Science, 242*(122), 130-134. https://doi.org/10.1038/physci242130a0

James, G. M., William, R. N., & Robin, T. H. (1994). Giant Hawaiian landslides. *Annual Review of Earth and Planetary Sciences, 22*(1), 119-144. https://doi.org/10.1146/annurev.ea.22.050194.001003

Jarosewich, E., Nelen, J. A., & Norberg, J. A. (1980). Reference Samples for Electron Microprobe Analysis*. *Geostandards and Geoanalytical Research, 4*, 43-47. https://doi.org/10.1111/j.1751-908X.1980.tb00273.x

Jarrad R, D. (1986). Relations among subduction parameters. *Review of Geophysics, 24*, 217-284. https://cir.nii.ac.jp/crid/1573950400479788032

Jaupart, C. (1998). Gas loss from magma through conduit walls during eruption. *The Physics of Explosive Volcanic Eruptions, 145*, 73-90. https://cir.nii.ac.jp/crid/1573105974654790784

Jaupart, C., & Allègre, C. J. (1991). Gas content, eruption rate and instabilities of eruption regime in silicic volcanoes. *Earth and planetary science letters, 102*(3), 413-429. https://doi.org/https://doi.org/10.1016/0012-821X(91)90032-D

Jaupart, C., & Vergniolle, S. (1988). Laboratory models of Hawaiian and Strombolian eruptions. *Nature, 331*(6151), 58-60. https://doi.org/10.1038/331058a0

Jeanloz, R. (1999). Mantle of the Earth. *Encyclopedia of Volcanoes*, 41.

Johnson, R. W. (1987). Large-scale volcanic cone collapse: The 1888 slope failure of Ritter volcano, and other examples from Papua New Guinea. *Bulletin of Volcanology, 49*(5), 669-679. https://doi.org/10.1007/BF01080358

Kamp, P. J. J., Vonk, A. J., Bland, K. J., Hansen, R. J., Hendy, A. J. W., McIntyre, A. P., Ngatai, M., Cartwright, S. J., Hayton, S., & Nelson, C. S. (2004). Neogene stratigraphic architecture and tectonic evolution of Wanganui, King Country, and eastern Taranaki Basins, New Zealand. *New Zealand Journal of Geology and Geophysics, 47*(4), 625-644. https://doi.org/10.1080/00288306.2004.9515080

Karig, D. E. (1970). Kermadec arc—New Zealand tectonic confluence. *New Zealand Journal of Geology and Geophysics, 13*(1), 21-29. https://doi.org/10.1080/00288306.1970.10428203

Karlstrom, L., Dufek, J., & Manga, M. (2010). Magma chamber stability in arc and continental crust. *Journal of Volcanology and Geothermal Research, 190*(3), 249-270. https://doi.org/https://doi.org/10.1016/j.jvolgeores.2009.10.00 3

Karstens, J., Berndt, C., Urlaub, M., Watt, S. F. L., Micallef, A., Ray, M., Klaucke, I., Muff, S., Klaeschen, D., Kühn, M., Roth, T., Böttner, C., Schramm, B., Elger, J., & Brune, S. (2019). From gradual spreading to catastrophic collapse – Reconstruction of the 1888 Ritter Island volcanic sector collapse from high-resolution 3D seismic data. *Earth and planetary science letters, 517*, 1-13. https://doi.org/https://doi.org/10.1016/j.epsl.2019.04.009

Keigler, R., Thouret, J.-C., Hodgson, K. A., Neall, V. E., Lecointre, J. A., Procter, J. N., & Cronin, S. J. (2011). The Whangaehu Formation: Debris-avalanche and lahar deposits from ancestral Ruapehu volcano, New Zealand. *Geomorphology, 133*(1), 57-79. https://doi.org/https://doi.org/10.1016/j.geomorph.2011.06.019

Kennedy, B., Spieler, O., Scheu, B., Kueppers, U., Taddeucci, J., & Dingwell, D. B. (2005). Conduit implosion during Vulcanian eruptions. *Geology, 33*(7), 581-584. https://doi.org/10.1130/g21488.1

Kent, A. J. R., Darr, C., Koleszar, A. M., Salisbury, M. J., & Cooper, K. M. (2010). Preferential eruption of andesitic magmas through recharge filtering. *Nature Geoscience, 3*(9), 631-636. https://doi.org/10.1038/ngeo924

Kerr, P. F., & Poldervaart, A. (1955). Hydrothermal Alteration and Weathering. In *Crust of the Earth: A Symposium* (Vol. 62, pp. 0). Geological Society of America. https://doi.org/10.1130/SPE62-p525

King, P. (1991). Physiographic maps of the Taranaki Basin—Late Cretaceous to recent. *New Zealand Geological Survey Report G, 155*.

King, P. R., & Thrasher, G. P. (1996). *Cretaceous Cenozoic geology and petroleum systems of the Taranaki Basin, New Zealand* (Vol. 2). Institute of Geological & Nuclear Sciences.

King, P. R., Thrasher, G. P., Watkins, J. S., Zhiqiang, F., & McMillen, K. J. (1992). Post-Eocene Development of the Taranaki Basin, New Zealand: Convergent Overprint of a Passive Margin. In

Geology and Geophysics of Continental Margins (Vol. 53, pp. 0). American Association of Petroleum Geologists. https://doi.org/10.1306/m53552c7

Klug, C., & Cashman, K. (1991). Effects of vesicle size and shape on the vesicularity of silicic magma fragmentation. *EOS Trans. Am. Geophys. Union, 72*, 312.

Klug, C., & Cashman, K. V. (1994). Vesiculation of May 18, 1980, Mount St. Helens magma. *Geology, 22*(5), 468-472. https://doi.org/10.1130/0091-7613(1994)022<0468:Vommsh>2.3.Co;2

Klug, C., & Cashman, K. V. (1996). Permeability development in vesiculating magmas: implications for fragmentation. *Bulletin of Volcanology, 58*(2), 87-100. https://doi.org/10.1007/s004450050128

Klug, C., Cashman, K., & Bacon, C. (2002). Structure and physical characteristics of pumice from the climactic eruption of Mount Mazama (Crater Lake), Oregon. *Bulletin of Volcanology, 64*(7), 486-501. https://doi.org/10.1007/s00445-002-0230-5

Knox, G. J. (1982). Taranaki Basin, structural style and tectonic setting. *New Zealand Journal of Geology and Geophysics, 25*(2), 125-140. https://doi.org/10.1080/00288306.1982.10421405

Koyaguchi, T., & Mitani, N. K. (2005). A theoretical model for fragmentation of viscous bubbly magmas in shock tubes. *Journal of Geophysical Research (Solid Earth), 110*, B10202. https://doi.org/10.1029/2004jb003513

Kroeger, K. F., Funnell, R. H., Nicol, A., Fohrmann, M., Bland, K. J., & King, P. R. (2013). 3D crustal-scale heat-flow regimes at a developing active margin (Taranaki Basin, New Zealand). *Tectonophysics, 591*, 175-193. https://doi.org/https://doi.org/10.1016/j.tecto.2012.04.005

Krumbein, W. C. (1934). Size frequency distributions of sediments. *Journal of sedimentary research, 4*(2), 65-77. https://doi.org/10.1306/d4268eb9-2b26-11d7-8648000102c1865d

Krumbein, W. C. (1938). Size frequency distributions of sediments and the normal phi curve. *Journal of sedimentary research, 8*(3), 84-90. https://doi.org/10.1306/d4269008-2b26-11d7-8648000102c1865d

Labazuy, P. (1996). Recurrent landslides events on the submarine flank of Piton de la Fournaise volcano (Reunion Island). *Geological Society of London Special Publications, 110*, 295-306. https://doi.org/10.1144/gsl.Sp.1996.110.01.23

Langmann, B., Folch, A., Hensch, M., & Matthias, V. (2012). Volcanic ash over Europe during the eruption of Eyjafjallajökull on Iceland, April–May 2010. *Atmospheric Environment, 48*, 1-8. https://doi.org/https://doi.org/10.1016/j.atmosenv.2011.03.054

Lara, L. E. (2010). The 2008 eruption of the Chaitén Volcano, Chile: a preliminary report. *Andean geology, 36*(1), 125-130.

Lautze, N. C., & Houghton, B. F. (2007). Linking variable explosion style and magma textures during 2002 at Stromboli volcano, Italy. *Bulletin of Volcanology, 69*(4), 445-460. https://doi.org/10.1007/s00445-006-0086-1

Lavigne, F. (2004). Rate of sediment yield following small-scale volcanic eruptions: a quantitative assessment at the Merapi and Semeru stratovolcanoes, Java, Indonesia. *Earth surface processes and Landforms, 29*(8), 1045-1058. https://doi.org/10.1002/esp.1092

Lavigne, F., & Thouret, J.-C. (2003). Sediment transportation and deposition by rain-triggered lahars at Merapi Volcano, Central Java, Indonesia. *Geomorphology, 49*(1), 45-69. https://doi.org/https://doi.org/10.1016/S0169-555X(02)00160-5

Le Maitre, R., W. (1989). A classification of igneous rocks and glossary of terms. *Recommendations of the International Union of Geological Sciences Subcommission on the Systematics of Igneous Rocks*. https://cir.nii.ac.jp/crid/1574231875719019520

Le Maitre, R. W., Streckeisen, A., Zanettin, B., Le Bas, M. J., Bonin, B., Bateman, P., Bellieni, G., Dudek, A., Efremova, S., Keller, J., & Lameyre, J. (2002). Igneous rocks: A classification and glossary of terms; Recommendations of the International Union of Geological Sciences. In Subcommission on the Systematics of Igneous rocks. Cambridge University Press.

Lénat, J.-F., Vincent, P., & Bachélery, P. (1989). The off-shore continuation of an active basaltic volcano: Piton de la Fournaise (Réunion Island, Indian Ocean); structural and geomorphological interpretation from sea beam mapping. *Journal of Volcanology and Geothermal Research, 36*(1), 1-36. https://doi.org/https://doi.org/10.1016/0377-0273(89)90003-6

Lerner, G. A., Cronin, S. J., & Turner, G. M. (2019a). Evaluating emplacement temperature of a 1000-year sequence of mass flows using paleomagnetism of their deposits at Mt. Taranaki, New Zealand. *Volcanica, 2*(1), 11-24.

Lerner, G. A., Cronin, S. J., Turner, G. M., & Rowe, M. C. (2019b). Paleomagnetic determination of the age and properties of the 1780–1800 AD dome effusion/collapse episode of Mt. Taranaki, New Zealand. *Bulletin of Volcanology, 81*(3), 15.

Lerner, G. A., Cronin, S. J., Turner, G. M., & Piispa, E. J. (2019c). Recognizing long-runout pyroclastic flow deposits using paleomagnetism of ash. *GSA Bulletin, 131*(11-12), 1783-1793. https://doi.org/10.1130/b35029.1

Lerner, G. A., Cronin, S. J., Bebbington, M. S., & Platz, T. (2019d). The characteristics of a multi-episode volcanic regime: the post-AD 960 Maero Eruptive Period of Mt. Taranaki (New Zealand). *Bulletin of Volcanology, 81*(11), 61. https://doi.org/10.1007/s00445-019-1327-4

Lin, Q., Neethling, S. J., Dobson, K. J., Courtois, L., & Lee, P. D. (2015). Quantifying and minimising systematic and random errors in X-ray micro-tomography based volume measurements. *Computers & Geosciences, 77*, 1-7. https://doi.org/https://doi.org/10.1016/j.cageo.2014.12.008

Lipman, P. W., & Mullineaux, D. R. (1981). *The 1980 eruptions of Mount St. Helens, Washington* [Report](1250). (Professional Paper, Issue. G. P. O. U.S. https://pubs.usgs.gov/publication/pp1250

Lissenberg, C. J., MacLeod, C. J., & Bennett, E. N. (2019). Consequences of a crystal mush-dominated magma plumbing system: a mid-ocean ridge perspective. *Philosophical Transactions of the Royal Society of London Series A, 377*, 20180014. https://doi.org/10.1098/rsta.2018.0014

Liu, Y., & Zhang, Y. (2000). Bubble growth in rhyolitic melt. *Earth and planetary science letters, 181*(1), 251-264. https://doi.org/https://doi.org/10.1016/S0012-821X(00)00197-7

Locke, C. A., Cassidy, J., & MacDonald, A. (1994). Constraints on the evolution of the Taranaki volcanoes, New Zealand, based on aeromagnetic data. *Bulletin of Volcanology, 56*(6), 552-560. https://doi.org/10.1007/BF00302835

Longpré, M. A., Troll, V. R., Walter, T. R., & Hansteen, T. H. (2009). Volcanic and geochemical evolution of the teno massif, tenerife, Canary Islands: Some repercussions of giant landslides on ocean island magmatism [Article]. *Geochemistry, Geophysics, Geosystems, 10*(12), Article Q12017. https://doi.org/10.1029/2009GC002892

Lormand, C., Zellmer, G. F., Sakamoto, N., Ubide, T., Kilgour, G., Yurimoto, H., Palmer, A., Németh, K., Iizuka, Y., & Moebis, A. (2021). Shallow magmatic processes revealed by cryptic microantecrysts: a case study from the Taupo Volcanic Zone. *Contributions to Mineralogy and Petrology, 176*(11), 97. https://doi.org/10.1007/s00410-021-01857-7

Lowe, D. J. (1986). Controls on the rates of weathering and clay mineral genesis in airfall tephras: A review and New Zealand case study. *Rates of chemical weathering of rocks and minerals.*, 265-330. https://cir.nii.ac.jp/crid/1571698599505034880

Lowe, D. J. (1988). Stratigraphy, age, composition, and correlation of late Quaternary tephras interbedded with organic sediments in Waikato lakes, North Island, New Zealand. *New Zealand Journal of Geology and Geophysics, 31*(2), 125-165.

Lowe, D. J. (1990). Tephra studies in New Zealand: an historical review. *Journal of the Royal Society of New Zealand, 20*(1), 119-150. https://doi.org/10.1080/03036758.1990.10426736

Lowe, D. J., Shane, P. A. R., Alloway, B. V., & Newnham, R. M. (2008). Fingerprints and age models for widespread New Zealand tephra marker beds erupted since 30,000 years ago: a framework for NZ-

INTIMATE. *Quaternary Science Reviews, 27*(1), 95-126. https://doi.org/https://doi.org/10.1016/j.quascirev.2007.01.013

Land Information New Zealand. (n.d). LINZ Data Service. https://data.linz.govt.nz/

Luhr, J. F., & Prestegaard, K. L. (1988). Caldera formation at Volcán Colima, Mexico, by a large large holocene volcanic debris avalanche. *Journal of Volcanology and Geothermal Research, 35*(4), 335-348. https://doi.org/https://doi.org/10.1016/0377-0273(88)90027-3

Lyakhovsky, V., Hurwitz, S., & Navon, O. (1996). Bubble growth in rhyolitic melts: experimental and numerical investigation. *Bulletin of Volcanology, 58*(1), 19-32. https://doi.org/10.1007/s004450050122

Macedonio, G., Dobran, F., & Neri, A. (1994). Erosion processes in volcanic conduits and application to the AD 79 eruption of Vesuvius. *Earth and planetary science letters, 121*(1), 137-152. https://doi.org/https://doi.org/10.1016/0012-821X(94)90037-X

Maclennan, J. (2019). Mafic tiers and transient mushes: evidence from Iceland. *Philosophical Transactions of the Royal Society of London Series A, 377*, 20180021. https://doi.org/10.1098/rsta.2018.0021

Mader, H. (1998). Conduit flow and fragmentation. *Geological Society, London, Special Publications, 145*(1), 51-71.

Manconi, A., Longpré, M.-A., Walter, T. R., Troll, V. R., & Hansteen, T. H. (2009). The effects of flank collapses on volcano plumbing systems. *Geology, 37*(12), 1099-1102. https://doi.org/10.1130/g30104a.1

Mangan, M., & Sisson, T. (2000). Delayed, disequilibrium degassing in rhyolite magma: decompression experiments and implications for explosive volcanism. *Earth and planetary science letters, 183*(3), 441-455. https://doi.org/https://doi.org/10.1016/S0012-821X(00)00299-5

Mangan, M. T., & Cashman, K. V. (1996). The structure of basaltic scoria and reticulite and inferences for vesiculation, foam formation, and fragmentation in lava fountains. *Journal of Volcanology and Geothermal Research, 73*(1), 1-18. https://doi.org/https://doi.org/10.1016/0377-0273(96)00018-2

Mangler, M. F., Petrone, C. M., & Prytulak, J. (2022). Magma recharge patterns control eruption styles and magnitudes at Popocatépetl volcano (Mexico). *Geology, 50*(3), 366-370. https://doi.org/10.1130/g49365. 1

Marschall, H. R., & Schumacher, J. C. (2012). Arc magmas sourced from mélange diapirs in subduction zones. *Nature Geoscience, 5*(12), 862-867. https://doi.org/10.1038/ngeo1634

Martel, C., & Iacono-Marziano, G. (2015). Timescales of bubble coalescence, outgassing, and foam collapse in decompressed rhyolitic melts. *Earth and planetary science letters, 412*, 173-185. https://doi.org/https://doi.org/10.1016/j.epsl.2014.12.010

Mason, R. M., Starostin, A. B., Melnik, O. E., & Sparks, R. S. J. (2006). From Vulcanian explosions to sustained explosive eruptions: The role of diffusive mass transfer in conduit flow dynamics. *Journal of Volcanology and Geothermal Research, 153*(1), 148-165. https://doi.org/https://doi.org/10.1016/j.jvolgeores.2005.08.011

Masson, D. G., Watts, A. B., Gee, M. J. R., Urgeles, R., Mitchell, N. C., Le Bas, T. P., & Canals, M. (2002). Slope failures on the flanks of the western Canary Islands. *Earth-Science Reviews, 57*(1), 1-35. https://doi.org/https://doi.org/10.1016/S0012-8252(01)00069-1

Mastin, L. G., Guffanti, M., Servranckx, R., Webley, P., Barsotti, S., Dean, K., Durant, A., Ewert, J. W., Neri, A., Rose, W. I., Schneider, D., Siebert, L., Stunder, B., Swanson, G., Tupper, A., Volentik, A., & Waythomas, C. F. (2009). A multidisciplinary effort to assign realistic source parameters to models of volcanic ash-cloud transport and dispersion during eruptions. *Journal of Volcanology and Geothermal Research, 186*(1), 10-21. https://doi.org/https://doi.org/10.1016/j.jvolgeores.2009.01.008

McBirney, A. R., & Murase, T. (1970). Factors governing the formation of pyroclastic rocks. *Bulletin Volcanologique, 34*(2), 372-384. https://doi.org/10.1007/BF02596762

McCulloch, M. T., & Gamble, J. A. (1991). Geochemical and geodynamical constraints on subduction zone magmatism. *Earth and planetary science letters, 102*(3), 358-374. https://doi.org/https://doi.org/10.1016/0012-821X(91)90029-H.

McDonald, G. W., Cronin, S. J., Kim, J. H., Smith, N. J., Murray, C. A., & Procter, J. N. (2017). Computable general equilibrium modelling of economic impacts from volcanic event scenarios at regional and national scale, Mt. Taranaki, New Zealand. *Bulletin of Volcanology, 79*(12), 87. https://doi.org/10.1007/s00445-017-1171-3

McGlone, M. S., & Neall, V. E. (1994). The late pleistocene and holocene vegetation history of Taranaki, North Island, New Zealand. *New Zealand journal of botany, 32*(3), 251-269. https://doi.org/10.1080/0028825X.1994.10410470

McGlone, M. S., Neall, V. E., & Clarkson, B. D. (1988). The effect of recent volcanic events and climatic changes on the vegetation of Mt Egmont (Mt Taranaki), New Zealand. *New Zealand journal of botany, 26*(1), 123-144. https://doi.org/10.1080/0028825X.1988.10410105

McGlone, M. S., Mildenhall, D. C., & Pole, M. S. (1996). History and paleoecology of New Zealand Nothofagus forests. *The Ecology and Biogeography of Nothofagus Forest. Yale University Press, New Haven*, 83-130.

McGuire, W. J. (1996). Volcano instability: a review of contemporary themes. *Geological Society of London Special Publications, 110*, 1-23. https://doi.org/10.1144/gsl.Sp.1996.110.01.01

Melekhova, E., Blundy, J., Robertson, R., & Humphreys, M. C. S. (2015). Experimental Evidence for Polybaric Differentiation of Primitive Arc Basalt beneath St. Vincent, Lesser Antilles. *Journal of Petrology, 56*(1), 161-192. https://doi.org/10.1093/petrology/egu074

Melekhova, E., Blundy, J., Martin, R., Arculus, R., & Pichavant, M. (2017). Petrological and experimental evidence for differentiation of water-rich magmas beneath St. Kitts, Lesser Antilles. *Contributions to Mineralogy and Petrology, 172*(11), 98. https://doi.org/10.1007/s00410-017-1416-3

Melnik, O., Sparks, R. S. J., Druitt, T. H., & Kokelaar, B. P. (2002). Modelling of conduit flow dynamics during explosive activity at Soufrière Hills Volcano, Montserrat. In *The Eruption of Soufrière Hills Volcano, Montserrat from 1995 to 1999* (Vol. 21, pp. 0). Geological Society of London. https://doi.org/10.1144/gsl.Mem.2002.021.01.14

Metcalfe, A., Moune, S., Komorowski, J.-C., Kilgour, G., Jessop, D. E., Moretti, R., & Legendre, Y. (2021). Magmatic Processes at La Soufrière de Guadeloupe: Insights from Crystal Studies and Diffusion Timescales for eruption onset. *Frontiers in Earth Science, 9*, 78. https://doi.org/10.3389/feart.2021.617294

Métrich, N., & Deloule, E. (2014). Water content, δD and δ11B tracking in the Vanuatu arc magmas (Aoba Island): Insights from olivine-hosted melt inclusions. *Lithos, 206-207*, 400-408. https://doi.org/https://doi.org/10.1016/j.lithos.2014.08.011

Miall, A. D. (1996). *The geology of fluvial deposits : sedimentary facies, basin analysis, and petroleum geology*. Springer-Verlag. https://cir.nii.ac.jp/crid/1130282268814866560

Mills, S. A. (2019). *Using Proximal Deposits to Understand the Physical Dynamics of the Largest Plinian Eruption from Tuhua (Mayor) Island* University of Auckland.

Moebis, A., Cronin, S. J., Neall, V. E., & Smith, I. E. (2011). Unravelling a complex volcanic history from fine-grained, intricate Holocene ash sequences at the Tongariro Volcanic Centre, New Zealand. *Quaternary international, 246*(1), 352-363. https://doi.org/https://doi.org/10.1016/j.quaint.2011.05.035

Mollo, S., Putirka, K., Iezzi, G., Del Gaudio, P., & Scarlato, P. (2011a). Plagioclase–melt (dis)equilibrium due to cooling dynamics: Implications for thermometry, barometry and hygrometry. *Lithos, 125*(1), 221-235. https://doi.org/https://doi.org/10.1016/j.lithos.2011.02.008

Mollo, S., Lanzafame, G., Masotta, M., Iezzi, G., Ferlito, C., & Scarlato, P. (2011b). Cooling history of a dike as revealed by mineral chemistry: A case study from Mt. Etna volcano. *Chemical Geology, 288*(1), 39-52. https://doi.org/https://doi.org/10.1016/j.chemgeo.2011.06.016

Molloy, C., Shane, P., & Augustinus, P. (2009). Eruption recurrence rates in a basaltic volcanic field based on tephra layers in maar sediments: implications for hazards in the Auckland volcanic field. *Geological Society of America Bulletin, 121*(11-12), 1666-1677.

Moore, J. G., Clague, D. A., Holcomb, R. T., Lipman, P. W., Normark, W. R., & Torresan, M. E. (1989). Prodigious submarine landslides on the Hawaiian Ridge. *Journal of Geophysical Research B: Solid Earth, 94*(B12), 17465-17484. https://doi.org/10.1029/JB094iB12p17465

Moriya, I. (1980). Bandaian eruption and landforms associated with it. *collection of articles in memory of retirement of Prof. K. Nishimura from Tohoku University. Fac Sci Tohoku Univ, Sendai*, 214-219.

Mortimer, N., Tulloch, A. J., & Ireland, T. R. (1997). Basement geology of Taranaki and Wanganui Basins, New Zealand. *New Zealand Journal of Geology and Geophysics, 40*(2), 223-236. https://doi.org/10.1080/00288306.1997.9514754

Mortimer, N., Herzer, R. H., Gans, P. B., Parkinson, D. L., & Seward, D. (1998). Basement geology from Three Kings Ridge to West Norfolk Ridge, southwest Pacific Ocean: evidence from petrology, geochemistry and isotopic dating of dredge samples. *Marine Geology, 148*(3), 135-162. https://doi.org/https://doi.org/10.1016/S0025-3227(98)00007-3

Mueller, S., Scheu, B., Kueppers, U., Spieler, O., Richard, D., & Dingwell, D. B. (2011). The porosity of pyroclasts as an indicator of volcanic explosivity. *Journal of Volcanology and Geothermal Research, 203*(3), 168-174. https://doi.org/https://doi.org/10.1016/j.jvolgeores.2011.04.006

Muller, J. R., Ito, G., & Martel, S. J. (2001). Effects of volcano loading on dike propagation in an elastic half-space [Article]. *Journal of Geophysical Research: Solid Earth, 106*(B6), 11101-11113, Article 2000jb900461. https://doi.org/10.1029/2000jb900461

Myeong, B., Regelous, M., Haase, K. M., & Münker, C. (2023). Effects of variable slab components and tectonics on magma composition in the intra-oceanic Kermadec Arc-Backarc system. *Chemical Geology, 616*, 121246. https://doi.org/https://doi.org/10.1016/j.chemgeo.2022.121246

Nakamura, K. (1977). Volcanoes as possible indicators of tectonic stress orientation — principle and proposal. *Journal of Volcanology and Geothermal Research, 2*(1), 1-16. https://doi.org/https://doi.org/10.1016/0377-0273(77)90012-9

Namur, O., Montalbano, S., Bolle, O., & Vander Auwera, J. (2020). Petrology of the April 2015 Eruption of Calbuco Volcano, Southern Chile. *Journal of Petrology, 61*(8). https://doi.org/10.1093/petrology/egaa084

Navon, O., Chekhmir, A., & Lyakhovsky, V. (1998). Bubble growth in highly viscous melts: theory, experiments, and autoexplosivity of dome lavas. *Earth and planetary science letters, 160*(3), 763-776. https://doi.org/https://doi.org/10.1016/S0012-821X(98)00126-5

Neall, V. (1979). Sheets P19, P20, and P21 New Plymouth, Egmont, and Manaia: New Zealand. *Department of Scientific and Industrial Research*.

Neall, V., & Jansen, H. (1984). Anomalous radiocarbon dates from Mt Egmont. Programme and Abstracts, Geological Society of New Zealand Conference. Geological Society ofNew Zealand miscellaneouspublication 31A,

Neall, V., & Alloway, B. (1996). Volcanic hazard map of Western Taranaki. *Massey Uni Dep Soil Sci Occ Report, 12*.

Neall, V. E. (1971). Volcanic Domes and lineations in Egmont National Park. *New Zealand Journal of Geology and Geophysics, 14*(1), 71-81. https://doi.org/10.1080/00288306.1971.10422461

Neall, V. E. (1972). Tephrochronology and tephrostratigraphy of western Taranaki (N108–109), New Zealand. *New Zealand Journal of Geology and Geophysics, 15*(4), 507-557. https://doi.org/10.1080/00288306.1972.10423983

Neall, V. E. (1975). Climate-controlled tephra redeposition on Pouakai ring plain, Taranaki, New Zealand. *New Zealand Journal of Geology and Geophysics, 18*(2), 317-326. https://doi.org/10.1080/00288306.1975.10418202

Neall, V. E. (1977). Genesis and weathering of andosols in Taranaki, New Zealand. *Soil Science, 123*(6). https://journals.lww.com/soilsci/fulltext/1977/06000/genesis_and_weathering_of_andosols_in_taranaki,.9.aspx

Neall, V. E. (2003). *The volcanic history of Taranaki*. Institute of Natural Resources, Massey University.

Neall, V. E., & Alloway, B. (2004). *Quaternary Geological Map of Taranaki, 1: 100 000*. Institute of Natural Resources, Massey University.

Neall, V.E., Stewart, R. B., Smith, I. E. M. (1986). History and petrology of the Taranaki volcanoes. In: Smith, I. E. M (ed) Late Cenozoic volcanism. Royal Society of New Zealand Bulletin 23, 251-263.

Neall, V. E., Smith, I. E., & Stewart, R. (1986). History and petrology of the Taranaki volcanoes.

Nelson, S. T., & Montana, A. (1992). Sieve-textured plagioclase in volcanic rocks produced by rapid decompression. *American Mineralogist, 77*(11-12), 1242-1249.

Németh, K., Risso, C., Nullo, F., & Kereszturi, G. (2011). The role of collapsing and cone rafting on eruption style changes and final cone morphology: Los Morados scoria cone, Mendoza, Argentina. *Central European Journal of Geosciences, 3*(2), 102-118. https://doi.org/10.2478/s13533-011-0008-4

Neri, A., Papale, P., & Macedonio, G. (1998). The role of magma composition and water content in explosive eruptions: 2. Pyroclastic dispersion dynamics. *Journal of Volcanology and Geothermal Research, 87*(1), 95-115. https://doi.org/https://doi.org/10.1016/S0377-0273(98)00102-4

Newhall C, G. (1996). FIRE and MUD, Eruptions and Lahars of Mount Pinatubo, Philippines. *Philippine Institute of Volcanology and Seismology, 1126*. https://cir.nii.ac.jp/crid/1571135649480409344

Newhall, C. G. (1979). Temporal variation in the lavas of Mayon volcano, Philippines. *Journal of Volcanology and Geothermal Research, 6*(1), 61-83. https://doi.org/https://doi.org/10.1016/0377-0273(79)90047-7

Newhall, C. G., & Self, S. (1982). The Volcanic Explosivity Index (VEI): An estimate of explosive magnitude for historical volcanism. *Journal of Geophysical Research, 87*, 1231-1238. https://doi.org/10.1029/JC087iC02p01231

Newnham, R., & Alloway, B. (2004). A terrestrial record of Last Interglacial climate preserved by voluminous debris avalanche inundation in Taranaki, New Zealand. *Journal of Quaternary Science, 19*, 299-314. https://doi.org/10.1002/jqs.834

Nicholls, I. A., & Ringwood, A. E. (1973). Effect of Water on Olivine Stability in Tholeiites and the Production of Silica-Saturated Magmas in the Island-Arc Environment. *Journal of Geology, 81*, 285-300. https://doi.org/10.1086/627871

Nicol, A., Mazengarb, C., Chanier, F., Rait, G., Uruski, C., & Wallace, L. (2007). Tectonic evolution of the active Hikurangi subduction margin, New Zealand, since the Oligocene. *Tectonics, 26*, TC4002. https://doi.org/10.1029/2006tc002090

Nodder, S. D. (1993). Neotectonics of the offshore Cape Egmont Fault Zone, Taranaki Basin, New Zealand. *New Zealand Journal of Geology and Geophysics, 36*(2), 167-184. https://doi.org/10.1080/00288306.1993.9514566

Norris, R. J., & Cooper, A. F. (2007). The Alpine Fault, New Zealand: Surface geology and field relationships. *Geophysical Monograph Series, 175*, 157-175. https://doi.org/10.1029/175gm09

O'Callaghan, L., & Francis, P. (1986). Volcanological and petrological evolution of San Pedro volcano, Provincia EI Loa, North Chile. *Journal of the Geological Society, 143*(2), 275-286. https://doi.org/10.1144/gsjgs.143.2.0275

Oehler, J.-F., Lénat, J.-F., & Labazuy, P. (2008). Growth and collapse of the Reunion Island volcanoes. *Bulletin of Volcanology, 70*(6), 717-742. https://doi.org/10.1007/s00445-007-0163-0

Okumura, S., Nakamura, M., Tsuchiyama, A., Nakano, T., & Uesugi, K. (2008). Evolution of bubble microstructure in sheared rhyolite: Formation of a channel-like bubble network. *Journal of Geophysical Research (Solid Earth), 113*, B07208. https://doi.org/10.1029/2007jb005362

Okumura, S., Nakamura, M., Nakano, T., Uesugi, K., & Tsuchiyama, A. (2010). Shear deformation experiments on vesicular rhyolite: Implications for brittle fracturing, degassing, and compaction of magmas in volcanic conduits. *Journal of Geophysical Research: Solid Earth, 115*(B6).

Okumura, S., Nakamura, M., Uesugi, K., Nakano, T., & Fujioka, T. (2013). Coupled effect of magma degassing and rheology on silicic volcanism. *Earth and planetary science letters, 362*, 163-170. https://doi.org/https://doi.org/10.1016/j.epsl.2012.11.056

Okumura, S., Nakamura, M., Takeuchi, S., Tsuchiyama, A., Nakano, T., & Uesugi, K. (2009). Magma deformation may induce non-explosive volcanism via degassing through bubble networks. *Earth and planetary science letters, 281*(3), 267-274. https://doi.org/https://doi.org/10.1016/j.epsl.2009.02.036

Oliver, W. R. B. (1931). An ancient Maori oven on Mount Egmont. *The Journal of the Polynesian Society, 40*(2(158)), 73-80. http://www.jstor.org/stable/20702353

Pallister, J. S., Clynne, M. A., Wright, H. M., Van Eaton, A. R., Vallance, J. W., Sherrod, D. R., & Kokelaar, B. P. (2017). *Field-trip guide to Mount St. Helens, Washington - An overview of the eruptive history and petrology, tephra deposits, 1980 pyroclastic density current deposits, and the crater* [Report](2017-5022D). (Scientific Investigations Report, Issue. U. S. G. Survey. https://pubs.usgs.gov/publication/sir20175022D

Palmer, B. A., & Neall, V. E. (1991). Contrasting lithofacies architecture in ring-plain deposits related to edifice construction and destruction, the Quaternary Stratford and Opunake Formations, Egmont Volcano, New Zealand. *Sedimentary Geology, 74*(1), 71-88. https://doi.org/https://doi.org/10.1016/0037-0738(91)90035-C

Palmer, B. A., Alloway, B. V., & Neall, V. E. (1991). Volcanic-debris-avalanche deposits in New Zealand—lithofacies organization in unconfined, wet-avalanche flows.

Pankhurst, M. J., Morgan, D. J., Thordarson, T., & Loughlin, S. C. (2018). Magmatic crystal records in time, space, and process, causatively linked with volcanic unrest. *Earth and planetary science letters, 493*, 231-241. https://doi.org/https://doi.org/10.1016/j.epsl.2018.04.025

Papale, P. (1999). Strain-induced magma fragmentation in explosive eruptions. *Nature, 397*(6718), 425-428. https://doi.org/10.1038/17109

Papale, P., Neri, A., & Macedonio, G. (1998). The role of magma composition and water content in explosive eruptions: 1. Conduit ascent dynamics. *Journal of Volcanology and Geothermal Research, 87*(1), 75-93. https://doi.org/10.1016/S0377-0273(98)00101-2

Parat, F., Streck, M. J., Holtz, F., & Almeev, R. (2014). Experimental study into the petrogenesis of crystal-rich basaltic to andesitic magmas at Arenal volcano. *Contributions to Mineralogy and Petrology, 168*(2), 1040. https://doi.org/10.1007/s00410-014-1040-4

Pardo, N., Cronin, S. J., Palmer, A. S., & Németh, K. (2012a). Reconstructing the largest explosive eruptions of Mt. Ruapehu, New Zealand: lithostratigraphic tools to understand subplinian–plinian eruptions at andesitic volcanoes. *Bulletin of Volcanology, 74*(3), 617-640. https://doi.org/10.1007/s00445-011-0555-z

Pardo, N., Cronin, S., Palmer, A., Procter, J., & Smith, I. (2012b). Andesitic Plinian eruptions at Mt. Ruapehu: quantifying the uppermost limits of eruptive parameters. *Bulletin of Volcanology, 74*(5), 1161-1185. https://doi.org/10.1007/s00445-012-0588-y

Pardo, N., Cronin, S. J., Wright, H. M. N., Schipper, C. I., Smith, I., & Stewart, B. (2014). Pyroclast textural variation as an indicator of eruption column steadiness in andesitic Plinian eruptions at Mt. Ruapehu. *Bulletin of Volcanology, 76*(5), 822. https://doi.org/10.1007/s00445-014-0822-x

Paredes-Mariño, J., Scheu, B., Montanaro, C., Arciniega-Ceballos, A., Dingwell, D. B., & Perugini, D. (2019). Volcanic ash generation: Effects of componentry, particle size and conduit geometry on size-reduction processes. *Earth and planetary science letters, 514*, 13-27. https://doi.org/https://doi.org/10.1016/j.epsl.2019.02.028

Parfitt, E. A., & Wilson, L. (1995). Explosive volcanic eruptions—IX. The transition between Hawaiian-style lava fountaining and Strombolian explosive activity. *Geophysical Journal International, 121*(1), 226-232. https://doi.org/10.1111/j.1365-246X.1995.tb03523.x

Parfitt, E. A., & Wilson, L. (2008). *Fundamentals of Physical volcanology*. Blackwell Pub. https://cir.nii.ac.jp/crid/1130000793727590528

Parfitt, E. A. (2004). A discussion of the mechanisms of explosive basaltic eruptions. *Journal of Volcanology and Geothermal Research, 134*(1), 77-107. https://doi.org/https://doi.org/10.1016/j.jvolgeores.2004.01.002

Parolari, M., Gómez-Tuena, A., Errázuriz-Henao, C., & Cavazos-Tovar, J. G. (2021). Orogenic andesites and their link to the continental rock cycle. *Lithos, 382-383*, 105958. https://doi.org/https://doi.org/10.1016/j.lithos.2020.105958

Parson, L. M., & Wright, I. C. (1996). The Lau-Havre-Taupo back-arc basin: A southward-propagating, multi-stage evolution from rifting to spreading. *Tectonophysics, 263*(1), 1-22. https://doi.org/https://doi.org/10.1016/S0040-1951(96)00029-7

Patterson, D. B., & Graham, I. J. (1988). Petrogenesis of andesitic lavas from Mangatepopo valley and Upper Tama lake, Tongariro volcanic centre, New Zealand. *Journal of Volcanology and Geothermal Research, 35*(1), 17-29. https://doi.org/https://doi.org/10.1016/0377-0273(88)90003-0

Pérez, W., Freundt, A., Kutterolf, S., & Schmincke, H. U. (2009). The Masaya Triple Layer: A 2100 year old basaltic multi-episodic Plinian eruption from the Masaya Caldera Complex (Nicaragua). *Journal of Volcanology and Geothermal Research, 179*(3), 191-205. https://doi.org/https://doi.org/10.1016/j.jvolgeores.2008.10.015

Perfit, M. R., & P, D. J. (2000). Plate Tectonics and Volcanism.

Petrone, C. M., Braschi, E., & Francalanci, L. (2009). Understanding the collapse–eruption link at Stromboli, Italy: A microanalytical study on the products of the recent Secche di Lazzaro phreatomagmatic activity. *Journal of Volcanology and Geothermal Research, 188*(4), 315-332. https://doi.org/https://doi.org/10.1016/j.jvolgeores.2009.09.016

Pillans, B. (1990). Pleistocene marine terraces in New Zealand: A review. *New Zealand Journal of Geology and Geophysics, 33*(2), 219-231. https://doi.org/10.1080/00288306.1990.10425680

Pillans, B. (1994). Direct marine-terrestrial correlations, Wanganui Basin, New Zealand: The last 1 million years. *Quaternary Science Reviews, 13*(3), 189-200. https://doi.org/https://doi.org/10.1016/0277-3791(94)90024-8

Pillans, B., McGlone, M., Palmer, A., Mildenhall, D., Alloway, B., & Berger, G. (1993). The last glacial maximum in central and southern North Island, New Zealand: a paleoenvironmental reconstruction using the Kawakawa Tephra Formation as a chronostratigraphic marker. *Palaeogeography, palaeoclimatology, palaeoecology, 101*(3), 283-304. https://doi.org/https://doi.org/10.1016/0031-0182(93)90020-J

Pinel, V., & Jaupart, C. (2000). The effect of edifice load on magma ascent beneath a volcano [Article]. *Philosophical Transactions of the Royal Society A: Mathematical, Physical and Engineering Sciences, 358*(1770), 1515-1532. https://doi.org/10.1098/rsta.2000.0601

Pinel, V., & Jaupart, C. (2003). Magma chamber behavior beneath a volcanic edifice. *Journal of Geophysical Research : Solid Earth, 108*, p. 289-310. https://doi.org/10.1029/2002jb001751

Pinel, V., & Jaupart, C. (2004). Magma storage and horizontal dyke injection beneath a volcanic edifice. *Earth and planetary science letters, 221*(1), 245-262. https://doi.org/https://doi.org/10.1016/S0012-821X(04)00076-7

Pinel, V., & Jaupart, C. (2005). Some consequences of volcanic edifice destruction for eruption conditions. *Journal of Volcanology and Geothermal Research, 145*(1), 68-80. https://doi.org/https://doi.org/10.1016/j.jvolgeores.2005.01.012

Pinel, V., & Albino, F. (2013). Consequences of volcano sector collapse on magmatic storage zones: Insights from numerical modeling. *Journal of Volcanology and Geothermal Research, 252*, 29-37. https://doi.org/https://doi.org/10.1016/j.jvolgeores.2012.11.009

Pinel, V., Jaupart, C., & Albino, F. (2010). On the relationship between cycles of eruptive activity and growth of a volcanic edifice. *Journal of Volcanology and Geothermal Research, 194*(4), 150-164. https://doi.org/https://doi.org/10.1016/j.jvolgeores.2010.05.006

Pinkerton, H., Wilson, L., & MacDonald, R. (2002). The transport and eruption of magma from volcanoes: A review. *Contemporary Physics, 43*(3), 197-210. https://doi.org/10.1080/00107510110097756

Pioli, L., Erlund, E., Johnson, E., Cashman, K., Wallace, P., Rosi, M., & Delgado Granados, H. (2008). Explosive dynamics of violent Strombolian eruptions: The eruption of Parícutin Volcano 1943–1952 (Mexico). *Earth and planetary science letters, 271*(1), 359-368. https://doi.org/https://doi.org/10.1016/j.epsl.2008.04.026

Pistone, M., Caricchi, L., Ulmer, P., Reusser, E., & Ardia, P. (2013). Rheology of volatile-bearing crystal mushes: Mobilization vs. viscous death. *Chemical Geology, 345*, 16-39. https://doi.org/https://doi.org/10.1016/j.chemgeo.2013.02.007

Pistone, M., Caricchi, L., Ulmer, P., Burlini, L., Ardia, P., Reusser, E., Marone, F., & Arbaret, L. (2012). Deformation experiments of bubble- and crystal-bearing magmas: Rheological and microstructural analysis. *Journal of Geophysical Research (Solid Earth), 117*, B05208. https://doi.org/10.1029/2011jb008986

Pistone, M., Arzilli, F., Dobson, K. J., Cordonnier, B., Reusser, E., Ulmer, P., Marone, F., Whittington, A. G., Mancini, L., Fife, J. L., & Blundy, J. D. (2015). Gas-driven filter pressing in magmas: Insights into in-situ melt segregation from crystal mushes. *Geology, 43*(8), 699-702. https://doi.org/10.1130/g36766.1

Platz, T. (2007). *Understanding aspects of andesitic dome-forming eruptions through the last 1000 yrs of volcanism at Mt. Taranaki, New Zealand: a dissertation presented in partial fulfilment of the*

requirements for the degree of Doctor of Philosophy in Earth Science, Massey University, Palmerston North, New Zealand Massey University].

Platz, T., Cronin, S. J., Cashman, K. V., Stewart, R. B., & Smith, I. E. M. (2007). Transition from effusive to explosive phases in andesite eruptions — A case-study from the AD1655 eruption of Mt. Taranaki, New Zealand. *Journal of Volcanology and Geothermal Research, 161*(1), 15-34. https://doi.org/https://doi.org/10.1016/j.jvolgeores.2006.11.005

Platz, T., Cronin, S. J., Procter, J. N., Neall, V. E., & Foley, S. F. (2012). Non-explosive, dome-forming eruptions at Mt. Taranaki, New Zealand. *Geomorphology, 136*(1), 15-30. https://doi.org/https://doi.org/10.1016/j.geomorph.2011.06.016

Polacci, M., Pioli, L., & Rosi, M. (2003). The Plinian phase of the Campanian Ignimbrite eruption (Phlegrean Fields, Italy): evidence from density measurements and textural characterization of pumice. *Bulletin of Volcanology, 65*(6), 418-432. https://doi.org/10.1007/s00445-002-0268-4

Polacci, M., Corsaro, R. A., & Andronico, D. (2006a). Coupled textural and compositional characterization of basaltic scoria: Insights into the transition from Strombolian to fire fountain activity at Mount Etna, Italy. *Geology, 34*(3), 201-204. https://doi.org/10.1130/g22318.1.

Polacci, M., Baker, D. R., Mancini, L., Tromba, G., & Zanini, F. (2006b). Three-dimensional investigation of volcanic textures by X-ray microtomography and implications for conduit processes. *Geophysical research letters, 33*, L13312. https://doi.org/10.1029/2006gl026241

Ponomareva, V., Kyle, P., Pevzner, M., Sulerzhitsky, L., & Hartman, M. (2007). Holocene eruptive history of Shiveluch Volcano, Kamchatka Peninsula, Russia. *Geophysical Monograph Series, 172*, 263-282. https://doi.org/10.1029/172gm19

Ponomareva, V. V., Pevzner, M. M., & Melekestsev, I. V. (1998). Large debris avalanches and associated eruptions in the Holocene eruptive history of Shiveluch Volcano, Kamchatka, Russia. *Bulletin of Volcanology, 59*(7), 490-505. https://doi.org/10.1007/s004450050206

Ponomareva, V. V., Melekestsev, I. V., & Dirksen, O. V. (2006). Sector collapses and large landslides on Late Pleistocene–Holocene volcanoes in Kamchatka, Russia. *Journal of Volcanology and Geothermal Research, 158*(1), 117-138. https://doi.org/https://doi.org/10.1016/j.jvolgeores.2006.04.016

Presley, T. K., Sinton, J. M., & Pringle, M. (1997). Postshield volcanism and catastrophic mass wasting of the Waianae Volcano, Oahu, Hawaii [Article]. *Bulletin of Volcanology, 58*(8), 597-616. https://doi.org/10.1007/s004450050165

Price, R. C., McCulloch, M. T., Smith, I. E. M., & Stewart, R. B. (1992). Pb-Nd-Sr isotopic compositions and trace element characteristics of young volcanic rocks from Egmont Volcano and comparisons with basalts and andesites from the Taupo Volcanic Zone, New Zealand. *Geochimica et cosmochimica acta, 56*(3), 941-953. https://doi.org/https://doi.org/10.1016/0016-7037(92)90038-K

Price, R. C., Stewart, R. B., Woodhead, J. D., & Smith, I. E. M. (1999). Petrogenesis of High-K Arc Magmas: Evidence from Egmont Volcano, North Island, New Zealand. *Journal of Petrology, 40*(1), 167-197. https://doi.org/10.1093/petroj/40.1.167

Price, R. C., Cronin, S. J., Smith, I. E. M., Ukstins, I. A., & Zernack, A. V. (2021). Formation of crystal-rich, mixed, intermediate lavas at Pouakai Volcano and the evolution of the Taranaki volcanic lineament, western North Island, New Zealand. *Lithos, 380-381*, 105850. https://doi.org/https://doi.org/10.1016/j.lithos.2020.105850

Price, R. C., Gamble, J. A., Smith, I. E. M., Stewart, R. B., Eggins, S., & Wright, I. C. (2005). An integrated model for the temporal evolution of andesites and rhyolites and crustal development in New Zealand's North Island. *Journal of Volcanology and Geothermal Research, 140*(1), 1-24. https://doi.org/https://doi.org/10.1016/j.jvolgeores.2004.07.013

Price, R. C., Smith, I. E. M., Stewart, R. B., Gamble, J. A., Gruender, K., & Maas, R. (2016). High-K andesite petrogenesis and crustal evolution: Evidence from mafic and ultramafic xenoliths, Egmont Volcano (Mt. Taranaki) and comparisons with Ruapehu Volcano, North Island, New Zealand. *Geochimica et cosmochimica acta, 185*, 328-357. https://doi.org/https://doi.org/10.1016/j.gca.2015.12.009

Price, R. C., Gamble, J. A., Smith, I. E. M., Maas, R., Waight, T., Stewart, R. B., & Woodhead, J. (2012). The Anatomy of an Andesite Volcano: a Time–Stratigraphic Study of Andesite Petrogenesis and Crustal Evolution at Ruapehu Volcano, New Zealand. *Journal of Petrology, 53*(10), 2139-2189. https://doi.org/10.1093/petrology/egs050

Procter, J. (2009). *Towards improving volcanic mass flow hazard assessment at New Zealand stratovolcanoes: a thesis presented in partial fulfilment of the requirements for the degree of Doctor of Philosophy in Earth Science at Massey University, Palmerston North, New Zealand* Massey University].

Procter, J., Cronin, S., & Zernack, A. (2009). Landscape and sedimentary response to catastrophic debris avalanches, western Taranaki, New Zealand. *Sedimentary Geology, 220*(3), 271-287. https://doi.org/https://doi.org/10.1016/j.sedgeo.2009.04.027

Procter, J. N., Zernack, A. V., & Cronin, S. J. (2021). Computer simulation of a volcanic debris avalanche from Mt. Taranaki, New Zealand. In *Volcanic Debris Avalanches* (pp. 281-310). Springer.

Procter, J. N., Cronin, S. J., Platz, T., Patra, A., Dalbey, K., Sheridan, M., & Neall, V. (2010). Mapping block-and-ash flow hazards based on Titan 2D simulations: a case study from Mt. Taranaki, NZ. *Natural Hazards, 53*(3), 483-501. https://doi.org/10.1007/s11069-009-9440-x

Prousevitch, A. A., Sahagian, D. L., & Anderson, A. T. (1993). Dynamics of diffusive bubble growth in magmas: Isothermal case. *Journal of Geophysical Research: Solid Earth, 98*(B12), 22283-22307. https://doi.org/10.1029/93jb02027

Proussevitch, A., & Sahagian, D. (2005). Bubbledrive-1: A numerical model of volcanic eruption mechanisms driven by disequilibrium magma degassing. *Journal of Volcanology and Geothermal Research, 143*(1), 89-111. https://doi.org/https://doi.org/10.1016/j.jvolgeores.2004.09.012

Proussevitch, A., A., & Sahagian, D., L. (1996). Dynamics of coupled diffusive and decompressive bubble growth in magmatic systems. *Journal of Geophysical Research: Solid Earth, 101*(B8), 17447-17455. https://doi.org/10.1029/96jb01342

Proussevitch, A. A., & Sahagian, D. L. (1998). Dynamics and energetics of bubble growth in magmas: Analytical formulation and numerical modeling. *Journal of Geophysical Research, 103*, 18,223-218,251. https://doi.org/10.1029/98jb00906

Proussevitch, A. A., Sahagian, D. L., & Kutolin, V. A. (1993). Stability of foams in silicate melts. *Journal of Volcanology and Geothermal Research, 59*(1), 161-178. https://doi.org/https://doi.org/10.1016/0377-0273(93)90084-5

Putirka, K., Johnson, M., Kinzler, R., Longhi, J., & Walker, D. (1996). Thermobarometry of mafic igneous rocks based on clinopyroxene-liquid equilibria, 0–30 kbar. *Contributions to Mineralogy and Petrology, 123*(1), 92-108. https://doi.org/10.1007/s004100050145

Putirka, K. D. (2008). Thermometers and Barometers for Volcanic Systems. *Reviews in Mineralogy and Geochemistry, 69*(1), 61-120. https://doi.org/10.2138/rmg.2008.69.3

Pyle, D. M. (2000) The sizes of volcanic eruptions. In Encyclopedia of volcanoes. In Sigurdsson H, Houghton B, McNutt S, Rymer H, & S. J (Eds) (pp. 263–269). London, UK: Academic Press.

Pyle, D. M. (1989). The thickness, volume and grainsize of tephra fall deposits. *Bulletin of Volcanology, 51*(1), 1-15. https://doi.org/10.1007/BF01086757

Pyle, D. M. (1995). Assessment of the minimum volume of tephra fall deposits. *Journal of Volcanology and Geothermal Research, 69*(3), 379-382. https://doi.org/https://doi.org/10.1016/0377-0273(95)00038-0

Pyle, D. M. (2015). The sizes of volcanic eruptions. In Encyclopedia of volcanoes. In H. Sigurdsson (Ed.), *The Encyclopedia of Volcanoes (Second Edition)* (pp. 257-264). Academic Press. https://doi.org/https://doi.org/10.1016/B978-0-12-385938-9.00013-4

Regassa, A., Van Daele, K., De Paepe, P., Dumon, M., Deckers, J., Asrat, A., & Van Ranst, E. (2014). Characterizing weathering intensity and trends of geological materials in the Gilgel Gibe catchment, southwestern Ethiopia. *Journal of African Earth Sciences, 99*, 568-580. https://doi.org/https://doi.org/10.1016/j.jafrearsci.2014.05.012

Reid, M. E., Sisson, T. W., & Brien, D. L. (2001). Volcano collapse promoted by hydrothermal alteration and edifice shape, Mount Rainier, Washington. *Geology, 29*(9), 779-782. https://doi.org/10.1130/0091-7613(2001)029<0779:Vcpbha>2.0.Co;2

Renjith, M. L. (2014). Micro-textures in plagioclase from 1994–1995 eruption, Barren Island Volcano: Evidence of dynamic magma plumbing system in the Andaman subduction zone. *Geoscience Frontiers, 5*(1), 113-126. https://doi.org/https://doi.org/10.1016/j.gsf.2013.03.006

Reubi, O., & Blundy, J. (2009). A dearth of intermediate melts at subduction zone volcanoes and the petrogenesis of arc andesites. *Nature, 461*(7268), 1269-1273. https://doi.org/10.1038/nature08510

Reyners, M. (1983). Lateral segmentation of the subducted plate at the Hikurangi Margin, New Zealand: Seismological evidence. *Tectonophysics, 96*(3), 203-223. https://doi.org/https://doi.org/10.1016/0040-1951(83)90218-4

Reyners, M., Eberhart-Phillips, D., & Bannister, S. (2011). Tracking repeated subduction of the Hikurangi Plateau beneath New Zealand. *Earth and planetary science letters, 311*(1), 165-171. https://doi.org/https://doi.org/10.1016/j.epsl.2011.09.011

Reyners, M., Eberhart-Phillips, D., Stuart, G., & Nishimura, Y. (2006). Imaging subduction from the trench to 300 km depth beneath the central North Island, New Zealand, with Vp and Vp/Vs. *Geophysical Journal International, 165*(2), 565-583. https://doi.org/10.1111/j.1365-246X.2006.02897.x

Ringwood, A. E. (1974). The petrological evolution of island arc systems. *Journal of the Geological Society, 130*(3), 183-204. https://doi.org/doi:10.1144/gsjgs.130.3.0183

Ritter, J. B., Miller, J. R., Enzel, Y., & Wells, S. G. (1995). Reconciling the roles of tectonism and climate in Quaternary alluvial fan evolution. *Geology, 23*(3), 245-248. https://doi.org/10.1130/0091-7613(1995)023<0245:Rtrota>2.3.Co;2

Robin, C., Komorowski, J.-C., Boudal, C., & Mossand, P. (1990). Mixed-magma pyroclastic surge deposits associated with debris avalanche deposits at Colima volcanoes, Mexico. *Bulletin of Volcanology, 52*(5), 391-403. https://doi.org/10.1007/BF00302051

Romagnoli, C., Casalbore, D., Chiocci, F. L., & Bosman, A. (2009). Offshore evidence of large-scale lateral collapses on the eastern flank of Stromboli, Italy, due to structurally-controlled, bilateral flank instability. *Marine Geology, 262*(1), 1-13. https://doi.org/https://doi.org/10.1016/j.margeo.2009.02.004

Rose, W. I. (1993). Comment on 'another look at the calculation of fallout tephra volumes' by Judy Fierstein and Manuel Nathenson. *Bulletin of Volcanology, 55*(5), 372-374.

Rose, W. I., Palma, J. L., Escobar Wolf, R., Matías Gomez, R. O., Rose, W. I., Palma, J. L., Granados, H. D., & Varley, N. (2013). A 50 yr eruption of a basaltic composite cone: Pacaya, Guatemala. In *Understanding Open-Vent Volcanism and Related Hazards* (Vol. 498, pp. 0). Geological Society of America. https://doi.org/10.1130/2013.2498(01)

Rosi, M. (1998). Plinian eruption columns: particle transport and fallout. *From magma to tephra. Elsevier, Amsterdam*, 139-172.

Rosi, M., Principe, C., & Vecci, R. (1993). The 1631 Vesuvius eruption. A reconstruction based on historical and stratigraphical data. *Journal of Volcanology and Geothermal Research, 58*(1), 151-182. https://doi.org/https://doi.org/10.1016/0377-0273(93)90106-2

Rotella, M. D., Wilson, C. J. N., Barker, S. J., Cashman, K. V., Houghton, B. F., & Wright, I. C. (2014). Bubble development in explosive silicic eruptions: insights from pyroclast vesicularity textures from Raoul volcano (Kermadec arc). *Bulletin of Volcanology, 76*(8), 826. https://doi.org/10.1007/s00445-014-0826-6

Roverato, M., & Dufresne, A. (2021). Volcanic debris avalanches: introduction and book structure. In M. Roverato, A. Dufresne, & J. Procter (Eds.), *Volcanic Debris Avalanches: From Collapse to Hazard* (pp. 1-10). Springer International Publishing. https://doi.org/10.1007/978-3-030-57411-6_5.

Roverato, M., Capra, L., Sulpizio, R., & Norini, G. (2011). Stratigraphic reconstruction of two debris avalanche deposits at Colima Volcano (Mexico): Insights into pre-failure conditions and climate influence. *Journal of Volcanology and Geothermal Research, 207*(1), 33-46. https://doi.org/https://doi.org/10.1016/j.jvolgeores.2011.07.003

Roverato, M., Cronin, S., Procter, J., & Capra, L. (2015). Textural features as indicators of debris avalanche transport and emplacement, Taranaki volcano. *GSA Bulletin, 127*(1-2), 3-18. https://doi.org/10.1130/b30946.1

Roverato, M., Di Traglia, F., Procter, J., Paguican, E., & Dufresne, A. (2021). Factors Contributing to Volcano Lateral Collapse. In M. Roverato, A. Dufresne, & J. Procter (Eds.), *Volcanic Debris Avalanches: From Collapse to Hazard* (pp. 91-119). Springer International Publishing. https://doi.org/10.1007/978-3-030-57411-6_5.

Rowan, C. J., Roberts, A. P., & Rait, G. J. (2005). Relocation of the tectonic boundary between the Raukumara and Wairoa Domains (East Coast, North Island, New Zealand): Implications for the rotation history of the Hikurangi margin. *New Zealand Journal of Geology and Geophysics, 48*(1), 185-196. https://doi.org/10.1080/00288306.2005.9515108

Rowell, C. R., Jellinek, A. M., Hajimirza, S., & Aubry, T. J. (2022). External Surface Water Influence on Explosive Eruption Dynamics, With Implications for Stratospheric Sulfur Delivery and Volcano-Climate Feedback. *Frontiers in Earth Science, 10*, 788294. https://doi.org/10.3389/feart.2022.78829410.31223/x5xp6z

Ruprecht, P., Bergantz, G. W., Cooper, K. M., & Hildreth, W. (2012). The Crustal Magma Storage System of Volcán Quizapu, Chile, and the Effects of Magma Mixing on Magma Diversity. *Journal of Petrology, 53*(4), 801-840. https://doi.org/10.1093/petrology/egs002

Rust, A. C., & Cashman, K. V. (2004). Permeability of vesicular silicic magma: inertial and hysteresis effects. *Earth and planetary science letters, 228*(1), 93-107. https://doi.org/https://doi.org/10.1016/j.epsl.2004.09.025

Rust, A., & Cashman, K. (2011). Permeability controls on expansion and size distributions of pyroclasts. *Journal of Geophysical Research: Solid Earth, 116*(B11).

Saar, M. O., & Manga, M. (1999). Permeability-porosity relationship in vesicular basalts. *Geophysical research letters, 26*, 111-114. https://doi.org/10.1029/1998gl900256

Sable, J., Houghton, B., Wilson, C., & Carey, R. (2006). Complex proximal sedimentation from Plinian plumes: the example of Tarawera 1886. *Bulletin of Volcanology, 69*(1), 89.

Sahagian, D. (1999). Volcanology: Magma fragmentation in eruptions. *Nature, 402*, 589-591. https://doi.org/10.1038/45099

Sahagian, D. (2005). Volcanic eruption mechanisms: Insights from intercomparison of models of conduit processes. *Journal of Volcanology and Geothermal Research, 143*(1), 1-15. https://doi.org/https://doi.org/10.1016/j.jvolgeores.2004.12.006

Salmon, M. L., Stern, T. A., & Savage, M. K. (2011). A major step in the continental Moho and its geodynamic consequences: the Taranaki-Ruapehu line, New Zealand. *Geophysical Journal International, 186*(1), 32-44. https://doi.org/10.1111/j.1365-246X.2011.05035.x

Samaniego, P., Barba, D., Robin, C., Fornari, M., & Bernard, B. (2012). Eruptive history of Chimborazo volcano (Ecuador): A large, ice-capped and hazardous compound volcano in the Northern Andes. *Journal of Volcanology and Geothermal Research, 221-222*, 33-51. https://doi.org/https://doi.org/10.1016/j.jvolgeores.2012.01.014

Sandiford, A., Alloway, B., & Shane, P. (2001). A 28 000–6600 cal yr record of local and distal volcanism preserved in a paleolake, Auckland, New Zealand. *New Zealand Journal of Geology and Geophysics, 44*(2), 323-336. https://doi.org/10.1080/00288306.2001.9514941

Sarna-Wojcicki A, M. (1981). Areal distribution, thickness, mass, volume, and grain size of air-fall ash from the six major eruptions of 1980. *The 1980 Eruptions of Mount St. Helens*, 577-601. https://cir.nii.ac.jp/crid/1571417124294377344

Sato, H., Fujii, T., & Nakada, S. (1992). Crumbling of dacite dome lava and generation of pyroclastic flows at Unzen volcano. *Nature, 360*(6405), 664-666. https://doi.org/10.1038/360664a0

Scandone, R., & Malone, S. D. (1985). Magma supply, magma discharge and readjustment of the feeding system of mount St. Helens during 1980. *Journal of Volcanology and Geothermal Research, 23*(3), 239-262. https://doi.org/https://doi.org/10.1016/0377-0273(85)90036-8

Scheu, B., Spieler, O., & Dingwell, D. B. (2006). Dynamics of explosive volcanism at Unzen volcano: an experimental contribution. *Bulletin of Volcanology, 69*(2), 175-187. https://doi.org/10.1007/s00445-006-0066-5

Schindlbeck, J. C., Freundt, A., & Kutterolf, S. (2014). Major changes in the post-glacial evolution of magmatic compositions and pre-eruptive conditions of Llaima Volcano, Andean Southern Volcanic Zone, Chile. *Bulletin of Volcanology, 76*(6), 830. https://doi.org/10.1007/s00445-014-0830-x

Schmidt, M. W., & Poli, S. (1998). Experimentally based water budgets for dehydrating slabs and consequences for arc magma generation. *Earth and planetary science letters, 163*(1), 361-379. https://doi.org/https://doi.org/10.1016/S0012-821X(98)00142-3

Schwarzkopf, L. M., Schmincke, H.-U., & Cronin, S. J. (2005). A conceptual model for block-and-ash flow basal avalanche transport and deposition, based on deposit architecture of 1998 and 1994 Merapi flows. *Journal of Volcanology and Geothermal Research, 139*(1), 117-134. https://doi.org/https://doi.org/10.1016/j.jvolgeores.2004.06.012

Scott, K. M., Vallance, J., & Pringle, P. T. (1995). Sedimentology, Behavior, and Hazards of Debris Flows at Mount Rainier, Washington. *Professional Paper*. https://doi.org/10.3133/pp1547

Scott, K. M., Vallance, J. W., Kerle, N., Luis Macías, J., Strauch, W., & Devoli, G. (2005). Catastrophic precipitation-triggered lahar at Casita volcano, Nicaragua: occurrence, bulking and transformation. *Earth surface processes and Landforms, 30*, 59-79. https://doi.org/10.1002/esp.1127

Scott, W. E., Iverson, R. M., Vallance, J. W., & Hildreth, W. (1995). *Volcano hazards in the Mount Adams region, Washington* [Report](95-492). (Open-File Report, Issue. U. S. G. Survey. https://pubs.usgs.gov/publication/ofr95492

Scott, W. E., Pierson, T. C., Schilling, S. P., Costa, J. E., Gardner, C. A., Vallance, J. W., & Major, J. J. (1997). *Volcano hazards in the Mount Hood region, Oregon* [Report](97-89). (Open-File Report, Issue. U. S. G. Survey. https://pubs.usgs.gov/publication/ofr9789

Searcy, C., Dean, K., & Stringer, W. (1998). PUFF: A high-resolution volcanic ash tracking model. *Journal of Volcanology and Geothermal Research, 80*(1), 1-16. https://doi.org/https://doi.org/10.1016/S0377-0273(97)00037-1

Shane, P. (2005). Towards a comprehensive distal andesitic tephrostratigraphic framework for New Zealand based on eruptions from Egmont volcano. *Journal of Quaternary Science, 20*(1), 45-57.

Shane, P., & Hoverd, J. (2002). Distal record of multi-sourced tephra in Onepoto Basin, Auckland, New Zealand: implications for volcanic chronology, frequency and hazards. *Bulletin of Volcanology, 64*(7), 441-454. https://doi.org/10.1007/s00445-002-0217-2

Shane, P., Maas, R., & Lindsay, J. (2017). History of Red Crater volcano, Tongariro Volcanic Centre (New Zealand): Abrupt shift in magmatism following recharge and contrasting evolution between neighboring volcanoes. *Journal of Volcanology and Geothermal Research, 340*, 1-15. https://doi.org/https://doi.org/10.1016/j.jvolgeores.2017.04.008

Shane, P., Costa, F., Cronin, S., Stirling, C., & Reid, M. (2023). Priming and eruption of andesite magmas at Taranaki volcano recorded in plagioclase phenocrysts. *Bulletin of Volcanology, 85*(9), 47. https://doi.org/10.1007/s00445-023-01661-0

Shea, T., Gurioli, L., & Houghton, B. F. (2012). Transitions between fall phases and pyroclastic density currents during the AD 79 eruption at Vesuvius: building a transient conduit model from the textural and volatile record. *Bulletin of Volcanology, 74*(10), 2363-2381. https://doi.org/10.1007/s00445-012-0668-z

Shea, T., Gurioli, L., Houghton, B. F., Cioni, R., & Cashman, K. V. (2011). Column collapse and generation of pyroclastic density currents during the A.D. 79 eruption of Vesuvius: The role of pyroclast density. *Geology, 39*(7), 695-698. https://doi.org/10.1130/g32092.1

Shea, T., Houghton, B. F., Gurioli, L., Cashman, K. V., Hammer, J. E., & Hobden, B. J. (2010). Textural studies of vesicles in volcanic rocks: An integrated methodology. *Journal of Volcanology and Geothermal Research, 190*(3), 271-289. https://doi.org/https://doi.org/10.1016/j.jvolgeores.2009.12.003

Sherburn, S., & White, R. S. (2006). Tectonics of the Taranaki region, New Zealand: Earthquake focal mechanisms and stress axes. *New Zealand Journal of Geology and Geophysics, 49*(2), 269-279. https://doi.org/10.1080/00288306.2006.9515165

Siebert, L. (1984). Large volcanic debris avalanches: Characteristics of source areas, deposits, and associated eruptions. *Journal of Volcanology and Geothermal Research, 22*(3), 163-197. https://doi.org/https://doi.org/10.1016/0377-0273(84)90002-7

Siebert, L. (1996). Hazards of large volcanic debris avalanches and associated eruptive phenomena. *Monitoring and Mitigation of Volcanic Hazards.*, 541-572. https://cir.nii.ac.jp/crid/1572824498950008576

Siebert, L., & Roverato, M. (2021). A Historical Perspective on Lateral Collapse and Volcanic Debris Avalanches. In M. Roverato, A. Dufresne, & J. Procter (Eds.), *Volcanic Debris Avalanches: From Collapse to Hazard* (pp. 11-50). Springer International Publishing. https://doi.org/10.1007/978-3-030-57411-6_2

Siebert, L., Glicken, H., & Ui, T. (1987). Volcanic hazards from Bezymianny- and Bandai-type eruptions. *Bulletin of Volcanology, 49*(1), 435-459. https://doi.org/10.1007/BF01046635

Siebert, L., Begét, J. E., & Glicken, H. (1995). The 1883 and late-prehistoric eruptions of Augustine volcano, Alaska. *Journal of Volcanology and Geothermal Research, 66*(1), 367-395. https://doi.org/https://doi.org/10.1016/0377-0273(94)00069-S

Siebert, L., Kimberly, P., Pullinger, C. R., Rose, W. I., Bommer, J. J., López, D. L., Carr, M. J., & Major, J. J. (2004). The voluminous Acajutla debris avalanche from Santa Ana volcano, western El Salvador, and comparison with other Central American edifice-failure events. In *Natural Hazards in El Salvador* (Vol. 375, pp. 0). Geological Society of America. https://doi.org/10.1130/0-8137-2375-2.5

Sieron, K., Capra, L., & Rodríguez-Elizararrás, S. (2014). Hazard assessment at San Martín volcano based on geological record, numerical modeling, and spatial analysis. *Natural Hazards, 70*(1), 275-297. https://doi.org/10.1007/s11069-013-0807-7

Silver, E., Day, S., Ward, S., Hoffmann, G., Llanes, P., Driscoll, N., Appelgate, B., & Saunders, S. (2009). Volcano collapse and tsunami generation in the Bismarck Volcanic Arc, Papua New Guinea. *Journal of Volcanology and Geothermal Research, 186*(3), 210-222. https://doi.org/https://doi.org/10.1016/j.jvolgeores.2009.06.013

Simkin, T., Siebert, L., & Sigurdsson, H. (2000). Earth's volcanoes and eruptions: An overview. In Sigurdsson H, Houghton B, McNutt S, Rymer H, & S. J (Eds.), *The Encyclopedia of Volcanoes (*pp. 249-262), Elsevier.

Sisson, T. W. (1995). Blast ashfall deposit of May 18, 1980 at Mount St. Helens, Washington. *Journal of Volcanology and Geothermal Research, 66*(1), 203-216. https://doi.org/https://doi.org/10.1016/0377-0273(94)00063-M

Skeet, H. M. (1901). Mt. Egmont and the Pouakai Range in N.Z. [Annual Report]. *Department of Lands Survey*, 136-137.

Smith, G. A., & Fritz, W. J. (1989). Volcanic influences on terrestrial sedimentation. *Geology, 17*(4), 375-376. https://doi.org/10.1130/0091-7613(1989)017<0375:Viots>2.3.Co;2

Song, S.-R., Jones, K. W., Lindquist, B. W., Dowd, B. A., & Sahagian, D. L. (2001). Synchrotron X-ray computed microtomography: studies on vesiculated basaltic rocks. *Bulletin of Volcanology, 63*(4), 252-263. https://doi.org/10.1007/s004450100141

Sparks, R. S. J. (1976). Grain size variations in ignimbrites and implications for the transport of pyroclastic flows. *Sedimentology, 23*(2), 147-188.

Sparks, R. S. J. (1978). The dynamics of bubble formation and growth in magmas: A review and analysis. *Journal of Volcanology and Geothermal Research, 3*(1), 1-37. https://doi.org/https://doi.org/10.1016/0377-0273(78)90002-1

Sparks, R. S. J., & Wilson, L. (1976). A model for the formation of ignimbrite by gravitational column collapse. *Journal of the Geological Society, 132*(4), 441-451. https://doi.org/doi:10.1144/gsjgs.132.4.0441

Sparks, R. S. J., & Brazier, S. (1982). New evidence for degassing processes during explosive eruptions. *Nature, 295*(5846), 218-220. https://doi.org/10.1038/295218a0

Sparks, R. S. J., Barclay, J., Jaupart, C., Mader, H. M., & Phillips, J. C. (1994). Physical aspects of magma degassing; 1, Experimental and theoretical constraints on vesiculation. *Reviews in Mineralogy and Geochemistry, 30*(1), 413-445.

Sparks, RSJ., Bursik, MI., Carey, SN., Gilbert, JS., Glaze, L., Sigurdsson, H., & Woods, AW. (1997). *Volcanic plumes*. John Wiley & Sons, Inc.

Sparks, S. R. J., Sigurdsson, H., & Wilson, L. (1977). Magma mixing: a mechanism for triggering acid explosive eruptions. *Nature, 267*(5609), 315-318. https://doi.org/10.1038/267315a0

Spieler, O., Dingwell, D. B., & Alidibirov, M. (2004). Magma fragmentation speed: an experimental determination. *Journal of Volcanology and Geothermal Research, 129*(1), 109-123. https://doi.org/https://doi.org/10.1016/S0377-0273(03)00235-X

Stern, T., Houseman, G., Salmon, M., & Evans, L. (2013). Instability of a lithospheric step beneath western North Island, New Zealand. *Geology, 41*(4), 423-426. https://doi.org/10.1130/g34028.1

Stern, T. A. (1985). A back-arc basin formed within continental lithosphere: The Central Volcanic region of New zealand. *Tectonophysics, 112*(1), 385-409. https://doi.org/https://doi.org/10.1016/0040-1951(85)90187-8

Stern, T. A. (1987). Asymmetric back-arc spreading, heat flux and structure associated with the Central Volcanic Region of New Zealand. *Earth and planetary science letters, 85*(1), 265-276. https://doi.org/https://doi.org/10.1016/0012-821X(87)90037-9

Stern, T. A., & Davey, F. J. (1987). A seismic investigation of the crustal and upper mantle structure within the Central Volcanic Region of New Zealand. *New Zealand Journal of Geology and Geophysics, 30*(3), 217-231. https://doi.org/10.1080/00288306.1987.10552618

Stern, T. A., & Holt, W. E. (1994). Platform subsidence behind an active subduction zone. *Nature, 368*(6468), 233-236. https://doi.org/10.1038/368233a0

Stern, T. A., Stratford, W. R., & Salmon, M. L. (2006). Subduction evolution and mantle dynamics at a continental margin: Central North Island, New Zealand. *Reviews of Geophysics, 44*(4). https://doi.org/10.1029/2005rg000171

Stewart, R. B., Price, R. C., & Smith, I. E. M. (1996). Evolution of high-K arc magma, Egmont volcano, Taranaki, New Zealand: evidence from mineral chemistry. *Journal of Volcanology and Geothermal Research, 74*(3), 275-295. https://doi.org/https://doi.org/10.1016/S0377-0273(96)00049-2

Stock, M. J., Bagnardi, M., Neave, D. A., Maclennan, J., Bernard, B., Buisman, I., Gleeson, M. L. M., & Geist, D. (2018). Integrated Petrological and Geophysical Constraints on Magma System Architecture in the Western Galápagos Archipelago: Insights From Wolf Volcano. *Geochemistry, Geophysics, Geosystems, 19*, 4722-4743. https://doi.org/10.1029/2018gc007936

Stoopes, G. R., & Sheridan, M. F. (1992). Giant debris avalanches from the Colima Volcanic Complex, Mexico: Implications for long-runout landslides (>100 km) and hazard assessment. *Geology, 20*(4), 299-302. https://doi.org/10.1130/0091-7613(1992)020<0299:Gdaftc>2.3.Co;2

Streck, M. J., Broderick, C. A., Thronber, C. R., Clynne, M. A., & Pallister, J. S. (2008). *Plagioclase populations and zoning in dacite of the 2004-2005 Mount St. Helens eruption: Constraints for magma origin and dynamics* [Report](1750-34). (Professional Paper, Issue. U. S. G. Survey. https://pubs.usgs.gov/publication/pp175034

Sueoka, T., Lee, I., Muramatsu, M., & Imamura, S. (1985). Geomechanical properties and engineering classification for decomposed granite soils in Kaduna district, Nigeria. Proceedings of the first international conference on geomechanics in tropical lateritic and saprolitic soils, Brasilia,

Sun, S.-s., & McDonough, W. F. (1989). Chemical and isotopic systematics of oceanic basalts: implications for mantle composition and processes. *Geological Society, London, Special Publications, 42*(1), 313-345. https://doi.org/doi:10.1144/GSL.SP.1989.042.01.19

Sutherland, R. (1999). Basement geology and tectonic development of the greater New Zealand region: an interpretation from regional magnetic data. *Tectonophysics, 308*(3), 341-362. https://doi.org/https://doi.org/10.1016/S0040-1951(99)00108-0

Sutherland, R., Toy, V. G., Townend, J., Cox, S. C., Eccles, J. D., Faulkner, D. R., Prior, D. J., Norris, R. J., Mariani, E., Boulton, C., Carpenter, B. M., Menzies, C. D., Little, T. A., Hasting, M., De Pascale, G. P., Langridge, R. M., Scott, H. R., Lindroos, Z. R., Fleming, B., & Kopf, A. J. (2012). Drilling reveals fluid control on architecture and rupture of the Alpine fault, New Zealand. *Geology, 40*(12), 1143-1146. https://doi.org/10.1130/g33614.1

Swanson, D. A., & Holcomb, R. T. (1990). Regularities in Growth of the Mount St. Helens Dacite Dome, 1980–1986. In J. H. Fink (Ed.), *Lava Flows and Domes: Emplacement Mechanisms and Hazard Implications* (pp. 3-24). Springer Berlin Heidelberg. https://doi.org/10.1007/978-3-642-74379-5_1

Sykes L, R. (1966). The seismicity and deep structure of island arcs. *J. Geophys. Res., 71*, 2981-3006. https://cir.nii.ac.jp/crid/1571698599953387776

Taddeucci, J., & Wohletz, K. H. (2001). Temporal evolution of the Minoan eruption (Santorini, Greece), as recorded by its Plinian fall deposit and interlayered ash flow beds. *Journal of Volcanology and Geothermal Research, 109*(4), 299-317. https://doi.org/https://doi.org/10.1016/S0377-0273(01)00197-4

Taddeucci, J., Alatorre-Ibargüengoitia, M., Cruz-Vázquez, O., Del Bello, E., Scarlato, P., & Ricci, T. (2017). In-flight dynamics of volcanic ballistic projectiles. *Reviews of Geophysics, 55*(3), 675-718. https://doi.org/10.1002/2017rg000564

Takeuchi, S., Nakashima, S., Tomiya, A., & Shinohara, H. (2005). Experimental constraints on the low gas permeability of vesicular magma during decompression. *Geophysical research letters, 32*, L10312. https://doi.org/10.1029/2005gl022491

Tanaka, H., Kawamura, K. i., Nagao, K., & Houghton, B. F. (1997). K-Ar Ages and Paleosecular Variation of Direction and Intensity from Quaternary Lava Sequences in the Ruapehu Volcano, New Zealand. *Journal of geomagnetism and geoelectricity, 49*, 587-599. https://doi.org/10.5636/jgg.49.587

Tanner, W. F. (1969). The particle size scale. *Journal of sedimentary research, 39*, 809-812. https://doi.org/10.1306/74d71d39-2b21-11d7-8648000102c1865d

Tatsumi, Y., & Eggins, S. (1995). *Subduction zone magmatism* (Vol. 1). Wiley.

Tatsumi, Y., Hamilton, D. L., & Nesbitt, R. W. (1986). Chemical characteristics of fluid phase released from a subducted lithosphere and origin of arc magmas: Evidence from high-pressure experiments and

natural rocks. *Journal of Volcanology and Geothermal Research, 29*(1), 293-309. https://doi.org/https://doi.org/10.1016/0377-0273(86)90049-1

Taylor, N. H. (1954). Soils of the North Island of New Zealand (with map of ash showers). *N.Z. Soil Bureau Bulletin, 5*.

Tepley, F. J., III, Davidson, J. P., Tilling, R. I., & Arth, J. G. (2000). Magma Mixing, Recharge and Eruption Histories Recorded in Plagioclase Phenocrysts from El Chichón Volcano, Mexico. *Journal of Petrology, 41*(9), 1397-1411. https://doi.org/10.1093/petrology/41.9.1397

Thomas, R. M. E., & Sparks, R. S. J. (1992). Cooling of tephra during fallout from eruption columns. *Bulletin of Volcanology, 54*(7), 542-553. https://doi.org/10.1007/BF00569939

Thorarinsson, S., & Sigvaldason, G. E. (1972). The Hekla Eruption of 1970. *Bulletin Volcanologique, 36*(2), 269-288. https://doi.org/10.1007/BF02596870

Thouret, J. C., Cantagrel, J. M., Robin, C., Murcia, A., Salinas, R., & Cepeda, H. (1995). Quaternary eruptive history and hazard-zone model at Nevado del Tolima and Cerro Machin volcanoes, Colombia. *Journal of Volcanology and Geothermal Research, 66*(1), 397-426. https://doi.org/https://doi.org/10.1016/0377-0273(94)00073-P

Thrasher, G., & Cahill, J. (1990). Subsurface maps of the Taranaki Basin region, New Zealand. *NZ Geol. Surv. Rep., 142*.

Thrasher, G. P. (1992). Last Cretaceous Geology of Taranaki Basin, New Zealand.

Tibaldi, A. (2001). Multiple sector collapses at Stromboli volcano, Italy: how they work. *Bulletin of Volcanology, 63*(2), 112-125.

Tibaldi, A. (2004). Major changes in volcano behaviour after a sector collapse: insights from Stromboli, Italy. *Terra Nova, 16*, 2-8. https://doi.org/10.1046/j.1365-3121.2003.00517.x

Tibaldi, A., Corazzato, C., Kozhurin, A., Lagmay, A. F. M., Pasquarè, F. A., Ponomareva, V. V., Rust, D., Tormey, D., & Vezzoli, L. (2008). Influence of substrate tectonic heritage on the evolution of composite volcanoes: Predicting sites of flank eruption, lateral collapse, and erosion. *Global and Planetary Change, 61*(3), 151-174. https://doi.org/https://doi.org/10.1016/j.gloplacha.2007.08.014

Tilling, R. I., Topinka, L. J., & Swanson, D. A. (1984). *Eruptions of Mount St. Helens; past, present, and future* [Report](General Interest Publication, Issue. https://pubs.usgs.gov/publication/7000044

Tonkin, P. J. (1970). The soils of the southeastern sector of Egmont National Park [Journal Article]. https://hdl.handle.net/10289/9159 (Earth Science Journal)

Topping, W. W. (1972). Burrell Lapilli eruptives, Mount Egmont, New Zealand. *New Zealand Journal of Geology and Geophysics, 15*(3), 476-490. https://doi.org/10.1080/00288306.1972.10422345

Topping, W. W. (1974). Some aspects of quaternary history of Tongariro volcanic centre.

Toramaru, A. (1988). Formation of propagation pattern in two-phase flow systems with application to volcanic eruptions. *Geophysical Journal International, 95*, 613-623. https://doi.org/10.1111/j.1365-246X.1988.tb06707.x

Toramaru, A. (1989). Vesiculation process and bubble size distributions in ascending magmas with constant velocities. *Journal of Geophysical Research: Solid Earth, 94*(B12), 17523-17542. https://doi.org/10.1029/jb094ib12p17523

Toramaru, A. (1995). Numerical study of nucleation and growth of bubbles in viscous magmas. *J. Geophys. Res., 100*, 1913-1931. https://cir.nii.ac.jp/crid/1570291226763431040

Toramaru, A. (2006). BND (bubble number density) decompression rate meter for explosive volcanic eruptions. *Journal of Volcanology and Geothermal Research, 154*(3), 303-316. https://doi.org/https://doi.org/10.1016/j.jvolgeores.2006.03.027

Toramaru, A. (2022). *Vesiculation and Crystallization of Magma*. Springer. https://doi.org/10.1007/978-981-16-4209-8

Tormey, D. (2010). Managing the effects of accelerated glacial melting on volcanic collapse and debris flows: Planchon–Peteroa Volcano, Southern Andes. *Global and Planetary Change, 74*(2), 82-90. https://doi.org/https://doi.org/10.1016/j.gloplacha.2010.08.003

Tormey, D. R., Frey, F. A., & Lopez-Escobar, L. (1995). Geochemistry of the Active Azufre—Planchon—Peteroa Volcanic Complex, Chile (35°15′S): Evidence for Multiple Sources and Processes in a Cordilleran Arc Magmatic System. *Journal of Petrology, 36*(2), 265-298. https://doi.org/10.1093/petrology/36.2.265

Torres-Orozco, R., Cronin, S. J., Damaschke, M., & Pardo, N. (2017a). Diverse dynamics of Holocene mafic-intermediate Plinian eruptions at Mt. Taranaki (Egmont), New Zealand. *Bulletin of Volcanology, 79*(11), 76. https://doi.org/10.1007/s00445-017-1162-4

Torres-Orozco, R., Cronin, S. J., Pardo, N., & Palmer, A. S. (2017b). New insights into Holocene eruption episodes from proximal deposit sequences at Mt. Taranaki (Egmont), New Zealand. *Bulletin of Volcanology, 79*(1), 3. https://doi.org/10.1007/s00445-016-1085-5

Torres-Orozco, R., Cronin, S. J., Pardo, N., & Palmer, A. S. (2018). Volcanic hazard scenarios for multiphase andesitic Plinian eruptions from lithostratigraphy: Insights into pyroclastic density current

diversity at Mount Taranaki, New Zealand. *GSA Bulletin, 130*(9-10), 1645-1663. https://doi.org/10.1130/b31850.1

Torres-Orozco, R., Cronin, S. J., Pardo, N., Kósik, S., Ukstins, I., Heinrich, M., & Lee, P. D. (2023). Complex decompression and fragmentation of mingled andesite magmas driving multi-phase Plinian eruptions at Mt. Taranaki, New Zealand. *Journal of Volcanology and Geothermal Research, 433*, 107728. https://doi.org/https://doi.org/10.1016/j.jvolgeores.2022.107728

Tost, M., & Cronin, S. J. (2015). Linking distal volcaniclastic sedimentation and stratigraphy with the development of Ruapehu volcano, New Zealand. *Bulletin of Volcanology, 77*(11), 94. https://doi.org/10.1007/s00445-015-0977-0

Tost, M., & Cronin, S. J. (2016). Climate influence on volcano edifice stability and fluvial landscape evolution surrounding Mount Ruapehu, New Zealand. *Geomorphology, 262*, 77-90. https://doi.org/https://doi.org/10.1016/j.geomorph.2016.03.017

Tost, M., Cronin, S. J., & Procter, J. N. (2014). Transport and emplacement mechanisms of channelised long-runout debris avalanches, Ruapehu volcano, New Zealand. *Bulletin of Volcanology, 76*(12), 881. https://doi.org/10.1007/s00445-014-0881-z

Tost, M., Price, R. C., Cronin, S. J., & Smith, I. E. M. (2016). New insights into the evolution of the magmatic system of a composite andesite volcano revealed by clasts from distal mass-flow deposits: Ruapehu volcano, New Zealand. *Bulletin of Volcanology, 78*(5), 38. https://doi.org/10.1007/s00445-016-1030-7

TRC, T. R. C. (2004). Taranaki Civil Defence Emergency Management Group Volcanic Strategy 2004. Taranaki Regional Council.

Tucker, J. M., Hauri, E. H., Pietruszka, A. J., Garcia, M. O., Marske, J. P., & Trusdell, F. A. (2019). A high carbon content of the Hawaiian mantle from olivine-hosted melt inclusions. *Geochimica et cosmochimica acta, 254*, 156-172. https://doi.org/https://doi.org/10.1016/j.gca.2019.04.001

Turner, G. M., Alloway, B. V., Dixon, B. J., & Atkins, C. B. (2018). Thermal history of volcanic debris flow deposits on the eastern flanks of Mt. Taranaki, New Zealand: Implications for future hazards. *Journal of Volcanology and Geothermal Research, 353*, 55-67. https://doi.org/https://doi.org/10.1016/j.jvolgeores.2018.01.017

Turner, M. B., Cronin, S. J., Bebbington, M. S., & Platz, T. (2008a). Developing probabilistic eruption forecasts for dormant volcanoes: a case study from Mt Taranaki, New Zealand. *Bulletin of Volcanology, 70*(4), 507-515. https://doi.org/10.1007/s00445-007-0151-4

Turner, M. B., Bebbington, M. S., Cronin, S. J., & Stewart, R. B. (2009). Merging eruption datasets: building an integrated Holocene eruptive record for Mt Taranaki, New Zealand. *Bulletin of Volcanology, 71*(8), 903-918. https://doi.org/10.1007/s00445-009-0274-x

Turner, M. B., Cronin, S. J., Smith, I. E., Stewart, R. B., & Neall, V. E. (2008b). Eruption episodes and magma recharge events in andesitic systems: Mt Taranaki, New Zealand. *Journal of Volcanology and Geothermal Research, 177*(4), 1063-1076. https://doi.org/https://doi.org/10.1016/j.jvolgeores.2008.08.001

Turner, M. B., Cronin, S. J., Bebbington, M. S., Smith, I. E., & Stewart, R. B. (2011). Integrating records of explosive and effusive activity from proximal and distal sequences: Mt. Taranaki, New Zealand. *Quaternary international, 246*(1-2), 364-373.

Turner, R., & Hurst, T. (2001). Factors influencing volcanic ash dispersal from the 1995 and 1996 eruptions of Mount Ruapehu, New Zealand. *Journal of applied meteorology, 40*(1), 56-69.

Turner, S., Bourdon, B., & Gill, J. (2003). Insights into Magma Genesis at Convergent Margins from U-series Isotopes. *Reviews in Mineralogy and Geochemistry, 52*(1), 255-315. https://doi.org/10.2113/0520255

Ubide, T., & Kamber, B. S. (2018). Volcanic crystals as time capsules of eruption history. *Nature Communications, 9*(1), 326. https://doi.org/10.1038/s41467-017-02274-w

Udden, J. A. (1914). Mechanical composition of clastic sediments. *Bulletin of the geological society of America, 25*(1), 655-744.

Ui, T. (1983). Volcanic dry avalanche deposits — Identification and comparison with nonvolcanic debris stream deposits. *Journal of Volcanology and Geothermal Research, 18*(1), 135-150. https://doi.org/https://doi.org/10.1016/0377-0273(83)90006-9

Ui, T., Yamamoto, H., & Suzuki-Kamata, K. (1986a). Characterization of debris avalanche deposits in Japan. *Journal of Volcanology and Geothermal Research, 29*(1), 231-243. https://doi.org/https://doi.org/10.1016/0377-0273(86)90046-6

Ui, T., Kawachi, S., & Neall, V. E. (1986b). Fragmentation of debris avalanche material during flowage — Evidence from the Pungarehu Formation, Mount Egmont, New Zealand. *Journal of Volcanology and Geothermal Research, 27*(3), 255-264. https://doi.org/https://doi.org/10.1016/0377-0273(86)90016-8

Ulmer, P. (2001). Partial melting in the mantle wedge — the role of H2O in the genesis of mantle-derived 'arc-related' magmas. *Physics of the Earth and Planetary Interiors, 127*(1), 215-232. https://doi.org/https://doi.org/10.1016/S0031-9201(01)00229-1

Valentine, G. A., & Groves, K. R. (1996). Entrainment of Country Rock during Basaltic Eruptions of the Lucero Volcanic Field, New Mexico. *Journal of Geology, 104*, 71-90. https://doi.org/10.1086/629802

Vallance, J. W., & Scott, K. M. (1997). The Osceola Mudflow from Mount Rainier: Sedimentology and hazard implications of a huge clay-rich debris flow. *Geological Society of America Bulletin, 109*(2), 143-163.

Vallance, J. W., Siebert, L., Rose, W. I., Girón, J. R., & Banks, N. G. (1995). Edifice collapse and related hazards in Guatemala. *Journal of Volcanology and Geothermal Research, 66*(1), 337-355. https://doi.org/https://doi.org/10.1016/0377-0273(94)00076-S

Vallance, J. W., Schilling, S. P., Matías, O., Rose Jr, W. I., & Howell, M. M. (2001). *Volcano hazards at Fuego and Acatenango, Guatemala* [Report](2001-431). (Open-File Report, Issue. U. S. G. Survey. https://pubs.usgs.gov/publication/ofr01431

Van Dissen, R., & Yeats, R. S. (1991). Hope fault, Jordan thrust, and uplift of the Seaward Kaikoura Range, New Zealand. *Geology, 19*(4), 393-396. https://doi.org/10.1130/0091-7613(1991)019<0393:Hfjtau>2.3.Co;2

Van Gerve, T. D., Neave, D. A., Almeev, R. R., Holtz, F., & Namur, O. (2020). Zoned Crystal Records of Transcrustal Magma Transport, Storage and Differentiation: Insights from the Shatsky Rise Oceanic Plateau. *Journal of Petrology, 61*(8). https://doi.org/10.1093/petrology/egaa080

Van Nieuwenhove, V., De Beenhouwer, J., De Carlo, F., Mancini, L., Marone, F., & Sijbers, J. (2015). Dynamic intensity normalization using eigen flat fields in X-ray imaging. *Optics Express, 23*(21), 27975-27989. https://doi.org/10.1364/OE.23.027975

van Westen, C. J., & Daag, A. S. (2005). Analysing the relation between rainfall characteristics and lahar activity at Mount Pinatubo, Philippines. *Earth surface processes and Landforms, 30*, 1663-1674. https://doi.org/10.1002/esp.1225

Vandergoes, M. J., Hogg, A. G., Lowe, D. J., Newnham, R. M., Denton, G. H., Southon, J., Barrell, D. J. A., Wilson, C. J. N., McGlone, M. S., Allan, A. S. R., Almond, P. C., Petchey, F., Dabell, K., Dieffenbacher-Krall, A. C., & Blaauw, M. (2013). A revised age for the Kawakawa/Oruanui tephra, a key marker for the Last Glacial Maximum in New Zealand. *Quaternary Science Reviews, 74*, 195-201. https://doi.org/https://doi.org/10.1016/j.quascirev.2012.11.006

Varekamp, J. C. (1993). Some remarks on volcanic vent evolution during plinian eruptions. *Journal of Volcanology and Geothermal Research, 54*(3), 309-318. https://doi.org/https://doi.org/10.1016/0377-0273(93)90069-4

Verhoogen, J. (1951). Mechanism of Ash Formation. *Am. J. Sci., 249*, 723-739. https://cir.nii.ac.jp/crid/1570572699522227328

Vezzoli, L., Renzulli, A., & Menna, M. (2014). Growth after collapse: the volcanic and magmatic history of the Neostromboli lava cone (island of Stromboli, Italy). *Bulletin of Volcanology, 76*(6), 821. https://doi.org/10.1007/s00445-014-0821-y

Viana, M., Jouannin, P., Pontier, C., & Chulia, D. (2002). About pycnometric density measurements. *Talanta, 57*(3), 583-593.

Villamor, P., & Berryman, K. (2001). A late Quaternary extension rate in the Taupo Volcanic Zone, New Zealand, derived from fault slip data. *New Zealand Journal of Geology and Geophysics, 44*(2), 243-269. https://doi.org/10.1080/00288306.2001.9514937

Voight, B. (1981). The 1980 eruptions of Mt. St. Helens, Washington. *Geol. Surv. Professional Paper, No. 1250*, 347-378. https://cir.nii.ac.jp/crid/1571980074057762176

Voight, B. (2000). Structural stability of andesite volcanoes and lava domes. *Philosophical Transactions of the Royal Society of London. Series A: Mathematical, Physical and Engineering Sciences, 358*(1770), 1663-1703. https://doi.org/10.1098/rsta.2000.0609

Voight, B., & Elsworth, D. (1997). Failure of volcano slopes. *Geotechnique, 47*(1), 1-31. https://doi.org/10.1680/geot.1997.47.1.1

Voloschina, M., Lube, G., Procter, J., Moebis, A., & Timm, C. (2020). Lithosedimentological and tephrostratigraphical characterisation of small-volume, low-intensity eruptions: The 1800 years Tufa Trig Formation, Mt. Ruapehu (New Zealand). *Journal of Volcanology and Geothermal Research, 402*, 106987. https://doi.org/https://doi.org/10.1016/j.jvolgeores.2020.106987

Voltolini, M., Zandomeneghi, D., Mancini, L., & Polacci, M. (2011). Texture analysis of volcanic rock samples: Quantitative study of crystals and vesicles shape preferred orientation from X-ray microtomography data. *Journal of Volcanology and Geothermal Research, 202*(1), 83-95. https://doi.org/https://doi.org/10.1016/j.jvolgeores.2011.02.003

Wadge, G., & Isaacs, M. C. (1988). Mapping the volcanic hazards from Soufriere Hills Volcano, Montserrat, West Indies using an image processor. *Journal of the Geological Society, 145*, 541-551. https://doi.org/10.1144/gsjgs.145.4.0541

Wadge, G., Young, P., & McKendrick, I. (1994). Mapping lava flow hazards using computer simulation. *Journal of Geophysical Research: Solid Earth, 99*(B1), 489-504. https://doi.org/10.1029/93jb01561

Waitt, R. B. (2010). *Ejecta and landslides from Augustine Volcano before 2006: Chapter 13 in The 2006 eruption of Augustine Volcano, Alaska* [Report](176913). (Professional Paper, Issue. U. S. G. Survey. https://pubs.usgs.gov/publication/pp176913

Walcott, R. I. (1978). Present tectonics and Late Cenozoic evolution of New Zealand. *Geophysical Journal International, 52*(1), 137-164. https://doi.org/10.1111/j.1365-246X.1978.tb04225.x

Walker, G. P. L. (1980). The Taupo pumice: Product of the most powerful known (ultraplinian) eruption? *Journal of Volcanology and Geothermal Research, 8*(1), 69-94. https://doi.org/https://doi.org/10.1016/0377-0273(80)90008-6

Walker, G. P. L. (1981a). Generation and dispersal of fine ash and dust by volcanic eruptions. *Journal of Volcanology and Geothermal Research, 11*(1), 81-92. https://doi.org/https://doi.org/10.1016/0377-0273(81)90077-9

Walker, G. P. L. (1981b). Characteristics of two phreatoplinian ashes, and their water-flushed origin. *Journal of Volcanology and Geothermal Research, 9*(4), 395-407. https://doi.org/https://doi.org/10.1016/0377-0273(81)90046-9

Wallace, L. M., Beavan, J., McCaffrey, R., & Darby, D. (2004). Subduction zone coupling and tectonic block rotations in the North Island, New Zealand. *Journal of Geophysical Research (Solid Earth), 109*, B12406. https://doi.org/10.1029/2004jb003241

Wallace, L. M., Beavan, J., Bannister, S., & Williams, C. (2012). Simultaneous long-term and short-term slow slip events at the Hikurangi subduction margin, New Zealand: Implications for processes that control slow slip event occurrence, duration, and migration. *Journal of Geophysical Research (Solid Earth), 117*, B11402. https://doi.org/10.1029/2012jb009489

Walter, T., & Schmincke, H. U. (2002). Rifting, recurrent landsliding and Miocene structural reorganization on NW-Tenerife (Canary Islands). *International Journal of Earth Sciences, 91*(4), 615-628. https://doi.org/10.1007/s00531-001-0245-8

Wanke, M., Karakas, O., & Bachmann, O. (2019). The genesis of arc dacites: the case of Mount St. Helens, WA. *Contributions to Mineralogy and Petrology, 174*(1), 7. https://doi.org/10.1007/s00410-018-1542-6

Waters, L. E., & Lange, R. A. (2015). An updated calibration of the plagioclase-liquid hygrometer-thermometer applicable to basalts through rhyolites. *American Mineralogist, 100*(10), 2172-2184. https://doi.org/10.2138/am-2015-5232

Watt, A., Karstens, J., & Berndt, C. (2020). Volcanic Island lateral collapse and submarine volcanic debris avalanche deposits. *Volcanic debris avalanches: from collapse to hazard. Springer book series advances in volcanology*.

Watt, S. F. L. (2019). The evolution of volcanic systems following sector collapse. *Journal of Volcanology and Geothermal Research, 384*, 280-303. https://doi.org/https://doi.org/10.1016/j.jvolgeores.2019.05.012

Watt, S. F. L., Talling, P. J., Vardy, M. E., Masson, D. G., Henstock, T. J., Hühnerbach, V., Minshull, T. A., Urlaub, M., Lebas, E., Le Friant, A., Berndt, C., Crutchley, G. J., & Karstens, J. (2012). Widespread and progressive seafloor-sediment failure following volcanic debris avalanche emplacement: Landslide dynamics and timing offshore Montserrat, Lesser Antilles. *Marine Geology, 323-325*, 69-94. https://doi.org/https://doi.org/10.1016/j.margeo.2012.08.002

Waythomas, C. F. (1999). Stratigraphic framework of Holocene volcaniclastic deposits, Akutan Volcano, east-central Aleutian Islands, Alaska. *Bulletin of Volcanology, 61*(3), 141-161. https://doi.org/10.1007/s004450050268

Waythomas, C. F., & Miller, T. P. (1999). *Preliminary volcano-hazard assessment for Iliamna Volcano, Alaska* [Report](99-373). (Open-File Report, Issue. U. S. G. Survey. https://pubs.usgs.gov/publication/ofr99373

Waythomas, C. F., & Wallace, K. L. (2002). Flank collapse at Mount Wrangell, Alaska, recorded by volcanic mass-flow deposits in the Copper River lowland. *Canadian Journal of Earth Sciences, 39*(8), 1257-1279. https://doi.org/10.1139/e02-032

Weir, A. M., Mead, S., Bebbington, M. S., Wilson, T. M., Beaven, S., Gordon, T., & Campbell-Smart, C. (2022). A modular framework for the development of multi-hazard, multi-phase volcanic eruption scenario suites. *Journal of Volcanology and Geothermal Research, 427*, 107557.

Wellman, H. (1962). Holocene of the North Island of New Zealand: a coastal reconnaissance. Transactions of the Royal Society of New Zealand,

Wentworth, C. K. (1922). A Scale of Grade and Class Terms for Clastic Sediments. *Journal of Geology, 30*, 377-392. https://doi.org/10.1086/622910

Westrich, H. R., & Eichelberger, J. C. (1994). Gas transport and bubble collapse in rhyolitic magma: an experimental approach. *Bulletin of Volcanology, 56*(6), 447-458. https://doi.org/10.1007/BF00302826

White, J. D. L., & Houghton, B. F. (2006). Primary volcaniclastic rocks. *Geology, 34*(8), 677-680. https://doi.org/10.1130/g22346.1

Whitehead, S. (1976). Granulometric studies on selected tephra eruptions, North Island, New Zealand. *Unpublished Honours Dissertation, Massey University, Palmerston North*.

Williams, H., & McBirney, A. (1979). Volcanology Freeman Cooper & Co. *San Francisco, USA*.

Williams, P. W., McGlone, M., Neil, H., & Zhao, J.-X. (2015). A review of New Zealand palaeoclimate from the Last Interglacial to the global Last Glacial Maximum. *Quaternary Science Reviews, 110*, 92-106. https://doi.org/https://doi.org/10.1016/j.quascirev.2014.12.017

Wilson, C., Houghton, B., McWilliams, M., Lanphere, M., Weaver, S., & Briggs, R. (1995). Volcanic and structural evolution of Taupo Volcanic Zone, New Zealand: a review. *Journal of Volcanology and Geothermal Research, 68*(1-3), 1-28.

Wilson, C. J. N. (1993). Stratigraphy, Chronology, Styles and Dynamics of Late Quaternary Eruptions from Taupo Volcano, New Zealand. *Philosophical Transactions of the Royal Society of London Series A, 343*, 205-306. https://doi.org/10.1098/rsta.1993.0050

Wilson, C. J. N. (2001). The 26.5ka Oruanui eruption, New Zealand: an introduction and overview. *Journal of Volcanology and Geothermal Research, 112*(1), 133-174. https://doi.org/https://doi.org/10.1016/S0377-0273(01)00239-6

Wilson, C. J. N., & Rowland, J. V. (2016). The volcanic, magmatic and tectonic setting of the Taupo Volcanic Zone, New Zealand, reviewed from a geothermal perspective. *Geothermics, 59*, 168-187. https://doi.org/https://doi.org/10.1016/j.geothermics.2015.06.013

Wilson, L. (1976). Explosive volcanic eruptions—III. Plinian eruption columns. *Geophysical Journal International, 45*(3), 543-556.

Wilson, L. (1980). Relationships between pressure, volatile content and ejecta velocity in three types of volcanic explosion. *Journal of Volcanology and Geothermal Research, 8*(2), 297-313. https://doi.org/https://doi.org/10.1016/0377-0273(80)90110-9

Wilson, L., Sparks, R. S. J., & Walker, G. P. L. (1980). Explosive volcanic eruptions — IV. The control of magma properties and conduit geometry on eruption column behaviour. *Geophysical Journal International, 63*(1), 117-148. https://doi.org/10.1111/j.1365-246X.1980.tb02613.x

Wilson, M. J. (2004). Weathering of the primary rock-forming minerals: processes, products and rates. *Clay Minerals, 39*(3), 233-266. https://doi.org/10.1180/0009855043930133

Wodzicki, A. (1974). Geology of the pre-Cenozoic basement of the Taranaki-Cook Strait-Westland area, New Zealand, based on recent drillhole data. *New Zealand Journal of Geology and Geophysics, 17*(4), 747-757. https://doi.org/10.1080/00288306.1974.10418224

Wohletz, K. H. (1986). Explosive magma-water interactions: Thermodynamics, explosion mechanisms, and field studies. *Bulletin of Volcanology, 48*(5), 245-264. https://doi.org/10.1007/BF01081754

Woods, A. W. (1995). The dynamics of explosive volcanic eruptions. *Reviews of Geophysics, 33*, 495-530. https://doi.org/10.1029/95rg02096

Woods, A. W., & Koyaguchi, T. (1994). Transitions between explosive and effusive eruptions of silicic magmas. *Nature, 370*(6491), 641-644. https://doi.org/10.1038/370641a0

Wright, H. M. N., Cashman, K. V., Rosi, M., & Cioni, R. (2007). Breadcrust bombs as indicators of Vulcanian eruption dynamics at Guagua Pichincha volcano, Ecuador. *Bulletin of Volcanology, 69*(3), 281-300. https://doi.org/10.1007/s00445-006-0073-6

Wright, H. M. N., Cashman, K. V., Gottesfeld, E. H., & Roberts, J. J. (2009). Pore structure of volcanic clasts: Measurements of permeability and electrical conductivity. *Earth and planetary science letters, 280*(1), 93-104. https://doi.org/https://doi.org/10.1016/j.epsl.2009.01.023

Zanchetta, G., Sulpizio, R., & Di Vito, M. A. (2004). The role of volcanic activity and climate in alluvial fan growth at volcanic areas: an example from southern Campania (Italy). *Sedimentary Geology, 168*(3), 249-280. https://doi.org/https://doi.org/10.1016/j.sedgeo.2004.04.001

Zandomeneghi, D., Voltolini, M., Mancini, L., Brun, F., Dreossi, D., & Polacci, M. (2010). Quantitative analysis of X-ray microtomography images of geomaterials: Application to volcanic rocks. *Geosphere, 6*(6), 793-804. https://doi.org/10.1130/ges00561.1

Zellmer, G. F., Edmonds, M., & Straub, S. M. (2015). Volatiles in subduction zone magmatism. *Geological Society, London, Special Publications, 410*(1), 1-17. https://doi.org/doi:10.1144/SP410.13

Zellmer, G. F., Hawkesworth, C. J., Sparks, R. S. J., Thomas, L. E., Harford, C. L., Brewer, T. S., & Loughlin, S. C. (2003). Geochemical Evolution of the Soufrière Hills Volcano, Montserrat, Lesser Antilles Volcanic Arc. *Journal of Petrology, 44*(8), 1349-1374. https://doi.org/10.1093/petrology/44.8.1349

Zemeny, A. (2021). *Deciphering magmatic processes in response to growth and destruction at Taranaki Volcano, New Zealand: a dissertation presented in partial fulfilment of the requirements for the degree of Doctor of Philosophy in Earth Sciences at Massey University (Manawatū campus), Palmerston North, New Zealand* Massey University].

Zemeny, A., Procter, J., Nemeth, K., Zellmer, G. F., Zernack, A. V., & Cronin, S. J. (2021). Elucidating stratovolcano construction from volcaniclastic mass-flow deposits: The medial ring-plain of Taranaki Volcano, New Zealand. *Sedimentology*.

Zemeny, A., Zellmer, G. F., Ubide, T., Smith, I. E. M., Procter, J., Tapu, A.-T., & Zernack, A. V. (2023). Investigation of the Mid-Age (65–34 ka) Period of Taranaki Volcano, New Zealand: Indications for the Effect of Volcano Growth. *Journal of Petrology, 64*(5). https://doi.org/10.1093/petrology/egad027

Zernack, A. V. (2008). *A sedimentological and geochemical approach to understanding cycles of stratovolcano growth and collapse at Mt Taranaki, New Zealand: a thesis presented in partial fulfilment of the requirements for the degree of Doctor of Philosophy in Earth Science at Massey University, Palmerston North, New Zealand* Massey University].

Zernack, A. V. (2021). Volcanic Debris-Avalanche Deposits in the Context of Volcaniclastic Ring Plain Successions—A Case Study from Mt. Taranaki. In M. Roverato, A. Dufresne, & J. Procter (Eds.), *Volcanic Debris Avalanches: From Collapse to Hazard* (pp. 211-254). Springer International Publishing. https://doi.org/10.1007/978-3-030-57411-6_9

Zernack, A. V., & Procter, J. N. (2021). Cyclic Growth and Destruction of Volcanoes. In M. Roverato, A. Dufresne, & J. Procter (Eds.), *Volcanic Debris Avalanches: From Collapse to Hazard* (pp. 311-355). Springer International Publishing. https://doi.org/10.1007/978-3-030-57411-6_12

Zernack, A. V., Procter, J. N., & Cronin, S. J. (2009). Sedimentary signatures of cyclic growth and destruction of stratovolcanoes: A case study from Mt. Taranaki, New Zealand. *Sedimentary Geology, 220*(3), 288-305. https://doi.org/https://doi.org/10.1016/j.sedgeo.2009.04.024

Zernack, A. V., Cronin, S. J., Neall, V. E., & Procter, J. N. (2011). A medial to distal volcaniclastic record of an andesite stratovolcano: detailed stratigraphy of the ring-plain succession of south-west Taranaki, New Zealand. *International Journal of Earth Sciences, 100*(8), 1937-1966. https://doi.org/10.1007/s00531-010-0610-6

Zernack, A. V., Price, R. C., Smith, I. E. M., Cronin, S. J., & Stewart, R. B. (2012a). Temporal Evolution of a High-K Andesitic Magmatic System: Taranaki Volcano, New Zealand. *Journal of Petrology, 53*(2), 325-363. https://doi.org/10.1093/petrology/egr064

Zernack, A. V., Cronin, S. J., Bebbington, M. S., Price, R. C., Smith, I. E. M., Stewart, R. B., & Procter, J. N. (2012b). Forecasting catastrophic stratovolcano collapse: A model based on Mount Taranaki, New Zealand. *Geology, 40*(11), 983-986. https://doi.org/10.1130/g33277.1

Zhang, Y. (1999). A criterion for the fragmentation of bubbly magma based on brittle failure theory. *Nature, 402*(6762), 648-650. https://doi.org/10.1038/45210

Zheng, Y., Chen, R., Xu, Z., & Zhang, S. (2016). The transport of water in subduction zones. *Science China Earth Sciences, 59*(4), 651-682. https://doi.org/10.1007/s11430-015-5258-4

Appendices

Appendix A: Stratigraphy

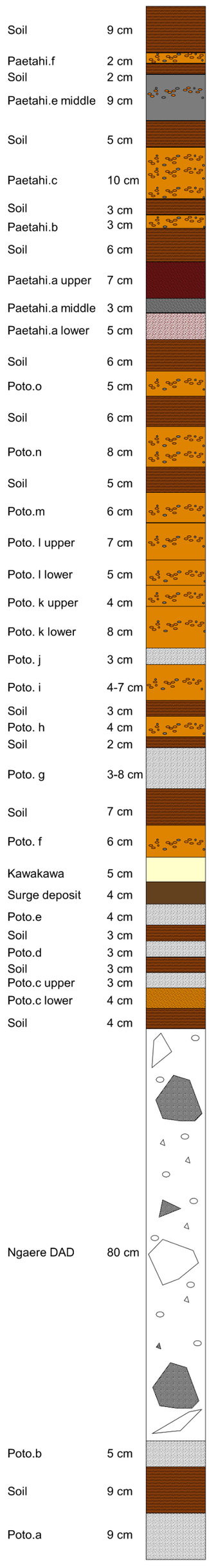
Appendix A1: Stratigraphic sections.

Stratigraphic sections for the eastern and southeastern ring plain locations.

1. Ronald Road: Poto Formation Reference Section.

Latitude/Longitude: -39.361454, 174.222222

The Poto Formation reference section is on a north-facing farm cutting 0.2 km east of Ronald Road along Opunake Road (Location 1; figure 2.1). The full Poto Formation is observable at this location, across a 0.06 km stretch. Poto.a is 18 cm above the Tuikonga Formation here accessible 0.1 km east of the farmer's gate. Poto.e through to the top of Paetahi.a upper is accessible 0.5m west of Poto.a. Poto.e is at the base of the outcrop. Paetahi.b-f is accessible 0.01 km west of Poto.e.



Soil	9 cm
Paetahi.f	2 cm
Soil	2 cm
Paetahi.e middle	9 cm
Soil	5 cm
Paetahi.c	10 cm
Soil	3 cm
Paetahi.b	3 cm
Soil	6 cm
Paetahi.a upper	7 cm
Paetahi.a middle	3 cm
Paetahi.a lower	5 cm
Soil	6 cm
Poto.o	5 cm
Soil	6 cm
Poto.n	8 cm
Soil	5 cm
Poto.m	6 cm
Poto. l upper	7 cm
Poto. l lower	5 cm
Poto. k upper	4 cm
Poto. k lower	8 cm
Poto. j	3 cm
Poto. i	4-7 cm
Soil	3 cm
Poto. h	4 cm
Soil	2 cm
Poto. g	3-8 cm
Soil	7 cm
Poto. f	6 cm
Kawakawa	5 cm
Surge deposit	4 cm
Poto.e	4 cm
Soil	3 cm
Poto.d	3 cm
Soil	3 cm
Poto.c upper	3 cm
Poto.c lower	4 cm
Soil	4 cm
Ngaere DAD	80 cm
Poto.b	5 cm
Soil	9 cm
Poto.a	9 cm

Paetahi.f **-** Yellow-brown matrix supported, poorly sorted layer. Large orange pumice clasts (very soft and erodible). Appears in pockets. Some lithics present. Gradual contacts.

Paetahi.e middle **-** Consolidated moderately well sorted layer. Grey pumice and lithic clasts. Some weathered large orange clasts present. Sharp contacts.

Paetahi.c **-** Heavily weathered yellow-brown matrix supported. Poorly sorted, Some large orange pumice clasts (very soft and erodible). Grey pumice and lithics present. Appears in pockets. Gradual contacts.

Paetahi.b **-** Heavily weathered yellow-brown matrix supported. Poorly sorted, Orange pumice clast dominated (very soft and erodible). Some grey pumice and lithics present. Appears in pockets. Gradual contacts.

Paetahi.a upper **-** Loosely consolidated orange matrix, moderately to poorly sorted orange coarse lapilli (7 mm). Slight reverse grading, more lithics present at the top. Gradual contacts.

Paetahi.a middle **-** Loosely consolidated, moderately sorted grey lapilli (2 mm). Higher percentage of lithics. Gradual contacts .

Paetahi.a lower **-** Unconsolidated, moderately sorted coarse orange lapilli. Sharp contact below with well defined soil. Start of new tephra formation. Gradual contact above.

Poto.o - Yellow-brown matrix supported, poorly sorted. Predominantly light grey clasts (5 mm to 1 cm). Darker orange band through it. Gradual and sharp contacts. Defined sharp contact at the top defining the end of the formation.

Poto.n - Yellow-brown matrix supported (matrix is well sorted). Large light grey pumice clasts present (1-3 cm). 3cm band near the top which contains more orange pumice clasts. Gradual contacts.

Poto.m -Yellowish-brown matrix supported heavily weathered poorly sorted layer. Pumice is soft and easily erodible. Light grey to orange/ brown clasts. Gradual contacts.

Poto.l upper - Yellow-brown matrix supported loosely consolidated; reverse graded layer. Moderately sorted reddish brown clasts (1 mm – 5 mm). Larger clasts are medium grey (5 mm to 1 cm). Gradual contacts.

Poto.l lower -Yellow-brown matrix supported; larger clasts are moderately sorted. Light grey pumice lapilli (5 mm to 1 cm). Gradual contacts.

Poto.k upper - Yellow-brown matrix supported, moderately to poorly sorted, heavily weathered orange/ red lapilli. Slightly normally graded. Gradual contacts.

Poto.k lower - Yellow-brown matrix supported, moderately to poorly sorted, light to dark grey ash to lapilli (1 mm to 1 cm). Sharp and gradual contacts.

Poto.j **-** Unconsolidated, moderately sorted, medium to dark grey coarse ash to fine lapilli, some larger clasts (7 mm to 1 cm) present. Band through the middle containing lighter grey (almost white) clasts. Appears in patches. Easily erodible. Sharp contacts.

Poto.i **-** Yellowish-brown, matrix supported, poorly sorted, consolidated layer. Light grey and yellow/ orange clasts (1 mm - 4.5 cm). Heavily weathered pumice clasts. Bands through layer containing more grey material. Gradual and sharp contacts.

Poto.h **-** Orange grey matrix supported, poorly sorted. Dominated by light grey pumice and lithic ash to lapilli (1 mm to 1 cm). Gradual contacts.

Poto.g **-** Unconsolidated, heavily eroded layer, thins and thickens in pockets across outcrop. Moderately sorted, light grey ash to lapilli, Largest clasts approximately (5 mm). Sharp contacts.

Poto.f **-** Orange to brown matrix supported, moderately sorted. Light grey to yellow/orange, fine ash to medium lapilli (1mm-7mm). Some larger 2-4 cm clasts dispersed through deposit. Sharp and gradual contacts.

Kawakawa tephra **-** White yellowish ash Rhyolitic tephra. Well sorted very fine glassy ash. Sharp contacts.

Surge deposit – dark brown/grey matrix supported. Predominantly fine grained with light grey flecks of pumice (1-2 mm) scale, moderately sorted. Appears in small pockets. Sharp and gradual contacts.

Poto.e **-** Unconsolidated, well sorted, grey fine lapilli, orange to light grey clasts (2mm-4mm) present at the top of the deposit. Sharp and gradual contacts.

Poto.d **-** Unconsolidated, moderately sorted, grey fine lapilli, surrounded by yellowish-brown matrix. Appears in pockets across the outcrop. Sharp contacts.

Poto.c upper **-** Unconsolidated, moderately sorted, medium grey fine ash to fine lapilli, normally graded. Appears in pockets across the outcrop. Sharp and gradual contacts.

Poto.c lower **-** Loosely consolidated, contained within a yellowish-brown matrix normally graded. Grey to orange/red clast coarse ash to medium lapilli. Gradual contacts.

Ngaere DAD **-** Massive debris-avalanche deposit. Yellowish-brown matrix supported, extremely poorly sorted. Well consolidated layer contains clasts from coarse ash (2mm) to boulder (>10 cm). Contains array of lithic (light grey/white to dark grey) and pumice (light grey to orange/red) clasts. Sharp below and gradual contact above.

Poto.b **-** Unconsolidated well sorted dark grey fine ash, small clasts present. Sharp contacts.

Poto.a **-** Unconsolidated, moderately well sorted, grey to reddish grey coarse ash (2mm) to fine lapilli (<1 cm) . Larger clasts are predominantly reddish-grey. Within a yellowish-brown matrix. Sharp contact at the bottom with a well-established soil 18cm thick. Gradual contact at the top.

Scale.

Thickness (cm): 50, 40, 30, 20, 10, 0

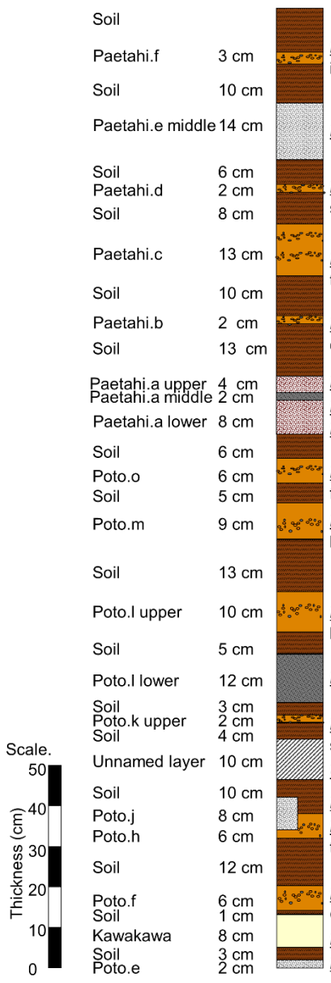
Key:

- Red Andesite tephra
- Soil
- Grey Andesite tephra
- Andesite tephra
- Kawakawa tephra
- Surge deposit
- Unconsolidated
- Ngaere DAD
- Loosely consolidated
- Matrix supported layer
- Reworking

5. Opunake Road: Paetahi Reference Section.

Latitude/Longitude: -39.355958, 174.244338

The Paetahi Formation reference section is a north-facing road cutting 3 km west of Stratford (Location 5; Figure 2.1). Poto.e is situated at the base of this outcrop.



Paetahi.f – Orange-brown matrix supported poorly sorted heavily weathered layer. Medium ash to fine lapilli dispersed throughout. Very soft coarse orange lapilli (3 cm). Appears in pockets clasts present. Gradual contacts.

Paetahi.e middle – Unconsolidated well sorted grey to dark grey coarse ash to fine lapilli. Well sorted fine to medium sized clasts. Gradual contacts.

Paetahi.d – Orange-brown matrix supported heavily weathered layer, appears in pockets. Medium ash to medium lapilli dispersed throughout. Large orange weathered lapilli very soft. Some lithics present. Gradual contacts.

Paetahi.c – Yellow-brown matrix supported consolidated poorly sorted layer. Heavily weathered orange coarse lapilli (very soft). Medium ash to coarse lapilli clasts dispersed throughout. Layer gets thicker and thinner across the deposit. Gradual and sharp contacts.

Paetahi.b – Yellow-brown matrix supported poorly sorted heavily weathered orange and grey pumice layer. Appears in pockets. Coarse ash to coarse orange lapilli (2-3cm) dispersed throughout. Large orange lapilli heavily weathered and soft. Gradual contacts

Paetahi.a upper – Unconsolidated moderately sorted fine medium orange lapilli, some lithics present. Very similar to Paetahi.a lower. Gradual and sharp contacts.

Paetahi.a middle – Loosely consolidated thin band of moderately to well sorted grey to dark grey fine lapilli. Gradual contacts.

Paetahi.a lower – Unconsolidated moderately sorted coarse orange lapilli, some lithics present. 8cm thick layer. Sharp and gradual contacts..

Poto.o – Yellow-brown matrix supported poorly sorted, heavily weathered layer. Thins and thickens across the outcrop. Large Orange and grey lapilli are very soft. Medium ash to fine/medium lapilli clasts are dispersed throughout. Some lithics present. Poorly sorted. Gradual contacts.

Poto.m – Yellow-brown matrix supported poorly sorted, heavily weathered layer. Medium ash to fine/medium lapilli dispersed throughout. Large orange lapilli (very soft). Some lithics present. Layer thickens and thins across the outcrop. Gradual contacts.

Poto.l upper – Yellow-brown matrix supported poorly sorted, heavily weathered layer. Coarse ash to fine/medium lapilli dispersed throughout. Some lithics present. Large orange lapilli pumice very soft. Gradual contacts

Poto.l lower – Loosely consolidated poorly sorted, grey lithic layer. Some orange and grey pumice present. Lithics range from (5 mm to >1 cm). Gradual contacts

Poto.k upper – Yellow-brown matrix supported, poorly sorted, heavily weathered layer. Coarse ash to fine lapilli dispersed throughout. Large orange lapilli very soft. Appears in small pockets. Some lithics present. Gradual contacts

Unknown (Reworking?)– Grey unconsolidated fine lapilli. Present in a couple of pockets. Appears to be potential reworking or deposit that has fallen into hole.

Poto.j – Unconsolidated grey moderately sorted fine lapilli some orange pumice clasts present in layer. Appears in pockets. Sharp contacts

Poto.h – Yellow-brown matrix supported poorly sorted, heavily weathered layer. Large orange lapilli very soft, heavily weathered. Coarse ash to medium lapilli clasts dispersed throughout. Some lithics present. Gradual and sharp contacts below.

Poto.f – Yellow-brown matrix supported, poorly to moderately sorted layer. Ash to lapilli sized clasts dispersed throughout. Pumice is heavily weathered. Lots of lithics present. Gradual contacts.

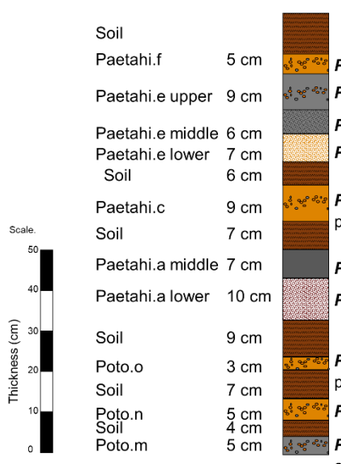
Kawakawa tephra – White-yellow very fine ash.

Poto.e – Unconsolidated well sorted, dark grey fine lapilli layer. Well sorted deposit. Sharp contact above. Base of outcrop.

6. Cardiff Road: Paetahi Reference section.

Latitude/Longitude: -39.342975, 174.2283056.

The Paetahi Formation reference section is a westerly facing road cutting 0.02 km south of the Paetahi Stream (Location 6; Figure 2.1). Poto.m is situated at the base of the outcrop.



Paetahi.f – Orange-brown matrix supported moderately sorted, grey medium lapilli and heavily weathered orange lapilli dispersed throughout. Gradual contacts.

Paetahi.e upper – Highly consolidated (hard to scrape) orange-brown matrix supported grey coarse ash to fine lapilli. Gradual contacts.

Paetahi.e middle – Loosely consolidated moderately sorted medium grey lapilli. Gradual contacts.

Paetahi.e lower – Unconsolidated poorly sorted very coarse orange-red lapilli. Some grey pumice/lithics. Sharp and gradual contacts.

Paetahi.c – Yellow-brown matrix supported, poorly sorted, heavily weathered layer. Coarse ash to coarse lapilli clasts dispersed throughout. Large (<1 cm) heavily weathered soft lapilli, predominant. More grey pumice/lithics near base of layer. Gradual contacts.

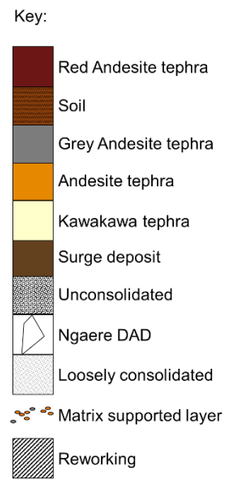
Paetahi.a middle– Consolidated moderately sorted, fine to medium grey lapilli. Gradual contacts.

Paetahi.a lower– Unconsolidated poorly sorted red and grey medium to coarse lapilli. Some grey lithics present. Sharp and gradual contact.

Poto.o – Yellow-brown matrix supported, poorly sorted layer. Medium ash to fine lapilli grey pumice/lithics and large weathered orange lapilli dispersed throughout. Clasts appear in pockets throughout the soil. Gradual contacts.

Poto.n – Yellow-brown matrix supported, poorly sorted, fine to coarse weathered orange lapilli dispersed throughout. Coarse ash to fine lapilli grey pumice/lithics present. Gradual contacts.

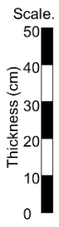
Poto.m – Grey matrix supported layer at the base of the outcrop. Medium ash to fine lapilli grey grey pumice/lithics and large weathered orange lapilli dispersed throughout. Gradual contact.



2. Climie Road:

Latitude/Longitude: -39.375576, 174.274383.

The outcrop is a south facing road cutting of a mound 2 km west of SH3 (Location 2; Figure 2.1). The Ngaere DAD is exposed <20 cm from the base of the outcrop near the centre of the mound. Poto.a is located 8cm from the base of the outcrop below the Ngaere DAD. Poto.k- Paetahi.d is located 0.01 km east of the Ngaere exposure at the base of the outcrop.



Soil		
Paetahi.d	1- 2 cm	***Paetahi.d*** **–** Heavily weathered yellow-brown matrix supported layer. Very soft orange pumice lapilli are dispersed throughout the matrix. Appears in small pockets across the outcrop. Gradual contacts.
Soil	9 cm	
Paetahi.c	11 cm	***Paetahi.c*** **–** Heavily weathered yellow-brown matrix supported layer. Very soft orange pumice lapilli. Some grey lapilli and lithics present. Appears in pockets across the outcrop. In small (2 cm by 3 cm) pockets directly underneath a layer of unconsolidated well sorted ash. Only a few sections. Gradual contacts.
Soil	12 cm	
Paetahi.b	3 cm	***Paetahi.b*** **–** Yellowish-brown matrix supported layer. Appears as heavily weathered large orange and grey pumice lapilli dispersed throughout the matrix. Present in small pockets across the outcrop. Some lithics present within the layer. Gradual contacts.
Soil	3 cm	
Paetahi.a lower	13 cm	***Paetahi.a lower*** **–** Unconsolidated poor to moderately sorted coarse orange lapilli layer. Sharp contact.
Soil	83 cm	
Poto.o	2-15 cm	***Poto.o*** **–** Yellow-brown matrix supported layers, poorly sorted. Appears in pockets. Yellow-orange and grey clasts present. Yellow-orange clasts (1-5 mm) in size dispersed throughout the layer. Some lithics but pumice seems to be dominant. Gradual contacts.
Poto.n	11 cm	***Poto.n*** **–** Yellow-brown matrix supported layers, poorly sorted. Yellow/orange clasts 1-5mm in size dispersed throughout the layer. Gradual contacts.
Poto.m	11 cm	***Poto. m*** **–** Yellow-orange matrix supported layer, poorly sorted, grey pumice and lithics throughout. Heavily weathered yellow/orange clasts (5 mm to 1 cm) present very soft. (Overthickening or potentially some reworking of the layer). Gradual contacts.
Poto.l upper	15 cm	***Poto.l upper*** **–** Yellow-orange matrix supported layer, poorly sorted, grey pumice and lithics throughout. Heavily weathered yellow/orange clasts (5 mm to 1 cm) present. (Overthickening or potentially some reworking of the layer).
Poto.l lower	5 cm	***Poto.l lower*** **–** Yellow-orange matrix supported layer, poorly sorted, grey pumice and lithics throughout. Heavily weathered yellow/orange clasts (5 mm to 1 cm) present. Appears as an orange band below Poto.l upper. Gradual contacts.
Soil	17cm	
Poto.k upper	>24 cm	***Poto.k upper*** - Yellowish/brown matrix dominated layer. Larger grey clasts poorly sorted. Some yellow/orange clasts present. (Overthickening or potentially some reworking of the layer).
		Gap in the sequence. DAD mound. Upper section present further along outcrop.
Ngaere DAD	31 cm	***Ngaere Formation*** –Thick massive unit. Poorly sorted flow unit clasts up to 10cm in diameter. Grey and yellow/orange clasts present.
Poto.b	3 cm	**Poto.b -** Unconsolidated material well sorted coarse ash to fine lapilli yellowish grey. Sharp contacts.
Poto.a	5 cm	***Poto.a*** – Unconsolidated moderately to well sorted. . Bottom 2.5cm of the layer is dominated by orange/red large ash to fine lapilli clasts. Top 2.5cm is dominated by well sorted medium grey coarse ash, which fines slightly upward. Sharp contacts.

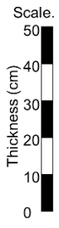
Key:

- Red Andesite tephra
- Soil
- Grey Andesite tephra
- Andesite tephra
- Kawakawa tephra
- Surge deposit
- Unconsolidated
- Ngaere DAD
- Loosely consolidated
- Matrix supported layer
- Reworking

3.Climie Road/SH3.

Latitude/Longitude: -39.375582, 174.296024.

The outcrop is a south facing road cutting 0.2 km west of SH3 next to farm entrance track (Location 3; Figure 2.1). Poto. h is situated 6 cm from the base of the outcrop.



Soil	10 cm	
Paetahi.f	2 cm	***Paetahi.f*** **–** Yellow-brown matrix supported**.** Heavily weathered orange pumice (very soft), some lithics and crystals present. Clasts are dispersed throughout the matrix. Gradual contacts.
Paetahi.e middle	7 cm	***Paetahi.e middle*** **–** Moderately to well sorted, matrix supported, grey pumice and lithics. Some orange pumice clasts present. Gradual contacts.
Soil	2 cm	
Paetahi.d	1-2 cm	***Paetahi.d*** **–** Yellow-brown matrix supported poorly sorted, layer. Appears in pockets, heavily weathered orange lapilli dispersed throughout. Some grey pumice, lithics and crystals present. Gradual contacts
Soil	3 cm	
Paetahi.c	5 cm	***Paetahi.c*** **–** Yellow-brown matrix supported, poorly sorted layer. Grey and heavily weathered orange pumice/ lapilli scattered throughout. Gradual contacts.
Soil	5 cm	
Paetahi.b	2 cm	***Paetahi.b*** **–** Yellow-brown matrix supported layer. Heavily weathered orange pumice. Some grey pumice and lithics present. Appears in pockets across the outcrop. Clasts are dispersed throughout the layer. Gradual contacts.
Paetahi.a upper	3 cm	***Paetahi.a upper*** –Moderately to well sorted orange to red lapilli. Some lithics present in the layer. Pumice clasts are finer than Paetahi.a lower. Gradual contacts.
Paetahi.a lower	11 cm	***Paetahi.a lower*** **–** Unconsolidated, poorly sorted orange to red lapilli. Sharp and gradual contacts.
Soil	2 cm	
Poto.o	3 cm	***Poto.o –*** Yellow-brown matrix supported layer. Pumice and lithics appear in pockets dispersed throughout. Heavily weathered orange lapilli present. Gradual contacts.
Soil	4 cm	
Poto.n	3 cm	***Poto.n –*** Matrix supported, moderately sorted grey pumice layer. Some larger more weathered lapilli present at the top of the layer. Weathered orange lapilli scattered throughout the outcrop. Gradual contacts.
Soil	7 cm	
Poto.m	8 cm	***Poto.m –*** Yellow-brown matrix supported, moderately to well sorted grey pumice dispersed throughout. Some lithics and crystals present. Weathered orange medium to coarse ash present more concentrated towards the base of the layer. Gradual contacts.
Soil	2 cm	
Poto.l upper	4 cm	***Poto.l upper –*** Yellow-brown matrix layer. Orange and grey heavily weathered pumice clasts dispersed throughout the layer. Grey dominated deposit. Some lithics and crystals present. Gradual contacts.
Soil		
Poto.l lower	2 cm	***Poto.l lower*** – Yellow-brown matrix supported heavily weathered layer. Grey clast dominated layer. Appears in pockets. Some lithics and crystals present. Clasts are dispersed throughout the layer. Gradual contacts.
Soil	1 cm	
Poto.k lower	5 cm	***Poto.k lower*** **–** Yellow-brown matrix supported heavily weathered layer. Grey and orange pumice to lapilli dispersed throughout, some lithics and crystals present. Gradual contacts.
Soil	17 cm	
Poto.j	2 cm	***Poto.j*** **–** Matrix supported, moderately sorted, heavily weathered medium to coarse grey ash and lithic dominated layer. Appears in patches across the outcrop. Gradual contacts.
Soil	1 cm	
Poto.h	7 cm	***Poto.h*** – Yellow-brown matrix supported, moderately sorted, heavily weathered layer. Grey dominated pumice lapilli clasts are >1cm. Very soft orange lapilli, lithics and crystals are present. Gradual contacts.
Soil	6 cm	

4. Meerman Farm (Finnerty Road):

Latitude/Longitude: -39.38985, 174.294782.

This is a north facing outcrop on Meerman Farm 0.4 km west of SH3, behind a farmhouse (Location 4; Figure 2.1). Poto.a is situated 30 cm from the base of the outcrop.



Soil
Paetahi.f 4 cm
Paetahi.f – Yellow-brown matrix supported layer**.** Weathered orange lapilli dispersed throughout. Grey pumice/lithics present. Appears in small pockets across the outcrop. Gradual contacts.

Soil 10 cm

Paetahi.e middle 10 cm
Paetahi.e middle – Matrix supported medium grey lapilli; lithic/pumice dominated layer. Some weathered orange pumice dispersed throughout. Gradual and wavy contact.

Paetahi.d 1 cm
Paetahi.d – Yellow-brown matrix dominated layer. Orange weathered pumice clasts dispersed across the outcrop. Appears in small pockets with 1-2 clasts grouped together. Gradual contacts.

Soil 16 cm

Paetahi.c 8 cm
Paetahi.c – Yellow-brown matrix supported grey pumice dominated with some orange weathered lapilli dispersed across the outcrop. Gradual contacts.

Soil 1 cm
Paetahi.b 6 cm
Paetahi.b – Yellow-brown matrix supported layer containing medium to coarse heavily weathered orange lapilli, grey pumice/lithics dispersed throughout. Appears in pockets. Gradual contacts

Paetahi.a middle 5 cm
Paetahi.a Middle –Grey pumice/lithic dominated fine to medium grained lapilli. Gradual contacts.

Paetahi.a lower 6 cm
Paetahi.a lower – Medium grained lapilli orange-red with some large orange weathered lapilli present at the base. Slight normal grading. Gradual contacts.

Soil 11 cm
Poto.n 1 cm
Poto.n – Yellow-brown matrix supported, appears in small pockets. Large 1cm heavily weathered orange/brown lapilli dispersed throughout. Some grey pumice/lithics. Gradual contacts.

Soil 6 cm
Poto.l upper 2 cm
Poto. l upper– Yellow-brown matrix supported, heavily weathered large orange/brown lapilli up to (2 – 4 cm) dispersed throughout. Smaller grey lithics/pumices present. Gradual contact.

Poto.l lower 2 cm
Poto. l lower– Yellow-brown matrix supported; heavily weathered large orange/brown lapilli dispersed throughout. Smaller grey lithics/pumices present. Gradual contact.

Soil 11 cm
Poto.f – Yellow-brown matrix supported. Grey lithics/pumice and heavily weathered brown lapilli dispersed throughout. Layer thins and thickens across outcrop.. Gradual contacts.

Poto.f 4 cm
Soil 4 cm
Kawakawa 1 cm
Kawakawa – White-yellow well sorted very fine ash appears in 1 cm by 1 cm pockets.

Poto.e 2 cm
Poto.e – Fine-grained lapilli at the bottom with a very fine ash layer along the top directly below the Kawakawa. It is very hard like cement. Appears in small pockets. Gradual contacts.

Soil 6 cm

Ngaere DAD 60-80 cm
Ngaere DAD – Massive unit across outcrop. Poorly sorted contains large blocks.

Poto.b 2 cm
Poto.b – Very well sorted dark grey fine-grained lapilli. Appears in pockets throughout the outcrop. Directly below the Ngaere DAD.

Soil 20 cm

Poto.a 10 cm
Poto.a – 30cm up from the base. Moderately sorted, grey pumice/lithics and weathered orange coarse ash. Gradual contacts.

Scale.
Thickness (cm)
50
40
30
20
10
0

Key:
- Red Andesite tephra
- Soil
- Grey Andesite tephra
- Andesite tephra
- Kawakawa tephra
- Surge deposit
- Unconsolidated
- Ngaere DAD
- Loosely consolidated
- Matrix supported layer
- Reworking

8.Eltham Road:

Latitude/Longitude: -39.426708, 174.179163.

This is a north facing road cutting 0.03 km east of Kapuni Stream (Location 8; Figure 2.1). The Ngaere DAD is present at the base of the outcrop.



Soil
Paetahi. e lower 3-6 cm
Paetahi.e lower – Unconsolidated moderately well sorted medium lapilli. Grey pumice/lithics present. Appears in pockets. Gradual contacts.

Paetahi. d 3 cm
Paetahi.d – Yellow-brown matrix supported poorly sorted layer. Heavily weathered orange lapilli dispersed throughout. Grey pumice/lithics present. Gradual contacts.

Soil 10 cm

Paetahi. c 4 cm
Paetahi.c – Predominantly yellow-brown matrix supported. Moderately well sorted heavily weathered medium orange lapilli, Some smaller grey pumice/lithics present. Tightly packed layer. Gradual contacts.

Soil 2 cm
Paetahi. b 3 cm
Paetahi.b – Yellow-brown matrix supported poorly sorted layer. Large weathered orange lapilli clasts dispersed throughout. Grey pumice/lithics present. Grey clasts are smaller than orange ones. Gradual contacts

Paetahi. a middle 4 cm
Paetahi.a middle – Moderately sorted fine to medium grey lapilli/lithics. Fine to medium. Some orange lapilli present. 4cm thick layer. Gradual contacts.

Paetahi. a lower 3 cm
Paetahi.a lower – Unconsolidated moderately well *sorted* fine to medium orange lapilli. Sharp and gradual contacts.

Soil 5 cm
Kawakawa 2 cm
Kawakawa tephra – white-yellow very fine ash.

Soil 5 cm
Poto.d 2 cm
Poto.d – *Yellow-brown matrix supported, m*edium to coarse grained heavily weathered orange lapilli dispersed throughout layer. A small amount of grey lithics/pumice present. Gradual contacts.

Soil 10 cm

Poto.c lower 3 cm
Poto.c lower- Yellow-brown matrix supported layer. Heavily weathered orange medium lapilli dispersed throughout. Grey lithics and pumice are present. Gradual contacts.

Soil 2 cm

Ngaere DAD >15 cm
Ngaere DAD - Massive unit. Poorly sorted.

Scale.
Thickness (cm)
50
40
30
20
10
0

9. Upper Palmer Road.

Latitude/Longitude: -39.365312, 174.169401.

This is an east facing road cutting 1.3 km north of Opunake Road next to a farm paddock entrance. The Ngaere DAD is present at the base of this outcrop.



Scale.
Thickness (cm)
50
40
30
20
10
0

Soil
Paetahi.f 3 cm
Paetahi.f – Yellow-brown matrix supported layer. Heavily weathered orange medium lapilli. Some grey pumice/lithics. The layer appears in pockets not continuous across the outcrop. Gradual contacts.

Paetahi.e upper 5 cm
Paetahi.e Upper – Matrix supported consolidated fine-grained grey lapilli, pumice/lithics. Moderately sorted there are some larger grey clasts deposited throughout. Gradual contacts.

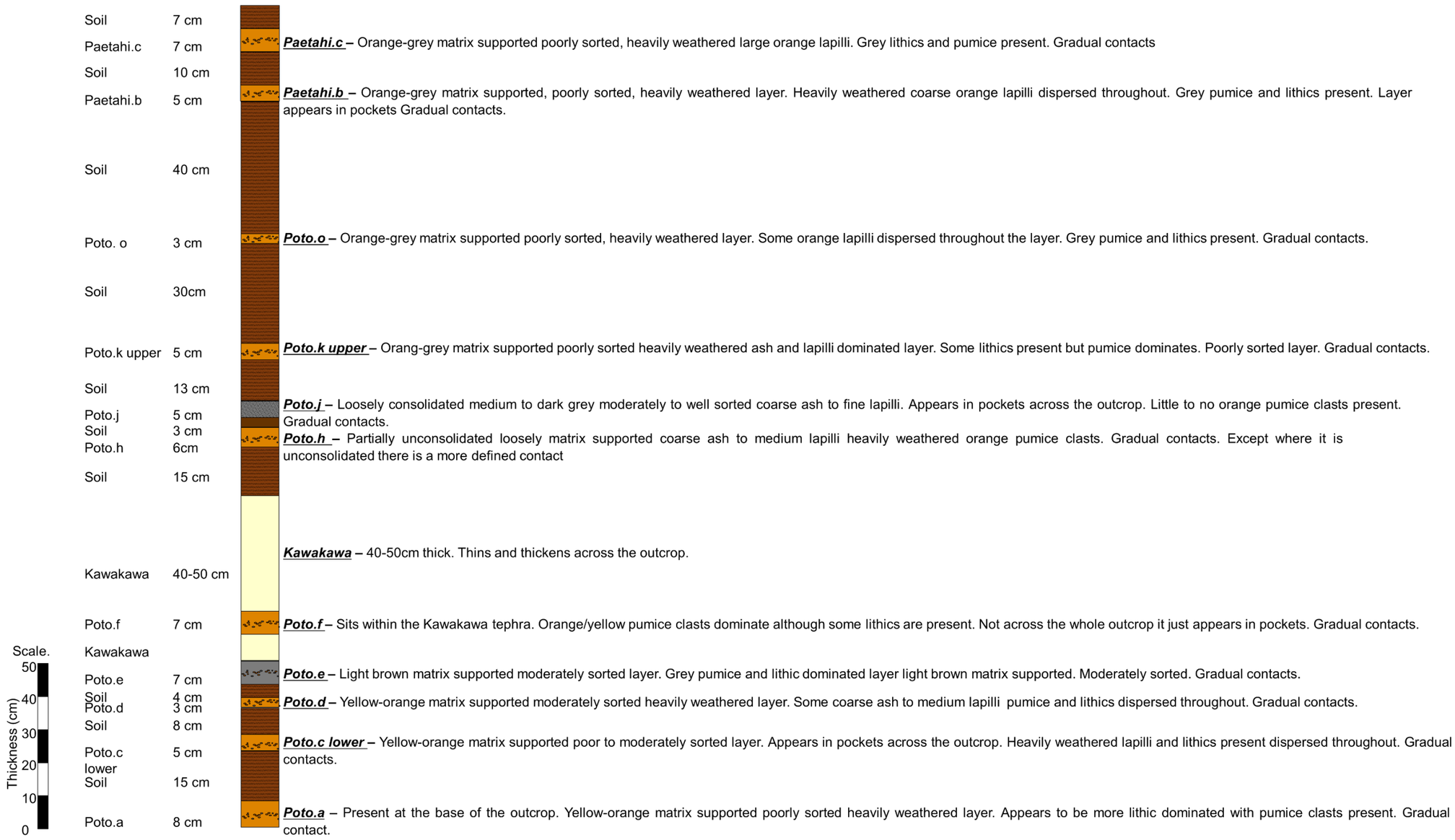
Paetahi.e middle 6 cm
Paetahi.e middle – Loosely consolidated poorly sorted, grey dominated medium lapilli. Some matrix present. Gradual contacts

Paetahi.e lower 5 cm
Paetahi.e lower – Unconsolidated moderately sorted very coarse orange lapilli. Grey pumice/lithics present. Gradual contacts. Ngaere DAD present >20 cm below.

10.Turuturu Road.

Latitude/Longitude: -39.566992, 174.293545.

This is an east facing road cutting 2 km north of Hawera and 0.3 km North of Turuturu Mokai Historic Reserve. Poto.a is present at the base of the outcrop. Over thickening of Kawakawa tephra here but all other layers do not appear reworked.



Paetahi.c **–** Orange-grey matrix supported poorly sorted, heavily weathered large orange lapilli. Grey lithics and pumice present. Gradual contacts

Paetahi.b **–** Orange-grey matrix supported, poorly sorted, heavily weathered layer. Heavily weathered coarse orange lapilli dispersed throughout. Grey pumice and lithics present. Layer appears in pockets Gradual contacts.

Poto.o **–** Orange-grey matrix supported poorly sorted, heavily weathered layer. Some orange lapilli dispersed throughout the layer. Grey pumice and lithics present. Gradual contacts.

Poto.k upper **–** Orang-grey matrix supported poorly sorted heavily weathered ash and lapilli dominated layer. Some lithics present but pumice dominates. Poorly sorted layer. Gradual contacts.

Poto.j **–** Loosely consolidated medium to dark grey moderately to well sorted coarse ash to fine lapilli. Appears in pockets across the outcrop. Little to no orange pumice clasts present. Gradual contacts.

Poto.h **–** Partially unconsolidated loosely matrix supported coarse ash to medium lapilli heavily weathered orange pumice clasts. Gradual contacts. Except where it is unconsolidated there is a more defined contact

Kawakawa **–** 40-50cm thick. Thins and thickens across the outcrop.

Poto.f **–** Sits within the Kawakawa tephra. Orange/yellow pumice clasts dominate although some lithics are present. Not across the whole outcrop it just appears in pockets. Gradual contacts.

Poto.e **–** Light brown matrix supported moderately sorted layer. Grey pumice and lithic dominated layer light brown matrix supported. Moderately sorted. Gradual contacts.

Poto.d **–** Yellow-orange matrix supported moderately sorted heavily weathered layer. Some coarse ash to medium lapilli pumice and lithics dispersed throughout. Gradual contacts.

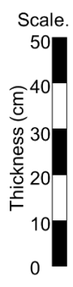
Poto.c lower **–** Yellow-orange matrix supported poor to moderately sorted layer. Appears in pockets across the outcrop. Heavily weathered lapilli and lithics present dispersed throughout. Gradual contacts.

Poto.a – Present at the base of the outcrop. Yellow-orange matrix supported poorly sorted heavily weathered layer. Appears to be more lithic dominated with pumice clasts present. Gradual contact.

11. 650 South Road.

Latitude/ Longitude: -39.616647, 174.338685.

This is a north facing road cutting 5 km east of Hawera (Location 11; Figure 2.1). Road cutting is next to the passing lane.



Poto.h 3.5 cm
Soil 7 cm
Kawakawa 4 cm
Soil 35 cm
Poto.b 1 cm

Poto.h – Matrix supported layer with heavily weathered orange-brown lapilli, lithics and free crystals distributed throughout.

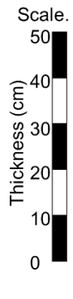
Kawakawa tephra – White-yellow very fine ash.

Poto.b – Unconsolidated well sorted dark grey ash. Gradual contacts.

12. 147 South Road.

Latitude/Longitude: -39.586839, 174.251921.

This is a south facing road cutting 2 km west of Hawera (Location 12; Figure 2.1). The Ngaere DAD is present at the base of the outcrop. A 40 cm sandy lahar unit is present above the tephra deposits.



Soil 24 cm
Poto.f 3 cm
Soil 15 cm
Poto.d 6 cm
Soil 9 cm
Poto.c lower 5 cm
Soil 3 cm
Ngaere DAD 39 cm

Poto.f **–** Yellow-orange matrix supported poor to moderately sorted heavily weathered orange lapilli layer. Appear in pockets Gradual contacts.

Poto.d **–** Yellow-orange matrix supported heavily weathered layer dominated by grey pumice and lithics. There are some much larger (4cm) lithics present. Gradual contacts.

Poto.c lower **–** Yellow-orange matrix supported heavily weathered layer. Grey and orange (weathered very soft) coarse ash to lapilli clasts distributed throughout. Gradual contacts.

Ngaere DAD – Massive unit poorly sorted.

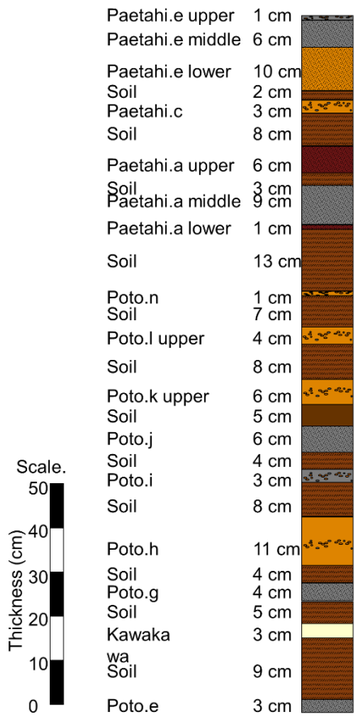
Key:

- Red Andesite tephra
- Soil
- Grey Andesite tephra
- Andesite tephra
- Kawakawa tephra
- Surge deposit
- Unconsolidated
- Ngaere DAD
- Loosely consolidated
- Matrix supported layer
- Reworking

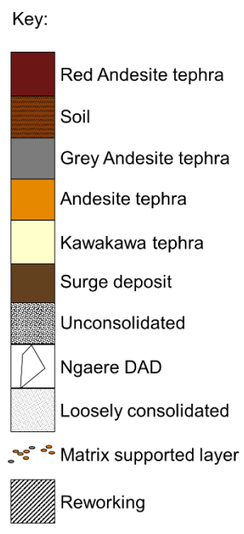
14.Tihi Road.

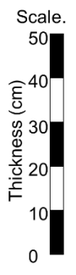
Latitude/Longitude: -39.585792, 174.40098.

This is an east facing farm track cutting 12 km northeast of Hawera (Location 14; Figure 2.1). Poto.e is situated 15 cm above a change in soil colours. Bottom section of the outcrop is dominated by a banded bright orange soil, before a changes to a brown defined soil found within the Poto and Paetahi Formations across the Taranaki ring plain.



Paetahi.e upper	1 cm	***Paetai.e upper*** T– Coarse orange lapilli clats directly along the top of Paetahi.e middle. Lapilli are (2 – 5 mm). Some grey clasts dispersed throughout.
Paetahi.e middle	6 cm	***Paetahi. e middle*** - Loosely consolidated grey fine lapilli. Some orange clasts present within the layer. Gradual contacts.
Paetahi.e lower	10 cm	***Paetahi.e lower*** **-** Loosely consolidated moderately sorted grey coarse ash to fine lapilli. Some slightly larger orange lapilli are present. Gradual contacts.
Soil	2 cm	
Paetahi.c	3 cm	***Paetahi.c*** – Yellow-brown matrix dominated moderately to well sorted medium to coarse grey ash. Small orange clasts present within the layer. This layer is moderately to well sorted fine grained. Gradual contacts.
Soil	8 cm	
Paetahi.a upper	6 cm	***Paetahi.a upper*** **–** Loosely consolidated moderately sorted grey medium to coarse ash. There are some orange and grey lapilli and lithics present. Gradual contacts.
Soil	3 cm	
Paetahi.a middle	9 cm	Paetahi.a middle – Loosely consolidated moderately sorted grey coarse ash to fine lapilli. Some orange coarse lapilli dispersed throughout. Fine grained orange band across the top 1cm. Gradual contacts.
Paetahi.a lower	1 cm	Paetahi.a lower – Loosely consolidated moderately sorted coarse orange lapilli clasts. Gradual contacts.
Soil	13 cm	
Poto.n	1 cm	***Poto.n*** – Yellow-brown matrix supported heavily weathered large lapilli clasts (5 mm to 1 cm) dispersed throughout. Gradual contacts.
Soil	7 cm	
Poto.l upper	4 cm	***Poto.l upper*** – Yellow-brown matrix supported poorly sorted, heavily weathered soft orange lapilli clasts. Some smaller grey and orange coarse ash to fine lapilli dispersed throughout. Appears in pockets across the outcrop. Gradual contact.
Soil	8 cm	
Poto.k upper	6 cm	***Poto.k upper-*** Yellow-brown matrix supported poorly sorted heavily weathered large orange lapilli which are very soft. There are some smaller grey and orange clasts present within the layer.
Soil	5 cm	
Poto.j	6 cm	***Poto.j*** – Loosely consolidated moderately to well sorted fine-grained grey ash. Some orange clasts are also present. Gradual contacts.
Soil	4 cm	
Poto.i	3 cm	***Poto.i*** – Yellow-matrix supported fine grained grey ash. Some heavily weathered orange lapilli (blobs) and slightly larger grey (coarse ash) lithics are present within the layer. Gradual contacts.
Soil	8 cm	
Poto.h	11 cm	***Poto.h*** – Yellow-brown matrix supported poorly sorted, heavily weathered orange lapilli (blobs). Some grey and orange clasts are dispersed throughout. Gradual contacts.
Soil	4 cm	
Poto.g	4 cm	***Poto.g*** – Loosely consolidated moderately sorted fine grained lapilli appears in small pockets. Some weathered orange clasts present. Gradual contacts.
Soil	5 cm	
Kawakawa	3 cm	***Kawakawa*** – Pinky brown very fine ash. Some specs of tephra clasts present in the soil above.
Soil	9 cm	
Poto.e	3 cm	***Poto.e*** – Loosely consolidated moderately sorted, fine to medium dark grey ash, appears in pockets 2.5-3cm thick. Gradual contacts.





15. Allen Road.

Latitude/Longitude: -39.58562, 174.43456.

This is a southwest facing farm cutting 20 km northwest of Hawera (Location 15; Figure 2.1). Poto.c lower is situated 15 cm from the base of the outcrop.



Paetahi.a lower	**6 cm**	**Paetahi.a lower –** Poorly sorted heavily weathered orange coarse lapilli. Gradual contacts.
Soil	**5 cm**	
Kawakawa	**1-3 cm**	**Kawakawa tephra –** White-yellow very fine ash appears as blotches across the outcrop. Gradual contacts.
Soil	**3 cm**	
Poto.c lower	**3 cm**	**Poto.c lower –** Poorly sorted yellow-brown matrix supported orange and grey coarse ash to fine lapilli sized clasts dispersed throughout..

Appendix A2: Sample Locations.

Locations of the thirteen sample locations across the eastern and southeastern sector of the Taranaki ring plain in latitude and longitude, their thickness and largest grain size (where applicable).

Location name	**Ronald Road**	Poto reference location		**Climie Rd**			**Climie Rd/SH3**		
Location number	**1**			**2**			**3**		
	Latitude	**Longitude**		**Latitude**	**Longitude**		**Latitude**	**Longitude**	
Co-ordinates Latitude/Longitude	-39.361454	174.222222		-39.375576	174.274383		-39.375582	174.296024	
	Poto type section	Thickness (cm)	**Max grain size (phi)**		Thickness (cm)	**Max grain size (phi)**		Thickness (cm)	**Max grain size (phi)**
	Paetahi.f	2		Paetahi.d	2		Paetahi.f	2	
	Paetahi.e middle	9	**-3**	Paetahi.c	11		Paetahi.e middle	7	**-2.5**
	Paetahi.c	10		Paetahi.b	3	**-4**	Paetahi.d	2	
	Paetahi.b	3	**-3**	Paetahi.a lower	13	**-4**	Paetahi.c	5	

	Paetahi.a upper	7	**-4**	Poto.o	15	**-3.5**	Paetahi.b	2	**-2.5**
	Paetahi.a middle	3	**-3.5**	Poto.n	11		Paetahi.a upper	3	
	Paetahi.a lower	5	**-3.5**	Poto.m	11		Paetahi.a lower	11	**-3**
	Poto.o	5	**-4**	Poto.l upper	15	**-2.5**	Poto.o	3	**-2.5**
	Poto.n	8	**-4**	Poto.l lower	5		Poto.n	3	
	Poto.m	6	**-4**	Poto.b	3		Poto.m	8	
	Poto.l upper	7	**-4**	Poto.a	5	**-3**	Poto.l upper	4	
	Poto.l lower	5	**-4**				Poto.l lower	2	**-3.5**
	Poto.k upper	4	**-3.5**				Poto.k lower	5	
	Poto.k lower	8	**-4**				Poto.j	2	
	Poto.j	3	**-3.5**				Poto.h	7	

	Poto.i	4_7	**-4**						
	Poto.h	4	**-3.5**						
	Poto.g	3_8	**-3**						
	Poto.f	6	**-3.5**						
	Poto.e	4	**-2**						
	Poto.d	3	**-2.5**						
	Poto.c upper	3	**-2.5**						
	Poto.c lower	4	**-3.5**						
	Poto.b	5	**-1.5**						
	Poto.a	9	**-3.5**						

Location name	**<u>Meerman Farm</u>**			**<u>Opunake Rd</u>**	Paetahi reference location		**<u>Cardiff Road</u>**	Paetahi reference location	
Location number	**4**			**5**			**6**		
	Latitude	**Longitude**		**Latitude**	**Longitude**		**Latitude**	**Longitude**	

Co-ordinates Latitude/Longitude	-39.38985	174.294782		-39.355958	174.244338		-39.342975	174.228305 6	
		Thickness (cm)	**Max grain size (phi)**		Thickness (cm)	**Max grain size (phi)**		Thickness (cm)	**Max grain size (phi)**
	Paetahi.f	4		Paetahi.f	3	**-3.5**	Paetahi.f	5	**-2.5**
	Paetahi.e middle	10	**-2.5**	Paetahi.e middle	14	**-3**	Paetahi.e upper	9	**-3**
	Paetahi.d	1	**-3**	Paetahi.d	2	**-4**	Paetahi.e middle	6	**-3.5**
	Paetahi.c	8	**-3**	Paetahi.c	13	**-3.5**	Paetahi.e lower	7	**-4**
	Paetahi.b	6	**-3.5**	Paetahi.b	2	**-3.5**	Paetahi.c	9	**-4**
	Paetahi.a middle	5	**-3.5**	Paetahi.a upper	4	**-3**	Paetahi.a middle	7	**-4**
	Paetahi.a lower	6	**-3**	Paetahi.a middle	2	**-3**	Paetahi.a lower	10	**-4**
	Poto.n	1	**-2**	Paetahi. a lower	8	**-3**	Poto.o	3	**-3**

	Poto.l upper	2		Poto.o	6		Poto.n	5	**-3**
	Poto.l lower	2	**-4**	Poto.m	9		Poto.m	5	**-2**
	Poto.f	4	**-2.5**	Poto.l upper	10				
	Poto.e	2	**-1.5**	Poto.l lower	12	**-4**			
	Poto.b	2	**-0.5**	Poto.k upper	2				
	Poto.a	10		Poto.j	8				
				Poto.h	6				
				Poto.f	6	**-3**			
				Poto.e	2	**-3**			

Location name	**Eltham Rd Kapuni Stream**			**Upper Palmer Rd**			**Turuturu Rd**		
Location number	**8**			**9**			**10**		

	Latitude	**Longitude**		**Latitude**	**Longitude**		**Latitude**	**Longitude**	
Co-ordinates Latitude/Longitude	-39.426708	174.179163		-39.365312	174.169401		-39.566992	174.293545	
		Thickness (cm)	**Max grain size (phi)**		Thickness (cm)	**Max grain size (phi)**		Thickness (cm)	**Max grain size (phi)**
	Paetahi.e lower	6		Paetahi.f	3		Paetahi.c	7	
	Paetahi.d	3		Paetahi.e upper	5		Paetahi.b	5	**-3**
	Paetahi.c	4		Paetahi.e middle	6	**-4**	Poto.o	3	**-2**
	Paetahi.b	3	**-4**	Paetahi.e lower	5		Poto.k upper	5	
	Paetahi.a middle	4					Poto.j	5	
	Paetahi.a lower	3	**-2.5**				Poto.h	6	
	Poto.d	2					Poto.f	7	**-1.5**
	Poto.c lower	3					Poto.e	7	**-2.5**

							Poto.c lower	5	
							Poto.a	8	**-2.5**

Location name	**650 South Rd SH3**			**147 South Rd SH45**			**Tihi Rd East**		
Location number	**11**			**12**			**14**		
	Latitude	**Longitude**		**Latitude**	**Longitude**		**Latitude**	**Longitude**	
Co-ordinates Latitude/Longitude	-39.616647	174.338685		-39.586839	174.251921		-39.585792	174.40098	
		Thickness (cm)	**Max grain size (phi)**		Thickness (cm)	**Max grain size (phi)**		Thickness (cm)	**Max grain size (phi)**
	Poto.h	3.5		Poto.f	3	**-2**	Paetahi.e upper	1	
	Poto.b	1		Poto.d	6		Paetahi.e middle	6	**-2.5**

				Poto.c lower	5		Paetahi.e lower	10	
							Paetahi.c	3	
							Paetahi.a upper	6	
							Paetahi.a middle	9	
							Paetahi.a lower	1	**-2.5**
							Poto.n	1	
							Poto.l upper	4	
							Poto.k upper	6	
							Poto.j	6	
							Poto.i	3	
							Poto.h	11	
							Poto.g	4	

							Poto.e	3	**-1.5**
Location name	**Allen rd.**								
Location number	**15**								
	Latitude	**Longitude**							
Co-ordinates Latitude/Longitude	-39.58562	174.43456							
		Thickness (cm)	**Max grain size (phi)**						
	Paetahi.a lower	6							
	Poto.c lower	3							

Appendix A3: Exposure locations across the west/southwestern ring plain.

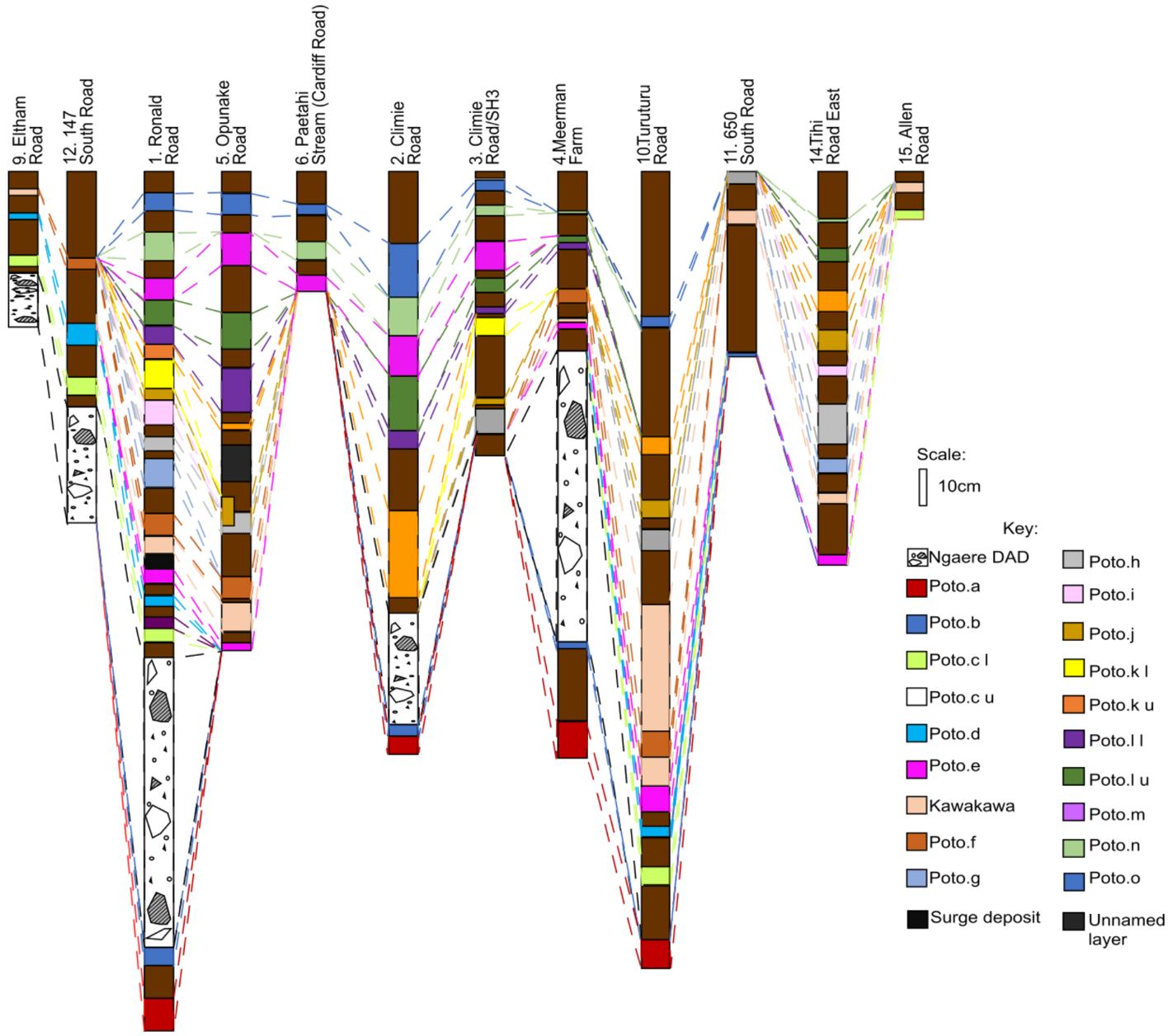
Exposure locations for Poto and Paetahi aged tephras within the coastal southwestern stratigraphy. Correlations with the eastern stratigraphy could not be completed due to lack of inland exposures. Location 16 Dover Road explored around the Carrington tephras due to a similar age of the deposits. Tephras between sites were also not able to be correlated due to similarities in features and small exposure regions.

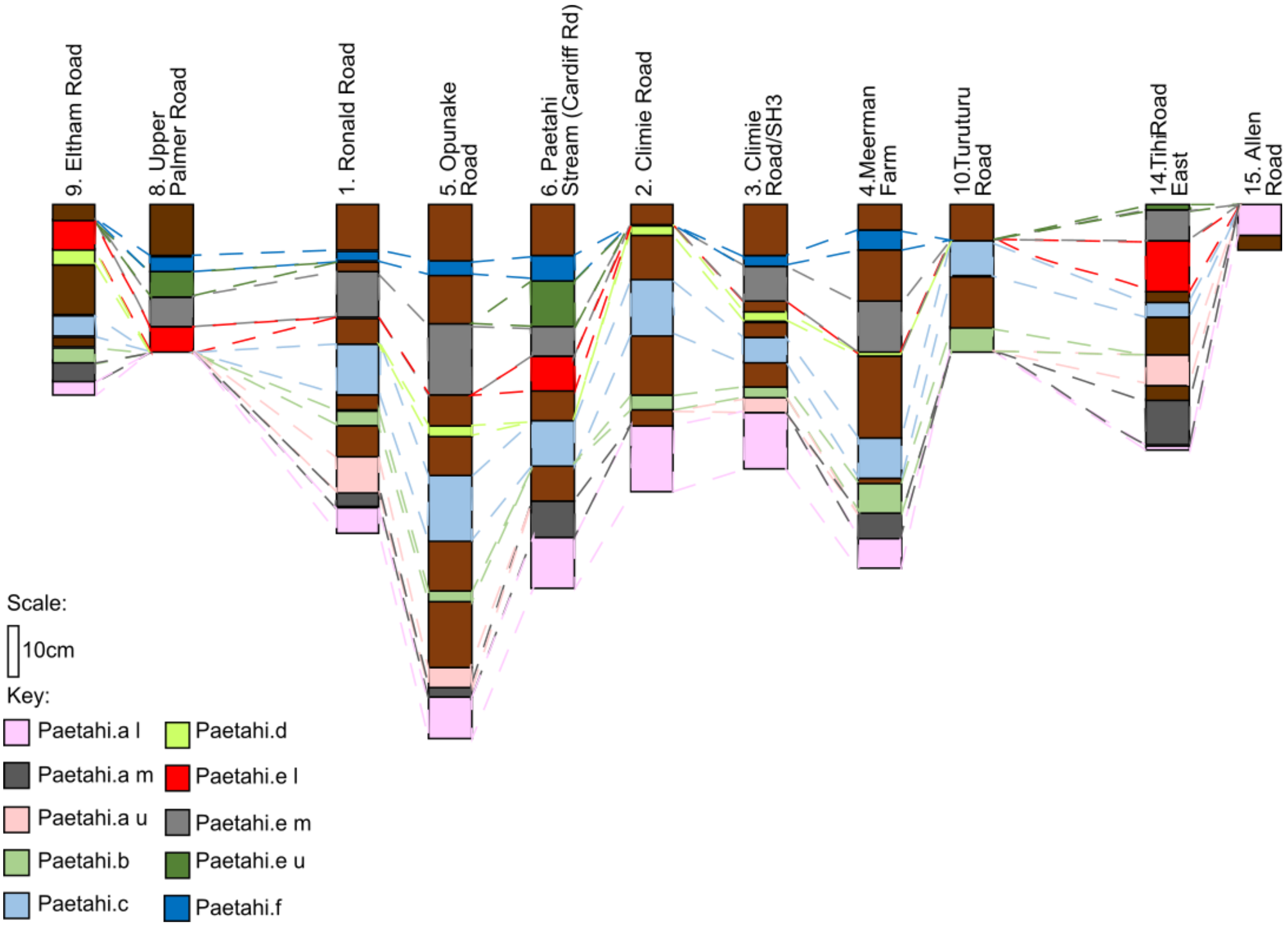
Location number	Location name	Latitude	Longitude	Number of identified tephras.	Thickness.	Notes.
7	**Okaweo Stream**	-39.432348	173.822413	1-2	1-3 cm	Fine grained ash very small area of access.
13	**Waste water station**	-39.443548	173.831382	4	T1 – 3-10cm T2 – 2.5 – 3cm T3 – 2.5 cm T4 – 1.5 – 4 cm	T1 -directly underneath Pungarehu DAD.
16	**Dover Rd**	-39.224503	173.966732	0	-	Carrington tephras here. No Poto or Paetahi identified.
17	**Middleton Bay**	-39.454227	173.849149	2	T1 – 2-4cm T2 2.5 cm	Kawakawa tephra present between tephras.
18	**Heimama 12**	-39.449254	173.839322	1	T1 – 2cm	Very silty tephra layer. Possible

						very thin layers around it.

Appendix A4: Stratigraphic Fence Diagrams.

Stratigraphic fence diagrams for the eastern and southeastern site locations.




9. Eltham Road
8. Upper Palmer Road
1. Ronald Road
5. Opunake Road
6. Paetahi Stream (Cardiff Rd)
2. Climie Road
3. Climie Road/SH3
4.Meerman Farm
10.Turuturu Road
14.TihiRoad East
15. Allen Road
Scale:
10cm
Key:
Paetahi.a l
Paetahi.a m
Paetahi.a u
Paetahi.b
Paetahi.c
Paetahi.d
Paetahi.e l
Paetahi.e m
Paetahi.e u
Paetahi.f

Appendix A5: Isopach Calculations.

Isopach thicknesses, area, and volumes for the twenty-eight Poto and Paetahi fall units.

Isopach – Poto Formation.												
T (m)	A (km²)	A½	√ area	Perimeter (km)	Shape factor	Long axis	Short axis	Aspect ratio	k	theta	lambda	AshCalc Volume (km³)
Poto.a									0.9774	0.01208	90.85	0.20
0.10	104.95	10.24	10.24	85.00	0.18	40.62	5.03	0.12				
0.05	340.01	18.44	18.44	97.00	0.45	43.93	13.78	0.31				
Poto.b									1.14	0.01138	40.1	0.03
0.05	37.71	6.14	6.14	34	0.066745	16.37	3.05	0.2				
0.03	116.31	10.78	10.78	47	0.061324	21.09	6.78	0.3				
0.02	192.86	13.89	13.89	57	0.053723	24.63	10.14	0.4				
0.01	595.26	24.40	24.4	106	0.027289	43.02	20.5	0.5				
Poto.c lower									0.3398	0.004603	79.62	0.17
0.05	185.03	13.60	13.6	83	0.34	39.68	7.54	0.19				
0.03	320.66	17.91	17.91	92	0.48	42.26	11.96	0.28				
Poto.c upper									0.1806	0.0274	12.69	0.05
0.03	53.82	7.34	7.34	36	0.521853	15.91	3.94	0.2				
Poto.d									0.4657	0.009935	49	0.10
0.06	120.26	10.97	10.97	46	0.714193	50.14	10.31	0.2				
0.02	407.38	20.18	20.18	106	0.455615	18.24	10.3	0.6				

Poto.e									1.105	0.2122	11.74	0.05
0.05	208.95	14.46	14.46	92	0.31	43.49	9.23	0.21				
0.02	423.48	20.58	20.58	109	0.45	50.56	16.48	0.33				
Poto.f									1.225	0.01908	73.86	0.17
0.06	201.42	14.19	14.19	92	0.299045	42.88	8.06	0.2				
0.03	776.4	27.86	27.86	135	0.535338	56.97	17.61	0.3				
Poto.g									1.409	0.02509	53.8	0.10
0.08	47.63	6.90	6.9	35	0.488601	16.35	3.86	0.2				
0.04	300.97	17.35	17.35	97	0.401966	43.7	8.13	0.2				
Poto.h									1.661	0.264	15.44	0.08
0.05	410.72	20.27	20.27	98	0.537407	45.47	14.8	0.3				
0.03	559.48	23.65	23.65	107	0.614083	49.1	18.07	0.4				
Poto.i									1.562	0.04235	30.08	0.05
0.07	54.55	7.39	7.38	34	0.592989	16.04	4.61	0.3				
0.03	396.8	19.92	19.92	96	0.541052	44.46	10.64	0.2				
Poto.j									1.975	0.04934	19.88	0.02
0.05	230.9	15.20	15.19	104.3	0.27	49.88	8.59	0.17				
0.02	313.4	17.70	17.7	109	0.33	51.47	10.58	0.21				
Poto.k lower									1.113	0.01081	65.35	0.08
0.08	39.68	6.30	6.3	33	0.457882	15.9	3.33	0.2				
0.05	102.01	10.10	10.1	50	0.512758	22.86	5.15	0.2				
Poto.k upper									1.639	0.207	10.31	0.03
0.05	153.63	12.39	12.39	105	0.18	50.21	6.77	0.13				

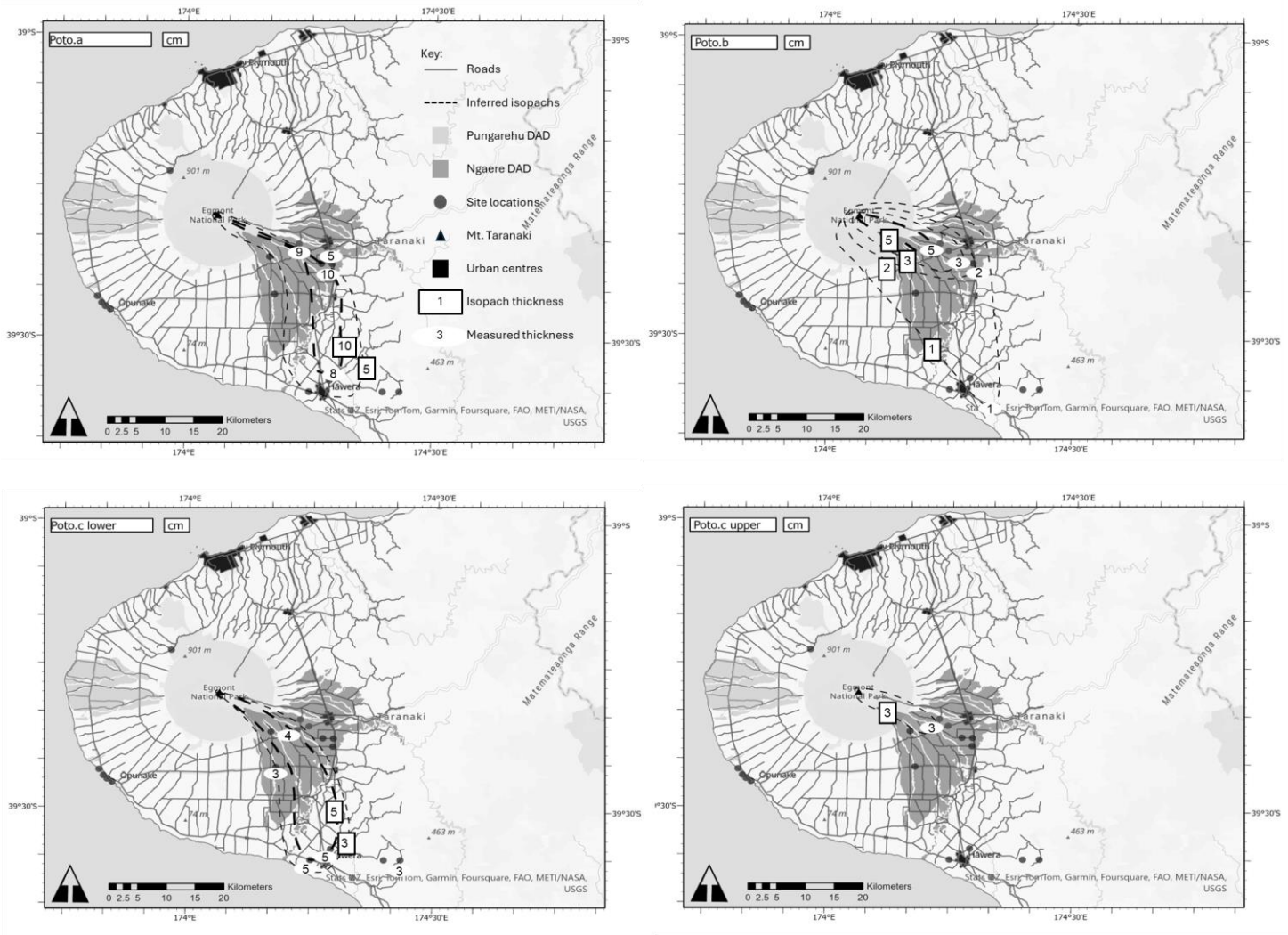
0.02	272.78	16.52	16.52	109	0.29	52.21	8.88	0.17				
Poto.l lower									1.953	0.2257	6.885	0.01
0.1	37.69	6.14	6.14	51	0.182094	24.48	1.83	0.1				
0.05	73.2	8.56	8.56	54	0.315452	25.5	3.67	0.1				
0.02	115.71	10.76	10.76	59	0.417712	26.75	5.12	0.2				
Poto.l upper									1.417	0.03813	32.03	0.06
0.15	8.35	2.89	2.89	42	0.059484	20.73	0.76	0.0				
0.1	28.95	5.38	5.38	45	0.179653	21.87	1.34	0.1				
0.04	246.08	15.69	15.69	99	0.315512	45.37	8.21	0.2				
Poto.m									1.13	0.04689	18.98	0.03
0.1	34.39	5.86	5.86	45	0.628629	21.88	2.03	0.1				
0.05	101.3	10.06	10.06	57	0.133012	26.29	4.95	0.2				
Poto.n									1.355	0.08397	12.08	0.02
0.1	29.78	5.46	5.46	46	0.176856	21.95	1.98	0.1				
0.05	85.15	9.23	9.23	48	0.464421	22.66	4.77	0.2				
0.01	357.56	18.91	18.91	99	0.458446	45.79	11.67	0.3				
Poto.o									1.498	0.01226	91.46	0.14
0.05	29.01	5.39	5.39	40	0.23	19.54	2.08	0.11				
0.03	187.18	13.68	13.68	90	0.29	43.13	7.16	0.17				

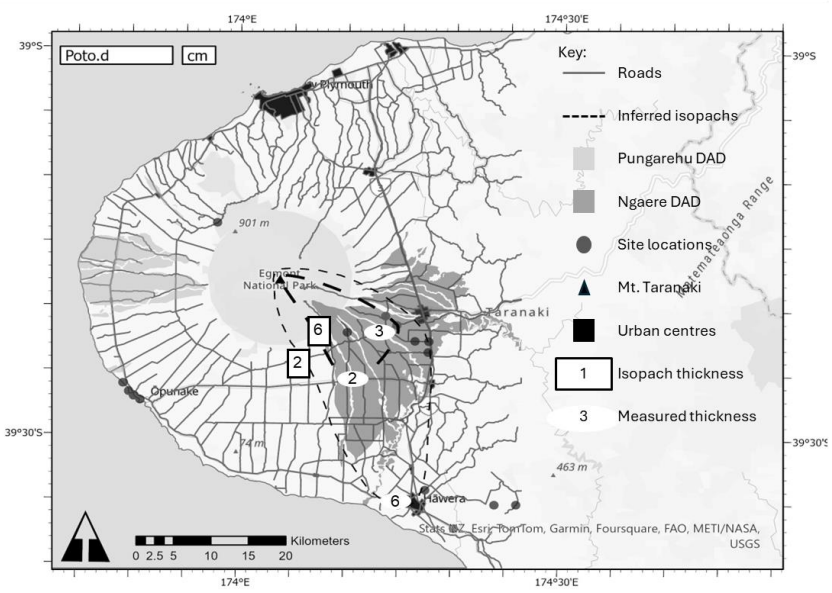
Isopach – Paetahi Formation.

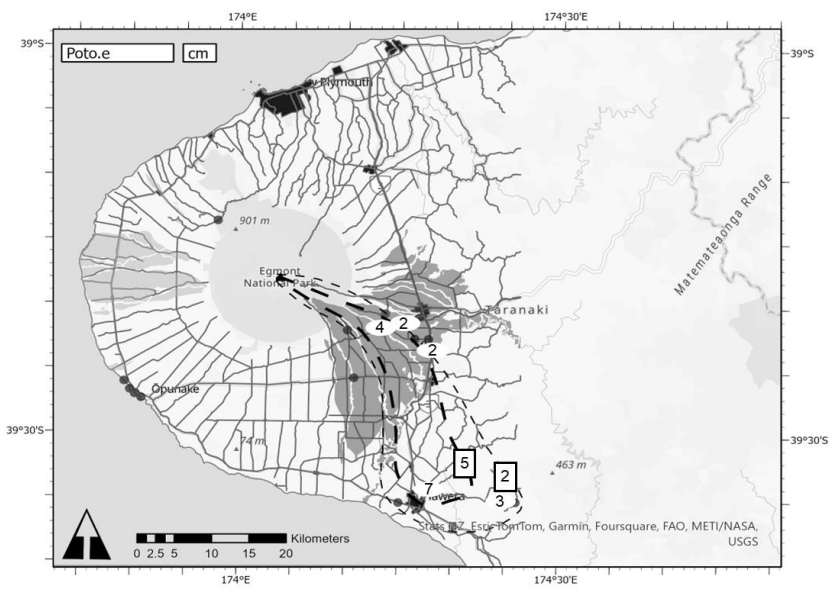
T (m)	A (km²)	A½	√ area	Perimeter (km)	Shape factor	Long axis	Short axis	Aspect ratio	k	theta	lambda	AshCalc Volume (km³)
Paetahi.a lower									0.93	0.01	99.36	0.26
0.10	157.23	12.54	12.54	93.00	0.23	43.43	7.58	0.17				
0.05	419.26	20.48	20.48	114.00	0.41	52.02	11.31	0.22				
0.03	1042.52	32.29	32.29	138.00	0.69	58.19	23.53	0.40				
Paetahi.a middle									1.13	0.02	41.16	0.06
0.05	131.87	11.48	11.48	103.00	0.16	50.10	5.75	0.11				
0.02	550.64	23.47	23.47	107.00	0.60	48.97	14.50	0.30				
Paetahi.a upper									1.31	0.01	70.97	0.11
0.07	44.04	6.64	6.64	34.00	0.48	15.68	7.31	0.5				
0.03	353.94	18.81	18.81	96.00	0.48	44.50	15.88	0.4				
Paetahi.b									0.78	0.16	11.91	0.06
0.05	168.41	12.98	12.98	89.00	0.27	42.89	7.31	0.17				
0.02	386.82	19.67	19.67	92.00	0.57	40.71	15.88	0.39				
Paetahi.c									1.91	0.09	24.75	0.06
0.10	22.78	4.77	4.77	45.00	0.14	21.68	2.81	0.1				
0.05	374.16	19.34	19.34	92.00	0.56	41.13	13.09	0.3				
0.04	502.33	22.41	22.41	99.00	0.64	41.80	16.23	0.4				
Paetahi.d									0.57	0.00	60.70	0.01
0.02	28.38	5.33	5.33	47.00	0.16	23.11	1.21	0.1				
0.01	67.89	8.24	8.24	52.00	0.32	24.45	2.98	0.1				

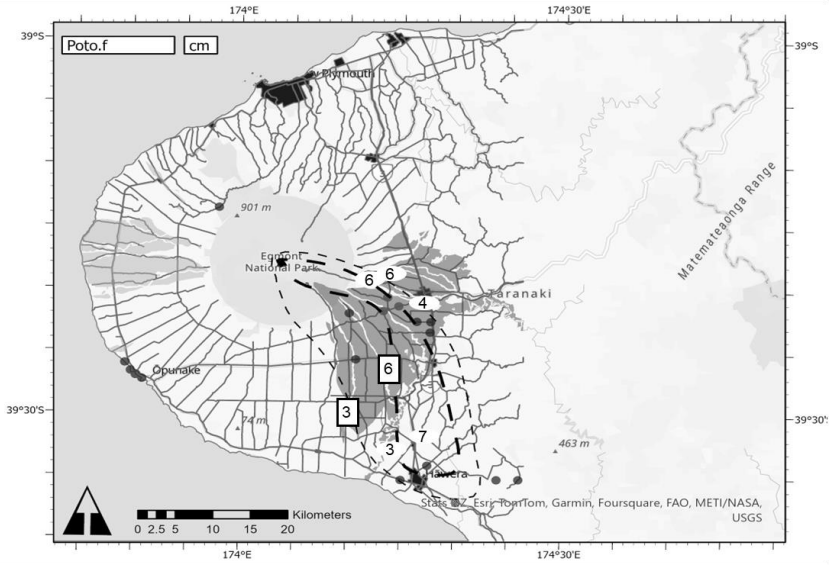
Paetahi.e lower									1.32	0.04	66.89	0.26
0.10	182.79	13.52	13.52	97.00	0.24	46.32	6.02	0.13				
0.05	789.35	28.10	28.09537	123	0.66	58	21.61	0.37				
Paetahi.e middle									1.50	0.02	89.86	0.26
0.10	27.15	5.21	5.21	47.00	0.15	22.82	2.16	0.09				
0.05	320.96	17.92	17.92	102.00	0.39	48.00	10.69	0.22				
Paetahi.e upper									0.36	6.22	2.60	0.24
0.10	131.73	11.48	11.48	49.00	0.69	21.04	9.69	0.46				
0.03	372.60	19.30	19.30	72.00	0.90	43.52	27.40	0.63				
0.01	918.84	30.31	30.31	116.00	0.86	27.30	18.19	0.67				
Paetahi.f									1.98	0.05	19.88	0.02
0.05	9.43	3.07	3.07	31.00	0.12	15.44	0.62	0.0				
0.03	254.42	15.95	15.95	78.00	0.53	35.92	9.32	0.3				
0.02	320.17	17.89	17.89	84.00	0.57	37.91	11.13	0.3				

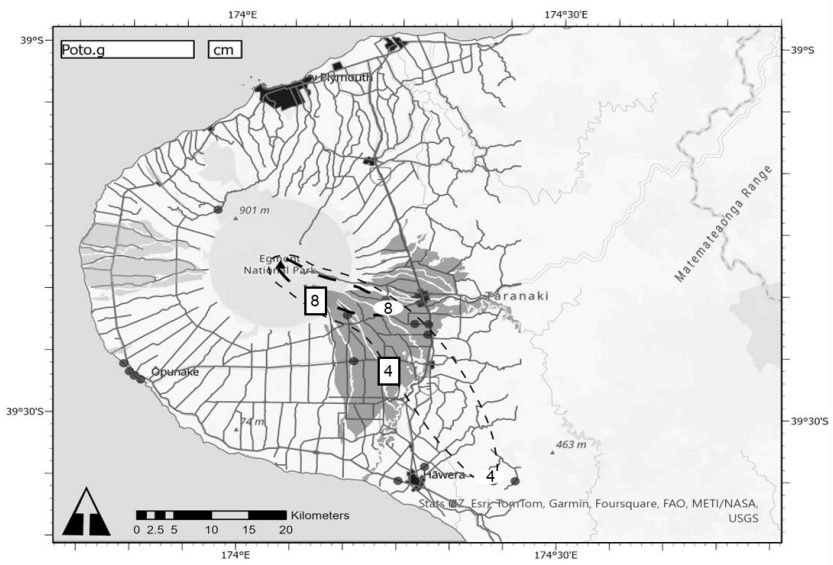
Appendix A6: Isopach maps. Isopach map images for all of the twenty-eight Poto and Paetahi Formations. Road and Topographic data sourced from the LINZ Data Service licensed for reuse under CC by 4.0.

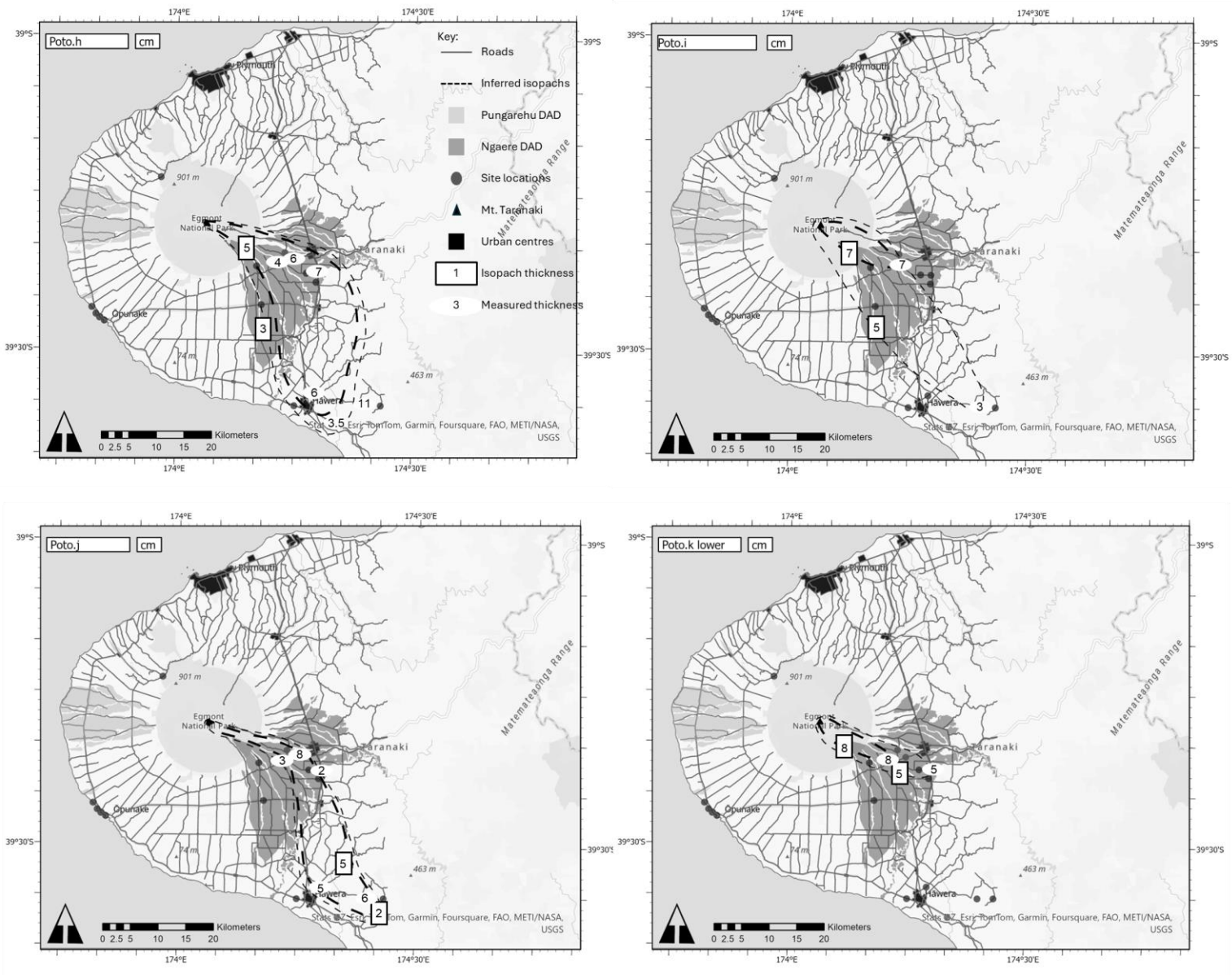


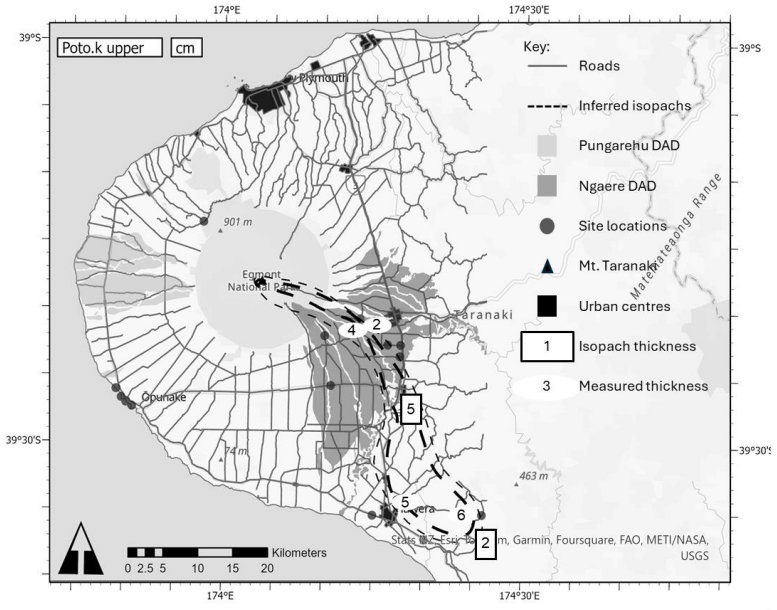

Poto.d
cm
Key:
Roads
Inferred isopachs
Pungarehu DAD
Ngaere DAD
Site locations
Mt. Taranaki
Urban centres
1 Isopach thickness
3 Measured thickness
174°E
174°30'E
39°S
39°30'S
Plymouth
Egmont National Park
Taranaki
Matemateaonga Range
Opunake
Hawera
901 m
74 m
463 m
6
3
2
2
6
Kilometers
0 2.5 5 10 15 20
Esri, TomTom, Garmin, Foursquare, FAO, METI/NASA, USGS

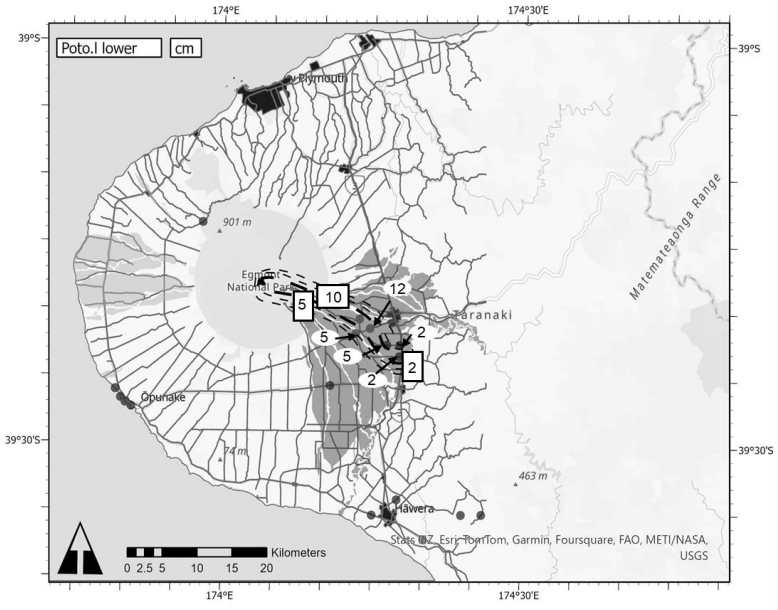

Poto.e
cm
174°E
174°30'E
39°S
39°30'S
Plymouth
Egmont National Park
Taranaki
Matemateaonga Range
Opunake
Hawera
901 m
74 m
463 m
4
2
2
5
2
3
7
Kilometers
0 2.5 5 10 15 20
Esri, TomTom, Garmin, Foursquare, FAO, METI/NASA, USGS

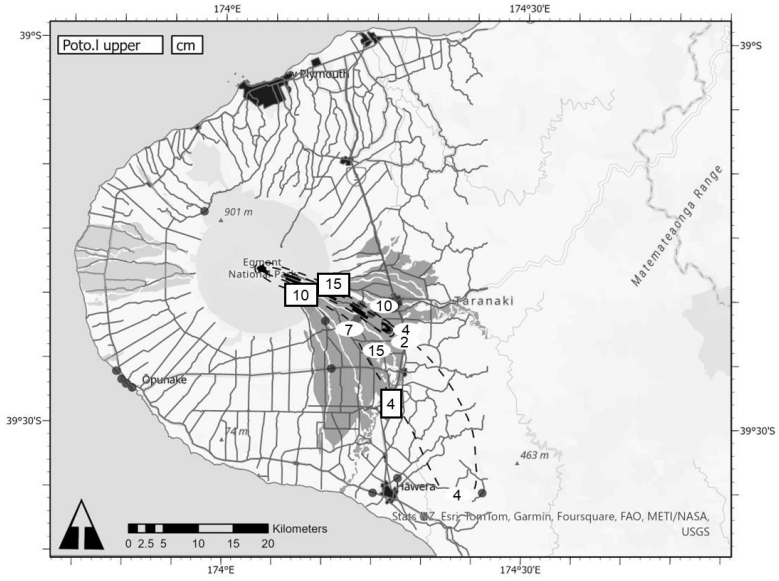

Poto.f
cm
174°E
174°30'E
39°S
39°30'S
Plymouth
Egmont National Park
Taranaki
Matemateaonga Range
Opunake
Hawera
901 m
74 m
463 m
6
6
4
6
3
3
7
Kilometers
0 2.5 5 10 15 20
Esri, TomTom, Garmin, Foursquare, FAO, METI/NASA, USGS

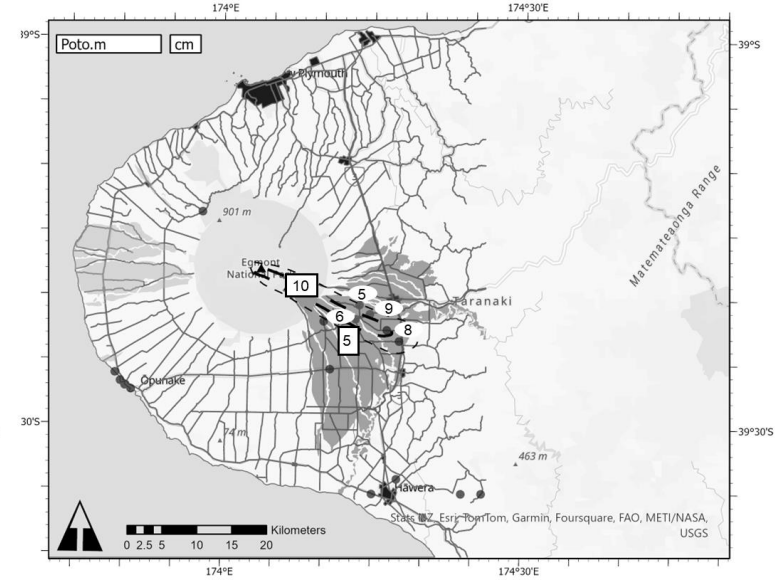

Poto.g
cm
174°E
174°30'E
39°S
39°30'S
Plymouth
Egmont National Park
Taranaki
Matemateaonga Range
Opunake
Hawera
901 m
74 m
463 m
8
8
4
4
Kilometers
0 2.5 5 10 15 20
Esri, TomTom, Garmin, Foursquare, FAO, METI/NASA, USGS

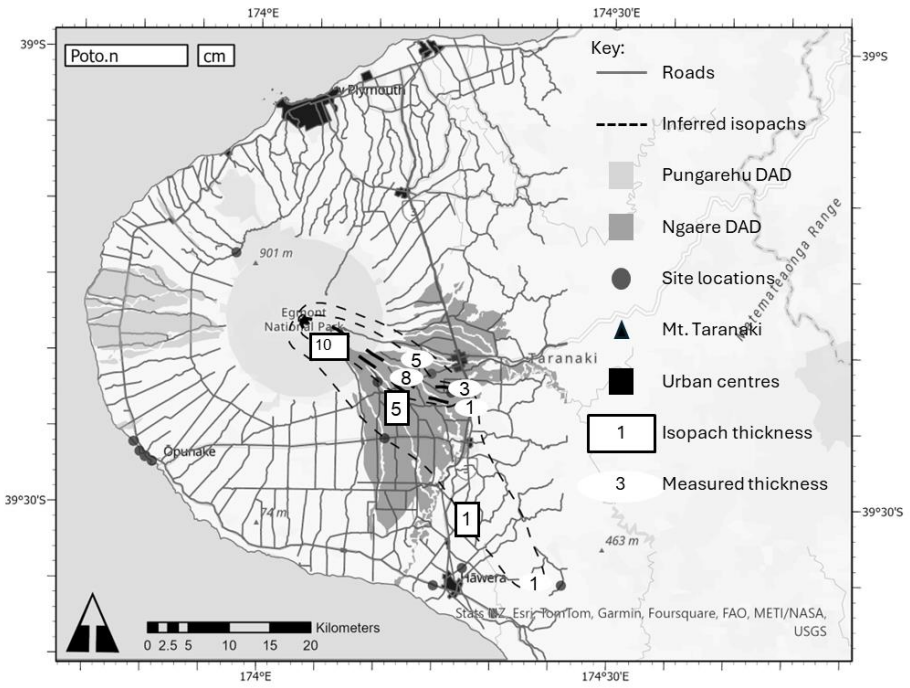

Poto.h
cm
Key:
Roads
Inferred isopachs
Pungarehu DAD
Ngaere DAD
Site locations
Mt. Taranaki
Urban centres
1 Isopach thickness
3 Measured thickness
Poto.i
Poto.j
Poto.k lower
174°E
174°30'E
39°S
39°30'S
Plymouth
Egmont National Park
Taranaki
Opunake
Hawera
Matemateaonga Range
901 m
74 m
463 m
Kilometers
0 2.5 5 10 15 20
Esri, TomTom, Garmin, Foursquare, FAO, METI/NASA, USGS

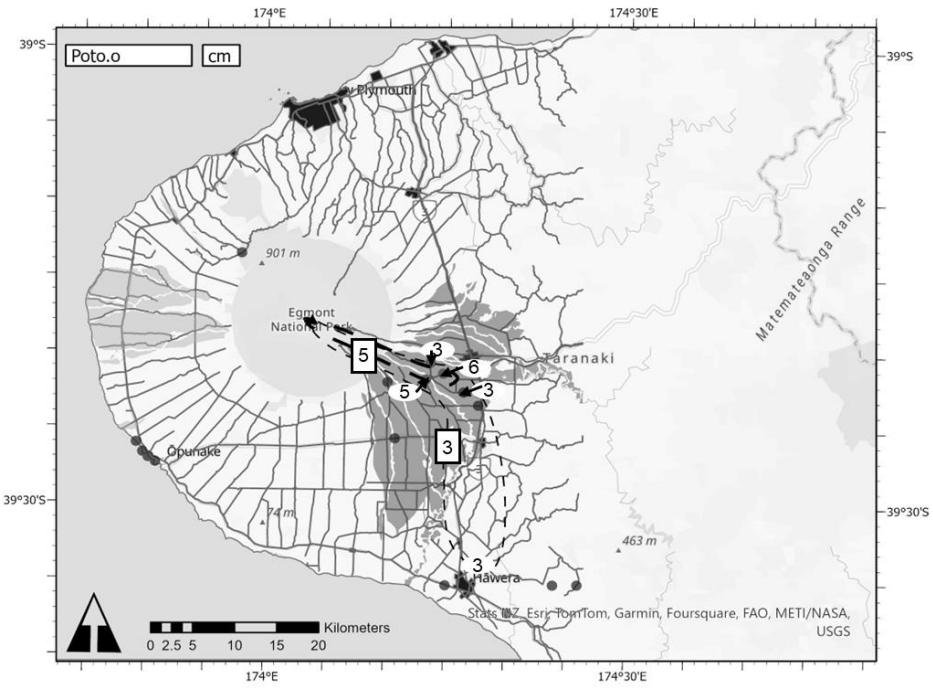

Poto.k upper
cm
Key:
Roads
Inferred isopachs
Pungarehu DAD
Ngaere DAD
Site locations
Mt. Taranaki
Urban centres
1 Isopach thickness
3 Measured thickness
Plymouth
Egmont National Park
Taranaki
Opunake
Hawera
Matemateaonga Range
901 m
74 m
463 m
174°E
174°30'E
39°S
39°30'S
Kilometers
0 2.5 5 10 15 20
Esri, TomTom, Garmin, Foursquare, FAO, METI/NASA, USGS

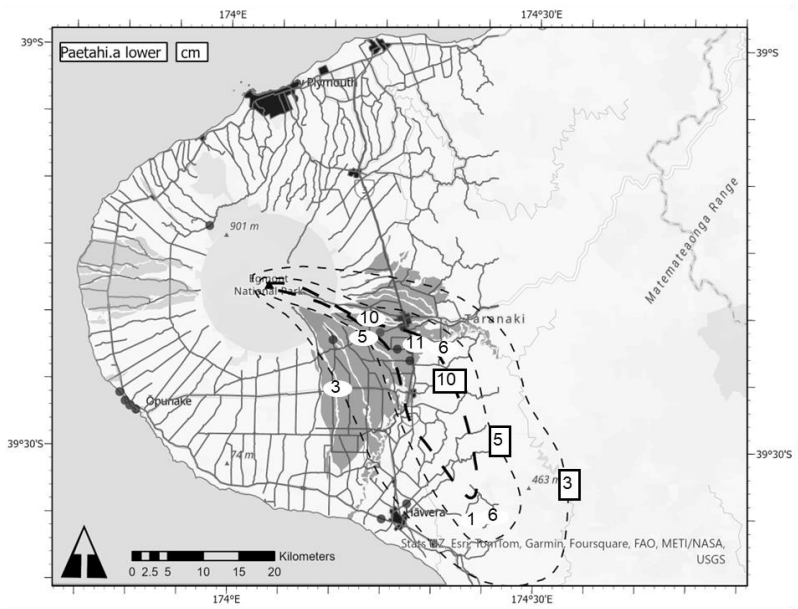

Poto.l lower
cm
Plymouth
Egmont National Park
Taranaki
Opunake
Hawera
Matemateaonga Range
901 m
74 m
463 m
174°E
174°30'E
39°S
39°30'S
Kilometers
0 2.5 5 10 15 20
Esri, TomTom, Garmin, Foursquare, FAO, METI/NASA, USGS

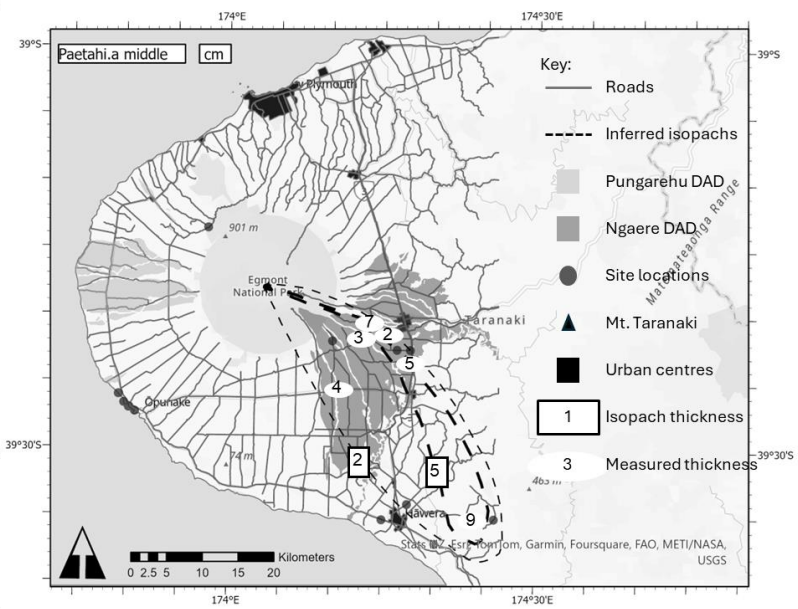

Poto.l upper
cm
Plymouth
Egmont National Park
Taranaki
Opunake
Hawera
Matemateaonga Range
901 m
74 m
463 m
174°E
174°30'E
39°S
39°30'S
Kilometers
0 2.5 5 10 15 20
Esri, TomTom, Garmin, Foursquare, FAO, METI/NASA, USGS

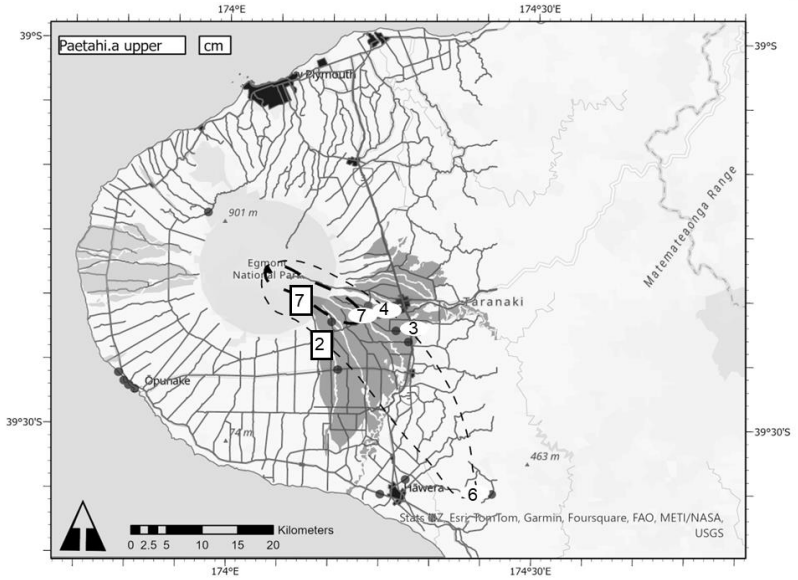

Poto.m
cm
Plymouth
Egmont National Park
Taranaki
Opunake
Hawera
Matemateaonga Range
901 m
74 m
463 m
174°E
174°30'E
39°S
39°30'S
Kilometers
0 2.5 5 10 15 20
Esri, TomTom, Garmin, Foursquare, FAO, METI/NASA, USGS

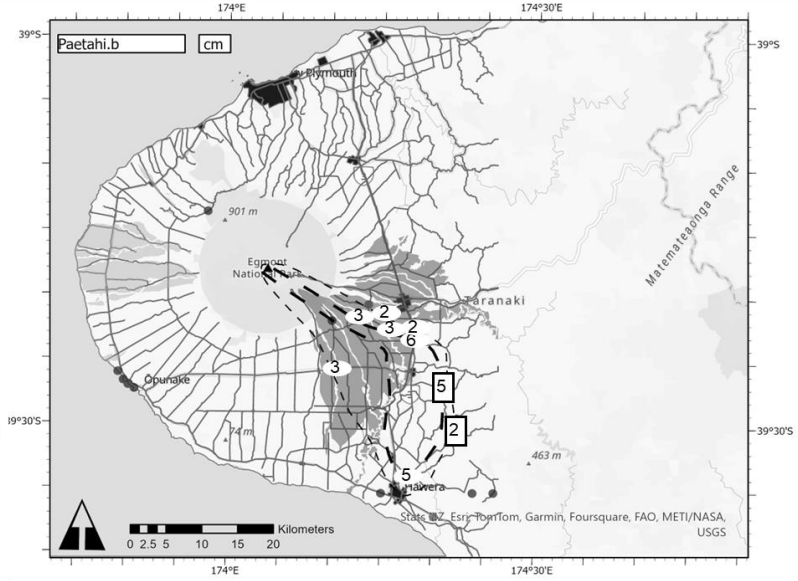

Poto.n
cm
Key:
Roads
Inferred isopachs
Pungarehu DAD
Ngaere DAD
Site locations
Mt. Taranaki
Urban centres
1 Isopach thickness
3 Measured thickness
174°E
174°30'E
39°S
39°30'S
Plymouth
Egmont National Park
Taranaki
Matemateaonga Range
Opunake
Hawera
901 m
74 m
463 m
10
5
8
3
1
5
1
1
Kilometers
0 2.5 5 10 15 20
Stats NZ, Esri, TomTom, Garmin, Foursquare, FAO, METI/NASA, USGS

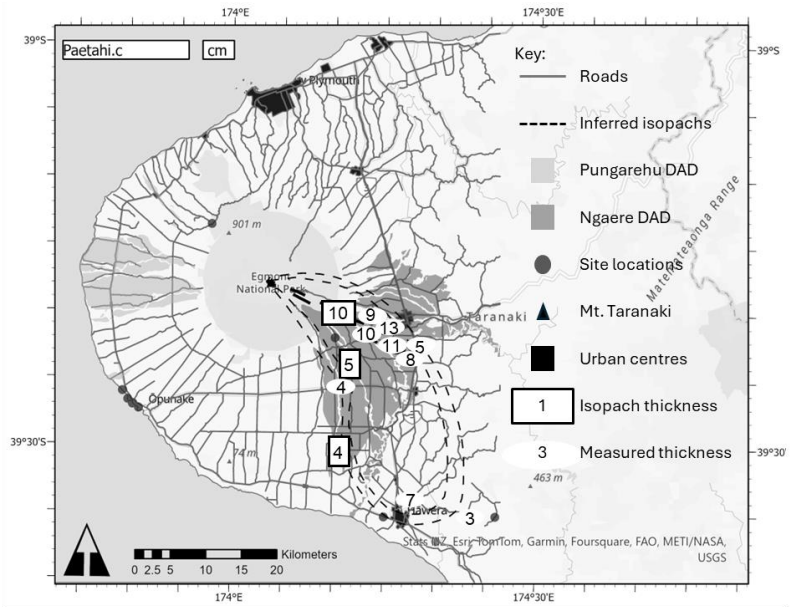

Poto.o
cm
174°E
174°30'E
39°S
39°30'S
Plymouth
Egmont National Park
Taranaki
Matemateaonga Range
Opunake
Hawera
901 m
74 m
463 m
5
3
6
5
3
3
3
Kilometers
0 2.5 5 10 15 20
Stats NZ, Esri, TomTom, Garmin, Foursquare, FAO, METI/NASA, USGS

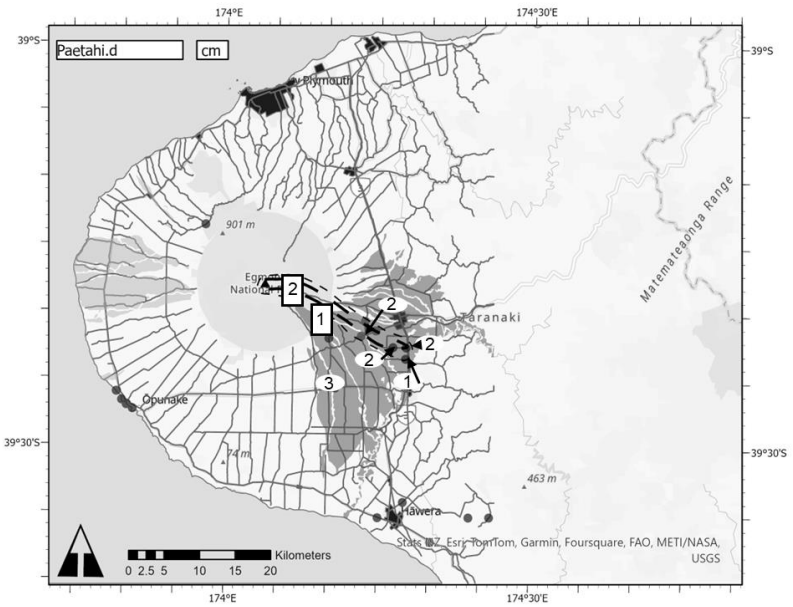

Paetahi.a lower
cm
174°E
174°30'E
39°S
39°30'S
Plymouth
Egmont National Park
Taranaki
Matemateaonga Range
Opunake
Hawera
901 m
74 m
463 m
10
5
11
6
10
3
5
3
1
6
Kilometers
0 2.5 5 10 15 20
Source: Esri, TomTom, Garmin, Foursquare, FAO, METI/NASA, USGS

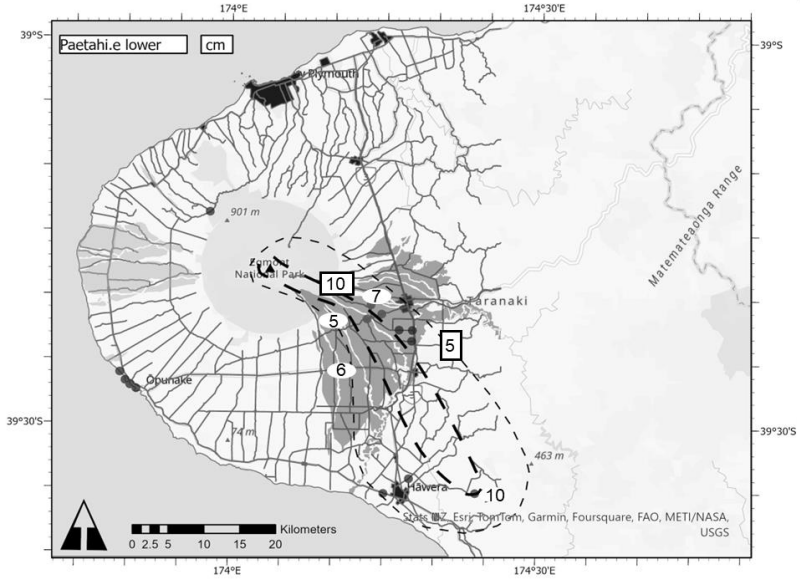

Paetahi.a middle
cm
Key:
Roads
Inferred isopachs
Pungarehu DAD
Ngaere DAD
Site locations
Mt. Taranaki
Urban centres
1 Isopach thickness
3 Measured thickness
174°E
174°30'E
39°S
39°30'S
Plymouth
Egmont National Park
Taranaki
Matemateaonga Range
Opunake
Hawera
901 m
74 m
463 m
7
3
2
5
4
2
5
9
Kilometers
0 2.5 5 10 15 20
Source: Esri, TomTom, Garmin, Foursquare, FAO, METI/NASA, USGS

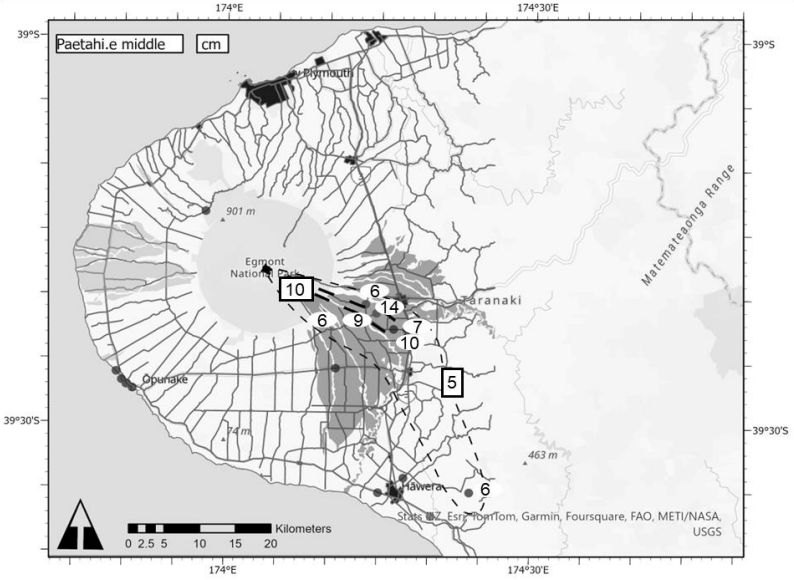

Paetahi.a upper
cm
174°E
174°30'E
39°S
39°30'S
Plymouth
Egmont National Park
Taranaki
Matemateaonga Range
Opunake
Hawera
901 m
74 m
463 m
7
7
4
3
2
6
Kilometers
0 2.5 5 10 15 20
Source: Esri, TomTom, Garmin, Foursquare, FAO, METI/NASA, USGS

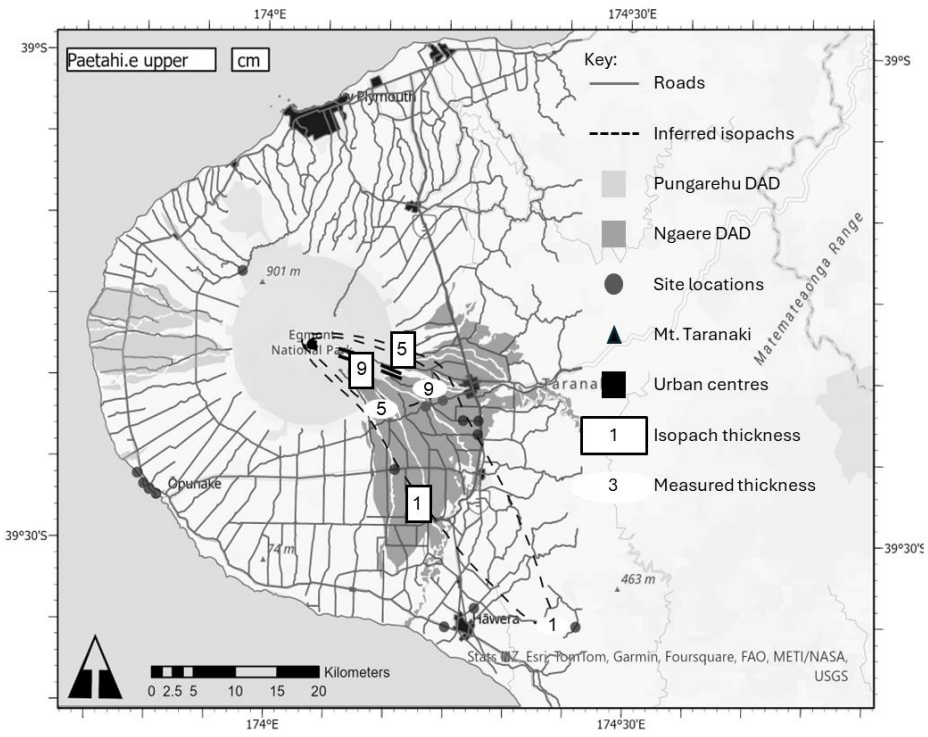

Paetahi.b
cm
174°E
174°30'E
39°S
39°30'S
Plymouth
Egmont National Park
Taranaki
Matemateaonga Range
Opunake
Hawera
901 m
74 m
463 m
3
2
3
2
6
3
5
2
5
Kilometers
0 2.5 5 10 15 20
Source: Esri, TomTom, Garmin, Foursquare, FAO, METI/NASA, USGS

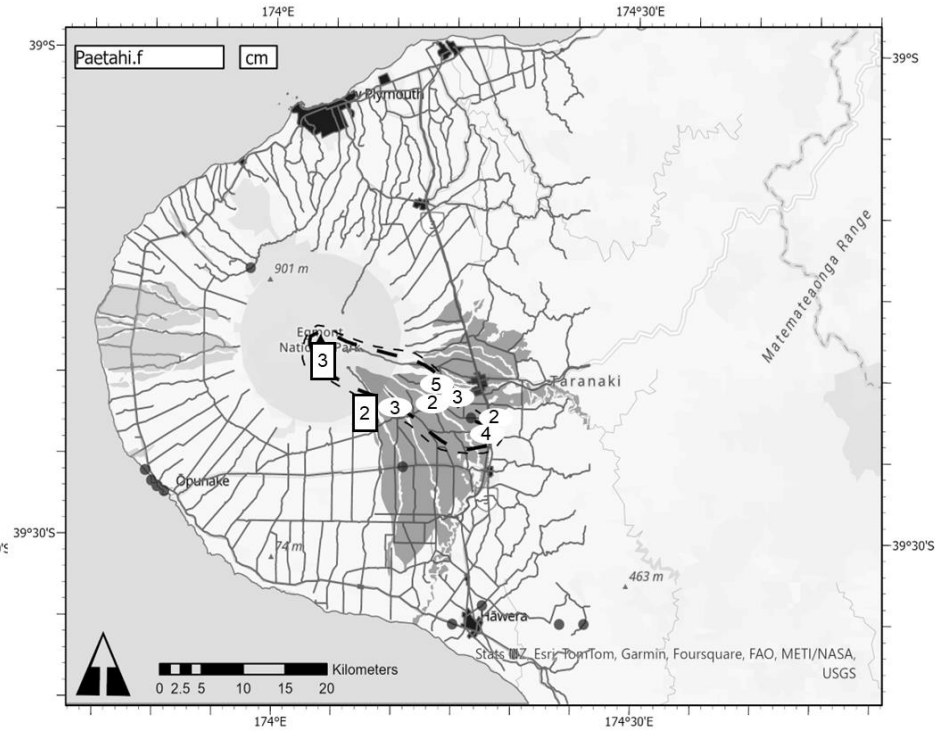

Paetahi.c
cm
Key:
Roads
Inferred isopachs
Pungarehu DAD
Ngaere DAD
Site locations
Mt. Taranaki
Urban centres
Isopach thickness
Measured thickness
Plymouth
Egmont National Park
Taranaki
Opunake
Hāwera
Matemateaonga Range
901 m
463 m
174°E
174°30'E
39°S
39°30'S
Kilometers
0 2.5 5 10 15 20
Esri, TomTom, Garmin, Foursquare, FAO, METI/NASA, USGS


Paetahi.d
cm
Plymouth
Taranaki
Opunake
Hāwera
Matemateaonga Range
901 m
463 m
174°E
174°30'E
39°S
39°30'S
Kilometers
0 2.5 5 10 15 20
Esri, TomTom, Garmin, Foursquare, FAO, METI/NASA, USGS


Paetahi.e lower
cm
Plymouth
Taranaki
Opunake
Hāwera
Matemateaonga Range
901 m
463 m
174°E
174°30'E
39°S
39°30'S
Kilometers
0 2.5 5 10 15 20
Esri, TomTom, Garmin, Foursquare, FAO, METI/NASA, USGS

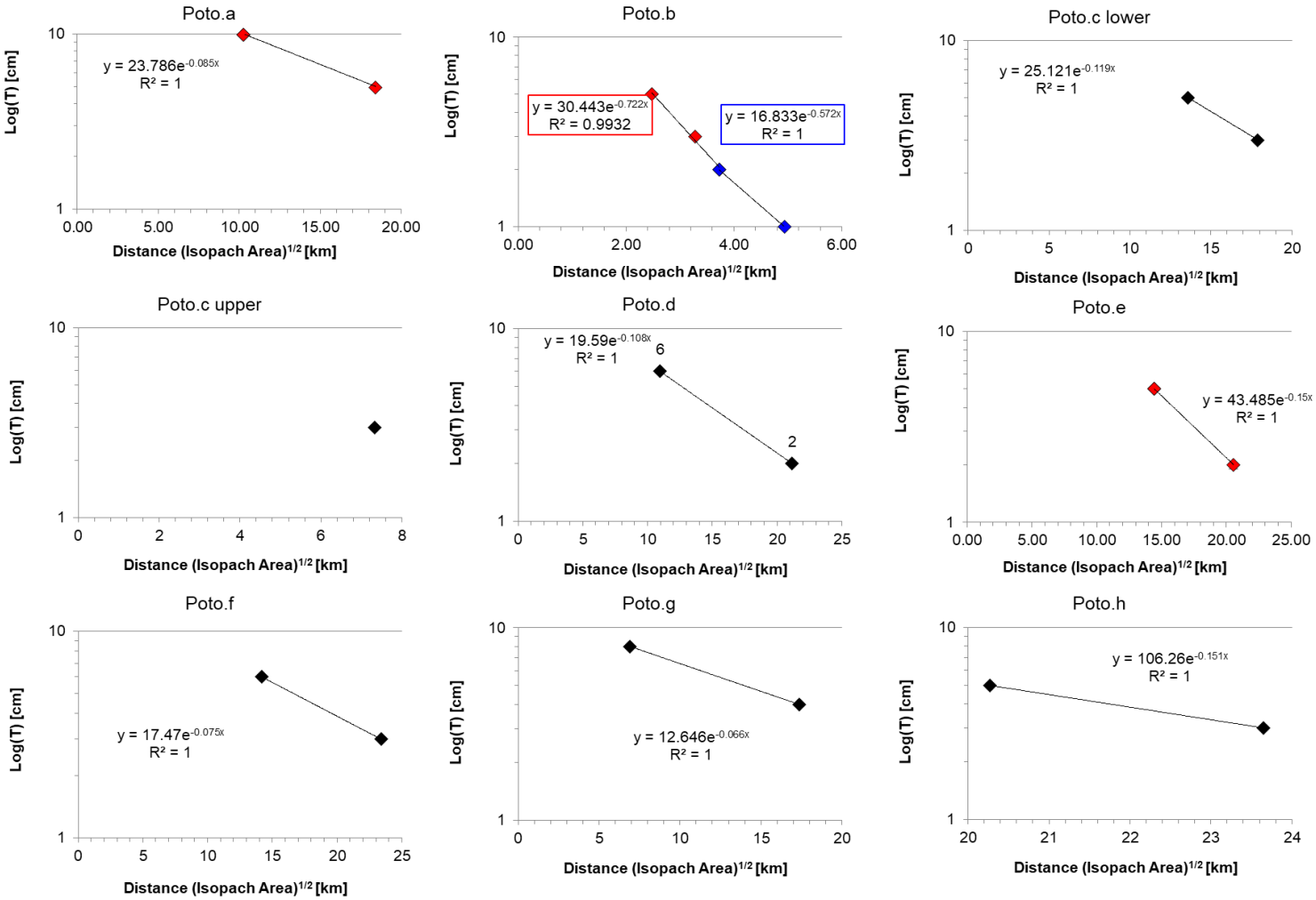

Paetahi.e middle
cm
Plymouth
Taranaki
Opunake
Hāwera
Matemateaonga Range
901 m
463 m
174°E
174°30'E
39°S
39°30'S
Kilometers
0 2.5 5 10 15 20
Esri, TomTom, Garmin, Foursquare, FAO, METI/NASA, USGS

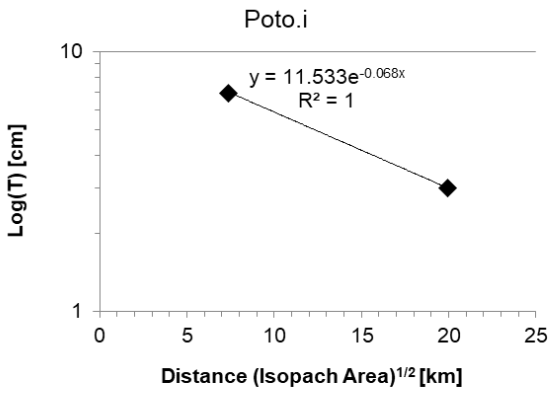

Paetahi.e upper
cm
Key:
Roads
Inferred isopachs
Pungarehu DAD
Ngaere DAD
Site locations
Mt. Taranaki
Urban centres
Isopach thickness
Measured thickness
Plymouth
Opunake
Hawera
Taranaki
Matemateaonga Range
901 m
74 m
463 m
174°E
174°30'E
39°S
39°30'S
Kilometers
0 2.5 5 10 15 20
Esri, TomTom, Garmin, Foursquare, FAO, METI/NASA, USGS

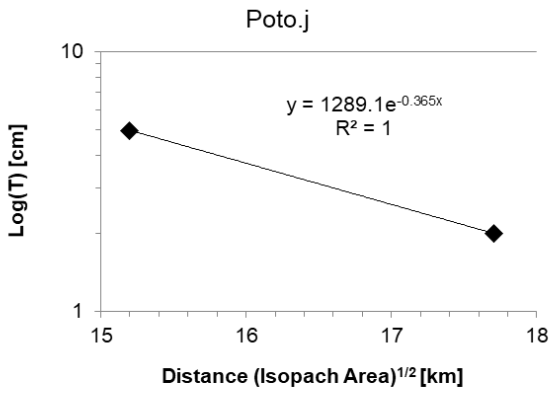

Paetahi.f
cm
Plymouth
Opunake
Hawera
Taranaki
Matemateaonga Range
901 m
74 m
463 m
174°E
174°30'E
39°S
39°30'S
Kilometers
0 2.5 5 10 15 20
Esri, TomTom, Garmin, Foursquare, FAO, METI/NASA, USGS

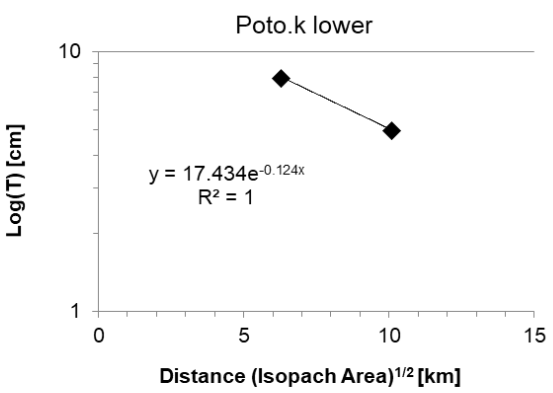
Appendix A7: Isopach graphs.

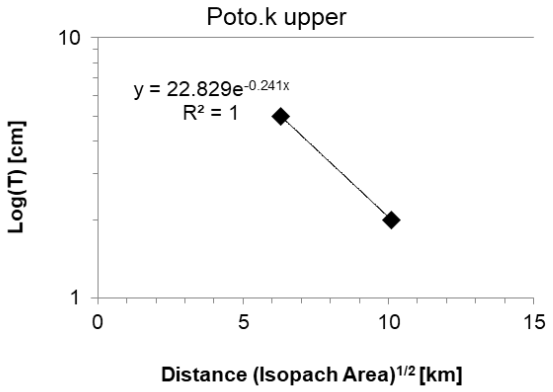
Isopach graphs of segments for volume calculation.

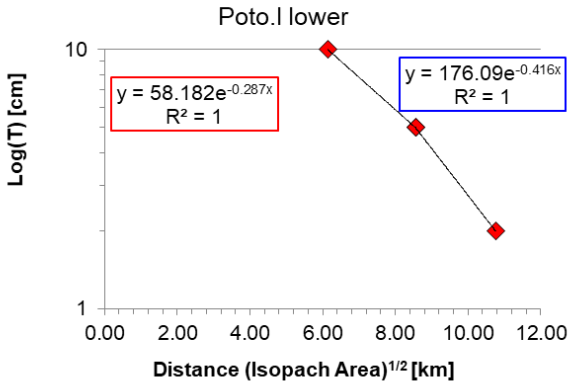


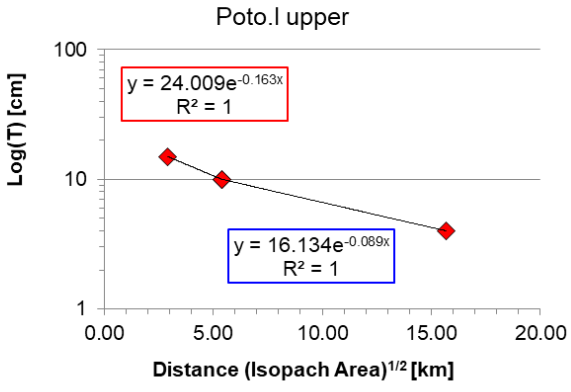

Poto.i
y = 11.533e-0.068x
R² = 1
Log(T) [cm]
Distance (Isopach Area)1/2 [km]

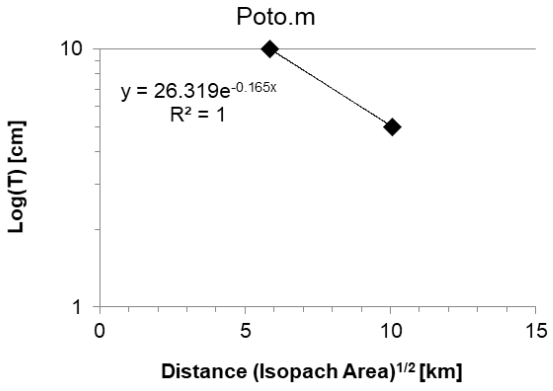

Poto.j
y = 1289.1e-0.365x
R² = 1
Log(T) [cm]
Distance (Isopach Area)1/2 [km]

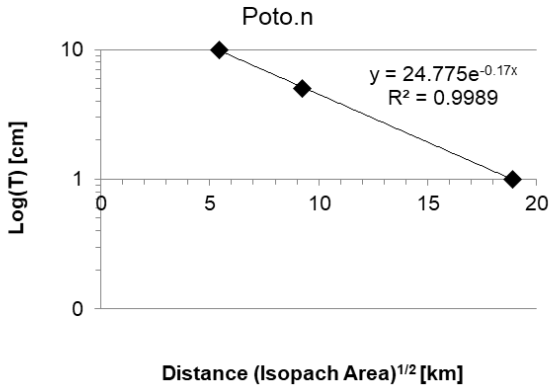

Poto.k lower
y = 17.434e-0.124x
R² = 1
Log(T) [cm]
Distance (Isopach Area)1/2 [km]

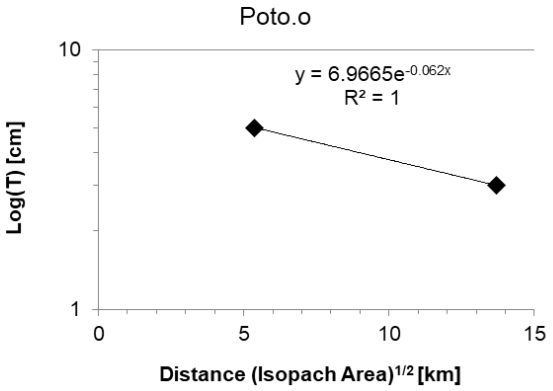

Poto.k upper
y = 22.829e-0.241x
R² = 1
Log(T) [cm]
Distance (Isopach Area)1/2 [km]

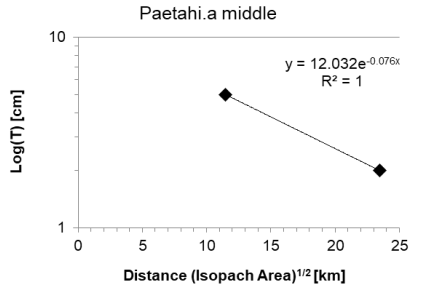

Poto.l lower
y = 58.182e-0.287x
R² = 1
y = 176.09e-0.416x
R² = 1
Log(T) [cm]
Distance (Isopach Area)1/2 [km]

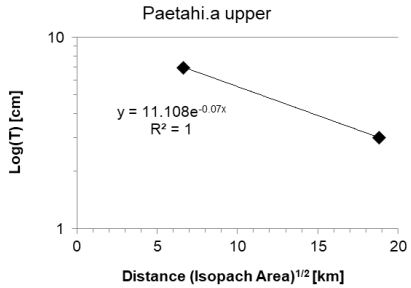

Poto.l upper
y = 24.009e-0.163x
R² = 1
y = 16.134e-0.089x
R² = 1
Log(T) [cm]
Distance (Isopach Area)1/2 [km]

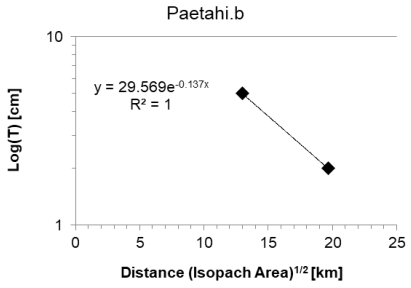

Poto.m
y = 26.319e-0.165x
R² = 1
Log(T) [cm]
Distance (Isopach Area)1/2 [km]

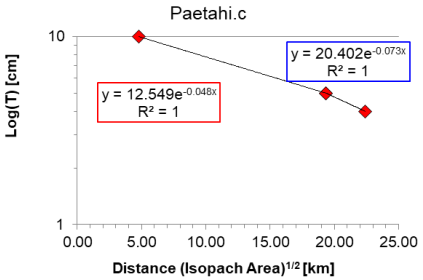

Poto.n
y = 24.775e-0.17x
R² = 0.9989
Log(T) [cm]
Distance (Isopach Area)1/2 [km]

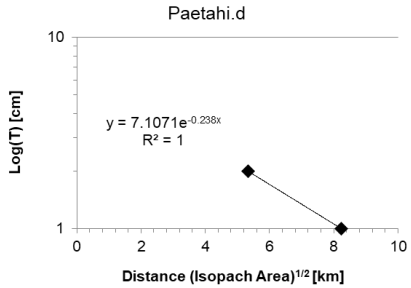

Poto.o
y = 6.9665e-0.062x
R² = 1
Log(T) [cm]
Distance (Isopach Area)1/2 [km]

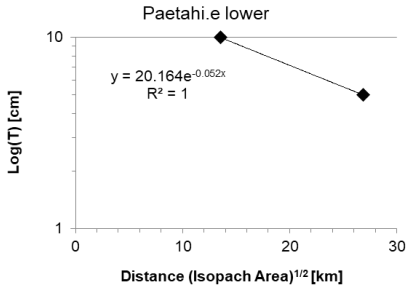

Paetahi.a middle
y = 12.032e-0.076x
R² = 1
Log(T) [cm]
Distance (Isopach Area)1/2 [km]

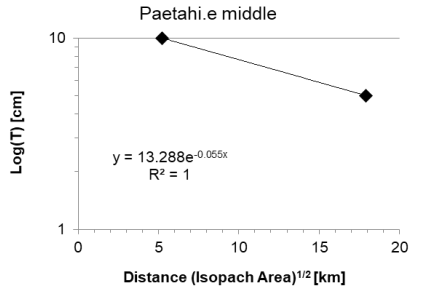

Paetahi.a upper
y = 11.108e-0.07x
R² = 1
Log(T) [cm]
Distance (Isopach Area)1/2 [km]

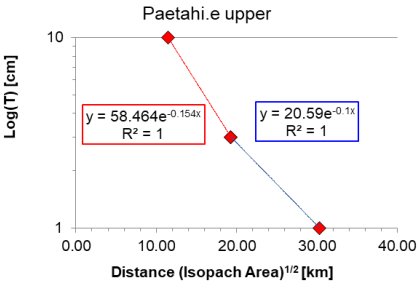

Paetahi.b
y = 29.569e-0.137x
R² = 1
Log(T) [cm]
Distance (Isopach Area)1/2 [km]

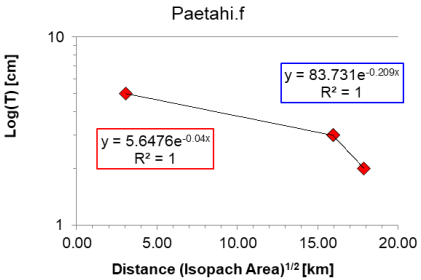

Paetahi.c
y = 20.402e-0.073x
R² = 1
y = 12.549e-0.048x
R² = 1
Log(T) [cm]
Distance (Isopach Area)1/2 [km]

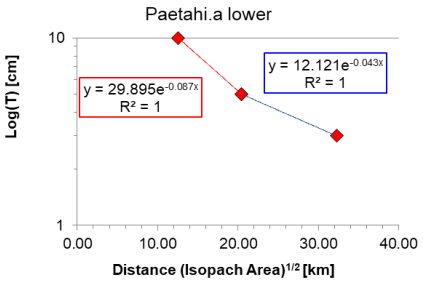

Paetahi.d
y = 7.1071e-0.238x
R² = 1
Log(T) [cm]
Distance (Isopach Area)1/2 [km]


Paetahi.e lower
y = 20.164e-0.052x
R² = 1
Log(T) [cm]
Distance (Isopach Area)1/2 [km]


Paetahi.e middle
y = 13.288e-0.055x
R² = 1
Log(T) [cm]
Distance (Isopach Area)1/2 [km]


Paetahi.e upper
y = 58.464e-0.154x
R² = 1
y = 20.59e-0.1x
R² = 1
Log(T) [cm]
Distance (Isopach Area)1/2 [km]


Paetahi.f
y = 83.731e-0.209x
R² = 1
y = 5.6476e-0.04x
R² = 1
Log(T) [cm]
Distance (Isopach Area)1/2 [km]


Paetahi.a lower
y = 12.121e-0.043x
R² = 1
y = 29.895e-0.087x
R² = 1
Log(T) [cm]
Distance (Isopach Area)1/2 [km]

Appendix A8: Isopleth Calculations.

Isopleth, grain size, area, and volumes for the twenty-eight Poto and Paetahi fall units.

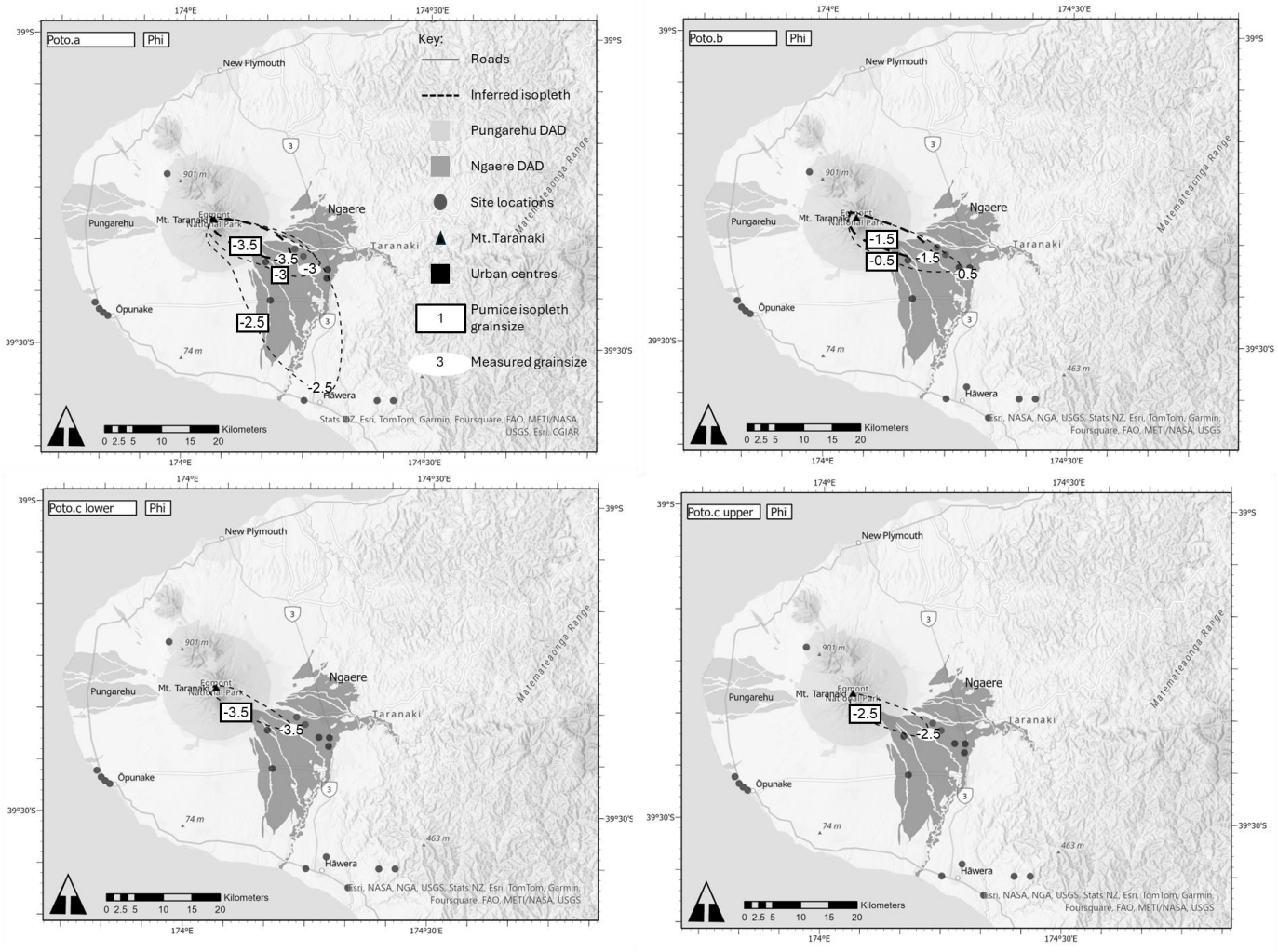
Isopleth					
Phi	A (km^2)	A1/2	√ area	Perimeter (km)	Shape factor
Poto.a					
-2.5	415	20.37	20.37	86	0.71
-3	112	10.58	10.58	47	0.64
-3.5	60	7.75	7.75	35	0.62
Poto.b					
-0.5	105	10.25	10.25	48	0.57
-1.5	61	7.81	7.81	37	0.56
Poto.c lower					
-0.5	43	6.56	6.56	29	0.64
-3.5	45	6.71	6.71	35	0.46
Poto.c upper					
-2.5	55	7.42	7.42	34	0.60
Poto.d					
-2.5	50	7.07		35	0.51
Poto.e					
-1.5	1155	33.99	33.99	145	0.69
-2	874	29.56	29.56	134	0.61
-2.5	491	22.16	22.16	105	0.56
-3	40	6.32	6.32	37	0.37
Poto.f					
-2	1168	34.18	34.18	130	0.87
-2.5	551	23.47	23.47	92	0.82
-3	334	18.28	18.28	73	0.79
-3.5	210	14.49	14.49	63	0.66
Poto.g					
-3	63	7.94	7.94	36	0.61
Poto.h					
-3.5	57	7.55	7.55	36	0.55

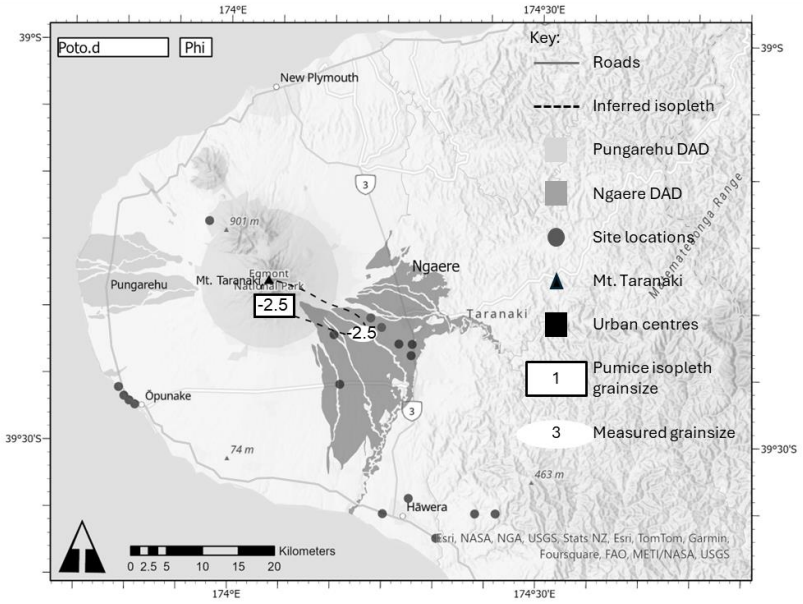
Poto.i					
-4	55	7.42	7.42	35	0.56
Poto.j					
-3.5	54	7.35	7.35	35	0.55
Poto.k lower					
-4	37	6.08	6.08	34	0.40
Poto.k upper					
-3.5	37	6.08	6.08	34	0.40
Poto.l lower					
-3.5	113	10.63	10.63	55	0.47
-4	54	7.35	7.35	50	0.27
Poto.l upper					
-2.5	71	8.43	8.43	46	0.42
-4	35	5.92	5.92	34	0.38
Poto.m					
-2	71	8.43	8.43	41	0.53
-4	35	5.92	5.92	35	0.36
Poto.n					
-2	122	11.05	11.05	53	0.55
-3	66	8.12	8.12	40	0.52
-4	36	6.00	6.00	36	0.35
Poto.o					
-2	449	21.19	21.19	99	0.58
-2.5	185	13.60	13.60	62	0.60
-3	123	11.09	11.09	56	0.49
-4	48	6.93	6.93	44	0.31

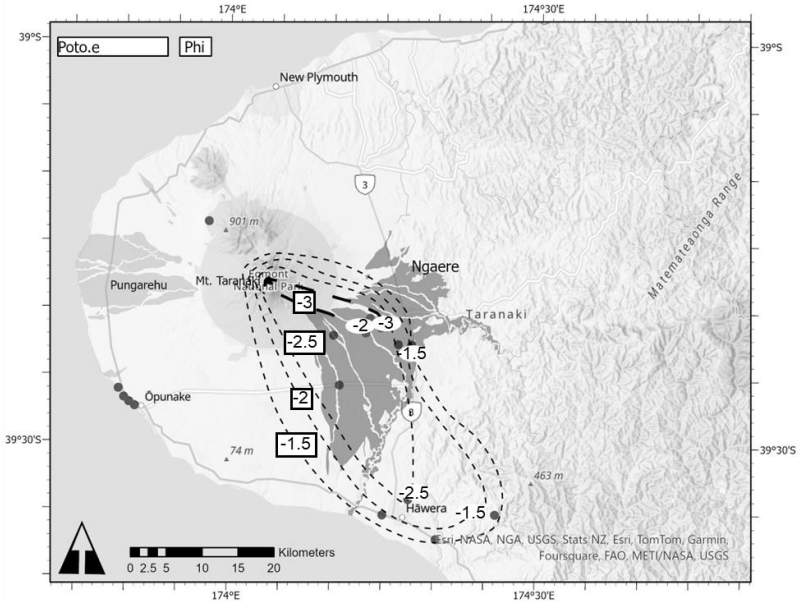
Isopleth					
Phi	A (km^2)	A1/2	√ area	Perimeter (km)	Shape factor
Paetahi.a lower					
-2.5	601	24.52	24.52	124	0.49
-3	206	14.35	14.35	77	0.44
-4	132	11.49	11.49	69	0.35

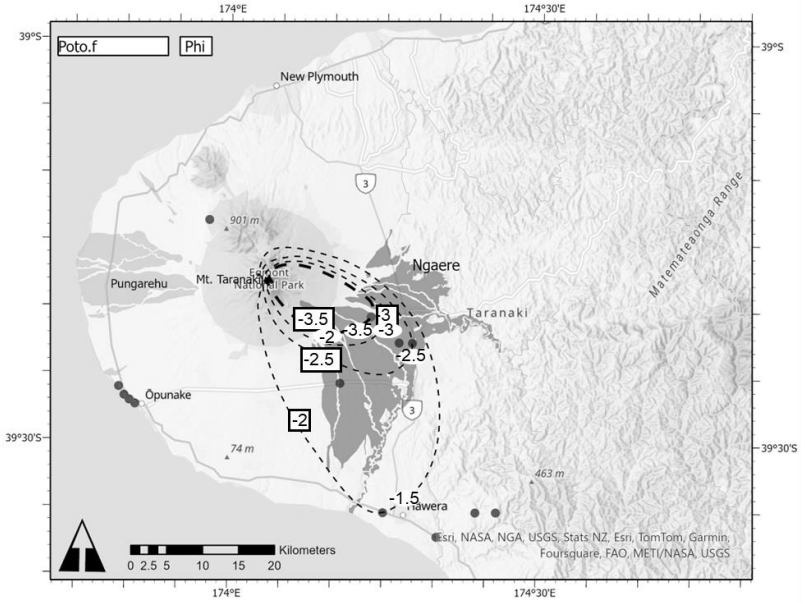
Paetahi.a middle					
-3.5	85	9.22	9.22	52	0.40
-4	26	5.10	5.10	34	0.28
Paetahi.a upper					
-3	86	9.27	9.27	44	0.56
-4	41	6.40	6.40	36	0.40
Paetahi.b					
-2.5	405	20.12	20.12	91	0.61
-3.5	312	17.66	17.66	85	0.54
-4	220	14.83	14.83	77	0.47
Paetahi.c					
-3	179	13.38	13.38	58	0.67
-3.5	84	9.17	9.17	43	0.57
-4	47	6.86	6.86	37	0.43
Paetahi.d					
-3	154	12.41	12.41	56	0.62
-4	73	8.54	8.54	42	0.52
Paetahi.e lower					
-4	41	6.40	6.40	36	0.40
Paetahi.e middle					
-2.5	448	21.17	21.17	105	0.51
-3	177	13.30	13.30	55	0.74
-3.5	124	11.14	11.14	45	0.77
-4	48	6.93	6.93	31	0.63
Paetahi.e upper					
-3	45	6.71	6.71	36	0.44
Paetahi.f					
-2.5	115	10.72	10.72	64	0.35
-3.5	36	6.00	6.00	39	0.30

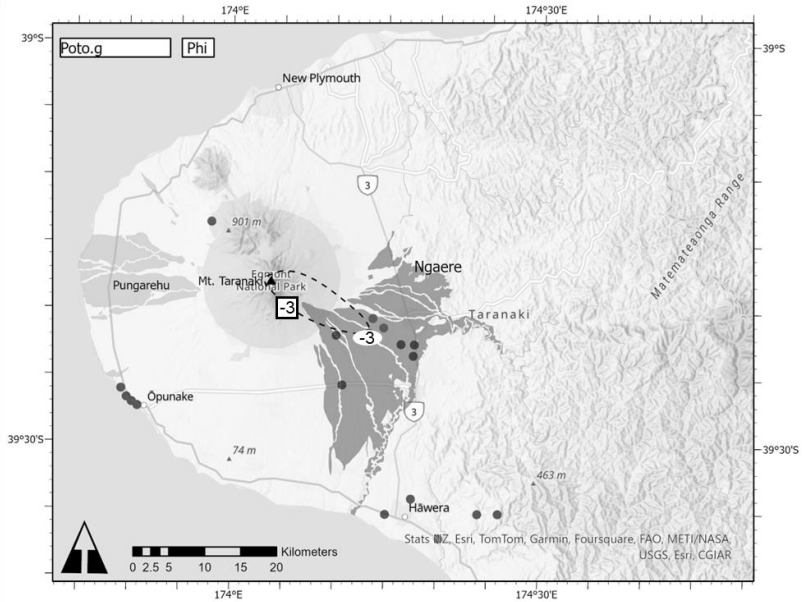
Appendix A9: Isopleth maps. Isopleth map images for all of the twenty-eight Poto and Paetahi Formations. Road and Topographic data sourced from the LINZ Data Service licensed for reuse under CC by 4.0

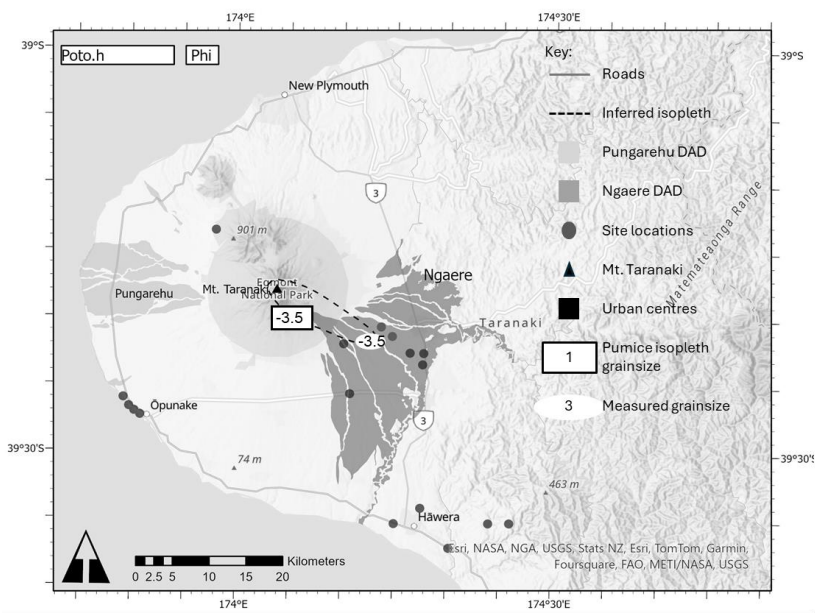


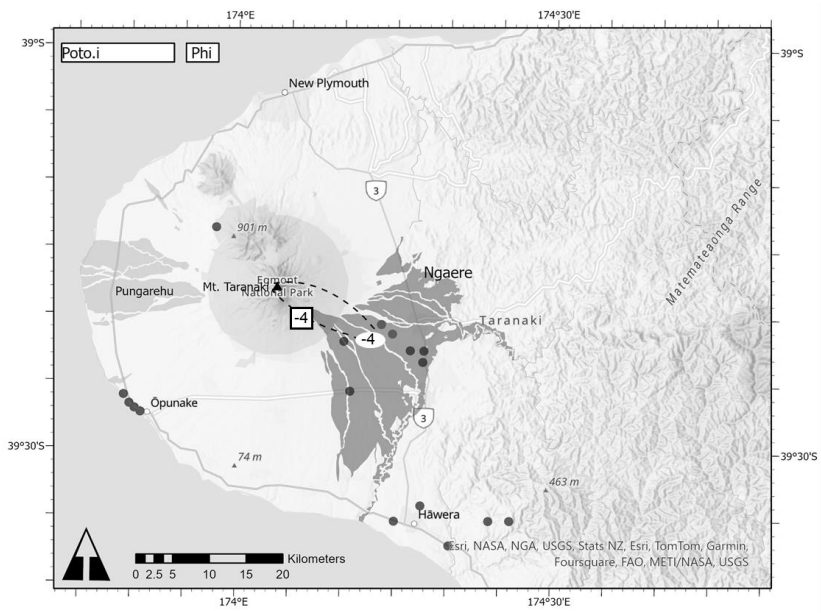

Poto.d
Phi
Key:
Roads
Inferred isopleth
Pungarehu DAD
Ngaere DAD
Site locations
Mt. Taranaki
Urban centres
Pumice isopleth grainsize
Measured grainsize
New Plymouth
Ngaere
Pungarehu
Mt. Taranaki
Egmont National Park
Taranaki
Matemategonga Range
Ōpunake
Hāwera
901 m
74 m
463 m
-2.5
-2.5
1
3
Kilometers
0 2.5 5 10 15 20
174°E
174°30'E
39°S
39°30'S
Esri, NASA, NGA, USGS, Stats NZ, Esri, TomTom, Garmin, Foursquare, FAO, METI/NASA, USGS

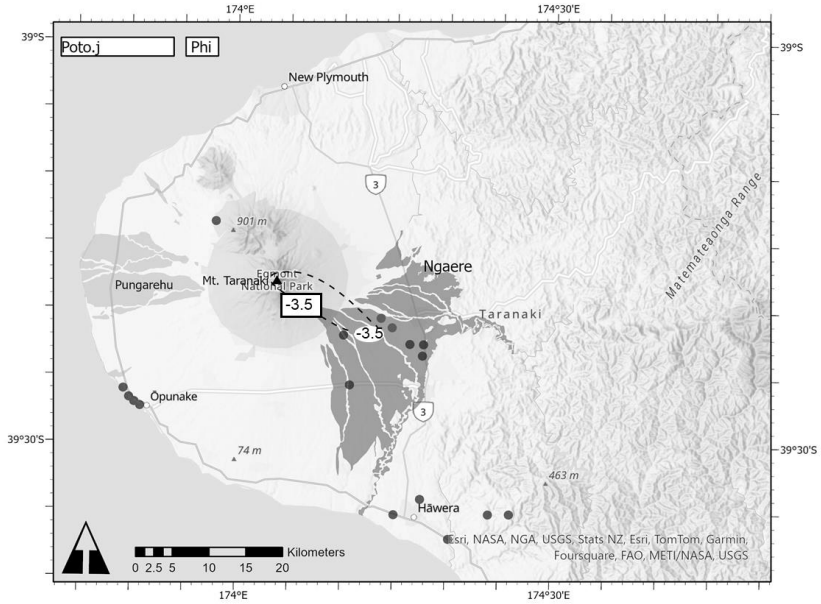

Poto.e
Phi
New Plymouth
Ngaere
Pungarehu
Mt. Taranaki
Egmont National Park
Taranaki
Matemategonga Range
Ōpunake
Hāwera
901 m
74 m
463 m
-3
-2
-3
-2.5
-1.5
-2
-1.5
-2.5
-1.5
Kilometers
0 2.5 5 10 15 20
174°E
174°30'E
39°S
39°30'S
Esri, NASA, NGA, USGS, Stats NZ, Esri, TomTom, Garmin, Foursquare, FAO, METI/NASA, USGS

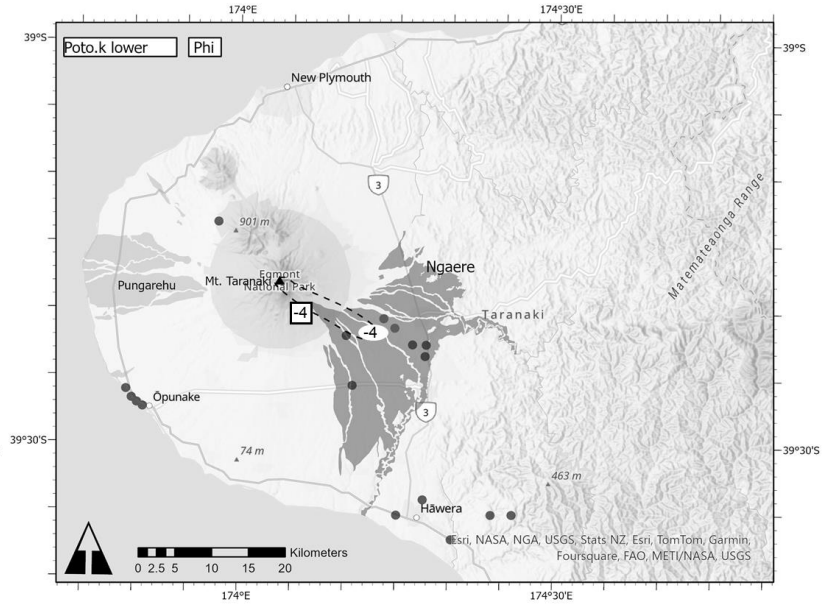

Poto.f
Phi
New Plymouth
Ngaere
Pungarehu
Mt. Taranaki
Egmont National Park
Taranaki
Matemategonga Range
Ōpunake
Hāwera
901 m
74 m
463 m
-3.5
-3
-2
-3.5
-3
-2.5
-2.5
-2
-1.5
Kilometers
0 2.5 5 10 15 20
174°E
174°30'E
39°S
39°30'S
Esri, NASA, NGA, USGS, Stats NZ, Esri, TomTom, Garmin, Foursquare, FAO, METI/NASA, USGS

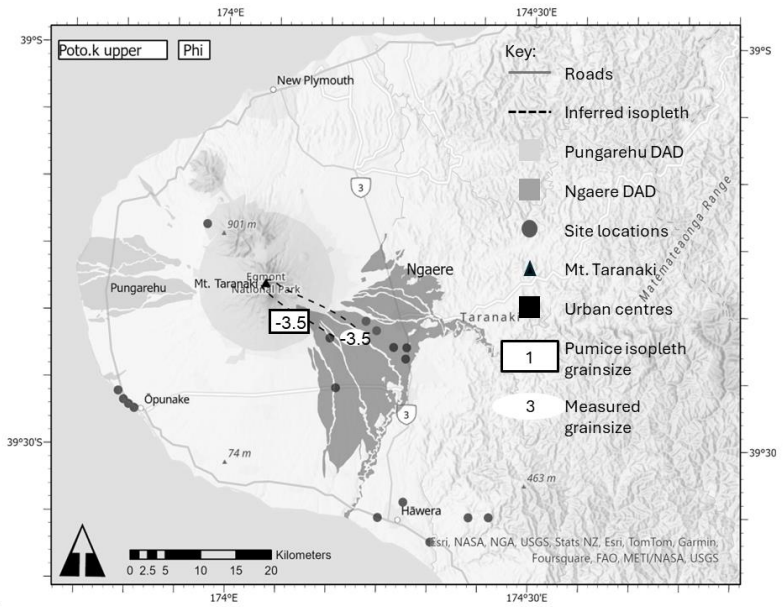

Poto.g
Phi
New Plymouth
Ngaere
Pungarehu
Mt. Taranaki
Egmont National Park
Taranaki
Matemategonga Range
Ōpunake
Hāwera
901 m
74 m
463 m
-3
-3
Kilometers
0 2.5 5 10 15 20
174°E
174°30'E
39°S
39°30'S
Stats NZ, Esri, TomTom, Garmin, Foursquare, FAO, METI/NASA, USGS, Esri, CGIAR

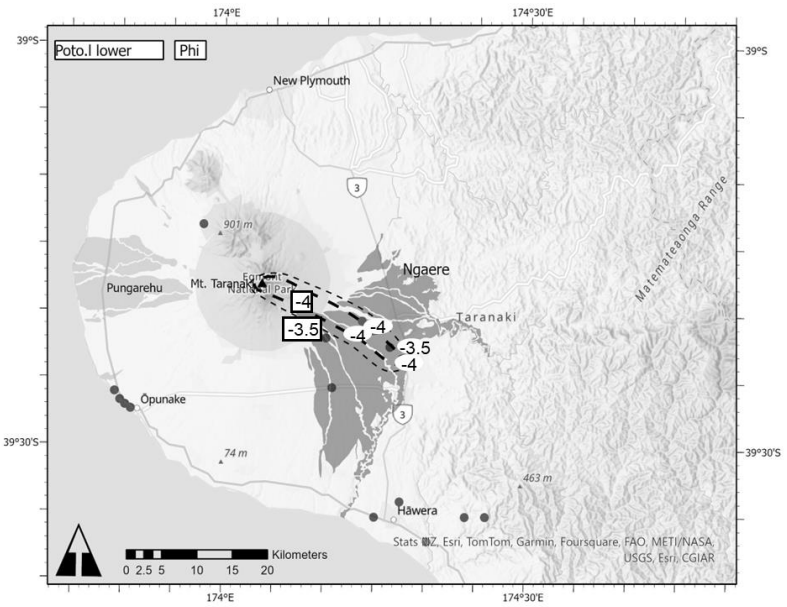

Poto.h
Phi
Key:
Roads
Inferred isopleth
Pungarehu DAD
Ngaere DAD
Site locations
Mt. Taranaki
Urban centres
1
Pumice isopleth grainsize
3
Measured grainsize
New Plymouth
Ngaere
Pungarehu
Mt. Taranaki
Egmont National Park
-3.5
-3.5
Taranaki
Matemateaonga Range
Ōpunake
Hāwera
901 m
74 m
463 m
174°E
174°30'E
39°S
39°30'S
Kilometers
0 2.5 5 10 15 20
Esri, NASA, NGA, USGS, Stats NZ, Esri, TomTom, Garmin, Foursquare, FAO, METI/NASA, USGS

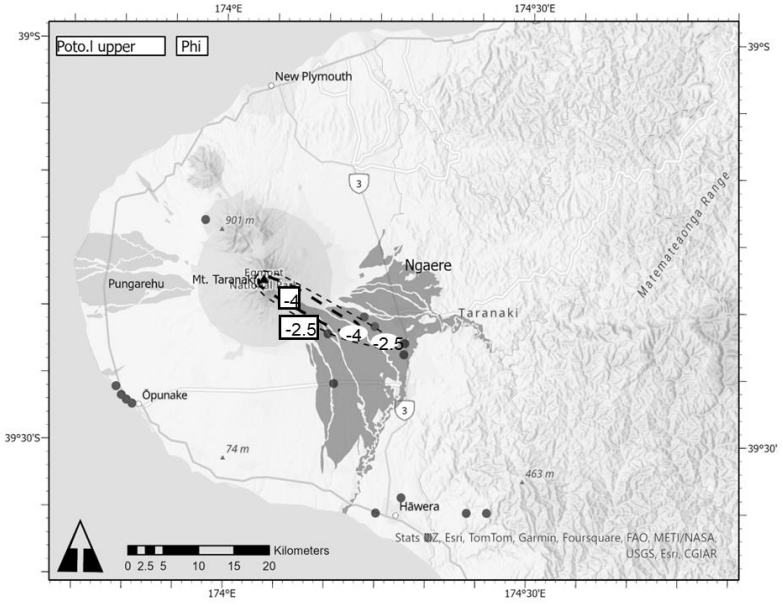

Poto.i
Phi
New Plymouth
Ngaere
Pungarehu
Mt. Taranaki
Egmont National Park
-4
-4
Taranaki
Matemateaonga Range
Ōpunake
Hāwera
901 m
74 m
463 m
174°E
174°30'E
39°S
39°30'S
Kilometers
0 2.5 5 10 15 20
Esri, NASA, NGA, USGS, Stats NZ, Esri, TomTom, Garmin, Foursquare, FAO, METI/NASA, USGS

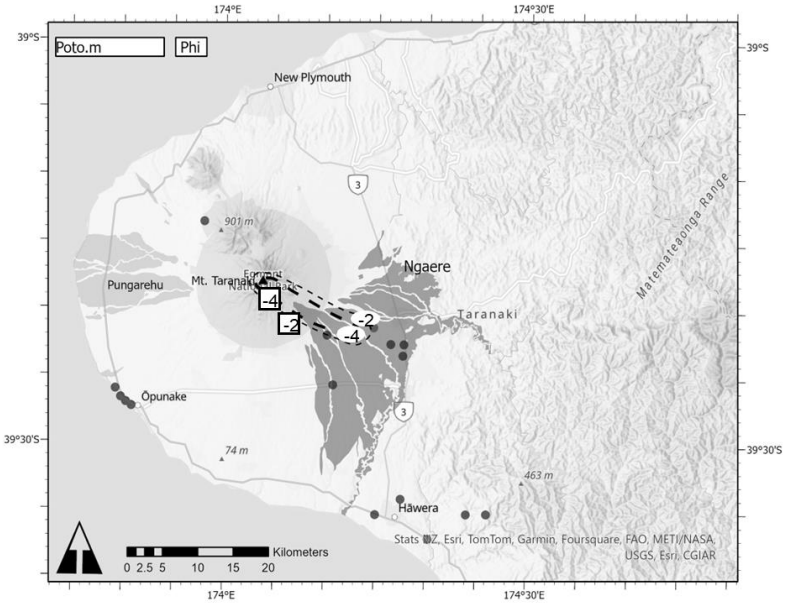

Poto.j
Phi
New Plymouth
Ngaere
Pungarehu
Mt. Taranaki
Egmont National Park
-3.5
-3.5
Taranaki
Matemateaonga Range
Ōpunake
Hāwera
901 m
74 m
463 m
174°E
174°30'E
39°S
39°30'S
Kilometers
0 2.5 5 10 15 20
Esri, NASA, NGA, USGS, Stats NZ, Esri, TomTom, Garmin, Foursquare, FAO, METI/NASA, USGS

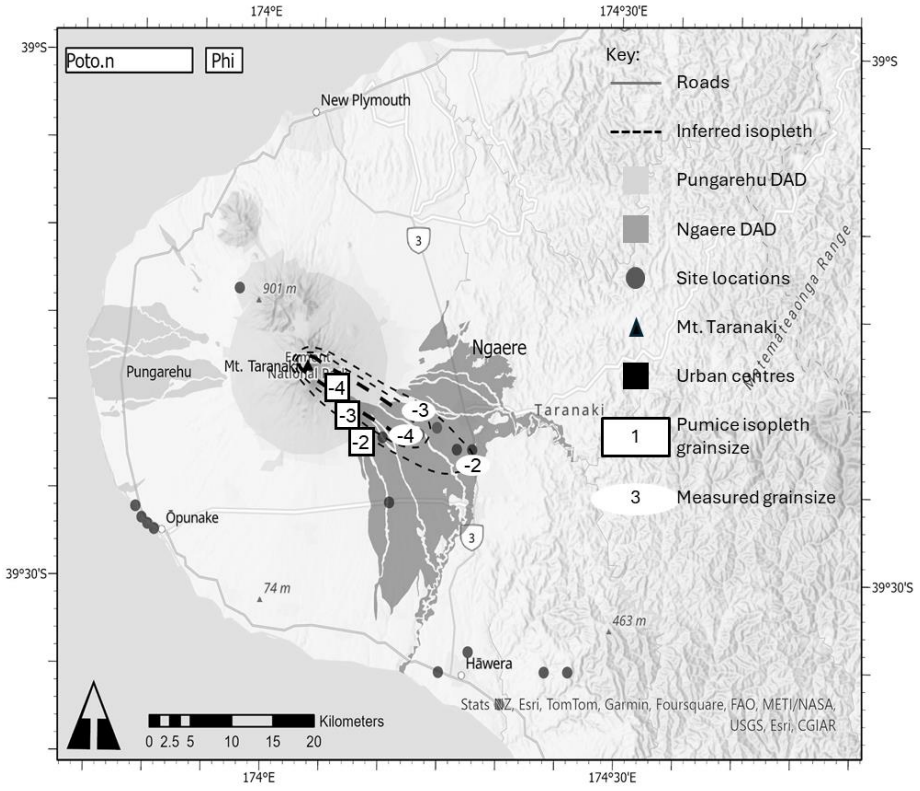

Poto.k lower
Phi
New Plymouth
Ngaere
Pungarehu
Mt. Taranaki
Egmont National Park
-4
-4
Taranaki
Matemateaonga Range
Ōpunake
Hāwera
901 m
74 m
463 m
174°E
174°30'E
39°S
39°30'S
Kilometers
0 2.5 5 10 15 20
Esri, NASA, NGA, USGS, Stats NZ, Esri, TomTom, Garmin, Foursquare, FAO, METI/NASA, USGS

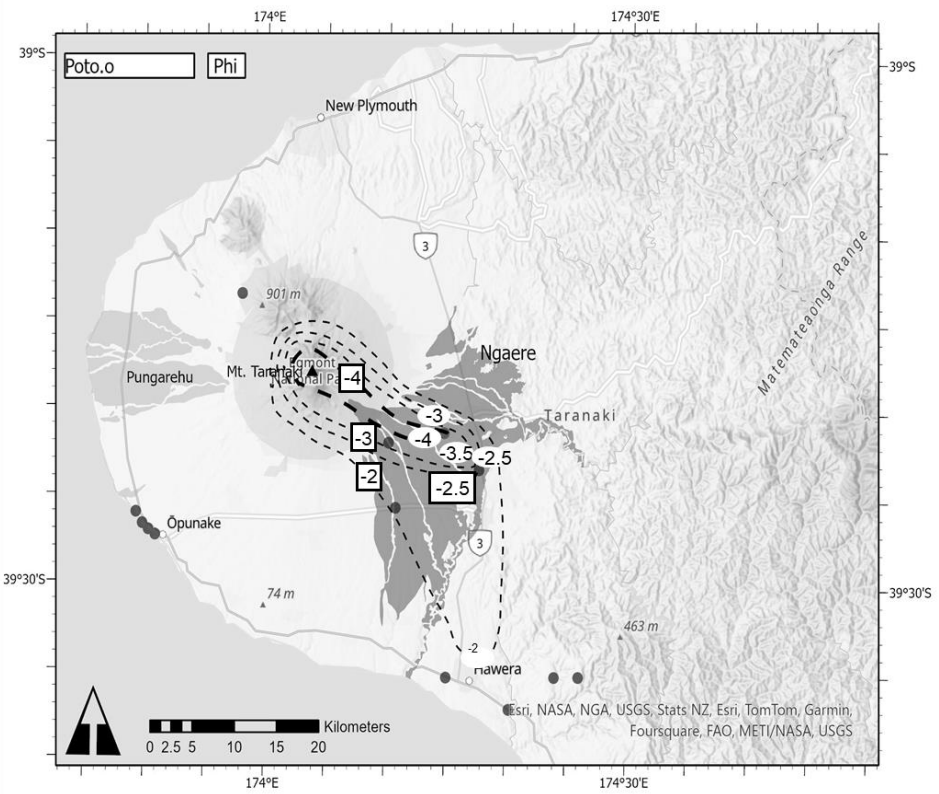

Poto.k upper
Phi
Key:
Roads
Inferred isopleth
Pungarehu DAD
Ngaere DAD
Site locations
Mt. Taranaki
Urban centres
1
Pumice isopleth grainsize
3
Measured grainsize
New Plymouth
Ngaere
Pungarehu
Mt. Taranaki
Egmont National Park
Taranaki
Matemāteāonga Range
Ōpunake
Hāwera
901 m
74 m
463 m
-3.5
-3.5
Kilometers
0 2.5 5 10 15 20
Esri, NASA, NGA, USGS, Stats NZ, Esri, TomTom, Garmin, Foursquare, FAO, METI/NASA, USGS
174°E
174°30'E
39°S
39°30'S

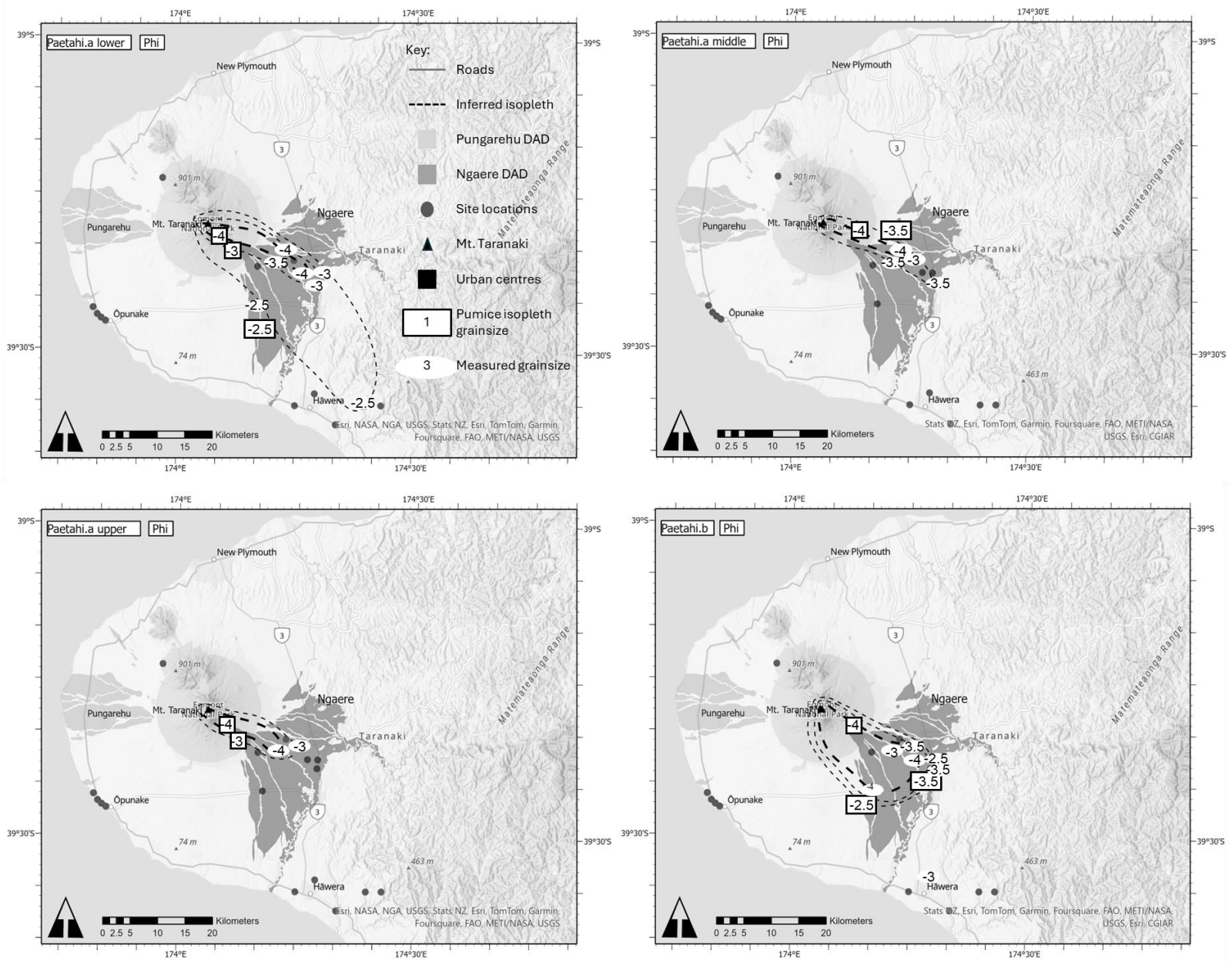

Poto.l lower
Phi
New Plymouth
Ngaere
Pungarehu
Mt. Taranaki
Taranaki
Matemāteāonga Range
Ōpunake
Hāwera
901 m
74 m
463 m
-4
-3.5
-4
-4
-3.5
-4
Kilometers
0 2.5 5 10 15 20
Stats NZ, Esri, TomTom, Garmin, Foursquare, FAO, METI/NASA, USGS, Esri, CGIAR
174°E
174°30'E
39°S
39°30'S

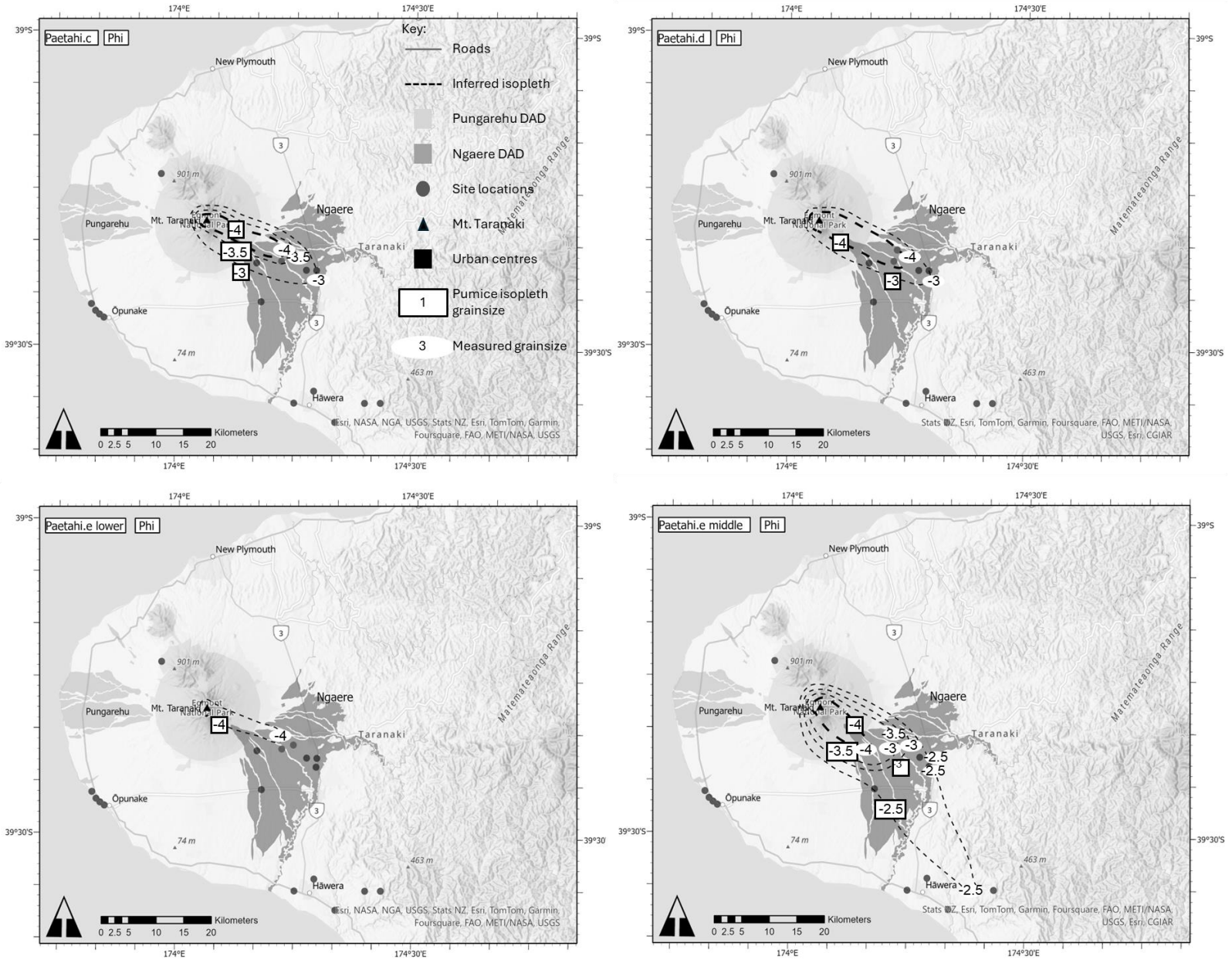

Poto.l upper
Phi
New Plymouth
Ngaere
Pungarehu
Mt. Taranaki
Taranaki
Matemāteāonga Range
Ōpunake
Hāwera
901 m
74 m
463 m
-4
-2.5
-4
-2.5
Kilometers
0 2.5 5 10 15 20
Stats NZ, Esri, TomTom, Garmin, Foursquare, FAO, METI/NASA, USGS, Esri, CGIAR
174°E
174°30'E
39°S
39°30'S

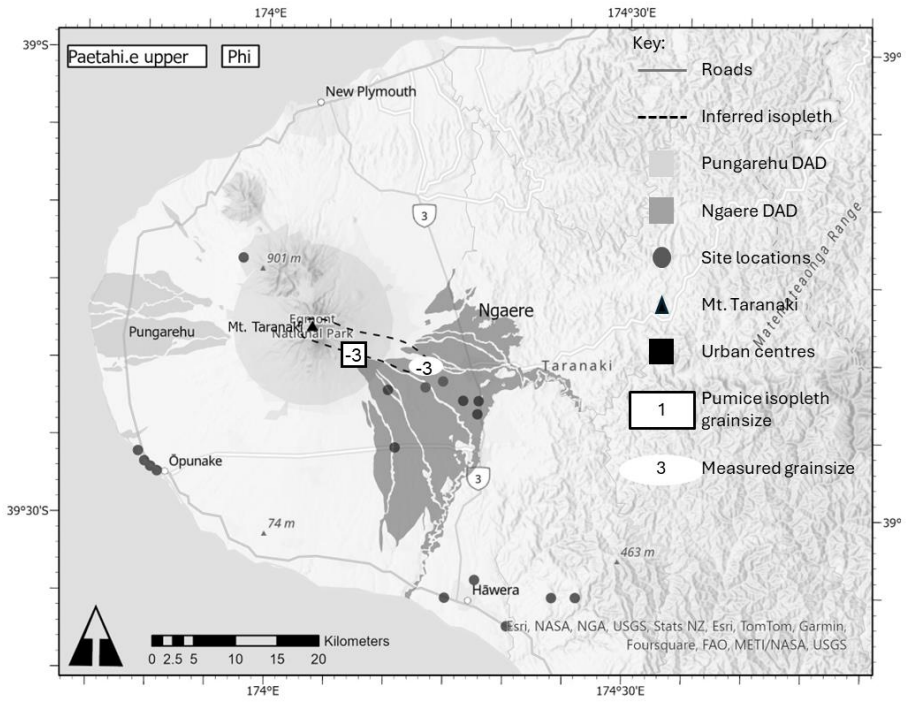

Poto.m
Phi
New Plymouth
Ngaere
Pungarehu
Mt. Taranaki
Taranaki
Matemāteāonga Range
Ōpunake
Hāwera
901 m
74 m
463 m
-4
-2
-2
-4
Kilometers
0 2.5 5 10 15 20
Stats NZ, Esri, TomTom, Garmin, Foursquare, FAO, METI/NASA, USGS, Esri, CGIAR
174°E
174°30'E
39°S
39°30'S

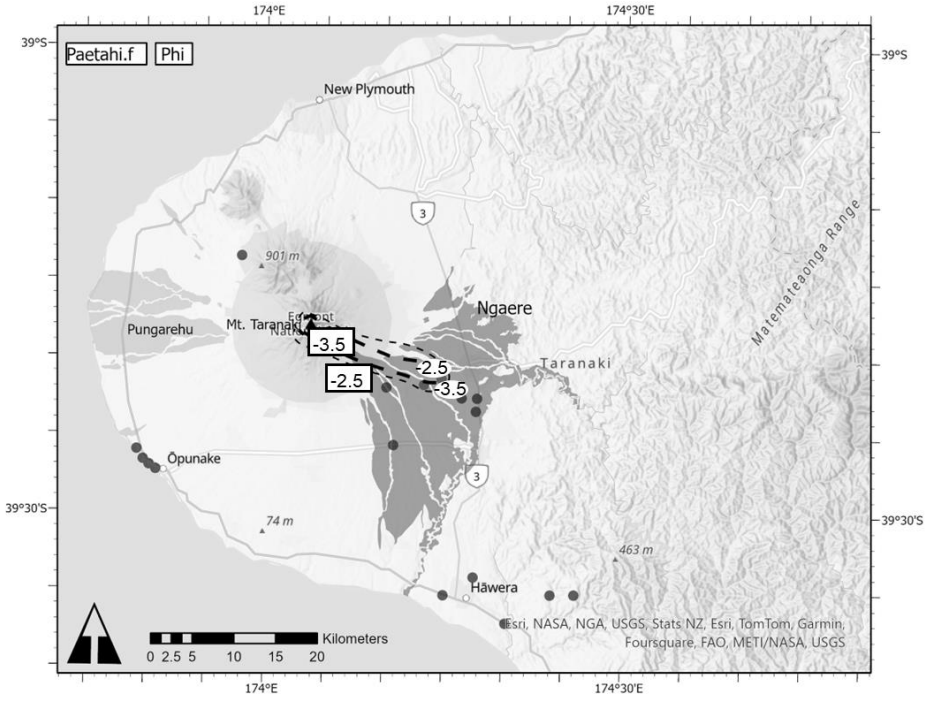

Poto.n
Phi
Key:
Roads
Inferred isopleth
Pungarehu DAD
Ngaere DAD
Site locations
Mt. Taranaki
Urban centres
Pumice isopleth grainsize
Measured grainsize
New Plymouth
Ngaere
Pungarehu
Mt. Taranaki
Taranaki
Matemateaonga Range
Ōpunake
Hāwera
901 m
74 m
463 m
-4
-3
-2
1
3
174°E
174°30'E
39°S
39°30'S
Kilometers
0 2.5 5 10 15 20
Stats NZ, Esri, TomTom, Garmin, Foursquare, FAO, METI/NASA, USGS, Esri, CGIAR


Poto.o
Phi
New Plymouth
Ngaere
Pungarehu
Taranaki
Matemateaonga Range
Ōpunake
Hāwera
901 m
74 m
463 m
-4
-3
-3.5
-2.5
-2
174°E
174°30'E
39°S
39°30'S
Kilometers
0 2.5 5 10 15 20
Esri, NASA, NGA, USGS, Stats NZ, Esri, TomTom, Garmin, Foursquare, FAO, METI/NASA, USGS


Paetahi.a lower
Phi
Key:
Roads
Inferred isopleth
Pungarehu DAD
Ngaere DAD
Site locations
Mt. Taranaki
Urban centres
Pumice isopleth grainsize
Measured grainsize
New Plymouth
Ngaere
Pungarehu
Mt. Taranaki
Taranaki
Matemateaonga Range
Ōpunake
Hāwera
901 m
74 m
463 m
-4
-3
-3.5
-2.5
Kilometers
0 2.5 5 10 15 20
174°E
174°30'E
39°S
39°30'S
Esri, NASA, NGA, USGS, Stats NZ, Esri, TomTom, Garmin, Foursquare, FAO, METI/NASA, USGS
Paetahi.a middle
Phi
Stats NZ, Esri, TomTom, Garmin, Foursquare, FAO, METI/NASA, USGS, Esri, CGIAR
Paetahi.a upper
Phi
Paetahi.b
Phi


Paetahi.c
Phi
Key:
Roads
Inferred isopleth
Pungarehu DAD
Ngaere DAD
Site locations
Mt. Taranaki
Urban centres
Pumice isopleth grainsize
Measured grainsize
New Plymouth
Ngaere
Pungarehu
Mt. Taranaki
Taranaki
Matemateaonga Range
Ōpunake
Hāwera
901 m
74 m
463 m
-4
-3.5
-3
Kilometers
0 2.5 5 10 15 20
Esri, NASA, NGA, USGS, Stats NZ, Esri, TomTom, Garmin, Foursquare, FAO, METI/NASA, USGS
Paetahi.d
Phi
Stats NZ, Esri, TomTom, Garmin, Foursquare, FAO, METI/NASA, USGS, Esri, CGIAR
Paetahi.e lower
Phi
Paetahi.e middle
Phi
-2.5


Paetahi.e upper
Phi
Key:
Roads
Inferred isopleth
Pungarehu DAD
Ngaere DAD
Site locations
Mt. Taranaki
Urban centres
1
Pumice isopleth grainsize
3
Measured grainsize
New Plymouth
Pungarehu
Mt. Taranaki
Egmont National Park
Ngaere
Taranaki
Matemateaonga Range
Ōpunake
Hāwera
901 m
74 m
463 m
-3
-3
174°E
174°30'E
39°S
39°30'S
Kilometers
0 2.5 5 10 15 20
Esri, NASA, NGA, USGS, Stats NZ, Esri, TomTom, Garmin, Foursquare, FAO, METI/NASA, USGS


Paetahi.f
Phi
New Plymouth
Pungarehu
Mt. Taranaki
Ngaere
Taranaki
Matemateaonga Range
Ōpunake
Hāwera
901 m
74 m
463 m
-3.5
-2.5
-2.5
-3.5
174°E
174°30'E
39°S
39°30'S
Kilometers
0 2.5 5 10 15 20
Esri, NASA, NGA, USGS, Stats NZ, Esri, TomTom, Garmin, Foursquare, FAO, METI/NASA, USGS

Appendix B: Grain Size distributions statistics.

Appendix B1: *Grain size distribution of each sample from the reference locations in half phi.*

Size fraction (phi)	**Poto a**	**Poto b**	**Poto c lower**	**Poto c upper**	**Poto d**	**Poto.e**	**Poto.f**	**Poto.g**	**Poto.h**	**Poto.i**	**Poto.j**	**Poto.k lower**
-4	0	0	0	0	0	0	0	0	0	0	0	0
-3.5	0	0	0	0	0	0	0	0	0	0	0	0
-3	43.4	0	20.85	0	0	4.01	59.38	0.43	55.5	177.49	4.4	52.74
-2.5	28.92	0	12.7	1.32	0.15	0	30.3	6.27	23.96	26.43	14.85	21.54
-2	33.41	0	14.69	0.54	1.23	1.6	24.95	17.12	16.67	29.87	16.99	17.37
-1.5	41.79	0.59	16.91	4.44	1.94	1.97	28.52	44.59	13.05	19.86	26.81	26.69
-1	44.66	1.44	8.75	7.45	2.6	2.88	24.83	62.56	12.55	18.25	23.86	23.76
-0.5	55.67	6.48	13.77	17.47	5.47	7.12	23.95	94.3	18.85	22.33	30.69	32.24
0	26.62	18.17	6.8	24.81	6.39	7.5	11.65	79.18	12.26	11.05	27.92	30.71
0.5	9.65	40.92	11.39	27.89	7.57	7.05	8.65	55.32	17.68	10.77	35.43	16.04
1	4.06	57.1	12.48	32.73	7.94	4.93	10.09	23.79	20.07	14.45	43.45	19.66
1.5	3.41	31.25	7.69	12.61	3.91	4.25	7.38	2.76	10.19	11.06	19.15	15.84
2	5.51	7.93	6.79	5.18	3.35	3.42	7.45	1.27	12.28	12.09	5.09	11.14
2.5	5.13	4.32	7.01	2.42	3.36	5.24	7.96	2.14	10.25	14.36	1.49	12.57
3	4.61	3.83	5.75	1.8	2.54	6.98	8.18	1.83	11.05	13.6	1.1	10.83
3.5	3.6	2.84	4.45	1.31	1.88	5.75	7.65	1.35	8.72	10.38	0.81	7.2

4	3.36	2.24	3.48	1.2	1.75	6.57	6.96	1.33	7.14	10.23	0.66	6.43
>4	3.76	3.51	6.79	2.15	3.65	19.78	18.08	2.62	14.3	20.98	1.3	12.22
Size fraction	**Poto.k Upper**	**Poto.l Lower**	**Poto.l Upper**	**Poto.m**	**Poto.n**	**Poto.o**	**Paetahi.a lower**	**Paetahi.a middle**	**Paetahi.a upper**	**Paetahi.b**	**Paetahi.c**	**Paetahi.d**
-4	0	0	0	32.95	0	0	0	0	0	0	0	3.37
-3.5	0	0	0	25.61	0	0	0	0	0	11.23	0.93	1.29
-3	30.27	78.76	77.5	28.38	68.24	34.22	9.84	0.52	3.93	6.85	2.57	4.96
-2.5	26.99	40.89	36.25	22.5	21.69	18.97	23.69	1.19	13.97	6.89	1.54	8.35
-2	29.99	28.68	21.24	27.48	22.54	11.26	40.85	1.86	30.02	5.12	5.19	9.54
-1.5	34.9	24.47	15.27	22.76	17.74	8.38	36.81	3.89	43.88	4.06	4.24	3.71
-1	25.37	14.73	9.16	16.22	13.34	8.41	37.05	6.9	33.15	2.66	7.34	3.29
-0.5	27.22	13.56	7.97	28.23	17.78	12.8	37.45	10.78	35.86	2.92	12.81	5.81
0	18.47	11.23	5.52	28.61	12.31	6.4	38.73	13	24.21	3.61	11.59	6.5
0.5	14.33	7.91	5.11	32.1	12.64	7.77	35.17	12.05	14.41	6.37	9.12	7.31
1	15.03	14.84	4.45	34.11	15.89	10.4	17.28	7.86	7.73	7.44	15.15	8.93
1.5	10.24	11.52	2.47	23.54	12.65	8.07	15.43	2.7	2.51	6.7	13.21	7.63
2	5.99	9.36	1.58	30.07	9.78	8.03	8.88	1.3	2.72	11.87	15.47	10.3
2.5	5.24	8.32	1.3	22.83	10.21	8.08	9.53	0.76	2.13	10.52	11.08	7.32
3	3.95	9.44	1.22	17.5	9.42	7.34	7.13	0.54	1.83	8.66	8.19	5.66
3.5	2.62	6.54	0.98	16.95	6.73	5.86	5.81	0.38	1.65	7.12	6.57	4.81
4	2.14	5.95	0.86	17.18	6.69	5.32	5.79	0.43	1.89	6.59	6.97	5.13
>4	3.91	13.36	1.19	36.88	13.98	11.68	15.72	0.7	4.07	14.13	9.23	10.49

Size fraction	**Paetahi.e lower**	**Paetahi.e Middle**	**Paetahi.e Upper**	**Paetahi.f**
-4	22.65	0	0	0
-3.5	97.56	34.03	0	0
-3			10.69	0
-2.5	65.45	23.7	25.05	4.65
-2	50.9	44.3	37.1	11.65
-1.5	35.36	76.57	38.4	18.26
-1	21.11	80.46	23.45	12.28
-0.5	22.86	86.91	29.32	17.84
0	14.22	51.19	30.34	7.2
0.5	13.7	38.2	38.49	6.25
1	8.55	29.07	43.39	18.57
1.5	2.94	9.97	20.57	11.87
2	4.85	5.84	15.55	12.91
2.5	3.9	2.65	11.85	7.75
3	3.15	2.51	12.57	8.64
3.5	3.12	3.23	10.87	7.93
4	3.19	5.84	12.06	9.09
>4	7.06	21.74	26.71	24.58

Appendix B2: Grain size distribution statistics.

Grain size distribution statistics of each sample from the Poto and Paetahi reference locations.

Poto.a			
	Geometric μm	Logarithmic ϕ	Description
Mean (x̄)	3021.5	-1.595	Very Fine Gravel
Sorting (σ)	3.025	1.597	Poorly Sorted
Skewness (*Sk*)	-0.101	0.101	Fine Skewed
Kurtosis (*K*)	1.166	1.166	Leptokurtic
Poto.b			
	Geometric μm	Logarithmic ϕ	Description
Mean (x̄)	608.6	0.716	Coarse Ash
Sorting (σ)	1.824	0.867	Moderately Sorted
Skewness (*Sk*)	-0.181	0.181	Fine Skewed
Kurtosis (*K*)	1.476	1.476	Leptokurtic
Poto.c lower			
	Geometric μm	Logarithmic ϕ	Description
Mean (x̄)	1277.5	-0.353	Very Coarse Ash
Sorting (σ)	4.900	2.293	Very Poorly Sorted
Skewness (*Sk*)	-0.216	0.216	Fine Skewed
Kurtosis (*K*)	0.887	0.887	Platykurtic
Poto.c upper			
	Geometric μm	Logarithmic ϕ	Description
Mean (x̄)	851.9	0.231	Coarse ash
Sorting (σ)	2.055	1.039	Poorly Sorted
Skewness (*Sk*)	-0.010	0.010	Symmetrical
Kurtosis (*K*)	1.231	1.231	Leptokurtic
Poto.d			
	Geometric μm	Logarithmic ϕ	Description
Mean (x̄)	552.3	0.857	Coarse Ash
Sorting (σ)	3.691	1.884	Poorly Sorted
Skewness (*Sk*)	-0.280	0.280	Fine Skewed
Kurtosis (*K*)	1.198	1.198	Leptokurtic
Poto.e			
	Geometric μm	Logarithmic ϕ	Description
Mean (x̄)	202.1	2.307	Fine Ash
Sorting (σ)	6.589	2.720	Very Poorly Sorted
Skewness (*Sk*)	-0.122	0.122	Fine Skewed
Kurtosis (*K*)	0.904	0.904	Mesokurtic
Poto.f			
	Geometric μm	Logarithmic ϕ	Description
Mean (x̄)	1417.3	-0.503	Very Coarse Ash
Sorting (σ)	6.020	2.590	Very Poorly Sorted
Skewness (*Sk*)	-0.451	0.451	Very Fine Skewed
Kurtosis (*K*)	1.027	1.027	Mesokurtic
Poto.g			
	Geometric μm	Logarithmic ϕ	Description

Mean (x̄)	1556.8	-0.639	Very Coarse Sand
Sorting (σ)	1.867	0.901	Moderately Sorted
Skewness (*Sk*)	0.004	-0.004	Symmetrical
Kurtosis (*K*)	1.012	1.012	Mesokurtic
Poto.h			
	Geometric μm	Logarithmic ϕ	Description
Mean (x̄)	901.1	0.150	Coarse Ash
Sorting (σ)	5.637	2.495	Very Poorly Sorted
Skewness (*Sk*)	-0.136	0.136	Fine Skewed
Kurtosis (*K*)	0.882	0.882	Platykurtic
Poto.i			
	Geometric μm	Logarithmic ϕ	Description
Mean (x̄)	2515.6	-1.331	Very Fine Lapilli
Sorting (σ)	7.091	2.826	Very Poorly Sorted
Skewness (*Sk*)	-0.455	0.455	Very Fine Skewed
Kurtosis (*K*)	0.800	0.800	Platykurtic
Poto.j			
	Geometric μm	Logarithmic ϕ	Description
Mean (x̄)	1370.6	-0.455	Very Coarse Ash
Sorting (σ)	2.505	1.325	Poorly Sorted
Skewness (*Sk*)	0.148	-0.148	Coarse Skewed
Kurtosis (*K*)	0.817	0.817	Platykurtic
Poto.k lower			
	Geometric μm	Logarithmic ϕ	Description
Mean (x̄)	1262.1	-0.336	Very Coarse Ash
Sorting (σ)	5.083	2.346	Very Poorly Sorted
Skewness (*Sk*)	-0.122	0.122	Fine Skewed
Kurtosis (*K*)	1.073	1.073	Mesokurtic
Poto.k upper			
	Geometric μm	Logarithmic ϕ	Description
Mean (x̄)	2.380.8	-1.251	Very Fine Lapilli
Sorting (σ)	3.457	1.789	Poorly Sorted
Skewness (*Sk*)	-0.269	0.269	Fine Skewed
Kurtosis (*K*)	0.971	0.971	Mesokurtic
Poto.l lower			
	Geometric μm	Logarithmic ϕ	Description
Mean (x̄)	1776.4	-0.829	Very Coarse Ash
Sorting (σ)	5.429	2.441	Very Poorly Sorted
Skewness (*Sk*)	-0.452	0.452	Very Fine Skewed
Kurtosis (*K*)	0.870	0.870	Platykurtic
Poto.l upper			
	Geometric μm	Logarithmic ϕ	Description
Mean (x̄)	2506.3	-1.326	Very Fine Lapilli
Sorting (σ)	3.705	1.889	Poorly Sorted
Skewness (*Sk*)	-0.275	0.275	Fine Skewed
Kurtosis (*K*)	0.999	0.999	Mesokurtic
Poto.m			
	Geometric μm	Logarithmic ϕ	Description
Mean (x̄)	1078.6	-0.109	Very Coarse Ash

Sorting (σ)	7.933	2.988	Very Poorly Sorted
Skewness (Sk)	-0.047	0.047	Symmetrical
Kurtosis (K)	0.919	0.919	Mesokurtic
Poto.n			
	Geometric μm	Logarithmic ϕ	Description
Mean (x̄)	1344.4	-0.427	Very Coarse Ash
Sorting (σ)	5.984	2.581	Very Poorly Sorted
Skewness (Sk)	-0.242	0.242	Fine Skewed
Kurtosis (K)	0.897	0.897	Platykurtic
Poto.o			
	Geometric μm	Logarithmic ϕ	Description
Mean (x̄)	835.5	0.259	Coarse Ash
Sorting (σ)	7.155	2.839	Very Poorly Sorted
Skewness (Sk)	-0.087	0.087	Symmetrical
Kurtosis (K)	1.004	1.004	Mesokurtic
Paetahi.a lower			
	Geometric μm	Logarithmic ϕ	Description
Mean (x̄)	1406.0	-0.492	Very Coarse Ash
Sorting (σ)	3.798	1.925	Poorly Sorted
Skewness (Sk)	-0.247	0.247	Fine Skewed
Kurtosis (K)	1.183	1.183	Leptokurtic
Paetahi.a middle			
	Geometric μm	Logarithmic ϕ	Description
Mean (x̄)	1181.8	-0.241	Very Coarse Ash
Sorting (σ)	2.153	1.106	Poorly Sorted
Skewness (Sk)	-0.002	0.002	Symmetrical
Kurtosis (K)	1.196	1.196	Leptokurtic
Paetahi.a upper			
	Geometric μm	Logarithmic ϕ	Description
Mean (x̄)	2133.1	-1.093	Very Fine Lapilli
Sorting (σ)	2.471	1.305	Poorly Sorted
Skewness (Sk)	-0.243	0.243	Fine Skewed
Kurtosis (K)	1.262	1.262	Leptokurtic
Paetahi.b			
	Geometric μm	Logarithmic ϕ	Description
Mean (x̄)	632.0	0.662	Coarse Ash
Sorting (σ)	8.706	3.122	Very Poorly Sorted
Skewness (Sk)	0.155	-0.155	Coarse Skewed
Kurtosis (K)	0.860	0.860	Platykurtic
Paetahi.c			
	Geometric μm	Logarithmic ϕ	Description
Mean (x̄)	494.4	1.016	Medium Ash
Sorting (σ)	4.259	2.091	Very Poorly Sorted
Skewness (Sk)	-0.048	0.048	Symmetrical
Kurtosis (K)	1.079	1.079	Mesokurtic
Paetahi.d			
	Geometric μm	Logarithmic ϕ	Description
Mean (x̄)	722.1	0.470	Coarse Ash
Sorting (σ)	7.025	2.813	Very Poorly Sorted

Skewness (Sk)	-0.007	0.007	Symmetrical
Kurtosis (K)	0.906	0.903	Mesokurtic
Paetahi.e lower			
	Geometric μm	Logarithmic ϕ	Description
Mean (x̄)	4590.2	-2.199	Fine Lapilli
Sorting (σ)	3.499	1.807	Poorly Sorted
Skewness (Sk)	-0.344	0.344	Very Fine Skewed
Kurtosis (K)	1.048	1.048	Mesokurtic
Paetahi.e middle			
	Geometric μm	Logarithmic ϕ	Description
Mean (x̄)	1886.5	-0.916	Very Coarse Ash
Sorting (σ)	3.406	1.768	Poorly Sorted
Skewness (Sk)	-0.191	0.191	Fine Skewed
Kurtosis (K)	1.721	1.721	Very Leptokurtic
Paetahi.e upper			
	Geometric μm	Logarithmic ϕ	Description
Mean (x̄)	927.1	0.109	Coarse Ash
Sorting (σ)	5.129	2.359	Very Poorly Sorted
Skewness (Sk)	-0.187	0.187	Fine Skewed
Kurtosis (K)	1.079	1.079	Mesokurtic
Paetahi.f			
	Geometric μm	Logarithmic ϕ	Description
Mean (x̄)	403.8	1.308	Medium Ash
Sorting (σ)	6.181	2.628	Very Poorly Sorted
Skewness (Sk)	0.039	-0.039	Symmetrical
Kurtosis (K)	1.383	1.383	Leptokurtic

Appendix C: Componentry.

Appendix C1: *Percentage measurements of the componentry in each unit from the Poto and Paetahi reference locations for -1.5 and 0.5 ϕ size fractions.*

Unit	Grain size (phi)	Grey Pumice	Brown Pumice	Altered Pumice	Grey Lithics	Altered Lithics	White clay material	Feldspar	Pyroxene	Amphibole	Cumulates
Poto.a	**-1.5**	31	36	1	27	4	0	0	0	0	1
	0.5	21	23	1	19	5	0	6	22	2	1
Poto.b	**-1.5**	7	0	0	87	7	0	0	0	0	0
	0.5	12	18	0	51	4	0	0	14	0	1
Poto.c lower	**-1.5**	11	64	0	21	0	0	0	3	0	1
	0.5	17	22	5	14	2	0	7	24	2	7
Poto.c upper	**-1.5**	33	33	2	29	2	0	0	1	0	1
	0.5	25	13	1	38	9	0	7	6	1	2
Poto.d	**-1.5**	55	31	2	10	2	0	0	0	0	0
	0.5	18	23	2	20	4	0	2	18	4	8
Poto.e	**-1.5**	36	5	0	59	0	0	0	0	0	0
	0.5	17	24	1	36	1	0	1	9	2	8
Poto.f	**-1.5**	10	53	2	26	8	0	0	1	0	0
	0.5	12	41	3	12	9	0	6	10	1	6

Poto.g	**-1.5**	43	4	0	53	1	0	0	0	0	0
	0.5	40	4	0	42	0	0	3	7	1	3
Poto.h	**-1.5**	24	15	1	51	4	0	0	4	0	0
	0.5	13	41	1	15	0	0	5	16	1	8
Poto.i	**-1.5**	11	75	3	0	4	7	0	0	0	0
	0.5	1	75	0	3	14	0	1	4	0	2
Poto.j	**-1.5**	31	13	0	42	13	0	0	1	0	1
	0.5	44	0	0	34	10	0	4	5	0	2
Poto.k	**-1.5**	22	4	0	25	18	29	0	0	0	2
lower	**0.5**	16	39	2	9	15	0	4	10	1	4
Poto.k	**-1.5**	32	59	0	7	1	0	0	0	0	0
upper	**0.5**	15	37	5	22	15	0	3	3	0	1
Poto.l	**-1.5**	22	27	0	40	10	0	0	1	0	0
lower	**0.5**	22	27	4	15	2	0	8	17	0	5
Poto.l	**-1.5**	15	53	0	27	4	0	0	0	0	1
upper	**0.5**	20	28	4	43	1	0	0	2	0	1
Poto.m	**-1.5**	28	25	6	37	1	0	0	1	0	1
	0.5	8	35	4	34	1	0	4	13	0	2
Poto.n	**-1.5**	27	42	0	18	1	0	0	8	0	4
	0.5	6	69	1	1	1	0	9	10	0	3
Poto.o	**-1.5**	15	12	10	46	0	0	0	5	0	12
	0.5	12	16	3	5	2	0	27	27	0	9

Paetahi.a lower	**-1.5**	48	17	0	26	9	0	0	0	0	0
	0.5	11	35	2	29	12	0	3	3	0	4
Paetahi.a middle	**-1.5**	70	8	4	13	6	0	0	0	0	0
	0.5	16	26	0	40	13	0	2	1	0	2
Paetahi.a upper	**-1.5**	42	50	0	5	2	0	0	0	0	0
	0.5	14	44	0	19	7	0	4	7	0	6
Paetahi.b	**-1.5**	42	7	0	44	6	0	0	0	0	1
	0.5	17	9	0	27	9	0	4	22	1	10
Paetahi.c	**-1.5**	18	5	0	74	0	0	0	0	0	3
	0.5	7	29	2	10	2	0	5	42	0	3
Paetahi.d	**-1.5**	37	17	0	33	3	0	0	4	0	6
	0.5	15	53	4	16	1	0	1	7	0	4
Paetahi.e lower	**-1.5**	33	36	0	24	5	0	0	2	0	0
	0.5	31	43	4	10	0	0	2	4	1	4
Paetahi.e middle	**-1.5**	21	10	0	62	6	0	0	0	0	0
	0.5	15	32	0	39	1	0	2	7	0	5
Paetahi.e upper	**-1.5**	12	29	2	50	7	0	0	0	0	0
	0.5	43	4	0	20	9	0	5	13	0	6
Paetahi.f	**-1.5**	19	22	0	55	2	0	0	0	0	1
	0.5	13	23	1	15	5	0	15	17	0	11

Appendix D: Density and vesicularity.

Appendix D1: Bulk density, and vesicularity measurements using pycnometry for pumices from -2 to -4 ϕ from the Poto and Paetahi Formations at the reference locations.

Layer	Clast	bulk density (g/cm^3)	Std %	Vesicularity (%)
Poto.a	1	1.22	0.12	49.24
	2	1.16	0.77	51.76
	3	1.27	0.65	46.94
	4	1.26	0.41	47.68
	5	1.17	0.80	51.30
	6	1.34	0.73	44.08
	7	1.18	0.48	51.00
	8	1.26	0.49	47.62
	9	1.25	0.85	47.87
	10	1.16	2.17	51.62
	11	1.43	0.74	40.40
	12	1.19	0.44	50.55
	13	1.48	0.25	38.52
	14	1.18	1.16	50.65

	16	1.00	1.06	58.44
	18	0.96	0.32	60.15
	19	1.30	0.91	45.68
	20	1.67	1.18	30.42
	22	1.01	0.42	57.98
Poto.c lower	1	1.07	1.24	55.26
	2	1.21	0.82	49.76
	3	1.16	0.92	51.60
	4	1.02	0.75	57.66
	5	0.99	0.94	58.61
Poto.c Upper	1	1.25	1.93	48.10
	2	1.16	0.96	51.53
	3	0.89	1.39	62.87
Poto.e	1	1.36	2.36	43.36
Poto.g	1	1.27	0.88	47.08
	2	1.59	1.40	33.89
	4	1.78	1.29	25.64
	5	1.71	2.03	28.81
Poto.h	1	1.41	1.26	41.37
	3	2.40	0.95	0.01
	7	1.30	0.75	45.90
	8	1.19	0.06	50.24

Poto.i	1	0.74	0.49	69.09
	2	0.87	0.94	63.62
	3	0.77	0.73	68.11
Poto.j	6	1.59	1.28	33.78
	7	1.47	1.21	38.73
	8	1.49	0.60	37.72
Poto.k lower	1	1.37	0.82	42.91
	2	1.08	0.73	54.95
	4	1.37	0.64	42.88
	5	1.16	0.32	51.87
	6	1.05	0.77	56.36
	7	1.40	0.80	41.84
	8	2.39	1.41	0.59
	9	2.33	1.56	3.03
	10	1.46	1.32	39.22
	11	1.35	1.33	43.81
	12	1.20	0.52	50.00
Poto.k Upper	1	1.25	2.88	47.94
	2	0.96	1.48	59.89
	3	1.12	0.88	53.33
	4	0.89	1.77	62.86
	6	0.77	0.52	68.10

	7	1.19	0.85	50.49
	12	0.92	1.02	61.73
Poto.l lower	2	1.21	2.96	49.47
	3	1.23	0.46	48.93
	4	1.22	2.17	49.18
	5	1.62	1.73	32.63
	6	1.74	1.00	27.51
	7	1.20	1.06	49.97
	8	1.74	0.29	27.54
	10	1.65	0.57	31.43
	11	1.96	0.66	18.48
	12	1.14	0.31	52.50
	15	1.34	0.25	44.35
	20	1.38	0.32	42.57
Poto.l Upper	2	1.57	0.24	34.50
	3	1.26	0.19	47.43
	4	1.03	0.27	56.95
	6	1.37	0.41	42.81
	8	1.20	1.04	49.83
	9	1.38	0.65	42.63
	10	1.28	0.52	46.80
	11	1.36	0.97	43.49

	12	1.27	1.02	47.04
	13	1.28	0.33	46.64
	14	1.43	0.16	40.53
	16	1.32	1.38	45.15
	17	1.37	1.87	42.98
	18	1.77	1.03	26.13
	19	1.45	0.44	39.63
	21	0.72	2.58	69.83
	22	1.48	1.33	38.27
	23	1.45	0.21	39.75
	24	1.59	0.64	33.60
	25	2.26	0.23	5.90
	26	1.29	0.61	46.14
	29	1.30	0.30	45.95
	30	1.50	1.99	37.51
	31	1.40	0.34	41.56
	32	1.32	0.60	44.82
	34	1.55	1.53	35.43
	35	1.71	0.93	28.89
	36	1.45	0.55	39.40
	37	1.36	1.10	43.30
	39	1.41	0.42	41.28
	40	1.35	0.33	43.58

Poto.n	2	1.26	2.28	47.54
	3	1.40	2.46	41.78
	4	1.30	1.70	45.83
	6	1.10	0.70	54.18
	7	1.16	0.22	51.47
	8	1.02	0.63	57.30
	9	0.99	0.77	58.88
	10	1.12	0.94	53.45
	11	1.16	0.49	51.86
	12	1.23	0.73	48.77
Poto.o	1.2	1.03	0.57	57.09
	1.4	1.58	0.88	34.05
	2.1	1.47	0.46	38.75
	2.2	1.21	0.84	49.63
	2.3	1.26	0.87	47.50
Paetahi.a	3	0.92	0.48	61.64
Bottom	5	0.94	0.88	60.84
	6	1.07	1.01	55.54
	8	0.95	0.20	60.37
	9	0.87	0.22	63.90
	11	1.08	0.60	55.19
	12	0.55	0.83	63.57

	13	0.97	0.66	59.75
	15	1.06	1.74	55.94
	16	1.07	1.59	55.60
Paetahi.a	2	1.15	1.02	52.01
Upper	4	1.11	0.64	53.61
	5	1.06	0.71	55.80
	6	0.97	1.18	59.74
	7	1.34	0.72	43.98
	8	0.90	0.66	62.62
	9	0.82	0.82	65.63
	10	0.94	1.20	60.82
	11	1.03	1.26	56.88
	12	1.27	0.21	47.24
	13	1.09	0.96	54.63
	14	1.16	0.61	51.67
	15	1.25	0.77	47.77
	16	1.08	0.54	55.04
	17	1.14	1.21	52.68
	18	1.12	0.71	53.43
	20	0.93	1.47	61.40
	21	1.35	0.93	43.67
	22	1.23	0.51	48.68
	24	1.07	0.44	55.49

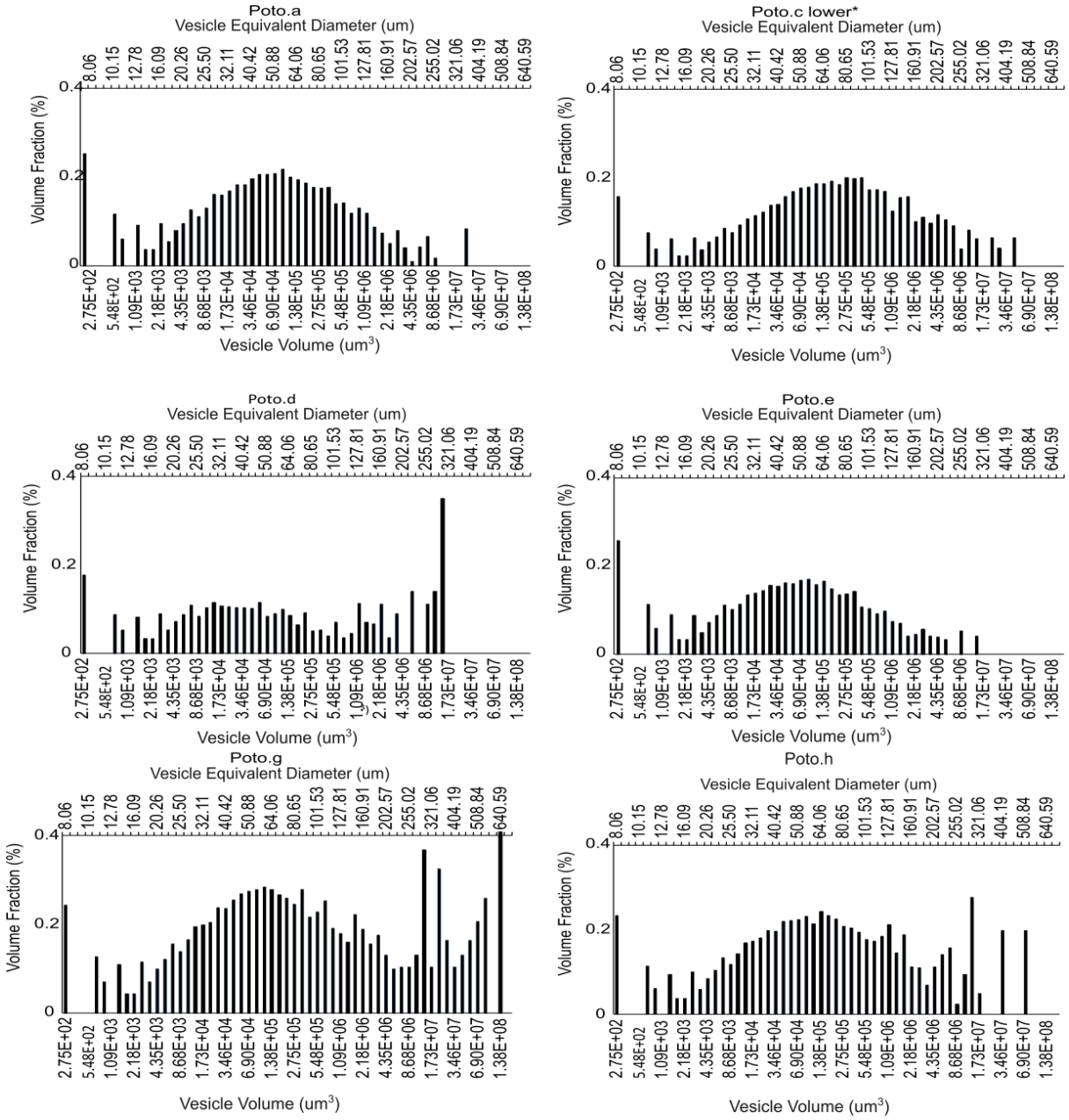
	28	1.27	0.38	47.13
	31	1.25	1.38	47.71
Paetahi.b	1	0.88	0.52	63.29
	2	1.00	1.18	58.27
	3	0.94	1.03	60.95
	4	0.77	1.42	68.00
	6	0.69	0.64	71.24
	7	1.05	0.89	56.39
	9	0.75	0.56	68.74
	10	1.04	1.04	56.87
Paetahi.d	3	1.03	0.80	57.29
	4	1.02	0.60	57.41
	5	1.28	0.47	46.63
	6	1.22	0.19	49.08
	7	1.27	0.94	47.18
	8	1.20	1.29	50.02
Paetahi.e	2	1.26	0.31	47.61
lower	3	1.53	2.34	36.45
	4	1.12	1.02	53.33
	5	1.38	1.20	42.53
	6	1.35	0.85	43.94
	7	1.31	0.43	45.40

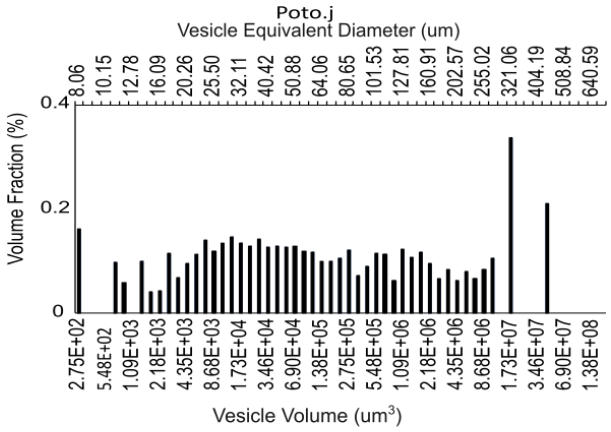
	8	1.37	0.44	43.01
	9	1.13	0.84	53.09
	10	1.17	1.03	51.22
	11	1.29	0.71	46.25
	12	1.27	1.17	47.13
Paetahi.e	1	1.36	0.63	43.49
Middle	3	1.21	1.74	49.58
	4	1.06	1.82	55.91
	5	0.96	0.65	60.15
	6	1.30	0.72	45.94
	7	1.10	0.39	54.35
	8	1.43	0.46	40.22
	9	1.36	1.10	43.30
	10	1.17	0.75	51.41
	11	1.12	0.66	53.39
Paetahi.f	1	1.28	0.50	46.80

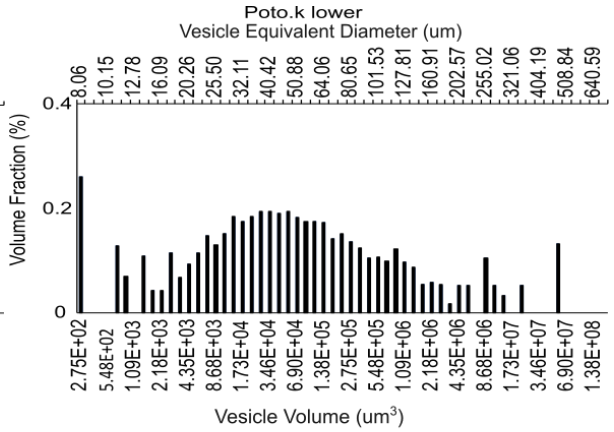
Appendix E: 3D X-ray Tomography.

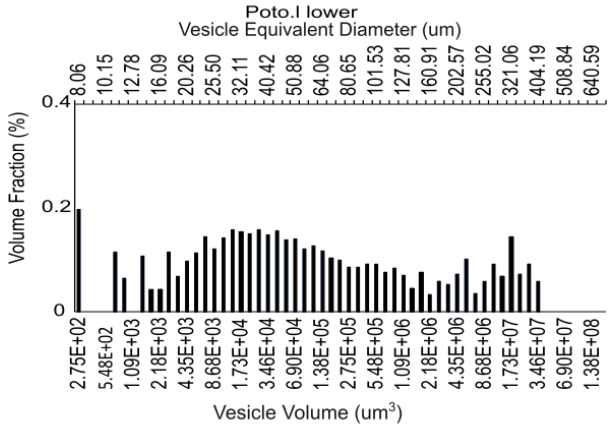
Appendix E1: Vesicle size distribution graphs.

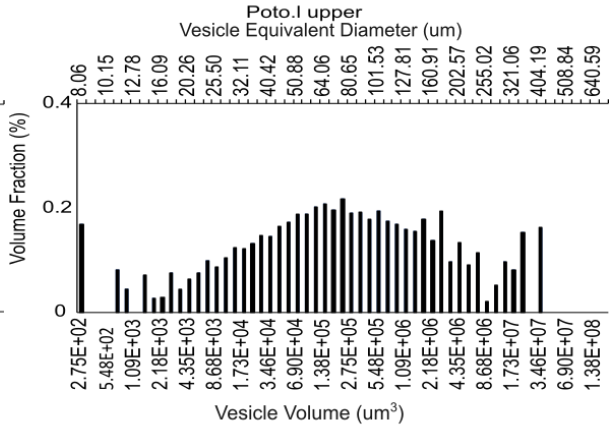
Vesicle size distribution graphs for 19 Poto and Paetahi units from the reference locations.

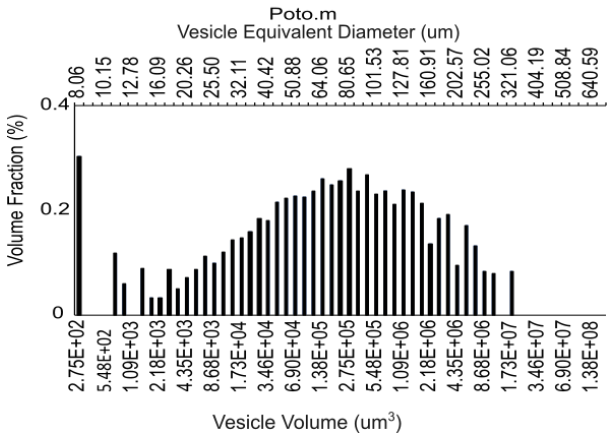


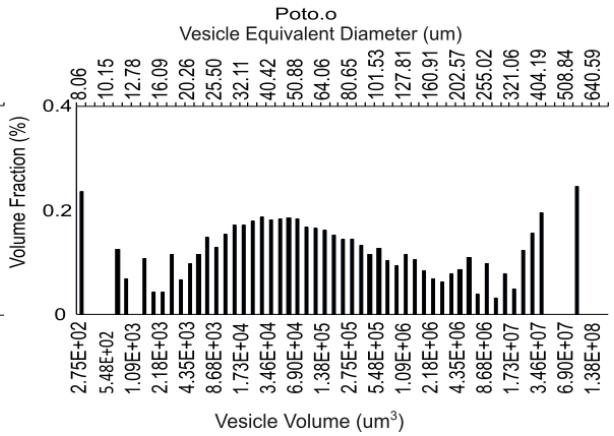

Poto.j
Vesicle Equivalent Diameter (um)
8.06 10.15 12.78 16.09 20.26 25.50 32.11 40.42 50.88 64.06 80.65 101.53 127.81 160.91 202.57 255.02 321.06 404.19 508.84 640.59
Volume Fraction (%)
0.4
0.2
0
2.75E+02 5.48E+02 1.09E+03 2.18E+03 4.35E+03 8.68E+03 1.73E+04 3.46E+04 6.90E+04 1.38E+05 2.75E+05 5.48E+05 1.09E+06 2.18E+06 4.35E+06 8.68E+06 1.73E+07 3.46E+07 6.90E+07 1.38E+08
Vesicle Volume (um3)

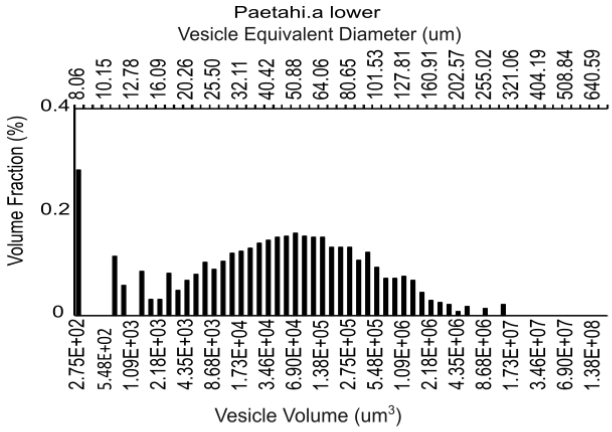

Poto.k lower
Vesicle Equivalent Diameter (um)
8.06 10.15 12.78 16.09 20.26 25.50 32.11 40.42 50.88 64.06 80.65 101.53 127.81 160.91 202.57 255.02 321.06 404.19 508.84 640.59
Volume Fraction (%)
0.4
0.2
0
2.75E+02 5.48E+02 1.09E+03 2.18E+03 4.35E+03 8.68E+03 1.73E+04 3.46E+04 6.90E+04 1.38E+05 2.75E+05 5.48E+05 1.09E+06 2.18E+06 4.35E+06 8.68E+06 1.73E+07 3.46E+07 6.90E+07 1.38E+08
Vesicle Volume (um3)

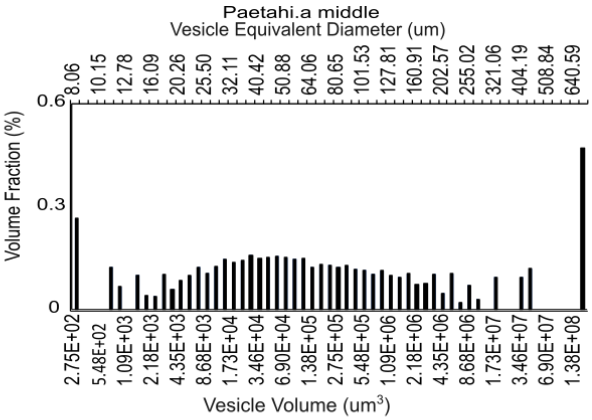

Poto.l lower
Vesicle Equivalent Diameter (um)
8.06 10.15 12.78 16.09 20.26 25.50 32.11 40.42 50.88 64.06 80.65 101.53 127.81 160.91 202.57 255.02 321.06 404.19 508.84 640.59
Volume Fraction (%)
0.4
0.2
0
2.75E+02 5.48E+02 1.09E+03 2.18E+03 4.35E+03 8.68E+03 1.73E+04 3.46E+04 6.90E+04 1.38E+05 2.75E+05 5.48E+05 1.09E+06 2.18E+06 4.35E+06 8.68E+06 1.73E+07 3.46E+07 6.90E+07 1.38E+08
Vesicle Volume (um3)

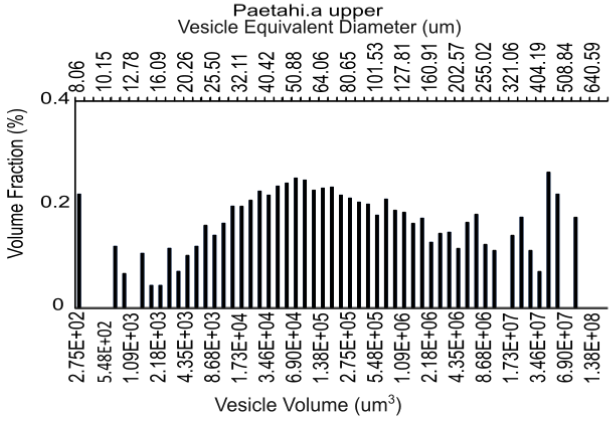

Poto.l upper
Vesicle Equivalent Diameter (um)
8.06 10.15 12.78 16.09 20.26 25.50 32.11 40.42 50.88 64.06 80.65 101.53 127.81 160.91 202.57 255.02 321.06 404.19 508.84 640.59
Volume Fraction (%)
0.4
0.2
0
2.75E+02 5.48E+02 1.09E+03 2.18E+03 4.35E+03 8.68E+03 1.73E+04 3.46E+04 6.90E+04 1.38E+05 2.75E+05 5.48E+05 1.09E+06 2.18E+06 4.35E+06 8.68E+06 1.73E+07 3.46E+07 6.90E+07 1.38E+08
Vesicle Volume (um3)

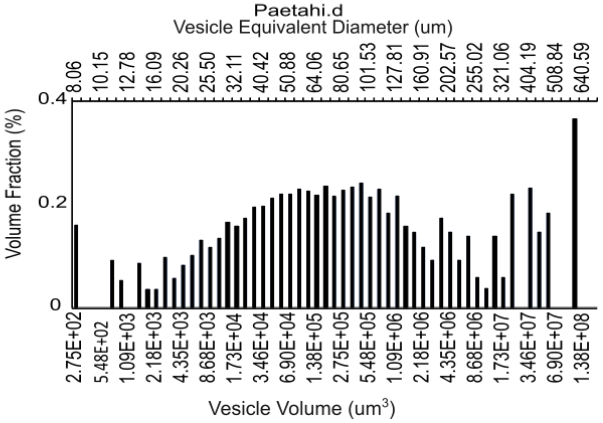

Poto.m
Vesicle Equivalent Diameter (um)
8.06 10.15 12.78 16.09 20.26 25.50 32.11 40.42 50.88 64.06 80.65 101.53 127.81 160.91 202.57 255.02 321.06 404.19 508.84 640.59
Volume Fraction (%)
0.4
0.2
0
2.75E+02 5.48E+02 1.09E+03 2.18E+03 4.35E+03 8.68E+03 1.73E+04 3.46E+04 6.90E+04 1.38E+05 2.75E+05 5.48E+05 1.09E+06 2.18E+06 4.35E+06 8.68E+06 1.73E+07 3.46E+07 6.90E+07 1.38E+08
Vesicle Volume (um3)

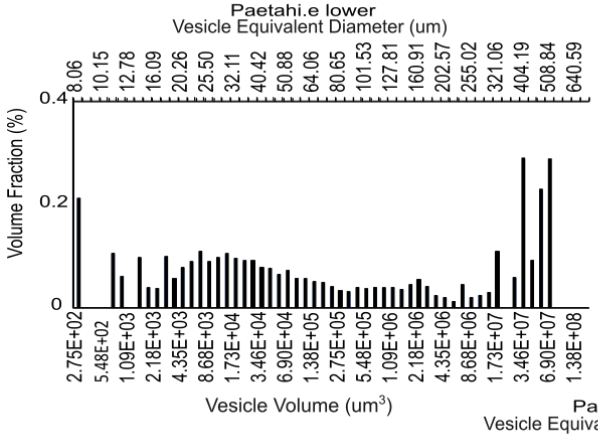

Poto.o
Vesicle Equivalent Diameter (um)
8.06 10.15 12.78 16.09 20.26 25.50 32.11 40.42 50.88 64.06 80.65 101.53 127.81 160.91 202.57 255.02 321.06 404.19 508.84 640.59
Volume Fraction (%)
0.4
0.2
0
2.75E+02 5.48E+02 1.09E+03 2.18E+03 4.35E+03 8.68E+03 1.73E+04 3.46E+04 6.90E+04 1.38E+05 2.75E+05 5.48E+05 1.09E+06 2.18E+06 4.35E+06 8.68E+06 1.73E+07 3.46E+07 6.90E+07 1.38E+08
Vesicle Volume (um3)

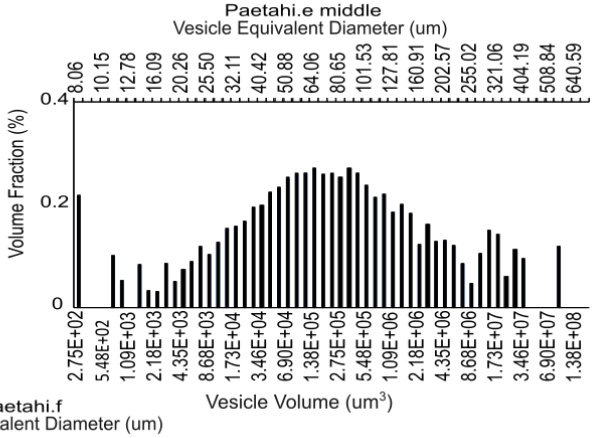

Paetahi.a lower
Vesicle Equivalent Diameter (um)
8.06 10.15 12.78 16.09 20.26 25.50 32.11 40.42 50.88 64.06 80.65 101.53 127.81 160.91 202.57 255.02 321.06 404.19 508.84 640.59
Volume Fraction (%)
0.4
0.2
0
2.75E+02 5.48E+02 1.09E+03 2.18E+03 4.35E+03 8.68E+03 1.73E+04 3.46E+04 6.90E+04 1.38E+05 2.75E+05 5.48E+05 1.09E+06 2.18E+06 4.35E+06 8.68E+06 1.73E+07 3.46E+07 6.90E+07 1.38E+08
Vesicle Volume (um3)

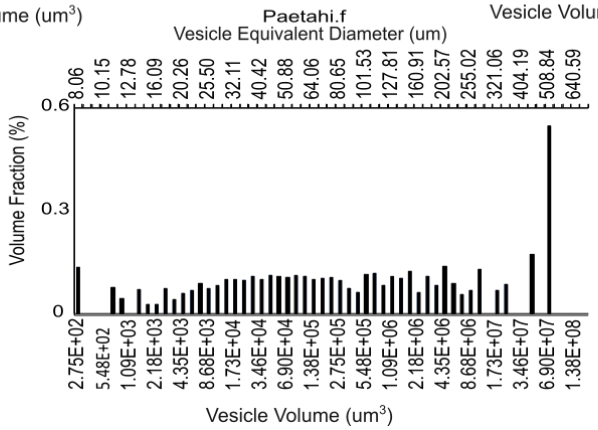

Paetahi.a middle
Vesicle Equivalent Diameter (um)
8.06 10.15 12.78 16.09 20.26 25.50 32.11 40.42 50.88 64.06 80.65 101.53 127.81 160.91 202.57 255.02 321.06 404.19 508.84 640.59
Volume Fraction (%)
0.6
0.3
0
2.75E+02 5.48E+02 1.09E+03 2.18E+03 4.35E+03 8.68E+03 1.73E+04 3.46E+04 6.90E+04 1.38E+05 2.75E+05 5.48E+05 1.09E+06 2.18E+06 4.35E+06 8.68E+06 1.73E+07 3.46E+07 6.90E+07 1.38E+08
Vesicle Volume (um3)


Paetahi.a upper
Vesicle Equivalent Diameter (um)
8.06 10.15 12.78 16.09 20.26 25.50 32.11 40.42 50.88 64.06 80.65 101.53 127.81 160.91 202.57 255.02 321.06 404.19 508.84 640.59
Volume Fraction (%)
0.4
0.2
0
2.75E+02 5.48E+02 1.09E+03 2.18E+03 4.35E+03 8.68E+03 1.73E+04 3.46E+04 6.90E+04 1.38E+05 2.75E+05 5.48E+05 1.09E+06 2.18E+06 4.35E+06 8.68E+06 1.73E+07 3.46E+07 6.90E+07 1.38E+08
Vesicle Volume (um3)


Paetahi.d
Vesicle Equivalent Diameter (um)
8.06 10.15 12.78 16.09 20.26 25.50 32.11 40.42 50.88 64.06 80.65 101.53 127.81 160.91 202.57 255.02 321.06 404.19 508.84 640.59
Volume Fraction (%)
0.4
0.2
0
2.75E+02 5.48E+02 1.09E+03 2.18E+03 4.35E+03 8.68E+03 1.73E+04 3.46E+04 6.90E+04 1.38E+05 2.75E+05 5.48E+05 1.09E+06 2.18E+06 4.35E+06 8.68E+06 1.73E+07 3.46E+07 6.90E+07 1.38E+08
Vesicle Volume (um3)


Paetahi.e lower
Vesicle Equivalent Diameter (um)
8.06 10.15 12.78 16.09 20.26 25.50 32.11 40.42 50.88 64.06 80.65 101.53 127.81 160.91 202.57 255.02 321.06 404.19 508.84 640.59
Volume Fraction (%)
0.4
0.2
0
2.75E+02 5.48E+02 1.09E+03 2.18E+03 4.35E+03 8.68E+03 1.73E+04 3.46E+04 6.90E+04 1.38E+05 2.75E+05 5.48E+05 1.09E+06 2.18E+06 4.35E+06 8.68E+06 1.73E+07 3.46E+07 6.90E+07 1.38E+08
Vesicle Volume (um3)


Paetahi.e middle
Vesicle Equivalent Diameter (um)
8.06 10.15 12.78 16.09 20.26 25.50 32.11 40.42 50.88 64.06 80.65 101.53 127.81 160.91 202.57 255.02 321.06 404.19 508.84 640.59
Volume Fraction (%)
0.4
0.2
0
2.75E+02 5.48E+02 1.09E+03 2.18E+03 4.35E+03 8.68E+03 1.73E+04 3.46E+04 6.90E+04 1.38E+05 2.75E+05 5.48E+05 1.09E+06 2.18E+06 4.35E+06 8.68E+06 1.73E+07 3.46E+07 6.90E+07 1.38E+08
Vesicle Volume (um3)


Paetahi.f
Vesicle Equivalent Diameter (um)
8.06 10.15 12.78 16.09 20.26 25.50 32.11 40.42 50.88 64.06 80.65 101.53 127.81 160.91 202.57 255.02 321.06 404.19 508.84 640.59
Volume Fraction (%)
0.6
0.3
0
2.75E+02 5.48E+02 1.09E+03 2.18E+03 4.35E+03 8.68E+03 1.73E+04 3.46E+04 6.90E+04 1.38E+05 2.75E+05 5.48E+05 1.09E+06 2.18E+06 4.35E+06 8.68E+06 1.73E+07 3.46E+07 6.90E+07 1.38E+08
Vesicle Volume (um3)

Appendix E2: Vesicle size distribution data for the Poto and Paetahi Formations.

Poto.a						**Poto.c lower**						**Poto.d**				
Volume bins in um	Frequency	Average volume of bin	volume fraction %	eqD (um)		Volume bins in um	Frequency	Average volume of bin	volume fraction %	eqD (um)		Volume bins in um	Frequency	Average volume of bin	volume fraction %	eqD (um)
2.75E+02	608326	167061527.8	0.252797003	8.06		2.75E+02	387087	106303767.4	0.156919059	8.06		2.75E+02	50416	13845494	0.175967507	8.06
3.46E+02	0	0	0	8.71		3.46E+02	0	0	0	8.71		3.46E+02	0	0	0	8.71
4.35E+02	0	0	0	9.40		4.35E+02	0	0	0	9.40		4.35E+02	0	0	0	9.40
5.48E+02	0	0	0	10.15		5.48E+02	0	0	0	10.15		5.48E+02	0	0	0	10.15
6.90E+02	111858	77162647.45	0.116762287	10.96		6.90E+02	73627	50789878.63	0.074972883	10.96		6.90E+02	9857	6799622.879	0.086418924	10.96
8.68E+02	45891	39853603.1	0.060306353	11.84		8.68E+02	30395	26396249.07	0.038964513	11.84		8.68E+02	4639	4028695.491	0.051202182	11.84
1.09E+03	0	0	0	12.78		1.09E+03	0	0	0	12.78		1.09E+03	0	0	0	12.78
1.38E+03	44054	60635284.19	0.09175313	13.80		1.38E+03	29926	41189710.69	0.060801708	13.80		1.38E+03	4618	6356147.964	0.080782637	13.80
1.73E+03	13585	23539634.36	0.035620104	14.90		1.73E+03	9203	15946651.09	0.023539462	14.90		1.73E+03	1490	2581822.245	0.032813334	14.90
2.18E+03	10904	23786246.36	0.035993277	16.09		2.18E+03	7297	15917850.3	0.023496948	16.09		2.18E+03	1145	2497730.382	0.03174458	16.09
2.75E+03	22830	62696887.5	0.094872742	17.37		2.75E+03	15509	42591591.25	0.062871078	17.37		2.75E+03	2539	6972728.75	0.08861899	17.37
3.46E+03	10485	36250041.22	0.054853454	18.76		3.46E+03	7147	24709494	0.03647463	18.76		3.46E+03	1182	4086556.864	0.051937564	18.76
4.35E+03	11997	52217097.62	0.079014755	20.26		4.35E+03	8360	36387008.09	0.053712255	20.26		4.35E+03	1278	5562511.524	0.070696018	20.26
5.48E+03	11486	62937412.18	0.095236703	21.87		5.48E+03	8108	44427697.89	0.065581425	21.87		5.48E+03	1241	6800046.013	0.086424301	21.87
6.90E+03	12038	83041351.54	0.125657924	23.62		6.90E+03	8410	58014434.83	0.085637327	23.62		6.90E+03	1230	8484869.778	0.10783735	23.62
8.68E+03	8409	73027161.85	0.110504482	25.50		8.68E+03	5924	51446415.36	0.075942022	25.50		8.68E+03	755	6556725.793	0.083331855	25.50
1.09E+04	7851	85835125.66	0.129885455	27.54		1.09E+04	5697	62285404.52	0.091941869	27.54		1.09E+04	733	8013902.32	0.10185165	27.54
1.38E+04	7686	105788984.9	0.160079575	29.73		1.38E+04	5257	72356582.6	0.10680832	29.73		1.38E+04	652	8974033.071	0.114054307	29.73
1.73E+04	6071	105196260.7	0.159182666	32.11		1.73E+04	4440	76934837.36	0.113566457	32.11		1.73E+04	479	8299952.049	0.105487162	32.11
2.18E+04	5092	111078105.7	0.168083056	34.67		2.18E+04	3778	82414195.49	0.121654747	34.67		2.18E+04	379	8267596.636	0.105075945	34.67
2.75E+04	4410	121109625	0.183262721	37.43		2.75E+04	3365	92411312.5	0.136411874	37.43		2.75E+04	294	8073975	0.102615136	37.43
3.46E+04	3494	120798897.5	0.182792529	40.42		3.46E+04	2721	94073783.65	0.138865912	40.42		3.46E+04	232	8020991.476	0.101941749	40.42
4.35E+04	2970	129269634	0.195610422	43.64		4.35E+04	2452	106723617	0.157538815	43.64		4.35E+04	182	7921573.532	0.10067821	43.64
5.48E+04	2473	135507766.2	0.205049945	47.12		5.48E+04	2073	113589809.7	0.167674264	47.12		5.48E+04	164	8986362.177	0.114211003	47.12
6.90E+04	1975	136240795.2	0.206159163	50.88		6.90E+04	1731	119409021	0.176264225	50.88		6.90E+04	94	6484372.026	0.082412284	50.88
8.68E+04	1574	136692535.1	0.206842734	54.94		8.68E+04	1388	120539541.7	0.17793303	54.94		8.68E+04	81	7034368.07	0.089402387	54.94
1.09E+05	1316	143878519.1	0.217716544	59.33		1.09E+05	1155	126276359.9	0.186401367	59.33		1.09E+05	71	7762442.902	0.09865576	59.33
1.38E+05	959	131995363.7	0.199734988	64.06		1.38E+05	918	126352183.4	0.186513293	64.06		1.38E+05	48	6606650.114	0.083966361	64.06
1.73E+05	738	127878175.6	0.193504872	69.17		1.73E+05	747	129437665.6	0.191067891	69.17		1.73E+05	29	5025023.161	0.063864879	69.17
2.18E+05	567	123686736	0.187162398	74.69		2.18E+05	572	124777447.9	0.184188765	74.69		2.18E+05	33	7198698.918	0.091490929	74.69
2.75E+05	427	117264875	0.177444857	80.65		2.75E+05	494	135664750	0.200259928	80.65		2.75E+05	14	3844750	0.048864351	80.65
3.46E+05	335	115820351.1	0.175259008	87.08		3.46E+05	387	133798435.4	0.19750499	87.08		3.46E+05	12	4148788.695	0.052728491	87.08
4.35E+05	269	117082597.8	0.177169036	94.03		4.35E+05	312	135798403.4	0.200457219	94.03		4.35E+05	7	3046759.051	0.038722388	94.03
5.48E+05	169	92603366.34	0.140127136	101.53		5.48E+05	212	116165169.6	0.171475852	101.53		5.48E+05	10	5479489.132	0.069640855	101.53
6.90E+05	135	93126619.52	0.140918921	109.63		6.90E+05	170	117270557.9	0.173107558	109.63		6.90E+05	4	2759307.245	0.035069057	109.63
8.68E+05	90	78159645.22	0.118270941	118.37		8.68E+05	132	114634146.3	0.16921585	118.37		8.68E+05	4	3473762.01	0.044149327	118.37
1.09E+06	78	85277541.74	0.12904172	127.81		1.09E+06	77	84184239.92	0.124267578	127.81		1.09E+06	8	8746414.537	0.111161419	127.81
1.38E+06	57	78453970.1	0.118716312	138.01		1.38E+06	76	104605293.5	0.154411876	138.01		1.38E+06	4	5505541.761	0.069971968	138.01
1.73E+06	33	57181298.04	0.086526569	149.02		1.73E+06	61	105698763	0.156025989	149.02		1.73E+06	3	5198299.822	0.066067116	149.02
2.18E+06	22	47991326.12	0.072620331	160.91		2.18E+06	31	67624141.35	0.099822583	160.91		2.18E+06	4	8725695.658	0.110898095	160.91
2.75E+06	12	32955000	0.049867407	173.75		2.75E+06	27	74148750	0.109453807	173.75		2.75E+06	1	2746250	0.034903108	173.75
3.46E+06	15	51859858.68	0.078474183	187.61		3.46E+06	19	65689154.33	0.096966274	187.61		3.46E+06	2	6914647.824	0.087880818	187.61
4.35E+06	6	26115077.58	0.039517257	202.57		4.35E+06	18	78345232.74	0.115648396	202.57		4.35E+06	0	0	0	202.57
5.48E+06	1	5479489.132	0.008291547	218.73		5.48E+06	13	71233358.72	0.105150286	218.73		5.48E+06	2	10958978.26	0.13928171	218.73
6.90E+06	4	27593072.45	0.041753754	236.18		6.90E+06	9	62084413.01	0.091645178	236.18		6.90E+06	0	0	0	236.18
8.68E+06	5	43422025.12	0.065706078	255.02		8.68E+06	3	26053215.07	0.038458148	255.02		8.68E+06	1	8684405.024	0.110373317	255.02
1.09E+07	1	10933018.17	0.01654381	275.37		1.09E+07	5	54665090.86	0.080693232	275.37		1.09E+07	1	10933018.17	0.138951774	275.37
1.38E+07	0	0	0	297.34		1.38E+07	3	41291563.21	0.060952056	297.34		1.38E+07	2	27527708.81	0.349859839	297.34
1.73E+07	0	0	0	321.06		1.73E+07	0	0	0	321.06		1.73E+07				321.06
2.18E+07	0	0	0	346.67		2.18E+07	2	43628478.29	0.064401666	346.67		2.18E+07				346.67
2.75E+07	2	54925000	0.083112345	374.32		2.75E+07	1	27462500	0.040538447	374.32		2.75E+07				374.32
3.46E+07				404.19		3.46E+07	0	0	0	404.19		3.46E+07				404.19
4.35E+07				436.43		4.35E+07	1	43525129.3	0.064249109	436.43		4.35E+07				436.43
5.48E+07				471.25		5.48E+07				471.25		5.48E+07				471.25
6.90E+07				508.84		6.90E+07				508.84		6.90E+07				508.84
8.68E+07				549.43		8.68E+07				549.43		8.68E+07				549.43
1.09E+08				593.26		1.09E+08				593.26		1.09E+08				593.26
1.38E+08				640.59		1.38E+08				640.59		1.38E+08				640.59
1.73E+08				691.69		1.73E+08				691.69		1.73E+08				691.69

Poto.e						**Poto.g**						**Poto.h**				
Volume bins in um	Frequency	Average volume of bin	volume fraction %	eqD (um)		Volume bins in um	Frequency	Average volume of bin	volume fraction %	eqD (um)		Volume bins in um	Frequency	Average volume of bin	volume fraction %	eqD (um)
2.75E+02	314681	86419269.63	0.258060177	8.06		2.75E+02	297325	81652878.13	0.242103483	8.06		2.75E+02	297107	81593009.88	0.233122885	8.06
3.46E+02	0	0	0	8.71		3.46E+02	0	0	0	8.71		3.46E+02	0	0	0	8.71
4.35E+02	0	0	0	9.40		4.35E+02	0	0	0	9.40		4.35E+02	0	0	0	9.40
5.48E+02	0	0	0	10.15		5.48E+02	0	0	0	10.15		5.48E+02	0	0	0	10.15
6.90E+02	54618	37676960.78	0.11250874	10.96		6.90E+02	61581	42480224.86	0.125955271	10.96		6.90E+02	57808	39877508.3	0.113935738	10.96
8.68E+02	22975	19952420.54	0.059580753	11.84		8.68E+02	26779	23255968.21	0.068954715	11.84		8.68E+02	24428	21214264.59	0.060612185	11.84
1.09E+03	0	0	0	12.78		1.09E+03	0	0	0	12.78		1.09E+03	0	0	0	12.78
1.38E+03	21635	29778099	0.08892162	13.80		1.38E+03	26631	36654520.66	0.108681866	13.80		1.38E+03	24031	33075918.52	0.094502624	13.80
1.73E+03	6571	11386009.38	0.034000236	14.90		1.73E+03	8170	14156703.18	0.041975093	14.90		1.73E+03	7548	13078922.35	0.03736835	14.90
2.18E+03	5018	10946385.2	0.032687456	16.09		2.18E+03	6558	14305778.03	0.042417105	16.09		2.18E+03	6122	13354677.21	0.038156221	16.09
2.75E+03	10826	29730902.5	0.088780685	17.37		2.75E+03	14093	38702901.25	0.114755382	17.37		2.75E+03	12822	35212417.5	0.100606907	17.37
3.46E+03	4828	16691959.85	0.049844556	18.76		3.46E+03	6673	23070722.47	0.068405455	18.76		3.46E+03	6010	20778516.71	0.059367191	18.76
4.35E+03	5547	24143389.22	0.072095579	20.26		4.35E+03	7576	32974637.96	0.097770892	20.26		4.35E+03	6815	29662375.62	0.084749645	20.26
5.48E+03	5375	29452254.09	0.087948601	21.87		5.48E+03	7395	40520822.13	0.120145577	21.87		5.48E+03	6709	36761892.59	0.105033979	21.87
6.90E+03	5410	37319630.49	0.111441701	23.62		6.90E+03	7559	52144008.66	0.15460871	23.62		6.90E+03	6818	47032391.99	0.134378263	23.62
8.68E+03	3881	33704175.9	0.100645442	25.50		8.68E+03	5340	46374722.83	0.137502586	25.50		8.68E+03	4787	41572246.85	0.118777848	25.50
1.09E+04	3483	38079702.29	0.113711383	27.54		1.09E+04	5074	55474134.2	0.164482642	27.54		1.09E+04	4585	50127888.32	0.143222538	27.54
1.38E+04	3256	44815109.94	0.133824264	29.73		1.38E+04	4723	65006684.35	0.192746968	29.73		1.38E+04	4309	59308448.62	0.16945271	29.73
1.73E+04	2658	46056936.42	0.137532534	32.11		1.73E+04	3846	66642203.72	0.197596337	32.11		1.73E+04	3506	60750797.25	0.173573706	32.11
2.18E+04	2213	48274911.23	0.144155721	34.67		2.18E+04	3137	68431268.2	0.202900973	34.67		2.18E+04	2900	63261293.52	0.180746553	34.67
2.75E+04	1907	52370987.5	0.156387185	37.43		2.75E+04	2898	79586325	0.235976085	37.43		2.75E+04	2514	69040725	0.197259214	37.43
3.46E+04	1485	51341260.1	0.153312273	40.42		3.46E+04	2296	79380157.02	0.23536479	40.42		3.46E+04	1988	68731599.37	0.196375998	40.42
4.35E+04	1248	54319361.36	0.162205305	43.64		4.35E+04	1961	85352778.55	0.25307381	43.64		4.35E+04	1760	76604227.56	0.218869222	43.64
5.48E+04	981	53753788.39	0.160516424	47.12		5.48E+04	1648	90301980.9	0.267748359	47.12		5.48E+04	1411	77315591.66	0.22090169	47.12
6.90E+04	812	56013937.07	0.167265548	50.88		6.90E+04	1340	92436792.71	0.274078147	50.88		6.90E+04	1137	78433308.44	0.224095167	50.88
8.68E+04	657	57056541.01	0.170378911	54.94		8.68E+04	1077	93531042.11	0.277322632	54.94		8.68E+04	935	81199186.98	0.231997677	54.94
1.09E+05	482	52697147.59	0.157361145	59.33		1.09E+05	871	95226588.27	0.282349983	59.33		1.09E+05	683	74672514.11	0.21335004	59.33
1.38E+05	402	55330694.7	0.16522529	64.06		1.38E+05	682	93869487.03	0.278326133	64.06		1.38E+05	619	85198258.76	0.243423596	64.06
1.73E+05	287	49730401.63	0.148502021	69.17		1.73E+05	516	89410756.94	0.265105851	69.17		1.73E+05	472	81786583.86	0.233675954	69.17
2.18E+05	207	45155475.03	0.134840643	74.69		2.18E+05	400	87256956.58	0.258719761	74.69		2.18E+05	360	78531260.93	0.224375031	74.69
2.75E+05	167	45862375	0.136951546	80.65		2.75E+05	300	82387500	0.244281661	80.65		2.75E+05	266	73050250	0.208715	80.65
3.46E+05	138	47711069.99	0.142472011	87.08		3.46E+05	271	93693478.02	0.27780426	87.08		3.46E+05	207	71566604.98	0.204476014	87.08
4.35E+05	82	35690606.02	0.106577204	94.03		4.35E+05	167	72686965.93	0.215519257	94.03		4.35E+05	156	67899201.7	0.193997719	94.03
5.48E+05	63	34520781.53	0.103083942	101.53		5.48E+05	140	76712847.85	0.22745613	101.53		5.48E+05	113	61918227.2	0.176909221	101.53
6.90E+05	45	31042206.51	0.092696424	109.63		6.90E+05	123	84848697.78	0.251579194	109.63		6.90E+05	88	60704759.39	0.17344217	109.63
8.68E+05	38	33000739.09	0.09854488	118.37		8.68E+05	74	64264597.18	0.190546655	118.37		8.68E+05	74	64264597.18	0.183613135	118.37
1.09E+06	23	25145941.79	0.075089343	127.81		1.09E+06	55	60131599.94	0.178292182	127.81		1.09E+06	68	74344523.57	0.212412924	127.81
1.38E+06	17	23398552.49	0.069871391	138.01		1.38E+06	39	53679032.17	0.159160105	138.01		1.38E+06	37	50926261.29	0.145503604	138.01
1.73E+06	8	13862132.86	0.041394292	149.02		1.73E+06	43	74508964.11	0.220921542	149.02		1.73E+06	38	65845131.08	0.188128946	149.02
2.18E+06	7	15269967.4	0.045598285	160.91		2.18E+06	29	63261293.52	0.187571827	160.91		2.18E+06	18	39265630.46	0.112187516	160.91
2.75E+06	7	19223750	0.05740484	173.75		2.75E+06	19	52178750	0.154711719	173.75		2.75E+06	14	38447500	0.10985	173.75
3.46E+06	4	13829295.65	0.041296235	187.61		3.46E+06	17	58774506.51	0.174268355	187.61		3.46E+06	7	24201267.38	0.069146478	187.61
4.35E+06	3	13057538.79	0.03899166	202.57		4.35E+06	10	43525129.3	0.129053447	202.57		4.35E+06	9	39172616.37	0.111921761	202.57
5.48E+06	2	10958978.26	0.032725061	218.73		5.48E+06	6	32876934.79	0.097481199	218.73		5.48E+06	9	49315402.19	0.140901149	218.73
6.90E+06	0	0	0	236.18		6.90E+06	5	34491340.56	0.102267965	236.18		6.90E+06	8	55186144.9	0.1576747	236.18
8.68E+06	2	17368810.05	0.051865726	255.02		8.68E+06	4	34737620.1	0.102998192	255.02		8.68E+06	1	8684405.024	0.024812586	255.02
1.09E+07	0	0	0	275.37		1.09E+07	4	43732072.69	0.129667041	275.37		1.09E+07	3	32799054.51	0.093711584	275.37
1.38E+07	1	13763854.4	0.041100818	297.34		1.38E+07	9	123874689.6	0.36729255	297.34		1.38E+07	7	96346980.82	0.275277088	297.34
1.73E+07				321.06		1.73E+07	2	34655332.15	0.102754206	321.06		1.73E+07	1	17327666.07	0.049507617	321.06
2.18E+07				346.67		2.18E+07	5	109071195.7	0.323399702	346.67		2.18E+07	0	0	0	346.67
2.75E+07				374.32		2.75E+07	2	54925000	0.162854441	374.32		2.75E+07	0	0	0	374.32
3.46E+07				404.19		3.46E+07	1	34573239.12	0.102510797	404.19		3.46E+07	2	69146478.24	0.197561366	404.19
4.35E+07				436.43		4.35E+07	1	43525129.3	0.129053447	436.43		4.35E+07	0	0	0	436.43
5.48E+07				471.25		5.48E+07	1	54794891.32	0.162468664	471.25		5.48E+07	0	0	0	471.25
6.90E+07				508.84		6.90E+07	1	68982681.13	0.20453593	508.84		6.90E+07	1	68982681.13	0.197093375	508.84
8.68E+07				549.43		8.68E+07	1	86844050.24	0.25749548	549.43		8.68E+07				549.43
1.09E+08				593.26		1.09E+08	0	0	0	593.26		1.09E+08				593.26
1.38E+08				640.59		1.38E+08	1	137638544	0.408102834	640.59		1.38E+08				640.59
1.73E+08				691.69		1.73E+08				691.69		1.73E+08				691.69

Poto.j						**Poto.k lower**						**Poto.l lower**				
Volume bins in um	Frequency	Average volume of bin	volume fraction %	eqD (um)		Volume bins in um	Frequency	Average volume of bin	volume fraction %	eqD (um)		Volume bins in um	Frequency	Average volume of bin	volume fraction %	eqD (um)
2.75E+02	120825	33181565.63	0.161395936	8.06		2.75E+02	393637	108102561.1	0.260095848	8.06		2.75E+02	429101	117841862.1	0.197991407	8.06
3.46E+02	0	0	0	8.71		3.46E+02	0	0	0	8.71		3.46E+02	0	0	0	8.71
4.35E+02	0	0	0	9.40		4.35E+02	0	0	0	9.40		4.35E+02	0	0	0	9.40
5.48E+02	0	0	0	10.15		5.48E+02	0	0	0	10.15		5.48E+02	0	0	0	10.15
6.90E+02	29188	20134664.97	0.097935496	10.96		6.90E+02	77382	53380178.31	0.128433245	10.96		6.90E+02	99487	68628799.97	0.11530633	10.96
8.68E+02	13844	12022690.32	0.058478656	11.84		8.68E+02	33058	28708906.13	0.069073917	11.84		8.68E+02	44681	38802790.09	0.065194311	11.84
1.09E+03	0	0	0	12.78		1.09E+03	0	0	0	12.78		1.09E+03	0	0	0	12.78
1.38E+03	14986	20626512.21	0.100327853	13.80		1.38E+03	32806	45153700.76	0.108640258	13.80		1.38E+03	46352	63798217.93	0.107190252	13.80
1.73E+03	4838	8383124.846	0.040775721	14.90		1.73E+03	10238	17740064.53	0.042682773	14.90		1.73E+03	14626	25343444.4	0.042580659	14.90
2.18E+03	4005	8736602.778	0.042495047	16.09		2.18E+03	7985	17418669.96	0.041909495	16.09		2.18E+03	12082	26355963.74	0.044281839	16.09
2.75E+03	8586	23579302.5	0.114690296	17.37		2.75E+03	17335	47606243.75	0.114541101	17.37		2.75E+03	24931	68466758.75	0.115034077	17.37
3.46E+03	4060	14036735.08	0.068275018	18.76		3.46E+03	8073	27910975.94	0.067154089	18.76		3.46E+03	11805	40813708.78	0.068572946	18.76
4.35E+03	4494	19560193.11	0.095141251	20.26		4.35E+03	8932	38876645.49	0.0935376	20.26		4.35E+03	13278	57792666.68	0.097100056	20.26
5.48E+03	4228	23167280.05	0.112686209	21.87		5.48E+03	8674	47529088.74	0.114355465	21.87		5.48E+03	12415	68027857.58	0.11429666	21.87
6.90E+03	4194	28931336.46	0.140722718	23.62		6.90E+03	8877	61235926.03	0.147334253	23.62		6.90E+03	12509	86290435.82	0.144980438	23.62
8.68E+03	2842	24681079.08	0.120049364	25.50		8.68E+03	6180	53669623.05	0.129129652	25.50		8.68E+03	8374	72723207.67	0.122185528	25.50
1.09E+04	2523	27584004.85	0.134169265	27.54		1.09E+04	5769	63072581.83	0.151753266	27.54		1.09E+04	7752	84752756.86	0.142396914	27.54
1.38E+04	2192	30170368.85	0.146749402	29.73		1.38E+04	5534	76169170.27	0.183263789	29.73		1.38E+04	6832	94034653.28	0.157991845	29.73
1.73E+04	1607	27845559.38	0.135441472	32.11		1.73E+04	4194	72672231.51	0.174850119	32.11		1.73E+04	5318	92148528.18	0.154822882	32.11
2.18E+04	1224	26700628.71	0.129872502	34.67		2.18E+04	3497	76284394.29	0.183541019	34.67		2.18E+04	4117	89809222.56	0.150892509	34.67
2.75E+04	1068	29329950	0.142661584	37.43		2.75E+04	2927	80382737.5	0.193401674	37.43		2.75E+04	3433	94278762.5	0.158401984	37.43
3.46E+04	761	26310234.97	0.127973618	40.42		3.46E+04	2322	80279061.24	0.193152228	40.42		3.46E+04	2549	88127186.52	0.148066445	40.42
4.35E+04	614	26724429.39	0.129988269	43.64		4.35E+04	1820	79215735.32	0.190593855	43.64		4.35E+04	2138	93056726.44	0.156348787	43.64
5.48E+04	478	26191958.05	0.127398316	47.12		5.48E+04	1466	80329310.68	0.193273129	47.12		5.48E+04	1508	82630696.12	0.138831545	47.12
6.90E+04	384	26489349.55	0.128844835	50.88		6.90E+04	1100	75880949.24	0.182570326	50.88		6.90E+04	1206	83193113.44	0.139776487	50.88
8.68E+04	281	24403178.12	0.118697647	54.94		8.68E+04	831	72167405.75	0.173635503	54.94		8.68E+04	836	72601626	0.121981253	54.94
1.09E+05	222	24271300.34	0.11805619	59.33		1.09E+05	665	72704570.84	0.174927928	59.33		1.09E+05	697	76203136.65	0.128032313	59.33
1.38E+05	149	20508143.06	0.099752103	64.06		1.38E+05	522	71847319.99	0.172865374	64.06		1.38E+05	510	70195657.46	0.117938878	64.06
1.73E+05	119	20619922.63	0.100295801	69.17		1.73E+05	340	58914064.65	0.141747831	69.17		1.73E+05	359	62206321.2	0.104515635	69.17
2.18E+05	100	21814239.15	0.106104985	74.69		2.18E+05	287	62606866.35	0.150632749	74.69		2.18E+05	271	59116588.09	0.099324435	74.69
2.75E+05	91	24990875	0.121556219	80.65		2.75E+05	206	56572750	0.136114605	80.65		2.75E+05	188	51629500	0.086745042	80.65
3.46E+05	43	14866492.82	0.07231098	87.08		3.46E+05	148	51168393.9	0.12311167	87.08		3.46E+05	147	50822661.51	0.085389437	87.08
4.35E+05	43	18715805.6	0.09103413	94.03		4.35E+05	100	43525129.3	0.104721898	94.03		4.35E+05	127	55276914.21	0.092873227	94.03
5.48E+05	43	23561803.27	0.114605179	101.53		5.48E+05	80	43835913.06	0.105469647	101.53		5.48E+05	100	54794891.32	0.092063359	101.53
6.90E+05	34	23454111.58	0.114081364	109.63		6.90E+05	59	40699781.86	0.097924084	109.63		6.90E+05	66	45528569.54	0.076494595	109.63
8.68E+05	15	13026607.54	0.063361733	118.37		8.68E+05	58	50369549.14	0.121189641	118.37		8.68E+05	58	50369549.14	0.084628142	118.37
1.09E+06	23	25145941.79	0.122310467	127.81		1.09E+06	37	40452167.23	0.097328321	127.81		1.09E+06	38	41545469.05	0.069802409	127.81
1.38E+06	16	22022167.05	0.107116352	138.01		1.38E+06	26	35786021.45	0.086101527	138.01		1.38E+06	20	27527708.81	0.04625054	138.01
1.73E+06	14	24258732.5	0.11799506	149.02		1.73E+06	13	22525965.89	0.0541977	149.02		1.73E+06	26	45051931.79	0.075693775	149.02
2.18E+06	9	19632815.23	0.095494487	160.91		2.18E+06	11	23995663.06	0.057733806	160.91		2.18E+06	9	19632815.23	0.032985975	160.91
2.75E+06	5	13731250	0.066789131	173.75		2.75E+06	8	21970000	0.052860041	173.75		2.75E+06	13	35701250	0.059983274	173.75
3.46E+06	5	17286619.56	0.084082535	187.61		3.46E+06	2	6914647.824	0.016636712	187.61		3.46E+06	9	31115915.21	0.052279247	187.61
4.35E+06	3	13057538.79	0.063512184	202.57		4.35E+06	5	21762564.65	0.052360949	202.57		4.35E+06	10	43525129.3	0.073128525	202.57
5.48E+06	3	16438467.4	0.079957102	218.73		5.48E+06	4	21917956.53	0.052734824	218.73		5.48E+06	11	60274380.46	0.101269694	218.73
6.90E+06	2	13796536.23	0.067106685	236.18		6.90E+06	0	0	0	236.18		6.90E+06	3	20694804.34	0.03477027	236.18
8.68E+06	2	17368810.05	0.084482311	255.02		8.68E+06	5	43422025.12	0.104473829	255.02		8.68E+06	4	34737620.1	0.058364236	255.02
1.09E+07	2	21866036.34	0.106356928	275.37		1.09E+07	2	21866036.34	0.052609903	275.37		1.09E+07	5	54665090.86	0.091845275	275.37
1.38E+07	0	0	0	297.34		1.38E+07	1	13763854.4	0.033115972	297.34		1.38E+07	3	41291563.21	0.06937581	297.34
1.73E+07	4	69310664.29	0.337128743	321.06		1.73E+07	0	0	0	321.06		1.73E+07	5	86638330.36	0.145564951	321.06
2.18E+07	0	0	0	346.67		2.18E+07	1	21814239.15	0.052485279	346.67		2.18E+07	2	43628478.29	0.073302166	346.67
2.75E+07	0	0	0	374.32		2.75E+07	0	0	0	374.32		2.75E+07	2	54925000	0.09228196	374.32
3.46E+07	0	0	0	404.19		3.46E+07	0	0	0	404.19		3.46E+07	1	34573239.12	0.058088052	404.19
4.35E+07	1	43525129.3	0.211707279	436.43		4.35E+07	0	0	0	436.43		4.35E+07				436.43
5.48E+07				471.25		5.48E+07	1	54794891.32	0.131837059	471.25		5.48E+07				471.25
6.90E+07				508.84		6.90E+07				508.84		6.90E+07				508.84
8.68E+07				549.43		8.68E+07				549.43		8.68E+07				549.43
1.09E+08				593.26		1.09E+08				593.26		1.09E+08				593.26
1.38E+08				640.59		1.38E+08				640.59		1.38E+08				640.59
1.73E+08				691.69		1.73E+08				691.69		1.73E+08				691.69

Poto.l upper						**Poto.m**						**Poto.o**				
Volume bins in um	Frequency	Average volume of bin	volume fraction %	eqD (um)		Volume bins in um	Frequency	Average volume of bin	volume fraction %	eqD (um)		Volume bins in um	Frequency	Average volume of bin	volume fraction %	eqD (um)
2.75E+02	262070	71970973.75	0.168787599	8.06		2.75E+02	459517	126194856.1	0.30431356	8.06		2.75E+02	303708	83405809.5	0.235706021	8.06
3.46E+02	0	0	0	8.71		3.46E+02	0	0	0	8.71		3.46E+02	0	0	0	8.71
4.35E+02	0	0	0	9.40		4.35E+02	0	0	0	9.40		4.35E+02	0	0	0	9.40
5.48E+02	0	0	0	10.15		5.48E+02	0	0	0	10.15		5.48E+02	0	0	0	10.15
6.90E+02	50163	34603782.33	0.081153402	10.96		6.90E+02	70949	48942522.43	0.118022824	10.96		6.90E+02	64320	44369660.5	0.125389301	10.96
8.68E+02	21863	18986714.7	0.044527979	11.84		8.68E+02	28719	24940742.79	0.060143547	11.84		8.68E+02	27757	24105303.03	0.068121934	11.84
1.09E+03	0	0	0	12.78		1.09E+03	0	0	0	12.78		1.09E+03	0	0	0	12.78
1.38E+03	22029	30320394.87	0.071107926	13.80		1.38E+03	26790	36873365.95	0.088918563	13.80		1.38E+03	27837	38314441.5	0.108277164	13.80
1.73E+03	6660	11540225.6	0.027064341	14.90		1.73E+03	7962	13796287.73	0.033269165	14.90		1.73E+03	8640	14971103.49	0.042308554	14.90
2.18E+03	5557	12122172.69	0.028429134	16.09		2.18E+03	6279	13697160.76	0.033030124	16.09		2.18E+03	6917	15088909.22	0.042641475	16.09
2.75E+03	11754	32279422.5	0.075702272	17.37		2.75E+03	13182	36201067.5	0.087297344	17.37		2.75E+03	14858	40803782.5	0.115312078	17.37
3.46E+03	5407	18693750.39	0.043840914	18.76		3.46E+03	6051	20920266.99	0.050448339	18.76		3.46E+03	6887	23810589.78	0.06728907	18.76
4.35E+03	6156	26794069.6	0.062837925	20.26		4.35E+03	6789	29549210.28	0.071256671	20.26		4.35E+03	7879	34293449.37	0.096913783	20.26
5.48E+03	5883	32235834.57	0.075600049	21.87		5.48E+03	6549	35885174.33	0.086535581	21.87		5.48E+03	7453	40838632.5	0.115410565	21.87
6.90E+03	6113	42169112.97	0.098895749	23.62		6.90E+03	6762	46646088.98	0.112485071	23.62		6.90E+03	7601	52433735.92	0.148178494	23.62
8.68E+03	4226	36700295.63	0.086070182	25.50		8.68E+03	4735	41120657.79	0.099160728	25.50		8.68E+03	5279	45844974.12	0.129558558	25.50
1.09E+04	4039	44158460.39	0.103561201	27.54		1.09E+04	4554	49788964.75	0.120063984	27.54		1.09E+04	4979	54435497.48	0.153835501	27.54
1.38E+04	3812	52467812.99	0.123048442	29.73		1.38E+04	4323	59501142.59	0.14348449	29.73		1.38E+04	4408	60671070.21	0.17145732	29.73
1.73E+04	2979	51619117.23	0.121058066	32.11		1.73E+04	3531	61183988.9	0.147542603	32.11		1.73E+04	3499	60629503.59	0.17139852	32.11
2.18E+04	2587	56433436.67	0.132348693	34.67		2.18E+04	3044	66402543.96	0.160126927	34.67		2.18E+04	2905	63370364.72	0.179085565	34.67
2.75E+04	2274	62449725	0.146458198	37.43		2.75E+04	2776	76235900	0.18383965	37.43		2.75E+04	2399	65882537.5	0.186185001	37.43
3.46E+04	1793	61989817.74	0.145379616	40.42		3.46E+04	2167	74920209.18	0.180666917	40.42		3.46E+04	1856	64167931.81	0.181339501	40.42
4.35E+04	1604	69814307.39	0.163729747	43.64		4.35E+04	2058	89574716.1	0.216005641	43.64		4.35E+04	1491	64895967.78	0.183396941	43.64
5.48E+04	1343	73589539.05	0.172583487	47.12		5.48E+04	1692	92712956.12	0.223573374	47.12		5.48E+04	1194	65425100.24	0.184892277	47.12
6.90E+04	1157	79812962.06	0.187178769	50.88		6.90E+04	1368	94368307.78	0.227565185	50.88		6.90E+04	940	64843720.26	0.183249289	50.88
8.68E+04	927	80504434.57	0.188800422	54.94		8.68E+04	1080	93791574.26	0.226174416	54.94		8.68E+04	681	59140798.22	0.167132749	54.94
1.09E+05	788	86152183.19	0.202045622	59.33		1.09E+05	897	98069173	0.236489665	59.33		1.09E+05	534	58382317.03	0.16498927	59.33
1.38E+05	643	88501583.81	0.207555478	64.06		1.38E+05	788	108459172.7	0.26154471	64.06		1.38E+05	415	57119995.77	0.161421932	64.06
1.73E+05	484	83865903.79	0.196683799	69.17		1.73E+05	596	103272889.8	0.249038208	69.17		1.73E+05	311	53889041.49	0.152291209	69.17
2.18E+05	426	92928658.76	0.217937932	74.69		2.18E+05	489	106671629.4	0.257234125	74.69		2.18E+05	233	50827177.21	0.143638336	74.69
2.75E+05	295	81014375	0.189996343	80.65		2.75E+05	422	115891750	0.279468055	80.65		2.75E+05	187	51354875	0.145129618	80.65
3.46E+05	236	81592844.33	0.19135298	87.08		3.46E+05	284	98187999.1	0.236776209	87.08		3.46E+05	135	46673872.81	0.131901038	87.08
4.35E+05	174	75733724.98	0.17761207	94.03		4.35E+05	255	110989079.7	0.267645473	94.03		4.35E+05	94	40913621.54	0.115622485	94.03
5.48E+05	151	82740285.9	0.19404398	101.53		5.48E+05	175	95891059.82	0.231237237	101.53		5.48E+05	82	44931810.89	0.126977946	101.53
6.90E+05	108	74501295.62	0.174721755	109.63		6.90E+05	143	98645234.01	0.237878811	109.63		6.90E+05	53	36560821	0.103321408	109.63
8.68E+05	83	72080561.7	0.169044607	118.37		8.68E+05	101	87712490.74	0.211514963	118.37		8.68E+05	38	33000739.09	0.093260565	118.37
1.09E+06	62	67784712.66	0.158969906	127.81		1.09E+06	91	99490465.36	0.239917051	127.81		1.09E+06	37	40452167.23	0.114318408	127.81
1.38E+06	48	66066501.14	0.154940326	138.01		1.38E+06	71	97723366.26	0.235655766	138.01		1.38E+06	27	37162406.89	0.105021498	138.01
1.73E+06	44	76241730.72	0.178803454	149.02		1.73E+06	51	88371096.97	0.213103164	149.02		1.73E+06	17	29457032.32	0.083245998	149.02
2.18E+06	27	58898445.69	0.138129675	160.91		2.18E+06	26	56717021.78	0.1367707	160.91		2.18E+06	11	23995663.06	0.06781209	160.91
2.75E+06	30	82387500	0.19321662	173.75		2.75E+06	28	76895000	0.185429042	173.75		2.75E+06	8	21970000	0.062087537	173.75
3.46E+06	12	41487886.95	0.097298125	187.61		3.46E+06	23	79518449.98	0.19175538	187.61		3.46E+06	8	27658591.3	0.078163578	187.61
4.35E+06	13	56582668.09	0.132698673	202.57		4.35E+06	9	39172616.37	0.094463108	202.57		4.35E+06	7	30467590.51	0.08610185	202.57
5.48E+06	7	38356423.93	0.089954163	218.73		5.48E+06	13	71233358.72	0.171776233	218.73		5.48E+06	7	38356423.93	0.108395807	218.73
6.90E+06	7	48287876.79	0.113245582	236.18		6.90E+06	8	55186144.9	0.133079055	236.18		6.90E+06	2	13796536.23	0.03898921	236.18
8.68E+06	1	8684405.024	0.02036682	255.02		8.68E+06	4	34737620.1	0.083768302	255.02		8.68E+06	4	34737620.1	0.098169016	255.02
1.09E+07	2	21866036.34	0.051280615	275.37		1.09E+07	3	32799054.51	0.079093533	275.37		1.09E+07	1	10933018.17	0.030896867	275.37
1.38E+07	3	41291563.21	0.096837703	297.34		1.38E+07	0	0	0	297.34		1.38E+07	2	27527708.81	0.077793702	297.34
1.73E+07	2	34655332.15	0.081274297	321.06		1.73E+07	2	34655332.15	0.083569868	321.06		1.73E+07	1	17327666.07	0.048968234	321.06
2.18E+07	3	65442717.44	0.153477417	346.67		2.18E+07				346.67		2.18E+07	2	43628478.29	0.123294709	346.67
2.75E+07	0	0	0	374.32		2.75E+07				374.32		2.75E+07	2	54925000	0.155218842	374.32
3.46E+07	2	69146478.24	0.162163542	404.19		3.46E+07				404.19		3.46E+07	2	69146478.24	0.195408945	404.19
4.35E+07				436.43		4.35E+07				436.43		4.35E+07	0	0	0	436.43
5.48E+07				471.25		5.48E+07				471.25		5.48E+07	0	0	0	471.25
6.90E+07				508.84		6.90E+07				508.84		6.90E+07	0	0	0	508.84
8.68E+07				549.43		8.68E+07				549.43		8.68E+07	1	86844050.24	0.245422539	549.43
1.09E+08				593.26		1.09E+08				593.26		1.09E+08				593.26
1.38E+08				640.59		1.38E+08				640.59		1.38E+08				640.59
1.73E+08				691.69		1.73E+08				691.69		1.73E+08				691.69

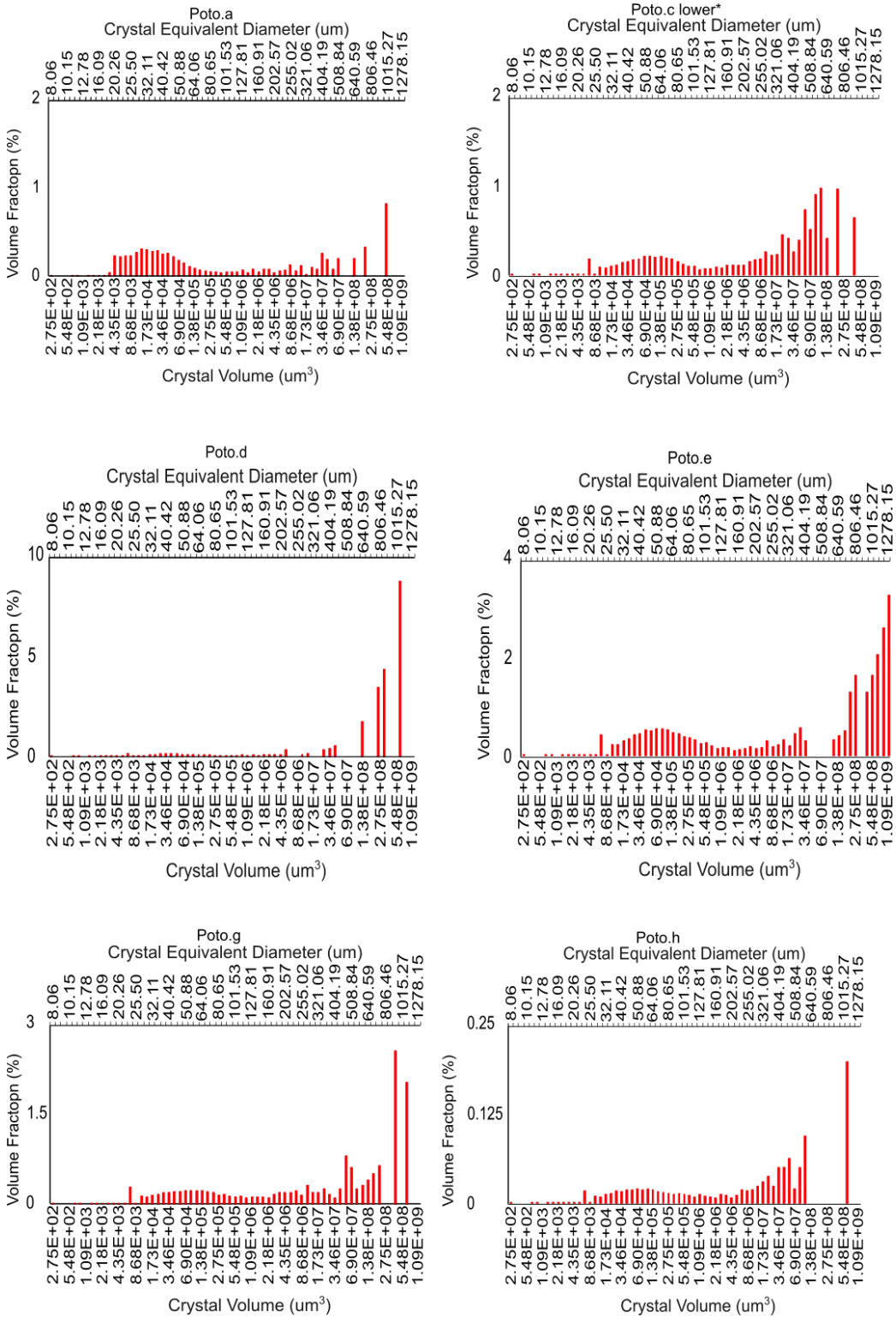
Paetahi.a lower						**Paetahi.a middle**						**Paetahi.a upper**				
Volume bins in um	Frequency	Average volume of bin	volume fraction %	eqD		Volume bins in um	Frequency	Average volume of bin	volume fraction %	eqD (um)		Volume bins in um	Frequency	Average volume of bin	volume fraction %	eqD (um)
2.75E+02	682289	187373616.6	0.280815434	8.06		2.75E+02	355970	97758261.25	0.265085729	8.06		2.75E+02	399787	109791504.9	0.219418114	8.06
3.46E+02	0	0	0	8.71		3.46E+02	0	0	0	8.71		3.46E+02	0	0	0	8.71
4.35E+02	0	0	0	9.40		4.35E+02	0	0	0	9.40		4.35E+02	0	0	0	9.40
5.48E+02	0	0	0	10.15		5.48E+02	0	0	0	10.15		5.48E+02	0	0	0	10.15
6.90E+02	110010	75887847.51	0.113732548	10.96		6.90E+02	65738	45347834.92	0.122967243	10.96		6.90E+02	85452	58947080.68	0.117805629	10.96
8.68E+02	44112	38308647.44	0.057412883	11.84		8.68E+02	27877	24209515.89	0.06564762	11.84		8.68E+02	37297	32390225.42	0.064731804	11.84
1.09E+03	0	0	0	12.78		1.09E+03	0	0	0	12.78		1.09E+03	0	0	0	12.78
1.38E+03	40989	56416662.81	0.084551229	13.80		1.38E+03	26671	36709576.08	0.099543349	13.80		1.38E+03	37922	52195288.67	0.104312185	13.80
1.73E+03	11908	20633784.76	0.030923698	14.90		1.73E+03	8280	14347307.51	0.038904809	14.90		1.73E+03	12223	21179606.24	0.042327403	14.90
2.18E+03	9445	20603548.87	0.030878384	16.09		2.18E+03	6545	14277419.52	0.038715297	16.09		2.18E+03	9638	21024563.69	0.042017551	16.09
2.75E+03	19722	54161542.5	0.081171497	17.37		2.75E+03	13506	37090852.5	0.100577236	17.37		2.75E+03	20887	57360923.75	0.114635697	17.37
3.46E+03	9117	31520422.11	0.04723942	18.76		3.46E+03	6241	21577158.54	0.0585096	18.76		3.46E+03	10058	34773763.91	0.069495301	18.76
4.35E+03	10241	44574084.91	0.066802847	20.26		4.35E+03	7040	30641691.03	0.083089397	20.26		4.35E+03	11511	50101776.33	0.100128305	20.26
5.48E+03	9527	52203092.97	0.078236384	21.87		5.48E+03	6627	36312574.48	0.098466822	21.87		5.48E+03	10785	59096290.29	0.118103824	21.87
6.90E+03	9901	68299752.58	0.102360327	23.62		6.90E+03	6551	45190554.41	0.122540754	23.62		6.90E+03	11439	78909288.94	0.157700064	23.62
8.68E+03	6778	58862897.25	0.088217383	25.50		8.68E+03	4465	38775868.43	0.105146401	25.50		8.68E+03	8069	70074464.14	0.140043683	25.50
1.09E+04	6361	69544928.59	0.104226463	27.54		1.09E+04	4183	45732815.01	0.124011173	27.54		1.09E+04	7453	81483784.43	0.162845188	27.54
1.38E+04	5867	80752533.79	0.121023217	29.73		1.38E+04	3938	54202058.64	0.146976757	29.73		1.38E+04	7132	98163809.61	0.196180187	29.73
1.73E+04	4784	82895554.49	0.124234946	32.11		1.73E+04	2911	50440835.94	0.136777655	32.11		1.73E+04	5624	97450793.99	0.194755226	32.11
2.18E+04	3971	86624343.65	0.129823254	34.67		2.18E+04	2410	52572316.34	0.142557474	34.67		2.18E+04	4736	103312236.6	0.206469308	34.67
2.75E+04	3391	93125337.5	0.139566245	37.43		2.75E+04	2126	58385275	0.158320156	37.43		2.75E+04	4112	112925800	0.225681997	37.43
3.46E+04	2805	96977935.74	0.145340105	40.42		3.46E+04	1572	54349131.9	0.147375568	40.42		3.46E+04	3153	109009422.9	0.217855124	40.42
4.35E+04	2312	100630098.9	0.150813574	43.64		4.35E+04	1282	55799215.76	0.151307681	43.64		4.35E+04	2704	117691949.6	0.235207137	43.64
5.48E+04	1856	101699318.3	0.152416005	47.12		5.48E+04	1043	57151071.65	0.154973434	47.12		5.48E+04	2196	120329581.3	0.240478439	47.12
6.90E+04	1531	105612484.8	0.158280639	50.88		6.90E+04	806	55600040.99	0.150767589	50.88		6.90E+04	1819	125479497	0.250770536	50.88
8.68E+04	1177	102215447.1	0.153189524	54.94		8.68E+04	620	53843311.15	0.146003961	54.94		8.68E+04	1423	123579083.5	0.246972563	54.94
1.09E+05	921	100693097.4	0.15090799	59.33		1.09E+05	497	54337100.31	0.147342942	59.33		1.09E+05	1037	113375398.4	0.226580518	59.33
1.38E+05	731	100613775.7	0.150789111	64.06		1.38E+05	329	45283080.99	0.122791653	64.06		1.38E+05	841	115754015.5	0.23133418	64.06
1.73E+05	506	87677990.33	0.131402346	69.17		1.73E+05	276	47824358.36	0.129682696	69.17		1.73E+05	673	116615192.7	0.233055241	69.17
2.18E+05	400	87256956.58	0.130771346	74.69		2.18E+05	217	47336898.95	0.128360879	74.69		2.18E+05	498	108634910.9	0.217106663	74.69
2.75E+05	320	87880000	0.131705097	80.65		2.75E+05	166	45587750	0.123617808	80.65		2.75E+05	386	106005250	0.21185129	80.65
3.46E+05	205	70875140.2	0.106220041	87.08		3.46E+05	136	47019605.21	0.127500491	87.08		3.46E+05	295	101991055.4	0.20382893	87.08
4.35E+05	186	80956740.49	0.12132926	94.03		4.35E+05	99	43089878	0.116844465	94.03		4.35E+05	230	100107797.4	0.200065243	94.03
5.48E+05	113	61918227.2	0.092796383	101.53		5.48E+05	77	42192066.32	0.114409918	101.53		5.48E+05	163	89315672.86	0.178497202	101.53
6.90E+05	70	48287876.79	0.072368679	109.63		6.90E+05	55	37940474.62	0.102881109	109.63		6.90E+05	152	104853675.3	0.209549871	109.63
8.68E+05	55	47764227.63	0.07158389	118.37		8.68E+05	48	41685144.12	0.113035325	118.37		8.68E+05	108	93791574.26	0.187442283	118.37
1.09E+06	46	50291883.59	0.075372069	127.81		1.09E+06	33	36078959.97	0.097833342	127.81		1.09E+06	84	91837352.64	0.183536775	127.81
1.38E+06	33	45420719.53	0.068071692	138.01		1.38E+06	25	34409636.01	0.093306728	138.01		1.38E+06	59	81206740.98	0.162291517	138.01
1.73E+06	17	29457032.32	0.044147033	149.02		1.73E+06	22	38120865.36	0.103370265	149.02		1.73E+06	50	86638330.36	0.173146538	149.02
2.18E+06	9	19632815.23	0.029423553	160.91		2.18E+06	12	26177086.98	0.070982975	160.91		2.18E+06	29	63261293.52	0.126427575	160.91
2.75E+06	6	16477500	0.024694706	173.75		2.75E+06	10	27462500	0.074468559	173.75		2.75E+06	26	71402500	0.14269776	173.75
3.46E+06	4	13829295.65	0.020725862	187.61		3.46E+06	11	38030563.03	0.103125397	187.61		3.46E+06	21	72603802.15	0.145098561	187.61
4.35E+06	1	4352512.93	0.006523078	202.57		4.35E+06	4	17410051.72	0.047209885	202.57		4.35E+06	13	56582668.09	0.113080355	202.57
5.48E+06	2	10958978.26	0.016424139	218.73		5.48E+06	7	38356423.93	0.104009016	218.73		5.48E+06	15	82192336.99	0.164261229	218.73
6.90E+06	0	0	0	236.18		6.90E+06	1	6898268.113	0.018705656	236.18		6.90E+06	13	89677485.46	0.179220284	236.18
8.68E+06	1	8684405.024	0.013015253	255.02		8.68E+06	3	26053215.07	0.070647078	255.02		8.68E+06	7	60790835.17	0.121490368	255.02
1.09E+07	0	0	0	275.37		1.09E+07	1	10933018.17	0.029646467	275.37		1.09E+07	5	54665090.86	0.10924808	275.37
1.38E+07	1	13763854.4	0.020627785	297.34		1.38E+07	0	0	0	297.34		1.38E+07	0	0	0	297.34
1.73E+07				321.06		1.73E+07	2	34655332.15	0.093972968	321.06		1.73E+07	4	69310664.29	0.138517231	321.06
2.18E+07				346.67		2.18E+07	0	0	0	346.67		2.18E+07	4	87256956.58	0.174382862	346.67
2.75E+07				374.32		2.75E+07	0	0	0	374.32		2.75E+07	2	54925000	0.109767508	374.32
3.46E+07				404.19		3.46E+07	1	34573239.12	0.093750361	404.19		3.46E+07	1	34573239.12	0.069094553	404.19
4.35E+07				436.43		4.35E+07	1	43525129.3	0.118024712	436.43		4.35E+07	3	130575387.9	0.260954664	436.43
5.48E+07				471.25		5.48E+07	0	0	0	471.25		5.48E+07	2	109589782.6	0.219014972	471.25
6.90E+07				508.84		6.90E+07	0	0	0	508.84		6.90E+07	0	0	0	508.84
8.68E+07				549.43		8.68E+07	0	0	0	549.43		8.68E+07	1	86844050.24	0.173557669	549.43
1.09E+08				593.26		1.09E+08	0	0	0	593.26		1.09E+08				593.26
1.38E+08				640.59		1.38E+08	0	0	0	640.59		1.38E+08				640.59
1.73E+08				691.69		1.73E+08	1	173276660.7	0.469864841	691.69		1.73E+08				691.69

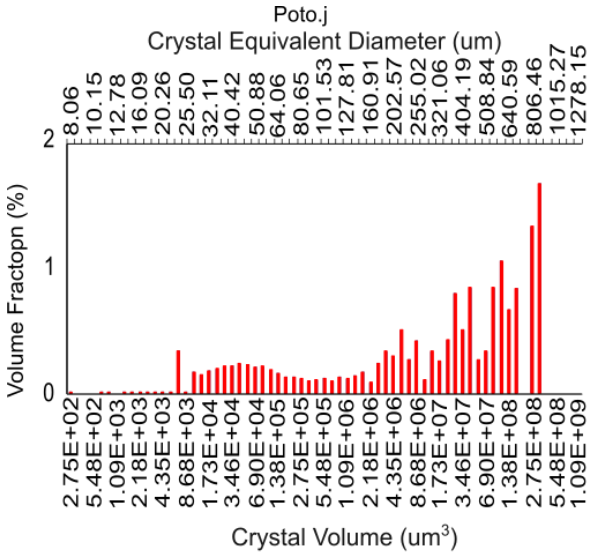
Paetahi.d						**Paetahi.e lower**				
Volume bins in um	Frequency	Average volume of bin	volume fraction %	eqD (um)		Volume bins in um	Frequency	Average volume of bin	volume fraction %	eqD (um)
2.75E+02	173468	47638649.5	0.159604383	8.06		2.75E+02	367330	100878001.3	0.210918141	8.06
3.46E+02	0	0	0	8.71		3.46E+02	0	0	0	8.71
4.35E+02	0	0	0	9.40		4.35E+02	0	0	0	9.40
5.48E+02	0	0	0	10.15		5.48E+02	0	0	0	10.15
6.90E+02	39093	26967399.53	0.090349227	10.96		6.90E+02	72940	50315967.61	0.10520183	10.96
8.68E+02	17880	15527716.18	0.052022708	11.84		8.68E+02	32940	28606430.15	0.059811009	11.84
1.09E+03	0	0	0	12.78		1.09E+03	0	0	0	12.78
1.38E+03	18558	25542961	0.085576913	13.80		1.38E+03	33379	45942369.61	0.096057407	13.80
1.73E+03	6156	10666911.23	0.035737491	14.90		1.73E+03	10291	17831901.16	0.037283366	14.90
2.18E+03	4871	10625715.89	0.035599473	16.09		2.18E+03	8102	17673896.56	0.036953006	16.09
2.75E+03	10519	28887803.75	0.096783182	17.37		2.75E+03	17130	47043262.5	0.09835918	17.37
3.46E+03	4939	17075722.8	0.057209015	18.76		3.46E+03	7678	26545333	0.055501618	18.76
4.35E+03	5645	24569935.49	0.082316973	20.26		4.35E+03	8458	36813554.36	0.076970661	20.26
5.48E+03	5457	29901572.2	0.100179624	21.87		5.48E+03	7682	42093435.52	0.088009963	21.87
6.90E+03	5662	39057994.05	0.130856503	23.62		6.90E+03	7531	51950857.16	0.108620096	23.62
8.68E+03	3977	34537878.78	0.115712702	25.50		8.68E+03	4882	42397265.33	0.088645218	25.50
1.09E+04	3658	39992980.47	0.133989	27.54		1.09E+04	4211	46038939.52	0.096259317	27.54
1.38E+04	3577	49233307.2	0.164946986	29.73		1.38E+04	3600	49549875.85	0.103600067	29.73
1.73E+04	2716	47061941.05	0.15767223	32.11		1.73E+04	2626	45502451.11	0.095137615	32.11
2.18E+04	2367	51634304.06	0.172991077	34.67		2.18E+04	1983	43257636.23	0.090444102	34.67
2.75E+04	2123	58302887.5	0.195332918	37.43		2.75E+04	1577	43308362.5	0.090550162	37.43
3.46E+04	1688	58359627.64	0.195523015	40.42		3.46E+04	1074	37131658.82	0.077635762	40.42
4.35E+04	1453	63242012.87	0.211880533	43.64		4.35E+04	828	36038807.06	0.075350801	43.64
5.48E+04	1198	65644279.81	0.219928879	47.12		5.48E+04	562	30794728.92	0.064386357	47.12
6.90E+04	951	65602529.75	0.219789004	50.88		6.90E+04	501	34560323.24	0.072259552	50.88
8.68E+04	791	68693643.74	0.230145203	54.94		8.68E+04	312	27095343.68	0.056651594	54.94
1.09E+05	617	67456722.12	0.226001128	59.33		1.09E+05	243	26567234.16	0.055547409	59.33
1.38E+05	472	64965392.78	0.217654395	64.06		1.38E+05	173	23811468.12	0.049785588	64.06
1.73E+05	405	70177047.59	0.23511507	69.17		1.73E+05	133	23045795.88	0.048184702	69.17
2.18E+05	295	64352005.48	0.215599356	74.69		2.18E+05	87	18978388.06	0.039680468	74.69
2.75E+05	247	67832375	0.227259683	80.65		2.75E+05	56	15379000	0.032154782	80.65
3.46E+05	202	69837943.03	0.233978964	87.08		3.46E+05	41	14175028.04	0.029637488	87.08
4.35E+05	166	72251714.63	0.242065854	94.03		4.35E+05	43	18715805.6	0.039131455	94.03
5.48E+05	117	64110022.85	0.214788639	101.53		5.48E+05	31	16986416.31	0.035515606	101.53
6.90E+05	99	68292854.31	0.228802433	109.63		6.90E+05	27	18625323.9	0.038942273	109.63
8.68E+05	63	54711751.65	0.183301489	118.37		8.68E+05	21	18237250.55	0.03813088	118.37
1.09E+06	59	64504807.21	0.21611129	127.81		1.09E+06	17	18586130.89	0.038860328	127.81
1.38E+06	34	46797104.97	0.156784946	138.01		1.38E+06	12	16516625.28	0.034533356	138.01
1.73E+06	25	43319165.18	0.145132759	149.02		1.73E+06	12	20793199.29	0.043474919	149.02
2.18E+06	16	34902782.63	0.116935244	160.91		2.18E+06	12	26177086.98	0.05473168	160.91
2.75E+06	10	27462500	0.092007969	173.75		2.75E+06	7	19223750	0.040193477	173.75
3.46E+06	15	51859858.68	0.173746755	187.61		3.46E+06	3	10371971.74	0.021685967	187.61
4.35E+06	10	43525129.3	0.145822803	202.57		4.35E+06	2	8705025.86	0.018200677	202.57
5.48E+06	5	27397445.66	0.091790016	218.73		5.48E+06	1	5479489.132	0.011456647	218.73
6.90E+06	6	41389608.68	0.138668141	236.18		6.90E+06	3	20694804.34	0.043269193	236.18
8.68E+06	2	17368810.05	0.058190949	255.02		8.68E+06	1	8684405.024	0.018157562	255.02
1.09E+07	1	10933018.17	0.036629032	275.37		1.09E+07	1	10933018.17	0.022859016	275.37
1.38E+07	3	41291563.21	0.138339658	297.34		1.38E+07	1	13763854.4	0.028777796	297.34
1.73E+07	1	17327666.07	0.058053104	321.06		1.73E+07	3	51982998.22	0.108687298	321.06
2.18E+07	3	65442717.44	0.219253582	346.67		2.18E+07	0	0	0	346.67
2.75E+07	0	0	0	374.32		2.75E+07	1	27462500	0.057419253	374.32
3.46E+07	2	69146478.24	0.23166234	404.19		3.46E+07	4	138292956.5	0.289146226	404.19
4.35E+07	1	43525129.3	0.145822803	436.43		4.35E+07	1	43525129.3	0.091003383	436.43
5.48E+07	1	54794891.32	0.183580033	471.25		5.48E+07	2	109589782.6	0.229132942	471.25
6.90E+07	0	0	0	508.84		6.90E+07	2	137965362.3	0.288461284	508.84
8.68E+07	0	0	0	549.43		8.68E+07				549.43
1.09E+08	1	109330181.7	0.366290321	593.26		1.09E+08				593.26
1.38E+08				640.59		1.38E+08				640.59
1.73E+08				691.69		1.73E+08				691.69

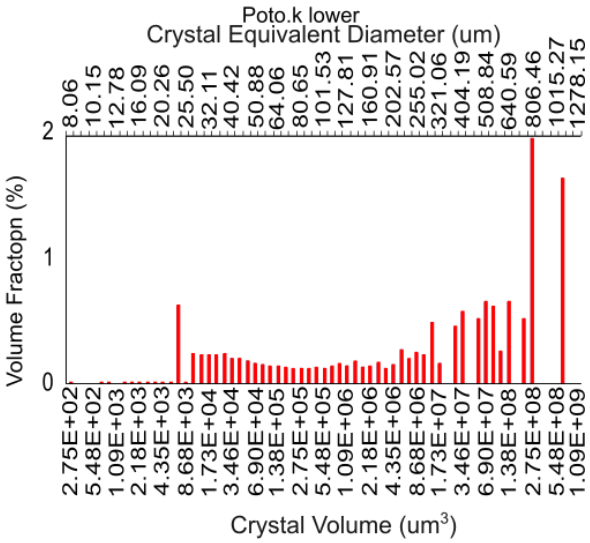
Paetahi.e middle						**Paetahi.f**				
Volume bins in um	Frequency	Average volume of bin	volume fraction %	eqD (um)		Volume bins in um	Frequency	Average volume of bin	volume fraction %	eqD (um)
2.75E+02	579562	159162214.3	0.218636894	8.06		2.75E+02	125096	34354489	0.13610218	8.06
3.46E+02	0	0	0	8.71		3.46E+02	0	0	0	8.71
4.35E+02	0	0	0	9.40		4.35E+02	0	0	0	9.40
5.48E+02	0	0	0	10.15		5.48E+02	0	0	0	10.15
6.90E+02	106619	73548644.79	0.101031814	10.96		6.90E+02	28313	19531066.51	0.077376227	10.96
8.68E+02	44817	38920898	0.053464601	11.84		8.68E+02	12707	11035273.46	0.043718443	11.84
1.09E+03	0	0	0	12.78		1.09E+03	0	0	0	12.78
1.38E+03	44255	60911937.66	0.083673106	13.80		1.38E+03	12766	17570936.53	0.06961078	13.80
1.73E+03	13706	23749299.12	0.03262378	14.90		1.73E+03	3899	6756057.002	0.026765471	14.90
2.18E+03	10676	23288881.71	0.031991316	16.09		2.18E+03	3098	6758051.287	0.026773372	16.09
2.75E+03	23004	63174735	0.086781451	17.37		2.75E+03	6654	18273547.5	0.072394314	17.37
3.46E+03	10799	37335640.93	0.051286975	18.76		3.46E+03	2896	10012410.05	0.039666165	18.76
4.35E+03	12343	53723067.09	0.073797946	20.26		4.35E+03	3411	14846421.6	0.058817069	20.26
5.48E+03	11873	65057974.47	0.089368406	21.87		5.48E+03	3164	17337103.62	0.068684404	21.87
6.90E+03	12503	86249046.21	0.118478017	23.62		6.90E+03	3257	22467659.24	0.089010127	23.62
8.68E+03	8645	75076681.43	0.103130837	25.50		8.68E+03	2129	18489098.3	0.073248261	25.50
1.09E+04	8467	92569864.86	0.127160757	27.54		1.09E+04	1893	20696203.4	0.08199215	27.54
1.38E+04	8134	111955191.7	0.153789864	29.73		1.38E+04	1821	25063978.87	0.099295966	29.73
1.73E+04	6679	115731481.7	0.158977253	32.11		1.73E+04	1431	24795890.15	0.098233879	32.11
2.18E+04	5635	122923237.6	0.168856377	34.67		2.18E+04	1122	24475576.32	0.096964892	34.67
2.75E+04	5184	142365600	0.195563832	37.43		2.75E+04	1003	27544887.5	0.109124582	37.43
3.46E+04	4206	145415043.7	0.199752772	40.42		3.46E+04	718	24823585.69	0.0983436	40.42
4.35E+04	3760	163654486.2	0.224807808	43.64		4.35E+04	651	28334859.17	0.112254213	43.64
5.48E+04	3112	170521701.8	0.234241119	47.12		5.48E+04	496	27178266.1	0.107672138	47.12
6.90E+04	2677	184666637.4	0.25367164	50.88		6.90E+04	388	26765280.28	0.106036012	50.88
8.68E+04	2193	190449002.2	0.261614721	54.94		8.68E+04	322	27963784.18	0.110784125	54.94
1.09E+05	1748	191109157.6	0.262521559	59.33		1.09E+05	253	27660535.97	0.109582746	59.33
1.38E+05	1438	197924226.3	0.271883237	64.06		1.38E+05	180	24774937.93	0.098150873	64.06
1.73E+05	1088	188525006.9	0.25897178	69.17		1.73E+05	151	26164775.77	0.103656993	69.17
2.18E+05	872	190220165.4	0.261300374	74.69		2.18E+05	121	26395229.37	0.104569981	74.69
2.75E+05	673	184822625	0.253885916	80.65		2.75E+05	88	24167000	0.095742405	80.65
3.46E+05	573	198104660.2	0.272131094	87.08		3.46E+05	54	18669549.13	0.073963154	87.08
4.35E+05	439	191075317.6	0.262475074	94.03		4.35E+05	36	15669046.55	0.062076062	94.03
5.48E+05	316	173151856.6	0.237854093	101.53		5.48E+05	52	28493343.49	0.11288208	101.53
6.90E+05	226	155900859.3	0.214156857	109.63		6.90E+05	43	29662552.88	0.117514137	109.63
8.68E+05	185	160661492.9	0.220696413	118.37		8.68E+05	24	20842572.06	0.082572019	118.37
1.09E+06	124	135569425.3	0.186228108	127.81		1.09E+06	25	27332545.43	0.108283346	127.81
1.38E+06	106	145896856.7	0.200414625	138.01		1.38E+06	19	26151323.37	0.103603699	138.01
1.73E+06	77	133423028.8	0.18327966	149.02		1.73E+06	18	31189798.93	0.123564628	149.02
2.18E+06	41	89438380.5	0.122859121	160.91		2.18E+06	7	15269967.4	0.06049503	160.91
2.75E+06	43	118088750	0.16221537	173.75		2.75E+06	10	27462500	0.108798187	173.75
3.46E+06	27	93347745.63	0.128229311	187.61		3.46E+06	6	20743943.47	0.082181282	187.61
4.35E+06	22	95755284.46	0.131536483	202.57		4.35E+06	8	34820103.44	0.137946805	202.57
5.48E+06	16	87671826.12	0.120432452	218.73		5.48E+06	4	21917956.53	0.086832369	218.73
6.90E+06	9	62084413.01	0.085283704	236.18		6.90E+06	2	13796536.23	0.054657738	236.18
8.68E+06	4	34737620.1	0.047718143	255.02		8.68E+06	2	17368810.05	0.068810015	255.02
1.09E+07	7	76531127.2	0.105128771	275.37		1.09E+07	3	32799054.51	0.129940016	275.37
1.38E+07	8	110110835.2	0.151256321	297.34		1.38E+07	0	0	0	297.34
1.73E+07	6	103965996.4	0.14281532	321.06		1.73E+07	1	17327666.07	0.068647015	321.06
2.18E+07	2	43628478.29	0.059931278	346.67		2.18E+07	1	21814239.15	0.086421472	346.67
2.75E+07	3	82387500	0.113173514	374.32		2.75E+07	0	0	0	374.32
3.46E+07	2	69146478.24	0.094984675	404.19		3.46E+07	0	0	0	404.19
4.35E+07	0	0	0	436.43		4.35E+07	1	43525129.3	0.172433507	436.43
5.48E+07	0	0	0	471.25		5.48E+07	0	0	0	471.25
6.90E+07	0	0	0	508.84		6.90E+07	2	137965362.3	0.546577381	508.84
8.68E+07	1	86844050.24	0.119295358	549.43		8.68E+07				549.43
1.09E+08				593.26		1.09E+08				593.26
1.38E+08				640.59		1.38E+08				640.59
1.73E+08				691.69		1.73E+08				691.69

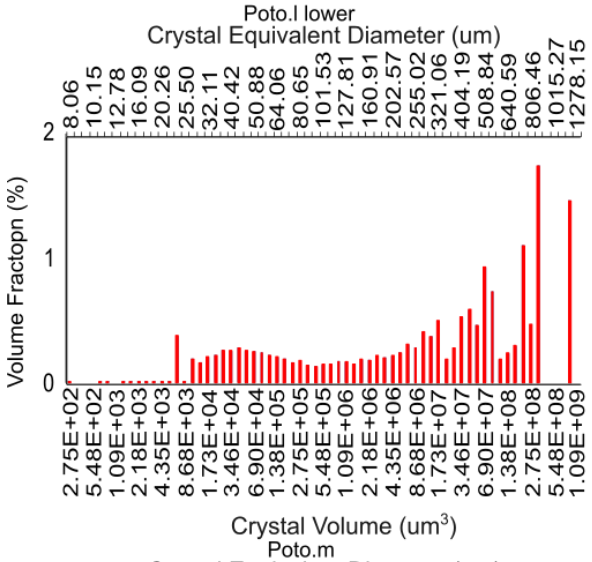
Appendix E3: Crystal Size distribution graphs.

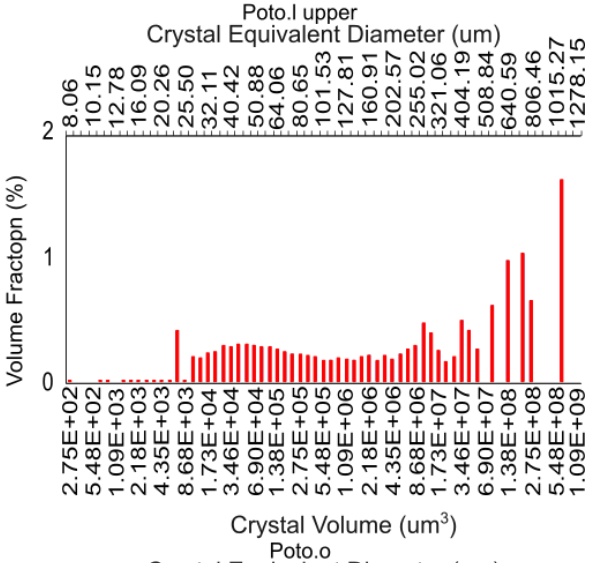
Crystal size distribution graphs for 19 Poto and Paetahi units from the reference locations.

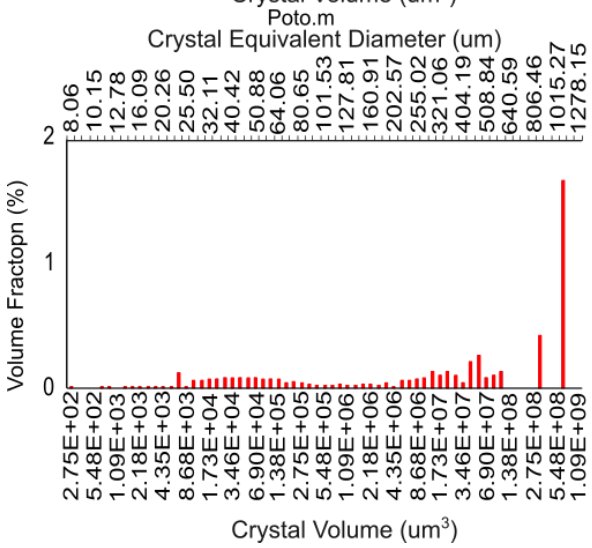


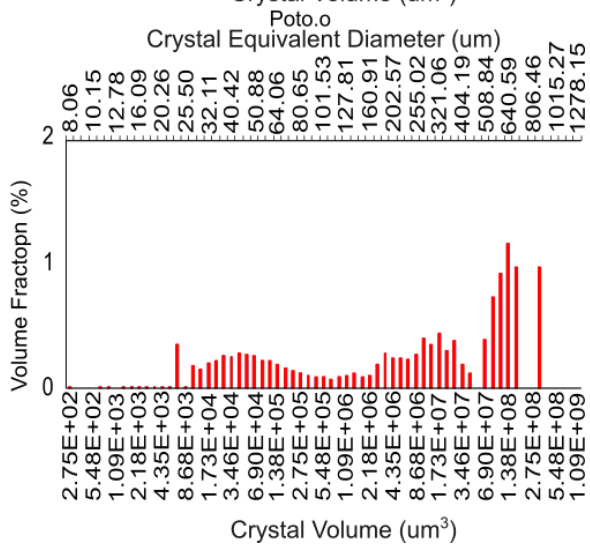

Poto.j
Crystal Equivalent Diameter (um)
Volume Fractopn (%)
Crystal Volume (um3)

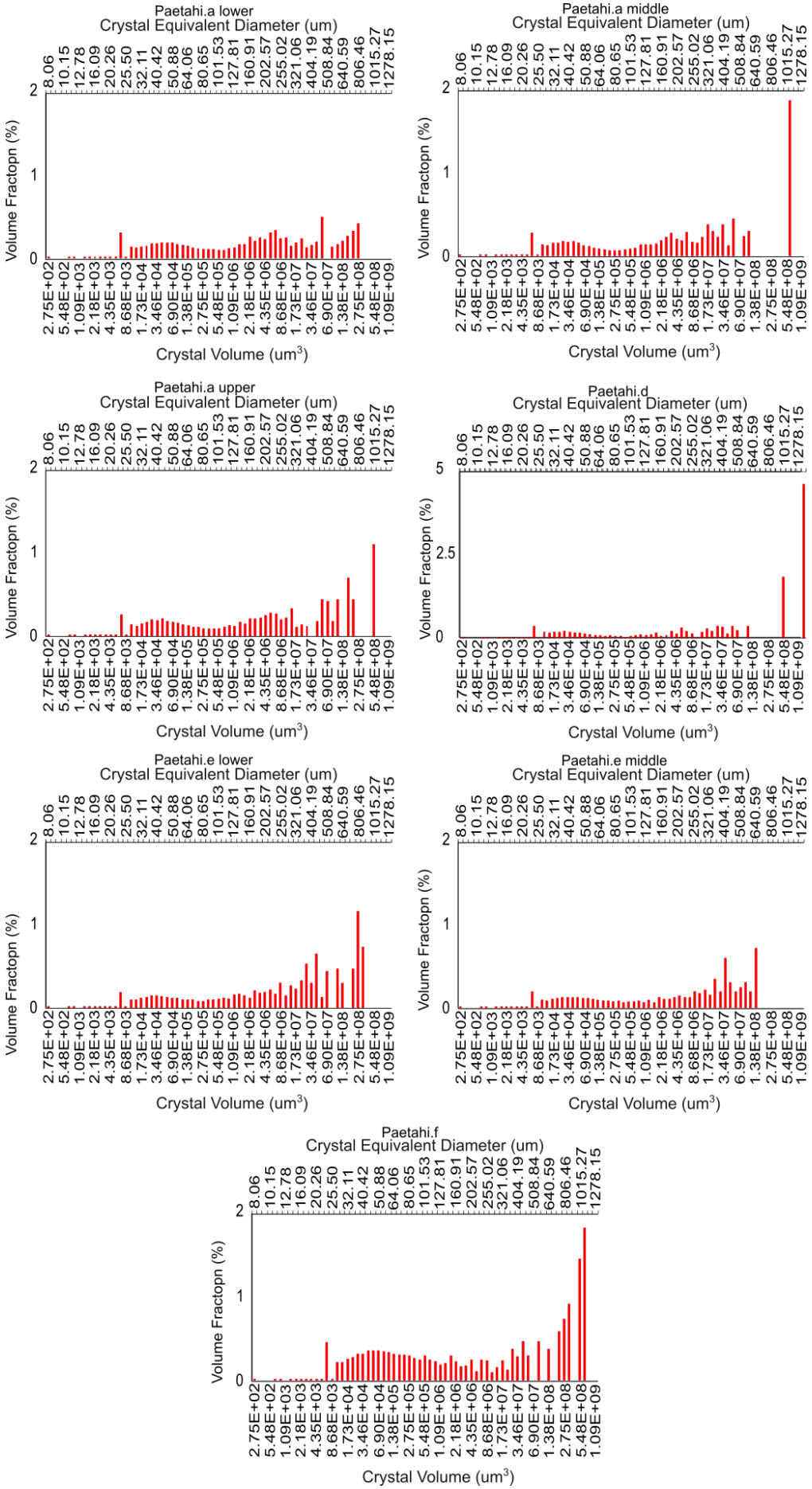

Poto.k lower
Crystal Equivalent Diameter (um)
Volume Fractopn (%)
Crystal Volume (um3)


Poto.l lower
Crystal Equivalent Diameter (um)
Volume Fractopn (%)
Crystal Volume (um3)


Poto.l upper
Crystal Equivalent Diameter (um)
Volume Fractopn (%)
Crystal Volume (um3)


Poto.m
Crystal Equivalent Diameter (um)
Volume Fractopn (%)
Crystal Volume (um3)


Poto.o
Crystal Equivalent Diameter (um)
Volume Fractopn (%)
Crystal Volume (um3)


Paetahi.a lower
Crystal Equivalent Diameter (um)
Volume Fractopn (%)
Crystal Volume (um3)
Paetahi.a middle
Crystal Equivalent Diameter (um)
Volume Fractopn (%)
Crystal Volume (um3)
Paetahi.a upper
Crystal Equivalent Diameter (um)
Volume Fractopn (%)
Crystal Volume (um3)
Paetahi.d
Crystal Equivalent Diameter (um)
Volume Fractopn (%)
Crystal Volume (um3)
Paetahi.e lower
Crystal Equivalent Diameter (um)
Volume Fractopn (%)
Crystal Volume (um3)
Paetahi.e middle
Crystal Equivalent Diameter (um)
Volume Fractopn (%)
Crystal Volume (um3)
Paetahi.f
Crystal Equivalent Diameter (um)
Volume Fractopn (%)
Crystal Volume (um3)

Appendix E4: Crystal size distribution data for the Poto and Paetahi Formations.

Poto.a						**Poto.c lower**						**Poto.d**				
Volume bins in um	Frequency	average volume of bin	volume fraction %	eqD (um)		Volume bins in um	Frequency	average volume of bin	volume fraction %	eqD (um)		Volume bins in um	Frequency	average volume of bin	volume fraction %	eqD (um)
2.75E+02	1197	328726.125	0.000497427	8.06		2.75E+02	781	214482.125	0.000316605	8.06		2.75E+02	224	61516	0.00078183	8.06
3.46E+02	0	0	0	8.71		3.46E+02	0	0	0	8.71		3.46E+02	0	0	0	8.71
4.35E+02	0	0	0	9.40		4.35E+02	0	0	0	9.40		4.35E+02	0	0	0	9.40
5.48E+02	0	0	0	10.15		5.48E+02	0	0	0	10.15		5.48E+02	0	0	0	10.15
6.90E+02	593	409067.2991	0.000618999	10.96		6.90E+02	144	99335.06082	0.000146632	10.96		6.90E+02	34	23454.11158	0.000298087	10.96
8.68E+02	507	440299.3347	0.00066626	11.84		8.68E+02	64	55580.19216	8.2044E-05	11.84		8.68E+02	14	12158.16703	0.000154523	11.84
1.09E+03	0	0	0	12.78		1.09E+03	0	0	0	12.78		1.09E+03	0	0	0	12.78
1.38E+03	698	960717.0374	0.001453754	13.80		1.38E+03	87	119745.5333	0.000176761	13.80		1.38E+03	23	31656.86513	0.000402339	13.80
1.73E+03	138	239121.7918	0.000361838	14.90		1.73E+03	129	223526.8923	0.000329957	14.90		1.73E+03	40	69310.66429	0.000880895	14.90
2.18E+03	122	266133.7176	0.000402713	16.09		2.18E+03	26	56717.02178	8.37222E-05	16.09		2.18E+03	7	15269.9674	0.000194072	16.09
2.75E+03	1708	4690595	0.007097794	17.37		2.75E+03	123	337788.75	0.000498623	17.37		2.75E+03	35	96118.75	0.001221609	17.37
3.46E+03	8413	29086466.07	0.044013553	18.76		3.46E+03	26	89890.42172	0.000132691	18.76		3.46E+03	7	24201.26738	0.000307583	18.76
4.35E+03	35793	155789495.3	0.235740197	20.26		4.35E+03	69	300323.3922	0.000443319	20.26		4.35E+03	19	82697.74567	0.001051036	20.26
5.48E+03	27195	149014707	0.225488608	21.87		5.48E+03	292	1600010.827	0.002361837	21.87		5.48E+03	48	263015.4784	0.003342761	21.87
6.90E+03	22265	153589939.5	0.232411836	23.62		6.90E+03	17415	120133339.2	0.177333419	23.62		6.90E+03	1993	13748248.35	0.174731576	23.62
8.68E+03	17925	155667960.1	0.23555629	25.50		8.68E+03	117	1016075.388	0.001499868	25.50		8.68E+03	27	234478.9357	0.00298008	25.50
1.09E+04	16441	179749751.8	0.271996785	27.54		1.09E+04	5462	59716145.25	0.088149287	27.54		1.09E+04	604	6603542.975	0.083926872	27.54
1.38E+04	14909	205205305.3	0.310516052	29.73		1.38E+04	3761	51765856.41	0.076413561	29.73		1.38E+04	479	6592886.259	0.083791431	29.73
1.73E+04	11451	198419104.2	0.300247193	32.11		1.73E+04	3950	68444280.99	0.101033222	32.11		1.73E+04	494	8559867.04	0.108790518	32.11
2.18E+04	8765	191201806.1	0.289325999	34.67		2.18E+04	3513	76633422.12	0.113121527	34.67		2.18E+04	381	8311225.115	0.105630436	34.67
2.75E+04	7050	193610625	0.292971017	37.43		2.75E+04	3454	94855475	0.140019796	37.43		2.75E+04	407	11177237.5	0.142055648	37.43
3.46E+04	4953	171241253.4	0.259121751	40.42		3.46E+04	2860	98879463.89	0.14595976	40.42		3.46E+04	328	11340022.43	0.144124542	40.42
4.35E+04	3940	171489009.4	0.259496655	43.64		4.35E+04	2692	117169648.1	0.172958601	43.64		4.35E+04	268	11664734.65	0.14825143	43.64
5.48E+04	2725	149316078.9	0.225944643	47.12		5.48E+04	2178	119343273.3	0.176167172	47.12		5.48E+04	225	12328850.55	0.156691924	47.12
6.90E+04	1785	123134085.8	0.186326129	50.88		6.90E+04	2009	138586206.4	0.204572402	50.88		6.90E+04	141	9726558.039	0.123618426	50.88
8.68E+04	1173	101868070.9	0.154146459	54.94		8.68E+04	1636	142076866.2	0.209725099	54.94		8.68E+04	113	9813377.677	0.124721849	54.94
1.09E+05	695	75984476.29	0.114979482	59.33		1.09E+05	1225	133929472.6	0.197698419	59.33		1.09E+05	87	9511725.809	0.120888043	59.33
1.38E+05	433	59597489.57	0.090182742	64.06		1.38E+05	1006	138464375.3	0.204392562	64.06		1.38E+05	62	8533589.73	0.10845655	64.06
1.73E+05	294	50943338.25	0.077087307	69.17		1.73E+05	739	128051452.3	0.189021648	69.17		1.73E+05	43	7450896.411	0.0946962	69.17
2.18E+05	188	41010769.59	0.062057374	74.69		2.18E+05	557	121505312	0.17935864	74.69		2.18E+05	33	7198698.918	0.091490929	74.69
2.75E+05	136	37349000	0.056516395	80.65		2.75E+05	362	99414250	0.146749178	80.65		2.75E+05	20	5492500	0.069806215	80.65
3.46E+05	99	34227506.73	0.051792961	87.08		3.46E+05	235	81247111.94	0.119931971	87.08		3.46E+05	20	6914647.824	0.087880818	87.08
4.35E+05	64	27856082.75	0.042151741	94.03		4.35E+05	147	63981940.07	0.09444619	94.03		4.35E+05	7	3046759.051	0.038722388	94.03
5.48E+05	60	32876934.79	0.049749279	101.53		5.48E+05	119	65205920.68	0.096252955	101.53		5.48E+05	12	6575386.959	0.083569026	101.53
6.90E+05	47	32421860.13	0.049060661	109.63		6.90E+05	54	37250647.81	0.054987107	109.63		6.90E+05	8	5518614.49	0.070138114	109.63
8.68E+05	40	34737620.1	0.052564863	118.37		8.68E+05	55	47764227.63	0.070506604	118.37		8.68E+05	10	8684405.024	0.110373317	118.37
1.09E+06	45	49198581.77	0.074447146	127.81		1.09E+06	43	47011978.14	0.06939618	127.81		1.09E+06	6	6559810.903	0.083371064	127.81
1.38E+06	20	27527708.81	0.041654846	138.01		1.38E+06	42	57808188.49	0.085332879	138.01		1.38E+06	6	8258312.642	0.104957952	138.01
1.73E+06	33	57181298.04	0.086526569	149.02		1.73E+06	30	51982998.22	0.076734093	149.02		1.73E+06	3	5198299.822	0.066067116	149.02
2.18E+06	16	34902782.63	0.052814786	160.91		2.18E+06	33	71986989.18	0.106262749	160.91		2.18E+06	5	10907119.57	0.138622619	160.91
2.75E+06	19	52178750	0.078956728	173.75		2.75E+06	28	76895000	0.113507652	173.75		2.75E+06	3	8238750	0.104709323	173.75
3.46E+06	16	55317182.59	0.083705795	187.61		3.46E+06	21	72603802.15	0.10717325	187.61		3.46E+06	3	10371971.74	0.131821227	187.61
4.35E+06	7	30467590.51	0.046103467	202.57		4.35E+06	17	73992719.81	0.109223485	202.57		4.35E+06	2	8705025.86	0.110635395	202.57
5.48E+06	8	43835913.06	0.066332372	218.73		5.48E+06	19	104110293.5	0.153681188	218.73		5.48E+06	5	27397445.66	0.348204276	218.73
6.90E+06	7	48287876.79	0.07306907	236.18		6.90E+06	17	117270557.9	0.173107558	236.18		6.90E+06	0	0	0	236.18
8.68E+06	10	86844050.24	0.131412156	255.02		8.68E+06	14	121581670.3	0.179471356	255.02		8.68E+06	0	0	0	255.02
1.09E+07	4	43732072.69	0.066175241	275.37		1.09E+07	16	174928290.7	0.258218343	275.37		1.09E+07	1	10933018.17	0.138951774	275.37
1.38E+07	6	82583126.42	0.124964539	297.34		1.38E+07	11	151402398.4	0.223490874	297.34		1.38E+07	1	13763854.4	0.174929919	297.34
1.73E+07	1	17327666.07	0.026220172	321.06		1.73E+07	9	155948994.7	0.230202278	321.06		1.73E+07	0	0	0	321.06
2.18E+07	3	65442717.44	0.099027724	346.67		2.18E+07	14	305399348	0.450811663	346.67		2.18E+07	0	0	0	346.67
2.75E+07	2	54925000	0.083112345	374.32		2.75E+07	10	274625000	0.405384471	374.32		2.75E+07	1	27462500	0.349031076	374.32
3.46E+07	5	172866195.6	0.261580609	404.19		3.46E+07	5	172866195.6	0.255174406	404.19		3.46E+07	1	34573239.12	0.439404091	404.19
4.35E+07	3	130575387.9	0.197586285	436.43		4.35E+07	6	261150775.8	0.385494653	436.43		4.35E+07	1	43525129.3	0.553176976	436.43
5.48E+07	1	54794891.32	0.082915465	471.25		5.48E+07	9	493154021.9	0.727963522	471.25		5.48E+07	0	0	0	471.25
6.90E+07	2	137965362.3	0.208768772	508.84		6.90E+07	5	344913405.6	0.509139876	508.84		6.90E+07	0	0	0	508.84
8.68E+07	0	0	0	549.43		8.68E+07	7	607908351.7	0.897356779	549.43		8.68E+07	0	0	0	549.43
1.09E+08	0	0	0	593.26		1.09E+08	6	655981090.3	0.968318787	593.26		1.09E+08	0	0	0	593.26
1.38E+08	1	137638544	0.208274232	640.59		1.38E+08	2	275277088.1	0.406347043	640.59		1.38E+08	1	137638544	1.749299193	640.59
1.73E+08	0	0	0	691.69		1.73E+08	0	0	0	691.69		1.73E+08	0	0	0	691.69
2.18E+08	1	218142391.5	0.330092412	746.87		2.18E+08	3	654427174.4	0.966024993	746.87		2.18E+08	0	0	0	746.87
2.75E+08	0	0	0	806.46		2.75E+08	0	0	0	806.46		2.75E+08	1	274625000	3.490310758	806.46
3.46E+08	0	0	0	870.79		3.46E+08	0	0	0	870.79		3.46E+08	1	345732391.2	4.394040908	870.79
4.35E+08	0	0	0	940.26		4.35E+08	1	435251293	0.642491088	940.26		4.35E+08	0	0	0	940.26
5.48E+08	1	547948913.2	0.829154652	1015.27		5.48E+08	0	0	0	1015.27		5.48E+08	0	0	0	1015.27
6.90E+08		0	0	1096.26		6.90E+08		0	0	1096.26		6.90E+08	1	689826811.3	8.767264234	1096.26
8.68E+08		0	0	1183.71		8.68E+08		0	0	1183.71		8.68E+08		0	0	1183.71
1.09E+09		0	0	1278.15		1.09E+09		0	0	1278.15		1.09E+09		0	0	1278.15

Poto.e						**Poto.g**						**Poto.h**				
Volume bins in um	Frequency	average volume of bin	volume fraction %	eqD (um)		Volume bins in um	Frequency	average volume of bin	volume fraction %	eqD (um)		Volume bins in um	Frequency	average volume of bin	volume fraction %	eqD (um)
2.75E+02	1436	394361.5	0.001177619	8.06		2.75E+02	847	232607.375	0.000689689	8.06		2.75E+02	587	161204.875	4.60585E-06	8.06
3.46E+02	0	0	0	8.71		3.46E+02	0	0	0	8.71		3.46E+02	0	0	0	8.71
4.35E+02	0	0	0	9.40		4.35E+02	0	0	0	9.40		4.35E+02	0	0	0	9.40
5.48E+02	0	0	0	10.15		5.48E+02	0	0	0	10.15		5.48E+02	0	0	0	10.15
6.90E+02	275	189702.3731	0.000566478	10.96		6.90E+02	172	118650.2115	0.000351802	10.96		6.90E+02	133	91746.9659	2.62134E-06	10.96
8.68E+02	69	59922.39467	0.000178937	11.84		8.68E+02	46	39948.26311	0.000118448	11.84		8.68E+02	39	33869.17959	9.67691E-07	11.84
1.09E+03	0	0	0	12.78		1.09E+03	0	0	0	12.78		1.09E+03	0	0	0	12.78
1.38E+03	126	173424.5655	0.00051787	13.80		1.38E+03	69	94970.59538	0.000281591	13.80		1.38E+03	55	75701.19922	2.16289E-06	13.80
1.73E+03	215	372544.8206	0.001112472	14.90		1.73E+03	203	351751.6213	0.001042955	14.90		1.73E+03	112	194069.86	5.54485E-06	14.90
2.18E+03	46	100345.5001	0.000299646	16.09		2.18E+03	31	67624.14135	0.000200508	16.09		2.18E+03	22	47991.32612	1.37118E-06	16.09
2.75E+03	172	472355	0.001410519	17.37		2.75E+03	123	337788.75	0.001001555	17.37		2.75E+03	78	214207.5	6.12021E-06	17.37
3.46E+03	48	165951.5478	0.000495555	18.76		3.46E+03	29	100262.3935	0.000297281	18.76		3.46E+03	19	65689.15433	1.87683E-06	18.76
4.35E+03	104	452661.3447	0.001351711	20.26		4.35E+03	66	287265.8534	0.000851753	20.26		4.35E+03	40	174100.5172	4.9743E-06	20.26
5.48E+03	271	1484941.555	0.004434246	21.87		5.48E+03	210	1150692.718	0.003411842	21.87		5.48E+03	150	821923.3699	2.34835E-05	21.87
6.90E+03	20765	143242537.4	0.427742501	23.62		6.90E+03	14105	97300071.73	0.28849793	23.62		6.90E+03	8507	58683566.83	0.001676673	23.62
8.68E+03	144	1250554.323	0.003734332	25.50		8.68E+03	93	807649.6673	0.002394708	25.50		8.68E+03	79	686067.9969	1.96019E-05	25.50
1.09E+04	7321	80040626.03	0.239012644	27.54		1.09E+04	4407	48181811.08	0.142860663	27.54		1.09E+04	3085	33728361.06	0.000963667	27.54
1.38E+04	5666	77985999.05	0.232877236	29.73		1.38E+04	2844	39144401.92	0.116064446	29.73		1.38E+04	2133	29358301.44	0.000838809	29.73
1.73E+04	5962	103307545.1	0.308490959	32.11		1.73E+04	2947	51064631.92	0.151408322	32.11		1.73E+04	2313	40078891.63	0.001145111	32.11
2.18E+04	5323	116117195	0.346742387	34.67		2.18E+04	2523	55037325.37	0.163187489	34.67		2.18E+04	2039	44479233.62	0.001270835	34.67
2.75E+04	5328	146320200	0.436932837	37.43		2.75E+04	2375	65223437.5	0.193389649	37.43		2.75E+04	2098	57616325	0.001646181	37.43
3.46E+04	4440	153505181.7	0.45838821	40.42		3.46E+04	1947	67314096.57	0.199588522	40.42		3.46E+04	1661	57426150.18	0.001640747	40.42
4.35E+04	4081	177626052.7	0.530416546	43.64		4.35E+04	1635	71163586.4	0.211002387	43.64		4.35E+04	1459	63503163.65	0.001814376	43.64
5.48E+04	3170	173699805.5	0.518692216	47.12		5.48E+04	1330	72877205.46	0.216083324	47.12		5.48E+04	1162	63671663.72	0.00181919	47.12
6.90E+04	2710	186943065.8	0.558238467	50.88		6.90E+04	1143	78847204.53	0.233784568	50.88		6.90E+04	995	68637767.72	0.001961079	50.88
8.68E+04	2115	183675166.3	0.548480056	54.94		8.68E+04	896	77812269.02	0.23071595	54.94		8.68E+04	735	63830376.93	0.001823725	54.94
1.09E+05	1650	180394799.8	0.538684417	59.33		1.09E+05	694	75875146.11	0.224972317	59.33		1.09E+05	614	67128731.57	0.001917964	59.33
1.38E+05	1152	158559602.7	0.473481427	64.06		1.38E+05	571	78591608.64	0.233026718	64.06		1.38E+05	468	64414838.61	0.001840424	64.06
1.73E+05	886	153523121.4	0.45844178	69.17		1.73E+05	403	69830494.27	0.207049724	69.17		1.73E+05	323	55968361.42	0.001599096	69.17
2.18E+05	605	131976146.8	0.394099463	74.69		2.18E+05	314	68496710.92	0.203095013	74.69		2.18E+05	241	52572316.34	0.001502066	74.69
2.75E+05	445	122208125	0.364930767	80.65		2.75E+05	192	52728000	0.156340263	80.65		2.75E+05	170	46686250	0.001333893	80.65
3.46E+05	319	110288632.8	0.329337475	87.08		3.46E+05	163	56354379.77	0.167092599	87.08		3.46E+05	128	44253746.08	0.001264393	87.08
4.35E+05	197	85744504.72	0.256045233	94.03		4.35E+05	104	45266134.47	0.134215585	94.03		4.35E+05	104	45266134.47	0.001293318	94.03
5.48E+05	162	88767723.95	0.265072994	101.53		5.48E+05	77	42192066.32	0.125100872	101.53		5.48E+05	77	42192066.32	0.001205488	101.53
6.90E+05	98	67603027.5	0.201872213	109.63		6.90E+05	67	46218396.35	0.137039073	109.63		6.90E+05	52	35870994.19	0.001024886	109.63
8.68E+05	60	52106430.15	0.155597179	118.37		8.68E+05	41	35606060.6	0.105573147	118.37		8.68E+05	31	26921655.58	0.00076919	118.37
1.09E+06	54	59038298.13	0.176296718	127.81		1.09E+06	36	39358865.42	0.116700337	127.81		1.09E+06	37	40452167.23	0.001155776	127.81
1.38E+06	41	56431803.05	0.168513355	138.01		1.38E+06	31	42667948.65	0.126511878	138.01		1.38E+06	23	31656865.13	0.000904482	138.01
1.73E+06	22	38120865.36	0.113834302	149.02		1.73E+06	23	39853631.97	0.118167336	149.02		1.73E+06	17	29457032.32	0.000841629	149.02
2.18E+06	21	45809902.21	0.136794855	160.91		2.18E+06	17	37084206.55	0.109955899	160.91		2.18E+06	11	23995663.06	0.00068559	160.91
2.75E+06	19	52178750	0.155813136	173.75		2.75E+06	20	54925000	0.162854441	173.75		2.75E+06	16	43940000	0.001255429	173.75
3.46E+06	19	65689154.33	0.196157117	187.61		3.46E+06	20	69146478.24	0.205021594	187.61		3.46E+06	11	38030563.03	0.001086588	187.61
4.35E+06	12	52230155.16	0.155966639	202.57		4.35E+06	15	65287693.95	0.193580171	202.57		4.35E+06	6	26115077.58	0.000746145	202.57
5.48E+06	11	60274380.46	0.179987835	218.73		5.48E+06	12	65753869.59	0.194962397	218.73		5.48E+06	7	38356423.93	0.001095898	218.73
6.90E+06	15	103474021.7	0.308988081	236.18		6.90E+06	11	75880949.24	0.224989523	236.18		6.90E+06	9	62084413.01	0.00177384	236.18
8.68E+06	7	60790835.17	0.181530042	255.02		8.68E+06	6	52106430.15	0.154497288	255.02		8.68E+06	7	60790835.17	0.001736881	255.02
1.09E+07	7	76531127.2	0.228532783	275.37		1.09E+07	10	109330181.7	0.324167604	275.37		1.09E+07	6	65598109.03	0.001874232	275.37
1.38E+07	8	110110835.2	0.328806546	297.34		1.38E+07	5	68819272.02	0.204051417	297.34		1.38E+07	6	82583126.42	0.002359518	297.34
1.73E+07	4	69310664.29	0.206971458	321.06		1.73E+07	4	69310664.29	0.205508411	321.06		1.73E+07	6	103965996.4	0.002970457	321.06
2.18E+07	7	152699674	0.45598285	346.67		2.18E+07	4	87256956.58	0.258719761	346.67		2.18E+07	6	130885434.9	0.003739584	346.67
2.75E+07	7	192237500	0.574048397	374.32		2.75E+07	2	54925000	0.162854441	374.32		2.75E+07	3	82387500	0.002353929	374.32
3.46E+07	3	103719717.4	0.309721763	404.19		3.46E+07	1	34573239.12	0.102510797	404.19		3.46E+07	5	172866195.6	0.004939034	404.19
4.35E+07	0	0	0	436.43		4.35E+07	2	87050258.6	0.258106895	436.43		4.35E+07	4	174100517.2	0.0049743	436.43
5.48E+07	0	0	0	471.25		5.48E+07	5	273974456.6	0.812343322	471.25		5.48E+07	4	219179565.3	0.006262273	471.25
6.90E+07	0	0	0	508.84		6.90E+07	3	206948043.4	0.613607791	508.84		6.90E+07	1	68982681.13	0.001970934	508.84
8.68E+07	0	0	0	549.43		8.68E+07	1	86844050.24	0.25749548	549.43		8.68E+07	2	173688100.5	0.004962517	549.43
1.09E+08	1	109330181.7	0.326475404	593.26		1.09E+08	1	109330181.7	0.324167604	593.26		1.09E+08	3	327990545.1	0.009371158	593.26
1.38E+08	1	137638544	0.411008183	640.59		1.38E+08	1	137638544	0.408102834	640.59		1.38E+08	0	0	0	640.59
1.73E+08	1	173276660.7	0.517428646	691.69		1.73E+08	1	173276660.7	0.513771028	691.69		1.73E+08	0	0	0	691.69
2.18E+08	2	436284782.9	1.302808143	746.87		2.18E+08	1	218142391.5	0.646799403	746.87		2.18E+08	0	0	0	746.87
2.75E+08	2	549250000	1.640138277	806.46		2.75E+08	0	0	0	806.46		2.75E+08	0	0	0	806.46
3.46E+08	0	0	0	870.79		3.46E+08	0	0	0	870.79		3.46E+08	0	0	0	870.79
4.35E+08	1	435251293	1.299721995	940.26		4.35E+08	2	870502586	2.581068949	940.26		4.35E+08	0	0	0	940.26
5.48E+08	1	547948913.2	1.636253048	1015.27		5.48E+08	0	0	0	1015.27		5.48E+08	0	0	0	1015.27
6.90E+08	1	689826811.3	2.059920542	1096.26		6.90E+08	1	689826811.3	2.045359303	1096.26		6.90E+08	1	689826811.3	0.019709337	1096.26
8.68E+08	1	868440502.4	2.593286317	1183.71		8.68E+08	0	0	0	1183.71		8.68E+08		0	0	1183.71
1.09E+09	1	1093301817	3.264754045	1278.15		1.09E+09	0	0	0	1278.15		1.09E+09		0	0	1278.15

Poto.j						**Poto.k lower**						**Poto.l lower**				
Volume bins in um	Frequency	average volume of bin	volume fraction %	eqD (um)		Volume bins in um	Frequency	average volume of bin	volume fraction %	eqD (um)		Volume bins in um	Frequency	average volume of bin	volume fraction %	eqD (um)
2.75E+02	732	201025.5	0.000977793	8.06		2.75E+02	1286	353167.75	0.000849725	8.06		2.75E+02	1208	331747	0.000557383	8.06
3.46E+02	0	0	0	8.71		3.46E+02	0	0	0	8.71		3.46E+02	0	0	0	8.71
4.35E+02	0	0	0	9.40		4.35E+02	0	0	0	9.40		4.35E+02	0	0	0	9.40
5.48E+02	0	0	0	10.15		5.48E+02	0	0	0	10.15		5.48E+02	0	0	0	10.15
6.90E+02	126	86918.17822	0.000422772	10.96		6.90E+02	143	98645.23401	0.000237341	10.96		6.90E+02	211	145553.4572	0.000244551	10.96
8.68E+02	44	38211.38211	0.000185861	11.84		8.68E+02	31	26921.65558	6.47738E-05	11.84		8.68E+02	68	59053.95416	9.92192E-05	11.84
1.09E+03	0	0	0	12.78		1.09E+03	0	0	0	12.78		1.09E+03	0	0	0	12.78
1.38E+03	51	70195.65746	0.000341433	13.80		1.38E+03	104	143144.0858	0.000344406	13.80		1.38E+03	85	116992.7624	0.000196565	13.80
1.73E+03	171	296303.0898	0.001441225	14.90		1.73E+03	226	391605.2532	0.000942206	14.90		1.73E+03	376	651520.2443	0.001094648	14.90
2.18E+03	24	52354.17395	0.000254652	16.09		2.18E+03	24	52354.17395	0.000125965	16.09		2.18E+03	43	93801.22833	0.0001576	16.09
2.75E+03	118	324057.5	0.001576223	17.37		2.75E+03	207	568473.75	0.001367754	17.37		2.75E+03	188	516295	0.00086745	17.37
3.46E+03	21	72603.80215	0.000353147	18.76		3.46E+03	37	127920.9847	0.000307779	18.76		3.46E+03	34	117549.013	0.000197499	18.76
4.35E+03	60	261150.7758	0.001270244	20.26		4.35E+03	91	396078.6766	0.000952969	20.26		4.35E+03	83	361258.5732	0.000606967	20.26
5.48E+03	192	1052061.913	0.005117255	21.87		5.48E+03	300	1643846.74	0.003955112	21.87		5.48E+03	381	2087685.359	0.003507614	21.87
6.90E+03	10139	69941540.39	0.34019734	23.62		6.90E+03	38194	263472452.3	0.633917367	23.62		6.90E+03	32046	221061899.9	0.371416029	23.62
8.68E+03	75	651330.3768	0.003168087	25.50		8.68E+03	98	851071.6924	0.002047687	25.50		8.68E+03	153	1328713.969	0.002232432	25.50
1.09E+04	3156	34504605.35	0.167831233	27.54		1.09E+04	9183	100397905.9	0.24155837	27.54		1.09E+04	10247	112030637.2	0.188227706	27.54
1.38E+04	2166	29812508.64	0.145008761	29.73		1.38E+04	6949	95645024.25	0.230122889	29.73		1.38E+04	6807	93690556.92	0.157413714	29.73
1.73E+04	2123	36786635.07	0.17893108	32.11		1.73E+04	5627	97502776.99	0.234592661	32.11		1.73E+04	6936	120184691.9	0.2019277	32.11
2.18E+04	1823	39767357.96	0.193429388	34.67		2.18E+04	4376	95459110.5	0.229675579	34.67		2.18E+04	5888	128442240.1	0.215801578	34.67
2.75E+04	1626	44654025	0.217198255	37.43		2.75E+04	3629	99661412.5	0.23978636	37.43		2.75E+04	5545	152279562.5	0.255851734	37.43
3.46E+04	1318	45567529.16	0.221641561	40.42		3.46E+04	2448	84635289.37	0.203633357	40.42		3.46E+04	4373	151188774.7	0.254019052	40.42
4.35E+04	1116	48574044.3	0.236265323	43.64		4.35E+04	1956	85135152.91	0.204836033	43.64		4.35E+04	3779	164481463.6	0.276352696	43.64
5.48E+04	868	47561965.67	0.231342548	47.12		5.48E+04	1417	77644361.01	0.186813113	47.12		5.48E+04	2762	151343489.8	0.254278996	47.12
6.90E+04	630	43459089.11	0.211386058	50.88		6.90E+04	997	68775733.08	0.165475105	50.88		6.90E+04	2154	148588695.1	0.249650542	50.88
8.68E+04	510	44290465.62	0.215429893	54.94		8.68E+04	746	64785661.48	0.155874952	54.94		8.68E+04	1628	141382113.8	0.237542441	54.94
1.09E+05	352	38484223.96	0.187188194	59.33		1.09E+05	543	59366288.67	0.142835887	59.33		1.09E+05	1192	130321576.6	0.218959135	59.33
1.38E+05	239	32895612.02	0.16000505	64.06		1.38E+05	425	58496381.21	0.140742881	64.06		1.38E+05	876	120571364.6	0.202577366	64.06
1.73E+05	153	26511329.09	0.128951744	69.17		1.73E+05	317	54928701.45	0.132159008	69.17		1.73E+05	651	112803106.1	0.189525566	69.17
2.18E+05	121	26395229.37	0.128387032	74.69		2.18E+05	232	50609034.82	0.121765846	74.69		2.18E+05	436	95110082.68	0.159798723	74.69
2.75E+05	85	23343125	0.113541523	80.65		2.75E+05	193	53002625	0.127524848	80.65		2.75E+05	380	104357500	0.175335724	80.65
3.46E+05	60	20743943.47	0.100899041	87.08		3.46E+05	148	51168393.9	0.12311167	87.08		3.46E+05	240	82975773.89	0.139411325	87.08
4.35E+05	49	21327313.36	0.103736567	94.03		4.35E+05	124	53971160.33	0.129855154	94.03		4.35E+05	174	75733724.98	0.127243634	94.03
5.48E+05	45	24657701.1	0.119935653	101.53		5.48E+05	97	53151044.59	0.127881947	101.53		5.48E+05	154	84384132.64	0.141777572	101.53
6.90E+05	29	20004977.53	0.097304693	109.63		6.90E+05	84	57945452.15	0.13941734	109.63		6.90E+05	125	86228351.41	0.144876127	109.63
8.68E+05	31	26921655.58	0.130947582	118.37		8.68E+05	76	66001478.18	0.15880022	118.37		8.68E+05	114	99002217.28	0.166338073	118.37
1.09E+06	22	24052639.98	0.116992621	127.81		1.09E+06	55	60131599.94	0.144677234	127.81		1.09E+06	88	96210559.91	0.161647684	127.81
1.38E+06	21	28904094.25	0.140590212	138.01		1.38E+06	54	74324813.78	0.178826249	138.01		1.38E+06	65	89465053.62	0.150314256	138.01
1.73E+06	20	34655332.15	0.168564371	149.02		1.73E+06	32	55448531.43	0.133409724	149.02		1.73E+06	63	109164296.3	0.183411838	149.02
2.18E+06	8	17451391.32	0.084883988	160.91		2.18E+06	27	58898445.69	0.141710252	160.91		2.18E+06	49	106889771.8	0.179590308	160.91
2.75E+06	18	49432500	0.240440872	173.75		2.75E+06	26	71402500	0.171795132	173.75		2.75E+06	46	126327500	0.212248508	173.75
3.46E+06	20	69146478.24	0.336330138	187.61		3.46E+06	15	51859858.68	0.124775341	187.61		3.46E+06	34	117549013	0.197499378	187.61
4.35E+06	14	60935181.02	0.29639019	202.57		4.35E+06	15	65287693.95	0.157082848	202.57		4.35E+06	29	126222875	0.212072723	202.57
5.48E+06	19	104110293.5	0.506394979	218.73		5.48E+06	21	115069271.8	0.276857824	218.73		5.48E+06	26	142466717.4	0.239364732	218.73
6.90E+06	8	55186144.9	0.26842674	236.18		6.90E+06	12	82779217.35	0.199167629	236.18		6.90E+06	26	179354970.9	0.301342344	236.18
8.68E+06	10	86844050.24	0.422411555	255.02		8.68E+06	12	104212860.3	0.250737189	255.02		8.68E+06	19	165003695.5	0.277230121	255.02
1.09E+07	2	21866036.34	0.106356928	275.37		1.09E+07	9	98397163.54	0.236744564	275.37		1.09E+07	22	240526399.8	0.40411921	275.37
1.38E+07	5	68819272.02	0.334738599	297.34		1.38E+07	15	206457816.1	0.49673958	297.34		1.38E+07	16	220221670.5	0.370004322	297.34
1.73E+07	3	51982998.22	0.252846557	321.06		1.73E+07	4	69310664.29	0.166762155	321.06		1.73E+07	17	294570323.2	0.494920834	321.06
2.18E+07	4	87256956.58	0.424419942	346.67		2.18E+07	0	0	0	346.67		2.18E+07	5	109071195.7	0.183255416	346.67
2.75E+07	6	164775000	0.801469575	374.32		2.75E+07	7	192237500	0.462525356	374.32		2.75E+07	6	164775000	0.27684588	374.32
3.46E+07	3	103719717.4	0.504495207	404.19		3.46E+07	7	242012673.8	0.582284925	404.19		3.46E+07	9	311159152.1	0.52279247	404.19
4.35E+07	4	174100517.2	0.846829115	436.43		4.35E+07	0	0	0	436.43		4.35E+07	8	348201034.4	0.585028201	436.43
5.48E+07	1	54794891.32	0.266523673	471.25		5.48E+07	4	219179565.3	0.527348236	471.25		5.48E+07	5	273974456.6	0.460316793	471.25
6.90E+07	1	68982681.13	0.335533425	508.84		6.90E+07	4	275930724.5	0.663892096	508.84		6.90E+07	8	551861449	0.927207213	508.84
8.68E+07	2	173688100.5	0.84482311	549.43		8.68E+07	3	260532150.7	0.626842972	549.43		8.68E+07	5	434220251.2	0.729552951	549.43
1.09E+08	2	218660363.4	1.063569282	593.26		1.09E+08	1	109330181.7	0.263049516	593.26		1.09E+08	1	109330181.7	0.18369055	593.26
1.38E+08	1	137638544	0.669477198	640.59		1.38E+08	2	275277088.1	0.66231944	640.59		1.38E+08	1	137638544	0.231252701	640.59
1.73E+08	1	173276660.7	0.842821857	691.69		1.73E+08	0	0	0	691.69		1.73E+08	1	173276660.7	0.291129902	691.69
2.18E+08	0	0	0	746.87		2.18E+08	1	218142391.5	0.524852786	746.87		2.18E+08	3	654427174.4	1.099532496	746.87
2.75E+08	1	274625000	1.335782624	806.46		2.75E+08	3	823875000	1.982251528	806.46		2.75E+08	1	274625000	0.4614098	806.46
3.46E+08	1	345732391.2	1.68165069	870.79		3.46E+08	0	0	0	870.79		3.46E+08	3	1037197174	1.742641567	870.79
4.35E+08		0	0	940.26		4.35E+08	0	0	0	940.26		4.35E+08	0	0	0	940.26
5.48E+08		0	0	1015.27		5.48E+08	0	0	0	1015.27		5.48E+08	0	0	0	1015.27
6.90E+08		0	0	1096.26		6.90E+08	1	689826811.3	1.659730239	1096.26		6.90E+08	0	0	0	1096.26
8.68E+08		0	0	1183.71		8.68E+08	0	0	0	1183.71		8.68E+08	1	868440502.4	1.459105902	1183.71
1.09E+09		0	0	1278.15		1.09E+09	0	0	0	1278.15		1.09E+09		0	0	1278.15

Poto.l upper						**Poto.m**						**Poto.o**				
Volume bins in um	Frequency	average volume of bin	volume fraction %	eqD (um)		Volume bins in um	Frequency	average volume of bin	volume fraction %	eqD (um)		Volume bins in um	Frequency	average volume of bin	volume fraction %	eqD (um)
2.75E+02	1384	380081	0.000891373	8.06		2.75E+02	733	201300.125	0.000485427	8.06		2.75E+02	1018	279568.25	0.000790064	8.06
3.46E+02	0	0	0	8.71		3.46E+02	0	0	0	8.71		3.46E+02	0	0	0	8.71
4.35E+02	0	0	0	9.40		4.35E+02	0	0	0	9.40		4.35E+02	0	0	0	9.40
5.48E+02	0	0	0	10.15		5.48E+02	0	0	0	10.15		5.48E+02	0	0	0	10.15
6.90E+02	233	160729.647	0.000376946	10.96		6.90E+02	102	70362.33475	0.000169676	10.96		6.90E+02	195	134516.2282	0.000380145	10.96
8.68E+02	65	56448.63266	0.000132384	11.84		8.68E+02	30	26053.21507	6.28262E-05	11.84		8.68E+02	45	39079.82261	0.00011044	11.84
1.09E+03	0	0	0	12.78		1.09E+03	0	0	0	12.78		1.09E+03	0	0	0	12.78
1.38E+03	107	147273.2421	0.000345388	13.80		1.38E+03	54	74324.81378	0.000179231	13.80		1.38E+03	82	112863.6061	0.000318954	13.80
1.73E+03	389	674046.2102	0.001580785	14.90		1.73E+03	174	301501.3897	0.000727058	14.90		1.73E+03	270	467846.984	0.001322142	14.90
2.18E+03	52	113434.0436	0.000266028	16.09		2.18E+03	17	37084.20655	8.9427E-05	16.09		2.18E+03	39	85075.53267	0.000240425	16.09
2.75E+03	216	593190	0.00139116	17.37		2.75E+03	107	293848.75	0.000708604	17.37		2.75E+03	184	505310	0.001428013	17.37
3.46E+03	43	148664.9282	0.000348652	18.76		3.46E+03	16	55317.18259	0.000133395	18.76		3.46E+03	33	114091.6891	0.000322425	18.76
4.35E+03	98	426546.2671	0.001000344	20.26		4.35E+03	55	239388.2111	0.000577275	20.26		4.35E+03	77	335143.4956	0.00094712	20.26
5.48E+03	347	1901382.729	0.004459156	21.87		5.48E+03	194	1063020.892	0.00256343	21.87		5.48E+03	280	1534256.957	0.004335832	21.87
6.90E+03	24792	171021863	0.401083494	23.62		6.90E+03	14627	100900967.7	0.243318418	23.62		6.90E+03	18257	125941680.9	0.355913007	23.62
8.68E+03	173	1502402.069	0.00352346	25.50		8.68E+03	95	825018.4773	0.001989497	25.50		8.68E+03	153	1328713.969	0.003754965	25.50
1.09E+04	7572	82784813.59	0.194148407	27.54		1.09E+04	4545	49690567.59	0.119826703	27.54		1.09E+04	6002	65619975.06	0.185442996	27.54
1.38E+04	5619	77339097.89	0.181377019	29.73		1.38E+04	3466	47705519.36	0.115039843	29.73		1.38E+04	4039	55592207.94	0.157104382	29.73
1.73E+04	5510	95475440.06	0.223910689	32.11		1.73E+04	3223	55847067.75	0.134672843	32.11		1.73E+04	4205	72862835.84	0.205911425	32.11
2.18E+04	4579	99887401.05	0.234257698	34.67		2.18E+04	2715	59225659.28	0.142820173	34.67		2.18E+04	3573	77942276.47	0.220265998	34.67
2.75E+04	4414	121219475	0.284286054	37.43		2.75E+04	2483	68189387.5	0.164435825	37.43		2.75E+04	3453	94828012.5	0.267985331	37.43
3.46E+04	3378	116788401.8	0.273894223	40.42		3.46E+04	1869	64617383.92	0.155822089	40.42		3.46E+04	2645	91446217.48	0.25842833	40.42
4.35E+04	2884	125526472.9	0.294386902	43.64		4.35E+04	1544	67202799.64	0.16205671	43.64		4.35E+04	2315	100760674.3	0.284751119	43.64
5.48E+04	2297	125863865.4	0.295178161	47.12		5.48E+04	1164	63781253.5	0.153805796	47.12		5.48E+04	1767	96822572.97	0.273621988	47.12
6.90E+04	1773	122306293.6	0.28683488	50.88		6.90E+04	985	67947940.91	0.163853587	50.88		6.90E+04	1340	92436792.71	0.26122771	50.88
8.68E+04	1337	116110495.2	0.272304384	54.94		8.68E+04	668	58011825.56	0.139893065	54.94		8.68E+04	918	79722838.12	0.225297891	54.94
1.09E+05	1065	116436643.5	0.273069273	59.33		1.09E+05	543	59366288.67	0.143159295	59.33		1.09E+05	715	78171079.92	0.2209126	59.33
1.38E+05	778	107082787.3	0.251132444	64.06		1.38E+05	401	55193056.16	0.133095721	64.06		1.38E+05	485	66754693.86	0.188649728	64.06
1.73E+05	570	98767696.61	0.231631747	69.17		1.73E+05	200	34655332.15	0.083569868	69.17		1.73E+05	330	57181298.04	0.161595173	69.17
2.18E+05	431	94019370.72	0.220495889	74.69		2.18E+05	186	40574484.81	0.097843655	74.69		2.18E+05	232	50609034.82	0.143021863	74.69
2.75E+05	329	90351625	0.211894227	80.65		2.75E+05	111	30483375	0.07350937	80.65		2.75E+05	163	44763875	0.126503357	80.65
3.46E+05	253	87470294.98	0.205136881	87.08		3.46E+05	64	22126873.04	0.053358019	87.08		3.46E+05	106	36647633.47	0.103566741	87.08
4.35E+05	189	82262494.37	0.192923455	94.03		4.35E+05	48	20892062.06	0.050380324	94.03		4.35E+05	73	31773344.39	0.08979193	94.03
5.48E+05	125	68493614.16	0.160632434	101.53		5.48E+05	31	16986416.31	0.040962025	101.53		5.48E+05	62	33972832.62	0.096007715	101.53
6.90E+05	104	71741988.37	0.168250579	109.63		6.90E+05	29	20004977.53	0.048241158	109.63		6.90E+05	36	24833765.21	0.070180579	109.63
8.68E+05	91	79028085.72	0.185338063	118.37		8.68E+05	27	23447893.57	0.056543604	118.37		8.68E+05	38	33000739.09	0.093260565	118.37
1.09E+06	67	73251221.75	0.171790059	127.81		1.09E+06	19	20772734.53	0.050092571	127.81		1.09E+06	32	34985658.15	0.098869975	127.81
1.38E+06	52	71572042.9	0.167852019	138.01		1.38E+06	13	17893010.72	0.043148239	138.01		1.38E+06	31	42667948.65	0.120580238	138.01
1.73E+06	48	83172797.15	0.195058313	149.02		1.73E+06	14	24258732.5	0.058498908	149.02		1.73E+06	19	32922565.54	0.093039645	149.02
2.18E+06	41	89438380.5	0.20975247	160.91		2.18E+06	10	21814239.15	0.052604115	160.91		2.18E+06	17	37084206.55	0.104800503	160.91
2.75E+06	25	68656250	0.16101385	173.75		2.75E+06	7	19223750	0.04635726	173.75		2.75E+06	25	68656250	0.194023553	173.75
3.46E+06	25	86433097.8	0.202704428	187.61		3.46E+06	9	31115915.21	0.075034714	187.61		3.46E+06	29	100262393.5	0.28334297	187.61
4.35E+06	17	73992719.81	0.173529034	202.57		4.35E+06	2	8705025.86	0.020991802	202.57		4.35E+06	20	87050258.6	0.246005287	202.57
5.48E+06	17	93151315.25	0.21846011	218.73		5.48E+06	9	49315402.19	0.118922007	218.73		5.48E+06	16	87671826.12	0.247761845	218.73
6.90E+06	16	110372289.8	0.258847044	236.18		6.90E+06	7	48287876.79	0.116444173	236.18		6.90E+06	12	82779217.35	0.233935263	236.18
8.68E+06	14	121581670.3	0.285135481	255.02		8.68E+06	7	60790835.17	0.146594529	255.02		8.68E+06	11	95528455.27	0.269964793	255.02
1.09E+07	18	196794327.1	0.461525532	275.37		1.09E+07	6	65598109.03	0.158187067	275.37		1.09E+07	13	142129236.2	0.401659272	275.37
1.38E+07	12	165166252.8	0.387350814	297.34		1.38E+07	8	110110835.2	0.265527624	297.34		1.38E+07	9	123874689.6	0.35007166	297.34
1.73E+07	6	103965996.4	0.243822891	321.06		1.73E+07	5	86638330.36	0.208924671	321.06		1.73E+07	9	155948994.7	0.440714109	321.06
2.18E+07	3	65442717.44	0.153477417	346.67		2.18E+07	5	109071195.7	0.263020577	346.67		2.18E+07	5	109071195.7	0.308236773	346.67
2.75E+07	3	82387500	0.19321662	374.32		2.75E+07	3	82387500	0.198673973	374.32		2.75E+07	5	137312500	0.388047106	374.32
3.46E+07	6	207439434.7	0.486490627	404.19		3.46E+07	1	34573239.12	0.083371904	404.19		3.46E+07	2	69146478.24	0.195408945	404.19
4.35E+07	4	174100517.2	0.408303609	436.43		4.35E+07	4	174100517.2	0.419836037	436.43		4.35E+07	1	43525129.3	0.123002643	436.43
5.48E+07	2	109589782.6	0.257011894	471.25		5.48E+07	4	219179565.3	0.528542255	471.25		5.48E+07	0	0	0	471.25
6.90E+07	0	0	0	508.84		6.90E+07	1	68982681.13	0.166348819	508.84		6.90E+07	2	137965362.3	0.389892104	508.84
8.68E+07	3	260532150.7	0.611004602	549.43		8.68E+07	1	86844050.24	0.209420756	549.43		8.68E+07	3	260532150.7	0.736267617	549.43
1.09E+08	0	0	0	593.26		1.09E+08	1	109330181.7	0.263645111	593.26		1.09E+08	3	327990545.1	0.926906013	593.26
1.38E+08	3	412915632.1	0.968377035	640.59		1.38E+08	0	0	0	640.59		1.38E+08	3	412915632.1	1.166905534	640.59
1.73E+08	0	0	0	691.69		1.73E+08	0	0	0	691.69		1.73E+08	2	346553321.5	0.979364686	691.69
2.18E+08	2	436284782.9	1.02318278	746.87		2.18E+08	0	0	0	746.87		2.18E+08	0	0	0	746.87
2.75E+08	1	274625000	0.644055401	806.46		2.75E+08	0	0	0	806.46		2.75E+08	0	0	0	806.46
3.46E+08	0	0	0	870.79		3.46E+08	1	345732391.2	0.833719045	870.79		3.46E+08	1	345732391.2	0.977044726	870.79
4.35E+08	0	0	0	940.26		4.35E+08	0	0	0	940.26		4.35E+08		0	0	940.26
5.48E+08	0	0	0	1015.27		5.48E+08	0	0	0	1015.27		5.48E+08		0	0	1015.27
6.90E+08	1	689826811.3	1.617794024	1096.26		6.90E+08	2	1379653623	3.326976382	1096.26		6.90E+08		0	0	1096.26
8.68E+08		0	0	1183.71		8.68E+08		0	0	1183.71		8.68E+08		0	0	1183.71
1.09E+09		0	0	1278.15		1.09E+09		0	0	1278.15		1.09E+09		0	0	1278.15

Paetahi.a lower						**Paetahi.a middle**						**Paetahi.a upper**				
Volume bins in um	Frequency	average volume of bin	volume fraction %	eqD (um)		Volume bins in um	Frequency	average volume of bin	volume fraction %	eqD (um)		Volume bins in um	Frequency	average volume of bin	volume fraction %	eqD (um)
2.75E+02	976	268034	0.000401701	8.06		2.75E+02	598	164225.75	0.000445322	8.06		2.75E+02	847	232607.375	0.000464865	8.06
3.46E+02	0	0	0	8.71		3.46E+02	0	0	0	8.71		3.46E+02	0	0	0	8.71
4.35E+02	0	0	0	9.40		4.35E+02	0	0	0	9.40		4.35E+02	0	0	0	9.40
5.48E+02	0	0	0	10.15		5.48E+02	0	0	0	10.15		5.48E+02	0	0	0	10.15
6.90E+02	144	99335.06082	0.000148873	10.96		6.90E+02	90	62084.41301	0.000168351	10.96		6.90E+02	198	136585.7086	0.000272966	10.96
8.68E+02	44	38211.38211	5.72671E-05	11.84		8.68E+02	30	26053.21507	7.06471E-05	11.84		8.68E+02	54	46895.78713	9.37211E-05	11.84
1.09E+03	0	0	0	12.78		1.09E+03	0	0	0	12.78		1.09E+03	0	0	0	12.78
1.38E+03	96	132133.0023	0.000198027	13.80		1.38E+03	64	88088.66818	0.000238865	13.80		1.38E+03	101	139014.9295	0.000277821	13.80
1.73E+03	178	308432.4561	0.000462245	14.90		1.73E+03	164	284173.7236	0.000770578	14.90		1.73E+03	256	443588.2515	0.00088651	14.90
2.18E+03	25	54535.59787	8.17321E-05	16.09		2.18E+03	22	47991.32612	0.000130135	16.09		2.18E+03	25	54535.59787	0.000108989	16.09
2.75E+03	142	389967.5	0.000584441	17.37		2.75E+03	89	244416.25	0.00066277	17.37		2.75E+03	161	442146.25	0.000883628	17.37
3.46E+03	28	96805.06954	0.000145081	18.76		3.46E+03	29	100262.3935	0.000271876	18.76		3.46E+03	25	86433.0978	0.000172736	18.76
4.35E+03	84	365611.0861	0.000547939	20.26		4.35E+03	62	269855.8016	0.000731753	20.26		4.35E+03	80	348201.0344	0.000695879	20.26
5.48E+03	228	1249323.522	0.001872352	21.87		5.48E+03	185	1013705.49	0.00274881	21.87		5.48E+03	269	1473982.577	0.002945751	21.87
6.90E+03	29127	200925855.3	0.301126072	23.62		6.90E+03	14687	101314863.8	0.274729973	23.62		6.90E+03	18377	126769473.1	0.253348551	23.62
8.68E+03	110	955284.5527	0.001431678	25.50		8.68E+03	76	660014.7818	0.001789726	25.50		8.68E+03	111	963968.9577	0.00192649	25.50
1.09E+04	8006	87529743.48	0.13118017	27.54		1.09E+04	4612	50423079.81	0.136729507	27.54		1.09E+04	6195	67730047.57	0.135358371	27.54
1.38E+04	5802	79857883.25	0.119682411	29.73		1.38E+04	3176	43714001.59	0.118536867	29.73		1.38E+04	4193	57711841.51	0.115337005	29.73
1.73E+04	5258	91108868.21	0.136544177	32.11		1.73E+04	3159	54738097.12	0.148430303	32.11		1.73E+04	4313	74734223.77	0.149356204	32.11
2.18E+04	4343	94739240.61	0.141984989	34.67		2.18E+04	2590	56498879.39	0.15320492	34.67		2.18E+04	3773	82305124.3	0.164486634	34.67
2.75E+04	4191	115095337.5	0.172492519	37.43		2.75E+04	2364	64921350	0.176043673	37.43		2.75E+04	3480	95569500	0.190995464	37.43
3.46E+04	3308	114368275	0.171402876	40.42		3.46E+04	1770	61194633.24	0.165938139	40.42		3.46E+04	2667	92206828.74	0.184275172	40.42
4.35E+04	2811	122349138.5	0.183363736	43.64		4.35E+04	1428	62153884.64	0.168539289	43.64		4.35E+04	2364	102893405.7	0.205632275	43.64
5.48E+04	2177	119288478.4	0.178776748	47.12		5.48E+04	1056	57863405.24	0.15690503	47.12		5.48E+04	1626	89096493.29	0.178059172	47.12
6.90E+04	1732	119478003.7	0.179060788	50.88		6.90E+04	651	44907725.41	0.121773822	50.88		6.90E+04	1202	82917182.71	0.165709832	50.88
8.68E+04	1222	106123429.4	0.159046387	54.94		8.68E+04	492	42727272.72	0.115861208	54.94		8.68E+04	880	76422764.21	0.152730749	54.94
1.09E+05	952	104082333	0.155987412	59.33		1.09E+05	326	35641639.24	0.096647483	59.33		1.09E+05	639	69861986.11	0.139619046	59.33
1.38E+05	695	95658788.1	0.143363108	64.06		1.38E+05	224	30831033.86	0.083602828	64.06		1.38E+05	454	62487898.99	0.124881947	64.06
1.73E+05	470	81440030.54	0.122053563	69.17		1.73E+05	160	27724265.72	0.075178375	69.17		1.73E+05	290	50250231.61	0.100424992	69.17
2.18E+05	340	74168413.1	0.111155644	74.69		2.18E+05	109	23777520.67	0.064476202	74.69		2.18E+05	233	50827177.21	0.101578017	74.69
2.75E+05	259	71127875	0.106598813	80.65		2.75E+05	79	21695375	0.058830161	80.65		2.75E+05	154	42292250	0.084520981	80.65
3.46E+05	208	71912337.37	0.107774481	87.08		3.46E+05	67	23164070.21	0.062812742	87.08		3.46E+05	121	41833619.34	0.083604409	87.08
4.35E+05	164	71381212.05	0.106978487	94.03		4.35E+05	65	28291334.04	0.076716063	94.03		4.35E+05	100	43525129.3	0.086984888	94.03
5.48E+05	118	64657971.76	0.096902417	101.53		5.48E+05	52	28493343.49	0.077263841	101.53		5.48E+05	78	42740015.23	0.085415839	101.53
6.90E+05	92	63464066.64	0.095113121	109.63		6.90E+05	49	33801513.75	0.091657716	109.63		6.90E+05	76	52426837.66	0.104774935	109.63
8.68E+05	90	78159645.22	0.117137274	118.37		8.68E+05	56	48632668.14	0.131874546	118.37		8.68E+05	72	62527716.17	0.124961522	118.37
1.09E+06	73	79811032.65	0.119612196	127.81		1.09E+06	45	49198581.77	0.133409103	127.81		1.09E+06	54	59038298.13	0.117987927	127.81
1.38E+06	81	111487220.7	0.167085061	138.01		1.38E+06	35	48173490.41	0.130629419	138.01		1.38E+06	60	82583126.42	0.165042221	138.01
1.73E+06	64	110897062.9	0.166200596	149.02		1.73E+06	31	53715764.83	0.145658101	149.02		1.73E+06	41	71043430.9	0.141980162	149.02
2.18E+06	77	167969641.4	0.251734841	160.91		2.18E+06	31	67624141.35	0.183372685	160.91		2.18E+06	47	102526924	0.204899863	160.91
2.75E+06	49	134566250	0.201673429	173.75		2.75E+06	30	82387500	0.223405677	173.75		2.75E+06	38	104357500	0.208558265	173.75
3.46E+06	47	162494223.9	0.243528874	187.61		3.46E+06	29	100262393.5	0.271876047	187.61		3.46E+06	31	107177041.3	0.214193113	187.61
4.35E+06	35	152337952.5	0.228307747	202.57		4.35E+06	17	73992719.81	0.20064201	202.57		4.35E+06	28	121870362	0.243557687	202.57
5.48E+06	37	202741097.9	0.303846562	218.73		5.48E+06	12	65753869.59	0.178301171	218.73		5.48E+06	25	136987228.3	0.273768715	218.73
6.90E+06	32	220744579.6	0.330828245	236.18		6.90E+06	15	103474021.7	0.280584844	236.18		6.90E+06	19	131067094.1	0.261937338	236.18
8.68E+06	18	156319290.4	0.234274548	255.02		8.68E+06	7	60790835.17	0.164843182	255.02		8.68E+06	11	95528455.27	0.190913436	255.02
1.09E+07	15	163995272.6	0.245778485	275.37		1.09E+07	5	54665090.86	0.148232336	275.37		1.09E+07	10	109330181.7	0.21849616	275.37
1.38E+07	7	96346980.82	0.144394497	297.34		1.38E+07	6	82583126.42	0.223936146	297.34		1.38E+07	12	165166252.8	0.330084442	297.34
1.73E+07	7	121293662.5	0.181781902	321.06		1.73E+07	8	138621328.6	0.375891873	321.06		1.73E+07	3	51982998.22	0.103887923	321.06
2.18E+07	7	152699674	0.228849856	346.67		2.18E+07	5	109071195.7	0.295762394	346.67		2.18E+07	3	65442717.44	0.130787146	346.67
2.75E+07	3	82387500	0.123473528	374.32		2.75E+07	3	82387500	0.223405677	374.32		2.75E+07	2	54925000	0.109767508	374.32
3.46E+07	3	103719717.4	0.155443962	404.19		3.46E+07	4	138292956.5	0.375001444	404.19		3.46E+07	0	0	0	404.19
4.35E+07	3	130575387.9	0.195692354	436.43		4.35E+07	1	43525129.3	0.118024712	436.43		4.35E+07	2	87050258.6	0.173969776	436.43
5.48E+07	6	328769347.9	0.492724155	471.25		5.48E+07	3	164384674	0.445752927	471.25		5.48E+07	4	219179565.3	0.438029944	471.25
6.90E+07	0	0	0	508.84		6.90E+07	0	0	0	508.84		6.90E+07	3	206948043.4	0.413585271	508.84
8.68E+07	1	86844050.24	0.130152527	549.43		8.68E+07	1	86844050.24	0.23549026	549.43		8.68E+07	1	86844050.24	0.173557669	549.43
1.09E+08	1	109330181.7	0.163852323	593.26		1.09E+08	1	109330181.7	0.296464673	593.26		1.09E+08	2	218660363.4	0.43699232	593.26
1.38E+08	1	137638544	0.206277853	640.59		1.38E+08	0	0	0	640.59		1.38E+08	0	0	0	640.59
1.73E+08	1	173276660.7	0.259688431	691.69		1.73E+08	0	0	0	691.69		1.73E+08	2	346553321.5	0.692586154	691.69
2.18E+08	1	218142391.5	0.326928366	746.87		2.18E+08	0	0	0	746.87		2.18E+08	1	218142391.5	0.435957154	746.87
2.75E+08	1	274625000	0.411578427	806.46		2.75E+08	0	0	0	806.46		2.75E+08	0	0	0	806.46
3.46E+08		0	0	870.79		3.46E+08	0	0	0	870.79		3.46E+08	0	0	0	870.79
4.35E+08		0	0	940.26		4.35E+08	0	0	0	940.26		4.35E+08	0	0	0	940.26
5.48E+08		0	0	1015.27		5.48E+08	0	0	0	1015.27		5.48E+08	1	547948913.2	1.095074861	1015.27
6.90E+08		0	0	1096.26		6.90E+08	1	689826811.3	1.870565626	1096.26		6.90E+08		0	0	1096.26
8.68E+08		0	0	1183.71		8.68E+08		0	0	1183.71		8.68E+08		0	0	1183.71
1.09E+09		0	0	1278.15		1.09E+09		0	0	1278.15		1.09E+09		0	0	1278.15

Paetahi.d						**Paetahi.e lower**				
Volume bins in um	Frequency	average volume of bin	volume fraction %	eqD (um)		Volume bins in um	Frequency	average volume of bin	volume fraction %	eqD (um)
2.75E+02	647	177682.375	0.000595292	8.06		2.75E+02	612	168070.5	0.000351406	8.06
3.46E+02	0	0	0	8.71		3.46E+02	0	0	0	8.71
4.35E+02	0	0	0	9.40		4.35E+02	0	0	0	9.40
5.48E+02	0	0	0	10.15		5.48E+02	0	0	0	10.15
6.90E+02	134	92436.79271	0.000309692	10.96		6.90E+02	131	90367.31227	0.000188942	10.96
8.68E+02	29	25184.77457	8.43769E-05	11.84		8.68E+02	37	32132.29859	6.7183E-05	11.84
1.09E+03	0	0	0	12.78		1.09E+03	0	0	0	12.78
1.38E+03	64	88088.66818	0.000295125	13.80		1.38E+03	44	60560.95938	0.000126622	13.80
1.73E+03	186	322294.589	0.001079788	14.90		1.73E+03	135	233923.492	0.000489093	14.90
2.18E+03	22	47991.32612	0.000160786	16.09		2.18E+03	23	50172.75004	0.000104902	16.09
2.75E+03	110	302087.5	0.001012088	17.37		2.75E+03	88	241670	0.000505289	17.37
3.46E+03	15	51859.85868	0.000173747	18.76		3.46E+03	14	48402.53477	0.000101201	18.76
4.35E+03	65	282913.3404	0.000947848	20.26		4.35E+03	62	269855.8016	0.000564221	20.26
5.48E+03	228	1249323.522	0.004185625	21.87		5.48E+03	148	810964.3916	0.001695584	21.87
6.90E+03	15821	109137499.8	0.365644777	23.62		6.90E+03	12204	84186464.05	0.176019075	23.62
8.68E+03	88	764227.6421	0.002560402	25.50		8.68E+03	75	651330.3768	0.001361817	25.50
1.09E+04	5240	57289015.22	0.191936128	27.54		1.09E+04	3845	42037454.87	0.087892917	27.54
1.38E+04	3370	46384189.34	0.155401549	29.73		1.38E+04	2931	40341857.26	0.084347721	29.73
1.73E+04	3307	57302591.7	0.191981614	32.11		1.73E+04	2993	51861704.56	0.108433694	32.11
2.18E+04	2456	53575771.34	0.179495599	34.67		2.18E+04	2557	55779009.5	0.116624089	34.67
2.75E+04	2299	63136287.5	0.21152632	37.43		2.75E+04	2426	66624025	0.139299107	37.43
3.46E+04	1567	54176265.7	0.181507443	40.42		3.46E+04	1898	65620007.85	0.137199884	40.42
4.35E+04	1186	51620803.35	0.172945845	43.64		4.35E+04	1435	62458560.54	0.130589854	43.64
5.48E+04	816	44712631.32	0.149801307	47.12		5.48E+04	1067	58466149.04	0.122242425	47.12
6.90E+04	579	39940972.37	0.133814756	50.88		6.90E+04	750	51737010.84	0.108172981	50.88
8.68E+04	408	35432372.5	0.118709536	54.94		8.68E+04	604	52453806.35	0.109671675	54.94
1.09E+05	263	28753837.79	0.096334355	59.33		1.09E+05	406	44388053.78	0.092807606	59.33
1.38E+05	169	23260913.94	0.077931341	64.06		1.38E+05	304	41842117.39	0.087484501	64.06
1.73E+05	119	20619922.63	0.069083193	69.17		1.73E+05	257	44532101.81	0.093108785	69.17
2.18E+05	101	22032381.54	0.073815373	74.69		2.18E+05	147	32066931.54	0.067046309	74.69
2.75E+05	69	18949125	0.063485499	80.65		2.75E+05	128	35152000	0.073496644	80.65
3.46E+05	54	18669549.13	0.062548832	87.08		3.46E+05	117	40450689.77	0.084575271	87.08
4.35E+05	32	13928041.38	0.046663297	94.03		4.35E+05	101	43960380.59	0.091913417	94.03
5.48E+05	31	16986416.31	0.05690981	101.53		5.48E+05	83	45479759.8	0.095090171	101.53
6.90E+05	36	24833765.21	0.083200885	109.63		6.90E+05	79	54496318.09	0.113942207	109.63
8.68E+05	34	29526977.08	0.098924613	118.37		8.68E+05	56	48632668.14	0.101682347	118.37
1.09E+06	25	27332545.43	0.09157258	127.81		1.09E+06	65	71064618.11	0.148583606	127.81
1.38E+06	24	33033250.57	0.110671727	138.01		1.38E+06	54	74324813.78	0.155400101	138.01
1.73E+06	28	48517465	0.16254869	149.02		1.73E+06	39	67577897.68	0.141293487	149.02
2.18E+06	10	21814239.15	0.073084527	160.91		2.18E+06	25	54535597.87	0.114024334	160.91
2.75E+06	10	27462500	0.092007969	173.75		2.75E+06	34	93372500	0.195225459	173.75
3.46E+06	19	65689154.33	0.220079223	187.61		3.46E+06	24	82975773.89	0.173487735	187.61
4.35E+06	9	39172616.37	0.131240523	202.57		4.35E+06	20	87050258.6	0.182006766	202.57
5.48E+06	17	93151315.25	0.312086056	218.73		5.48E+06	18	98630804.38	0.206219648	218.73
6.90E+06	9	62084413.01	0.208002212	236.18		6.90E+06	11	75880949.24	0.158653706	236.18
8.68E+06	5	43422025.12	0.145477372	255.02		8.68E+06	16	138950480.4	0.290520992	255.02
1.09E+07	1	10933018.17	0.036629032	275.37		1.09E+07	6	65598109.03	0.137154097	275.37
1.38E+07	4	55055417.61	0.184452878	297.34		1.38E+07	9	123874689.6	0.259000168	297.34
1.73E+07	5	86638330.36	0.290265518	321.06		1.73E+07	6	103965996.4	0.217374595	321.06
2.18E+07	3	65442717.44	0.219253582	346.67		2.18E+07	7	152699674	0.319268136	346.67
2.75E+07	4	109850000	0.368031875	374.32		2.75E+07	9	247162500	0.516773275	374.32
3.46E+07	3	103719717.4	0.34749351	404.19		3.46E+07	4	138292956.5	0.289146226	404.19
4.35E+07	1	43525129.3	0.145822803	436.43		4.35E+07	7	304675905.1	0.63702368	436.43
5.48E+07	2	109589782.6	0.367160066	471.25		5.48E+07	1	54794891.32	0.114566471	471.25
6.90E+07	1	68982681.13	0.231113569	508.84		6.90E+07	3	206948043.4	0.432691926	508.84
8.68E+07	0	0	0	549.43		8.68E+07	0	0	0	549.43
1.09E+08	1	109330181.7	0.366290321	593.26		1.09E+08	2	218660363.4	0.457180325	593.26
1.38E+08	0	0	0	640.59		1.38E+08	1	137638544	0.287777964	640.59
1.73E+08	0	0	0	691.69		1.73E+08	0	0	0	691.69
2.18E+08	0	0	0	746.87		2.18E+08	1	218142391.5	0.456097337	746.87
2.75E+08	0	0	0	806.46		2.75E+08	2	549250000	1.148385055	806.46
3.46E+08	0	0	0	870.79		3.46E+08	1	345732391.2	0.722865564	870.79
4.35E+08	0	0	0	940.26		4.35E+08		0	0	940.26
5.48E+08	1	547948913.2	1.835800329	1015.27		5.48E+08		0	0	1015.27
6.90E+08	0	0	0	1096.26		6.90E+08		0	0	1096.26
8.68E+08	0	0	0	1183.71		8.68E+08		0	0	1183.71
1.09E+09	0	0	0	1278.15		1.09E+09		0	0	1278.15

Paetahi.e middle						**Paetaih.f**				
Volume bins in um	Frequency	average volume of bin	volume fraction %	eqD (um)		Volume bins in um	Frequency	average volume of bin	volume fraction %	eqD (um)
2.75E+02	835	229311.875	0.000315	8.06		2.75E+02	2318	636580.75	0.002521942	8.06
3.46E+02	0	0	0	8.71		3.46E+02	0	0	0	8.71
4.35E+02	0	0	0	9.40		4.35E+02	0	0	0	9.40
5.48E+02	0	0	0	10.15		5.48E+02	0	0	0	10.15
6.90E+02	177	122099.3456	0.000167725	10.96		6.90E+02	400	275930.7245	0.001093155	10.96
8.68E+02	44	38211.38211	5.249E-05	11.84		8.68E+02	133	115502.5868	0.000457587	11.84
1.09E+03	0	0	0	12.78		1.09E+03	0	0	0	12.78
1.38E+03	87	119745.5333	0.000164491	13.80		1.38E+03	165	227103.5977	0.000899716	13.80
1.73E+03	240	415863.9857	0.000571261	14.90		1.73E+03	454	786676.0397	0.003116574	14.90
2.18E+03	27	58898.44569	8.09072E-05	16.09		2.18E+03	87	189783.8806	0.000751867	16.09
2.75E+03	158	433907.5	0.000596047	17.37		2.75E+03	300	823875	0.003263946	17.37
3.46E+03	37	127920.9847	0.000175722	18.76		3.46E+03	71	245469.9978	0.000972479	18.76
4.35E+03	66	287265.8534	0.000394609	20.26		4.35E+03	117	509244.0128	0.002017472	20.26
5.48E+03	240	1315077.392	0.001806487	21.87		5.48E+03	426	2334262.37	0.009247647	21.87
6.90E+03	19674	135716526.8	0.186430177	23.62		6.90E+03	24427	168503995.2	0.667562285	23.62
8.68E+03	105	911862.5275	0.001252601	25.50		8.68E+03	210	1823725.055	0.007225052	25.50
1.09E+04	6286	68724952.22	0.094405636	27.54		1.09E+04	7227	79012922.32	0.313025498	27.54
1.38E+04	4066	55963832	0.076876025	29.73		1.38E+04	5704	78509025.52	0.31102921	29.73
1.73E+04	4261	73833185.14	0.10142268	32.11		1.73E+04	5464	94678367.42	0.375087292	32.11
2.18E+04	3581	78116790.38	0.107306954	34.67		2.18E+04	4668	101828868.3	0.403415432	34.67
2.75E+04	3211	88182087.5	0.121133384	37.43		2.75E+04	4301	118116212.5	0.467941004	37.43
3.46E+04	2611	90270727.35	0.124002493	40.42		3.46E+04	3403	117652732.7	0.466104836	40.42
4.35E+04	2015	87703135.54	0.120475461	43.64		4.35E+04	2995	130357762.2	0.516438352	43.64
5.48E+04	1667	91343083.84	0.125475561	47.12		5.48E+04	2388	130850200.5	0.518389245	47.12
6.90E+04	1183	81606511.77	0.112100691	50.88		6.90E+04	1891	130446250	0.516788914	50.88
8.68E+04	952	82675535.83	0.113569181	54.94		8.68E+04	1461	126879157.4	0.502657163	54.94
1.09E+05	680	74344523.57	0.102125092	59.33		1.09E+05	1141	124745737.3	0.494205193	59.33
1.38E+05	461	63451368.8	0.087161455	64.06		1.38E+05	834	114790545.7	0.45476571	64.06
1.73E+05	356	61686491.22	0.08473709	69.17		1.73E+05	659	114189319.4	0.452383831	69.17
2.18E+05	259	56498879.39	0.077611006	74.69		2.18E+05	510	111252619.6	0.440749508	74.69
2.75E+05	194	53277250	0.073185539	80.65		2.75E+05	390	107103750	0.424312931	80.65
3.46E+05	166	57391576.94	0.07883728	87.08		3.46E+05	278	96113604.76	0.380773272	87.08
4.35E+05	93	40478370.25	0.055604059	94.03		4.35E+05	208	90532268.94	0.358661694	94.03
5.48E+05	91	49863351.11	0.068495957	101.53		5.48E+05	199	109041833.7	0.431991037	101.53
6.90E+05	75	51737010.84	0.071069754	109.63		6.90E+05	131	90367312.27	0.358008185	109.63
8.68E+05	64	55580192.16	0.076349029	118.37		8.68E+05	95	82501847.73	0.326847574	118.37
1.09E+06	43	47011978.14	0.064579102	127.81		1.09E+06	60	65598109.03	0.259880031	127.81
1.38E+06	47	64690115.7	0.088863089	138.01		1.38E+06	54	74324813.78	0.294452618	138.01
1.73E+06	25	43319165.18	0.059506383	149.02		1.73E+06	62	107431529.7	0.425611495	149.02
2.18E+06	41	89438380.5	0.122859121	160.91		2.18E+06	37	80712684.84	0.319759447	160.91
2.75E+06	26	71402500	0.098083712	173.75		2.75E+06	22	60417500	0.239356012	173.75
3.46E+06	22	76061126.07	0.104483143	187.61		3.46E+06	18	62231830.42	0.246543845	187.61
4.35E+06	21	91402771.53	0.125557552	202.57		4.35E+06	21	91402771.53	0.362110364	202.57
5.48E+06	19	104110293.5	0.143013537	218.73		5.48E+06	7	38356423.93	0.151956646	218.73
6.90E+06	13	89677485.46	0.123187573	236.18		6.90E+06	13	89677485.46	0.355275298	236.18
8.68E+06	10	86844050.24	0.119295358	255.02		8.68E+06	10	86844050.24	0.344050077	255.02
1.09E+07	13	142129236.2	0.195239146	275.37		1.09E+07	3	32799054.51	0.129940016	275.37
1.38E+07	9	123874689.6	0.170163361	297.34		1.38E+07	4	55055417.61	0.21811305	297.34
1.73E+07	9	155948994.7	0.21422298	321.06		1.73E+07	5	86638330.36	0.343235077	321.06
2.18E+07	5	109071195.7	0.149828196	346.67		2.18E+07	2	43628478.29	0.172842944	346.67
2.75E+07	9	247162500	0.339520542	374.32		2.75E+07	5	137312500	0.543990937	374.32
3.46E+07	4	138292956.5	0.18996935	404.19		3.46E+07	3	103719717.4	0.410906409	404.19
4.35E+07	10	435251293	0.597893106	436.43		4.35E+07	4	174100517.2	0.689734026	436.43
5.48E+07	4	219179565.3	0.30108113	471.25		5.48E+07	2	109589782.6	0.434161846	471.25
6.90E+07	2	137965362.3	0.189519343	508.84		6.90E+07	0	0	0	508.84
8.68E+07	2	173688100.5	0.238590717	549.43		8.68E+07	2	173688100.5	0.688100155	549.43
1.09E+08	2	218660363.4	0.300367916	593.26		1.09E+08	0	0	0	593.26
1.38E+08	1	137638544	0.189070401	640.59		1.38E+08	1	137638544	0.545282626	640.59
1.73E+08	3	519829982.2	0.714076598	691.69		1.73E+08	0	0	0	691.69
2.18E+08		0	0	746.87		2.18E+08	1	218142391.5	0.864214721	746.87
2.75E+08		0	0	806.46		2.75E+08	1	274625000	1.087981874	806.46
3.46E+08		0	0	870.79		3.46E+08	1	345732391.2	1.369688028	870.79
4.35E+08		0	0	940.26		4.35E+08	0	0	0	940.26
5.48E+08		0	0	1015.27		5.48E+08	1	547948913.2	2.170809232	1015.27
6.90E+08		0	0	1096.26		6.90E+08	1	689826811.3	2.732886906	1096.26
8.68E+08		0	0	1183.71		8.68E+08	0	0	0	1183.71
1.09E+09		0	0	1278.15		1.09E+09	0	0	0	1278.15

Appendix E5: Vesicle number densities.

Vesicle number densities for 19 units within the Poto and Paetahi Formations from the reference locations.

Formation	Sample	um^{-3}	mm^{-3}	cm^{-3}	No. of bubbles
Poto Formation	**Poto.a**				**960700**
	Total Volume	6.61E+10	66.08525	6.61E-11	
	Total bubble volume	3.22E+09	3.223683	3.22E-12	
	Total crystal + melt volume	6.29E+10	62.86157	6.29E-11	
	VND	1.53E-05	15282.79	1.53E+16	
	Poto.c lower				**629340**
	Total Volume	6.77E+10	67.74433	6.77E-11	
	Total bubble volume	3.27E+09	3.268726	3.27E-12	
	Total crystal + melt volume	6.45E+10	64.47561	6.45E-11	
	VND	9.76E-06	9760.901	9.76E+15	
	Poto.d				**83940**
	Total Volume	7.87E+09	7.868211	7.87E-12	
	Total bubble volume	2.69E+08	0.269064	2.69E-13	
	Total crystal + melt volume	7.6E+09	7.599146	7.6E-12	
	VND	1.1E-05	11045.98	1.1E+16	
	Poto.e				**482050**
	Total Volume	3.35E+10	33.48803	3.35E-11	
	Total bubble volume	1.31E+09	1.314353	1.31E-12	
	Total crystal + melt volume	3.22E+10	32.17368	3.22E-11	
	VND	1.5E-05	14982.74	1.5E+16	
	Poto.g				**507479**
	Total Volume	3.37E+10	33.72644	3.37E-11	
	Total bubble volume	3.02E+09	3.021591	3.02E-12	
	Total crystal + melt volume	3.07E+10	30.70485	3.07E-11	
	VND	1.65E-05	16527.65	1.65E+16	
	Poto.h				**489311**
	Total Volume	3.5E+10	35	3.5E-11	
	Total bubble volume	2.27E+09	2.26508	2.27E-12	
	Total crystal + melt volume	3.27E+10	32.73492	3.27E-11	

	VND	1.49E-05	14947.68	1.49E+16	
	Poto.j				**228170**
	Total Volume	2.06E+10	20.55911	2.06E-11	
	Total bubble volume	9.22E+08	0.922217	9.22E-13	
	Total crystal + melt volume	1.96E+10	19.63689	1.96E-11	
	VND	1.16E-05	11619.46	1.16E+16	
	Poto.k lower				**645219**
	Total Volume	4.16E+10	41.56259	4.16E-11	
	Total bubble volume	1.97E+09	1.972228	1.97E-12	
	Total crystal + melt volume	3.96E+10	39.59036	3.96E-11	
	VND	1.63E-05	16297.38	1.63E+16	
	Poto.l lower				**768014**
	Total Volume	5.95E+10	59.51868	5.95E-11	
	Total bubble volume	2.55E+09	2.551803	2.55E-12	
	Total crystal + melt volume	5.7E+10	56.96687	5.7E-11	
	VND	1.35E-05	13481.77	1.35E+16	
	Poto.l upper				**434047**
	Total Volume	4.26E+10	42.63997	4.26E-11	
	Total bubble volume	2.32E+09	2.321217	2.32E-12	
	Total crystal + melt volume	4.03E+10	40.31875	4.03E-11	
	VND	1.08E-05	10765.39	1.08E+16	
	Poto.m				**675356**
	Total Volume	4.15E+10	41.46869	4.15E-11	
	Total bubble volume	2.69E+09	2.694374	2.69E-12	
	Total crystal + melt volume	3.88E+10	38.77432	3.88E-11	
	VND	1.74E-05	17417.61	1.74E+16	
	Poto.o				**515709**
	Total Volume	3.54E+10	35.38552	3.54E-11	
	Total bubble volume	1.93E+09	1.929038	1.93E-12	
	Total crystal + melt volume	3.35E+10	33.45649	3.35E-11	
	VND	1.54E-05	15414.32	1.54E+16	
Paetahi Formation	**Paetahi.a lower**				**1001721**
	Total Volume	6.67E+10	66.72483	6.67E-11	
	Total bubble volume	2.34E+09	2.342755	2.34E-12	

	Total crystal + melt volume	6.44E+10	64.38207	6.44E-11	
	VND	1.56E-05	15559	1.56E+16	
	Paetahi.a middle				**558436**
	Total Volume	3.69E+10	36.87798	3.69E-11	
	Total bubble volume	1.8E+09	1.797308	1.8E-12	
	Total crystal + melt volume	3.51E+10	35.08067	3.51E-11	
	VND	1.59E-05	15918.62	1.59E+16	
	Paetahi.a upper				**700143**
	Total Volume	5E+10	50.03758	5E-11	
	Total bubble volume	3.71E+09	3.714519	3.71E-12	
	Total crystal + melt volume	4.63E+10	46.32306	4.63E-11	
	VND	1.51E-05	15114.35	1.51E+16	
	Paetahi.d				**319625**
	Total Volume	2.98E+10	29.84796	2.98E-11	
	Total bubble volume	2.11E+09	2.10747	2.11E-12	
	Total crystal + melt volume	2.77E+10	27.74049	2.77E-11	
	VND	1.15E-05	11521.97	1.15E+16	
	Paetahi.e lower				**596557**
	Total Volume	4.78E+10	47.82803	4.78E-11	
	Total bubble volume	1.58E+09	1.584118	1.58E-12	
	Total crystal + melt volume	4.62E+10	46.24392	4.62E-11	
	VND	1.29E-05	12900.23	1.29E+16	
	Paetahi.e middle				**936905**
	Total Volume	7.28E+10	72.79751	7.28E-11	
	Total bubble volume	4.98E+09	4.975013	4.98E-12	
	Total crystal + melt volume	6.78E+10	67.8225	6.78E-11	
	VND	1.38E-05	13814.07	1.38E+16	
	Paetahi.f				
	Total Volume	2.52E+10	25.24169	2.52E-11	
	Total bubble volume	1.05E+09	1.050597	1.05E-12	
	Total crystal + melt volume	2.42E+10	24.19109	2.42E-11	
	VND	9.03E-06	9025.926	9.03E+15	

Appendix E6: Crystal number densities.

Crystal number densities for nineteen units within the Poto and Paetahi Formations from the reference locations.

Formation	Sample	um^{-3}	mm^{-3}	cm^{-3}	**No. of Crystals**
Poto	**Poto.a**				**192013**
	Total Volume	6.61E+10	66.08525	6.61E-11	
	Total Crystals	4.37E+09	4.370349	4.37E-12	
	Bubbles+Melt	6.17E+10	61.7149	6.17E-11	
	Crystals	3.11E-06	3111.291	3.11E+15	
	Poto.c lower				**55655**
	Total Volume	6.77E+10	67.74433	6.77E-11	
	Total Crystals	6.91E+09	6.911778	6.91E-12	
	Bubbles+Melt	6.08E+10	60.83255	6.08E-11	
	Crystals	9.15E-07	914.8884	9.15E+14	
	Poto.d				**6255**
	Total Volume	7.87E+09	7.868211	7.87E-12	
	Total Crystals	1.59E+09	1.58632	1.59E-12	
	Bubbles+Melt	6.28E+09	6.28189	6.28E-12	
	Crystals	9.96E-07	995.7194	9.96E+14	
	Poto.e				**75630**
	Total Volume	3.35E+10	33.48803	3.35E-11	
	Total Crystals	8.19E+09	8.191773	8.19E-12	
	Bubbles+Melt	2.53E+10	25.29626	2.53E-11	
	Crystals	2.99E-06	2989.77	2.99E+15	
	Poto.g				**40902**
	Total Volume	3.37E+10	33.72644	3.37E-11	
	Total Crystals	4.62E+09	4.621334	4.62E-12	
	Bubbles+Melt	2.91E+10	29.1051	2.91E-11	
	Crystals	1.41E-06	1405.321	1.41E+15	
	Poto.h				**29900**
	Total Volume	3.5E+10	35	3.5E-11	
	Total Crystals	3.37E+09	3.368258	3.37E-12	
	Bubbles+Melt	3.16E+10	31.63174	3.16E-11	

	Crystals	9.45E-07	945.253	9.45E+14	
	Poto.j				**28450**
	Total Volume	2.06E+10	20.55911	2.06E-11	
	Total Crystals	3.04E+09	3.03667	3.04E-12	
	Bubbles+Melt	1.75E+10	17.52244	1.75E-11	
	Crystals	1.62E-06	1623.632	1.62E+15	
	Poto.k lower				**80638**
	Total Volume	4.16E+10	41.56259	4.16E-11	
	Total Crystals	5.54E+09	5.540383	5.54E-12	
	Bubbles+Melt	3.6E+10	36.0222	3.6E-11	
	Crystals	2.24E-06	2238.564	2.24E+15	
	Poto.l lower				**89894**
	Total Volume	5.95E+10	59.51868	5.95E-11	
	Total Crystals	8.99E+09	8.991884	8.99E-12	
	Bubbles+Melt	5.05E+10	50.52679	5.05E-11	
	Crystals	1.78E-06	1779.135	1.78E+15	
	Poto.l upper				**71583**
	Total Volume	4.26E+10	42.63997	4.26E-11	
	Total Crystals	5.62E+09	5.623207	5.62E-12	
	Bubbles+Melt	3.7E+10	37.01676	3.7E-11	
	Crystals	1.93E-06	1933.8	1.93E+15	
	Poto.m				**40645**
	Total Volume	4.15E+10	41.46869	4.15E-11	
	Total Crystals	5.98E+08	0.598023	5.98E-13	
	Bubbles+Melt	4.09E+10	40.87067	4.09E-11	
	Crystals	9.94E-07	994.4784	9.94E+14	
	Poto.o				**53400**
	Total Volume	3.54E+10	35.38552	3.54E-11	
	Total Crystals	4.2E+09	4.199571	4.2E-12	
	Bubbles+Melt	3.12E+10	31.18595	3.12E-11	
	Crystals	1.71E-06	1712.309	1.71E+15	
Paetahi	**Paetahi.a lower**				**73990**
	Total Volume	6.67E+10	66.72483	6.67E-11	
	Total Crystals	5.12E+09	5.123472	5.12E-12	
	Bubbles+Melt	6.16E+10	61.60136	6.16E-11	

	Crystals	1.2E-06	1201.11	1.2E+15	
	Paetahi.a middle				**38871**
	Total Volume	3.69E+10	36.87798	3.69E-11	
	Total Crystals	2.95E+09	2.951657	2.95E-12	
	Bubbles+Melt	3.39E+10	33.92632	3.39E-11	
	Crystals	1.15E-06	1145.748	1.15E+15	
	Paetahi.a upper				**53814**
	Total Volume	5E+10	50.03758	5E-11	
	Total Crystals	4.33E+09	4.330328	4.33E-12	
	Bubbles+Melt	4.57E+10	45.70725	4.57E-11	
	Crystals	1.18E-06	1177.363	1.18E+15	
	Paetahi.d				**39728**
	Total Volume	2.98E+10	29.84796	2.98E-11	
	Total Crystals	3.43E+09	3.431123	3.43E-12	
	Bubbles+Melt	2.64E+10	26.41683	2.64E-11	
	Crystals	1.5E-06	1503.889	1.5E+15	
	Paetahi.e lower				**36122**
	Total Volume	4.78E+10	47.82803	4.78E-11	
	Total Crystals	4.34E+09	4.338607	4.34E-12	
	Bubbles+Melt	4.35E+10	43.48943	4.35E-11	
	Crystals	8.31E-07	830.5927	8.31E+14	
	Paetahi.e middle				**54302**
	Total Volume	7.28E+10	72.79751	7.28E-11	
	Total Crystals	4.49E+09	4.493527	4.49E-12	
	Bubbles+Melt	6.83E+10	68.30398	6.83E-11	
	Crystals	7.95E-07	795.0049	7.95E+14	
	Paetahi.f				**73395**
	Total Volume	2.52E+10	25.24169	2.52E-11	
	Total Crystals	5.53E+09	5.534484	5.53E-12	
	Bubbles+Melt	1.97E+10	19.70721	1.97E-11	
	Crystals	3.72E-06	3724.272	3.72E+15	

Appendix E7: Vesicle Volume.

Vesicle volume calculations for the percentage of bubbles per mm^{-3} in each of the 19 grains analysed for 3D tomography.

Formation	Sample	Volume	Percent %
Poto	**Poto.a**	**mm^{-3}**	**Percent %**
	Total volume	66.08525	
	Total Bubble	3.223683	4.878068
	Total Crystal + Melt	62.86157	95.12193
	Total		100
	Poto.c lower	**mm^{-3}**	**Percent %**
	Total volume	67.74433	
	Total Bubble	3.268726	4.825091
	Total Crystal + Melt	64.47561	95.17491
	Total		100
	Poto.d	**mm^{-3}**	**Percent %**
	Total volume	7.868211	
	Total Bubble	0.269064	3.419635
	Total Crystal + Melt	7.599146	96.58036
	Total		100
	Poto.e	**mm^{-3}**	**Percent %**
	Total volume	33.48803	
	Total Bubble	1.314353	3.924844
	Total Crystal + Melt	32.17368	96.07516
	Total		100

	Poto.g	**mm^{-3}**	**Percent %**
	Total volume	33.72644	
	Total Bubble	3.021591	8.959118
	Total Crystal + Melt	30.70485	91.04088
	Total		100
	Poto.h	**mm^{-3}**	**Percent %**
	Total volume	35	
	Total Bubble	2.26508	6.471657
	Total Crystal + Melt	32.73492	93.52834
	Total		100
	Poto.j	**mm^{-3}**	**Percent %**
	Total volume	20.55911	
	Total Bubble	1.123936	5.466852
	Total Crystal + Melt	19.43517	94.53315
	Total		100
	Poto.k lower	**mm^{-3}**	**Percent %**
	Total volume	41.56259	
	Total Bubble	2.190588	5.270576
	Total Crystal + Melt	39.372	94.72942
	Total		100
	Poto.l lower	**mm^{-3}**	**Percent %**
	Total volume	59.51868	
	Total Bubble	3.000459	5.041207
	Total Crystal + Melt	56.51822	94.95879
	Total		100

	Poto.l upper	**mm^{-3}**	**Percent %**
	Total volume	42.63997	
	Total Bubble	2.721388	6.382248
	Total Crystal + Melt	39.91858	93.61775
	Total		100
	Poto.m	**mm^{-3}**	**Percent %**
	Total volume	41.46869	
	Total Bubble	2.694374	6.497369
	Total Crystal + Melt	38.77432	93.50263
	Total		100
	Poto.o	**mm^{-3}**	**Percent %**
	Total volume	35.38552	
	Total Bubble	1.929038	5.451488
	Total Crystal + Melt	33.45649	94.54851
	Total		100
Paetahi	**Paetahi.a lower**	**mm^{-3}**	**Percent %**
	Total volume	66.72483	
	Total Bubble	2.342755	3.511069
	Total Crystal + Melt	64.38207	96.48893
	Total		100
	Paetahi.a middle	**mm^{-3}**	**Percent %**
	Total volume	36.87798	
	Total Bubble	1.797308	4.873661
	Total Crystal + Melt	35.08067	95.12634
	Total		100

	Paetahi.a upper	**mm^{-3}**	**Percent %**
	Total volume	50.03758	
	Total Bubble	4.099423	8.19269
	Total Crystal + Melt	45.93815	91.80731
	Total		100
	Paetahi.d	**mm^{-3}**	**Percent %**
	Total volume	29.84796	
	Total Bubble	2.10747	7.060682
	Total Crystal + Melt	27.74049	92.93932
	Total		100
	Paetahi.e lower	**mm^{-3}**	**Percent %**
	Total volume	47.82803	
	Total Bubble	1.584118	3.312111
	Total Crystal + Melt	46.24392	96.68789
	Total		100
	Paetahi.e middle	**mm^{-3}**	**Percent %**
	Total volume	72.79751	
	Total Bubble	4.975013	6.834043
	Total Crystal + Melt	67.8225	93.16596
	Total		100
	Paetahi.f	**mm^{-3}**	**Percent %**
	Total volume	25.24169	
	Total Bubble	1.050597	4.162149
	Total Crystal + Melt	24.19109	95.83785
	Total		100

Appendix E8: Crystal volume.

Crystal volume calculations for the percentage of bubbles per mm^{-3} in each of the 19 grains analysed for 3D tomography.

Formation	Sample	Volume	Percent %
Poto	**Poto.a**	**mm^{-3}**	**Percent %**
	Total volume	66.08525	
	Total crystal	4.370349	6.613199
	Total bubble + Melt	61.7149	93.3868
	Total		100
	Poto.c lower	**mm^{-3}**	**Percent %**
	Total volume	67.74433	
	Total crystal	6.911778	10.20274
	Total bubble + Melt	60.83255	89.79726
	Total		100
	Poto.d	**mm^{-3}**	**Percent %**
	Total volume	7.868211	
	Total crystal	1.58632	20.16113
	Total bubble + Melt	6.28189	79.83887
	Total		100
	Poto.e	**mm^{-3}**	**Percent %**
	Total volume	33.48803	
	Total crystal	8.191773	24.4618
	Total bubble + Melt	25.29626	75.5382
	Total		100

	Poto.g	**mm^{-3}**	**Percent %**
	Total volume	33.72644	
	Total crystal	4.621334	13.70241
	Total bubble + Melt	29.1051	86.29759
	Total		100
	Poto.h	**mm^{-3}**	**Percent %**
	Total volume	35	
	Total crystal	3.368258	9.623594
	Total bubble + Melt	31.63174	90.37641
	Total		100
	Poto.j	**mm^{-3}**	**Percent %**
	Total volume	20.55911	
	Total crystal	3.03667	14.77044
	Total bubble + Melt	17.52244	85.22956
	Total		100
	Poto.k lower	**mm^{-3}**	**Percent %**
	Total volume	41.56259	
	Total crystal	5.540383	13.33022
	Total bubble + Melt	36.0222	86.66978
	Total		100
	Poto.l lower	**mm^{-3}**	**Percent %**
	Total volume	59.51868	
	Total crystal	8.991884	15.10767
	Total bubble + Melt	50.52679	84.89233
	Total		100

	Poto.l upper	**mm^{-3}**	**Percent %**
	Total volume	42.63997	
	Total crystal	5.623207	13.18764
	Total bubble + Melt	37.01676	86.81236
	Total		100
	Poto.m	**mm^{-3}**	**Percent %**
	Total volume	41.46869	
	Total crystal	0.598023	1.442107
	Total bubble + Melt	40.87067	98.55789
	Total		100
	Poto.o	**mm^{-3}**	**Percent %**
	Total volume	35.38552	
	Total crystal	4.199571	11.86805
	Total bubble + Melt	31.18595	88.13195
	Total		100
Paetahi	**Paetahi.a lower**	**mm^{-3}**	**Percent %**
	Total volume	66.72483	
	Total crystal	5.123472	7.678509
	Total bubble + Melt	61.60136	92.32149
	Total		100
	Paetahi.a middle	**mm^{-3}**	**Percent %**
	Total volume	36.87798	
	Total crystal	2.951657	8.003847
	Total bubble + Melt	33.92632	91.99615
	Total		100

	Paetahi.a upper	**mm^{-3}**	**Percent %**
	Total volume	50.03758	
	Total crystal	4.330328	8.654153
	Total bubble + Melt	45.70725	91.34585
	Total		100
	Paetahi.d	**mm^{-3}**	**Percent %**
	Total volume	29.84796	
	Total crystal	3.431123	11.49534
	Total bubble + Melt	26.41683	88.50466
	Total		100
	Paetahi.e lower	**mm^{-3}**	**Percent %**
	Total volume	47.82803	
	Total crystal	4.338607	9.071264
	Total bubble + Melt	43.48943	90.92874
	Total		100
	Paetahi.e middle	**mm^{-3}**	**Percent %**
	Total volume	72.79751	
	Total crystal	4.493527	6.172638
	Total bubble + Melt	68.30398	93.82736
	Total		100
	Paetahi.f	**mm^{-3}**	**Percent %**
	Total volume	25.24169	
	Total crystal	5.534484	21.92596
	Total bubble + Melt	19.70721	78.07404
	Total		100

Appendix F: Geochemical analysis.

Geochemical analysis of the Poto and Paetahi Formations from deposits at the reference locations.

Appendix F1: Major elements for whole rock analyses using XRF.

Appendix F2: Trace elements for whole rock analyses using ICP-MS.

Appendix F3: Major element EMPA analyses of glass from epoxy plugs.

Appendix F4: Major element EMPA analysis of pyroxene crystals from epoxy plugs.

Appendix F5: Major element EMPA analyses of plagioclase crystals from epoxy plugs

Appendix F1: Major elements for whole rock analyses using XRF.

Formation	Layer	SiO2 (%)	Al2O3 (%)	TiO2 (%)	MnO (%)	Fe2O3 (%)	MgO (%)	CaO (%)	Na2O (%)	K2O (%)	P2O5 (%)	LOI (%)	Sum with LOI (%)
Poto Formation	Poto a	45.69	21.46	1.099	0.147	9.84324	3.548	8.075	2.469	0.57	0.402	7.73	101.031
	Poto b	49.17	20.32	1.078	0.156	9.45052	3.955	8.093	3.281	1.47	0.342	3.34	100.668
	Poto c lower	43.37	21.15	1.255	0.158	10.90263	4.234	9.159	2.136	0.38	0.329	7.96	101.044
	Poto c upper	45.49	21.15	1.158	0.172	10.12225	4.275	9.163	2.559	0.81	0.341	5.58	100.828
	Poto d	43.4	21.82	1.259	0.145	10.96257	3.988	9.271	2.101	0.33	0.363	7.19	100.843
	Poto e	45.74	20.51	1.194	0.155	10.50329	4.255	8.657	2.394	0.69	0.309	6.42	100.842
	Poto f	48.04	20.26	1.041	0.16	8.96552	3.532	8.257	3.532	1.08	0.34	5.67	100.894
	Poto g	48.85	19.46	1.106	0.183	9.995	4.338	8.847	3.05	1.21	0.312	3.63	100.98
	Poto h	42.36	20.72	1.188	0.159	10.70545	4.108	8.782	2.982	0.37	0.392	9.35	101.111
	Poto i	44.94	21.41	1.055	0.163	9.47707	3.672	8.826	2.999	0.54	0.373	7.59	101.054
	Poto j	50.56	19.05	1.001	0.177	8.8938	3.825	8.885	3.498	1.43	0.323	3.27	100.923
	Poto k lower	43.53	21.03	1.056	0.156	9.54907	3.797	8.305	2.744	0.52	0.346	9.94	100.983
	Poto k upper	44.15	19.8	1.068	0.19	9.99945	4.324	8.178	3.085	0.62	0.34	9.47	101.238
	Poto l lower	44.29	20.62	1.204	0.158	10.80298	4.535	8.986	2.584	0.44	0.334	6.98	100.934
	Poto l upper	44.02	19.87	1.209	0.16	10.88281	4.883	9.309	2.9	0.44	0.349	6.97	100.996
	Poto m	47.37	19.62	1.111	0.166	9.63518	4.046	8.147	3.294	0.91	0.334	6.2	100.834
	Poto n	47.38	20.77	1.055	0.175	9.43372	3.529	7.695	2.748	0.92	0.358	7.15	101.212
	Poto o	45.66	21.03	1.108	0.196	10.11908	3.889	8.182	2.394	0.56	0.336	7.49	100.961
Paetahi Formation	Paetahi a bottom	49.44	21.14	0.905	0.156	8.11947	2.899	7.888	3.642	1.09	0.377	5.4	101.052
	Paetahi a middle	48.77	21.54	0.946	0.162	8.56785	3.146	8.173	3.364	0.92	0.383	4.96	100.941
	Paetahi a upper	48.25	21.56	0.949	0.16	8.72977	3.192	8.285	3.245	0.82	0.387	5.5	101.088
	Paetahi b	45.68	22.57	1.073	0.165	9.58763	3.441	7.937	2.375	0.72	0.429	6.72	100.694
	Paetahi c	43.47	22.53	1.212	0.161	10.5518	3.71	8.323	2.075	0.42	0.393	7.62	100.463
	Paetahi d	42.53	22.78	1.165	0.141	10.40104	3.288	7.369	2.165	0.37	0.384	9.31	99.91
	Paetahi e bottom	43.16	24.52	1.087	0.128	9.76025	2.879	7.071	2.171	0.39	0.419	8.95	100.543
	Paetahi e middle	50.78	21.31	0.969	0.121	7.88848	3.243	6.319	3.106	1.8	0.319	4.65	100.502
	Paetahi e upper	49.58	20.61	1.008	0.171	9.21608	3.563	7.995	3.147	1.22	0.37	3.91	100.801
	Paetahi f	46.3	22.69	0.95	0.154	8.85322	2.933	7.323	2.685	0.8	0.405	7.43	100.528

Appendix F2: Trace elements for whole rock analyses using ICP-MS.

Formation	Layer	Ca43	Sc45	V51	Cr53	Ni60	Sr88	Y89	Zr90	Nb93	Pr141	Nd146	Sm147	Eu151	Gd157	Tb159	Dy163	Ho165	Er166	Tm169	Yb172	Lu175	Pb208	Th232	U238	Eu153	Si29	Hf177	P31	K39	Ca44	Pb207	Pb206	Co59	Rb85	Ce140	Ti49	Ba137	La139	Cs133
Poto Formation	**Poto.a**	57712.02	19.83	248.90	30.09	16.13	532.87	22.46	133.04	5.06	4.44	20.53	4.98	1.43	4.97	0.60	4.39	0.70	2.52	0.31	2.08	0.33	10.92	6.01	1.10	1.48	207822.29	4.35	1537.68	4571.66	57534.26	11.01	11.12	37.38	9.56	22.09	6346.81	387.37	14.00	0.70
	Poto.b	57840.67	19.71	277.97	31.20	21.60	567.18	19.11	110.05	4.68	4.00	18.02	4.63	1.39	4.47	0.62	3.77	0.77	2.12	0.32	1.97	0.27	9.45	5.17	1.02	1.41	224594.90	3.56	1286.42	11900.23	58139.87	9.56	9.89	46.05	26.40	26.45	6281.48	710.70	13.76	1.46
	Poto.c lower	65459.37	26.82	327.13	20.50	16.80	516.09	21.90	104.10	3.94	4.34	19.49	4.49	1.29	4.87	0.80	4.49	0.90	2.77	0.38	2.37	0.31	10.47	5.06	0.78	1.38	190888.51	3.28	1257.85	2916.58	64435.73	10.78	11.44	39.29	2.85	22.73	7176.10	446.18	11.61	0.08
	Poto.c upper	65487.96	23.10	303.70	30.75	17.07	554.75	20.50	108.23	3.97	3.71	18.23	4.55	1.43	4.57	0.70	4.43	0.84	2.55	0.38	2.15	0.32	9.06	5.12	0.74	1.40	206515.41	3.38	1269.79	6536.37	65359.07	8.98	10.12	95.86	13.65	23.30	6640.09	509.92	11.42	0.72
	Poto.d	66259.84	23.50	315.05	24.57	13.76	553.13	21.32	115.25	3.94	4.34	19.31	5.42	1.37	5.16	0.75	4.73	0.87	2.42	0.38	2.25	0.31	10.91	5.55	0.73	1.50	197158.44	3.67	1335.57	2686.70	65936.76	10.69	11.12	47.52	4.28	20.88	7274.03	331.38	11.86	0.30
	Poto.e	61871.58	27.55	302.55	30.46	28.46	514.71	19.69	107.76	3.88	3.92	17.75	4.67	1.31	4.73	0.71	4.04	0.82	2.42	0.36	2.32	0.33	11.23	5.41	0.93	1.40	208736.99	3.41	1137.69	5720.71	62286.43	10.74	11.68	65.61	12.01	25.95	7026.60	453.60	11.64	0.78
	Poto.f	59012.78	17.65	255.12	21.02	12.45	611.93	19.92	111.72	3.94	4.05	17.13	3.45	1.58	4.47	0.63	3.84	0.86	2.46	0.35	2.22	0.35	9.61	5.40	0.86	1.54	218705.48	2.90	1137.86	9192.53	59027.03	8.73	10.68	50.61	20.99	25.19	6100.55	597.25	13.32	1.37
	Poto.g	63229.51	24.10	294.36	20.45	13.95	539.28	19.66	89.89	3.08	3.40	16.14	4.43	1.25	4.44	0.65	3.90	0.84	2.43	0.32	1.95	0.26	9.09	3.99	0.83	1.37	220631.63	3.03	1120.17	9615.89	63062.06	8.67	9.63	55.98	21.79	23.07	6391.78	554.37	11.19	1.27
	Poto.h	62764.95	23.96	296.68	42.77	17.62	558.55	20.36	125.69	4.27	3.69	18.03	5.27	1.32	4.65	0.74	4.02	0.87	2.26	0.30	1.97	0.31	10.03	5.53	0.66	1.38	194470.58	4.05	1516.39	2944.58	64346.78	9.26	10.79	81.79	5.31	17.49	7245.02	335.13	9.23	0.33
	Poto.i	63079.42	19.53	256.01	16.29	13.00	625.91	18.79	118.05	4.09	3.57	16.80	3.50	1.35	3.83	0.69	3.77	0.74	1.98	0.24	2.22	0.22	8.58	5.59	0.54	1.33	198772.91	3.60	1345.10	4277.04	61432.36	8.73	9.13	103.23	8.67	17.66	6065.00	341.63	9.74	0.64
	Poto.j	63501.09	19.30	255.86	25.95	34.99	620.38	22.37	97.94	3.70	4.02	18.31	4.57	1.31	4.25	0.68	4.23	0.91	2.13	0.32	2.20	0.30	9.43	4.36	0.78	1.25	228594.14	3.34	1181.73	12361.26	63762.57	9.60	9.27	101.04	30.40	27.45	5884.06	637.30	13.64	1.84
	Poto.k lower	59355.84	20.79	258.58	68.52	75.33	523.62	20.13	113.14	4.25	4.04	17.90	4.51	1.33	4.61	0.67	4.13	0.84	2.40	0.33	2.25	0.24	10.66	5.29	0.83	1.32	197982.78	3.49	1284.98	4304.10	59341.28	10.51	11.75	149.40	10.61	23.00	6289.04	344.20	12.70	0.80
	Poto.k upper	58448.17	21.09	271.76	43.49	28.65	478.41	18.59	106.20	3.68	3.59	15.65	3.82	1.21	4.03	0.61	3.88	0.74	2.27	0.30	1.97	0.26	9.83	4.72	0.83	1.22	192713.72	2.91	1237.61	4977.72	57274.01	10.35	10.77	114.74	13.18	23.43	6107.89	337.79	11.01	1.05
	Poto.l lower	64222.94	26.86	295.88	39.68	25.03	535.15	18.58	106.25	6.90	3.66	17.06	4.42	1.30	4.19	0.66	4.01	0.78	1.91	0.27	1.95	0.26	8.38	4.29	0.73	1.29	194635.69	3.17	1263.15	3511.34	62906.66	9.33	9.21	77.01	6.26	24.46	6808.05	358.96	11.45	0.39
	Poto.l upper	66531.42	27.28	306.92	90.74	24.72	559.93	17.00	118.14	7.59	3.24	15.36	3.40	1.10	3.93	0.52	3.45	0.66	1.75	0.23	1.55	0.20	9.44	4.78	0.49	1.21	196829.50	3.67	1252.00	3542.00	66151.93	9.27	10.07	245.43	7.65	17.94	7006.94	390.12	10.20	0.65
	Poto.m	58226.61	24.31	287.03	15.70	17.29	556.13	22.65	114.20	5.29	4.39	20.55	4.72	1.42	5.17	0.73	4.43	0.91	2.65	0.28	2.38	0.34	10.68	5.55	0.96	1.41	214487.56	3.05	1250.77	7702.76	60171.28	11.42	11.80	211.83	19.52	26.75	6667.57	604.59	14.67	1.18
	Poto.n	54996.17	19.50	243.60	17.11	13.05	495.05	22.14	116.76	4.74	4.20	18.79	4.09	1.14	4.93	0.71	4.09	0.84	2.37	0.34	2.05	0.30	11.68	5.26	1.10	1.31	208322.37	3.48	1318.81	7476.22	53877.30	12.01	12.35	60.48	18.53	25.83	6066.97	465.24	13.09	1.16
	Poto.o	58476.75	22.93	257.06	12.39	11.47	497.44	24.53	122.89	4.62	4.43	20.27	5.14	1.41	4.66	0.69	4.51	0.85	2.32	0.36	2.20	0.31	10.77	5.96	1.07	1.32	200690.56	3.63	1204.94	4333.73	56466.17	10.47	11.61	95.72	11.14	27.64	6454.76	382.31	15.01	0.88
Paetahi Formation	**Paetahi.a lower**	56375.54	14.29	185.89	13.91	16.99	609.32	20.11	122.72	4.93	4.37	18.04	4.45	1.27	4.48	0.66	4.17	0.73	2.19	0.30	2.14	0.23	7.85	5.96	0.85	1.51	205373.94	3.21	1106.83	8547.53	54069.73	7.99	11.47	45.81	22.02	29.47	5111.96	529.25	13.81	1.29
	Paetahi.a middle	58412.43	16.11	206.71	17.95	10.40	631.69	19.41	123.35	4.71	3.79	16.85	4.40	1.39	4.56	0.64	4.07	0.79	2.32	0.34	2.38	0.33	11.31	6.03	0.86	1.46	219517.72	3.81	1384.67	7376.56	58636.39	11.10	11.99	40.09	16.82	25.55	5414.59	517.78	12.62	0.90
	Paetahi.a upper	59212.89	16.36	206.07	18.58	13.85	606.37	18.41	121.84	4.61	3.71	16.97	4.28	1.13	4.01	0.63	3.62	0.76	2.11	0.32	1.97	0.31	10.41	5.61	0.79	1.29	225790.91	3.74	1491.17	6572.36	58444.12	10.18	11.16	181.49	14.62	24.02	5427.53	440.90	11.85	0.83
	Paetahi.b	56725.74	18.10	245.04	21.16	21.21	507.22	20.46	141.63	4.99	4.25	19.17	4.84	1.28	4.97	0.67	4.42	0.83	2.24	0.36	2.16	0.35	11.52	6.66	0.98	1.29	209417.52	4.42	1620.15	5739.18	55985.70	11.21	12.32	92.28	14.42	25.33	6142.71	357.22	13.19	0.79
	Paetahi.c	59484.48	20.30	282.10	19.03	13.63	533.38	20.19	140.56	5.15	4.05	18.60	4.69	1.30	4.65	0.66	3.93	0.84	2.33	0.36	1.95	0.30	10.94	7.78	0.95	1.42	199165.62	4.31	1494.71	3333.24	58970.10	10.33	11.60	93.67	7.16	18.20	6882.75	307.47	11.68	0.42
	Paetahi.d	52666.24	17.92	269.10	16.84	16.11	526.01	18.81	144.62	5.21	4.11	18.36	4.60	1.33	4.50	0.67	3.98	0.75	2.25	0.37	2.02	0.27	13.41	7.21	1.13	1.39	193723.79	4.15	1463.60	3004.61	52882.49	12.69	13.79	46.88	5.65	18.90	6769.22	328.14	10.93	0.38
	Paetahi.e lower	50536.44	16.19	237.77	13.49	10.63	527.60	15.10	131.78	5.20	3.39	15.31	4.19	1.14	3.38	0.55	3.31	0.62	2.02	0.25	1.72	0.31	13.31	6.53	1.00	1.20	198088.31	3.81	1553.66	3139.00	50683.72	12.75	14.50	50.73	5.96	20.08	6271.28	312.54	8.89	0.29
	Paetahi.e middle	45161.89	17.62	206.37	39.07	19.39	490.05	18.79	144.86	6.33	4.33	18.18	4.39	1.36	4.19	0.64	3.51	0.74	2.25	0.33	2.25	0.29	8.90	7.66	1.19	1.42	228671.34	4.62	1177.79	14365.80	45008.95	8.65	9.34	71.70	36.98	30.78	5558.84	663.71	16.05	1.43
	Paetahi.e upper	57140.26	17.53	246.61	20.21	21.85	582.87	19.27	114.48	4.38	3.84	17.02	4.48	1.29	4.25	0.61	3.89	0.78	2.38	0.31	2.13	0.33	10.28	5.68	1.06	1.37	226955.46	3.72	1373.20	9974.72	57460.37	10.12	10.82	68.38	25.04	27.76	5828.72	598.77	13.48	1.44
	Paetahi.f	52337.48	14.28	211.49	17.83	20.19	559.52	18.46	139.42	5.20	3.99	17.60	4.08	1.23	4.16	0.64	3.63	0.77	2.20	0.31	1.89	0.00	10.93	6.34	1.02	1.38	201538.31	4.21	1317.39	6339.06	51977.36	10.55	7.29	57.58	16.90	20.42	5450.29	406.11	12.52	0.95

Appendix F3: Major element EMPA analyses of glass from epoxy plugs.

	SAMPLE	SiO2	TiO2	Al2O3	FeO	MnO	MgO	CaO	SrO	BaO	Na2O	K2O	P2O5	SO3	Cl	F	TOTAL	O
Poto Formation	Poto.a	58.09	0.61	22.19	3.76	0.11	0.99	6.84	0.09	0.10	4.38	2.76	0.28	0.00	0.13	0.05	100.34	-0.05
	Poto.b	57.63	0.51	23.45	2.44	0.06	0.86	6.94	0.08	0.11	5.55	1.98	0.51	0.01	0.07	0.04	100.23	-0.04
	Poto.c lower	54.48	0.13	26.89	1.42	0.05	1.16	10.94	0.12	0.07	4.51	1.57	0.03	0.00	0.01	0.00	101.38	0.00
	Poto.c upper	59.81	0.48	23.07	2.03	0.06	0.43	5.56	0.07	0.12	5.29	3.70	0.20	0.01	0.11	0.06	100.95	-0.05
	Poto.d	56.25	0.43	22.44	2.96	0.10	2.25	9.44	0.11	0.09	4.43	1.80	0.16	0.01	0.10	0.03	100.57	-0.03
	Poto.e	60.91	0.78	19.80	3.40	0.11	1.21	4.12	0.04	0.12	5.47	3.79	0.35	0.01	0.15	0.05	100.26	-0.06
	Poto.f	55.66	0.26	26.01	1.47	0.04	0.35	8.41	0.13	0.08	5.28	1.51	0.11	0.01	0.08	0.47	99.64	-0.22
	Poto.g	60.94	0.73	20.39	3.75	0.12	0.90	4.59	0.07	0.12	4.86	3.23	0.34	0.01	0.19	0.06	100.23	-0.07
	Poto.h	60.65	0.58	21.68	2.76	0.11	0.69	5.33	0.08	0.10	5.01	3.06	0.25	0.01	0.17	0.03	100.46	-0.05
	Poto.i	64.13	0.44	20.38	2.39	0.10	0.96	2.72	0.04	0.12	5.63	4.32	0.18	0.01	0.12	0.02	101.53	-0.03
	Poto.j	59.96	0.40	23.10	2.25	0.08	0.54	6.53	0.10	0.10	4.82	2.40	0.16	0.01	0.12	0.03	100.56	-0.04
	Poto.k lower	56.85	0.32	25.82	1.88	0.06	0.59	8.69	0.11	0.07	4.38	1.59	0.11	0.01	0.10	0.00	100.55	-0.02
	Poto.k Upper	62.97	0.81	18.35	3.84	0.14	1.20	3.22	0.06	0.13	4.73	3.76	0.29	0.01	0.17	0.04	99.67	-0.06
	Poto. L lower	60.94	0.90	17.57	4.92	0.17	1.62	3.43	0.04	0.11	4.89	3.64	0.38	0.02	0.23	0.04	98.85	-0.07
	Poto.L Upper	57.23	0.87	21.07	4.69	0.14	1.43	6.56	0.08	0.09	4.43	2.76	0.35	0.01	0.19	0.05	99.88	-0.06
	Poto.m	59.35	0.66	21.49	3.36	0.10	1.02	5.43	0.07	0.11	5.13	2.58	0.24	0.01	0.16	0.04	99.69	-0.05
	Poto.n	58.11	0.51	22.86	2.96	0.10	1.16	7.25	0.09	0.08	4.33	2.01	0.18	0.01	0.10	0.04	99.74	-0.04
	Poto. O	54.39	0.08	29.04	0.89	0.01	0.09	10.73	0.14	0.05	5.24	0.60	0.01	0.00	0.01	0.00	101.28	0.00
Paetahi Formation	Paetahi.a lower	53.39	0.21	27.01	1.80	0.03	0.36	10.35	0.16	0.07	4.62	0.94	0.09	0.01	0.03	0.01	99.06	-0.01
	Paetahi.a middle	57.99	0.65	20.70	4.28	0.16	2.14	7.86	0.07	0.08	3.93	2.02	0.21	0.01	0.10	0.01	100.19	-0.03
	Paetahi.a upper	57.50	0.66	21.76	3.84	0.12	1.78	7.77	0.09	0.09	4.15	1.87	0.21	0.01	0.09	0.02	99.94	-0.03
	Paetahi.b	61.25	0.69	19.89	3.61	0.14	1.26	4.68	0.07	0.11	4.69	2.84	0.27	0.02	0.15	0.03	99.64	-0.04
	Paetahi.c	58.04	0.46	23.93	3.09	0.08	0.99	7.67	0.10	0.09	4.50	1.75	0.21	0.01	0.09	0.02	101.02	-0.03
	Paetahi.d	59.68	0.78	21.33	4.82	0.11	0.66	5.13	0.08	0.13	5.14	2.31	0.17	0.01	0.10	0.02	100.42	-0.03
	Paetahi.e lower	57.37	0.41	24.57	2.47	0.07	0.66	7.64	0.12	0.09	4.92	1.61	0.18	0.01	0.07	0.03	100.19	-0.03
	Paetaih.e middle	57.50	0.39	24.65	2.42	0.08	0.76	7.70	0.12	0.08	4.87	1.69	0.20	0.00	0.07	0.02	100.54	-0.03
	Paetahi.e upper	56.06	0.28	26.34	1.86	0.04	0.39	9.06	0.13	0.09	4.81	1.31	0.38	0.01	0.06	0.03	100.81	-0.03
	Paetahi.f	54.09	0.25	24.29	3.35	0.18	3.13	10.55	0.11	0.04	3.21	0.97	0.07	0.00	0.06	0.00	100.29	-0.02

Appendix F4: Major element EMPA analysis of pyroxene crystals from epoxy plugs.

Formation	Layer	Sample	SiO2	TiO2	Al2O3	V2O3	Cr2O3	FeO	NiO	MnO	MgO	CaO	Na2O	K2O	O	Total
Poto	Poto.a	Poto.a Grain 1 cpx 1	51.95453	0.538367	2.023445	0.040517	0.007223	9.08157	0.008192	0.44354	15.20295	20.1269	0.349324	0.008055	2.5E-06	99.78463
		Poto.a Grain 1 cpx 2	51.59123	0.598004	2.249408	0.028067	0.002353	9.099505	0.005027	0.444529	15.04915	20.06303	0.349195	0.007853	0.000002	99.4873
		Poto.a Grain 1 cpx 3	53.57925	0.261177	0.944207	0.008787	0.00276	17.21775	0.014425	0.739475	24.81218	1.594118	0.032112	0.00377	0.000004	99.21003
		Poto.a Grain 3 cpx 1	51.52445	0.559658	2.092983	0.032012	0.001483	9.104733	0.004277	0.445552	15.07613	20.0463	0.368873	0.000564	0	99.25698
		Poto.a Grain 3 cpx 2	51.68988	0.590635	2.138378	0.038586	0.000646	9.107903	0.008733	0.431856	15.05735	20.1759	0.357013	0.000915	0.000002	99.5978
		Poto.a Grain 3 cpx 3	51.851	0.526411	2.11014	0.036946	0.001582	8.971775	0.009507	0.446618	15.01523	20.1084	0.359464	0.003318	-1.5E-06	99.4405
		Poto.a Grain 4 cpx 1	51.6755	0.512942	1.916553	0.031626	0.000679	8.833643	0.001219	0.449822	15.08773	20.22748	0.364361	0.013485	-2.5E-06	99.11505
		Poto.a Grain 4 cpx 2	51.78065	0.553292	2.278763	0.038458	0.001635	8.39394	0.000496	0.379444	15.16928	20.57555	0.352539	0.02326	1.25E-06	99.54728
	Poto.b	Poto.b Grain 1 cpx 2	50.4104	0.807798	12.75559	0.038219	0.003794	6.293721	0.002227	0.191604	9.446686	17.48467	1.934522	0.17329	0.000004	99.5424
		Poto.b Grain 7 cpx 1	51.0378	0.717303	2.74292	0.044852	0.0061	8.91151	0	0.350785	15.5612	19.7864	0.312762	0.016173	0	99.4878
		Poto.b Grain 6 cpx 1	50.49708	0.805644	3.300745	0.034431	0.001845	7.976395	0.003922	0.282349	14.7386	21.43445	0.409599	0.025329	0.000002	99.51038
	Poto.c lower	Poto.c lower Grain 3 cpx 1	44.34022	2.052988	9.46534	0.07828	0.002308	9.447436	0.002846	0.161411	11.24238	22.27356	0.333478	0.003629	0	99.40388
		Poto.c lower Grain 3 cpx 3	41.7712	3.23565	12.6525	0.121675	0.00056	13.2088	0.003762	0.197508	12.8099	11.5255	2.33946	0.847416	0	98.7138
		Poto.c lower Grain1 cpx 1	52.22743	0.549696	2.085268	0.033312	0.003914	7.561238	0.002043	0.417227	15.26373	21.2555	0.389052	0.021966	-5E-07	99.81043
		Poto.c lower Grain1 cpx 2	51.99784	0.570022	2.122368	0.034903	0.001897	7.784168	0.000785	0.42007	15.39416	21.07972	0.383179	0.017863	0.000007	99.80694
		Poto.c lower Grain1 cpx 3	51.6221	0.640425	2.587263	0.036773	0.002665	7.695388	0.002867	0.374283	14.9942	21.40948	0.403026	0.013082	0.000001	99.78153
		Poto.c lower Grain1 cpx 4	51.6763	0.633868	2.42098	0.032069	0.001983	7.67183	0.014097	0.402285	15.11623	21.31043	0.412936	0.014369	0.000007	99.70735
	Poto.c upper	Poto.c upper Grain 1 cpx 1	50.9417	0.791618	3.096482	0.035159	0	8.371465	0.001105	0.416852	14.54732	21.03195	0.407664	0.033051	6.67E-07	99.67438
		Poto.c upper Grain 1 cpx 2	50.87453	0.793002	3.111368	0.039848	0.001682	7.91594	0.002473	0.372929	14.72075	21.27665	0.399173	0.030812	0.000002	99.53913
		Poto.c upper Grain 3 cpx 1	47.54932	1.42316	6.170964	0.058747	0.001788	8.934282	0.001326	0.246113	12.99292	21.61944	0.412635	0.003873	4.8E-06	99.41464
		Poto.c upper Grain 3 cpx 2	51.4019	0.668152	2.63616	0.037831	0.001846	7.86063	0	0.332273	15.14043	21.30427	0.359561	0.002971	0	99.74623
		Poto.c upper Grain 4 cpx 1	51.04115	0.758567	3.11803	0.039608	0.000844	7.708683	0.000363	0.33607	14.8445	21.46143	0.408541	0.002349	0.000002	99.7201
	Poto.d	Poto.d Grain 1 cpx 1	50.75937	0.789532	3.055677	0.041476	0.001157	8.301567	0.009959	0.333844	14.68507	21.05027	0.414822	0.000984	-2E-06	99.44377
		Poto.d Grain 2 cpx 1	49.62925	0.959046	4.143498	0.044733	0.001681	8.328178	0.002974	0.317317	14.07108	21.2608	0.384675	0.013863	-5E-07	99.15708
		Poto.d Grain 4 cpx 1	50.07835	0.883151	3.752348	0.033861	0.001142	8.982565	0.004894	0.35391	14.66163	20.21593	0.32033	0.004067	0	99.29208
		Poto.d Grain 4 cpx 2	48.586	1.124716	5.2824	0.050656	0.001766	8.818213	0.005207	0.248732	13.2229	21.61063	0.342243	0.003639	0.000004	99.29717
	Poto.e	Poto.e Grain 1 CPX 1	50.92445	0.810169	3.341423	0.040033	0.005629	8.224168	0.008201	0.334239	14.64648	21.09238	0.415468	0.015042	0.000003	99.85765
		Poto.e Grain 1 CPX 2	50.86472	0.758476	3.14468	0.042428	0.001822	8.22901	0.002379	0.349181	14.66252	21.06216	0.396922	0.011615	2.4E-06	99.52588
		Poto.e Grain 3 CPX 1	50.7552	0.756495	3.570983	0.037012	0.000339	8.428147	0.005893	0.297366	14.6035	20.86743	0.354206	0.017745	-6.7E-07	99.6943
		Poto.e Grain 3 CPX 2	47.69093	1.195284	6.851077	0.064647	0.095109	8.201023	0.005495	0.135017	12.82043	22.50703	0.308845	0.009196	1.33E-06	99.88417
		Poto.e Grain 3 CPX 3	51.64733	0.678438	2.663873	0.02543	0.002446	7.809773	0	0.348127	15.00025	21.14448	0.392096	0.004996	0.000002	99.7172
	Poto.f	Poto_f_Grain_1_CPX1	51.174	0.75808	3.258	0.04026	0.00164	8.394	0.00212	0.3239	15.164	20.814	0.29596	0.00666		100.2326
		Poto_f_Grain_1_CPX2	51.87	0.7052	2.975	0.0344	0.0057	8.325	0	0.349	15.265	20.75	0.31145	0.0161		100.6069
		Poto_f_Grain_1_CPX3	42.155	2.985	13.185	0.0911	0.01705	11.585	0.00015	0.2066	14.5	11.065	2.64	0.82865		99.25855
		Poto_f_Grain_1_CPX4	54.385	1.2888	14.155	0.04195	0.0027	6.49	0.00245	0.14175	6.33505	13.295	2.09635	1.32685		99.5609
		Poto_f_Grain_1_CPX5	50.1	1.062	4.68	0.0449	0.0076	9.21	0.0089	0.389	13.97	19.99	0.3984	0.0861		99.9469
		Poto_f_Grain_5_CPX1	52.455	0.5715	2.2126	0.02705	0.0077	7.925	0.0051	0.44115	15.425	20.8	0.3639	0.003		100.237
		Poto_f_Grain_5_CPX2	53.22	0.44405	1.76655	0.02035	0.0038	8.08	0	0.5348	15.86	20.62	0.3413	0.0053		100.8962
		Poto_f_Grain_5_CPX3	51.555	0.69195	2.665	0.041	0.0003	8.36	0.002125	0.393825	15.26	20.695	0.3684	0.002875		100.0355
		Poto_f_Grain_5_CPX4	51.79	0.65255	2.545	0.0424	0.00015	7.95	0.00875	0.34225	15.145	21.06	0.35595	0.005		99.89705
		Poto_f_Grain_5_CPX5	44.8	3.265	12.03	0.07505	0.00795	10.915	0	0.28725	14.305	10.63	2.595	0.82115		99.7314
	Poto.g	Poto.g Grain 1 cpx 2	52.28228	0.750441	4.407568	0.036655	0.004254	7.956678	0.005778	0.374107	13.48776	19.55352	0.635481	0.272337	-5.2E-06	99.76696
		Poto.g Grain 1 cpx 3	48.8894	1.101738	7.47946	0.044493	0.003251	8.230333	0.003904	0.220274	12.03035	21.3141	0.608338	0.041148	0	99.96673
		Poto.g Grain 4 cpx 1	52.03018	0.615495	2.62432	0.039543	0.00163	7.680445	0.000584	0.379656	15.21133	21.2662	0.374248	0.009462	2.5E-06	100.2331
		Poto.g Grain 4 cpx 2	51.4249	0.695553	3.095793	0.032513	0.001898	7.83588	0.004471	0.359695	14.82798	21.3404	0.376872	0.008769	4.75E-06	100.0048
	Poto.h	Poto.h Grain 3 cpx 1	52.63224	0.477963	2.065172	0.02424	0.001602	7.78397	0.001649	0.466748	15.62998	20.88126	0.342834	0.002493	0	100.31
		Poto.h Grain 3 cpx 2	52.00433	0.621436	2.626903	0.022842	0.00114	7.976023	0.002401	0.44397	15.24445	20.9598	0.376782	0.002041	0	100.2823
		Poto.h Grain 4 cpx 1	49.72985	1.227205	4.60018	0.038519	0.001662	8.9951	0	0.435059	14.91683	18.2044	0.917735	0.226443	-2.5E-06	99.293
		Poto.h Grain 4 cpx 2	52.5934	0.505216	2.064108	0.029955	0.00327	7.617103	0.000141	0.454604	15.4964	21.01193	0.348538	0.005003	0.000003	100.1296
	Poto.i	Poto.i Grain 1 cpx 1	51.98175	0.512998	2.252728	0.031213	0.005327	7.663138	0.000161	0.493823	15.36978	21.24788	0.378362	0.008909	0.000001	99.94603
		Poto.i Grain 1 cpx 2	52.9848	0.504285	3.05888	0.027959	0.003302	7.830133	0.004073	0.507782	14.32543	19.57338	0.557759	0.309991	-2.5E-06	99.6877
		Poto.i Grain 4 cpx 1	50.47727	0.700452	2.850357	0.040127	0.003009	8.526613	0.001956	0.481097	14.3762	21.44433	0.344472	0.019391	6.33E-06	99.26527
		Poto.i Grain 4 cpx 2	52.19625	0.484501	2.097775	0.028399	0.003133	7.69128	0	0.526109	15.5268	20.99775	0.385617	0.030809	-5E-06	99.96845
	Poto.j	Poto.j Grain 1 cpx 2	50.7988	0.608614	3.434895	0.035431	0.005013	8.524895	0.001302	0.393172	13.9777	21.28773	0.511755	0.010065	-5E-07	99.58933
		Poto.j Grain 1 cpx 3	50.86538	0.62766	3.633623	0.038756	0.003623	8.707668	0.005282	0.430291	13.9675	21.048	0.481594	0.01327	0.000001	99.82268
		Poto.j Grain 3 cpx 1	52.4479	0.477626	2.289313	0.031507	0.002527	7.605018	0.001308	0.502054	15.38023	20.79155	0.402977	0.037301	0.000002	99.96953
		Poto.j Grain 3 cpx 2	50.64555	0.60227	2.64105	0.026564	0.000479	8.22663	0	0.475674	14.7919	21.33895	0.35821	0.010301	-5E-06	99.11775
	Poto.k lower	Poto.k lower Grain 1 cpx 2	51.10563	0.613184	3.085153	0.030031	0.003007	8.70221	0.000417	0.487012	14.37977	20.61677	0.477311	0.013176	2.67E-06	99.51367
		Poto.k lower Grain 4 cpx 1	51.39715	0.648194	2.77944	0.03537	0.00455	7.737285	0.00403	0.385639	15.24178	21.10518	0.356041	0.002566	0	99.69713
		Poto.k lower Grain 4 cpx 2	51.45503	0.572147	2.609403	0.034159	0.003239	8.07297	0	0.423198	15.05455	20.84573	0.388895	0.000972	0.000001	99.46028
	Poto.k upper	Poto.k upper Grain 1 cpx 2	51.71983	0.618253	2.719207	0.039462	0.001679	7.739227	0.006372	0.373707	15.3129	21.1523	0.345859	0.010579	0	100.0393
		Poto.k upper Grain 1 cpx 1	52.00865	0.63873	2.623933	0.033831	0.000526	7.715615	0.001117	0.396448	15.39463	21.03428	0.374884	0.008302	0.000001	100.231
		Poto.k upper Grain 3 cpx 1	52.12773	0.56471	2.36213	0.034684	0.002107	7.710293	0.003541	0.426007	15.48145	20.75298	0.395396	0.002896	0.000002	99.86393
		Poto.k upper Grain 3 cpx 2	52.01668	0.58097	2.550075	0.023264	0.003841	7.757478	0.004866	0.409104	15.43753	20.83988	0.349586	0.002804	0.000001	99.97595
		Poto.k upper Grain 2 cpx 1	52.1236	0.614028	2.938517	0.027103	0.003511	7.776893	0.011778	0.417719	15.22457	20.33467	0.371272	0.021365	2.67E-06	99.865
	Poto.l lower	Poto.l lower Grain 1 cpx 1	50.2594	0.645253	4.117028	0.037579	0.08256	7.699593	0.00353	0.188353	15.24673	20.8516	0.335874	0.005089	3.75E-06	99.4726
		Poto.l lower Grain 1 cpx 2	51.3755	0.669249	2.49032	0.035758	0.001869	8.640443	0.013437	0.407569	15.004	20.67905	0.387987	0.001594	-2.5E-06	99.70675
		Poto.l lower Grain 3 cpx 1	51.87477	0.546666	2.259353	0.035639	0.007392	8.186757	0.006758	0.405345	15.42157	20.78253	0.390266	0.001292	2.67E-06	99.9186
		Poto.l lower Grain 3 cpx 2	51.3471	0.618102	2.4835	0.041685	0.000774	8.26143	0.0191	0.430493	15.4085	20.9429	0.379211	0.005497	0	99.9383
	Poto.l upper	Poto.l upper Grain 2 cpx 1	51.23725	0.684225	2.672245	0.036861	0	8.20605	0.003082	0.368636	14.94765	20.9303	0.38659	0.006513	0.000004	99.4794
		Poto.l upper Grain 2 cpx 2	51.45695	0.593306	2.281168	0.027561	0.002081	7.94253	0.005359	0.357472	15.18713	21.11423	0.370284	0.015166	-5E-07	99.3532
		Poto.l upper Grain 5 cpx 1	48.6739	1.210293	5.02415	0.051495	0.009888	8.904973	0	0.280783	13.69193	21.17393	0.374568	0.00113	5.33E-06	99.39703
		Poto.l upper Grain 5 cpx 2	48.33383	1.274405	5.580863	0.057917	0.00572	8.90133	0.000982	0.27209	13.25223	20.82107	0.399105	0.006285	5.33E-06	98.9058
	Poto.m	Poto.m Grain 1 cpx 1	51.19553	0.619299	2.4671	0.035222	0.010499	7.882548	0.001834	0.343147	15.18813	20.98955	0.382106	0.000626	0.000004	99.11555
		Poto.m Grain 1 cpx 2	49.8397	0.973458	4.408233	0.051719	0	9.202473	0	0.320543	14.4184	19.92757	0.404635	0.007232	2.67E-06	99.55403
		Poto.m Grain 3 cpx 1	51.06483	0.711176	2.992728	0.035354	0.007698	8.183843	0.0013	0.339108	14.92978	20.99473	0.398827	0.007196	0.000002	99.66658
		Poto.m Grain 3 cpx 2	51.88873	0.585378	2.311348	0.030349	0.005538	8.20438	0.001969	0.386188	15.22683	20.84313	0.361062	0.005807	0.000001	99.85068
		Poto.m Grain 4 cpx 1	51.511	0.607228	2.514422	0.033887	0.003038	8.053092	0.002253	0.386338	15.0942	20.97022	0.3996	0.010814	3.2E-06	99.5861
	Poto.n	Poto.n Grain 1 cpx 1	51.15583	0.645734	2.56738	0.040774	0.001497	9.522773	0.000737	0.496455	14.3703	19.98423	0.436474	0.026843	0.000003	99.249
		Poto.n Grain 1 cpx 2	50.43747	0.84626	3.32697	0.044838	0.003763	8.412593	0.000127	0.328587	14.93967	20.59403	0.337905	0.017264	0	99.28943
		Poto.n Grain 3 cpx 1	51.46863	0.598803	2.282413	0.038385	0.000225	8.28959	0.000536	0.425696	15.46575	20.37475	0.354283	0.006196	0.000002	99.30525
		Poto.n Grain 3 cpx 2	51.7119	0.539295	2.000625	0.031706	0.001971	8.218818	0.001048	0.431667	15.54278	20.39403	0.336106	0.016451	-3E-06	99.2264
	Poto.o	Poto.o Grain 2 cpx 1	50.1938	0.724696	3.668817	0.033777	0.002312	8.664647	0.01149	0.428586	14.12807	21.16813	0.382319	0.011649	-6.7E-06	99.41833
		Poto.o Grain 3 cpx 1	51.60498	0.545902	2.31735	0.025077	0.002382	7.975333	0.005292	0.432396	15.30028	20.82345	0.325269	0.003603	0.000002	99.3613
		Poto.o Grain 4 cpx 1	50.38683	0.931425	3.864793	0.032295	0.000577	8.660803	0	0.348445	14.35237	20.75747	0.334577	0.00108	2.67E-06	99.67053
		Poto.o Grain 4 cpx 2	52.32415	0.471385	1.935663	0.028599	0	8.034128	0	0.456355	15.79783	20.39718	0.304942	0.001667	0.000004	99.75188

Formation	Layer	Sample	SiO2	TiO2	Al2O3	V2O3	Cr2O3	FeO	NiO	MnO	MgO	CaO	Na2O	K2O	O	Total
	Paetahi.a lower	Paetahi.a lower Grain 1 cpx 1	53.4904	0.265906	1.197455	0.010405	0.001695	17.04135	0.0037	0.913818	25.26485	1.66991	0.034062	0.004596	0	99.89805
		Paetahi.a lower Grain 1 cpx 2	52.32597	0.501966	2.012083	0.026702	0.000892	8.6282	0.005575	0.507226	15.61123	20.4049	0.360293	0.002397	-3.3E-06	100.3877
		Paetahi.a lower Grain 2 cpx 1	51.97935	0.523553	2.20755	0.023948	0.002651	8.69379	0	0.525279	15.42103	20.1881	0.358684	0.009055	0.000002	99.93315
		Paetahi.a lower Grain 2 cpx 2	50.63697	0.808361	3.682778	0.040243	0.00142	12.18276	0.002895	0.559043	17.48093	14.22095	0.282749	0.008594	-3.3E-06	99.90767
		Paetahi.a lower Grain 3 cpx 1	51.62985	0.57439	2.552378	0.032045	0.002274	8.874638	0.003085	0.469841	15.11685	20.5465	0.365774	0.001462	-1.5E-06	100.1692
		Paetahi.a lower Grain 3 cpx 2	51.66303	0.645032	2.961633	0.027323	0.005083	11.8876	0.00231	0.560186	18.13713	14.26073	0.228049	0.003248	-3.3E-06	100.3813
	Paetahi.a middle	Paetahi.a middle Grain 1 cpx 1	52.16315	0.564081	2.93463	0.024741	0.000851	8.58981	0.004251	0.489137	14.7023	20.21058	0.337493	0.015765	-2.5E-06	100.0368
		Paetahi.a middle Grain 1 cpx 2	52.20348	0.491508	1.84782	0.02504	0.001822	8.87088	0.003678	0.456089	15.0357	20.46083	0.333079	0.011573	-5E-07	99.74155
		Paetahi.a middle Grain 3 cpx 1	52.44538	0.482909	1.996448	0.021314	0.001061	10.47339	0.000426	0.603081	17.59698	15.55829	0.248895	0.009929	-1.5E-06	99.4381
		Paetahi.a middle Grain 3 cpx 2	52.00218	0.571197	2.70907	0.027283	0.00115	8.431323	0.000515	0.471969	14.78635	20.14985	0.388375	0.036907	0.000002	99.5761
	Paetahi.a upper	Paetahi.a upper Grain 1 cpx 1	51.71103	0.561246	2.478832	0.030256	0.0015	8.579653	0.000592	0.491972	14.8809	20.67593	0.364186	0.002021	6.67E-07	99.77808
		Paetahi.a upper Grain 1 cpx 2	52.19475	0.502402	2.14895	0.024093	0	8.298348	0.006798	0.497218	15.44323	20.36553	0.31505	0.004159	3.75E-06	99.80048
		Paetahi.a upper Grain 1 cpx 3	53.79753	0.276305	1.262248	0.018028	0.000777	16.63	0.002923	0.896665	25.30655	1.447365	0.027343	0.005803	-5E-07	99.67163
		Paetahi.a upper Grain 1 cpx 4	51.88913	0.574584	2.380097	0.03529	0	8.810347	0.003874	0.491511	15.1257	20.10033	0.355274	0.009417	-6.7E-06	99.77553
		Paetahi.a upper Grain 3 cpx 2	50.79308	0.807712	2.112968	0.045516	0.001212	10.4512	0.001361	0.513858	15.12046	19.75391	0.343857	0.007308	1.25E-06	99.95243
		Paetahi.a upper Grain 3 cpx 3	48.88257	1.066366	5.65935	0.04659	0.002141	10.02862	0.004305	0.328016	12.70043	20.55463	0.371548	0.032428	0	99.6769
		Paetahi.a upper Grain 3 cpx 4	44.45175	2.01792	8.65704	0.071506	0	10.97	0.007854	0.23822	11.00915	21.35745	0.359645	0.003853	-5E-06	99.1444
		Paetahi.a upper Grain 4 cpx 1	51.41864	0.604002	2.743717	0.028406	0.006328	10.43236	0	0.532456	16.64236	16.93588	0.292405	0.007026	-4.4E-06	99.64354
	Paetahi.b	Paetahi.b Grain 1 cpx 1	51.45845	0.605126	2.626728	0.028769	0.000711	8.164503	0	0.388803	15.3899	20.6479	0.349229	0.00417	0.000002	99.6644
		Paetahi.b Grain 1 cpx 2	52.40175	0.473594	1.459635	0.028309	0.001879	10.26394	0.002262	0.678725	14.37545	19.57518	0.393251	0.022636	-1.5E-06	99.6766
		Paetahi.b Grain 1 cpx 3	51.36135	0.635329	2.61312	0.031713	0	9.076455	0	0.4887	15.05165	19.8973	0.374834	0.010564	0.000004	99.54095
		Paetahi.b Grain 4 cpx 1	51.39588	0.56266	2.38295	0.031467	0.001386	8.048588	0.007031	0.461304	15.403	20.61922	0.356293	0.006519	1.6E-06	99.2763
		Paetahi.b Grain 4 cpx 2	51.14495	0.610202	2.611085	0.02418	0.001787	8.30371	0.005293	0.448853	15.41913	20.46028	0.361836	0.005323	0.000001	99.3966
		Paetahi.b Grain 4 cpx 4	48.97393	1.141743	4.715398	0.045609	0.001071	9.361348	0.0026	0.385571	13.80098	20.5988	0.384576	0.017455	0.000002	99.42905
	Paetahi.c	Paetahi_c_Grain_1_CPX1	50.14667	0.929233	3.91	0.0367	0.008167	9.293333	0.008367	0.397867	14.77	20.38333	0.364833	0.002367		100.2509
		Paetahi_c_Grain_1_CPX2	52.79	0.5199	2.22	0.0425	0.0098	8.33	0.0134	0.4146	15.83	20.43	0.3508	0.0037		100.9547
		Paetahi_c_Grain_1_CPX3	51.04	0.8412	3.86	0.0357	0	8.65	0	0.3791	14.72	21.07	0.3853	0.0017		100.983
		Paetahi_c_Grain_1_CPX4	50.965	0.77045	3.35165	0.03705	0.00045	9.325	0.00395	0.41305	14.935	20.39	0.321	0.00185		100.5145
		Paetahi_c_Grain_1_CPX5	51.88	0.6826	2.9	0.0279	0.0033	9.05	0	0.4786	15.71	19.89	0.3517	0.004		100.9781
		Paetahi_c_Grain_3_CPX1	52.46	0.52078	2.1528	0.02978	0.00492	8.346	0.0015	0.46262	15.894	20.312	0.32126	0.00438		100.51
		Paetahi_c_Grain_3_CPX2	52.125	0.6281	2.605	0.0287	0.01415	8.755	0	0.4451	15.29	20.4	0.3416	0.00765		100.6403
		Paetahi_c_Grain_3_CPX3	50.715	0.807575	3.99	0.047425	0.00315	8.465	0.003775	0.288675	14.425	21.4125	0.355225	0.006425		100.5198
		Paetahi_c_Grain_3_CPX4	51.7325	1.088425	6.0725	0.036775	0	9.575	0	0.346275	12.2275	17.5775	0.55945	0.467		99.68293
		Paetahi_c_Grain_3_CPX5	51.9875	0.52415	2.82	0.032125	0	7.955	0.001825	0.302075	15.33	21.3875	0.287975	0.00405		100.6322
		Paetahi_c_Grain_7_CPX1	52.41	0.6134	2.645	0.02745	0.00545	8.7	0.0056	0.42695	15.425	20.275	0.3768	0.01035		100.921
		Paetahi_c_Grain_7_CPX2	51.455	0.750767	3.34	0.0387	0.003167	9.141667	0.006067	0.45335	15.51167	19.345	0.324683	0.01575		100.3858
		Paetahi_c_Grain_7_CPX3	52.4	0.5706	2.39344	0.02916	0.00284	8.764	0.00426	0.47866	15.598	20.146	0.34602	0.00622		100.7392
		Paetahi_c_Grain_7_CPX4	51.625	0.717283	3.185	0.033967	0.004283	9.055	0.005417	0.447117	15.375	20.02167	0.355367	0.000983		100.8261
		Paetahi_c_Grain_7_CPX5	51.8925	0.6307	2.875	0.03065	0.001225	8.67	0.003725	0.419475	15.06	20.7225	0.3424	0.003825		100.652
	Paetahi.d	Paetahi_d_Grain_1_CPX1	51.97	0.649914	2.895714	0.037371	0.003957	8.571429	0.002729	0.419214	15.29857	20.53714	0.329271	0.010871		100.7262
		Paetahi_d_Grain_1_CPX2	52.835	0.4843	1.9498	0.02765	0.006	8.81	0.00265	0.47055	15.995	19.78	0.3072	0.01555		100.6837
		Paetahi_d_Grain_1_CPX3	52.45	0.5373	2.24	0.024067	0.012133	9.686667	0.003367	0.547533	14.91333	19.41	0.433267	0.074633		100.3323
		Paetahi_d_Grain_1_CPX4	52.28	0.5969	2.28195	0.0278	0.00205	9.535	0.00675	0.5104	15.63	19.47	0.2982	0.02305		100.6621
		Paetahi_d_Grain_1_CPX5	51.4775	0.662975	3.0925	0.033525	0.0007	9.7	0.0092	0.499575	14.475	19.905	0.444675	0.0669		100.3676
		Paetahi_d_Grain_4_CPX1	51.645	0.5324	2.49	0.02805	0.0058	8.285	0	0.41955	15.525	20.43	0.35045	0		99.71125
		Paetahi_d_Grain_4_CPX2	51.56667	0.692167	3.013333	0.0348	0.001633	8.583333	0.0001	0.458267	15.36333	19.89	0.335833	0.005		99.94447
		Paetahi_d_Grain_4_CPX3	51.70667	0.607667	3.3	0.037433	0.001333	8.536667	0.003367	0.380767	15.10333	20.29667	0.391233	0.007967		100.3731
		Paetahi_d_Grain_4_CPX4	50.13	1.003	4.05	0.0523	0.0133	9.67	0	0.415	14.7	19.98	0.3574	0		100.371
		Paetahi_d_Grain_4_CPX5	51.60667	0.638633	2.803333	0.025767	0.000667	8.193333	0.0009	0.404167	15.53	20.63667	0.3316	0.002867		100.1746
	Paetahi.e lower	Paetahi.e lower Grain 1 cpx 1	48.69228	1.047208	5.461673	0.058459	0.002323	9.233988	0.005058	0.297451	13.21083	21.15202	0.416535	0.016058	3.33E-07	99.59383
		Paetahi.e lower Grain 2 cpx 1	48.11683	1.249548	5.720755	0.052005	0.003278	9.3993	0.002844	0.272366	13.0075	21.23543	0.374076	0.024005	-1.5E-06	99.45793
		Paetahi.e lower Grain 3 cpx 1	49.8383	0.79556	3.70982	0.040104	0	8.775567	0.001838	0.349454	14.26577	20.77227	0.336391	0.008934	-5.3E-06	98.89407
		Paetahi.e lower Grain 3 cpx 2	50.45777	0.672212	2.83992	0.033863	0.001561	8.878167	0	0.424712	14.56533	20.43837	0.386358	0.008495	1.33E-06	98.70677
	Paetahi.e middle	Paetahi_emiddle_Grain_1_CPX1	48.875	1.127675	4.1525	0.054025	0.003925	10.66	0.00155	0.300425	14.025	20.8125	0.32555	0.01625		100.3544
		Paetahi_emiddle_Grain_1_CPX2	49.73	1.01065	6.15	0.0459	0.0105	9.295	0.00495	0.3114	13.24	19.775	0.5618	0.03905		100.1743
		Paetahi_emiddle_Grain_1_CPX3	49.58	0.9862	4.32	0.04065	0.0041	9.505	0	0.38155	14.04	20.22	0.3845	0.02755		99.48955
		Paetahi_emiddle_Grain_1_CPX4	51.79167	0.672467	2.978333	0.031917	0.002117	8.728333	0.0083	0.405067	15.25333	20.38833	0.341033	0.0148		100.6157
		Paetahi_emiddle_Grain_1_CPX5	52.29	0.5079	2.05	0.0374	0.0028	8.4	0.0083	0.4522	15.62	20.39	0.3547	0.0067		100.12
		Paetahi_emiddle_Grain_4_CPX1	51.32333	0.7226	3.553333	0.0323	0.004033	9.04	0.002367	0.3714	14.80333	20.51333	0.320167	0.0107		100.6969
		Paetahi_emiddle_Grain_4_CPX2	50.52667	0.899033	4.44	0.032133	0	9.806667	0.0046	0.3708	14.40333	19.59333	0.3529	0.020133		100.4496
		Paetahi_emiddle_Grain_4_CPX3	49.55667	1.072633	4.096667	0.044867	0.005	12.36	0	0.432167	14.46	17.73	0.4728	0.088433		100.3192
		Paetahi_emiddle_Grain_4_CPX4	51.5	0.55215	2.16	0.03135	0.00085	8.6	0	0.39025	15.385	20.45	0.2679	0.01155		99.34905
		Paetahi_emiddle_Grain_4_CPX5	50.935	1.2662	9.285	0.05835	0.0068	9.535	0	0.3685	10.18	16.36	1.414	0.49755		99.9064
	Paetahi.e upper	Paetahi.e upper Grain 1 cpx 1	51.08205	0.920214	7.123073	0.033465	0	8.612955	0.004077	0.381425	12.33098	18.41445	1.061672	0.196654	0	100.1612
		Paetahi.e upper Grain 1 cpx 2	51.76428	0.559105	2.616975	0.032615	0.004083	7.403465	0.001066	0.2991	15.22378	21.48643	0.349201	0.004856	0	99.74495
		Paetahi.e upper Grain 1 cpx 3	45.67658	1.759593	8.027765	0.057618	0.00178	10.28978	0.005772	0.23799	11.7278	21.31318	0.376673	0.024221	0.000002	99.49873
		Paetahi.e upper Grain 1 cpx 4	48.46893	1.262944	6.378848	0.042402	0.004837	9.645698	0	0.301657	12.68215	19.93208	0.547252	0.103832	-2.5E-06	99.37068
	Paetahi.f	Paetahi.f Grain 1 cpx 1	52.01613	0.430745	1.69456	0.026154	0.001388	10.57484	0.001747	0.660736	17.86463	15.67656	0.271119	0.006923	-3E-06	99.22555
		Paetahi.f Grain 1 cpx 2	51.133	0.530892	2.442728	0.026804	0.00089	8.063043	0.000327	0.432957	15.00975	21.21998	0.368926	0.002668	0	99.23198
		Paetahi.f Grain 1 cpx 3	50.89608	0.595902	2.642803	0.028224	0.001742	8.995935	0.001352	0.454778	14.99013	20.10468	0.386768	0.006854	5E-07	99.10523
		Paetahi.f Grain 3 cpx 1	50.02116	0.800487	4.148816	0.036282	0.001827	8.873583	0.004223	0.358496	14.0931	20.6793	0.34557	0.005812	0.000001	99.36859
		Paetahi.f Grain 3 cpx 2	50.78587	0.638943	2.894	0.037803	0.001736	8.352127	0.000868	0.447523	14.82193	20.59637	0.350102	0.006852	0.000004	98.93413
		Paetahi.f Grain 3 cpx 3	51.81535	0.465197	1.9738	0.02788	0.000076	8.428155	0.00332	0.505812	15.0281	20.7459	0.376776	0.00819	0	99.37855
		Paetahi.f Grain 3 cpx 4	51.41918	0.515062	2.40454	0.02133	0.003282	8.339333	0	0.429614	15.08518	20.8727	0.33965	0.017919	0.000004	99.44778
		Paetahi.f Grain 4 cpx 1	51.52078	0.561136	2.34749	0.026729	0.003353	8.334623	0.000719	0.510658	15.2648	20.51418	0.365051	0.007764	0.000003	99.45728
		Paetahi.f Grain 4 cpx 2	51.7354	0.512344	2.12403	0.02426	0.000404	8.286377	0.004596	0.52007	15.28377	20.673	0.389705	0.012252	1.33E-06	99.56633
		Paetahi.f Grain 4 cpx 3	51.10115	0.578972	2.770858	0.03308	0.003727	8.0685	0.003621	0.453604	15.10765	20.67868	0.347216	0.015281	0.000002	99.16235
Paetahi		Paetahi.f Grain 4 cpx 4	52.14923	0.537726	2.602647	0.026151	0.001512	8.311403	0.005988	0.535885	15.13113	19.46543	0.368158	0.127421	-6.7E-07	99.26267

Appendix F5: Major element EMPA analyses of plagioclase crystals from epoxy plugs

Formation	Layer	SAMPLE	SiO2	TiO2	Al2O3	FeO	MnO	MgO	CaO	SrO	BaO	Na2O	K2O	O	Total
Poto	Poto.a	Poto.a Grain 1 Feld 1	54.8072	0.038943	28.8172	0.672584	0.004711	0.069014	10.71468	0.145353	0.061269	5.090173	0.465029	-5E-07	100.8863
		Poto_a_Grain_1_Feldspar1	59.4	0.05065	25.445	0.66275	0.00435	0.04265	7.535	#DIV/0!	0.1693	6.51	1.0254		100.8451
		Poto_a_Grain_1_Feldspar2	55.1775	0.039075	28.5975	0.667525	0.011925	0.064875	10.9	#DIV/0!	0.055375	5.1025	0.43575		101.052
		Poto_a_Grain_1_Feldspar3	55.65286	0.043571	28.24571	0.706314	0.0116	0.065214	10.62714	#DIV/0!	0.061429	5.288571	0.463343		101.1658
		Poto_a_Grain_1_Feldspar4	54.36	0.03305	28.475	0.643	0.00525	0.0644	11.37	#DIV/0!	0.053175	4.8075	0.4194		100.2308
		Poto_a_Grain_1_Feldspar5	54.4975	0.07205	28.4	0.849475	0.007775	0.11165	11.375	#DIV/0!	0.0502	4.6225	0.547675		100.5338
		Poto_a_Grain_2_Feldspar1	55.4925	0.042725	28.2725	0.704275	0.0101	0.063525	10.615	#DIV/0!	0.059175	5.145	0.46695		100.8718
		Poto_a_Grain_2_Feldspar2	53.6425	0.031925	29.47	0.644225	0.00845	0.051225	12.105	#DIV/0!	0.046425	4.47	0.32625		100.796
		Poto_a_Grain_2_Feldspar3	55.7225	0.042225	27.5975	0.687425	0.010975	0.0631	10.2375	#DIV/0!	0.06795	5.37	0.502125		100.3013
		Poto_a_Grain_2_Feldspar4	55.4075	0.043725	28.38	0.6845	0.007975	0.0623	10.72	#DIV/0!	0.063775	5.18	0.435975		100.9858
		Poto_a_Grain_3_Feldspar1	55.1425	0.043325	28.695	0.7162	0.004175	0.05915	10.9475	#DIV/0!	0.053025	5.0225	0.41765		101.101
		Poto_a_Grain_3_Feldspar2	55.2675	0.03955	28.3275	0.6762	0.0081	0.059625	10.535	#DIV/0!	0.060475	5.2625	0.45525		100.6917
		Poto_a_Grain_3_Feldspar3	53.265	0.280675	1.0028	18.1275	0.76765	24.805	1.6425	#DIV/0!	0.000975	0.035275	0.001475		99.92885
		Poto_a_Grain_3_Feldspar4	55.635	0.04585	28.725	0.7117	0.01445	0.06425	10.71	#DIV/0!	0.0424	5.135	0.4407		101.5244
		Poto_a_Grain_3_Feldspar5	55.25667	0.037967	28.17333	0.619167	0.009	0.057067	10.56333	#DIV/0!	0.0677	5.183333	0.460567		100.4281
		Poto_a_Grain_4_Feldspar1	55.10667	0.037167	28.76667	0.649633	0.005033	0.057767	11.05667	#DIV/0!	0.0577	5.15	0.412367		101.2997
		Poto_a_Grain_4_Feldspar2	52.2675	0.02975	30.235	0.668475	0.01395	0.060675	12.8375	#DIV/0!	0.037925	4.07	0.2783		100.4991
		Poto_a_Grain_4_Feldspar3	55.07	0.0454	28.17	0.663367	0.009233	0.058733	10.69667	#DIV/0!	0.0649	5.17	0.452367		100.4007
		Poto_a_Grain_4_Feldspar4 4	57.01	0.0762	27.325	0.82955	0.0089	0.103275	9.4825	#DIV/0!	0.076925	5.4225	0.6313		100.9662
		Poto_a_Grain_4_Feldspar5	54.955	0.038225	28.6725	0.7165	0.00215	0.05885	11.045	#DIV/0!	0.05305	4.99	0.414175		100.9455
		Poto_a_Grain_8_Feldspar1	55.97	0.0397	27.9225	0.670225	0.0055	0.0545	10.1175	#DIV/0!	0.069975	5.38	0.512975		100.7429
	Poto.b	Poto.b Grain 2 Feld 1	52.0507	0.092544	29.0448	0.913512	0.000258	0.078585	11.4437	0.136864	0.07101	4.43326	0.389141	0.000008	98.6543
		Poto.b Grain 2 Feld 4	52.1288	0.154359	29.1627	1.28916	0	0.084985	10.9907	0.14244	0.058829	4.49433	0.457211	0	98.9636
		Poto.b Grain 5 Feld 2	53.1105	0.167204	27.8486	1.47043	0.01694	0.31932	9.72019	0.129149	0.075381	4.58702	0.689973	0	98.1347
		Poto.b Grain 5 Feld 5	52.6132	0.0898	29.4844	0.893201	0	0.118637	11.5415	0.161359	0.053586	4.48067	0.491161	0.000004	99.9276
		Poto.b Grain 7 Feld 1	54.1215	0.238274	26.5074	1.59801	0.029606	0.345065	9.56414	0.128478	0.087262	4.82724	0.974076	0.000008	98.4211
		Poto.b Grain 7 Feld 2	52.6708	0.114669	29.6731	0.962215	0	0.091759	11.363	0.153829	0.075364	4.27038	0.438747	0.000008	99.8139
	Poto.c lower	Poto.c lower Grain 1 Feld 1	55.1746	0.112109	27.5949	1.003767	0.019899	0.180265	9.83629	0.142461	0.080714	5.024245	0.896063	0.000002	100.0652
		Poto.c lower Grain 1 Feld 2	55.12793	0.156541	26.94813	1.527837	0.01737	0.183972	9.322445	0.143831	0.086279	5.284513	0.838876	0.000002	99.6379
		Poto.c lower Grain 1 Feld 3	55.9702	0.076163	27.1604	0.737129	0.015601	0.114792	9.236777	0.125952	0.049156	5.44081	0.811472	2.67E-06	99.7383
		Poto.c lower Grain 1 Feld 4	57.5069	0.235531	25.40865	1.501587	0.041221	0.359294	8.181673	0.124178	0.10043	5.28172	1.545372	2.5E-06	100.2865
		Poto.c lower Grain 1 Feld 5	57.328	0.291348	24.875	1.66944	0.048875	0.406922	7.90469	0.108222	0.104215	5.06774	1.82278	0	99.6272
		Poto.c lower Grain 2 Feld 2	53.0683	0.042322	30.13	0.641113	0.001685	0.071021	12.1725	0.154712	0.052605	4.31319	0.331038	0.000008	100.978
		Poto.c lower Grain 3 Feld 1	58.34915	0.046811	25.96865	0.567128	0.000894	0.038836	7.540265	0.127459	0.070536	6.58703	0.698979	0	99.99595
		Poto.c lower Grain 3 Feld 2	58.54833	0.01325	26.60998	0.432418	0.003471	0.020366	7.974163	0.115431	0.045481	6.481865	0.589275	0	100.8339
		Poto.c lower Grain 3 Feld 5	56.3403	0.181004	25.0344	1.642659	0.042193	0.936451	8.80659	0.109108	0.037006	5.52277	0.819084	0.000002	99.47135
	Poto.c upper	Poto.c upper Grain 1 Feld 1	54.67578	0.050546	28.8738	0.636136	0.007263	0.035513	10.91075	0.075269	0.047559	5.12919	0.36655	0.000002	100.8085
		Poto.c upper Grain 1 Feld 2	56.0457	0.071514	27.78423	0.662735	0.009359	0.037888	9.729175	0.076873	0.043668	5.529033	0.664897	-3E-06	100.6553
		Poto.c upper Grain 2 Feld 1	51.39305	0.044673	30.20775	0.738881	0.009003	0.067325	12.72725	0.15791	0.039112	3.865505	0.290565	0.000004	99.541
		Poto.c upper Grain 2 Feld 2	51.56295	0.036493	31.3149	0.858684	0.003135	0.106561	13.4761	0.131033	0.029015	3.484845	0.240348	0.000004	101.244
		Poto.c upper Grain 3 Feld 1	53.27265	0.047438	30.08905	0.756433	0.005941	0.080454	11.98508	0.141587	0.04508	4.435885	0.352582	0.000002	101.2125
	Poto.d	Poto.d Grain 1 Feld 1	51.9992	0.055353	29.1029	0.761395	0.005683	0.085223	11.4023	0.165481	0.056827	4.54243	0.352108	0.000008	98.5289
		Poto.d Grain 1 Feld 2	53.97437	0.115745	28.52593	1.186958	0.020332	0.68691	11.27157	0.131669	0.067304	4.50919	0.412536	1.33E-06	100.9024
		Poto.d Grain 1 Feld 4	53.74167	0.044618	30.3551	0.646054	0.000881	0.073425	12.05947	0.153178	0.052644	4.25707	0.325027	1.33E-06	101.709
		Poto.d Grain 2 Feld 1	54.1618	0.211761	27.2155	1.55632	0.032309	0.373864	9.36993	0.132554	0.085869	4.6814	0.921399	0	98.7427
		Poto.d Grain 3 Feld 1	54.0166	0.067936	29.1393	0.807042	0.003368	0.086815	11.0227	0.153761	0.061013	4.84813	0.436985	0.000004	100.644
		Poto.d Grain 3 Feld 2	52.66533	0.080105	29.4128	1.061467	0.010605	0.341968	11.61973	0.13891	0.05003	4.122927	0.338148	-2E-06	99.842
		Poto.d Grain 4 Feld 1	52.3821	0.208863	29.6519	1.64499	0.006572	0.167818	10.27129	0.133179	0.05858	4.03018	0.391849	0.000002	98.94735
		Poto.d Grain 4 Feld 3	53.3881	0.091164	30.4919	1.031453	0.01311	0.131603	10.8074	0.137049	0.048561	4.391785	0.368557	-1.5E-05	100.9007
	Poto.e	Poto.e Grain 1 Feld 1	54.37013	0.096593	27.8406	1.451591	0.027811	0.884597	10.07537	0.107183	0.052234	4.979483	0.738407	0	100.6239
		Poto.e Grain 1 Feld 2	52.13355	0.04322	30.2023	0.696905	0.007687	0.063893	12.30475	0.150068	0.047399	4.380193	0.305432	0.000001	100.3356
		Poto.e Grain 3 Feld 1	51.17013	0.036288	30.83073	0.723218	0.004445	0.103075	13.2024	0.146231	0.03709	3.695295	0.2503	0.000005	100.199
		Poto.e Grain 3 Feld 2	53.53307	0.044932	29.89837	0.691719	0.003679	0.0749	11.81737	0.160176	0.04673	4.553763	0.338149	1.33E-06	101.1627
	Poto.f	Poto_f_Grain_1_Feldspar1	52.79333	0.0377	29.57	0.8133	0.0101	0.0989	12.89	#DIV/0!	0.0385	4.023333	0.332167		100.6073
		Poto_f_Grain_1_Feldspar2	54.1875	0.043825	29.1675	0.7355	0.008275	0.08905	11.7225	#DIV/0!	0.0718	4.6675	0.39375		101.0872
		Poto_f_Grain_1_Feldspar3	54.345	0.041425	29.12	0.7135	0.007025	0.075275	11.65	#DIV/0!	0.0436	4.745	0.344825		101.0857
		Poto_f_Grain_1_Feldspar4	54.8925	0.036975	28.5475	0.60095	0.005	0.06295	11.195	#DIV/0!	0.0515	4.965	0.3946		100.752
		Poto_f_Grain_1_Feldspar5	53.0975	0.04205	29.77	0.813725	0.007625	0.095825	12.41	#DIV/0!	0.03245	4.29	0.309175		100.8684
		Poto_f_Grain_5_Feldspar1	59.32	0.1774	25.17333	1.3985	0.034633	0.3073	8.34	#DIV/0!	0.072333	5.133333	1.192233		101.1491
		Poto_f_Grain_5_Feldspar2	54.215	0.04	29.4325	0.71245	0.006125	0.0709	11.56	#DIV/0!	0.052175	4.8075	0.349575		101.2462
		Poto_f_Grain_5_Feldspar3	54.73	0.046633	28.88667	0.622433	0.0168	0.054667	11.20667	#DIV/0!	0.050967	4.993333	0.361733		100.9699
		Poto_f_Grain_5_Feldspar4	54.75667	0.0366	28.55667	0.5759	0.009367	0.061	11.04333	#DIV/0!	0.054967	4.816667	0.3769		100.2881
		Poto_f_Grain_5_Feldspar5	57.10167	0.26905	25.59333	1.96415	0.059317	0.51875	9.416667	#DIV/0!	0.07375	4.256667	1.224467		100.4778
	Poto.g	Poto.g Grain 1 Feld 1	53.29885	0.037876	30.5922	0.6898	0.011096	0.069323	12.1338	0.149305	0.043805	4.24915	0.277958	0.000002	101.5535
		Poto.g Grain 1 Feld 2	52.41587	0.040038	30.51123	0.684063	0.007672	0.075955	12.25203	0.153039	0.035886	4.242747	0.275791	3.67E-06	100.6947
		Poto.g Grain 4 Feld 1	54.32125	0.050691	29.0605	0.778516	0.005337	0.093022	10.78585	0.173505	0.075972	4.94928	0.391589	0.000002	100.6856
		Poto.g Grain 4 Feld 2	55.09113	0.304458	25.26398	2.806584	0.105499	1.938527	9.873695	0.106345	0.054674	4.167375	1.011765	-2.5E-06	100.724
	Poto.h	Poto.h Grain 1 Feld 1	53.1851	0.038375	30.06577	0.675097	0.004081	0.071164	11.79637	0.155887	0.04373	4.457843	0.329274	2.67E-06	100.8227
		Poto.h Grain 4 Feld 1	56.03843	0.034458	28.8099	0.594668	0.011545	0.068122	10.1466	0.163553	0.070698	5.439143	0.411343	2.67E-06	
		Poto.h Grain 4 Feld 2	53.72297	0.038126	30.04477	0.57166	0.008686	0.06123	11.68203	0.148985	0.039456	4.51507	0.298054	-3.3E-06	101.131
		Poto.h Grain 3 Feld 1	57.0493	0.147087	27.11397	1.084349	0.029832	0.233531	9.391693	0.157703	0.081334	5.14024	0.92336	5.33E-06	101.3527
	Poto.i	Poto.i Grain 1 Feld 1	58.03123	0.026111	27.24143	0.559808	0.007781	0.0216	8.419857	0.128954	0.099677	6.13867	0.671472	2.67E-06	101.3467
		Poto.i Grain 1 Feld 2	52.5795	0.035598	30.5367	0.720682	0.010422	0.066252	12.4101	0.144863	0.036831	4.216183	0.304549	1.33E-06	101.0617
		Poto.i Grain 4 Feld 1	56.3829	0.032113	28.21027	0.596376	0.007542	0.047087	9.366883	0.137075	0.072914	5.58728	0.49007	0	100.9303
		Poto.i Grain 4 Feld 2	56.41983	0.093513	27.3493	1.011238	0.016528	0.117936	9.18371	0.130445	0.084465	5.09392	0.795212	3.67E-06	100.2963
	Poto.j	Poto.j Grain 1 Feld 1	56.17128	0.080589	27.62755	1.011753	0.019172	0.315966	9.77066	0.142775	0.079084	5.160265	0.589759	5.5E-06	100.9685
		Poto.j Grain 1 Feld 2	57.83205	0.208195	25.30685	1.536383	0.04072	0.211763	8.06436	0.120439	0.092952	5.0501	1.359286	0.000004	99.8232
		Poto.j Grain 3 Feld 1	54.42733	0.034896	29.08327	0.565048	0.002431	0.059532	10.813	0.17811	0.052289	5.168353	0.326157	6.67E-07	100.7103
		Poto.j Grain 3 Feld 2	57.33048	0.102776	27.30273	0.87972	0.016606	0.181439	9.27878	0.145748	0.05963	5.210723	0.77124	0.000001	101.28
	Poto.k lower	Poto.k lower Grain 1 Feld 1	51.29458	0.033224	31.10783	0.770449	0.003167	0.097493	13.3513	0.149511	0.0338	3.662738	0.234185	1.25E-06	100.7383
		Poto.k lower Grain 1 Feld 2	56.73193	0.060438	27.07313	0.859687	0.019342	0.350635	8.982943	0.141345	0.080174	5.496938	0.598901	-3E-06	100.3955
		Poto.k lower Grain 4 Feld 1	52.91285	0.040557	30.03375	0.650791	0.004575	0.078893	12.0354	0.159497	0.053478	4.306375	0.291653	-5E-06	100.568
		Poto.k lower Grain 4 Feld 2	51.53097	0.038365	30.66207	0.672582	0.007436	0.082534	12.7199	0.150347	0.030286	3.94407	0.241155	5.33E-06	100.0797
		Poto.k lower Grain 3 Feld 1	53.7181	0.030759	29.7552	0.667899	0.011227	0.069913	11.8385	0.156109	0.039647	4.50031	0.303506	0.000004	101.091
	Poto.k upper	Poto.k upper Grain 1 Feld 1	57.73427	0.16361	25.8111	1.047011	0.025907	0.232171	7.96658	0.164817	0.119053	5.839273	0.950083	-3.3E-06	100.0539
		Poto.k upper Grain 1 Feld 2	60.4661	0.476474	21.7629	2.52516	0.05814	0.775967	5.76173	0.077655	0.089207	5.88477	2.31347	0	100.192
		Poto.k upper Grain 2 Feld 1	52.45777	0.038524	29.9464	0.66406	0.008863	0.067233	12.08433	0.166255	0.039649	4.368253	0.287343	0	100.1287
		Poto.k upper Grain 3 Feld 1	54.966	0.049685	27.8483	0.661962	0.006746	0.071745	9.91129	0.172162	0.062325	5.44309	0.416808	0.000004	99.6101
	Poto.l lower	Poto.l lower Grain 2 Feld 1	53.43058	0.051496	29.7022	0.713432	0.007947	0.072858	11.56405	0.151434	0.043771	4.67938	0.344056	2.5E-07	100.7611
		Poto.l lower Grain 2 Feld 2	53.1843	0.045127	29.6361	0.680815	0.004162	0.069303	11.53035	0.155207	0.051678	4.603805	0.334119	0.000002	100.295
		Poto.l lower Grain 2 Feld 3	51.5775	0.043104	30.40975	0.802989	0.008426	0.096182	12.8102	0.154999	0.038099	4.1369	0.254883	0.000002	100.333
		Poto.l lower Grain 5 Feld 1	53.6496	0.065333	29.45405	0.842976	0.011087	0.075003	11.3311	0.147665	0.051499	4.479745	0.337376	5.5E-06	100.4453
		Poto.l lower Grain 4 Feld 1	53.97035	0.055833	29.56525	0.740124	0.005672	0.080669	11.49175	0.152793	0.036685	4.632715	0.318505	0.000002	101.0505
	Poto.l upper	Poto.l upper Grain 1 Feld 1	53.92347	0.041755	29.71997	0.651347	0.004937	0.067378	11.3856	0.143742	0.046876	4.628807	0.329688	1.33E-06	100.9436
		Poto.l upper Grain 1 Feld 2	53.8292	0.053192	29.55797	0.788187	0.010073	0.100678	11.5825	0.131597	0.038928	4.598177	0.365977	-2E-06	101.0563
		Poto.l upper Grain 3 Feld 1	52.1396	0.025753	30.81435	0.694295	0.000958	0.070859	12.73198	0.15357	0.031129	4.061638	0.249754	0.000001	100.974
		Poto.l upper Grain 3 Feld 2	52.4783	0.035995	30.2791	0.722779	0.003243	0.093751	12.2997	0.165097	0.039955	4.13332	0.272525	0	100.524
		Poto.l upper Grain 2 Feld 1	53.79535	0.038713	29.9673	0.660974	0.011834	0.063625	11.64025	0.148033	0.039369	4.689345	0.30044	-5E-06	101.355
	Poto.m	Poto.m Grain 1 Feld 2	53.8681	0.06575	29.49535	0.81525	0.009458	0.094557	11.14825	0.133657	0.049692	4.823255	0.356744	0	100.86
		Poto.m Grain 3 Feld 1	52.36203	0.050006	30.4987	0.813644	0.004796	0.119995	12.8724	0.167987	0.046422	3.837715	0.28075	1.5E-06	101.0545
		Poto.m Grain 3 Feld 2	52.5491	0.050744	30.246	0.788836	0.007141	0.072254	12.3717	0.146839	0.031033	4.14033	0.29722	0	100.701
		Poto.m Grain 4 Feld 1	55.38967	0.080201	29.3492	0.755211	0.011804	0.105425	10.66444	0.138759	0.047835	4.719113	0.491954	0.000005	101.7537
	Poto.n	Poto.n Grain 1 Feld 1	57.60075	0.044113	27.2479	0.627841	0.001211	0.037062	8.38054	0.104912	0.132673	5.95827	1.013702	0.000002	101.149
		Poto.n Grain 1 Feld 2	56.97675	0.065244	26.87153	0.677963	0.004663	0.049637	8.2848	0.116759	0.132593	5.84718	1.054937	0	100.0821
		Poto.n Grain 3 Feld 1	54.1638	0.042607	29.1119	0.637318	0.002597	0.067274	10.90257	0.147647	0.05164	4.871653	0.36921	0.000005	100.368
		Poto.n Grain 3 Feld 2	54.6125	0.042815	29.2273	0.614914	0.004232	0.06945	10.92557	0.155726	0.057183	4.801733	0.382468	1.33E-06	100.894
		Poto.n Grain 4 Feld 1	54.71647	0.042873	29.3128	0.651933	0.001248	0.065385	10.93327	0.133312	0.049956	4.99271	0.379078	-6.7E-07	101.2793
	Poto.o	Poto.o Grain 4 Feld 1	52.72183	0.05598	30.1275	0.839441	0.005266	0.102926	12.1773	0.142553	0.044539	4.214713	0.282518	0.000002	100.7147
		Poto.o Grain 4 Feld 2	52.39095	0.041604	29.6524	0.831623	0.005704	0.108107	12.11858	0.146023	0.044413	4.368453	0.29213	0.000001	100.0001
		Poto.o Grain 3 Feld 1	52.1088	0.030164	30.0434	0.655701	0.012272	0.065805	12.3694	0.137584	0.037513	4.26129	0.265126	0.000004	99.987
		Poto.o Grain 2 Feld 1	56.47325	0.043698	27.08848	0.59905	0.008419	0.052684	8.612078	0.117617	0.122458	5.037603	1.790503	-1.5E-06	99.94578

Formation	Layer	SAMPLE	SiO2	TiO2	Al2O3	FeO	MnO	MgO	CaO	SrO	BaO	Na2O	K2O	O	Total
	Paetahi.a lower	Paetahi.a lower Grain 1 Feld 2	52.7146	0.212218	27.4941	2.38001	0.032926	0.442192	10.0177	0.107605	0.051209	4.07295	0.597811	0	98.1233
		Paetahi.a lower Grain 3 Feld 2	53.0226	0.140145	28.1137	1.35659	0.021556	0.503467	10.7237	0.133213	0.047493	4.79573	0.39311	0	99.2514
		Paetahi.a lower_Grain_1_Feldspar1	55.395	0.03505	28.6325	0.6871	0.005825	0.0593	10.99	#DIV/0!	0.053675	5.0625	0.39905		101.32
		Paetahi.a lower_Grain_1_Feldspar2	52.315	0.037775	29.98	1.0851	0.005175	0.1512	13.4075	#DIV/0!	0.02625	3.7375	0.248825		100.9943
		Paetahi.a lower_Grain_1_Feldspar3	54.67333	0.080033	27.83333	1.436667	0.019067	0.2477	11.02667	#DIV/0!	0.0684	4.756667	0.435633		100.5775
		Paetahi.a lower_Grain_1_Feldspar4	54.66	0.03038	28.822	0.63954	0.01236	0.05858	11.326	#DIV/0!	0.05378	4.852	0.37022		100.8249
		Paetahi.a lower_Grain_1_Feldspar5	54.512	0.02986	28.726	0.65802	0.00856	0.05704	11.418	#DIV/0!	0.05038	4.782	0.37142		100.6133
		Paetahi.a lower_Grain_4_Feldspar1	55.07667	0.038967	28.55	0.658467	0.005033	0.056167	10.55667	#DIV/0!	0.054933	4.91	0.407067		100.314
		Paetahi.a lower_Grain_4_Feldspar2	52.175	0.03505	30.025	0.94405	0.004875	0.135525	13.29	#DIV/0!	0.0372	3.6875	0.226825		100.561
		Paetahi.a lower_Grain_4_Feldspar3	55.59	0.035567	28.35667	0.657867	0.002367	0.0558	10.61	#DIV/0!	0.056933	5.223333	0.434833		101.0234
		Paetahi.a lower_Grain_4_Feldspar4	54.285	0.46425	22.015	4.115	0.11955	3.135	12.185	#DIV/0!	0.0439	3.315	0.5174		100.1951
		Paetahi.a lower_Grain_4_Feldspar5	53.575	0.0388	29.44	0.8645	0.004	0.0963	12.335	#DIV/0!	0.04905	4.46	0.3156		101.1783
		Paetahi.a lower_Grain_7_Feldspar1	54.44667	0.027433	29.09	0.615467	0.004633	0.0561	11.68	#DIV/0!	0.052867	4.65	0.354133		100.9773
		Paetahi.a lower_Grain_7_Feldspar2	54.56667	0.034033	28.68333	0.660533	0.009867	0.055	11.10667	#DIV/0!	0.053933	4.923333	0.409567		100.5029
		Paetahi.a lower_Grain_7_Feldspar3	54.3625	0.05735	29.1925	1.1114	0.028425	0.2606	11.46	#DIV/0!	0.0526	4.4875	0.3465		101.3594
		Paetahi.a lower_Grain_7_Feldspar4	54.15	0.07565	27.99	1.48435	0.02485	0.6617	11.04	#DIV/0!	0.05155	4.57	0.35455		100.4027
		Paetahi.a lower_Grain_7_Feldspar5	55.65	0.0328	27.73	0.6485	0.0048	0.0589	10.44	#DIV/0!	0.0688	5.29	0.4614		100.3852
	Paetahi.a middle	Paetahi.a middle Grain 1 Feld 1	53.63078	0.034292	29.53003	0.64592	0.011984	0.054468	11.49545	0.144049	0.05025	4.67129	0.370209	-1.5E-06	100.6386
		Paetahi.a middle Grain 1 Feld 2	54.18533	0.04459	29.35903	0.850168	0.010565	0.104728	11.4382	0.133325	0.049632	4.671505	0.37938	-1.5E-06	101.2265
		Paetahi.a middle Grain 3 Feld 1	54.42613	0.042017	29.2309	0.678482	0.004976	0.062324	10.77733	0.145351	0.054571	4.99286	0.417531	0	100.8323
		Paetahi.a middle Grain 3 Feld 2	54.69993	0.029798	29.39575	0.599322	0.007763	0.061996	10.96685	0.148104	0.056282	4.559883	0.40462	1.5E-06	100.93
	Paetahi.a upper	Paetahi.a upper Grain 3 Feld 2	53.8458	0.054574	28.6764	1.03514	0.009111	0.285321	10.881	0.13408	0.050172	4.67003	0.436713	0.000004	100.078
		Paetahi_aupper_Grain_2_Feldspar1	55.1975	0.03375	28.3525	0.65935	0.0102	0.061125	11.045		0.054525	4.9625	0.393325		100.7698
		Paetahi_aupper_Grain_2_Feldspar2	53.46	0.0343	29.30667	0.663667	0.022767	0.0578	12.08333		0.0524	4.47	0.338033		100.489
		Paetahi_aupper_Grain_2_Feldspar3	54.695	0.03365	27.605	0.5369	0.0131	0.0417	9.985		0.0563	5.055	0.43475		98.4564
		Paetahi_aupper_Grain_2_Feldspar4	55.435	0.0324	28.33	0.62255	0	0.06	10.68		0.05475	5.15	0.4205		100.7852
		Paetahi_aupper_Grain_2_Feldspar5	56.325	0.0279	27.045	0.535	0.00605	0.0286	9.39		0.0848	5.67	0.605		99.71735
		Paetahi_aupper_Grain_6_Feldspar1	54.76333	0.031067	29.00667	0.694133	0.010433	0.061667	11.26667		0.049333	4.853333	0.374833		101.1115
		Paetahi_aupper_Grain_6_Feldspar2	54.60667	0.034067	28.83667	0.647267	0.009433	0.059467	11.04		0.051433	4.763333	0.374367		100.4227
		Paetahi_aupper_Grain_6_Feldspar3	54.31667	0.032067	28.62333	0.730167	0.009433	0.080633	11.47667		0.057567	4.673333	0.376567		100.3764
		Paetahi_aupper_Grain_6_Feldspar5	54.105	0.0449	29.025	0.8433	0.01055	0.15035	11.665		0.04335	4.655	0.33945		100.8819
	Paetahi.b	Paetahi.b Grain 4 Feld 1	54.28605	0.130689	28.6895	1.098543	0.022314	0.233767	11.11173	0.149474	0.054106	4.351775	0.64836	9.5E-06	100.7765
	Paetahi.c	Paetahi_c_Grain_1_Feldspar2	53.85333	0.0401	28.22667	0.790533	0.014367	0.0937	11.73		0.054833	4.85	0.338133		99.99167
		Paetahi_c_Grain_1_Feldspar3	56.82	0.211	24.99	1.750367	0.0305	0.57	9.286667		0.100033	4.893333	1.0244		99.6763
		Paetahi_c_Grain_1_Feldspar4	57.52	0.3358	24.74333	2.293833	0.067133	0.4966	8.653333		0.080533	4.02	1.582367		99.79293
		Paetahi_c_Grain_3_Feldspar1	57.45	0.244475	25.585	1.732075	0.049525	0.3571	9.4075		0.081275	4.3525	1.249875		100.5093
		Paetahi_c_Grain_3_Feldspar2	57.18667	0.1766	25.28	1.333933	0.027233	0.298867	8.933333		0.0891	5.316667	1.047667		99.69007
		Paetahi_c_Grain_3_Feldspar3	58.925	0.3766	23.205	2.35805	0.05495	0.4426	7.43		0.10285	4.84	1.9737		99.70875
		Paetahi_c_Grain_3_Feldspar4	55.025	0.09325	27.715	1.31995	0.0239	0.48975	10.495		0.04445	4.92	0.38585		100.5122
		Paetahi_c_Grain_3_Feldspar5	54.33667	0.074433	27.83333	1.041433	0.017133	0.169633	11.23333		0.054267	4.736667	0.463767		99.96067
		Paetahi_c_Grain_7_Feldspar1	55.495	0.0458	27.8	0.68225	0.01605	0.07545	10.58		0.06165	5.255	0.4029		100.4141
		Paetahi_c_Grain_7_Feldspar2	53.85	0.04105	28.845	0.81255	0.0119	0.14485	12.025		0.0477	4.4775	0.295525		100.5511
		Paetahi_c_Grain_7_Feldspar3	54.75875	0.044388	28.3525	0.791638	0.011125	0.09695	11.27875		0.052175	4.91625	0.351063		100.6536
		Paetahi_c_Grain_7_Feldspar4	56.1	0.067233	26.67333	0.9953	0.020767	0.470733	9.746667		0.0716	5.416667	0.4596		100.0219
		Paetahi_c_Grain_7_Feldspar5	55.28	0.035633	28.13667	0.702	0	0.071767	10.8		0.062	5.206667	0.4054		100.7001
	Paetahi.d	Paetahi_d_Grain_1_Feldspar1	58.82667	0.0774	25.37	0.7007	0.017467	0.028433	7.716667		0.1872	5.466667	2.3019		100.6931
		Paetahi_d_Grain_1_Feldspar2	52.255	0.465975	1.725125	9.535	0.5715	15.6275	19.655		0.0005	0.32225	0.028		100.1859
		Paetahi_d_Grain_1_Feldspar3	64.075	0.075025	21.065	0.598675	0.004975	0.00265	2.69775		0.38035	6.1725	5.13		100.2019
		Paetahi_d_Grain_1_Feldspar4	58.46	0.0517	26.005	0.682	0.01105	0.0283	8.3		0.1797	5.96	1.05475		100.7325
		Paetahi_d_Grain_1_Feldspar5	58.3375	0.049075	25.77	0.708325	0.009675	0.022875	7.9675		0.19185	5.635	1.930475		100.6223
		Paetahi_d_Grain_4_Feldspar1	54.08	0.0496	28.475	0.80295	0.0025	0.113725	11.6375		0.0634	4.6025	0.3767		100.2039
		Paetahi_d_Grain_4_Feldspar2	53.905	0.03915	28.9725	0.689025	0.01015	0.07515	11.87		0.0489	4.6175	0.303225		100.5306
		Paetahi_d_Grain_4_Feldspar3	53.635	0.039475	28.635	0.6954	0.009425	0.077475	11.795		0.059725	4.53	0.29835		99.77485
		Paetahi_d_Grain_4_Feldspar4	53.66667	0.038633	28.58	0.737567	0.0067	0.0831	11.79		0.045233	4.59	0.301233		99.83913
		Paetahi_d_Grain_4_Feldspar5	53.64333	0.032917	28.97333	0.690567	0.00795	0.064517	11.90167		0.042633	4.541667	0.290183		100.1888
	Paetahi.e lower	Paetahi.e lower Grain 1 Feld 1	57.86603	0.322156	24.99573	2.226992	0.062072	0.557438	8.489837	0.100979	0.075476	4.42717	1.535329	2.67E-06	100.6589
		Paetahi.e lower Grain 1 Feld 2	53.2579	0.049469	30.01697	0.941235	0.005659	0.191869	12.18937	0.149596	0.034796	4.273633	0.293185	1.33E-06	101.404
		Paetahi.e lower Grain 3 Feld 1	53.07163	0.036355	29.91555	0.717062	0.004981	0.086387	11.94893	0.156624	0.043374	4.372283	0.280709	-3E-06	100.6336
		Paetahi.e lower Grain 3 Feld 2	53.49435	0.037555	29.50318	0.689395	0.007843	0.066293	11.32665	0.14971	0.047193	4.57066	0.311693	1.5E-06	100.2045
		Paetahi.e lower Grain 2 Feld 1	56.2439	0.042126	28.1773	0.671381	0.006729	0.05488	9.793685	0.146578	0.07317	5.444538	0.524262	0.000005	101.1788
		Paetahi.e lower_Grain_1_Feldspar1	53.66	0.03245	29.665	0.7456	0.01025	0.0711	12.165		0.0403	4.535	0.2915		101.2162
		Paetahi.e lower_Grain_1_Feldspar2	54.39333	0.0423	28.68	0.805633	0.0029	0.090167	11.40333		0.055167	4.763333	0.372633		100.6088
		Paetahi.e lower_Grain_1_Feldspar3	55.16333	0.037967	28.64167	0.766033	0.00805	0.065183	11.115		0.0549	5.098333	0.378533		101.329
		Paetahi.e lower_Grain_1_Feldspar4	54.9125	0.0371	28.6825	0.70905	0.007425	0.0732	11.33		0.0474	4.8675	0.337625		101.0043
		Paetahi.e lower_Grain_1_Feldspar5	55.9025	0.034725	28.585	0.701425	0.0102	0.064	10.575		0.066375	5.07	0.44745		101.4567
		Paetahi.e lower_Grain_5_Feldspar1	55.05333	0.062533	27.73333	0.87215	0.0156	0.262033	10.94333		0.05715	5.015	0.386183		100.4007
		Paetahi.e lower_Grain_5_Feldspar2	56.9175	0.160725	26.87	1.229675	0.032525	0.185225	9.6375		0.07645	4.7775	0.91475		100.8019
		Paetahi.e lower_Grain_5_Feldspar3	55.2825	0.037975	28.5425	0.6767	0.011125	0.06615	10.985		0.05455	5.0975	0.4011		101.1551
		Paetahi.e lower_Grain_5_Feldspar4	55.47333	0.055967	27.93667	0.873067	0.001933	0.240767	10.91		0.0736	5.113333	0.438867		101.1175
		Paetahi.e lower_Grain_5_Feldspar5	56.91667	0.1457	25.80667	1.915333	0.0543	1.000167	9.746667		0.072433	4.98	0.756767		101.3947
		Paetahi.e lower_Grain_8_Feldspar1	51.545	0.03435	30.0825	0.777975	0.008925	0.10155	13.61		0.028475	3.645	0.214125		100.0479
		Paetahi.e lower_Grain_8_Feldspar2	55.1475	0.04025	28.875	0.735025	0.0078	0.0734	11.26		0.051175	4.9875	0.355425		101.5331
		Paetahi.e lower_Grain_8_Feldspar3	54.91667	0.041233	28.15333	0.7314	0.012567	0.078267	11.13		0.0643	5.006667	0.347067		100.4815
		Paetahi.e lower_Grain_8_Feldspar4	53.42	0.03605	29.465	0.815125	0.008675	0.082525	12.35		0.034675	4.4225	0.285675		100.9202
		Paetahi.e lower_Grain_8_Feldspar5	53.94333	0.044233	29.05667	0.810667	0.0021	0.091367	11.71333		0.047767	4.62	0.3371		100.6666
	Paetahi.e middle	Paetahi.e middle_Grain_1_Feldspar1	55.1975	0.04335	28.225	0.847925	0.006275	0.128475	11.1175		0.0605	5.045	0.398775		101.0703
		Paetahi.e middle_Grain_1_Feldspar2	54.57167	0.035433	28.665	0.755683	0.012733	0.079567	11.54667		0.051017	4.743333	0.378517		100.8396
		Paetahi.e middle_Grain_1_Feldspar3	53.65	0.037275	29.4775	0.8432	0.01185	0.093425	12.24		0.045275	4.4475	0.3255		101.1715
		Paetahi.e middle_Grain_1_Feldspar4	55.2625	0.035425	28.3325	0.60785	0.0051	0.0491	10.8525		0.074575	5.1975	0.409575		100.8266
		Paetahi.e middle_Grain_1_Feldspar5	55.27	0.02955	28.105	0.72105	0.013025	0.065725	10.8175		0.06045	5.12	0.417075		100.6194
		Paetahi.e middle_Grain_1_Feldspar6	53.585	0.03995	29.045	0.887675	0.007775	0.111675	12.3225		0.05775	4.355	0.307225		100.7196
		Paetahi.e middle_Grain_4_Feldspar1	54.834	0.04326	28.582	0.76082	0.01246	0.07928	11.276		0.058	4.81	0.36088		100.8167
		Paetahi.e middle_Grain_4_Feldspar2	54.5	0.06095	28.5425	1.06055	0.011125	0.137975	11.6425		0.057625	4.585	0.42945		101.0277
		Paetahi.e middle_Grain_4_Feldspar3	54.2	0.043167	29.11	0.7695	0.008533	0.142233	12		0.0481	4.54	0.297667		101.1592
		Paetahi.e middle_Grain_4_Feldspar4	53.0325	0.0299	29.41	0.72235	0.0214	0.09615	12.595		0.03625	4.16	0.26755		100.3711
		Paetahi.e middle_Grain_4_Feldspar5	54.33	0.04375	28.72	0.76895	0.00595	0.1134	11.79		0.0611	4.6	0.3293		100.7625
	Paetahi.e upper	Paetahi_eupper_Grain_1_Feldspar1	57.945	0.039575	26.135	0.58935	0.002175	0.04515	8.565		0.131525	5.9725	0.87875		100.304
		Paetahi_eupper_Grain_1_Feldspar2	54.26	0.034425	28.4625	0.74785	0.007175	0.087025	11.485		0.0515	4.745	0.35185		100.2323
		Paetahi_eupper_Grain_1_Feldspar3	53.4425	0.02715	29.43	0.6455	0.009775	0.065875	12.2525		0.038775	4.4125	0.3093		100.6339
		Paetahi_eupper_Grain_1_Feldspar4	54.035	0.036225	28.905	0.669125	0.0085	0.0728	11.81		0.048575	4.62	0.33115		100.5364
		Paetahi_eupper_Grain_1_Feldspar5	54.5425	0.038475	28.7025	0.76245	0.011625	0.0867	11.51		0.05035	4.8075	0.3544		100.8665
		Paetahi_eupper_Grain_3_Feldspar1	55.1825	0.039525	27.7475	0.697725	0.009225	0.05685	10.515		0.0734	5.245	0.436175		100.0029
		Paetahi_eupper_Grain_3_Feldspar2	55.25	0.0269	28.24	0.6547	0.0007	0.0559	10.64		0.0529	5.26	0.3965		100.5776
		Paetahi_eupper_Grain_3_Feldspar3	53.53	0.209867	27.73333	2.0617	0.0593	0.471033	11.96333		0.0488	3.78	0.614233		100.4716
		Paetahi_eupper_Grain_3_Feldspar4	54.8625	0.04305	28.245	0.78835	0.009825	0.09565	11.0125		0.059925	4.9875	0.396425		100.5007
		Paetahi_eupper_Grain_3_Feldspar5	54.36	0.0471	28.93	0.662	0.0063	0.0652	11.43		0.0483	4.85	0.3599		100.7588
		Paetahi_eupper_Grain_5_Feldspar1	52.37	0.04345	29.82	0.858	0.012125	0.115925	12.96		0.033	3.965	0.294275		100.4718
		Paetahi_eupper_Grain_5_Feldspar2	52.8475	0.06775	28.715	1.144875	0.01175	0.6131	12.805		0.037225	4.0525	0.277625		100.5723
		Paetahi_eupper_Grain_5_Feldspar3	54.41	0.039375	29.32	0.747375	0.013875	0.099075	11.4175		0.05035	4.625	0.33525		101.0578
		Paetahi_eupper_Grain_5_Feldspar4	54.15	0.07015	28.57	0.988125	0.016025	0.253575	11.4475		0.05885	4.285	0.458625		100.2979
		Paetahi_eupper_Grain_5_Feldspar5	54.4525	0.1219	27.92	1.23755	0.019125	0.20775	11.6675		0.05575	4.1325	0.67		100.4846
		Paetahi_eupper_Grain_5_Feldspar6	58.9825	0.03655	25.4675	0.5825	0.00805	0.02635	7.5925		0.15525	6.425	1.06815		100.3444
	Paetahi.f	Paetahi.f Grain 1 Feld 2	55.6279	0.030542	28.519	0.650249	0.009678	0.046165	10.35	0.143698	0.055134	5.21823	0.426515	0	101.077
		Paetahi.f Grain 1 Feld 4	52.5585	0.041379	30.3941	0.620892	0.003024	0.060554	12.3347	0.154541	0.041547	4.21959	0.260174	0.000008	100.689
		Paetahi.f Grain 3 Feld 1	55.3079	0.124516	27.21415	1.124056	0.027565	0.227924	9.685605	0.145481	0.067013	4.886155	0.816067	0.000002	99.62635
		Paetahi.f Grain 3 Feld 2_5	47.7703	0.028975	33.5902	0.665179	0.011903	0.055173	15.992	0.143499	0.021518	2.32589	0.103838	-0.00001	100.709
		Paetahi.f Grain 3 Feld 3	56.4498	0.221113	25.1107	1.65676	0.048621	0.487913	8.5851	0.132563	0.071092	5.08072	1.22736	0	99.0716
		Paetahi.f Grain 3 Feld 4	54.97555	0.047221	28.5886	0.669471	0.007166	0.084445	10.6033	0.16422	0.060462	5.131345	0.394113	0	100.726
		Paetahi.f Grain 3 Feld 5	56.1654	0.037168	28.1415	0.706089	0	0.082193	9.8626	0.155885	0.062703	5.3043	0.447976	0.000004	100.966
		Paetahi.f Grain 4 Feld 1	54.0714	0.031522	28.9559	0.649833	0.011733	0.059791	10.4958	0.148891	0.045526	4.93359	0.353369	0	99.7573
		Paetahi.f Grain 4 Feld 2	57.7953	0.237328	25.12715	1.625152	0.046292	0.403311	8.462205	0.124577	0.088641	4.716845	1.513842	-5E-06	100.1406
		Paetahi.f Grain 4 Feld 3	53.6587	0.036941	29.2468	0.709095	0.021449	0.080574	11.2444	0.156121	0.05579	4.72274	0.331125	0.000004	100.264
		Paetahi.f Grain 4 Feld 4	55.4918	0.072844	27.79935	0.796405	0.01457	0.128964	10.03572	0.159138	0.057608	4.98926	0.609401	0.000002	100.155
		Paetahi.f Grain 4 Feld 5	59.06825	0.299696	23.4687	1.826996	0.05979	0.462823	7.16727	0.098082	0.094615	4.92245	1.769921	0.000002	99.23865

Appendix G: DRC16 Contributions Form.

DRC 16

MASSEY UNIVERSITY
TE KUNENGA KI PŪREHUROA
UNIVERSITY OF NEW ZEALAND

GRADUATE RESEARCH SCHOOL

STATEMENT OF CONTRIBUTION
DOCTORATE WITH PUBLICATIONS/MANUSCRIPTS

We, the candidate and the candidate's Primary Supervisor, certify that all co-authors have consented to their work being included in the thesis and they have accepted the candidate's contribution as indicated below in the *Statement of Originality*.

Name of candidate:	Shannen Mills
Name/title of Primary Supervisor:	Professor Jonathan Procter
In which chapter is the manuscript /published work:	Chapter 3

Please select one of the following three options:

○ The manuscript/published work is published or in press

x Please provide the full reference of the Research Output:

○ The manuscript is currently under review for publication – please indicate:

x The name of the journal:
N

x The percentage of the manuscript/published work that was contributed by the candidate:

x Describe the contribution that the candidate has made to the manuscript/published work:
Conceptualization, Sampling, Formal analysis, Investigation, Methodology, Writing (original draft), Writing (review and editing)

◉ It is intended that the manuscript will be published, but it has not yet been submitted to a journal

Candidate's Signature:	Shannen Mills
Date:	28-Apr-2024
Primary Supervisor's Signature:	
Date:	29/9/24

This form should appear at the end of each thesis chapter/section/appendix submitted as a manuscript/ publication or collected as an appendix at the end of the thesis.

GRS Version 5 – 13 December 2019
DRC 19/09/10

MASSEY UNIVERSITY
TE KUNENGA KI PŪREHUROA
UNIVERSITY OF NEW ZEALAND

GRADUATE RESEARCH SCHOOL

STATEMENT OF CONTRIBUTION
DOCTORATE WITH PUBLICATIONS/MANUSCRIPTS

We, the candidate and the candidate's Primary Supervisor, certify that all co-authors have consented to their work being included in the thesis and they have accepted the candidate's contribution as indicated below in the *Statement of Originality*.

Name of candidate:	Shannen Mills
Name/title of Primary Supervisor:	Professor Jonathan Procter
In which chapter is the manuscript /published work:	Chapter 4

Please select one of the following three options:

○ The manuscript/published work is published or in press

- x Please provide the full reference of the Research Output:

○ The manuscript is currently under review for publication – please indicate:

- x The name of the journal:
- x The percentage of the manuscript/published work that was contributed by the candidate:
- x Describe the contribution that the candidate has made to the manuscript/published work:

Conceptualization, Sampling, Formal analysis, Investigation, Methodology, Writing (original draft), Writing (review and editing)

◉ It is intended that the manuscript will be published, but it has not yet been submitted to a journal

Candidate's Signature:	Shannen Mills
Date:	28-Apr-2024
Primary Supervisor's Signature:	
Date:	29/4/24

This form should appear at the end of each thesis chapter/section/appendix submitted as a manuscript/ publication or collected as an appendix at the end of the thesis.

GRS Version 5 – 13 December 2019
DRC 19/09/10

DRC 16

MASSEY UNIVERSITY
TE KUNENGA KI PŪREHUROA
UNIVERSITY OF NEW ZEALAND

GRADUATE RESEARCH SCHOOL

STATEMENT OF CONTRIBUTION
DOCTORATE WITH PUBLICATIONS/MANUSCRIPTS

We, the candidate and the candidate's Primary Supervisor, certify that all co-authors have consented to their work being included in the thesis and they have accepted the candidate's contribution as indicated below in the *Statement of Originality*.

Name of candidate:	Shannen Mills
Name/title of Primary Supervisor:	Professor Jonathan Procter
In which chapter is the manuscript /published work:	Chapter 5

Please select one of the following three options:

○ The manuscript/published work is published or in press

- Please provide the full reference of the Research Output:

○ The manuscript is currently under review for publication – please indicate:

- The name of the journal:

- The percentage of the manuscript/published work that was contributed by the candidate:

- Describe the contribution that the candidate has made to the manuscript/published work:

Conceptualization, Sampling, Formal analysis, Investigation, Methodology, Writing (original draft), Writing (review and editing)

◉ It is intended that the manuscript will be published, but it has not yet been submitted to a journal

Candidate's Signature:	Shannen Mills
Date:	28-Apr-2024
Primary Supervisor's Signature:	
Date:	29/4/24

This form should appear at the end of each thesis chapter/section/appendix submitted as a manuscript/ publication or collected as an appendix at the end of the thesis.

GRS Version 5 – 13 December 2019
DRC 19/09/10